

Permeability Anisotropy and Resistivity Anisotropy of Mechanically Compressed Mudrocks

by

Amy Lynn Adams

Honours Bachelor of Applied Science in Geological Engineering, Cooperative Program
University of Waterloo, Waterloo, Ontario, Canada (2008)

Master of Science in Civil and Environmental Engineering
Massachusetts Institute of Technology, Cambridge, Massachusetts, USA (2011)

Submitted to the Department of Civil and Environmental Engineering
in Partial Fulfillment of the Requirements for the Degree of

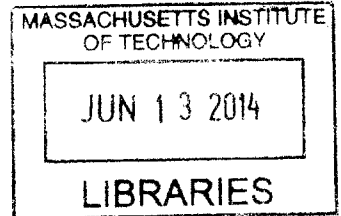
Doctor of Philosophy in the field of Geotechnical and Geoenvironmental Engineering

at the

MASSACHUSETTS INSTITUTE OF TECHNOLOGY

June 2014

ARCHIVES



© 2014 Massachusetts Institute of Technology. All rights reserved.

Signature redacted

Signature of Author
Department of Civil and Environmental Engineering
May 2, 2014

Signature redacted

Certified by
John T. Germaine
Senior Research Associate and Senior Lecturer of Civil and Environmental Engineering
Thesis Supervisor

Signature redacted

Accepted by
Heidi M. Nepf
Chair, Departmental Committee for Graduate Students

Permeability Anisotropy and Resistivity Anisotropy of Mechanically Compressed Mudrocks

by

Amy Lynn Adams

Submitted to the Department of Civil and Environmental Engineering on May 2, 2014
in Partial Fulfillment of the Requirements for the Degree of
Doctor of Philosophy in the field of Geotechnical and Geoenvironmental Engineering

ABSTRACT

Permeability anisotropy (the ratio of the horizontal to vertical permeability) is an important parameter used in sedimentary basin models and geotechnical design to model fluid flow, locate hydrocarbon reserves and estimate stress and pressure evolution. The magnitude of the permeability anisotropy for a given mudrock is difficult to measure; further, whether the permeability anisotropy is a constant value or evolves with the basin state is of active debate.

This thesis experimentally investigates the development of permeability anisotropy in mechanically compressed mudrocks. A novel measurement method is developed using resedimented cubic specimens. The permeability anisotropy of Resedimented Boston Blue Clay (RBBC) is systematically measured to determine both the magnitude and evolution of the permeability anisotropy. The permeability anisotropy predicted using measurements of the mudrock fabric is compared with the measured permeability anisotropy to understand the relationship between fabric evolution and permeability anisotropy. Finally, resistivity anisotropy is compared with permeability anisotropy to reveal useful field correlations. The results of the RBBC study are contrasted with additional measurements made using mudrocks covering a range of plasticity, clay fraction and mineralogical composition.

The permeability anisotropy and the conductivity anisotropy (inverse of the resistivity anisotropy) of uniform RBBC increase from 1.2 to 1.9 as the porosity decreases from 0.49 to 0.36. The permeability decreases by over one order of magnitude and the formation factor triples over this porosity range. Platy particles rotate from ~ 42 to 28 degrees to the horizontal, driving permeability anisotropy development. Further decreasing the porosity of RBBC below porosity 0.36 decreases both the permeability anisotropy and the conductivity anisotropy. Finally, the conductivity anisotropy is shown to equal to the permeability anisotropy within $\pm 20\%$. This general behaviour is characteristic of all mudrocks studied.

Though small (< 2), the permeability anisotropy of uniform mudrocks can significantly increase the permeability anisotropy of larger systems, as shown through layered system models. These models also reveal that the large scale conductivity anisotropy is not equal to the permeability anisotropy, though the relationship identified for uniform mudrocks may still be useful for sites with high measurement resolution.

Thesis Supervisor: John T. Germaine

Title: Senior Research Associate and Senior Lecturer of Civil and Environmental Engineering

Acknowledgements

First and foremost I would like to thank my advisor Dr. John T. Germaine (aka Dr. G) for teaching me so much over the past few years with so much patience. Dr. G always seems to have time to listen and help despite being one of the busiest people around. He is modest and respectful of everybody he meets and has a true 'can do' attitude. Thank you, Dr. G, for being such a great teacher, role model, and friend.

I would like to thank my committee for the time and energy they spent helping guide and improve my research. Dr. Peter Flemings was particularly instrumental in teaching me to write technical papers and prepare presentations. I enjoyed many technical discussions over hot chocolates with Dr. Richard Plumb. I am always struck by the depth of Professor Charles C. Ladd's knowledge in soil behaviour, and by that of Professor Brian Evans in rock mechanics. Finally, Dr. Lucy Jen has been a valued mentor and I have enjoyed discussing topics ranging from soil mechanics to life with her.

A number of other people have helped shape my time here at MIT. Professor Einstein continually reminds me that age is just a number and that true greatness is supported by kindness and caring. I have shared many laughs with Sheila Fay and Caroline Jundzilo Cromer. Finally Steve Rudolph was always happy to discuss equipment design, help me find parts, or to share a cookie or brownie.

I have been fortunate to have my studies at MIT fully funded. I would like to thank the Linde Family for the Presidential Fellowship in my first year which allowed me time to adjust and choose my project. Thank you to UT Geofluids and MIT CEE for supporting me for the remainder of my studies.

I would not have survived MIT without the help, support and distraction of my friends. Over the years my especially talented and lively lab mates and office friends including Brendan, Jana, Aiden, Brian, Amer, Taylor, Chunwei, Steve, Ale, Bruno, Gonzalo, Nina and Sherif made coming to school every day, even when nothing was working, an enjoyable experience.

My friends outside of lab also deserve special mention. I spent five amazing seasons with the MIT Women's Club Ice Hockey Team who inspire me with their skills, accomplishments and attitudes both on and off the ice. My culture has been enriched by friends, interesting talks and events organized by the MIT Canadians Club. And finally, many of my friends from home and Waterloo have kept in touch and visited or hosted me. Thanks to everybody for all of the good times we've had so far, and I look forward to all the great times we have ahead of us!

Last but certainly not least, I would like to thank my family for their support, encouragement and love. You've driven tens of thousands of kilometers over the past 11 years moving me back and forth to school, or shuffling me to and from airports or bus stations. And, you've racked up an equally high number of long distance minutes. Getting here would have been infinitely harder without you; thank you for being the constants – the ones who care, and the ones who can be counted on.

To the courageous among us –

Who approach this life with wonder and curiosity;
Who cultivate the will to get back up and climb when obstacles present;
Who value truth but remain aware of the power of fiction;
Whose forward momentum is fueled by the confidence
to look, listen, think, learn and evolve; and
Who are too busy dreaming to be afraid.

I dedicate this thesis to *you*.

“In life, as in engineering and laboratory experimentation, the examples that we learn the most
from often aren’t even good examples at all”

Table of Contents

Abstract	3
Acknowledgements	5
Table of Contents.....	9
List of Tables.....	11
List of Figures.....	13
List of Symbols.....	19
1 Introduction	23
1.1 Problem Statement.....	23
1.2 Thesis Scope and Objectives.....	25
1.3 Organization of the Thesis.....	26
2 Background	29
2.1 Intact vs. Resedimented Specimens	30
2.2 Mudrock Fabric	31
2.3 Permeability & Permeability Anisotropy	34
2.4 Resistivity & Resistivity Anisotropy.....	43
2.5 Relationship between Permeability Anisotropy and Resistivity Anisotropy.....	52
2.6 Summary.....	53
3 Materials and Specimen Fabrication.....	75
3.1 Mudrock Powder Source and Preparation	76
3.2 Resedimentation.....	78
3.3 Salts	86
3.4 Index Properties	90
4 Equipment and Procedures	121
4.1 Specimen Preparation.....	122
4.2 Permeability and Permeability Anisotropy Measurement	122
4.3 Resistivity and Conductivity Anisotropy Measurement	125
4.4 Measurement Sequence Bias Adjustment.....	127
4.5 Fabric Imaging and Analysis.....	130

5	Results and Analysis	145
5.1	Resedimentation Results	146
5.2	Permeability Measurements: Experimental Parameters	151
5.3	Permeability and Permeability Anisotropy Results.....	156
5.4	Resistivity Measurements	167
5.5	Particle Fabric Characterisation	171
5.6	Summary of Results.....	180
6	Interpretation	241
6.1	Permeability Anisotropy Development in Uniform Mudrocks	242
6.2	Permeability Anisotropy vs. Conductivity Anisotropy in Uniform Mudrocks	252
6.3	Extension to Layered Systems	258
6.4	Summary and Field Extension	267
7	Conclusions and Recommendations	299
7.1	Overview.....	300
7.2	Key Findings and Conclusions	301
7.3	Summary of Experimental Program Results.....	304
7.4	Recommendations for Future Research	308
	Bibliography	313
	Appendix 1: Raw Data	325
	Appendix 2: Permeability Anisotropy Measurement: Equipment, Methods and Analysis.....	371
	Appendix 3: Resistivity and Conductivity Anisotropy Measurement.....	419
	Appendix 4: Bench Top Resistivity Measurements: Summary of Results	461
	Appendix 5: Cation Exchange Capacity (CEC) and Specific Surface Area (SSA) Analysis	485
	Appendix 6: Equipment CAD Drawings	509
	Appendix 7: Sample Data Sheets.....	529
	Appendix 8: Constant Head Hydraulic Conductivity Program Code	537

List of Tables

Table 2-1: Mudrock terminology proposed by Stow (1981) to improve communication within the earth sciences field.....	55
Table 2-2: Permeability anisotropy measurement techniques.....	56
Table 2-3: Summary of mudrock permeability anisotropy measurements (after from Chapuis and Gill, 1989).....	57
Table 2-4: Permeability anisotropy measurements and findings.....	58
Table 2-5: Conductivity anisotropy of compressed mudrocks (after Mousseau and Trump, 1967)..	61
Table 3-1: Resedimentation water content and salinity values for different mudrocks.....	94
Table 3-2: Mudrock Index Properties.....	95
Table 3-3: Clay Mineralogy of < 2 μ m size fraction.....	96
Table 3-4: Specific Surface Area (SSA) measurements.....	96
Table 3-5: Laboratory Salt Solution Mixing Guide - Sea Salt Solution.....	97
Table 3-6: Laboratory Salt Solution Mixing Guide - NaCl Solution.....	98
Table 3-7: AIN Plastics acrylic data sheet.....	99
Table 3-8: Reinforced sedimentation column design: Sample calculation.....	100
Table 3-9: Resedimentation Load Frame Specifics.....	101
Table 3-10: Index properties of RBBC Series I to III (after Cauble, 1996).....	102
Table 3-11: Index properties of RBBC Series IV (after Abdulhadi, 2009).....	103
Table 5-1: Summary of specimen characteristics: RBBC.....	182
Table 5-2: Summary of specimen characteristics: 39% Clay RBBC.....	183
Table 5-3: Summary of specimen characteristics: RGoM-EI, RSFBM, Leached RBBC & Leached RSFBM.....	183
Table 5-4: Specimen metrics: stress and volume change (1 of 4).....	184
Table 5-5: Salinity measurements (1 of 2).....	188
Table 5-6: Compression index (c_c) and swelling index (c_s) for RBBC, RGoM-EI and RSFBM.....	189
Table 5-7: RBBC permeability summary.....	190
Table 5-8: 39% Clay RBBC permeability summary.....	191
Table 5-9: RGoM-EI, RSFBM, Leached RBBC & Leached RSFBM permeability summary.....	191
Table 5-10: RBBC measured permeability for measurement sequence bias determination.....	192
Table 5-11: 39% Clay RBBC measured permeability for Measurement Sequence Bias Determination.....	193
Table 5-12: Measurement Sequence Bias summary for Permeability.....	193
Table 5-13: Permeability anisotropy as a function of maximum effective stress and sidewall friction for RBBC OCR 4.....	193
Table 5-14: Porosity as a function of stress level and sidewall friction for RBBC at OCR 4.....	194
Table 5-15: RBBC measured resistivity for Measurement Sequence Bias Determination.....	194
Table 5-16: Measurement Sequence Bias summary for Resistivity.....	194
Table 5-17: Resistivity Measurements Summary (Triaxial Cell Measurements).....	195
Table 5-18: Summary of Bench top conductivity measurements for 39% Clay RBBC, RGoM-EI and RSFBM.....	196

Table 5-19: Summary of image analysis	197
Table 5-20: Image analysis results: particle orientation and aspect ratio for each image	198
Table 5-21: Particle orientation measurements for RBBC (UT Images)	199
Table 5-22: Particle orientation measurements for RBBC (MIT Images)	199
Table 5-23: Particle orientation as a function of size and stress level for RBBC (UT Images, 1D analysis, Cheong)	200
Table 5-24: Particle orientation as a function of size and stress level for RBBC (MIT Images, 1D analysis, Durant)	200
Table 5-25: Aspect ratio measurements for RBBC (UT Images).....	200
Table 5-26: Particle aspect ratio as a function of particle size for RBBC (UT Images).....	201
Table 5-27: Particle orientation as a function of aspect ratio and stress level for UT Images	201
Table 5-28: Aspect ratio as a function of size for RBBC (UT Images)	201
Table 6-1: Summary of 1D Particle Orientation Analysis for RBBC	269
Table 6-1: Clay and Silt Porosities for RBBC and 39% Clay RBBC	269
Table 6-2: Permeability and Resistivity Equation Analogies	270
Table 6-3: Formation factor as a function of a and m using literature bounds	271
Table 6-4: Archie parameters for RBBC.....	271
Table 6-5: RGoM-EI and RBBC compression and permeability parameters for layered permeability anisotropy and resistivity models	271
Table 6-6: Compressing layer permeability anisotropy model results summary for layered RBBC and RGoM-EI at OCR 1	272
Table 6-7: Comparison of permeability and resistivity for a layered RBBC at OCR 1 with thickness contrast of unity	272

List of Figures

Figure 2-1: Particle orientation in a) flocculated and b) dispersed structures (Lambe and Whitman, 1969).....	62
Figure 2-2: Schematic representation of the flow through i) loosely and ii) densely packed elliptical grains (Scholes et al, 2007)	62
Figure 2-3: Orientation vs. stress for slurry resedimented Kaolinite measured using peak ratio XRD analysis (after Martin and Ladd, 1975)	63
Figure 2-4: Orientation vs. porosity and strain for slurry resedimented Kaolinite measured using peak ratio XRD analysis, assuming $G_s = 2.65$ (adapted from Martin and Ladd, 1975)....	63
Figure 2-5: Particle orientation vs. strain and porosity for RBBC predicted using the March (1932) model assuming a random initial particle orientation (45 degrees) at zero effective stress and 100% water content.....	64
Figure 2-6: Cubic specimen test procedure suggested by Chan and Kenney (1973).....	65
Figure 2-7: Permeability anisotropy measurements in the literature (small plot)	66
Figure 2-8: Permeability anisotropy measurements in the literature (extended version of Figure 2-7)	67
Figure 2-9: Dual porosity structure create by inclusion of silt in clay rich mudrocks (Schneider et al, 2011).....	68
Figure 2-10: Model Geometry: (a) Idealized platy particle packing; and (b) fluid flow paths (Daigle and Dugan, 2011)	68
Figure 2-11: Tortuosity vs. angle of flow for uniaxially compressed mudrocks (Arch and Maltman, 1990).....	69
Figure 2-12: Uniaxial strain vs. permeability anisotropy predicted by Arch and Maltman (1990)....	69
Figure 2-13: Electrical conduction paths through varying fabric structures (Blewett et al, 2001)....	70
Figure 2-14: Effect of increasing brine conductivity on measured rock conductivity (after Waxman and Smits, 1968)	71
Figure 2-15: Effect of increasing pore fluid salinity (specific conductance) on the apparent formation factor of clean sands (after Huntley, 1986).....	71
Figure 2-16: Graphic determination of matrix resistivity and intrinsic formation factor using equation 2-21 (after Patnode and Wyllie, 1950).....	72
Figure 2-17: Comparison between and Waxman and Smits model (left) and Dual Water model (right) (Clavier et al, 1984).....	72
Figure 2-18: Ionic conduction path anisotropy through a stacked structure (McCarter et al, 2005) 73	
Figure 2-19: Conductivity anisotropy prediction compared with field measurements for the Green Canyon, GoM (after Bachrach, 2011).....	73
Figure 2-20: Relation between hydraulic conductivity and formation factor for a well sorted clay free sand (Huntley, 1986)	74
Figure 3-1: GPX Disc Grinder (Horan, 2012).....	104
Figure 3-2: Index map showing location of wells A-12 and A-20 (after Stump & Flemings, 2002). 105	
Figure 3-3: Leaching via dialysis tubing	105
Figure 3-4: Bath concentration vs. time curve during the leaching process for RBBC.....	106

Figure 3-5: Resedimentation: Mixing dry soil powder with salt water in an electric mixer	106
Figure 3-6: Resedimentation: Transferring the sediment slurry to a vacuum cylinder for de-airing	107
Figure 3-7: Resedimentation: Pouring the sediment slurry into 3" ID settling columns using a funnel method	107
Figure 3-8: Resedimentation: Configuration of base porous stone and filter paper in sedimentation column	108
Figure 3-9: Sample resedimentation log.....	109
Figure 3-10: Steel reinforced sedimentation tube (without protective rubber membranes).....	110
Figure 3-11: Direct loading (gravity) load frame with hanger setup.....	111
Figure 3-12: Low- medium stress moment arm load frame.....	112
Figure 3-13: Medium - high stress air pressure load frame	113
Figure 3-14: High stress Baldwin hydraulic load frame.....	114
Figure 3-15: High stress load frame control cart with computer, MAX 100 and PVA	115
Figure 3-16: Illustrative resedimentation stress path	115
Figure 3-17: Lateral stress ratio, K_0 vs. OCR for Boston Blue Clay (Ladd, 1965).....	116
Figure 3-18: NaCl calibration curve for conductivity meter model 23226-505 VWR International. Co = 1 g/L NaCl solution.....	116
Figure 3-19: Casagrande chart.....	117
Figure 3-20: Mudrock particle size distribution.....	118
Figure 3-21: Clay Fraction Triangle Plot.....	119
Figure 3-22: Clay Mineralogy Triangle Plot.....	119
Figure 4-1: Completed resedimented specimen prior to extrusion	134
Figure 4-2: Extruding a resedimented specimen using the manual hydraulic jack.....	135
Figure 4-3: Trimming a high stress specimen	136
Figure 4-4: Dimensioning the cubic specimen	136
Figure 4-5: Solid view of the low stress triaxial cell (modified for permeability measurement) with manifold and cubic shaped specimen	137
Figure 4-6: Dimensioned section of the low stress triaxial cell (modified for permeability measurement) with cubic specimen.....	138
Figure 4-7: Vertical and Horizontal order testing sequences illustrated.....	139
Figure 4-8: Illustration of specimen stress and porosity change during application of a hydraulic gradient.....	139
Figure 4-9: Horizontal Measurement Sequence Bias for RBBC.....	140
Figure 4-10: Single specimen measurement sequence bias with correction method (after Chan and Kenney, 1973).....	140
Figure 4-11: 4-Probe resistivity diagram	141
Figure 4-12: Drawing: Cubic end adapters modified for resistivity measurements	142
Figure 4-13: Imaging specimen configuration (image courtesy of Amer Deirieh)	143
Figure 4-14: SEM image of an ion milled cross section (image courtesy of Amer Deirieh)	143
Figure 4-15: Pore scale mechanisms that contribute to a dual porosity structure and lead to heterogeneous fabric at the microscale (Schneider et al, 2011).....	144
Figure 5-1: Salinity vs. maximum effective stress for RBBC.....	202

Figure 5-2: Comparison between trimmings salinity and specimen salinity (before vs. after permeability measurement, all mudrocks)	202
Figure 5-3: Void ratio vs. log axial consolidation stress compression curve: RBBC.....	203
Figure 5-4: Porosity vs. log axial consolidation stress compression curve: RBBC.....	203
Figure 5-5: Void Ratio vs. log axial consolidation stress compression curve: RBBC & 39% Clay RBBC - effect of clay fraction	204
Figure 5-6: Porosity vs. log axial consolidation stress compression curve: RBBC & 39% Clay RBBC - effect of clay fraction	204
Figure 5-7: Void Ratio vs. log axial consolidation stress compression curve: RGoM-EI	205
Figure 5-8: Porosity vs. log axial consolidation stress compression curve: RGoM-EI	205
Figure 5-9: Void Ratio vs. log axial consolidation stress compression curve: RSFBM.....	206
Figure 5-10: Porosity vs. log axial consolidation stress compression curve: RSFBM.....	206
Figure 5-11: Void Ratio vs. log axial consolidation stress compression curve: RBBC - effect of leaching.....	207
Figure 5-12: Porosity vs. log axial consolidation stress compression curve: RBBC - effect of leaching	207
Figure 5-13: Swelling index vs. maximum vertical effective stress as a function of OCR for RBBC K ₀ Consolidated in the triaxial cell (data from Abdulhadi, 2009)	208
Figure 5-14: Porosity deviation from CRS OCR 4 line vs. maximum effective stress for RBBC	208
Figure 5-15: Plot of hydraulic conductivity vs. time for a constant hydraulic gradient (HC027, 39% Clay RBBC).....	209
Figure 5-16: Horizontal permeability cross plot to determine measurement sequence bias, x_H , for RBBC	209
Figure 5-17: Vertical permeability cross plot to determine measurement sequence bias, x_V , for RBBC	210
Figure 5-18: Horizontal permeability cross plot to determine measurement sequence bias, x_H , for 39% Clay RBBC.....	210
Figure 5-19: Vertical permeability cross plot to determine measurement sequence bias, x_V , for 39% Clay RBBC.....	211
Figure 5-20: Comparison of horizontal permeability adjusted using the global and single specimen methods for RBBC	211
Figure 5-21: Comparison of vertical permeability adjusted using the global and single specimen methods for RBBC	212
Figure 5-22: Comparison of permeability anisotropy computed using permeability adjusted using the global and single specimen methods for RBBC	212
Figure 5-23: Effect of measurement sequence bias adjustment on the permeability anisotropy of RBBC	213
Figure 5-24: Permeability vs. porosity for RBBC	213
Figure 5-25: Permeability vs. maximum axial effective stress for RBBC	214
Figure 5-26: Permeability vs. porosity with trend lines for RBBC.....	214
Figure 5-27: Permeability anisotropy vs. porosity for RBBC.....	215
Figure 5-28: Permeability vs. porosity for RBBC and Leached RBBC.....	215
Figure 5-29: Permeability vs. maximum axial effective stress for RBBC and Leached RBBC.....	216

Figure 5-30: Permeability anisotropy vs. porosity for RBBC and Leached RBBC	216
Figure 5-31: Permeability vs. porosity for RBBC and 39% Clay RBBC	217
Figure 5-32: Permeability vs. maximum axial effective stress for RBBC and 39% Clay RBBC	217
Figure 5-33: Permeability anisotropy vs. porosity for RBBC and 39% Clay RBBC	218
Figure 5-34: Permeability vs. porosity for RGoM-EI	218
Figure 5-35: Permeability anisotropy vs. porosity for RGoM-EI	219
Figure 5-36: Permeability vs. porosity for RSFBM	219
Figure 5-37: Permeability anisotropy vs. porosity for RSFBM	220
Figure 5-38: Horizontal cracking of RGoM-EI specimens during permeability measurement	220
Figure 5-39: Permeability vs. porosity: Comparison between RBBC, RGoM-EI and RSFBM	221
Figure 5-40: Permeability vs. maximum axial effective stress: Comparison between RBBC, RGoM-EI and RSFBM	221
Figure 5-41: Permeability anisotropy vs. porosity: Comparison between RBBC, RGoM-EI and RSFBM	222
Figure 5-42: Coefficient of Variation as a function of porosity for all mudrocks measured	222
Figure 5-43: Coefficient of variation as a function of permeability for all mudrocks measured	223
Figure 5-44: Layering due to sidewall friction	223
Figure 5-45: Model: Permeability anisotropy of compressing anisotropic mudrock layers: sidewall friction analysis	224
Figure 5-46: Horizontal resistivity cross plot to determine measurement sequence bias, $x_{H\rho}$, for RBBC ($\Delta n = 1$ for all points)	225
Figure 5-47: Vertical resistivity cross plot to determine measurement sequence bias, $x_{V\rho}$, for RBBC	225
Figure 5-48: Comparison of horizontal resistivity adjusted using the global and single specimen methods for RBBC	226
Figure 5-49: Comparison of vertical resistivity adjusted using the global and single specimen methods for RBBC	226
Figure 5-50: Comparison of conductivity anisotropy computed using resistivity adjusted using the global and single specimen methods for RBBC	227
Figure 5-51: Resistivity vs. porosity for RBBC	227
Figure 5-52: Log of apparent formation factor vs. porosity for RBBC. Trend lines are fit for the porosity > 0.36 data	228
Figure 5-53: Resistivity anisotropy vs. porosity for RBBC	228
Figure 5-54: Conductivity anisotropy vs. porosity for RBBC	229
Figure 5-55: Resistivity vs. porosity for RBBC and Leached RBBC	229
Figure 5-56: Apparent formation factor vs. porosity for RBBC and Leached RBBC	230
Figure 5-57: Conductivity anisotropy vs. porosity for RBBC and Leached RBBC	230
Figure 5-58: First version bench top resistivity measurement set up used to measure the conductivity anisotropy of larger specimens	231
Figure 5-59: Conductivity anisotropy vs. porosity: Comparison between RBBC, 39% Clay RBBC, RGoM-EI, RSFBM, Leached RBBC and Leached RSFBM	231
Figure 5-60: BSEM images of the vertical plane of RBBC at (a) 0.1 MPa (b) 1.0 MPa, and (c) 10 MPa [Emmanuel and Day-Stirrat, 2011]	232

Figure 5-61: Repeatability of Image Analysis for a single RBBC image analyzed by different users and using different techniques	233
Figure 5-62: Particle orientation vs. porosity for RBBC measured using UT Images	233
Figure 5-63: RBBC Particle orientation measured using MIT and UT Images (1D Analysis)	234
Figure 5-64: Particle Orientation measured using 1D analysis for RBBC prepared at MIT compared with March 1932 Model	235
Figure 5-65: Histograms showing particle orientation as a function of particle size for images of RBBC obtained at UT, analyzed using the 1D technique by Cheong	236
Figure 5-66: Histograms showing particle orientation as a function of particle size for images of RBBC obtained at MIT, analyzed using the 1D technique by Durant	237
Figure 5-67: Histograms showing particle orientation as a function of particle size for images of RBBC obtained at MIT, analyzed using the 1D technique by Adams	238
Figure 5-68: Particle aspect ratio as a function of size for 2D analysis of UT Images	239
Figure 5-69: Particle orientation as a function of particle aspect ratio for 2D analysis of UT Images	239
Figure 6-1: Three zones of distinct permeability anisotropy behaviour noted RBBC are related to different deformation mechanisms	273
Figure 6-2: Permeability anisotropy vs. porosity for RBBC and 39% Clay RBBC	274
Figure 6-3: Conductivity anisotropy vs. porosity for RBBC	274
Figure 6-4: Particle Orientation for RBBC prepared at MIT compared with March 1932 Model	275
Figure 6-5: Comparison of Daigle and Dugan (2011) model prediction using measured particle orientation with measured RBBC permeability anisotropy	276
Figure 6-6: Comparison of Daigle and Dugan (2011) model prediction computed using March (1932) modelled particle orientation with measured RBBC permeability anisotropy	276
Figure 6-7: Permeability vs. porosity with trend lines for RBBC	277
Figure 6-8: Resistivity vs. porosity for RBBC	277
Figure 6-9: Formation factor vs. porosity for RBBC	278
Figure 6-10: Axial strain vs. log of axial consolidation stress for RBBC	278
Figure 6-11: Permeability anisotropy vs. vertical effective stress for various mudrocks (Grande and Mondol, 2013)	279
Figure 6-12: Permeability anisotropy vs. porosity for RBBC, RGoM-EI and RSFBM	279
Figure 6-13: Conductivity anisotropy vs. porosity: Comparison between RBBC, 39% Clay RBBC, RGoM-EI, RSFBM, Leached RBBC and Leached RSFBM	280
Figure 6-14: Casagrande chart showing variation in mudrock plasticity	280
Figure 6-15: Clay Fraction Triangle Plot	281
Figure 6-16: Clay Mineralogy Triangle Plot	281
Figure 6-17: Permeability vs. porosity: Comparison between RBBC, RGoM-EI and RSFBM	282
Figure 6-18: Log of apparent formation factor vs. porosity for RBBC (fit does not include data for porosity <0.36)	282
Figure 6-19: Cross plot of conductivity anisotropy vs. permeability anisotropy for RBBC	283
Figure 6-20: Illustration of electrical tortuosity concept	283
Figure 6-21: Cross plot of conductivity anisotropy vs. permeability anisotropy for RBBC, RGoM-EI and RSFBM	284

Figure 6-22: Equivalent Two Layer System	284
Figure 6-23: 2 Layer system permeability anisotropy, permeability contrast 1 to 20.....	285
Figure 6-24: 2 Layer system permeability anisotropy, permeability contrast 1 to 100.....	285
Figure 6-25: 2 Layer system permeability anisotropy, fixed layer thickness contrast = 1.....	286
Figure 6-26: Schematic of a compressing layered system.....	286
Figure 6-27: CRS compression curve in void ratio-log stress space for RBBC (CRS 1219) and RGoM-EI (CRS 109).....	287
Figure 6-28: CRS compression curves in porosity – log stress space for RBBC (CRS 1219) and RGoM-EI (CRS 109).....	287
Figure 6-29: Graphic illustration of model compression parameters for RBBC (CRS 1219).....	288
Figure 6-30: CRS vertical permeability curves for RBBC and RGoM-EI.....	288
Figure 6-31: Graphic illustration of model permeability parameters.....	289
Figure 6-32: Graphic illustration of model permeability anisotropy parameters.....	289
Figure 6-33: Model: Permeability anisotropy of compressing layered RBBC and RGoM-EI mudrock	290
Figure 6-34: Permeability anisotropy of a layered system vs. maximum effective stress.....	291
Figure 6-35: Permeability anisotropy and resistivity anisotropy model scenarios	291
Figure 6-36: Layered permeability anisotropy model: RBBC layers	292
Figure 6-37: Permeability anisotropy of different model scenarios.....	293
Figure 6-38: Layered resistivity and conductivity anisotropy model: RBBC layers.....	294
Figure 6-39: Conductivity anisotropy of different model scenarios	295
Figure 6-40: Conductivity anisotropy vs. permeability anisotropy for a layered system of RBBC at OCR 1 (layers compressed to different maximum effective stresses).....	296
Figure 6-41: Partitioning of horizontal fluid and electric flow in layered systems	297
Figure 6-42: Relation between hydraulic conductivity and formation factor for a well sorted clay free sand (Huntley, 1986)	298

List of Symbols

<u>Symbol</u>	<u>Typical Units</u>	<u>Description</u>
a		Archie's Law fitting parameter (tortuosity parameter)
A		Alternate permeability anisotropy definition suggested by Meegoda et al (1989)
A, a	m ²	Area for falling head test (big and small, respectively)
A/D		Analogue-to-Digital Converter
AC		Alternating Current
a _H		Archie's Law fitting parameter (tortuosity parameter) in the horizontal direction
a _σ		Archie's Law fitting parameter (tortuosity parameter) for the conductivity anisotropy
a _v		Archie's Law fitting parameter (tortuosity parameter) in the vertical direction
BASIC		Beginner's All Purpose Symbolic Instruction Code
C	nF, mF, F	Capacitance
c _c		Slope of virgin compression line e vs. log stress space (space assumed)
c _{c-e}		Slope of virgin compression line e vs. log stress space (space defined)
c _{c-e}		Slope of swelling line e vs. log stress space (space defined)
c _{c-n}		Slope of virgin compression line n vs. log stress space (space defined)
c _{c-n}		Slope of swelling line n vs. log stress space (space defined)
CEC	equivalents/ kg	Cation Exchange Capacity
CF		Clay Fraction
CH		High Plasticity Clay
c _k		Slope of permeability curve in log permeability vs. n space
CL		Low Plasticity Clay
Co	unit/m ³	Initial Concentration. Unit may be charge, volume or mass.
CRS		Constant Rate of Strain
c _s		Slope of swelling line e vs. log stress space (space assumed)
C _v	cm ² /s	Coefficient of consolidation
c _α		Log time rate of secondary compression
D/A		Digital-to-Analogue Converter
DC		Direct Current
dr _k /dn		Slope of permeability anisotropy curve in permeability anisotropy vs. porosity space
e		Void ratio. Equal V _v /V _s
e _o		Initial void ratio OR void ratio intercept fixed at e = 1.0; corresponds to n _o

Symbol	Typical Units	Description
F		Formation factor (general) or intrinsic formation factor
g	9.807 cm/s ²	Gravitational Constant
G _s		Specific gravity
h	m	Hydraulic head
H	cm, m	Height of sample
H _o	cm, m	Initial height of sample
i	-	Gradient
k	m ² , millidarcy	Permeability. Property of the medium. Also known as intrinsic permeability.
K	cm/s, m/s	Hydraulic conductivity. Property of the medium and the fluid.
k _H	m ² , millidarcy	Horizontal or radial permeability
K _H	cm/s, m/s	Horizontal or radial hydraulic conductivity.
K _o		Coefficient of Lateral Earth Pressure at rest
k _V	m ² , millidarcy	Vertical permeability
K _V	cm/s, m/s	Vertical hydraulic conductivity.
L	cm, m	Length
LIR		Load Increment Ratio
L _o	cm, m	Direct path length
log K _o	cm/s, m/s	intercept of permeability model (at either n = 0 c/o Julia or n = 0.5 c/o Amy & Brendan)
LVDT		Linear Variable Differential Transformer
M		Mass
m		Aspect Ratio
m		Archie's Law cementation exponent
m _H		Archie's Law cementation exponent in the horizontal direction
MIT		Massachusetts Institute of Technology
M _s		Mass of solids
m _σ		Archie's Law cementation exponent for the conductivity anisotropy
M _t		Total mass
m _V		Archie's Law cementation exponent in the vertical direction
m _v	1/MPa	Coefficient of volume compressibility
n		Porosity. Equal to V _v /V _t .
n		Measurement number in measurement sequence bias correction
NC		Normally Consolidated
n _o		Initial porosity OR porosity intercept fixed at n = 0.5; corresponds to e _o
OC		Over Consolidated
OCR		Over Consolidation Ratio
P	MPa, kPa	Pressure

Symbol	Typical Units	Description
PC		Personal Computer
PI	%	Plasticity Index
PVA		Pressure Volume Actuator
PVC		Pressure Volume Controller
θ	degrees	Particle orientation relative to the horizontal
Q	cm ³ /s, m ³ /s	Volumetric flow Rate
q	cm/s, m/s	Linear flow rate
θ_0	degrees	Initial particle orientation
θ_{EV}	degrees	Particle orientation relative to the horizontal at a fixed volumetric strain ϵ_V
R	Ω	Resistance
RBBC		Resedimented Boston Blue Clay
RGoM-EI		Resedimented Gulf of Mexico Clay from the Eugene Island Block
r_k		Permeability anisotropy
r_{k0}		Permeability anisotropy intercept at porosity 0.5
RMS		Root Mean Squared
RSFBM		Resedimented San Francisco Bay Mud
r_ρ		Resistivity anisotropy
r_σ		Conductivity anisotropy
S	m ² /g, m ² /kg	Mass based specific surface area. Equal to the surface area per unit mass.
S		Saturation
Sa	1/m	Volumetric specific surface area. Equal to the surface area per unit volume.
σ'_p	MPa, kPa	Maximum past pressure
T	Degrees Celcius, Degrees Kelvin	Temperature
t	s	Time
t_D	nm	Debye Length
u	MPa, kPa	Pore pressure
u_b	MPa, kPa	Back pressure (pore pressure in a laboratory experiment)
UT		University of Texas
V		Volume
V	V, mV	Voltage
V_s	cm ³ , m ³	Volume of the solid grains
V_t	cm ³ , m ³	Total volume
V_v	cm ³ , m ³	Volume of the voids
w _l	%	Liquid limit

Symbol	Typical Units	Description
w_p	%	Plastic limit
x		Successive measurement sequence bias correction factor
x'		Non-successive measurement sequence bias correction factor
γ_p	kN/m^3	Unit weight of permeant. Equal to γ_w if the permeant is water.
γ_w	kN/m^3	Unit weight of water
Δ		Change (in a parameter that follows)
ϵ		Strain; strain rate with dot on top
ϵ_v		Volumetric strain
λ	$\text{cm}^2/\text{eq } \Omega$	Equivalent Ionic conductance
μ_p	$\text{Pa}\cdot\text{s}$, g/cms	Dynamic viscosity of the permeant.
ν	m^2/s	Kinematic viscosity
ρ	g/cm^3 , kg/m^3	Mass density
ρ	Ωm	Electrical resistivity
ρ_w	Ωm	Pore fluid resistivity
σ	S/m	Electrical conductivity
τ		Tortuosity, equal to L/L_0
τ_H		Horizontal Tortuosity
τ_V		Vertical Tortuosity

1 Introduction

1	Introduction	23
1.1	Problem Statement.....	23
1.2	Thesis Scope and Objectives.....	25
1.3	Organization of the Thesis.....	26

1.1 Problem Statement

Mudrocks are sedimentary rocks with more than 50% siliclastic grains less than 0.0625 mm (Boggs 2006). The term ‘mudrock’ is a general term that can be applied to any hardened sediment that is comprised of silt and/or clay (Nichols, 2009). Mudrocks are the most abundant sedimentary rock but are the least understood compared to other types of rocks such as sandstones (Middleton, 2003). Mudrocks can be subdivided many ways, however the general divisions are distinguish whether they are non-lithified, lithified and non-fissile or lithified and fissile (Stow, 1981). The research will focus on non lithified and thus non fissile mudrocks.

Mudrock porosity can decrease from 0.9 to as little as 0.05 over a few kilometers depth with a corresponding decrease in permeability of up to 8 orders of magnitude (Neuzil, 1994). The log of permeability generally decreases linearly with porosity, and at a given porosity mudrock permeability can vary by up to 3 orders of magnitude (Neuzil, 1994). The permeability anisotropy of uniform (non-layered) mudrocks, defined as the ratio of the horizontal to vertical permeability, typically increases with compression (Basak, 1972; Daigle and Dugan, 2011; Dewhurst et al, 1998; Yang and Aplin, 2007).

The study of mudrocks, and particularly the evolution of mudrocks as they are buried and compressed, is important for a number of engineering problems. Oil reservoirs form in, are often located near to, or are constrained by mudrock formations. These formations develop permeability anisotropy with increasing stress and decreasing porosity. Changing mudrock porosity, and hence permeability, in a sedimentary basin directly affects fluid migration, consolidation rates and overpressure generation (see Broichhausen et al, 2005, Bethke, 1989). Basin models are often used to simulate the evolution of sedimentary basins with time and compression. These models require numerous inputs, and the accuracy and representativeness of such inputs directly affects the accuracy and representativeness of the model predictions. The permeability anisotropy parameter is often neglected (assumed isotropic, e.g. Ungerer et al, 1990) or included as a constant (e.g. Bekele et al, 2001). A more mature approach is to include permeability anisotropy as an evolving parameter, however it is not easy to determine 1) what magnitude to assign to the permeability anisotropy or 2) how to model the permeability anisotropy (constant or evolving), or 3) whether it really even matters.

There have been limited experimental studies measuring the development of permeability anisotropy in mudrocks during compression (e.g. Clennell et al 1999, Leroueil et al 1990, Basak 1972 and Yang and Aplin 1998 and 2007). These studies used a variety of measurement techniques to measure the permeability anisotropy development in either resedimented, remoulded or intact mudrocks with increasing mechanical compression. All of these studies suggest that in uniform mudrocks, the permeability anisotropy varies modestly between 1 and at most 3 or 4 in the first few kilometers below seafloor. Conversely, permeability anisotropy models, based on particle orientations (e.g. Daigle and Dugan, 2011) or pore orientations (e.g. Yang and Aplin, 1998 & 2007) have been developed but have not yet been experimentally validated. These models suggest that permeability anisotropy is low (~ 1) at high porosities and will increase rapidly (ranging from 1 to > 10) as mudrocks compress and particles become more aligned.

It is costly and difficult to obtain undisturbed, representative samples of deeply buried mudrocks. Even if a sample can be obtained, measuring the permeability or permeability anisotropy is a challenging task. However, downhole logging while drilling (LWD) resistivity measurements are standard procedure on most boreholes, though commonly only the horizontal resistivity is measured. New downhole tools allow for continuous measurement of the resistivity in the vertical and horizontal directions, relative to the borehole axis. An ideal solution to assess the permeability anisotropy of a sedimentary basin might be to first understand the relationship between permeability anisotropy and resistivity anisotropy. Then, downhole measurements of the resistivity anisotropy could be used to infer the permeability anisotropy.

There has been limited work investigating the link between permeability anisotropy and resistivity anisotropy. Some authors assume that the two quantities are equal for granular materials (e.g. Meegoda et al, 1989); this combined with the theoretical similarity between fluid and electric flow concepts suggests that the resistivity anisotropy might be a useful field correction for the permeability anisotropy. However this equality has not been proven for fine-grained materials which are comprised of charged particles. McCarter et al (2005) measured the conductivity anisotropy (inverse of the resistivity anisotropy) of Kaolinite and reported results in a similar range to the permeability anisotropy measured by other researchers (e.g. Basak, 1972). Georgi et al (2011) use theoretical models to suggest that the permeability anisotropy should not equal the conductivity anisotropy for layered systems, but do not address the case of uniform mudrocks.

The present research seeks to measure and understand the development of permeability anisotropy and resistivity anisotropy in uniform, mechanically compressed mudrocks. The degree of permeability anisotropy that can be developed from mechanical compression is evaluated first using a systematic study of Resedimented Boston Blue Clay, a low plasticity Illite rich mudrock. The experimental results are compared to available models in order to interpret the causes of permeability anisotropy in mechanically compressed mudrocks. Additional permeability anisotropy measurements are made using additional resedimented mudrocks with varying clay fraction, mineralogy and plasticity for comparison. Further, the magnitude and causes of resistivity anisotropy of these same mudrocks is evaluated. Finally, the relationship between permeability

anisotropy and resistivity anisotropy is explored with the goal that this relationship may be useful in interpreting the permeability anisotropy of natural mudrocks using downhole resistivity measurements.

1.2 Thesis Scope and Objectives

This thesis summarizes work done as part of the experimental investigation to examine the permeability, electrical and fabric properties of uniform, resedimented mudrocks that are one dimensionally and mechanically compressed over a stress range of 0.4 to 40 MPa. In addition to developing the relevant methods to measure the permeability, resistivity and fabric structure of mudrocks, this thesis summarizes numerous experiments including 1) permeability anisotropy measurements of various mudrocks at different stress levels, 2) resistivity anisotropy measurements on various mudrocks at different stress levels, and 3) fabric imaging of different mudrocks at different stress levels. The research program measured the permeability, permeability anisotropy, resistivity, formation factor, and resistivity anisotropy of a variety of resedimented mudrocks with varying clay fraction, plasticity and mineralogy. The control of mudrock composition on anisotropy development is experimentally explored, and the relationship between permeability anisotropy and resistivity is analyzed. The effect of additional alteration is not explored (e.g. temperature alteration, cementation, different stress path), nor is the effect of varying OCR explored.

A cubic specimen technique previously applied at MIT was used as the starting point to measure the permeability anisotropy of resedimented mudrocks as a function of stress level and porosity at a fixed OCR of 4. This resulted in the development of new analysis techniques to determine the undisturbed permeability and permeability anisotropy from the measured results. The permeability anisotropy of Resedimented Boston Blue Clay is measured over the full applied stress range from 0.4 to 40 MPa; additionally 5 other mudrocks compressed to effective stresses ranging from 1.2 to 10 MPa were measured.

The cubic specimen permeability measurement technique was later adapted to include measurement of the resistivity. This required development of an analog resistivity measurement method that uses a fixed frequency (10 kHz) and sinusoidal wave form to evaluate the specimen resistance using a 4-probe technique. Again, measurements were restricted to specimens compressed to effective stresses ranging from 0.4 to 40 MPa and rebounded to a fixed OCR of 4.

Finally, numerical models were employed to understand the development of permeability anisotropy and resistivity anisotropy. First, images of the mudrock fabric were obtained and analyzed to evaluate the particle orientation, particle size and particle aspect ratio as a function of stress level and porosity. These results are used as input for particle orientation models used to predict the permeability anisotropy. The model results are compared to the experimental measurements to understand how the mudrock fabric is related to the mudrock permeability anisotropy. Second, a model for the permeability and resistivity anisotropy of layered mudrocks was created to analyze the effect of scale. This model reveals the complex relationships between 1)

uniform layer and system permeability anisotropy; and 2) permeability anisotropy and resistivity anisotropy.

1.3 Organization of the Thesis

This thesis is organized into seven chapters complimented by numerous appendices. The chapters are organized to provide the reader with a complete picture of the problem investigated, including background, materials, experimental methods, results and interpretation. The appendices provide more detailed laboratory procedures, tabulated experimental results, data sheets, codes and supplemental studies.

Chapter 2 presents the required background information needed for the current research program. This chapter begins by discussing the evolution of fabric structure during compression and the measurement of mudrock permeability. These two concepts are then used to introduce the mudrock permeability anisotropy, including the permeability anisotropy measurement technique, the relation between permeability anisotropy and mudrock fabric, and available permeability anisotropy models. This is followed by a similar discussion covering mudrock resistivity. The concepts of Archie's law and Formation factor are used alongside parallel resistor models to highlight the challenges inherent in interpreting clay resistivity measurements. This chapter concludes with a discussion of the resistivity anisotropy, including a review of the measurement methods, available models and its relation to the permeability anisotropy.

Chapter 3 presents an overview of the mudrocks studied in this testing program, including their origins, index properties, and the specific material processing that was performed for each mudrock. The salinity measurement technique and salt mixing protocols are described in detail, as is the leaching procedure used to remove natural salt from some of the mudrock powder. Finally, the process of resedimentation is outlined, including the parameters, procedure and equipment.

Chapter 4 provides a brief description of the experimental methods. The experimental methods are divided into three categories: 1) permeability and permeability anisotropy measurement, 2) resistivity and resistivity anisotropy measurement and 3) image analysis. Appendix 2 provides a more detailed overview of the equipment and procedures relevant to the permeability anisotropy measurement; Appendix 3 does the same for the resistivity measurement.

Chapter 5 summarizes the experimental results. The testing program included measurement of the permeability and permeability anisotropy of 36 resedimented specimens made from 6 different mudrocks. The resistivity and resistivity anisotropy was measured on 18 of these specimens. Finally, image analysis was undertaken using SEM images of RBBC obtained by researchers at both at the University of Texas at Austin and MIT. Image analysis revealed trends in particle size, aspect ratio and orientation.

The results of the testing program are interpreted in Chapter 6. First, the permeability anisotropy results of all mudrocks are analyzed and compared with model predictions to estimate the

maximum permeability anisotropy achievable from mechanical compression. Next, the relationship between the permeability anisotropy and the conductivity anisotropy (inverse of the resistivity anisotropy) in uniform mudrocks is examined by combining the experimental results with theoretical analogies. Next, a numerical model simulating the permeability anisotropy of a layered mudrock system is developed to extend these two concepts. This model is applied to 1) evaluate the permeability anisotropy of a layered system as a function of the uniform layer anisotropy, and 2) evaluate the link between permeability anisotropy and conductivity anisotropy for layered (non-uniform) mudrocks. Finally, this chapter concludes by briefly discussing how the results of this work might be applied in the field.

Chapter 7 is a summary of the main results and findings of this research. This chapter also presents recommendations for future research.

(Page intentionally left blank)

2 Background

2	Background	29
2.1	Intact vs. Resedimented Specimens	30
2.2	Mudrock Fabric	31
2.2.1	Influence of compression	31
2.2.2	Influence of pore fluid salinity	32
2.3	Permeability & Permeability Anisotropy	34
2.3.1	Mudrock Permeability	34
2.3.2	Permeability Anisotropy	35
2.3.3	Permeability Anisotropy Measurement Techniques	37
2.3.4	Permeability Anisotropy and Fabric Measurements	38
2.3.5	Permeability Anisotropy Models	40
2.4	Resistivity & Resistivity Anisotropy	43
2.4.1	Resistivity, Formation Factor & Archie's Law	43
2.4.2	Resistivity in Practice	45
2.4.3	Clay Resistivity and Parallel Resistor Models	46
2.4.4	Resistivity Anisotropy	50
2.4.5	Resistivity Anisotropy Measurements & Models	51
2.5	Relationship Between Permeability Anisotropy and Resistivity Anisotropy	52
2.6	Summary	53

This chapter begins by introducing mudrocks, their relevance, and how their permeability and resistivity are measured and understood. The discussion continues by highlighting the difference between intact and resedimented specimens, which justifies the benefit of using resedimented specimens in a systematic study of elemental mudrock behaviour. Next, the evolution of fabric during compression is discussed with emphasis on fabric structure and pore fluid salinity. This is followed by two sections covering mudrock permeability & permeability anisotropy, and mudrock resistivity & resistivity anisotropy. These sections introduce basic concepts and include literature reviews that relate to the interrelation of mudrock permeability anisotropy, resistivity anisotropy and fabric anisotropy.

Mudrocks are sedimentary rocks with more than 50% siliclastic grains less than 0.0625 mm (Boggs 2006). The term 'mudrock' is a general term that can be applied to any hardened sediment that is comprised of silt and/or clay (Nichols, 2009). Mudrocks are the most abundant sedimentary rock but are the least understood compared to other types of rocks such as sandstones (Middleton, 2003). Stow (1981) suggested standard mudrock terminology and classification for use in the earth sciences field (Table 2-1) based on texture, fissility and grain size. Mudrocks can be subdivided many ways, however the general divisions are distinguish whether they are non-lithified, lithified and non-fissile or lithified and fissile (Stow, 1981). The research will focus on non lithified and thus non fissile mudrocks.

Mudrocks are of key interest because they can contain or trap hydrocarbons and other fluids. However, mudrock permeability, and permeability anisotropy in particular, are poorly understood owing to measurement difficulties and a general lack of understanding of the micro scale behavior. Borehole logs include measurements of density, porosity and resistivity (e.g. Sawyer, 2009), but little direct insight about the mudrock permeability can be easily derived from these measurements. This chapter begins by describing the mudrock fabric, including the difference between intact and resedimented specimens and the impact of pore fluid salinity on the fabric structure. Next, mudrock permeability and permeability anisotropy are discussed focusing on theory, measurement methods, results and models. A similar approach is used to describe mudrock resistivity and resistivity anisotropy. The relationship between mudrock permeability anisotropy and resistivity anisotropy measurements is discussed, and the last section of this chapter provides a summary of what is known, understood, measured and what remains to be learned concerning mudrock permeability anisotropy and resistivity anisotropy.

2.1 Intact vs. Resedimented Specimens

Intact specimens are cut from core samples. Though representative of the natural conditions, intact specimens are costly and difficult to acquire and often undergo lengthy storage times between acquisition and measurement. The use of intact specimens has many disadvantages, most notably the high potential for sampling disturbance such as drying, stress changes and loss of maximum past pressure, σ'_p , due to mistreatment during extraction, handling, storage and transportation (Germaine 2009, Ladd 1996). Intact specimens are not ideal for use in lengthy laboratory investigations because of their uncontrolled stress history, mineralogy and chemistry, as well as the high specimen variability between depths in the same hole, and between drill holes.

Resedimented specimens are ideal for lengthy laboratory investigations. They are fabricated in the laboratory from a uniform, pre-prepared soil powder; as a result they have a known mineralogy, chemistry and stress history. The process of resedimentation produces uniform, repeatable specimens with a known stress history and composition. The main advantage of resedimented specimens is that differences in behavior between two specimens can be attributed to true material behavior related to the manner in which the specimens were prepared (differing stress history, chemistry etc.) as opposed to specimen variability. Further, resedimented specimens are often less costly to prepare, can be prepared as required thus bypassing the need for storage, and can be

safely and readily prepared within laboratory time scales. The process of resedimentation is described in detail in Chapter 3.

2.2 Mudrock Fabric

The 'mudrock fabric' (sometimes called soil structure) refers to the orientation and distribution of the particles in a soil mass (Lambe and Whitman, 1969). This includes the particle shape, size, and orientation. The fabric of mechanically compressed mudrocks is a combined result of the sedimentation environment, the salinity and chemistry of the permeating fluid, mineralogy of the constituent particles, and stress history of the deposit.

During sedimentation, mudrock particles become flocculated in high salinity or oceanic environments or dispersed in low salinity or lacustrine environments. Flocculated particles form aggregate structures (flocs, clusters) with edge-to-face contacts (Figure 2-1 a) while dispersed particles behave more as individual particles and form more face-to-face contacts (Figure 2-1 b) (Lambe and Whitman, 1969). Once deposited, mudrocks are compressed and densified by the weight of the overlying sediments as well as the other externally applied forces (glaciers, fault zones, tectonics etc.). Compression occurs through porosity reduction as the pore fluids are squeezed out and the mudrock fabric structure comes to bear the applied loads.

The following sections describe the formation of the mudrock fabric under the influences of compression and pore fluid salinity.

2.2.1 Influence of compression

Numerous theories describe the process of mudrock compression. Olsen (1962) suggests that at high porosities compression occurs primarily through cluster rearrangement, with only inter-cluster or inter-aggregate porosity reduction. Once the large inter-cluster pores are removed, the clusters themselves begin to compress. Delage and Lefebvre (1984) also found evidence of a progressively collapsing aggregate structure. They suggest that the mudrock pore network may develop 'significant anisotropy' during compression, as identified through microscopic analysis, though they are unable to quantify the anisotropy.

Some researchers (e.g. Olsen 1962, Lambe 1958, and Mitchell 1956) believe that particle orientation plays a large role in mudrock compression and fabric anisotropy development. These researchers' work suggests that the degree of particle orientation increases with increasing uniaxial compression and with increasing dispersion (decreasing salinity).

If particles rotate and realign relative to the applied stress as mudrocks are compressed (e.g. Figure 2-2, Scholes et al 2007), then interparticle bonds will be progressively ruptured to ultimately create an aligned, anisotropic fabric most similar to fissile shales.

Clay platelets will reorient into the plane perpendicular to the major principal consolidation pressure once the preconsolidation pressure is exceeded, even when the direction of this pressure is changed (Quigley and Thompson, 1966). Mudrocks with higher clay content reach higher degrees of preferred orientation (Voltolini et al, 2009). Martin and Ladd (1975) measured the particle orientation of Kaolinite slurries using peak ratio X-ray Diffraction (XRD) pole figure analysis (Figure 2-3 and Figure 2-4). They show that the majority of orientation occurs at low stress, below 0.1 MPa and 60% strain. McCarter et al (2005) find a similar result, suggesting that the most rapid changes in orientation occur below 50 kPa for slurry resedimented Kaolinites. Day Stirrat et al (2011) show that the particle orientation of Resedimented Boston Blue clay measured by X Ray diffraction varies by less than 1 degree (from ~25 to ~24 degrees to the horizontal) as the stress increases from 0.1 To 10 MPa.

March (1932) suggests that pore collapse and particle orientation occur simultaneously. He proposed a model to predict the rotation of a platy particle in response to an applied uniaxial strain:

$$\theta_{\varepsilon_v} = \tan^{-1}[(1 - \varepsilon_v)\tan\theta_o] \quad 2-1$$

Where ε_v is the volumetric (uniaxial) strain and θ is the mean particle orientation relative to the horizontal. Figure 2-5 gives the predicted orientation vs. strain, converted to porosity for the case of Resedimented Boston Blue Clay computed assuming an initially random particle orientation ($\theta_o = 45$ degrees) for high water contents and zero strain. This March model predicts that the majority of particle orientation will occur below 60% strain, as was measured by Martin and Ladd (1965) for Kaolinite (Figure 2-4).

However, March's model includes important assumptions. The model maps the rotation of the hypotenuse of a right angle triangle as the height of the triangle decreases as a result of vertical strain. The particle angle asymptotically approaches zero. When applied to mudrocks, as is commonly done, this model implies that compression occurs via realignment of the particles for every increment of strain. Further, this model it assumes that particles are freely able to rotate and can slip past each other uninhibited by other particles.

2.2.2 Influence of pore fluid salinity

Salinity can both directly and indirectly affect the permeability and resistivity of mudrocks. Salinity directly affects mudrock permeability and resistivity by affecting the physical characteristics of the measurement fluid such as the density, viscosity and resistivity. These parameters are used to compute the permeability and formation factor and are discussed in sections 2.3.1 and 2.4.1. Salinity indirectly affects mudrock permeability and resistivity via the mudrock fabric and porosity. The difference between flocculated or dispersed fabrics (Figure 2-1) is a function of salinity: mudrocks deposited in high salinity environments form flocculated fabrics and those deposited in low salinity environments form dispersed fabrics (Lambe and Whitman, 1969).

Mudrocks exist at a wide range of pore fluid salinity and pore fluid chemistry. The salinity of sea water is ~ 35 g/L (~3.5%) and is dominantly NaCl. The composition of mudrock formation waters (fluid filling the pore spaces) has been shown to vary by nearly 3 orders of magnitude (von Engelhardt and Gaida, 1963).

Horan (2011) found insignificant differences in the compression and permeability behavior of RBBC that was resedimented with salt concentration ranging from 4 to 256 g/L sea salt. Horan (2011) also leached RBBC to remove the salt and noted changes in the physical structure of the material. These changes were attributed to the destruction of flocs that were formed during initial sedimentation of the material and that survived the grinding process (see Chapter 3 covering resedimentation). The leached RBBC was resedimented with varying salt concentrations ranging from 0 g/L to 256 g/L. The compressibility increases with increasing salinity at low stress levels and converges to be salinity independent at high stress. No definitive trend in the permeability with salinity was noted for porosities below 0.5 (strain 0.47). Above porosity 0.5, the permeability appears to vary with salinity however there is not a consistent trend of increasing or decreasing permeability with increasing pore fluid salinity.

von Engelhardt and Gaida (1963) find that the salt content of the pore fluid has no influence on the final porosity for a given applied stress for high stress levels. However, increasing the salt concentration of the pore fluid increases the coefficient of consolidation (c_v) and speeds up compression.

Fahy (2014) also found that the coefficient of consolidation increases with increasing salinity for Resedimented Gulf of Mexico mudrock. Gulf of Mexico mudrock resedimented with low pore fluid salinity (1 g/L) has a relatively constant coefficient of consolidation, whereas that resedimented with a higher pore fluid salinity (up to 256 g/L) has a coefficient of consolidation that is initially higher, but decreases with increasing effective stress and eventually converges with that of the low salinity resedimented mudrock. Further, both the compression and permeability curves exhibit salinity dependence at low stress (0.1 MPa) only and converge to become salinity independent with increasing effective stress (> 10 MPa).

Olsen (1962) noted that at a given porosity, the measured permeability varied with the chemical composition of the pore fluid (amount of dispersant). Olsen describes the mudrock fabric as being composed of individual soil clusters. The cluster mass and structure is controlled by the pore fluid salinity, and this in turn affects the compression and permeability behavior.

The salinity of the pore fluid itself may change with mudrock compression. For Montmorillonite rich mudrocks v. Engelhardt and Gaida (1963) show that the salinity decreases with increasing compression as the mobile pore fluid (fluid in the pore space) is removed and the bound fluid remains. Once the porosity reaches a certain threshold however, the salinity begins to rise as pores become cut off and saline pore fluid is trapped. Further compression reduces the total pore volume and increases the ratio of trapped porosity to total porosity, leading to an increase in bulk salinity.

2.3 Permeability & Permeability Anisotropy

This section is divided into five sections. The first section describes the factors influencing mudrock permeability and briefly introduces a common empirical method to estimate mudrock permeability. The second section introduces the concept of permeability anisotropy, and defines permeability anisotropy at the macro and micro scales. The third section discusses numerous techniques that have been applied in the literature to measure the permeability anisotropy, highlighting the advantages and disadvantages of each technique. The fourth section summarizes the permeability anisotropy measurements documented in the literature and focuses on both the magnitude of the anisotropy as well as the cause of the permeability anisotropy where possible. Finally, the fifth section discusses theoretical models that have been developed to explain mudrock permeability anisotropy.

2.3.1 Mudrock Permeability

Hydraulic conductivity is a measure of the rate of flow of a particular fluid through a medium. Its value varies as a function of the fluid and the medium. Permeability is a property of the medium itself and is not related to the density or viscosity of the fluid flowing through the fabric. The hydraulic conductivity (K) and permeability (k) are related by:

$$k = \frac{K\mu}{\rho g} \quad 2-2$$

Where k is the permeability, ρ and μ are the mass density (g/cm^3) and the dynamic viscosity (g/cms) respectively, of the permeant fluid and g is the gravitational constant (cm/s^2). Assuming constant fluid properties, the hydraulic conductivity and permeability are directly proportional.

As the porosity in natural sedimentary basins decreases from 0.9 to as little as 0.05 over a few kilometers depth, the permeability can correspondingly decrease by up to 8 orders of magnitude Neuzil (1994). Many researchers (e.g. Neuzil, 1994, Dewhurst and Aplin, 1999, Clennell et al, 1999, Tavenas et al, 1984) note that permeability (k) of mudrocks decreases logarithmically with an increase in density, typically decreasing void ratio (e) or porosity (n). However, alternate trends such as $\log(e)$ vs. $\log(k)$ and $\log(e)$ vs. $\log(k)(1+e)$ have been applied to better linearize the permeability-density relationship of some materials (e.g. Tavenas et al, 1984).

Mudrock permeability is affected by a number of parameters, including but not limited to: particle size, shape, aspect ratio, mineralogy, particle packing, pore fluid chemistry and salinity, and bound water layers surrounding charged particles. Many of these factors are in turn inter-related. The initial particle packing influences the evolution of pore fluid salinity during compression (e.g. von Engelhardt and Gaida, 1963). Further, Clavier et al (1984) describe the thickness and composition of the bound and unbound water layers as a functions of the clay counterions (ions bound by the double layer), pore fluid chemistry, and the total water content defined by the particle packing and fabric.

Many empirical equations have been derived to estimate the permeability of soils as a function of measurable soil properties. Most equations were initially defined for use in coarse grained materials (e.g. sands and gravels) and attempts have been made to modify them for use with fine grained materials (e.g. clays and silts). First proposed by Kozeny (1927) and later modified by Carman (1937, 1956), the Kozeny-Carman equation considers flow through porous media as analogous to laminar flow through a bundle of capillary tubes. The Navier-Stokes equation is applied to compute the permeability of isotropic media:

$$k = \frac{n^3}{v\tau^2(1-n)^2G_s^2S_a^2} \quad 2-3$$

Where k is the permeability, n is the porosity, τ is the flow tortuosity, G_s is the specific gravity and S_a is the volumetric specific surface area and v is a dimensionless constant. The constant accounts for variations in pore shape. Many modifications of the Kozeny Carman equation exist in the literature.

Although widely applied for granular soils, Olsen (1962) showed that the Kozeny Carman equation is not applicable to mudrocks. The permeability predicted using the Kozeny Carman relation deviates from the measured permeability by greater than one order of magnitude due to the prevalence of uneven pore sizes.

2.3.2 Permeability Anisotropy

Permeability anisotropy (r_k) is defined as the ratio of the horizontal permeability (k_H) divided by the vertical permeability (k_V):

$$r_k = \frac{K_H}{K_V} = \frac{k_H}{k_V} \quad 2-4$$

Permeability anisotropy can be written in terms either the permeability (k) or the hydraulic conductivity (K).

There are three main causes of permeability anisotropy: 1) macro-stratification (layering), 2) micro-stratification (layering), and 3) flatness plus orientation of particles (Witt and Brauns, 1983). Additionally, researchers have suggested that the permeability anisotropy of non-stratified mudrocks is related to particle clustering (Olsen (1962), the aggregate or floc structure related to clay fraction (e.g. Clennell et al, 1999, Dewhurst et al, 1996), micro cracks and stress relief cracks, and other small scale heterogeneities at the fabric level (e.g. Bolton et al, 2000).

Macro-stratification occurs when different sedimentary units are layered. The permeability of individual layers is measured and the permeability anisotropy is computed knowing the thickness of each layer:

$$k_{\perp} = \frac{\sum_{i=1}^n L_i}{\sum_{i=1}^n L_i / k_i} \quad 2-5$$

$$k_{\parallel} = \frac{\sum_{i=1}^n k_i L_i}{\sum_{i=1}^n L_i} \quad 2-6$$

$$r_k = \frac{k_{\parallel}}{k_{\perp}} \quad 2-7$$

Where k_{\perp} is the permeability perpendicular to layering, k_{\parallel} is the permeability parallel to layering, L_i is the individual layer thickness of the i^{th} layer, k_i is the individual layer permeability of the i^{th} layer and there are n layers. The permeability k_i used for calculation is typically assumed isotropic; however more correctly k_i is the permeability in the direction of interest, either perpendicular or parallel.

Micro-stratification is similar to macro-stratification however the layers are not easily delineated and the individual layer permeability cannot be measured. The layer thicknesses are much smaller in micro-stratified units (e.g. varved clays) and pump tests or measurements of the layered system itself are required to determine the permeability anisotropy.

Permeability anisotropy can develop in homogeneous materials or homogeneous layers due to flatness and orientation of particles. As they are mechanically loaded, the fabric structure changes and becomes more aligned, as discussed in Section 2.2.1.

Scholes et al (2007) provide an excellent description of the basis of particle orientation theory (Figure 2-2). In the loose state, the elliptical grains are randomly oriented such that the flow path is equally tortuous (see Eq. 2-9) in the vertical (white) and horizontal (black) directions. With increasing compression, the pore space is reduced and the grains realign. At maximum density the grains are horizontally aligned and the flow path in the vertical direction is much more tortuous than that in the horizontal direction.

Witt and Brauns (1981) showed that the permeability anisotropy (r_k) is equal to the inverse of the square of the tortuosity anisotropy:

$$r_k = \frac{\tau_V^2}{\tau_H^2} \quad 2-8$$

Where τ_V is the vertical tortuosity and τ_H is the horizontal tortuosity. The tortuosity is given by:

$$\tau = l/l_o \quad 2-9$$

Where l is the path actually traversed by a fluid particle and l_o is the direct, uninterrupted path.

2.3.3 Permeability Anisotropy Measurement Techniques

There are a number of different measurement techniques applied by researchers to measure the permeability anisotropy. Each experimental set up is slightly different and the specific details of each perturbation will not be described in detail herein; Chapuis and Gill (1989) provide a detailed description of a number of permeability anisotropy measurement techniques described in the literature. The experimental techniques may be classified based on the types of equipment they use (e.g. oedometers, pressure cells, permeameters), the measurement procedures they apply (e.g. consolidation theory, constant head or constant flow methods), and more importantly whether they measure the permeability anisotropy using multiple (two) specimens or a single specimen. Table 2-2 provides a summary of the common methods.

Permeability anisotropy can be indirectly measured using consolidation theory and the oedometer. Two oedometer cells are required, one each configured for either vertical or radial drainage with vertical loading. The permeability is computed from Terzaghi's theory of consolidation:

$$k = \gamma C_v m_v \quad 2-10$$

Where k is the vertical or radial permeability depending on the drainage configuration, γ is the unit weight of the fluid, C_v is the coefficient of consolidation for vertical loading and m_v is the coefficient of volume compressibility for vertical loading.

Permeability anisotropy is also commonly measured using either a constant head test (e.g. Leroueil et al 1990; Basak 1972) or a constant flow test (e.g. Clennell et al 1999, Dewhurst et al 1996, Bolton et al 2000) performed on two specimens of the same material oriented in different directions. This can be achieved using a variety of physical setups, such as an oedometer modified with a flow pump so that the permeability is measured between load increments. Again, two different set ups and specimens are required to measure the permeability anisotropy, one with vertical drainage and one with radial drainage. This method is also easily adaptable to the Constant Rate of Strain (CRS) device (Wissa et al, 1971) or for use in the triaxial cell. Adams (2011) showed that the permeability obtained using the CRS technique and the constant head techniques are the same. More recently, the solution for the horizontal permeability under a constant rate of strain was published by Yune and Jung (2011), paving the way for rapid collection of continuous permeability measurements in both the vertical and horizontal direction using two specimens.

Alternatively, a standard permeameter can measure the permeability of specimens trimmed in the direction of interest. One specimen is trimmed and installed for measurement in the vertical direction using either a constant head, constant flow or falling head permeability measurement technique. A second specimen is trimmed at 90 degrees for measurement of the horizontal permeability.

Finally, Chan and Kenney (1973) developed a measurement method using cubic specimens which measures both the horizontal and vertical permeability of the same specimen, allowing direct measurement of the permeability anisotropy of a specimen.

The cubic specimen method applied by Chan and Kenney (1973) uses 2.5 in (6.4 cm) cubes trimmed in line with the varved layers. The permeability is measured via a constant head test in a pressurized cell. The permeability is first measured in one direction, then the specimen is rotated 90 degrees and the permeability is measured in the perpendicular direction. This process was repeated multiple times on the same specimen to determine the effects of specimen recompression. Chan and Kenney (1973) noted that re-measurement of the permeability of the same specimen lead to a decrease in the measured permeability, due to recompression effects and smearing across the varve interfaces. They provide a procedure (Figure 2-6) for correctly determining the permeability anisotropy of a specimen. The procedure requires that the second permeability measurement be repeated and the permeability at measurement number 1 be extrapolated for use in the anisotropy calculation.

The cubic specimen method is further developed in this thesis for use with uniform mudrocks.

2.3.4 Permeability Anisotropy and Fabric Measurements

There are a limited number of directional permeability measurements for mudrocks available on the literature. Of those studies, fewer still go so far as to compute and analyze the permeability anisotropy. Further, not all studies measure the directional permeability oriented to the principal axes (i.e. parallel and perpendicular to the axial loading direction).

Chapuis and Gill (1989) provide an excellent summary (Table 2-3) of the historic anisotropy measurements made on mudrocks using a variety of laboratory and field methods which are well detailed in their paper. The majority of measurements are performed using multiple specimens and variations of the techniques described in section 2.3.3. Based on this summary, the permeability anisotropy of the majority of cohesive soils falls within the range of 0.7 to 4. The horizontal permeability is most often higher than the vertical permeability except in the case of very shallow soils where the vertical permeability may be affected by root and worm holes.

Significant additional work has been completed since 1989. Figure 2-7 and Figure 2-8 compare the range of permeability anisotropy as a function of porosity that researchers have measured for different mudrocks for selected studies. Table 2-4 summarizes the key findings of permeability anisotropy studies that focused on determining the causes of permeability anisotropy development in addition to the magnitude of the permeability anisotropy.

Numerous experimental conclusions have been reached concerning the magnitude of the permeability anisotropy of uniform cohesive mudrocks. Some have found that mudrocks can remain isotropic ($r_k = k_h/k_v = 1$) despite increasing compression (e.g. Clennell et al, 1999, Dewhurst et al, 1996, Basak, 1972, Leroueil et al, 1990 and Tavenas et al, 1983) whereas other experiments

showed permeability anisotropy develops with increased compression (e.g. Clennell et al, 1999, Basak, 1972, Leroueil et al, 1990) and with shear (e.g. Dewhurst et al, 1996, Arch and Maltman, 1990). Bolton et al (2000) found that intact mudrocks exhibit high anisotropy at very low (< 0.6 MPa) confining stress owing to the presence of stress relief micro cracks; increasing the effective stress seals these cracks and yields an isotropic mudrock.

Some researchers (e.g. Leroueil et al, 1990, Tavenas 1983, Dewhurst et al, 1996) suggested that small measured permeability anisotropy increases or decreases may in fact be due to specimen variability stemming from measurement techniques requiring the use of two separate specimens. Two studies applied experimental techniques requiring only 1 specimen. New Liskeard Varved clay is micro stratified and has relatively low permeability anisotropy that does not exceed 4 due to the small difference in the absolute permeability between the high and low permeability layers (Chan and Kenney, 1973). Witt and Brauns (1983) measured the permeability of uniform lenticular gravel to be 2.3 and suggested the limit of permeability anisotropy for an assemblage of uniform, lenticular particles to be 2.5.

Overall, the permeability anisotropy of uniform mechanically compressed mudrocks is low, certainly below 10, and is closer to isotropic for most materials, especially for silty materials (Table 2-2, Table 2-3, and Figure 2-7).

Many experimental investigations quoted above have undertaken additional analysis of the mudrock fabric, either qualitatively using Scanning Electron Microscope (SEM) images, or quantitatively using Mercury Intrusion Porosimetry techniques. Based on these analyses, the permeability anisotropy may, or may not, be linked to measurable fabric parameters.

SEM images reveal micro scale heterogeneities such as clay grains wrapping around silt grains (e.g. Dewhurst et al, 1996, Schneider et al, 2011). Some authors (e.g. Clennell et al, 1999, Dewhurst et al, 1996) failed to note bulk alignment of clay particles but were able to note alignment of larger silt particles, and for clay particles within domains and aggregate groupings. Other authors (e.g. Dewhurst et al, 1996, Arch and Maltman, 1990) could not identify alignment of platy particles within mechanically compressed mudrocks, but were able to identify platy particle alignment within mechanically compressed and sheared mudrocks.

Schneider et al (2011) suggest a mechanism to limit platy particle alignment in mudrocks with non-uniform particle size distributions: As the clay fraction decreases and silt particles form the dominant structure, stress bridges form which act to preserve large pores and cause the non-uniform compression of clay particles (Figure 2-9). Olsen (1962) proposed a similar idea with his particle clustering model. He showed that unequal pore sizes develop in clays due to particle clustering and that this is the cause for the discrepancies between the measured permeability and that predicted by the Kozeny-Carmen equation (eq. 2-3).

Further, Basak (1972) showed that dispersed fabrics develop permeability anisotropy with increasing compression, whereas flocculated fabrics remain isotropic. Basak's (1972) results

suggest that particle orientation may lead to higher anisotropy, but also beg the question as to whether fabric evolution is significant once deposition has occurred.

Leroueil et al (1990) interpret that the pore space undergoes a progressive collapse as mudrocks compress. First the large, inter-aggregate pores are removed, followed by the smaller intra-aggregate pores. As a result, the aggregates remain intact to very high levels of compression before being integrated into a homogeneous fabric.

Overall the above studies highlight the variety of findings related to the magnitude and causes of permeability anisotropy in mechanically compressed mudrocks.

2.3.5 Permeability Anisotropy Models

A number of models have been developed to estimate the permeability and/or permeability anisotropy based on observations of the influence of fabric, specifically the influence of particles and pores. Each model is based on an underlying assumption that some parameter, be it particle orientation, pore shape, particle shape, etc. controls the development of permeability anisotropy. This section describes a number of relevant models.

Olsen (1962) describes a model to predict the permeability anisotropy due to tortuous flow paths based on geometric analysis. Olsen does not develop his model into a single equation. The anisotropy of an assemblage of particles with a given orientation, aspect ratio and spacing is determined by first computing the tortuosity ratio for flow in varying directions. Based on his model, Olsen predicts the permeability anisotropy for Kaolinites will vary between 1 and 20, and will increase to a maximum of 100 for Illite rich clays with a higher mean aspect ratio.

Daigle and Dugan (2011) apply a similar method using a geometry based approach to relate the permeability anisotropy to the particle orientation, aspect ratio and porosity. They assume an idealized assemblage of platy particles (Figure 2-10 a) with aspect ratio m and orientation θ to the horizontal. The porosity is a function of particle spacing defined by the face to face spacing, ε and the edge to edge spacing, ζ (see Figure 2-9) Three fluid flow paths are identified (Figure 2-10 b): free flow through the pore space (path A), flow encountering the particle face (path B) and flow encountering the particle edge (path C). They apply the Kozeny Carmen relation (eq. 2-3) to predict the permeability anisotropy of the idealized assemblage. Because all parameters except for the tortuosity are isotropic, the permeability anisotropy reduces to:

$$r_k = \frac{k_H}{k_V} = \frac{\tau_V^2}{\tau_H^2} \quad 2-11$$

Where τ_V is the vertical tortuosity and τ_H is the horizontal tortuosity. Equation 2-11 yields the same result as equation 2-8, proven more rigorously by Witt and Brauns (1981).

Daigle and Dugan (2011) compute the average tortuosity in both the vertical and horizontal directions as a function of the particle aspect ratio, spacing and orientation given the three possible flow paths. They derive an equation relating the permeability anisotropy to the particle aspect ratio (m), mean particle orientation (θ) and porosity (n):

$$\tau_k = \frac{k_H}{k_V} = \frac{\left[1 + \frac{\left[\frac{8m}{9} \cos(\theta) + \frac{2}{\pi} \sin(\theta) \right]}{\left[\frac{3\pi}{8(1-n)} - \frac{1}{2} \right]} \right]^2}{\left[1 + \frac{\left[\frac{8m}{9} \sin(\theta) + \frac{2}{\pi} \cos(\theta) \right]}{\left[\frac{3\pi}{8(1-n)} - \frac{1}{2} \right]} \right]^2} \quad 2-12$$

For mudrocks comprised of assemblages of grains with non-uniform aspect ratios, Daigle and Dugan (2011) define an equivalent aspect ratio m_{eq} :

$$\frac{1}{m_{eq}^2} = \frac{f_{m1}}{m_1^2} + \frac{f_{m2}}{m_2^2} + \dots \quad 2-13$$

Where m_{eq} is the equivalent aspect ratio, and m_1 and m_2 are the aspect ratios of grain volume fractions f_1 and f_2 , respectively. This equation is based on electric circuit analogies but is not well explained. Daigle and Dugan suggest that mudrocks comprised of mixed aspect ratio grains will have their permeability behavior dominated by the lowest aspect ratio grains because those grains reduce the difference in tortuosity between the horizontal and vertical directions, thus reducing the permeability anisotropy. Higher aspect ratios lead to high permeability anisotropies. As a result, high permeability anisotropies are not expected from mudrocks containing silt which reduces the equivalent aspect ratio; contrarily pure clays with higher mean aspect ratios should expect to achieve higher permeability anisotropy.

Based on equation 2-12, Daigle and Dugan (2011) validate their model against the permeability anisotropy derived for similar particle assemblages modeled using computer simulations and the lattice Boltzmann method. They simulate the rigid rotation of particles as a function of strain using the March (1932) model (equation 2-1). They show that as the porosity decreases, preferential grain orientation is capable of producing high permeability anisotropies ~ 10 , even for mudrocks with modest particle aspect ratios such as Illite. The permeability anisotropy of compressed mudrocks increases as the particle aspect ratio increases and the porosity decreases. Further, very high permeability anisotropy is possible when compression is combined with shear phases. An extensive discussion of shear induced permeability anisotropy is beyond the scope of this work.

Yang and Aplin developed (1998) and calibrated (2007) a pore-based model to predict the directional permeability, and indirectly the permeability anisotropy, of mudrocks as a function of pore radius, porosity and clay content. Their model assumes biconical shaped pores and incorporates anisotropy using an assumed pore angle distribution as a function of effective stress. The model is calibrated using an extensive data set of measurements on intact marine mudrocks

and can predict the permeability to within +/- 3 for both horizontal and vertical permeabilities. The calibration makes many assumptions explained as 'arbitrary' by the authors. The Yang and Aplin (1998) model does not predict the permeability anisotropy, rather the directional permeability. Because the permeability anisotropy is a ratio of the vertical and horizontal permeability, each with a +/- 3 error band, any predictions of the permeability anisotropy made using this model are expected to have a very large error band.

Arch and Maltman (1990) created a computer model to simulate the variation in tortuosity with direction of flow through argillaceous sediments. Their model is based on findings from their permeability experiments on sheared Ball clay which showed that both the primary (undeformed) and the secondary (sheared) fabric controlled the permeability anisotropy development. The model consists of 2 separate computer programs. The first program creates a virtual specimen. The second program computes the flow tortuosity through the virtual specimen created by the first program. The computed tortuosity is inversely related to the permeability through equation 2-3. Unfortunately, the specific details of the computer program used to generate these results are not given and the model cannot be readily adapted or applied to other materials and situations.

Arch and Maltman (1990) find that high degrees of uniaxial shortening (>2, equal to > 50% strain) are required to produce significant changes in tortuosity with specimen orientation (see Figure 2-11). The permeability anisotropy can be computed by inputting directional tortuosity data from Figure 2-11 into eq. 2-8. Figure 2-12 plots the predicted permeability anisotropy as a function of uniaxial strain. For a uniaxial shortening of 1.5, corresponding to a uniaxial strain of 33%, the model predicts the permeability anisotropy of the primary, unsheared fabric to be 2.3. This increases to as high as 22 for a uniaxial shortening of 10 corresponding to 90% strain. Much higher tortuosity differentials are produced when simple shear is combined with uniaxial strain.

Scholes et al (2007) measured the permeability anisotropy of lignite which consists of compressible particles; for this reason the permeability anisotropy results are not included in Figure 2-7. The permeability anisotropy of lignite is shown to increase exponentially from 1 to 8, and varies with temperature. Scholes et al (2007) derive an empirical model for use in mudrocks with particles of any shape. Their model estimates the permeability anisotropy (r_k) as a function of strain:

$$r_k = r_1 \left(\frac{1 + e_1}{1 + e} \right)^{x'} \quad 2-14$$

Where r_k is the permeability anisotropy at the current void ratio e , r_1 is the permeability anisotropy at void ratio e_1 , and x' is an empirical fitting parameter. The value of x' is determined experimentally.

The Scholes et al (2007) model is useful only if measurements of the permeability anisotropy exist to show the trend; it is more of an empirical fit to existing data rather than a model based on the factors controlling the permeability anisotropy such as particle orientation as in the Daigle and Dugan (2011) model.

2.4 Resistivity & Resistivity Anisotropy

This section is divided into five sections. The first section defines resistivity and formation factor, and presents Archie's law which relates resistivity to porosity and saturation. The second section describes how resistivity is used in practice. The third section introduces the concept of parallel resistor models used to adjust the measured resistivity to correct for clay surface conductivity. The fourth introduces the concept of resistivity anisotropy, and the fifth section discusses the limited experimental and theoretical models that have been published in the literature exploring the magnitude and causes of mudrock resistivity anisotropy.

2.4.1 Resistivity, Formation Factor & Archie's Law

Electrical resistivity is a material property. It is symbolized by ρ and is the length (L) and area (A) normalized resistance (R) of a material and has units of ohm meters (Ωm):

$$\rho = \frac{RA}{L} \quad 2-15$$

The inverse of the resistivity is the conductivity (σ) with units of Siemens per meter (S/m):

$$\sigma = \frac{1}{\rho} \quad 2-16$$

The formation factor normalizes the resistivity by the pore fluid resistivity and allows comparison between mudrocks of varying pore fluid salinity and ionic composition:

$$F = \frac{\rho}{\rho_w} \quad 2-17$$

Where F is the formation factor (unitless), ρ is the soil or rock resistivity and ρ_w is the resistivity of the saturating pore fluid for mudrocks saturated with a single phase (e.g. only salt water, not mixed water and oil).

It is important to use the formation factor and not the resistivity when comparing mudrocks at different depths, locations, and of different lithology, mineralogy, salinity etc. The use of formation factor normalizes the effects of varying pore fluid salinity, which directly affects the magnitude of the resistivity.

Mudrock resistivity is a function of the porosity, the pore fluid salinity, the saturation and the tortuosity of the flow path (McCarter et al, 2005), the mineral grains, the temperature and the measurement frequency (Clavier et al, 1984, Bešter-Rogač and Habe 2006, Abu-hassanein et al, 1996). The flow path tortuosity is controlled by the fabric structure of the mudrock. For a constant porosity, a flocculated type structure will produce a higher resistivity than flow parallel to bedding

in a dispersed structure because of a higher tortuosity (Figure 2-13, Blewett et al 2001). Electrical current can flow both through fluid filled pores, and along charged surfaces, therefore multiple flow paths are possible. Typical values of resistivity for clay rich mudrocks are in the range of 1 to 100 Ωm or more (McNeill, 1980). Many correction factors are developed in the literature to adjust the measured resistivity for the surface conductivity interference. This concept is further discussed in Sections 2.4.2 and 2.4.3. As a result, resistivity is not a proxy for permeability because of the differing path tortuosity.

Archie (1942) defined the relationship between the resistivity of a soil or rock and its brine saturation and porosity (equation 2-18):

$$\rho = \frac{a\rho_w}{n^m S_w^k} \quad 2-18$$

Where ρ is the soil or rock resistivity, a is the tortuosity factor or cementation intercept, ρ_w is the resistivity of the brine saturating the pore space, n is the soil or rock porosity, m is the cementation exponent, S is the degree of brine saturation, and k is the saturation exponent.

Archie postulated that the formation factor should be independent of the brine resistivity and therefore depend only on the pore network and soil fabric. However, Archie's law applies only to soils or rocks with non-conductive solid grains where the flow of ions is constrained to the continuous aqueous phase within the pore space. All solid particles have some degree of surface conductivity. Clay minerals in particular have significant surface conductivity owing to the presence of the charged surfaces and the double layer (e.g. Waxman and Smits 1968, Patnode and Wyllie 1950). Therefore, resistivity measurements made in clays yield only *apparent* resistivity and *apparent* formation factor as they incorporate the effects of the soil particles themselves in addition to the pore space and the soil fabric.

Many researchers have attempted to define relations to correct the resistivity of soils containing clay minerals based on modified Archie equations and parallel resistor models (e.g. Waxman and Smits, 1969, Clavier et al, 1984 and de Lima and Sharma, 1990, to name a few). These are described in detailed in Section 2.4.2. Appendix 4 summarizes experiments that demonstrate surface conductivity is significant even for glass beads and sands that do not have conductive double layers.

Ignoring the effects of conductive solid grains and assuming that the electrically conductive path is through the connected pore space only, the formation factor may be written in terms of Archie's law:

$$F = \frac{a}{n^m S_w^k} \quad 2-19$$

The three Archie parameters are: the tortuosity parameter, a , the cementation exponent, m and the saturation exponent, k .

The cementation exponent m is the slope of the log of formation factor (F) vs. porosity (n). The literature suggests the minimum value of m is 1, and m increases >1 as the porosity decreases (Ransom, 2011). The cementation exponent is typically in the range of 1.3 to >2 : Unconsolidated sands have a cementation exponent closer to 1.3 and consolidated sandstones have a cementation exponent in the range of 1.8 to 2.0 (Archie, 1942). Clay bearing rocks have higher cementation exponents up to 3.3 (Atkins and Smith, 1961).

The Saturation exponent, k , is an extension of the cementation exponent. Archie (1942) found that $k \sim 2$ for both clean unconsolidated sand as well as consolidated sands. When the brine saturation is 1, meaning the pore space is fully saturated with a conductive phase, the saturation exponent falls out of the calculation. However, the saturation exponent becomes increasingly important when the brine saturation is less than 1 (partially saturated) or there are multiple phases saturating the pore space, for example brine and oil, or brine and gas. Applying Archie's Law to multi-phase systems can underestimate the water phase saturation because of the influence of the non-water phase (oil, gas etc.) on the resistivity measurements (Ransom, 2011).

The parameter, a , is poorly documented in the literature. Though sometimes referred to as the tortuosity, it is most appropriately termed the cementation intercept (Archie, 1942). It is widely accepted as a constant value for a given material. Formation factor varies as a function of porosity and the constant a . Many authors assume that $a = 1$ (e.g. Bourlange et al, 2003, Archie, 1942), however others suggest that ' a ' can range from 0.5 to 1.5 (e.g. Crain, 2013). No advice on constraining ' a ' was found.

2.4.2 Resistivity in Practice

In practice, resistivity is used as a comparative tool (e.g. Evans, 2007), and can be analyzed to yield the porosity and saturation of formations through relations such as Archie's Law (Archie, 1942). Resistivity is commonly used to delineate oil bearing formations by noting abnormalities. Downhole horizontal resistivity anisotropy profiles can also reveal bedding and structure in geologic formations.

As a comparative tool, differences in the resistivity between two measurement points separated by a difference in elevation, lateral spacing or time may be indicative of a change in structure, porosity, saturation, or saturating fluid. A given mudrock with constant porosity will show a much higher resistivity when saturated with oil (non-conductive) than when saturated with salt water brine. It is best to use formation factor when comparing different mudrocks as in Archie (1942) rather than resistivity itself since resistivity is affected by pore fluid salinity.

In practice, field resistivity measurements may be corrected for clay surface conductivity (discussed in Section 2.4.3). Bourlange et al (2003) apply Archie's law to estimate the porosity from borehole resistivity logs and compare the results to porosity derived from density. They find that the two porosities (resistivity-derived and density-derived) compare well in intact (un-fractured) mudrocks when a careful clay surface conductivity correction is applied.

2.4.3 Clay Resistivity and Parallel Resistor Models

This section briefly discusses several key parallel resistor models used to adjust the measured resistivity to account for particle surface conductivity. Such models require complex inputs that are difficult and labour intensive to determine and often poorly constrained. This thesis focuses on unadjusted or *apparent* measurements and investigates correlations between permeability anisotropy and the apparent resistivity anisotropy in an attempt to bypass the need to apply such complex correction factors. Nevertheless, this section summarizes the need for correction factors and introduces some of the empirical methods that are commonly applied to adjust the measured mudrock resistivity.

While fluid flows through mudrock pores, electric current flows through a combination of pathways including fluid filled pores, charged particle surfaces, and even through the particles themselves. Electric current flow dominates along the path of least resistance. The ratio of flow through each pathway varies with varying pore fluid salinity for a given mineralogy, porosity and fabric structure. So too does the measured resistivity.

The apparent formation factor (F_a) in mudrocks is defined as the measured formation factor. The apparent formation factor includes current pathways through the fluid filled pore space and through and along grain surfaces. The intrinsic formation factor (F or F_o) is the formation factor that would be measured for current flow through the fluid filled pore space only; it does not include the resistive effects of current paths through or along grain surfaces.

Even clean sands and glass beads exhibit particle surface conductivity (Appendix 4). Urish (1981) showed that decreasing grain size and porosity increase the surface conductivity component of flow through clean sands. Corrections to the measured resistivity and formation are required to account for particle surface conductivity affected by two key factors: 1) the pore fluid salinity, and 2) the mudrock mineralogy.

Patnode and Wyllie (1950) and Waxman and Smits (1968) both propose parallel resistor models to describe the flow of ions through porous media. The specific details of each model vary slightly, but the governing concepts are the same. Ionic flow is partitioned through various flow paths, including through the grains, along grain surfaces, and through the brine filled pore space, and via mobile cations. Each flow path can be considered as a separate resistor, with all resistors arranged in parallel. As the relative resistances of each of these components changes, the easiest flow path for electric charge also changes. Electric current prefers the path of least resistance. The measured resistance is the net resistance of all flow paths through the mudrock, for example as shown by Patnode and Wyllie (1950):

$$\frac{1}{R_t} = \frac{1}{R_w} + \frac{1}{R_g} + \frac{1}{R_m} \quad 2-20$$

Where R_t is the bulk measured resistance of the sample, R_w is the resistance of fluid in the pores, R_g is the resistance of the grains or rock and R_m is the resistance along the surface of grains or rock due to surface conductance effects, referred to as matrix conduction. The grain resistance $R_g \gg R_w$ and R_m , therefore its contribution is negligible.

Changing pore fluid salinity changes the path of least resistance through the mudrock (Figure 2-14). At low pore fluid salinities (high pore fluid resistance), flow is partitioned through various flow paths, including through the grains, along grain surfaces, and through the brine filled pore space, and via mobile cations. As pore fluid salinity increases (R_w decreases) the relative resistance of each component changes, the easiest flow path for electric charge also changes until it reaches the path of least resistance through the pore space. At this point, increasing the brine conductivity has no additional effect the flow path and the true formation factor can be measured. The true formation factor is measured as the inverse of the slope of a plot of rock conductivity vs. brine conductivity (e.g. Figure 2-14). The apparent formation factor will asymptotically approach the intrinsic formation factor for a clean sand as the pore fluid salinity increases (Figure 2-15, Huntley, 1986).

Adding charged clay particles into the system will magnify the dependence of apparent formation factor on the pore fluid salinity by decreasing R_m relative to R_w , especially at lower pore fluid salinities. More flow will be partitioned along grain surfaces, increasing the difference between the apparent and intrinsic formation factor as a function of the salinity.

The apparent formation factor can be related to the intrinsic formation factor using eq. 2-20 (Patnode and Wyllie, 1950) by incorporating concepts of resistivity (eq. 2-15) and formation factor (eq. 2-17):

$$\frac{1}{F_a} = \frac{1}{F} + \frac{\rho_w}{\rho_m} \quad 2-21$$

Where F_a is the apparent formation factor, F is the intrinsic formation factor, ρ_w is the pore fluid resistivity, and ρ_m is the matrix resistivity. This method relies on the matrix resistivity of the clay particles being independent of the pore fluid salinity.

Equation 2-21 can be used to measure the formation factor and the matrix resistivity by making measurements of the same mudrock at a variety of pore fluid brine concentrations (Figure 2-16, Patnode and Wyllie, 1950). This method requires long time periods to replace the pore fluid of materials, days to weeks for sands, and weeks to months and even years for materials with clays. As an alternative, a relatively good estimate of the true formation factor can be determined by making a single measurement using a low resistivity, high salinity saturating pore fluid. Still, this method requires careful and time consuming laboratory measurement.

Alternatively, some researchers (e.g. Waxman and Smits 1968, Clavier et al, 1984, Bourlange et al, 2003) have proposed equations based on measurable clay properties, such as the cation exchange capacity, and the pore fluid composition to correct the measured resistivity, conductivity or

formation factor. These equations require the field measured resistivity, as well as measurements of the clay specific properties and pore fluid chemistry, rather than long laboratory measurements.

Waxman and Smits (1968) correct the measured conductivity based on the clay cation exchange capacity and numerous parameters relating to the pore fluid chemistry and conductivity:

$$C_o = \frac{1}{F_a} (BQ_v + C_w) \quad 2-22$$

$$B = 0.001\lambda_{Na}^e [1 - a \exp\left(\frac{-C_w}{\gamma}\right)] \quad 2-23$$

$$a = 1 - \frac{(\lambda_{Na}^e)'}{\lambda_{Na}^e} \quad 2-24$$

Where C_o is the specific conductance of clean sand rock core with clay conductance effects removed ($1/\Omega\text{cm}$), F_a is the shaly sand formation resistivity factor. Also the apparent formation factor (measured, dimensionless), B is the equivalent conductance of the clay exchange ions as a function of solution conductivity ($\text{cm}^2/\Omega \text{ meq}$), Q_v is the cation Exchange Capacity per unit volume (equivalent / L), C_w is the specific conductance of the equilibrating salt solution ($1/\Omega\text{cm}$), λ_{Na}^e is the maximum equivalent ionic conductance of Na exchange ions at 25°C ($\text{cm}^2/\text{eq } \Omega$), $(\lambda_{Na}^e)'$ is the equivalent ionic conductance of Na exchange ions at 25°C ($\text{cm}^2/\text{eq } \Omega$), and γ is a constant defined by rate of increase in cation exchange mobility from zero water conductivity to its constant value at higher water conductivities.

The dual water model (Clavier et al, 1984) is also well applied in the literature. This model separates the water in the pore space into two domains:

1. Clay water that surrounds the particles, has a conductivity independent of the type and amount of clay that comes exclusively from the clay counterions (cations, related to cation exchange capacity) and is dependent upon the counterion concentration and the temperature; and
2. Far water that fills the rest of the pores and has conductivity and salinity equal to that of the bulk formation water.

The dual water model computed the intrinsic formation factor by equation 2-25:

$$F_o = F_a(1 - v_{Q^H} Q_v) \quad 2-25$$

Where F_o is the intrinsic formation factor, F_a is the apparent (measured) formation factor, v_{Q^H} is the volume of clay water per unit charge for the case where diffuse layer thickness exceeds the Helmholtz plane, and Q_v is the volumetric counter ion charge concentration. The terms v_{Q^H} and Q_v are obtained from experiments and this model is theoretically based. This correction reduces

scatter in plot of formation factor vs. porosity by two times over the Waxman Smits Model (eq. 2-22, Figure 2-17).

Temperature is the main factor that is not accounted for in either of the above relations. Changes in temperature affect the mobility of the counter ions, the thickness of the diffuse layer, and thus the parameters ν_Q^H and Q_v . Temperature affects the clay water conductivity much more than the far water conductivity. Therefore, temperature is only important in shaly soils, not clean sands. In the dual water model, the type or amount of clay is unimportant in the correction of the formation factor.

Finally, Revil et al (1998) derive a complex model based upon the Waxman and Smits (1968) model that differentiates between anionic and cationic flow paths. Anionic flow paths experience the pore space tortuosity; however cationic flow is routed both through the pore space and along the grain water interface dependent on the easiest flow path which is a function of the pore fluid salinity. The specific details of this model are beyond the scope of this discussion but are well covered in their paper. Revil et al. (1998) apply their model to predict the electrical conductivity of mudrocks measured by Waxman and Smits (1968). Using their new model, the predicted values compare much more closely to the measured values than by using the Waxman and Smits model ($r = 0.94$ vs. $r = 0.87$).

Bourlange et al (2003) apply a simplified version of the Revil et al (1998) model. They obtain downhole resistivity logs and correct for clay surface conduction by:

$$\sigma_s = \frac{2}{3} \rho_g CEC \beta_s \quad 2-26$$

Where σ_s is the surface conductivity of the clays that is removed from the measured resistivity, ρ_g is the grain density, CEC is the cation exchange capacity, measured on cores or cuttings, and β_s is the equivalent surface mobility given by a linear combination of the surface mobility of all contributing ions, mainly Na^+ , K^+ , NH_4^+ , Ca^{2+} , Mg^{2+} :

$$\beta_s = \frac{\sum_i \beta_s^i Z_i C_i}{\sum_j Z_j C_j} \quad 2-27$$

Where β_s is the ion surface mobility (available in tables), Z is the ionic charge, and C is the ionic concentration of each ion. In the above equation, the values are summed up over ions 1 though $i = j$ to represent the contribution of each individual ion in solution. This equation is a charge and concentration weighted average surface mobility.

Once corrected, the resistivity is converted to formation factor using the measured pore fluid salinity as a function of depth. The pore fluid salinity, and ionic composition, as well as clay CEC, are all measured as a function of depth via sampling during drilling to allow these calculations and conversions.

The surface conductivity, σ_s , in eq. 2-26 is not necessarily the same as the inverse of the matrix resistivity ρ_m in eq. 2-21. Both equations attempt to quantify the surface conductance or resistance of the particles but use different approaches (experimental vs. theoretical) and may not result in similar quantities.

There are other models available to correct the measured resistivity, conductivity or formation factor to obtain the true resistivity, conductivity or formation factor. Most models are perturbations of the Waxman and Smits (1968), Patnode and Wyllie (1950), Clavier et al (1984) or Revil et al (1998) models. Each model works well for a particular situation, however the art is to determine what model will work, how well it will work, and how to obtain the parameters necessary to apply the model correctly. At minimum the models require complex knowledge of the pore fluid chemistry and the clay composition. Even though measurements are sometimes possible, as shown by Bourlange et al (2003), the accuracy, representativeness and variability of such parameters must always be considered.

2.4.4 Resistivity Anisotropy

Mousse au and Trump (1967) are one of the first to discuss the concept of electrical anisotropy. Electrical anisotropy occurs because the electrical conduction path is different in the vertical and horizontal direction in an anisotropic fabric. Figure 2-18 shows the ionic conduction path through a dispersed (stacked) fabric structure (McCarter et al, 2005). It is important to recall that the electrical flow path might not be constrained to the fluid filled pore spaces, and may flow along particle surfaces or through particles as discussed in Section 2.4.3.

The resistivity anisotropy, r_ρ is defined similarly to the permeability anisotropy as the ratio of the horizontal to the vertical resistivity, ρ :

$$r_\rho = \frac{\rho_H}{\rho_V} \quad 2-28$$

In order to allow comparison to the permeability anisotropy, which is a ratio of directional fluid *conductivity*, the conductivity anisotropy, r_σ , is defined as the ratio of the horizontal to the vertical electrical conductivity.

$$r_\sigma = \frac{\sigma_H}{\sigma_V} = \frac{\rho_V}{\rho_H} = \frac{F_V}{F_H} \quad 2-29$$

By equation 2-16 the conductivity anisotropy is also equal to the ratio of the vertical to horizontal resistivity or formation factor.

2.4.5 Resistivity Anisotropy Measurements & Models

Appendix 3 describes various methods that are commonly applied to measure the resistivity of mudrocks.

McCarter et al (2005) measured the conductivity anisotropy of compressing mudrocks using a modified Rowe cell. Their results show only slight anisotropy development in Kaolinites (up to $r_\sigma = 1.5$) that levels off by 100 – 200 kPa effective stress. Conductivity anisotropy is an inelastic process, and does not decrease with rebound, suggesting that particle orientation is the cause of electric anisotropy.

Mousseau and Trump (1967) measured the conductivity anisotropy of various mudrocks (Table 2-5) and suggested that the anisotropy evolution is related to the evolution of the particle orientation during compression. They did not discuss any relation to permeability or permeability anisotropy. Their results suggest that particle orientation and particle aspect ratio, combined with the manner of preparation, influence the electrical anisotropy. The manner of preparation, interpreted to influence the initial particle orientation, leads to significant differences in the Bentonite specimens, with anisotropy ranging from nearly isotropic for packed dry Bentonite and increasing to 18 for salt water (flocculated) slurry preparation and 25.5 for freshwater (dispersed) slurry preparation. The particle aspect ratio is shown to influence anisotropy development, with mudrocks containing higher aspect ratio particles such as bentonite developing higher conductivity anisotropy.

Mousseau and Trump (1967) also created a simple stacked particle model similar to the dispersed structure shown in Figure 2-1b and use geometry to predict the conductivity anisotropy of the assemblage as a function of particle aspect ratio. This method is similar to that applied by Olsen (1962) and Daigle and Dugan (2011) to predict the permeability anisotropy. Mousseau and Trump (1967) find that that electrical conductivity anisotropy increases with increasing particle aspect ratio.

Bachrach (2011) proposed a much more complex compressing shale resistivity anisotropy model that simulates the change in pore aspect ratio with compression. The changing pore aspect ratio is linked to changing particle orientation. Compression is modeled by a two parameter orientation distribution function. The model is able to capture behavior across the Smectite to Illite (S/I) transition. A differential effective media (DEM) scheme is applied to compute the behavior of the material comprised of individual particles and pores of varying size, shape and orientation. Bacharach applies his model to predict the conductivity anisotropy of an assemblage of individual, oriented Illite particles with particle conductivity anisotropy of 4 and a pore fluid salinity equal to sea water. The model predicts the conductivity anisotropy to be < 3 for porosities > 0.2 , increasing exponentially with further porosity decrease (Figure 2-19). Field measurements from Green Canyon, Gulf of Mexico obtained using Schlumberger's RT Scanner tool yield conductivity anisotropy values ranging from 2-3.

2.5 Relationship between Permeability Anisotropy and Resistivity Anisotropy

In academia, students are often taught that fluid flow is analogous to electric flow and that the governing equations for both processes are similar. Thus, it should be expected that resistivity, like permeability, is a directional parameter and will vary with the axis of measurement and that resistivity anisotropy could be used as an approximate measure of permeability anisotropy, at least in non-conductive granular materials. This concept is briefly suggested first by Meegoda et al (1989).

Meegoda et al (1989) suggest that the permeability anisotropy can be estimated using the electrical anisotropy for granular soils (eq. 2-31 and 2-33). However, this relation may or may not hold for clay rich soils because the fluid flow path and the electric current flow path may differ due to the influence of particle surface conductivity. Thus far, no research is available comparing the permeability anisotropy and resistivity anisotropy of uniform mudrocks.

Meegoda et al (1989) develop an equation similar to the Kozeny Carmen relation to compute the permeability in anisotropic granular media. This equation is based on computer simulations of fluid flow around spheroid particles solved using the Navier Stokes equation:

$$k_{\alpha} = \frac{1}{3} \frac{e^3}{(1+e)S_a^2} \frac{T}{A} \quad 2-30$$

$$A = \left(K_{\alpha} / K_{\alpha+90^{\circ}} \right)^{2/3} \quad 2-31$$

$$T = \left(\frac{r+r_0}{r'} \right)^{-0.5} \quad 2-32$$

Where e is the void ratio, S_a is the volumetric specific surface area, A relates to the permeability anisotropy where K_{α} and $K_{\alpha+90^{\circ}}$ are the permeability measured at right angles, and T is the tortuosity term. Three radii are defined in the tortuosity term. A particle is simulated by a spheroid consisting of two spheres, one larger sphere with radius r and one smaller sphere with radius r_0 . Together they have a total volume V , equal to the volume of an equivalent sphere with radius r' . Equation 2-30 predicts the permeability of anisotropic granular media (permeability range 10^{-14} m^2) to within 3% (Meegoda et al, 1989).

Given the difficulty in measuring the directional permeability of granular materials, Meegoda et al (1989) suggest that the permeability anisotropy term A can be estimated using electrical conductivity measurements:

$$A \approx \left(\frac{\sigma_H}{\sigma_V} \right)^{2/3} \quad 2-33$$

Where σ_H and σ_V are the horizontal and vertical DC electrical conductivity, respectively (refer to Section 2.4 for more details). This is the first direct reference in the literature linking the electrical anisotropy to the permeability anisotropy.

The above relation was developed for granular materials. Granular materials are generally non-conductive and behave very differently than mudrocks; therefore the link between electrical anisotropy and permeability anisotropy for mudrocks is not immediately intuitive.

In mudrocks, the permeability and formation factor both vary logarithmically with porosity. It would be ideal to link permeability with formation factor given the availability and low cost of downhole resistivity measurements compared to field and laboratory permeability measurements. However, no such relations have been identified, or are expected to exist. Both permeability and resistivity are highly dependent on mudrock structure. Further, resistivity measurements may take a variety of conduction paths through a mudrock dependent on the mudrock properties and the pore fluid salinity. Neither the conversion to formation factor nor the careful application of correction factors (Section 2.4.3) can yield sufficient accuracy to estimate the permeability to within an order of magnitude. Even for clay free sands, with minimal surface conductivity, Huntley (1986) shows that the relation between hydraulic conductivity and formation factor is sufficiently steep to render it useless (Figure 2-20).

For similar reason, Georgi et al (2011) showed that the conductivity anisotropy of layered systems does not equal the permeability anisotropy due to of the vastly different permeability and resistivity contrasts between layers.

2.6 Summary

Researchers have investigated the development of permeability anisotropy and resistivity anisotropy (conductivity anisotropy) from both an experimental and modeling perspective.

There are a number of different permeability anisotropy measurement methods in use, the majority of which require one specimen and apparatus to measure the vertical permeability and a separate specimen and apparatus to measure the radial or horizontal permeability. As a result, small measured anisotropy can be associated with experimental errors or specimen variability. The use of cubic specimens allows measurement of both the vertical and horizontal permeability on the same specimen. This method is further developed in this thesis.

The permeability anisotropy of an assemblage of non-aggregated uniform lenticular particles is suggested to be limited to ~ 2.5 (Witt and Brauns, 1983), however pure clays achieve higher levels of permeability anisotropy (~ 10). Many researchers have found that mudrocks with mixed grain sizes exhibit little to no permeability anisotropy. Fewer studies have been conducted to measure the conductivity anisotropy, but similar results are given.

As described in section 2.3.4, the scientific community is divided concerning the causes of permeability anisotropy. Specimen variability (e.g. Leroueil et al, 1990, Tavenas 1983, Dewhurst et al, 1996), micro cracking (e.g. Bolton et al, 2000), micro stratification (e.g. Chan and Kenney, 1974), particle orientation (e.g. Witt and Brauns, 1983, Olsen 1962, Daigle and Dugan 2011), and pore orientation (e.g. Yang and Aplin 1998 and 2007) are among suggested causes of permeability anisotropy development. There has been much focus on developing conceptual models to predict the permeability anisotropy as a function of particle and pore alignment. None of these models have been proven using real mudrocks. On the other hand, increased alignment of platy particles may lead to increased permeability anisotropy especially in shear zones where intense particle alignment creates fluid conduits (e.g. Arch and Maltman 1990, Daigle and Dugan 2011, Dewhurst et al, 1996). However results show that more complex behavior is at play. Though alignment of larger silt particles is well documented, smaller clay particles do not consistently exhibit preferential alignment. Floccs or aggregates form, clay grains are seen to wrap around silt grains, and silt grains are shown to form stress bridges suppressing clay particle compression and alignment. Similar causes are associated with electrical anisotropy development, though fewer studies have investigated the electrical anisotropy of mudrocks.

Models are available to predict the permeability anisotropy based on particle orientation (e.g. Daigle and Dugan, 2011, Arch and Maltman, 1990) pore shape and orientation (e.g. Yang and Aplin, 1998), and empirical relations (e.g. Scholes et al, 2007). The most prevalent and easy to implement models apply the theory of particle orientation to predict the permeability anisotropy. However, particle orientation models have not yet been experimentally validated with real mudrocks. Particle orientation models predict that the permeability anisotropy will increase significantly as grains become more uniformly and horizontally aligned. The permeability anisotropy of natural mudrocks is expected to behave more complexly than predicted by models, owing to diagenetic effects, grain clustering, and mineral inhomogeneities (Daigle and Dugan, 2011), and perhaps even sample size and the effects of layering, as is evident from the array of conclusions drawn from experimental investigations.

Similarly, particle orientation and pore orientation models are used to compute the electrical resistivity. These models are significantly more complex than permeability anisotropy models to account for varying electric flow paths.

Studies have been conducted to link the formation factor (resistivity) and the permeability. Because these two properties are not related, even site specific correlations result in predictions with significant error bands. However, no work has been identified linking the permeability and conductivity anisotropy of uniform mudrocks, despite the significant parallels presented in this chapter.

Table 2-1: Mudrock terminology proposed by Stow (1981) to improve communication within the earth sciences field.

Mudrock (>50% siliclastic, >50% less than 63 μm)			
<i>Basic terms</i>			
<i>Unlithified</i>	<i>Lithified/non-fissile</i>	<i>Lithified/fissile</i>	<i>Approx. proportions/grain-size</i>
Silt	Siltstone	Silt-shale	> $\frac{2}{3}$ silt-sized (4–63 μm)
Mud	Mudstone	Mud-shale	silt and clay mixture (<63 μm)
Clay	Claystone	Clay-shale	> $\frac{2}{3}$ clay-sized (<4 μm)
<i>Metamorphic terms</i>			
Argillite	slightly metamorphosed/non-fissile		silt and clay mixture
Slate	metamorphosed/fissile		silt and clay mixture
<i>Textural descriptors</i>			
		<i>Approx. proportions</i>	
Silty		>10% silt-size	
Muddy		>10% silt- or clay-size (applied to non-mudrock sediments)	
Clayey		>10% clay size	
Sandy, pebbly, etc		>10% sand-size, pebble-size, etc.	
<i>Compositional descriptors</i>			
Calcareous		<i>Approx. proportions</i>	
		>10% CaCO_3 (foraminiferal, nannofossil, etc)	
Siliceous		>10% SiO_2 (diatomaceous, radiolarian, etc)	
Carbonaceous		>1% Organic carbon	
Pyritiferous	} Commonly used for contents greater than about 1–5%		
Ferruginous			
Micaceous			
and others			

Table 2-2: Permeability anisotropy measurement techniques

Method	Number of Specimens / Specimen Shape	Equipment	Permeability measurement Technique	Reference
Oedometer	2 short cylinders ("hockey pucks")	Oedometer	Consolidation Theory	Chan and Kenney, 1973
Flow Pump	2 cylinders	Oedometer or CRS or Triaxial (Pressure) cell connected to flow pump allowing for measurement of inflow and outflow in desired direction	Constant Head Constant Flow	Glennell et al, 1999 Leroueil et al, 1990 Dewhurst et al, 1996
Permeameter	2 cylinders or cubes	Pressure cell	Constant Flow Constant Head	Bolton et al, 2000 Basak, 1972
Permeameter	1 cube	Pressure cell	Constant head Constant Flow	Chan and Kenney, 1973 This work

Table 2-3: Summary of mudrock permeability anisotropy measurements (after from Chapuis and Gill, 1989)

Mudrock	Method	Permeability Anisotropy $r_k = k_h/k_v$	Reference
Boston Blue Clay	Cut Samples	1.7 to 3.6	Mitchell (1956)
Boston Blue Clay	Cut Samples	0.9 to 4.0	Olsen (1962)
Boston Blue Clay	Cut Samples	0.7 to 3.3	Haley & Aldrich (1969)
Chicago	Cut Samples	1.4	Mitchell (1956)
Cincinnati	Cut Samples	2.2	Mitchell (1956)
Dow Field	Cut Samples	1.2	Mitchell (1956)
Enköping	Cut Samples	1.1 to 1.3	Jakobson (1955)
Fore River	Cut Samples	2.2	Mitchell (1956)
Goose Bay	Cut Samples	3.4	Mitchell (1956)
London	Cut Samples	2	Leroueil (1988, pers. Comm)
Louisiana	Cut Samples	0.9	Mitchell (1956)
Mexico	Cut Samples	0.60	Mitchell (1956)
Pump Site	Cut Samples	0.30	Mitchell (1956)
Silty	Cut Samples	1 to 15	Johnson & Morris (1962)
Texas	Cut Samples	3.9	Mitchell (1956)
Vasby	Cut Samples	0.8 to 1.3	Jakobson (1955)
Fissured	Cut Samples	0.7 to 4.6	Garga (1988)
Marine	Cut Samples	0.7 to 1.4	Lumb and Holt (1968)
Marine	Cut Samples	1.05	Subbaraju et al (1973)
Backebol	Cut Samples	1.0	Larsson (1981)
Many clays	Cut Samples	0.9 to 1.4	Tavenas et al (1983)
Atchafalaya	Cut Samples	2.2 to 2.5	Tavenas et al (1983)
Sensitive	Cut Samples	8 to 12	Wu et al (1978)
Varved	Cut Samples	1.5	Bazett and Brodie (1961)
Varved	Cut samples + radial permeability	1.5 to 3.7	Chan and Kenney (1973)
Varved	Cut Samples	3 to 8	Wu et al (1978)
Varved	Cut Samples	4 to 40	Casagrande & Poulos (1969)
Varved	Cut Samples	1.2 to 1.3	Tavenas et al (1983)
Flocculated Kaolin	Radial permeameter	1	Basak (1972)
Dispersed Kaolin	Radial permeameter	1 to 1.6	Basak (1972)
Dispersed Kaolin	Radial permeameter	1 to 2.8	Al-Tabbaa & Wood (1987)
Dispersed Kaolin	Radial permeameter	0.8	Wilkinson & Shipley (1969)
Dispersed Kaolin	Air injected by tubes	1.1 to 2.1	De Boodt & Kirkham (1953)
Dispersed Kaolin	Air injected by tubes	1.6 to 13	Masland & Kirkham (1955)
Kaolinite	Cut samples	1.3 to 1.7	Olsen (1962)
Kaolinite	Oedometer Tests	2.3 to 2.8	Morgenster & Tchalenko (1967)

Table 2-4: Permeability anisotropy measurements and findings

Permeability Measurement Method	Number of Specimens Required	Mudrocks Measured	Permeability Anisotropy k_H/k_V	Additional Work	Key findings	Researcher
CRS with flow pump (constant flow)	2	Kaolinite Silty Clay Marine Mudrock Ca Mont.	0.9 to 1.9 0.9 1.2 to 9.1 6.7 to 11.6	SEM images	<ol style="list-style-type: none"> 1) Alignment of larger silt particles; clays within domains. 2) Particle clustering interrupts particle alignment and limits permeability anisotropy development. 3) Oedometer devices cause edge effects leading to vertical particle alignment along specimen edges, skewing radial permeability measurements. 	Glennell et al (1999)
Oedometer with flow pump, triaxial	2	Sensitive Clay Sensitive Clay Sensitive Clay Marine Clay	1.4 to 1.5 1.2 to 1.1 1.5 to 1.3 1.15 to 1.3	None	<ol style="list-style-type: none"> 1) Isotropic permeability 2) Measured permeability anisotropy clouded by specimen variability 3) Progressive collapse of pore structure (inter-aggregate first, then intra-aggregate) limits permeability anisotropy development 4) Fabric anisotropy not linked to permeability anisotropy 5) Negligible difference between horizontal permeability of specimens that were compressed a) vertically and b) horizontally 	Leroueil et al (1990)
Oedometer with flow pump	2	Champlain Sea Clays, Canadian Clays & Marine Clays Atchafalaya clay	Nearly isotropic 2.2-2.5	None	<ol style="list-style-type: none"> 1) Mudrocks are mostly isotropic with some exceptions 2) Measured permeability anisotropy clouded by specimen variability 	Tavenas et al (1983)
Oedometer with flow pump	2	Compressed Silty Clay Sheared Silty Clay	1.0 3 to 16	SEM Images	<ol style="list-style-type: none"> 1) Silt grains show alignment, clays wrap around silt grains. 2) Particle alignment only evident in shear zones after excessive shear. 	Dewhurst et al (1996)

Table 2-4 Page 1/3

Table 2-4: Permeability anisotropy measurements and findings

Permeability Measurement Method	Number of Specimens Required	Mudrocks Measured	Permeability Anisotropy $\Gamma_k = k_H/k_V$	Additional Work	Key findings	Researcher
Triaxial	2	Intact Marine Mudrocks	1.0 to 1.0	Mercury Porosimetry	<ol style="list-style-type: none"> 1) Stress relief cracks / micro cracks cause high anisotropy at low stress 2) Permeability anisotropy decreases to isotropic as stress increases for intact mudrocks 3) No particle alignment seen in SEM images 	Bolton et al (2000)
Directional Permeameter	2	Kaolinite Flocculated Kaolinite Dispersed Kaolinite	1.0 to 1.1 1.0 1.04 to 1.5	None	<ol style="list-style-type: none"> 1) The degree of initial particle alignment during placement affects the permeability anisotropy 2) Permeability anisotropy is a function of mudrock fabric structure 	Basak (1972)
Permeameter	2	Ball Clay	N/A	Thin Section Analysis	<ol style="list-style-type: none"> 1) SEM images showed the presence of primary (undeformed) and secondary (deformed) fabric 2) The primary fabric developed appreciable particle orientation, but particle orientation became intense within the shear zones. 	Arch and Maltman (1990)
Unknown	Unknown	Kaolinite Illite Boston Blue Clay	1.3 to 1.7 N/A 0.9 to 4.0		<ol style="list-style-type: none"> 1) Unequal pore sizes develop in clays due to particle clustering 	Olsen (1962)
Permeameter	1	Uniform lenticular gravel	2.3	Tortuosity Analysis via Digital Planimeter	<ol style="list-style-type: none"> 1) Permeability anisotropy of uniform oriented particles limited to 2.5 2) Measured tortuosity predicts permeability anisotropy 	Witt and Brauns (1983)

Table 2-4 Page 2/3

Table 2-4: Permeability anisotropy measurements and findings

Permeability Measurement Method	Number of Specimens Required	Mudrocks Measured	Permeability Anisotropy $\Gamma_k = k_H/k_V$	Additional Work	Key findings	Researcher
Permeameter	1 (Cubic)	New Liskeard Varved Soil	4	None	1) Permeability anisotropy low due to low permeability contrast between varved layers 2) Cubic specimen permeability decreases with repetitive measurement, can be corrected	Chan and Kenny (1974)
Permeameter	1 (Cubic)	Resedimented Boston Blue Clay	1.2 – 1.9	Image Analysis Fabric measurements	1) Permeability anisotropy increases as particles rotate to the horizontal 2) Permeability anisotropy of cubic specimens decreases with measurement; can be corrected using method by Chan and Kenny (1974) or global specimen method 3) Resedimentation is useful for laboratory studies to understand development of permeability anisotropy in mechanically compressed mudrocks	Adams et al (2013)

Table 2-4 Page 3/3

Table 2-5: Conductivity anisotropy of compressed mudrocks (after Mousseau and Trump, 1967)

Sample	Method of Preparation	Conductivity Anisotropy $r_{\sigma} = \sigma_H / \sigma_V = \rho_V / \rho_H$
Ohio shale	Natural	5.53
Conemaugh shale	Natural	4.95
Kaolinite (4 MPa)	Slurry	3.92
Bentonite (3.3 MPa)	Packed dry	1.10
Bentonite (2.65 MPa)	Packed dry	1.22
Bentonite (7.8 MPa)	Fresh Water Slurry	25.5
Bentonite (7.2 MPa)	0.5 M NaCl Slurry	18.2

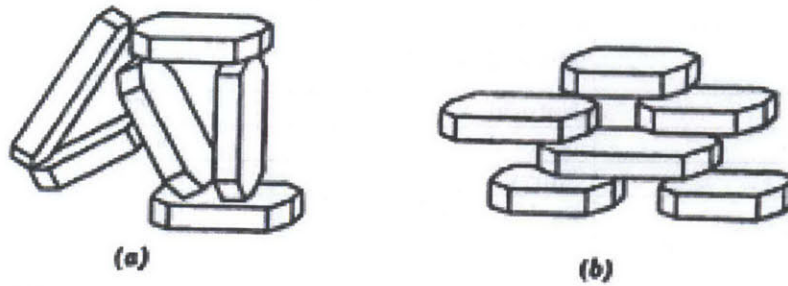
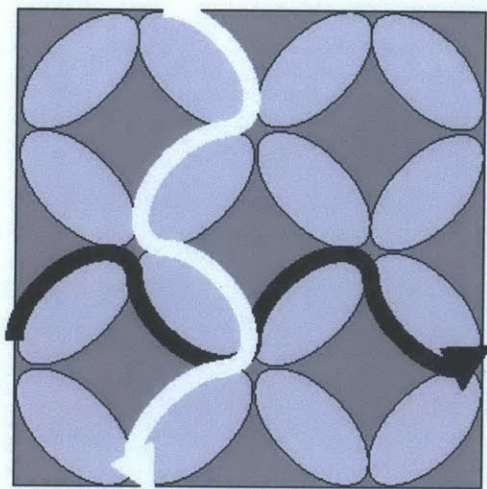
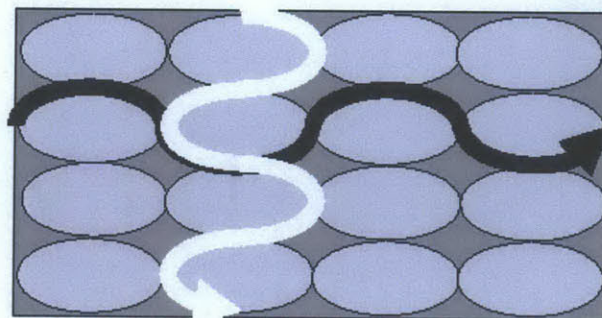


Figure 2-1: Particle orientation in a) flocculated and b) dispersed structures (Lambe and Whitman, 1969)



(i) Loosely Packed, Isotropic State



(ii) Tightly Packed, Anisotropic State

Figure 2-2: Schematic representation of the flow through i) loosely and ii) densely packed elliptical grains (Scholes et al, 2007)

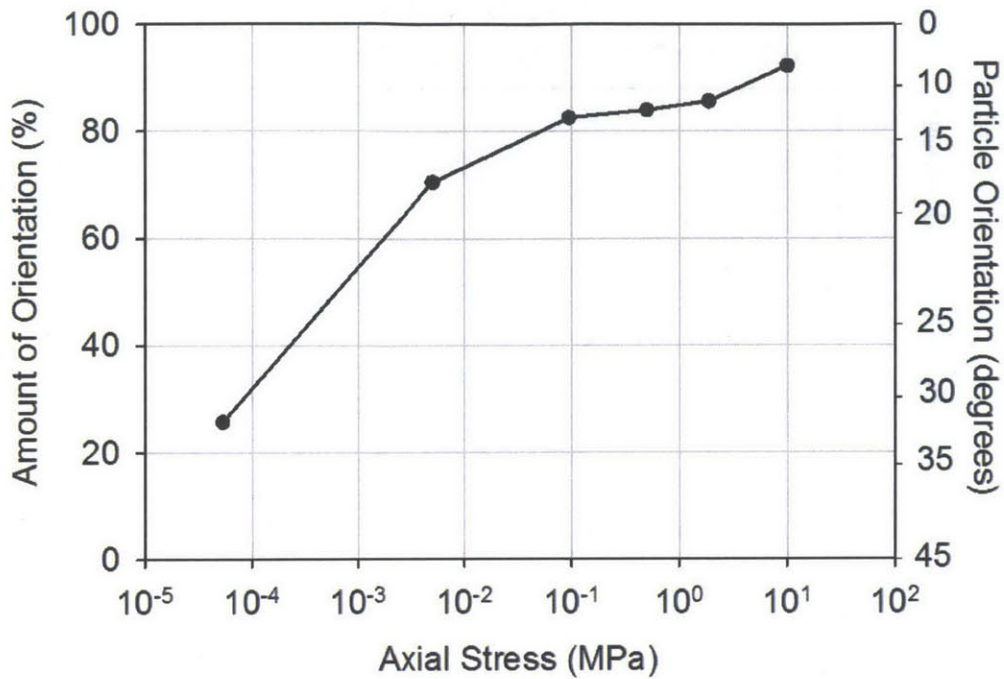


Figure 2-3: Orientation vs. stress for slurry resedimented Kaolinite measured using peak ratio XRD analysis (after Martin and Ladd, 1975)

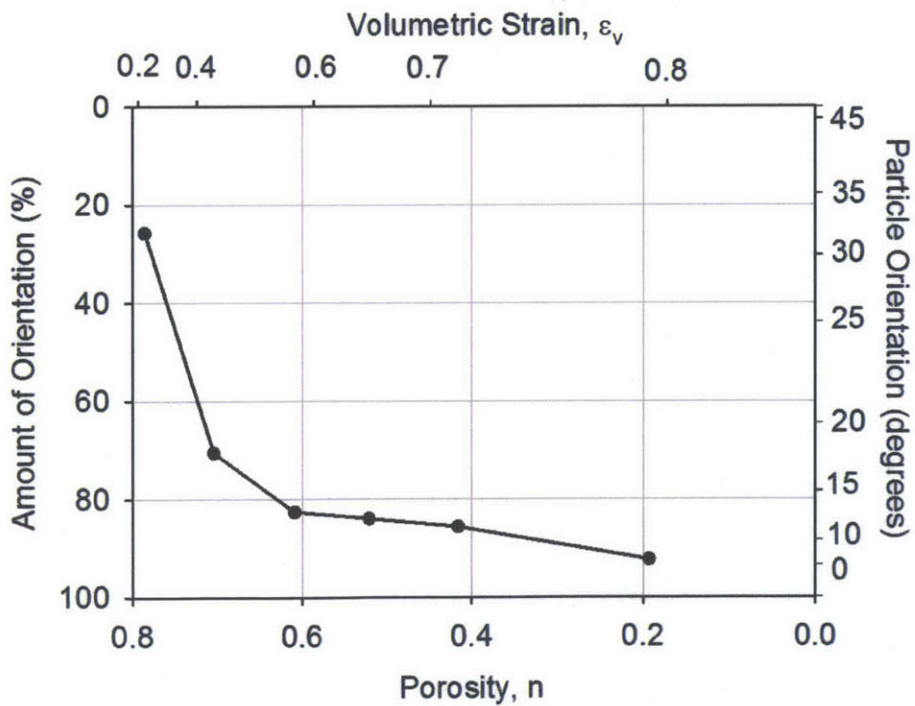


Figure 2-4: Orientation vs. porosity and strain for slurry resedimented Kaolinite measured using peak ratio XRD analysis, assuming $G_s = 2.65$ (adapted from Martin and Ladd, 1975)

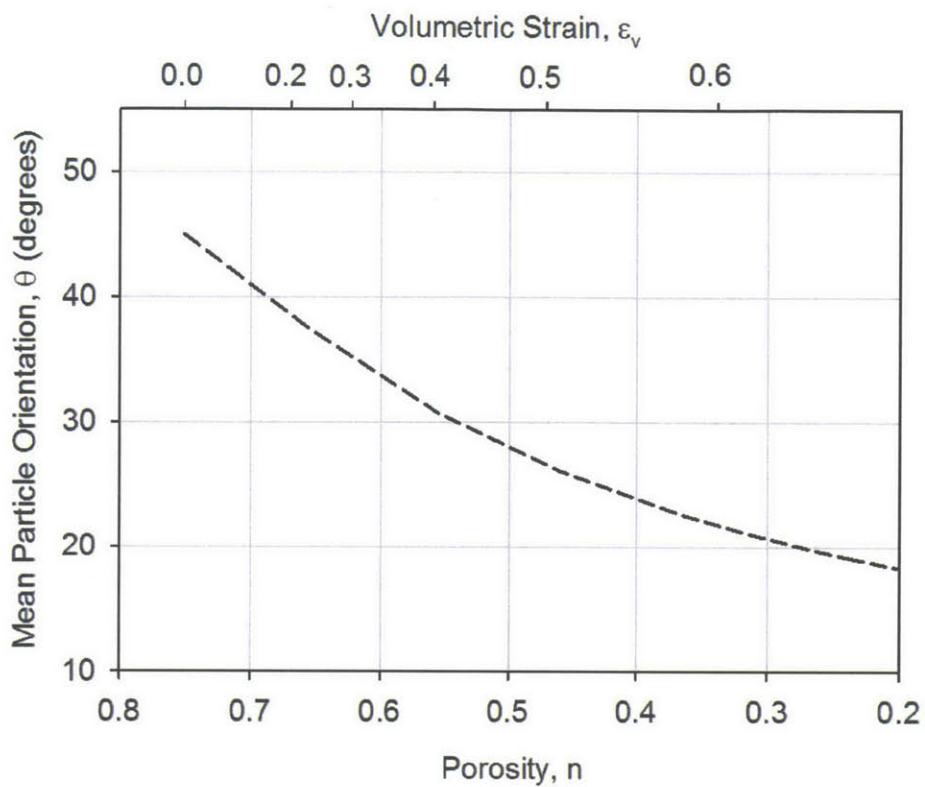
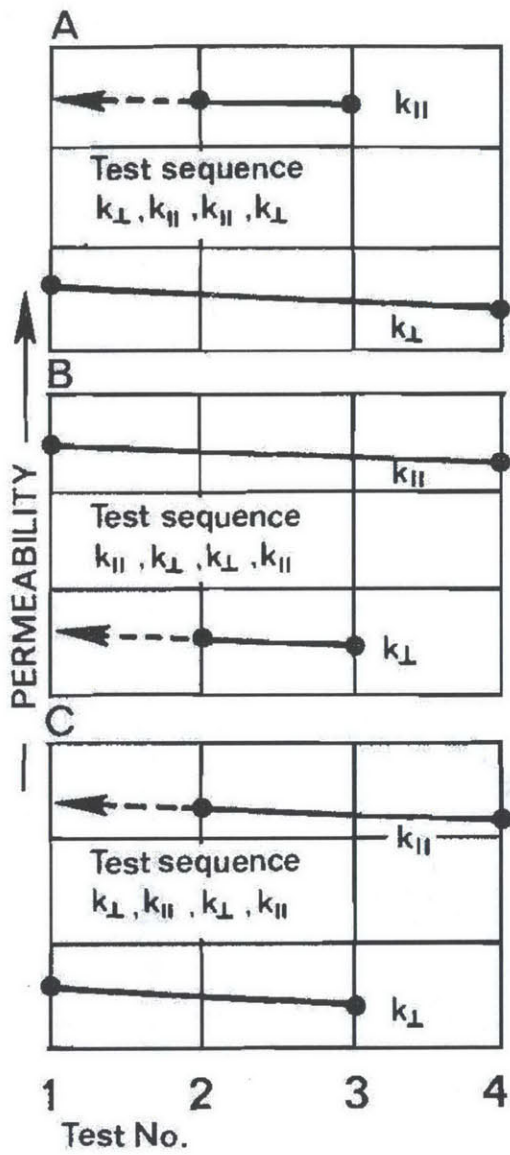


Figure 2-5: Particle orientation vs. strain and porosity for RBBC predicted using the March (1932) model assuming a random initial particle orientation (45 degrees) at zero effective stress and 100% water content.



TEST PROCEDURE

1. Follow test sequence A, B, or C.

2. Extrapolate results to obtain $k_{||}$ and k_{\perp} for test No. 1

3. Calculate $r_K = k_{||}/k_{\perp}$

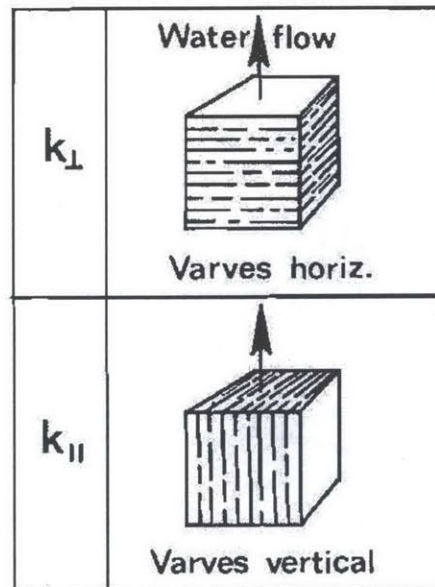


Figure 2-6: Cubic specimen test procedure suggested by Chan and Kenney (1973)

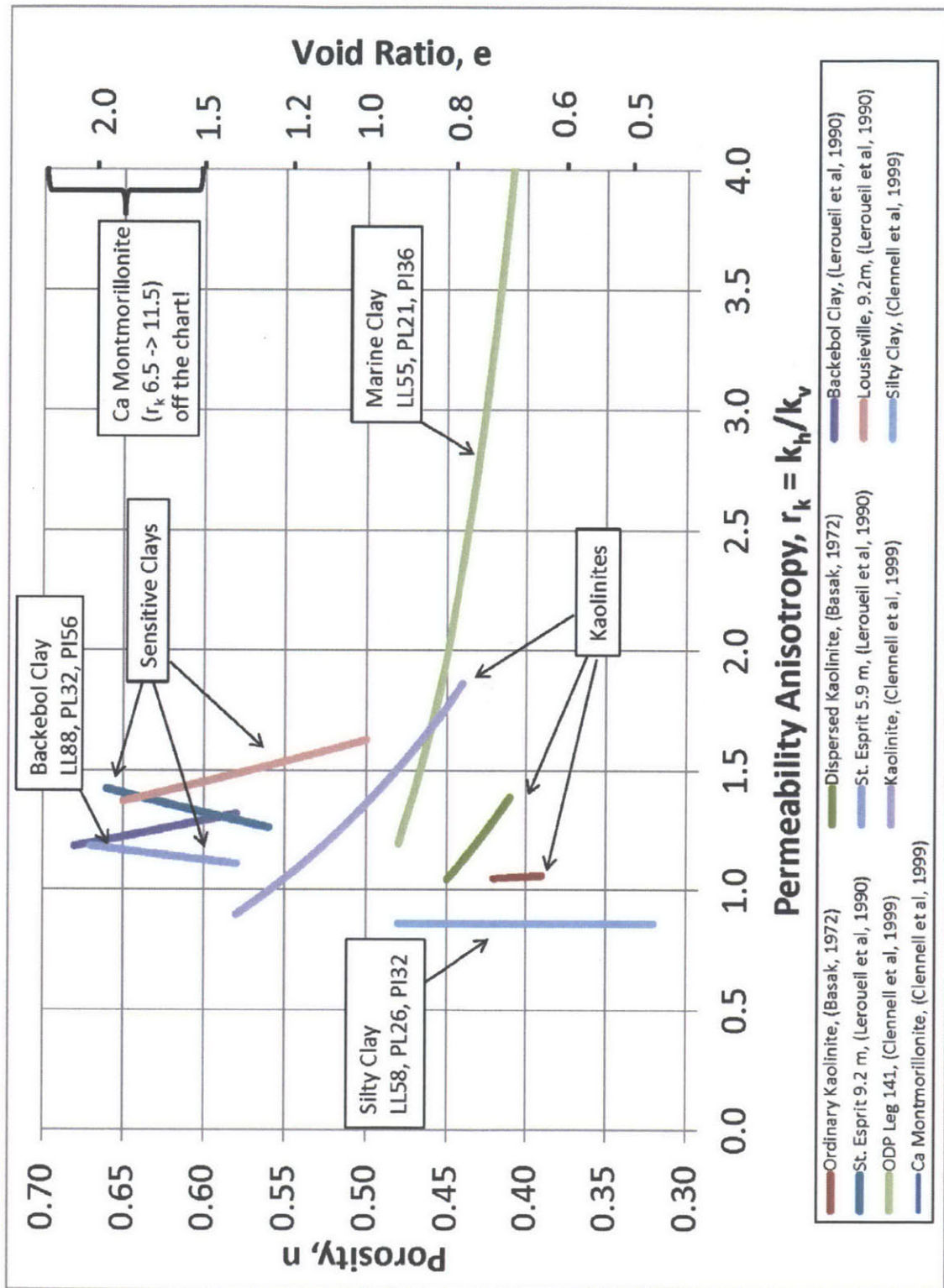


Figure 2-7: Permeability anisotropy measurements in the literature (small plot)

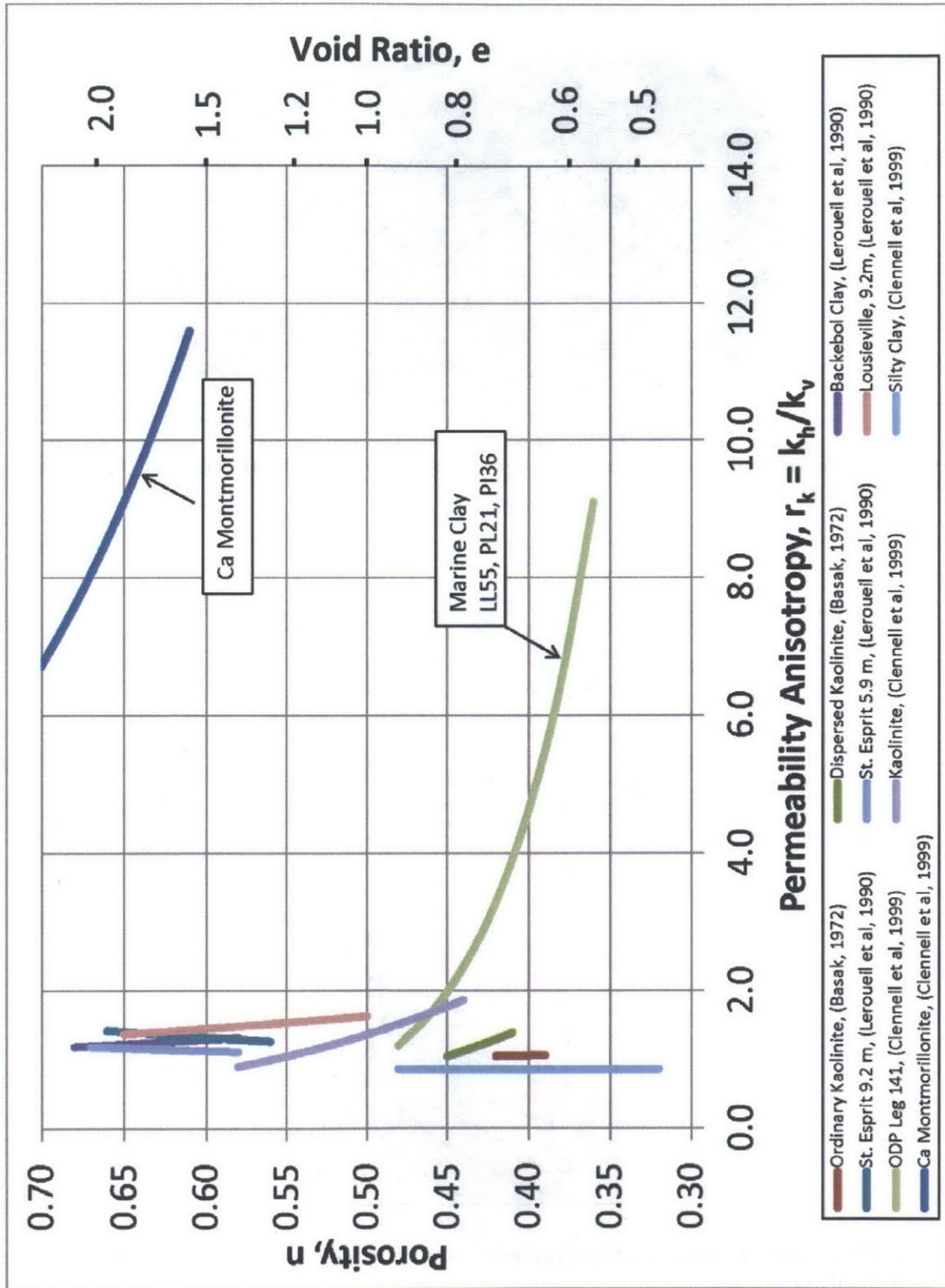


Figure 2-8: Permeability anisotropy measurements in the literature (extended version of Figure 2-7)

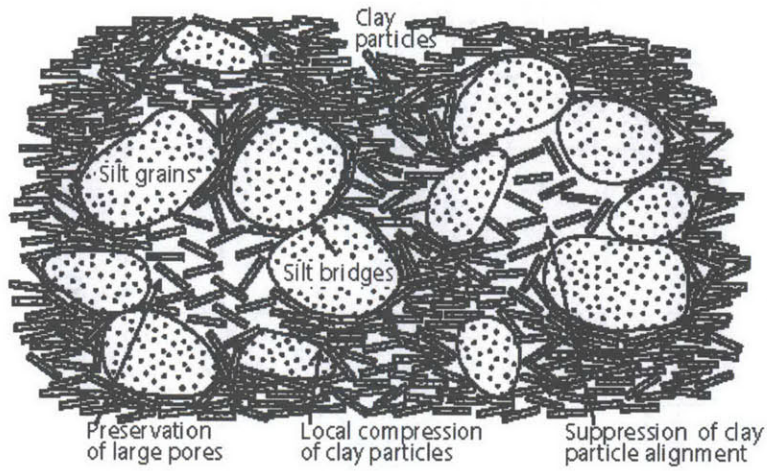
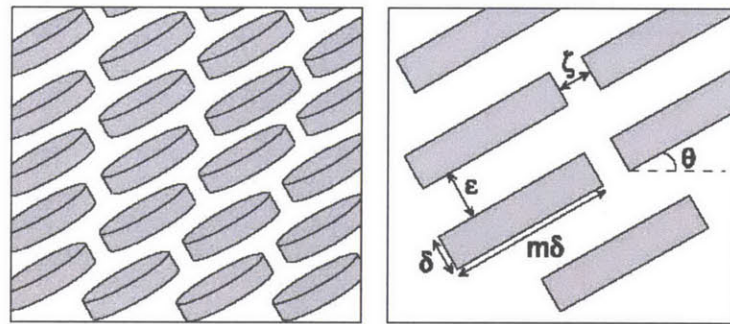
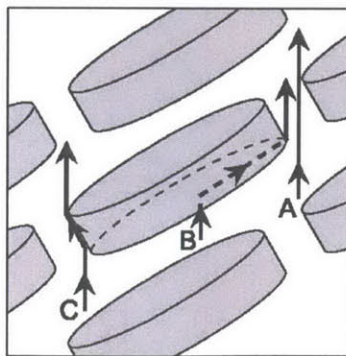


Figure 2-9: Dual porosity structure create by inclusion of silt in clay rich mudrocks (Schneider et al, 2011)



(a)



(b)

Figure 2-10: Model Geometry: (a) Idealized platy particle packing; and (b) fluid flow paths (Daigle and Dugan, 2011)

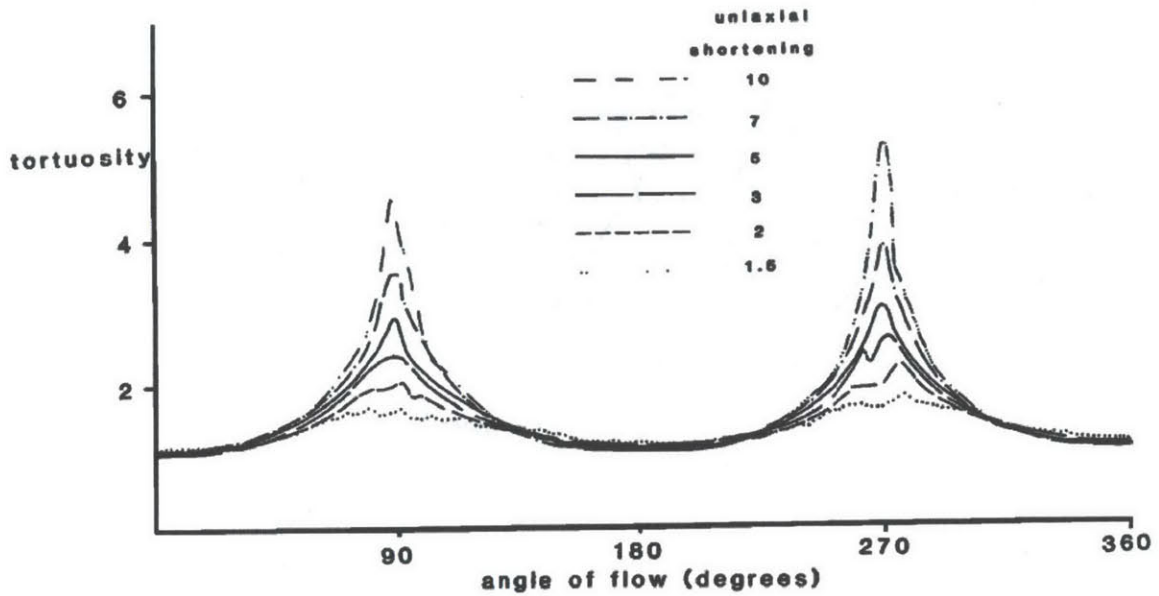


Figure 2-11: Tortuosity vs. angle of flow for uniaxially compressed mudrocks (Arch and Maltman, 1990)

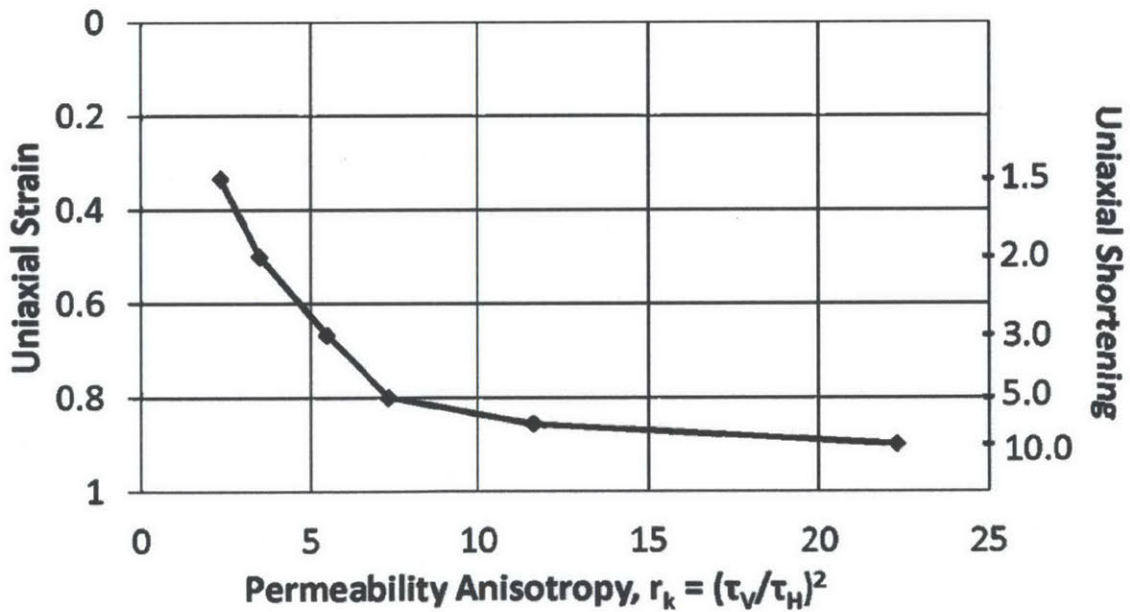
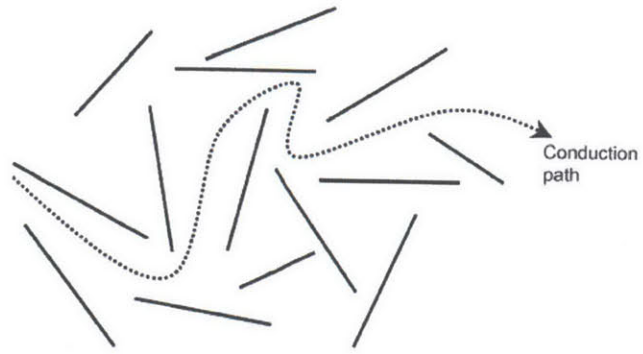
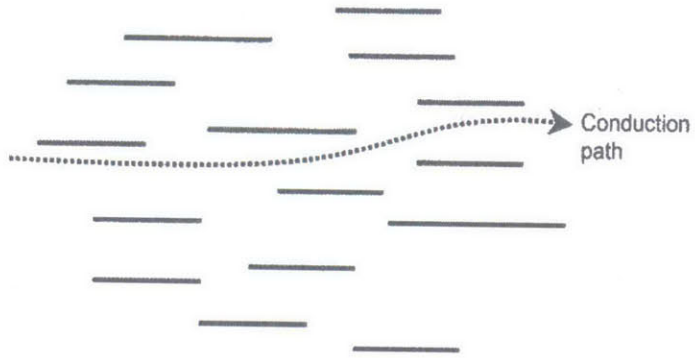


Figure 2-12: Uniaxial strain vs. permeability anisotropy predicted by Arch and Maltman (1990)



a) Cardhouse structure



b) Aligned structure

Figure 2-13: Electrical conduction paths through varying fabric structures (Blewett et al, 2001)

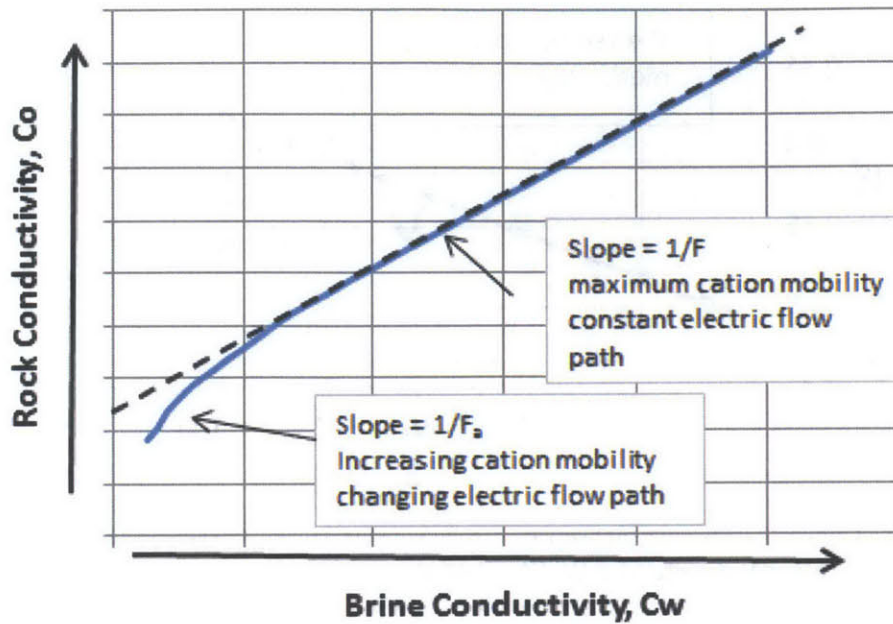


Figure 2-14: Effect of increasing brine conductivity on measured rock conductivity (after Waxman and Smits, 1968)

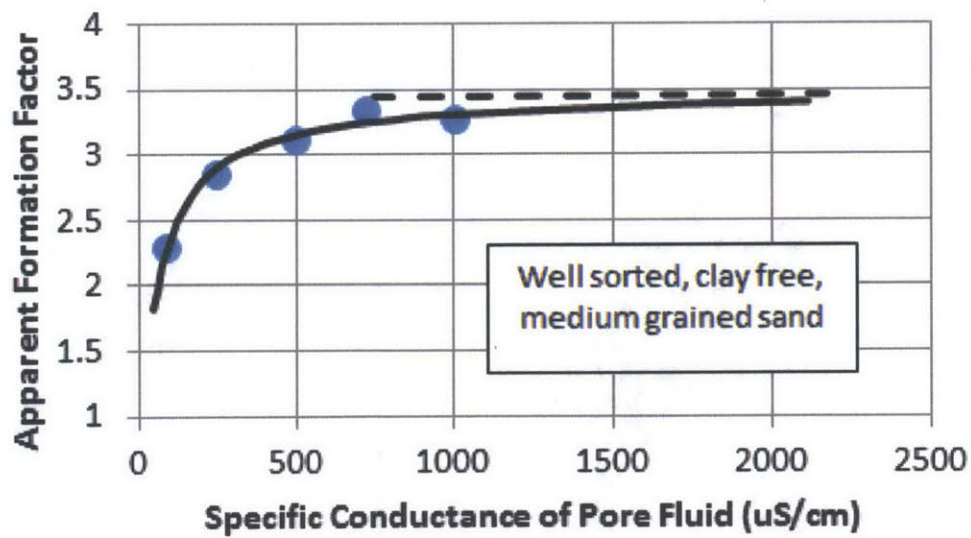


Figure 2-15: Effect of increasing pore fluid salinity (specific conductance) on the apparent formation factor of clean sands (after Huntley, 1986)

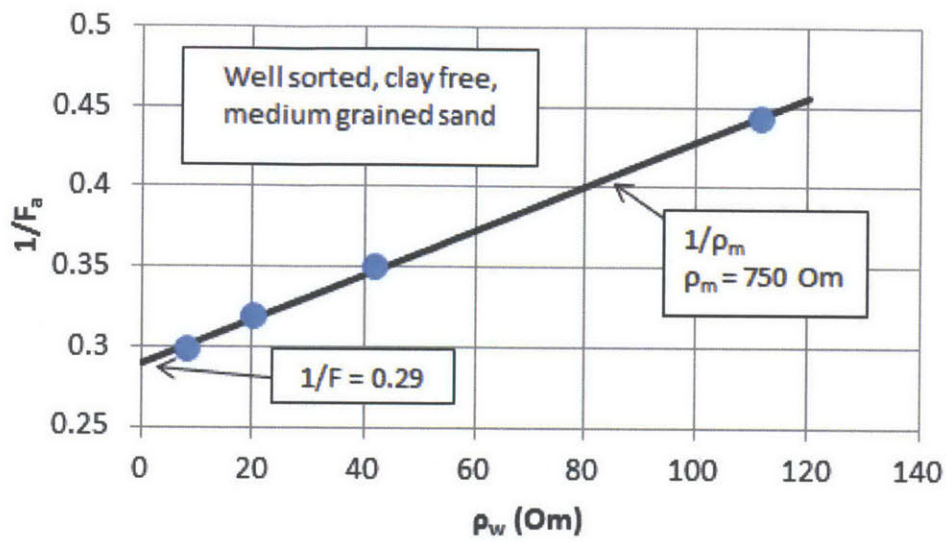


Figure 2-16: Graphic determination of matrix resistivity and intrinsic formation factor using equation 2-21 (after Patnode and Wyllie, 1950)

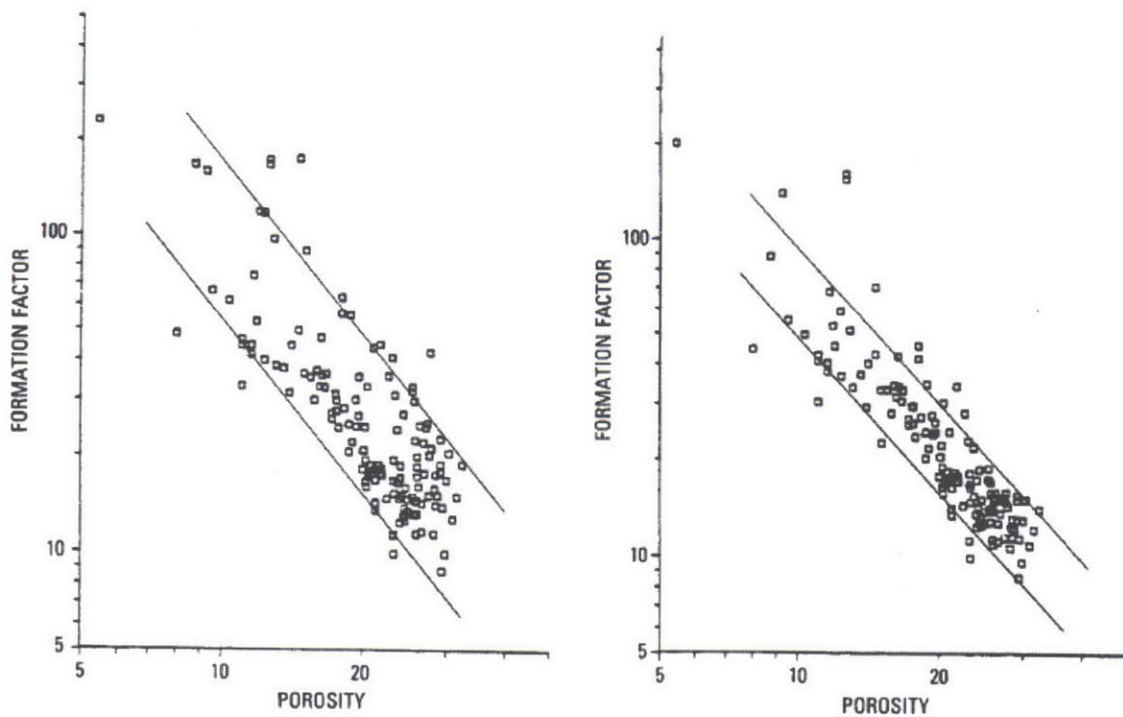


Figure 2-17: Comparison between Waxman and Smits model (left) and Dual Water model (right) (Clavier et al, 1984)

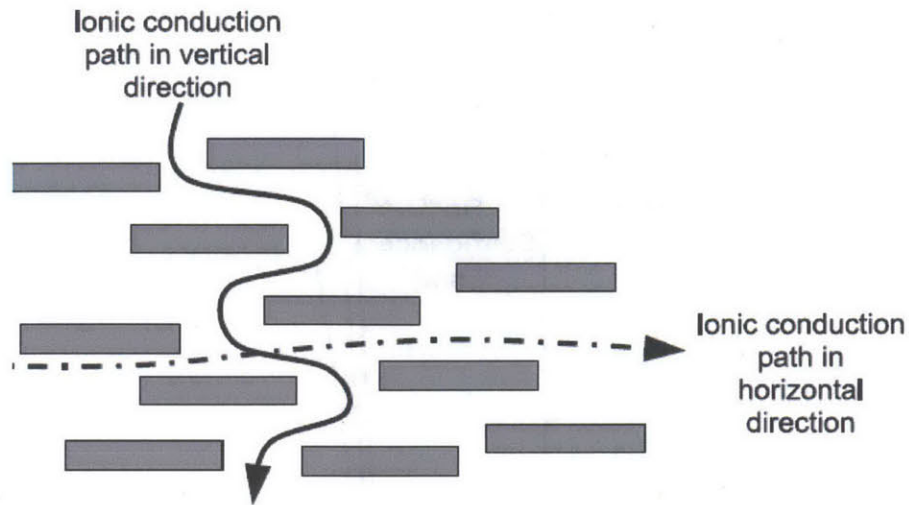


Figure 2-18: Ionic conduction path anisotropy through a stacked structure (McCarter et al, 2005)

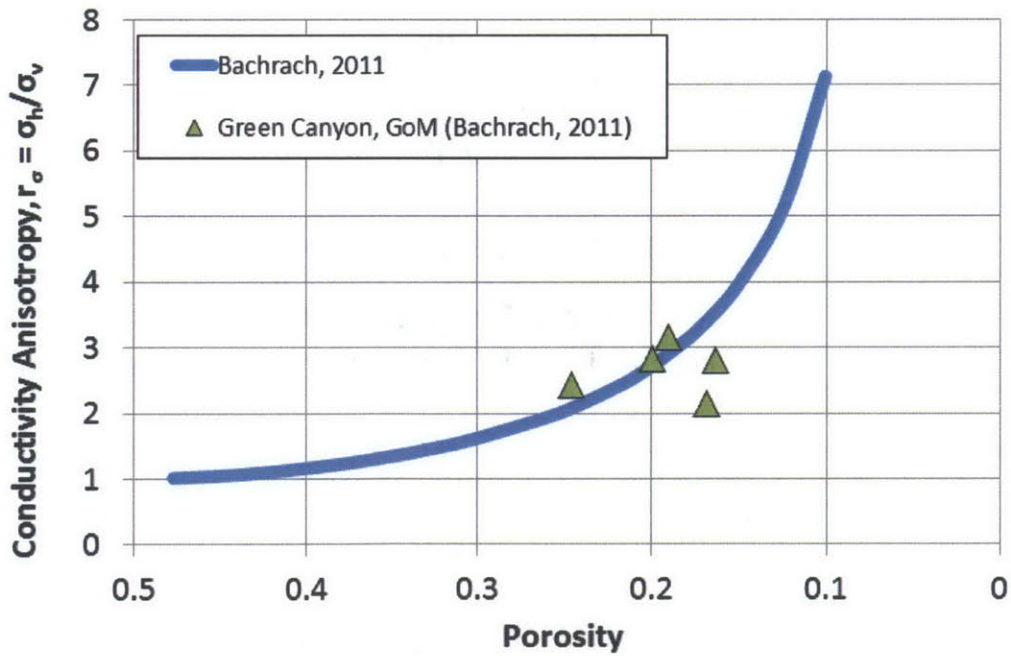


Figure 2-19: Conductivity anisotropy prediction compared with field measurements for the Green Canyon, GoM (after Bachrach, 2011)

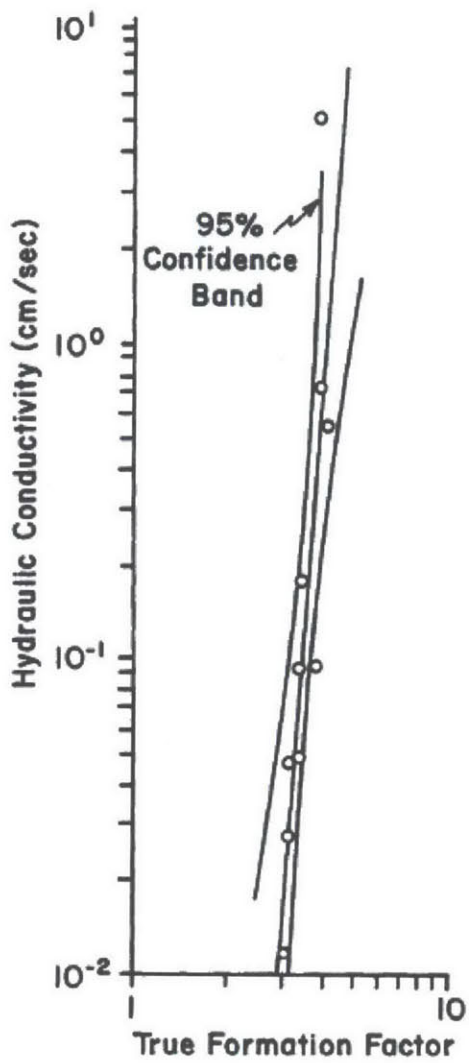


Figure 2-20: Relation between hydraulic conductivity and formation factor for a well sorted clay free sand (Huntley, 1986)

3 *Materials and Specimen Fabrication*

3	Materials and Specimen Fabrication.....	75
3.1	Mudrock Powder Source and Preparation	76
3.1.1	Resedimented Boston Blue Clay.....	76
3.1.2	Resedimented Gulf of Mexico Clay – Eugene Island 330 Block.....	76
3.1.3	Resedimented San Francisco Bay Mud.....	77
3.1.4	Deflocculation via Soil Leaching.....	77
3.2	Resedimentation.....	78
3.2.1	Effect of OCR 4	80
3.2.2	Mass of Solids, Water Content & Salinity.....	81
3.2.3	Sedimentation Column Design.....	82
3.2.4	Resedimentation Load Frames	84
3.3	Salts.....	86
3.3.1	Salt Mixing Guide	86
3.3.2	Salinity Measurement.....	88
3.4	Index Properties	90
3.4.1	Resedimented Boston Blue Clay.....	91
3.4.2	Min-u-Sil 40 and 39% Clay RBBC.....	92
3.4.3	Resedimented Gulf of Mexico Clay – Eugene Island Block 330	92
3.4.4	Resedimented San Francisco Bay Mud.....	92

To enable the systematic study of the evolution of permeability and resistivity with mechanical compression, mudrock specimens are fabricated in the laboratory using a process termed resedimentation. Resedimentation produces uniform, repeatable mudrock specimens with a known stress history and chemistry. Intact mudrocks are sourced, dried and ground using a variety of methods to produce uniform soil powders with 99% passing the #100 US sieve. The ground mudrock powder is combined with salt and water to form slurry that is incrementally compressed to produce test specimens. This chapter begins by describing the source and method used to prepare each of the dry soil powders used in this research. The process of resedimentation is described next, followed by a section describing the treatment and measurement of salts. Finally, this chapter concludes with a summary of the index properties of each mudrock studied.

3.1 Mudrock Powder Source and Preparation

Mudrock powder used in the laboratory is the dried, ground product of intact materials that originate from either block or tube samples. An intact sample is obtained, transported, sieved, air dried and ground to >95% passing the #100 sieve before it is ready to be used for resedimentation. The first three sections describe the specific source and processes applied to produce the mudrock powders used in this research. The fourth section describes the process of leaching which was used to remove the salt from the mudrock powder in some cases.

3.1.1 Resedimented Boston Blue Clay

Series IV Boston Blue Clay powder is produced from block samples of Boston Blue Clay that were obtained from under the Biology building (#62, GPS Coordinates 42° 21.706', -71° 5.317') on the MIT campus in Cambridge, MA in 1992. Approximately 2500 kg of soil was obtained from a depth of 12 m (Abdulhadi, 2009). Cauble (1996) describes the material processing procedure. The material was softened with tap water and mixed into a thick slurry which was then passed through a #10 US Standard sieve to remove all large particles including gravels, shell fragments and non-natural particles. The soil passing the #10 sieve was then oven dried at a temperature of 60 degrees Centigrade and ground by the Stuartevant Company to 95% passing the #100 standard US sieve using a roller mill process. Because the material was not processed as one unit, two blending operations were employed to mix and manually randomize the powder before storing in sealed 40 gallon drums.

3.1.2 Resedimented Gulf of Mexico Clay – Eugene Island 330 Block

Series I Gulf of Mexico Clay from the Eugene Island Block was sourced from two separate wells in the Eugene Island Oil Field in the Gulf of Mexico: Well A-12, located in Block 316, and Well A-20, located in Block 330 (Figure 3-2). The Pathfinder well extension of well A-20 yielded 107 m of 4" core beginning at a depth of 2234 m. Additionally, 43.2 m of 4" core were obtained from well A-12 between 2369 m and 2476 m measured depth. Coring occurred in 1993 and 1994. Cores were stabilized with epoxy resin, sealed with wax and stored in cold storage first in Houston, and then at the University of Pennsylvania, before being transported to room temperature storage at the Austin Core Research Center (Losh et al., 1994; Stump and Flemings, 2002). In 2010, the cores were opened. Sandy intervals were removed and the remaining material was separated into fist sized intervals and laid on plastic sheets to air dry for 18 days. The dried mudrock was shipped to Metso Minerals (York, PA.) and Custom Processing Services (Reading, PA.), where it was crushed to the specification that 99% should pass through a #100 mesh sieve (150 microns), and homogenized (Will Betts, Personal Communication).

3.1.3 Resedimented San Francisco Bay Mud

Series II San Francisco Bay Mud powder was used in this study. Kontopoulos (2012) describes San Francisco Bay Mud as originating from a mix of alluvial deposits, intermittent silt, organic and inorganic deposits during periods of glaciation, and the influences of human activities such as infilling and mining. San Francisco Bay Mud was obtained from numerous Shelby tube samples available in the MIT Geotechnical Laboratory from previous studies. Specimens of San Francisco Bay Mud (both intact and resedimented) previously tested by Kontopoulos (2012) were air-dried and re-ground using a GPX Disc-Style Grinder acquired from Modern Process Equipment, Chicago, IL (shown in Figure 3-1). This grinder has the ability to grind material to 100% passing a US #100 sieve (Horan, 2011). The air-dried material was first broken into small chunks (<1 – 2 inches) and fed through the grinder on a coarse setting. The soil was re-ground on a finer setting, achieved by reducing the spacing between the grinding discs via adjustment of a set screw. The fine ground powder was stored in a sealed 5 gallon pail.

3.1.4 Deflocculation via Soil Leaching

To investigate the effects soil structure influenced by salt chemistry on anisotropy, some test specimens were made using leached mudrock powder. Leaching removes the salt from the soil in stages by diffusion into distilled water. Leaching is accomplished using one of two methods: centrifuge or dialysis tubing.

Horan (2011) describes the process of leaching via the centrifuge. This process is similar to a salinity test (described in Section 3.3.2) repeated numerous times, each time reducing the salt content by approximately one half. The centrifuge method is labour intensive but quick and effective for small quantities of soil.

Leaching via dialysis tubing requires more time but is well suited for larger quantities of soil. Clay powder is mixed with distilled water to form a slurry of pourable consistency. The slurry is poured into ~ 1 foot lengths of dialysis tubing that are sealed at both ends using chip bag clips. 1 5/16" dialysis tubing was sourced in 50 foot lengths from Carolina Biological Supply. This size tubing was ideal to fit over standard plastic laboratory funnels which aided in filling the tubing. Pouring is a messy process and 10% of the original material is easily lost. The filled tubes or 'sausages' are arranged in a large container filled with a quantity of distilled water. Fickian dispersion causes migration of the salt through the semi-permeable membrane as a function of salinity gradient and time. A peristaltic pump is useful to apply a small degree of agitation to the leaching tank and speed up the diffusion process. Figure 3-3 shows a set up with only two sausages, sealed at each end using chip clips, and submersed in a bath of distilled water. Tubing connects the water bath to a peristaltic pump (not shown). Typically 10 to 15 sausages are processed at a time to yield ~ 1 to 1.2 kg of leached soil, enough to produce one 3" resedimented specimen.

The water bath is changed at regular intervals, typically 6, 12 or 24 hours as schedules permit. The used water is removed from the tank via syphon and the salinity measured and recorded on the data sheet. The tank is refilled with the same volume of distilled water and let sit again. The salinity of a solution of 1 g/L salt solution is also recorded as a control. Over time, the equilibrium salinity of the bath water decreases, typically halving at each water change. After approximately 6 to 10 days, depending on the mass of clay being leached, the salinity measurement will become constant (between 10 and 20 $\mu\text{S}/\text{cm}$) and leaching is deemed complete. It has been found that leaching past ~ 12 - 14 days results in breakdown of the dialysis tubing; if the measurement has not leveled off by this point, the soil should be removed from the tubes and new tubes filled to continue the process. Figure 3-4 gives a typical bath water concentration vs. time plot of the leaching process. The curve appears slightly jagged due to a) slight variations in the volume of the bath water at each water change and b) variations in the time between water changes.

The leached clay is removed from the dialysis tubes using a three stage process. It is important to minimize loss of valuable leached material while at the same time minimizing the need for addition of water which will need to be removed later. First, one sausage is opened and emptied into a large container or bucket. The emptied sausage is then cut into 2" lengths and placed into a medium bowl with a small amount of water, just enough to cover the cut pieces of tubing. The tubing is agitated in the water to remove the attached clay particles. The tubing pieces are then placed in a third smaller bowl, with a smaller amount of water than the second. They are further agitated to remove the finest of particles. Once cleaned, the tubing pieces are removed as a collection and the excess water squeezed into the third bowl. The cleaned tubing pieces are discarded. To save water, the contents of the second bowl, if too dirty, are poured into the first, and those of the third into the second. The process is repeated for each sausage. Each stage progressively cleans the dialysis tubing and removes finer and finer particles, ensuring that all material is retained. Done carefully, losses during this process should be minimal.

Once complete, all material should be in the large container. The water content of this material is very high; air drying with the aid of a table top fan is used to reduce the water content until a slurry of the desired consistency is reached (described in Section 3.2.2).

3.2 Resedimentation

Resedimentation is the process of mixing a uniform, homogeneous and workable sediment slurry of desired water content and salinity and then incrementally, and uniaxially, loading it to a desired axial effective stress in a rigid walled sedimentation column called a consolidometer. Resedimentation produces a uniform, repeatable soil sample that can be cut into one or more specimens and trimmed to the desired size and shape for testing.

Resedimentation of BBC was first undertaken at MIT in 1961 by Bailey (Abdulhadi, 2009). Series IV BBC is currently being used, and has been in use since the early 1990's. Resedimentation has been used to produce fully saturated and uniform samples (Germaine, 1982) using RBBC with a salt

concentration of 16 g/L, and resedimentation techniques at MIT have been evolving ever since (e.g. Seah 1990, Abdulhadi 2009, Adams 2011, Casey 2011 and Horan 2012).

Dry, ground soil powder (described in Section 3.1) is mixed with salt water to a pre-determined water content and salinity (see section 3.2.2). The dry and ground soil powder is gradually added to the salt water solution in a standard kitchen electric mixer fitted with a flat beater attachment for mixing (Figure 3-5). The batter is mixed on low speed for approximately 20 minutes, wiping the sides of the bowl at intervals to ensure full and complete mixing. Once a smooth, uniform slurry is generated, the slurry is transferred under vacuum into a vacuum cylinder (Figure 3-6) and de-aired under approximately 15 to 25 inches of Mercury (in Hg) vacuum pressure for 20 – 30 minutes to remove any air bubbles. Longer de-airing times have been noted to non-uniformly reduce the water content of the slurry. The slurry is shaken regularly during the de-airing process.

For this research, a 3" (7.62 cm) inside-diameter (ID) rigid walled sedimentation column of varying height (14" to 18", 25.6 to 45.7 cm) is cleaned and coated with a thin layer of silicone oil prior to slurry placement to help minimize friction during consolidation. The base of the column is plugged by a porous stone and an oversized filter screen (Figure 3-8) made of 05/15 nylon mesh by Sefar Nitrex. The filter screen is placed adjacent the soil slurry. Initially, the stone is propped on a 4" (10.1 cm) tall, 2.9" (7.4 cm) diameter PVC spacer (as in Figure 3-8). The sedimentation column is set up in a reservoir that can be filled with water later but is drained during pouring of the slurry to prevent leakage around the base porous stone. Once the applied stress reaches ~ 100 kPa and the soil column is stable enough, this spacer is replaced by a 6" (15.2 cm) tall spacer, creating a floating sedimentation tube to further reduce sidewall friction during compression.

The de-aired slurry is carefully poured into the sedimentation column using an extended funnel to minimize air inclusion during the pouring process (Figure 3-7). Two people are required to pour the slurry; the first person holds the funnel ensuring that the base of the funnel is kept just at the top of the rising column of slurry. The second person pours the slurry into the funnel gradually ensuring that pressure flow does not develop (i.e. the funnel should not ever flow full). This method both minimizes the potential for air bubbles to form during pouring and allows bubbles that do form to escape upon exit from the funnel. Upon exit, the freefall distance is limited, minimizing air inclusion in the sedimentation column. Though pouring the slurry seems straightforward, it is deceptively challenging to do well.

Once the slurry is placed, a filter screen and porous stone are placed on top with the filter screen adjacent to the slurry. This set up provides two-way drainage (top and bottom). Often, placement of the top filter screen and porous stone requires the use of a shop vacuum to suspend and lower the stone onto the slurry, removing the vacuum as the stone approaches the slurry (i.e. within about 1 cm of the top of the slurry). The reservoir is then filled to a level above the base of the slurry column with saline water of the same salinity as the sediment slurry. The water level in the reservoir is marked so it can be maintained via addition of distilled water on a daily basis to account for evaporation losses, maintaining a constant salinity. Finally, the top of the sedimentation

column is carefully filled to a depth of 1 in with saline water of the same salinity as the sediment slurry.

A resedimentation log is filled out (Figure 3-9) and the specimen is incrementally loaded over time using a load increment ratio (LIR) of approximately 1. PVC Spacers measuring 2.9" (7.4 cm) diameter are initially used to apply load and fill the sedimentation column until a hanger can be applied. Spacer heights of 2,4,6,8 and 12 inches (5.1, 10.2, 15.2, 20.3, and 30.5 cm, respectively) are used as necessary. The specimen is loaded through a series of load frames (see Section 3.2.4) to the desired maximum applied stress and then unloaded to an over consolidation ratio (OCR) of 4 prior to extrusion and trimming. Figure 3-16 illustrates the resedimentation stress path.

The following sections discuss different components of the resedimentation procedure in detail. The first section describes the effect of and reason for the OCR 4 criteria. The second section gives guidelines to determine the mass of solids, water content and salinity to prepare a batch of resedimented mudrock. Subsection three describes the design of the resedimentation column with particular focus on the maximum stress level that the sedimentation column can withstand. Finally, the fourth subsection describes the four different load frames that are used to apply a range of axial stress to the resedimented specimen.

3.2.1 Effect of OCR 4

The over consolidation ratio (OCR) is the ratio between the maximum and current applied effective stresses. Ladd (1965) showed for BBC that an OCR of 4 produced a lateral stress ratio, K_o , equal to 1 providing hydrostatic effective stress conditions (Figure 3-17). K_o is defined by:

$$K_o = \frac{\sigma'_H}{\sigma'_V} \quad 3-1$$

As a result, the shear strains during sample extrusion and trimming should be minimal and the sample should be close to a perfect sampling condition.

The OCR 4 requirement for a hydrostatic effective stress condition is well known for BBC, however this condition is not well known for other soils resedimented in this study. A general relation for the lateral stress ratio K_o as a function of OCR was proposed by Ladd (1998):

$$K_o = K_{oNC}(OCR)^N \quad 3-2$$

$$N \sim 1 - K_{oNC} \quad 3-3$$

Where K_{oNC} is the K_o at OCR = 1. For clays, Ladd (1996) gives K_{oNC} as varying between 0.45 and 0.7. Therefore, given the potential variance in the normally consolidated K_o , the OCR which produces a K_o of 1 can vary from 3.28 for $K_{oNC} = 0.7$ to 4.27 for $K_{oNC} = 0.45$. Given this small variation,

uncertainties in K_{oNC} and the amount of sidewall friction, all specimens were unloaded to an OCR of 4 during resedimentation prior to trimming.

3.2.2 Mass of Solids, Water Content & Salinity

Clay powder is mixed with water and salt at a pre-determined initial water content and salinity. Phase relations are used to determine the quantity of material required to produce a final specimen with the desired dimension and void ratio.

$$M_s = \left(\frac{V_f G_s}{1 + e_f} \right) (1 + LF) \quad 3-4$$

Where M_s is the mass of soil, V_f is the final specimen volume, G_s is the specific gravity of solids, e_f is the final void ratio, and LF is the loss factor. Material loss occurs during mixing and pouring because the material sticks to the mixing bowl, beaters, vacuum cylinder and funnel. Loss factors range from 0.1 to 0.2 depending on the surface area of the equipment and the experience of the investigator.

Once the quantity of material is determined, the quantity of water and salt are determined using the water content and salinity.

Slurry resedimentation has been applied at a varying range of water contents. Burland (1990) suggested a value 1.0 to 1.5 times the liquid limit; other researchers have suggested other values ranging from 0.75 to 2.0 times the liquid limit (Sheeran and Kirzek, 1977, Allman and Atkinson, 1992, Cotecchia and Chandler, 1997, and Skempton, 1944). The initial water content affects the intrinsic compression line (Burland, 1990), and more noticeably controls the workability of the soil slurry. During resedimentation the soil must be mixed, de-aired and poured. To achieve this goal, the slurry must neither be too thin nor too thick. An ideal consistency is that of a cake mix that one would make in the kitchen; thin enough to pour, but thick enough to remain homogeneous (not separate) while pouring slowly without splatter. Abdulhadi (2009) found that mixing BBC powder at 100% water content, roughly twice the liquid limit, results in a workable slurry that has no lumps, is stable, does not exhibit particle segregation during consolidation and does not produce free water without the addition of applied forces on a slurry column.

In the MIT Geotechnical Laboratory, we have found that there is no single water content as a function of the liquid limit that works for all soils. The salinity and plasticity of the soil affect the water content required to form a stable slurry. Increasing the salinity decreases the required water content. Therefore, a rule of twice the liquid limit is used as a starting point, and the slurry water content is increased or decreased until a stable slurry as described by Abdulhadi (2009) is formed. For some soils, for example RGoM-EI, the stable water content range is very small, varying from 115 – 120 % for 80 g/L salinity, but other mudrocks are more forgiving.

Pure sea salt is mixed with distilled water using the salt mixing guide (Section 3.3.1) to create a solution of the desired salinity. Adding salt produces a flocculated soil structure and helps reduce

particle segregation during sedimentation (Abdulhadi, 2009) in addition to mimicking a natural brackish marine depositional environment. The salinity is chosen to be representative of in situ conditions or varied to study pore fluid chemistry effects.

Table 3-1 gives a summary of batching water contents and salinities used for this research. Boston Blue Clay forms in brackish water and is resedimented at a salinity of 16 g/L, half that of sea water. San Francisco Bay Mud was also resedimented at this salinity. Measurements on cores from the Eugene Island block in the Gulf of Mexico report the in situ salinity as ranging from (Losh et al, 2002) 63 g/L to 116 g/L. Horan (2011) showed insignificant changes in permeability behavior resultant from changes in pore fluid salinity beyond ~ 16 g/L; therefore 80 g/L salinity was selected for resedimentation. Leached soils (see Section 3.1.4) are at very high water contents following completion of the leaching process. These soils are air dried until a pourable consistency is reached and as a result the batching water content is unknown. Salt is not added to leached soils prior to sedimentation.

The dry mudrock powder is obtained from either a brackish (e.g. BBC) or sea salt water environment (e.g. SFBM and GoM-EI) and therefore already has a certain salt content related to the salinity and porosity of the parent deposit. Table 3-2 summarizes the salt content of the mudrock powder in g / kg. This salt content is converted to pore fluid salinity during batching using the batching water content. For example, BBC powder has 1.242 g of salt per kg of solid grains. BBC is batched at 100% water content (Table 3-1). One kilogram of batched BBC will thus have a salinity of 1.242 g of salt per kg of water, or roughly 1.2 g/L. Technically only ~ 14.8 g/L additional salinity need be added to reach 16 g/L salinity. This is a rough estimate because salinity in g/L is defined as grams of salt per liter of *solution* and accounts for the volume of the salt; it is not grams of salt per liter of water. However the small salinity added by the mudrock powder in this case is often ignored. The mudrock salt content is only considered when it will offset the salinity by $> 5 - 10$ g/L. For this research, the mudrock salt content was not considered during resedimentation and all mudrocks were mixed with salt water at the salinity given in Table 3-1.

3.2.3 Sedimentation Column Design

Sedimentation columns are 3" (7.62 cm) ID acrylic cylinders with wall thickness varying based on the final stress of the specimen to be resedimented. Three categories of sedimentation columns are used: low stress (< 2 MPa) sedimentation columns have $\frac{1}{4}$ " (0.64 cm) wall thickness and are cheaply sourced from McMaster Carr. Medium stress (up to 10 MPa) sedimentation columns have $\frac{1}{2}$ " (1.27 cm) wall thickness and are custom made by AIN Plastics (see physical properties, Table 3-7). High Stress sedimentation columns (> 10 MPa) are made of low stress, $\frac{1}{4}$ " (0.64 cm) thick cylinders that are reinforced with 0.375" (0.95 cm) steel sleeves. These are custom designed in the MIT Geotechnical laboratory to withstand the required hoop stresses generated from incremental K_0 consolidation to the desired stress level.

The hoop stress is computed using hollow cylinder theory. Both thin-walled and thick-walled theory is applied as the final wall thickness to internal radius ratio is initially unknown. The hoop

stress under thin-walled theory is valid when the wall thickness is less than $\sim 1/10$ of the internal radius, and is given by:

$$\sigma_{\theta} = \frac{\sigma_r r_i}{t} \quad 3-5$$

The thick walled hoop stress is computed at the inside diameter and is given by the simplified equation:

$$\sigma_{\theta} = \sigma_r \frac{(r_o^2 + r_i^2)}{(r_o^2 - r_i^2)} \quad 3-6$$

Where σ_{θ} is the hoop stress, σ_r is the radial stress exerted by the consolidating specimen on the inside of the sedimentation column, r_i is the inside radius of the cylinder, r_o is the outside radius of the cylinder, t is the wall thickness. In this case, σ_r is equal to the horizontal effective stress in the soil, σ'_H plus the pore pressure.

During resedimentation, an incremental load is applied and this load is taken by the pore pressure. The full increment is taken by the pore pressure and thus is added to both the axial and radial stresses. With time, the radial stress decreases as the excess pore pressure dissipates and the soil consolidates to a K_o state of stress. Therefore, the maximum radial stresses occur immediately following the application of an incremental load and the long term state of stress has a higher factor of safety.

Table 3-8 gives an example calculation using equations 3-5 and 3-6 to determine the required wall thickness and loading sequence for a steel reinforcement. This example determines the loading sequence and wall thickness required to reach a maximum applied stress of 100 MPa given the initial conditions characteristic of RBBC. A steel sleeve with 0.375" (0.95 cm) wall thickness, along with a modified loading sequence where the load increment ratio (LIR) is reduced below 1 is required to maintain hoop stresses within a factor of safety of 1.1.

Two reinforced sedimentation columns were constructed. Their capacity is 40 MPa using a standard loading sequence, or up to 100 MPa using a modified (LIR<1) loading sequence. The cylinders are constructed using 3" (7.62 cm) ID, ¼" (0.64 cm) wall thickness acrylic cylinders from McMaster Carr, reinforced with standard steel with 0.375" (0.95 cm) wall thickness. The purchased steel ID was slightly larger than the OD of the acrylic. This allowed it to easily slide over the inside acrylic cylinder and provided a volume for epoxy infilling to bond the two cylinders. Tyfo S Saturant Epoxy sourced from Fyfe Co. LLC was used to bond the steel to the acrylic; this particular epoxy has a high tensile modulus (3.18 GPa) yet boasts a long workable time (> ½ hour flowable and 2-3 days to fully cure) and a low viscosity (600 – 700 cP) making it easy to work with and pour into the tight void between the steel and acrylic cylinders.

Only the region of the sedimentation column containing the mudrock specimen needed to be reinforced. To minimize cost and weight, the steel cylinder was cut shorter than the acrylic cylinder.

Standard 4" (10.1 cm) spacers are applied at the base of the columns. Therefore, 4" (10.1 cm) was left unreinforced at the base of the cylinder, and 3" (7.62 cm) at the top to account for strain occurring at low stresses.

Once bonded to the acrylic, the reinforcing steel was sealed to protect it from corrosion due to exposure to water and salt during resedimentation. Initially the steel sleeve was painted with marine grade waterproofing spray paint, applying two coats of an undercoating and two coats of a black top coat. This did not work, and the steel quickly began to rust when placed in the sedimentation reservoirs. An effective and easy solution was to encase the steel sleeve in two overlapping 2.5" (6.35 cm) diameter, 0.025" (0.06 cm) thick triaxial rubber membranes sealed at each end with O-rings. The membranes are replaced for each specimen. Figure 3-10 is an image of the completed steel reinforced sedimentation column without the rubber membranes installed.

3.2.4 Resedimentation Load Frames

Four types of load frames are used to apply increasingly higher applied stresses: direct loading (gravity), lever arm, air pressure, and hydraulic. When combined, these load frames can be used to produce specimens with maximum applied stresses ranging from 100 kPa up to greater than 40 MPa. Table 3-9 lists the maximum capacity, gives a typical applied stress range given a 3" (7.62 cm) diameter specimen, and provides a figure reference for each load frame.

Low Stress Direct Loading (Gravity) Load Frame

The direct loading or gravity driven load frame is the most common in the MIT Geotechnical Laboratory. This load frame is capable of applying loads varying from the porous stone (0.7 N, equivalent to 69 g mass) up to 590 N (equivalent to 60 kg mass) of force to a specimen. The applied stress varies as a function of the specimen area; 3" (7.62 cm) diameter specimens are typically loaded to between 390 N and 490 N (equivalent to 40 and 50 kg mass), corresponding to ~ 100 kPa effective stress for a 3" diameter specimen, at this stage.

The direct loading load frame sits on top of the spacers protruding from the sedimentation column. The frame is installed through two holes in the table and weights are loaded onto a hanger below, shown in Figure 3-11. This is a safe and stable way to apply load to the top of the specimen. Specimens spend the most time at this low stress stage and experience the highest number of load increments at this stage.

Low-Medium Stress Gravity Load Frame

A gravity load frame is used to apply loads from 440 N (equivalent to 45 kg mass) up to ~ 8.7 kN (equivalent to 890 kg mass) corresponding to stresses of 100 to 1900 kPa using a lever arm. The specimen is placed on a table through which a frame is installed (Figure 3-12). The table and specimen are raised or lowered using a crank wheel. Lowering the reaction cross bar to push the specimen spacers against the frame increases the applied stress. A lever arm with a hanger allows

application of counter weight. When the lever arm is levelled, the mass applied to the specimen is equal to the counter weight mass (scale mass) times the lever arm factor.

The scale mass is computed by:

$$S = F_{kg}(2.2) + T \quad 3-7$$

Where S is the scale reading (lb), F_{kg} is the desired applied load (kg), and T is the scale tare reading at zero applied mass. The tare is obtained by placing the specimen on the table and measuring the load required to level the lever arm when the specimen is not in contact with the load frame.

High – Medium Stress Air Pressure Load Frame

An air pressure load frame is used to apply loads up to 45 kN (equivalent to 4600 kg mass), reaching applied effective stresses of up to 10 MPa for a 3" diameter specimen. The reservoir and sedimentation are installed on top of a piston (Figure 3-13). Air pressure forces a piston upwards and the top of the specimen contacts the top cross bar of the load frame. The load frame itself has a capacity of 89.3 kN (20,000 lbf or 9100 kg mass), however the laboratory air supply limits the maximum applied load to 45.1 kN (equivalent to 4600 kg mass).

High Stress Baldwin Hydraulic Load Frame

The Baldwin frame a 267.6 kN (60,000 lbf or 27,280 kg mass) hydraulic load frame capable of reaching applied stresses of 60 MPa given a 3" (7.62 cm) diameter specimen. However, the maximum stress applied was only 178.4 kN (40,000 lbf, equivalent to 18,182 kg mass or 40 MPa on a 3" diameter specimen) because of permeameter stress level restrictions.

The applied load is set using a pressure volume actuator (PVA) controlled by a modified version of the Laboratory Triaxial program (Appendix 2) connected to a Max 100 (shown in Figure 3-15; described in Appendix 2). The Baldwin operates using two hydraulic reservoirs. The lower reservoir is a closed system and the pressure in this reservoir is monitored to provide a measurement of the force applied to the specimen. The upper reservoir is connected to an external reservoir and filled or emptied to control the applied force. When the upper reservoir is filled, the pressure increases, causing the table to rise, pushing the specimen against the load frame, increasing the applied stress (Figure 3-14).

Using one axis of control in the triaxial program, the program monitors the pressure in the lower reservoir, which is a measure of the stress applied to the specimen. Fluid is injected or withdrawn from the upper reservoir using the PVA in order to adjust the stress applied to the specimen.

3.3 Salts

The salt concentration of the pore fluid is known to affect soil fabric structure which can in turn affect soil strength, compressibility and permeability, as well as electrical and sonic properties. Further, the physical properties of salt water are required to convert measured hydraulic conductivity to permeability. The density and viscosity of salt water are functions of the salinity and the temperature.

A salt mixing guide was created to 1) simplify the process of mixing salt solutions in the geotechnical laboratory, ensuring salinities are consistent despite varying users, temperatures, and laboratories; and 2) simplify the calculation of the required physical properties of salt water. The salinity of resedimented specimens is measured to confirm the repeatability of the process and to identify outliers, if any. This section presents the salt mixing guide and provides a procedure for testing the salinity of fine grained soils using a centrifuge.

3.3.1 Salt Mixing Guide

Salt solutions are commonly used in the geotechnical laboratory. One liter of 16 g/L salt solution has 16 g salt in a total solution volume of one liter. A common error is to mix 16 g of salt with 1 liter of water. Because salt has a non-trivial volume, the resultant solution volume is greater than 1 liter and the salinity is less than 16 g/L. A salt mixing guide was designed to address this problem. This guide is a detailed spreadsheet, consisting of calculation forms, mixing tables for commonly used salts, and relevant equations.

The density of salt water varies as a function of temperature and is a non-linear function of salinity. Simple phase relations that are commonly applied in geotechnical engineering, such as relationships between mass and volume via density and specific gravity, cannot be applied to a mixture of salt and water because molecular spacing, and hence density, vary as a function of salinity. This variation is unfortunate because masses are easier to accurately measure in the laboratory and do not require correction for daily temperature fluctuations.

Look up tables are often used to determine the density of salt water as a function of salinity and temperature. A solution to avoid needing complex tables was to trick the problem by back calculating the specific gravity of salt required to make common geotechnical phase relations (equation 3-8) work given a known density and salinity.

$$\rho = \frac{M_{salt} + M_w}{V_{salt} + V_{water}} = \frac{M_{salt} + M_w}{\frac{M_{salt}}{G_{salt}\rho_w^{20}} + \frac{M_w}{\rho_w^T}} \quad 3-8$$

Where ρ is the density of the salt solution [g/cm^3], M_{salt} and M_w are the masses [g] of salt and water, respectively, V_{salt} and V_{water} are the volumes [cm^3] of salt and water, respectively, G_{salt} is the specific gravity of the salt [dimensionless], and $\rho_w^{T,20}$ is the density of distilled water [g/cm^3] at temperature

T. For a constant salt composition, this method assigns a varying specific gravity to the solid phase. This is physically incorrect but serves as a useful mathematical trick.

We tabulated salinity vs. density data for various salts of interest and computed the specific gravity of the salt grains as a function of salinity. We assumed that the specific gravity of salt was not temperature dependent; therefore temperature dependence mirrored that of distilled water.

The specific gravity of sea salt grains is given by:

$$G_{sea\ salt} = (1.06 * 10^{-5})c^2 + (-0.0075)c + 4.17 \quad 3-9$$

Where $G_{sea\ salt}$ is the specific gravity of the sea salt and c is the salt concentration in g/L of the related solution. Data for this fit were obtained from Sharqawy et al (2010) via their MatLab code available at <http://web.mit.edu/seawater/>.

The specific gravity of pure NaCl grains is given by:

$$G_{NaCl} = (2 * 10^{-6})c^2 + (-0.0028)c + 3.4 \quad 3-10$$

Where G_{NaCl} is the specific gravity of the sea salt and c is the salt concentration in g/L of the related solution. Data for this fit were obtained from the CRC Handbook (1994).

The density of distilled water (ρ_{H2O}) as a function of temperature (T) in degrees Celcius is given by (ASTM D854):

$$\rho_{H2O} = (-4.95 * 10^{-6})T^2 + (-7.77 * 10^{-6})T + 1.00034 \quad 3-11$$

Table 3-5 is a laboratory guide for preparing 1 liter of sea salt solution at 20 degrees Centigrade, with the mass of salt and the mass of water tabulated as a function of salinity. Table 3-6 gives the same for NaCl solutions.

Sharqawy et al (2010) also provide the viscosity of sea water as a function of salinity and temperature. Linear interpolation was used to determine the viscosity as a function of salinity at fixed temperature points between 20°C and 30°C, bounding the temperature ranges of our laboratory. The data were fit to a curve of the form $\mu(T)=m(T)c^2+n(T)c+p(T)$ where $\mu(T)$ is the dynamic viscosity in g/cms and m , n , and p are the temperature dependent constants. Experiments in the MIT Geotechnical Laboratory are performed in temperature controlled enclosures where possible and the temperature of each enclosure varies based on its unique mercury switch. Therefore the viscosity - concentration relation was determined for multiple temperatures to span the needs of the laboratory. Equations 3-12 through 3-15 give the empirical relations:

20°C	$\mu = (5.0 * 10^{-9})c^2 + (2.25 * 10^{-5})c + 1.0 * 10^{-2}$	3-12
24°C	$\mu = (5.0 * 10^{-8})c^2 + (2.0 * 10^{-5})c + 9.2 * 10^{-3}$	3-13
25.3°C	$\mu = (2.3 * 10^{-8})c^2 + (1.95 * 10^{-5})c + 8.9 * 10^{-3}$	3-14
26°C	$\mu = (3.2 * 10^{-8})c^2 + (1.8 * 10^{-5})c + 8.8 * 10^{-3}$	3-15

Where μ is the dynamic viscosity of sea water in g/cms at the specified temperature and c is the concentration in g/L. Permeability anisotropy measurement is undertaken at 25.3°C and constant rate of strain measurements are performed at 25.3°C when temperature controlled, and assumed ~ 20°C otherwise. Our partner laboratory at the University of Texas at Austin performs experiments in a temperature controlled laboratory set at 24°C.

The dynamic viscosity of sea water is assumed equal to the dynamic viscosity of sea salt mixed with water to the same concentration. This assumption leads to a small degree of error when converting hydraulic conductivity to permeability. However, this error is significantly less than that resulting from ignoring the effect of salinity and temperature on viscosity and using values representative of distilled water, as was found to be the previous practice in the laboratory.

3.3.2 Salinity Measurement

A trace portable conductivity meter, model 23226-505 from VWR International was used for salinity measurements. The salinity meter was calibrated using NaCl and normalized to 1 g/L solution to obtain the relationship between measured conductivity and salinity. This calibration was performed by John Grennan (2010) by testing various concentrations of sea salt and measuring the electrical conductivity. Figure 3-18 gives the calibration curve.

There is currently no ASTM standard test method for soil salinity analysis. The following protocol is used at MIT (Martin 1982, Grennan 2010, Germaine and Germaine, 2009)

1. Tare the centrifuge tube
2. Add moist, not oven dried soil to the tube to equivalent of 15 g dry mass;
3. Record the mass of moist soil added to the tube;
4. Add distilled water to the tube to approximately 45 g total mass including previously added moist soil (approximately 200% water content, w_c);
5. Record the mass of distilled water added;
6. Fill a total of 4 tubes with soil for testing;
7. Fill an additional 4 tubes with a reference salt solution. 1 g/L sea salt solution was used;
8. Cap tube, shake soil tubes vigorously, let sit overnight in humid container;
9. Shake soil tubes in wrist action shaker for 20 minutes;

10. Place all tubes in centrifuge and run at approximately 5000 RPM for 20-30 minutes. A Damon/IEC Division, IEC HT Centrifuge was used in this study;
11. Turn on the conductivity meter and allow about 30 minutes to warm up while the tubes spin in the centrifuge. Clean two 20 mL graduated cylinders.
12. Decant the supernatant liquid from each tube into a clean 10 mL glass beaker;
13. Pair each soil tube with a reference salt solution tube (4 pairs);
14. Pour the supernatant of soil 1 into one graduated cylinder and some of the corresponding reference solution into the other graduated cylinder.
15. Clean the probe with distilled water and dry;
16. Measure the conductance of the reference salt solution;
17. Clean the probe with distilled water and dry;
18. Measure the conductance of the soil supernatant liquid;
19. Repeat from step 15 until at least 2 consistent readings of each of the soil supernatant and reference salt solution have been obtained;
20. Return the supernatant into the corresponding 10 mL glass beaker from step 12;
21. Clean all equipment, repeat from step 14 with each other the other 3 soil reference salt solution pairs;
22. Clean and store the probe and all equipment.
23. Meanwhile, obtain 4 large oven safe tares of minimum 1.5L volume. Record the mass and ID of each tare and assign one tare to each soil tube.
24. Carefully remove all soil from each tube into the assigned tare. Do so by flushing with water (tap water is OK). Add the corresponding supernat from step 12. Oven dry the tares and soils for 24 hours or until all water is completely removed.
25. Record the mass of each tare with the soil. Compute the mass of soil and water content for each tube (w_n)

Using the calibration relationship in Figure 3-18 the salinity of the supernatant liquid can be found when compared to the salinity of the reference salt solution. The use of the reference salt solution helps eliminate temperature effects. The salinity of the specimen can then be computed by multiplying the salinity measurement computed by the testing water content and dividing it by the natural water content (equation 4-2):

$$RSS = SS \times \frac{w_c}{w_n} \quad 3-16$$

Where RSS is the salinity of the test specimen (g/L), SS is the salinity of the supernatant liquid (g/L), w_c is the water content of the soil specimen during salinity measurement (%), and w_n is the natural water content of the soil specimen (%). The water content, w , is defined by:

$$w = \frac{m_w}{m_s} \quad 3-17$$

Where w is the water content (unitless), m_w is the mass of water in the specimen and m_s is the mass of solids. Equation 3-17 can be applied to compute either the natural water content (w_n) or actual water content (w_c).

The resolution of the conductivity meter is $\pm 1 \mu\text{S}/\text{cm}$, but the readings vary by approximately $\pm 5 \mu\text{S}/\text{cm}$. This corresponds to a supernatant liquid resolution of $\pm 0.003 \text{ g}/\text{L}$ using the calibration curve for NaCl. For RBBC measured at 200% water content with a natural moisture content of 20%, using equation 3-16, the resolution in the salinity measurement is $0.02 \text{ g}/\text{L}$.

The water content of the soil during salinity testing is approximately 200% given the testing methodology. Salinity measurement of resedimented specimens is performed on either the specimen trimmings or on a piece of the specimen itself after all measurements have been completed. It is well documented in the MIT Geotechnical Laboratory that there is a variation in water content between specimen trimmings and the actual specimen. The actual specimen always has a higher water content, sometimes by up to 2%. As a result, the water content of the actual specimen, back calculated using phase relations and the experimental set up data, is used to compute the salinity of the pore fluid in (g/L) of the specimen. The trimmings water content is not used in calculations.

One potential problem associated with the salinity measurement method is that the reference salt solution is centrifuged (step 10). This is done to maintain temperature consistency between the reference solution and the specimens. However, centrifuging the reference solution may cause separation of the salts and an unrepresentative measurement. Further, the use of 4 reference solution tubes (Step 13) required to balance the centrifuge may incorporate additional variability into the measurement. Finally, the measurement probe uses a 2 probe resistivity approach (further described in Appendix 3) to measure the fluid conductance and is subject to polarization. This effect is especially evident when measuring the reference solution which requires approximately 5 minutes to reach a stable reading. Further work should be done to assess the variability introduced by 1) centrifuging the reference solution and 2) using multiple reference solution tubes, as well as to assess whether electrode polarization affects the salinity measurement.

Errors in the measured salinity affect formation factor calculations and are further discussed in Chapters 5 and 6.

3.4 Index Properties

This section presents the index properties of the materials where available. All index properties have been tested as per the ASTM standard method unless otherwise stated.

Clay size and clay mineralogy can be easily confused. In this work, 'clay' refers to clay size, defined as the fraction of particles $< 2\mu\text{m}$. Clay mineralogy will be used to refer to the clay minerals (such as Illite, Smectite, Kaolinite, etc.). Mineralogy measurements measure both the whole rock and clay fraction mineralogy. In the whole rock mineralogy, specific minerals are targeted. These minerals

may or may not be clay minerals. In the clay fraction mineralogy, only those particles that are clay size ($<2\mu\text{m}$) are measured, and the percentage of specific clay minerals are measured.

Mineralogy was determined by Macaulay Scientific Consulting Ltd. Analysis of the bulk mineralogy was performed using X-ray powder diffraction (XRDP) analysis. The clay fraction ($<2\mu\text{m}$) was separated via timed sedimentation and were glycolated, heated and then air dried prior to XRDP analysis. The cation exchange capacity (CEC) was measured by copper adsorption by the SUNY lab at the University of Buffalo. The external specific surface area (SSA) was measured by gas (N_2) adsorption using the BET method by Micromeritics. The total SSA was measured using the methylene blue spot test method, and the internal SSA was computed as the difference between the total and external SSA. The CEC and SSA methods, results and data reports are provided in Appendix 5 along with a discussion of the validity of the results.

Table 3-2 summarizes the Atterberg limits, clay fractions, specific gravities and Unified Soil Classification System (USCS) classifications of all materials, where available. Table 3-3 summaries the clay fraction mineralogy where available, and Table 3-4 summaries the specific surface area measurements. Figure 3-19 plots all mudrocks on the Casagrande plasticity chart, and Figure 3-20 compares the grain size distributions measured via sedimentation analysis. Figure 3-21 is a triangle plot comparing the clay fraction obtained by sedimentation analysis for all mudrocks. Figure 3-22 is a triangle plot comparing the clay fraction mineralogy obtained via XRD analysis where available. Triangle plots were generated using an excel file prepared and described by Graham and Midgley (2000). The source of information for each measurement is given in Table 3-1, and is also described in the following sections.

3.4.1 Resedimented Boston Blue Clay

Resedimented Boston Blue Clay (RBBC) has been extensively tested at MIT. Boston Blue Clay was deposited in the Boston, MA region about 12,000 years ago and is a marine clay (Barosh et al, 1989). Series IV BBC powder is used in this study.

Table 3-10 presents the index properties of Series I - III BBC powder (after Cauble, 1996) and Table 3-11 presents the index properties of Series IV BBC Powder (after Abdulhadi, 2009). Abdulhadi (2009) measured the Atterberg limits as: plastic limit 23%, liquid limit 46% and plasticity index 23%. The specific gravity is measured as 2.780. The particle size distribution of RBBC was re-measured for this research and is given in Figure 3-20. The clay fraction is 53%, and the clay fraction is dominated by 92% Illite with only 1.4% Smectite and 7% other minerals. The soil is classified as a-low plasticity clay (CL) according to the Unified Soil Classification System (USCS). The CEC is 10.7 meq / 100 g and the external, internal, and total SSA are 24, 25, and 49 m^2/g , respectively. The dry soil powder has 1.2 g of salt per kg of dry soil. Leaching via the dialysis tubing method (described in section 3.1.4) reduced the salt content of the powdered soil to 0.08 g/kg and increased the total SSA to 60 m^2/g .

3.4.2 Min-u-Sil 40 and 39% Clay RBBC

Min-u-Sil 40 is a commercially available silt sized silica product with only 5% clay sized particles. To reduce the clay fraction, RBBC powder was admixed with Min-u-Sil 40 in the proportion of 68% RBBC to 32% Min-u-Sil 40, by mass. The resultant mixture has a clay fraction, and is called '39% clay RBBC'. The Atterberg limits of this mixture were not measured. The particle size distributions of both the pure Min-u-Sil 40 and the 39% Clay RBBC mixture are given in Figure 3-20. The specific gravity of Min-u-Sil 40 is 2.67 and that of the 39% clay RBBC mixture is 2.75. The external SSA was not measured, but the total SSA is 43 m²/g, less than that of BBC.

3.4.3 Resedimented Gulf of Mexico Clay – Eugene Island Block 330

Resedimented Gulf of Mexico Clay from the Eugene Island Block 330 (RGoM-EI) is being extensively studied by the UT Geofluids Initiative due to its availability and representativeness of the Gulf of Mexico Soils. Julia Schneider (2011) measured both the Atterberg limits and the particle size distribution. The plastic limit is 24%, the liquid limit 87%, and the plasticity index 63%. Figure 3-20 gives the particle size distribution. The clay fraction is 65%, much higher than RBBC, and is dominated by 74% Smectite with only 21% Illite, and 5% other minerals. The specific gravity is 2.775, very close to that of RBBC. Both the CEC and the SSA are higher than BBC, measuring 32.4 meq / 100 g and 43 m²/ g, respectively. The CEC is 32.4 +/- 1.7 meq / 100 g and the external, internal, and total SSA are 43, 224, and 267 m²/g, respectively. RGoM-EI has significantly more internal SSA than BBC, likely due to the higher Smectite. The salt content of RGoM-EI has been measured by multiple researchers and varies between 7.9 g/kg (Brian Fahy, MIT) and 10.5 to 11.4 g/kg (Will Betts, University of Texas at Austin). Leaching via the centrifuge method (Horan, 2012) reduced the salt content of the powdered soil to 0.8 g/kg.

3.4.4 Resedimented San Francisco Bay Mud

Series II San Francisco Bay mud is the dried and re-ground material previously studied by Kontopoulos (2012). The original material is a blend from numerous tubes of in-situ material from the San Francisco Bay area. Kontopoulos (2012) measured the particle size distribution (Figure 3-20) and determined the clay fraction to be 52%, roughly the same as RBBC. These data are assumed representative and were not re-measured after the material was re-ground to form series II RSFMB. Brendan Casey of MIT measured the Atterberg Limits as: plastic limit 32%, liquid limit 60% and plasticity index 29%. The clay mineralogy has roughly equal parts Illite (47%) and Smectite (45%) with 8% other minerals. SFBM falls between BBC and GoM-EI in the mineralogy triangle plot (Figure 3-22). The CEC is intermediate between BBC and GoM-EI, measuring 28.1 meq / 100 g. The external, internal, and total SSA are 21, 100, and 121 m²/g, respectively. The external SSA is lower than that of BBC, but the internal and total SSA are intermediate between BBC and GoM-EI, as expected based on Smectite content. The discrepancy in external SSA is potentially a result of a small sample size and the presence of millimetre sized particles in the powder leading to

inhomogeneities. The dry soil powder has 3.8 g of salt per kg of dry soil. Leaching via the dialysis tubing method (described in section 3.1.4) reduced the salt content of the powdered soil to 0.1 g/kg.

Table 3-1: Resedimentation water content and salinity values for different mudrocks

Material	Water content	Salinity
	%	g/L
RBBC	100	16
Leached RBBC	pourable	0
39% Clay RBBC	86	16
RSFBM	90	16
Leached RSFBM	pourable	0
RGoM-EI	120	80

Notes:

- 1) RSFBM was initially batched at 0.4 g/L. Future batches should be made at 16 g/L.
- 2) Leached batches were air dried following the leaching process until a pourable consistency was reached. Exact water contents are unknown.

Table 3-2: Mudrock Index Properties

Material	Series	Atterberg Limits			Specific Gravity	Clay Fraction	Cation Exchange Capacity ^b meq / 100 g	Salt	
		Liquid Limit	Plastic Limit	Plasticity Index				Regular g/kg	Leached State g/kg
BBC	IV	46 ^a	23 ^a	23 ^a	2.780	53%	10.7	1.242	0.08
39% Clay BBC	IV	N/A	N/A	N/A	2.750	39%	N/A	N/A	N/A
GoM-EI	I	87 ^b	24 ^b	63 ^b	2.775	65% ^b	32.4 +/- 1.7	7.9-11.4 ^{e,g}	0.8 ^g
Min-u-Sil	N/A	N/A	N/A	N/A	2.670	5%	N/A	N/A	N/A
SFBM	II	60 ^c	32 ^c	29 ^c	2.690 ^c	52% ^d	28.1 +/- 2.4	3.84	0.14

Note:

The letters indicate data that were obtained from other sources or other personnel, as described below:

- a) Abdulhadi, 2009
- b) Julia Schneider, University of Texas at Austin
- c) Brendan Casey, MIT
- d) Nick Kontopoulos, MIT (2012)
- e) William Betts, University of Texas at Austin
- f) Richard Baker Harrison Ltd
- g) Brian Fahy, MIT
- h) Appendix 5

Table 3-3: Clay Mineralogy of < 2 μ m size fraction

Mudrock	Mineralogy Summary				Additional Data	
	Illite	Smectite	Other	Total	% Illite - Smectite	Expandability
	%	%	%	%	%	%
BBC	92	1	7	100	28	5
GoM-EI	30	65	5	100	87	70-80
SFBM	47	45	8	100	81	50-60

Table 3-4: Specific Surface Area (SSA) measurements

Mudrock	(a) External SSA BET Method	(b) Internal SSA Difference (c-a)	(c) Total SSA MB Spot Test Method
	m ² /g	m ² /g	m ² /g
BBC	24	25	49
39% Clay BBC	N/A	N/A	43
Leached BBC	N/A	N/A	60
SFBM	21	100	121
GoM-EI	43	224	267

Table 3-5: Laboratory Salt Solution Mixing Guide - Sea Salt Solution

MIT Geotechnical Laboratory
Sea Salt Solution Mixing Guide

Temperature 20 deg C
Density of Pure Water 0.99820 g/cm³ Volume: 1 L

Salt Concentration = Mass of Salt	Effective Density of Salt	Density of Salt Water at 20 ° C	Mass of Water
g/L	g/cm ³	g/cm ³	g
1.00	4.163	0.999	997.96
4.00	4.140	1.001	997.24
10.00	4.096	1.006	995.77
16.00	4.053	1.010	994.26
20.00	4.024	1.013	993.24
36.00	3.914	1.025	989.02
64.00	3.733	1.045	981.09
80.00	3.638	1.056	976.25
100.00	3.526	1.070	969.89
128.00	3.384	1.088	960.44
200.00	3.094	1.134	933.68
256.00	2.945	1.167	911.42

Notes and Assumptions

- 1) Table values are computed for a temperature of 20°C.
- 2) We compute the effective salt density a function of salinity.
This makes the density of salt water an additive function of salt and water components.

Equations:

- 1) Density of Pure Water (ρ) as a function of temperature (t):

$$\rho = (-4.95 * 10^{-6})T^2 + (-7.77 * 10^{-6})T + 1.00034$$

- 2) Effective density of Sea Salt (ρ) as a function of salinity (c):

$$\rho = (1.06 * 10^{-5})c^2 + (-0.0075)c + 4.17$$

Table 3-6: Laboratory Salt Solution Mixing Guide - NaCl Solution

MIT Geotechnical Laboratory

NaCl Sodium Chloride Solution Mixing Guide

Temperature 20 deg C
 Density of Pure Water 0.99820 g/cm³ Volume: 1 L

Salt Concentration = Mass of Salt	Effective Density of Salt	Density of Salt Water at 20 ° C	Mass of Water
g/L	g/cm ³	g/cm ³	g
1.00	3.397	0.999	997.91
4.00	3.389	1.001	997.03
10.00	3.372	1.005	995.24
16.00	3.356	1.009	993.45
20.00	3.345	1.012	992.24
36.00	3.302	1.023	987.32
64.00	3.229	1.042	978.42
80.00	3.189	1.053	973.16
100.00	3.140	1.066	966.41
128.00	3.074	1.085	956.64
200.00	2.920	1.130	929.83
256.00	2.814	1.163	907.40

Notes and Assumptions

- 1) Table values are computed for a temperature of 20°C.
- 2) We compute the effective salt density a function of salinity.
 This makes the density of salt water an additive function of salt and water components.

Equations:

- 1) Density of Pure Water (ρ) as a function of temperature (t):

$$\rho = (-4.95 * 10^{-6})T^2 + (-7.77 * 10^{-6})T + 1.00034$$

- 2) Effective Density of NaCl (Sodium Chloride) Salt (ρ) as a function of salinity (c):

$$\rho = (2 * 10^{-6})c^2 + (-0.0028)c + 3.4$$

Table 3-7: AIN Plastics acrylic data sheet

Physical Properties of Townsend Cast Acrylic

PROPERTY	TEST METHOD	VALUE
Mechanical Properties:		
Specific Gravity	ASTM D792	1.17 - 1.20
Tensile Strength, min. psi 73° F	ASTM D638 (Test speed B)	6,038
Tensile Elongation at Rupture, min. % 73° F	ASTM D638 (Test speed B)	2.7
Impact Strength (Izod II lbs. per inch notch)	ASTM D256	0.4 - 0.5 or 0.3
Tensile Modulus of Elasticity, PSI 73° F	ASTM D638	350,000 - 500,000
Flexural Strength, PSI 73° F	ASTM D790	12,000
Compressive Strength, 10% Deflection, PSI	ASTM D695	11,000 - 19,000
Hardness, Rockwell, 73° F	ASTM D785	M80 - M100
Electrical Properties:		
Volume Resistivity OHM/cm	ASTM D251	10 ¹⁴
Dielectric Strength short time 125° thickness, Volts/Mil	ASTM D149	450 - 550
Dielectric Strength step by step 125° thickness, Volts/Mil	ASTM D149	350 - 400
Dissipation (Power) Factor 60 Cycles	ASTM D150	0.05 - 0.06
10 ³ Cycles	ASTM D150	0.04 - 0.06
10 ⁶ Cycles	ASTM D150	0.02 - 0.03
Arc Resistance, sec	ASTM D495	No Track
Optical Properties:		
Clarity - Light transmission %	ASTM D791	92
Index of Refraction at 23° C	ASTM D542	1.491
Spectral Transmittance at 290-330 nm, 0.250 in. thickness max. percent	LP-391-D (4.3.7)	250 - 47.2 300 - 55.5 310 - 60.4 320 - 62.8 330 - 64.9
Thermal Properties:		
Coefficient of Linear Thermal Expansion, in./in./°F	ASTM D696	3 - 5 x 10 ⁻⁵
Continuous Service Temperature in Air (Maximum), °F		150
Thermal Conductivity 10 ⁻⁴ cal/sec/cm. ² /°C/CM	ASTM D177	4 - 6
Deflection Temperature under load of 264 psi, min. °C	ASTM D648	65
Flammability Property:		
Burning Rate	ASTM D635	Slow
Flammability Property	ASTM D635	1.75
Burning rate in per min. max.		
Stability Property:		
Water absorption, 24 hrs., 1/8" thickness, % max.	ASTM D570	4
Chemical Properties:		
Resistance to	ASTM D543	
Weak Acids		Practically No
Strong Acids		Attacked only by high concentration oxidizing acids
Weak Alkalies		Practically No
Strong Alkalies		Attacked
Organic Solvents		Scrubable in ketones, esters, aromatic chlorinated hydrocarbon

The above property data represent typical average values and will vary on specific production lots. They should be used only as a guide for application of this specification purposes.

Flammability data: Townsend Cast Acrylic Rod and Tube meet the requirements of FEDSPEC SPEC LP-051-D ITEM B & C.

This information based on experience is in line with accepted engineering practice and is believed to be reliable. However, we do not warrant the suitability of this material in the listed applications, unless specified for that material in a particular purpose. This data can vary on the use of the material.

Table 3-8: Reinforced sedimentation column design: Sample calculation

Amy Adams

**Determination of Required Loading Sequence
and Maximum allowable Hoop Stress In
AIN Plastic 3" ID 3.5" OD Acrylic Resedimentation Tubes
MIT Geotechnical Laboratory**

Tube Area	45.6036731	cm ²
Starting Stress	100	ksc
Starting Load	4560.36731	kg
Assumed Ko	0.5	(actually 0.48)
1 ksc=	98.07	kPa
1 kPa=	0.14503774	psi
1 ksc=	14.223851	psi
po	0	psi
ri	1.75	inches
t	0.375	inches
ro	2.125	inches
σt max	50000	psi
FS	1.1	

$$\frac{(r_o^2 + r_i^2)}{(r_o^2 - r_i^2)} = 5.215054$$

OD of 3", 1/4" thick tube

OD of Steel Tube

AIN Tubes data sheet = 6038

Steel tube = 60000 psi

Sequence	Hoop Stress							
	Axial Stress		Radial Stress (pi)			Thin Walled		
	Δσa	σa	σa	σr	σr	σt	FS	OK?
	ksc	ksc	psi	ksc	psi	psi		
Start	0	100	1422	50	711	3319	15.1	
Increment	100	200	2845	150	2134	9957	5.0	
Equilibrated	0	200	2845	100	1422	6638	7.5	
Increment	200	400	5690	300	4267	19913	2.5	
Equilibrated	0	400	5690	200	2845	13276	3.8	
Increment	200	600	8534	400	5690	26551	1.9	
Equilibrated	0	600	8534	300	4267	19913	2.5	
Increment	200	800	11379	500	7112	33189	1.5	
Equilibrated	0	800	11379	400	5690	26551	1.9	
Increment	200	1000	14224	600	8534	39827	1.3	
Equilibrated	0	1000	14224	500	7112	33189	1.5	

Sequence	Hoop Stress							
	Axial Stress		Radial Stress (pi)			Thick Walled		
	Δσa	σa	σa	σr	σr	σt	FS	OK?
	ksc	ksc	psi	ksc	psi	psi		
Start	0	100	1422	50	711	3709	13.5	
Increment	100	200	2845	150	2134	11127	4.5	
Equilibrated	0	200	2845	100	1422	7418	6.7	
Increment	200	400	5690	300	4267	22253	2.2	
Equilibrated	0	400	5690	200	2845	14836	3.4	
Increment	100	500	7112	300	4267	22253	2.2	
Equilibrated	0	500	7112	250	3556	18545	2.7	
Increment	50	550	7823	300	4267	22253	2.2	
Equilibrated	0	550	7823	275	3912	20399	2.5	
Increment	50	600	8534	325	4623	24108	2.1	
Equilibrated	0	1000	14224	500	7112	37089	1.3	

Table 3-9: Resedimentation Load Frame Specifics

Load Frame	Type	Load Capacity		Typical Applied Stress Range (3" diameter specimen)	Figure Reference
		kg	kN		
Low Stress (gravity)	Gravity	40 – 60	0.4-0.6	0-100 kPa	Figure 3-11
Low-Medium Stress	Gravity	890	8.73	100 – 1900 kPa	Figure 3-12
High – Medium Stress	Air Pressure	4 600	45.1	1.5 - 10 MPa	Figure 3-13
High Stress Baldwin	Hydraulic	27 280	267.6	10 – 40 MPa	Figure 3-14

Table 3-10: Index properties of RBBC Series I to III (after Cauble, 1996)

Year	Researcher	Series	Source Batch	G _s	w _i	w _p	l _p	Clay Frac. <2µm (%)	Salt (g/l)	
1961	Bailey	Ia	MIT 1139	2.77	30.0	17.5	12.5	40	2-3	
					34.7	17.7	17.0		35	
1963	Jackson				36.2	19.5	16.7		16.7	
1964	Varallyay		S4		32.6	19.5	13.1	35	16.8	
			S5		33.3	20.4	12.9			
			S6		32.8	20.3	12.5			
1965	Ladd, R.S.		Ib		2.77	45	22	23		16
1965	Preston			S1	2.77	45.6	23.4	22.2	35	24
1966	Branthen			S2	2.77	45.4	23.1	22.3		22
1967	Dickey					34.5	23.9	19.6		
1970	Kinner	100		2.78	43.5	19.6	23.9	50		
		150			43.5	19.6	23.9			
		200			38.1	17.8	20.3	52	8	
		300			39.7	21.6	18.1		10	
		400			39.4	21.3	18.1	52	10	
		800			41.5	19.5	22.0	48	16	
		900		41.2	18.7	22.5	54	16		
		1000		41.1	19.5	22.6	58	16		
		1100		42.0	20.6	21.4		16		
		1200		40.2	18.6	21.6	48	16		
		M101		40.7	19.6	21.1	52			
		M104		40.3	19.6	20.7				
		M107		41.3	19.6	21.7				
		M200		42.3	18.5	23.8	52			
M400		39.8	18.9	20.9	47					
1971	Ladd et al.	160	2.78	38.1	17.8	20.3		8		
		1300		42.1	22.1	20.0		16		
		1500		43.8	20.6	23.2		16		
1984	Bensari	II	105	2.75	47.6	23.3	24.3		16	
			111	2.75	47.1	24.9	22.2		16	
1985	O'Neill		105-112	2.78	41.3	22.1	19.2	52	16	
1989	Seah	III	200-207	2.78	45.2	21.7	23.5	58	16	
1991	Sbeahan		210,214, 216		45.6	21.4	24.2			
1993	Cauble		217-218	2.78	37.0	21.3	15.7			
1994	Santagata		219-220		40.4	20.9	19.5			

Table 3-11: Index properties of RBBC Series IV (after Abdulhadi, 2009)

Year	Researcher	Batch	w _l (%)	w _p (%)	I _p (%)	G _s	Clay fraction (%)	Salt g/L
1994	Zriek	powder	46.4	22.5	23.9	2.78	60.1	
1994	Sinfield	powder 402 403	47.0 46.8 47.2	23.8 22.4 23.3	23.2 24.4 23.9	2.79		
1996	Cauble	powder 401 404 405 406 407 408 409 410 411 413 414 415 416 417	46.7 47.4 45.2 45.0 44.6 44.7 45.4 46.6 46.7 45.5 46.3 46.1 46.7 47.2	21.8 21.9 22.1 22.6 23.0 23.9 24.0 25.0 24.5 24.3 24.3 24.7 24.0 24.5	24.9 25.5 23.1 22.4 21.6 20.8 21.4 21.6 22.2 21.2 22.0 21.4 22.7 22.7	2.81	57.6 57.8 58.7 56.8 56.9	10.4 10.0 12.5 13.1 10.1 13.0 13.4 10.2 9.7 12.0 10.5 12.9 13.2
1998	Santagata	418 419	47.8	23.3	24.5			
1998	Force	420	45.2	22.6	22.6			
2009	Abdulhadi	powder	46.5	23.5	23.0	2.81	56.0	11.1

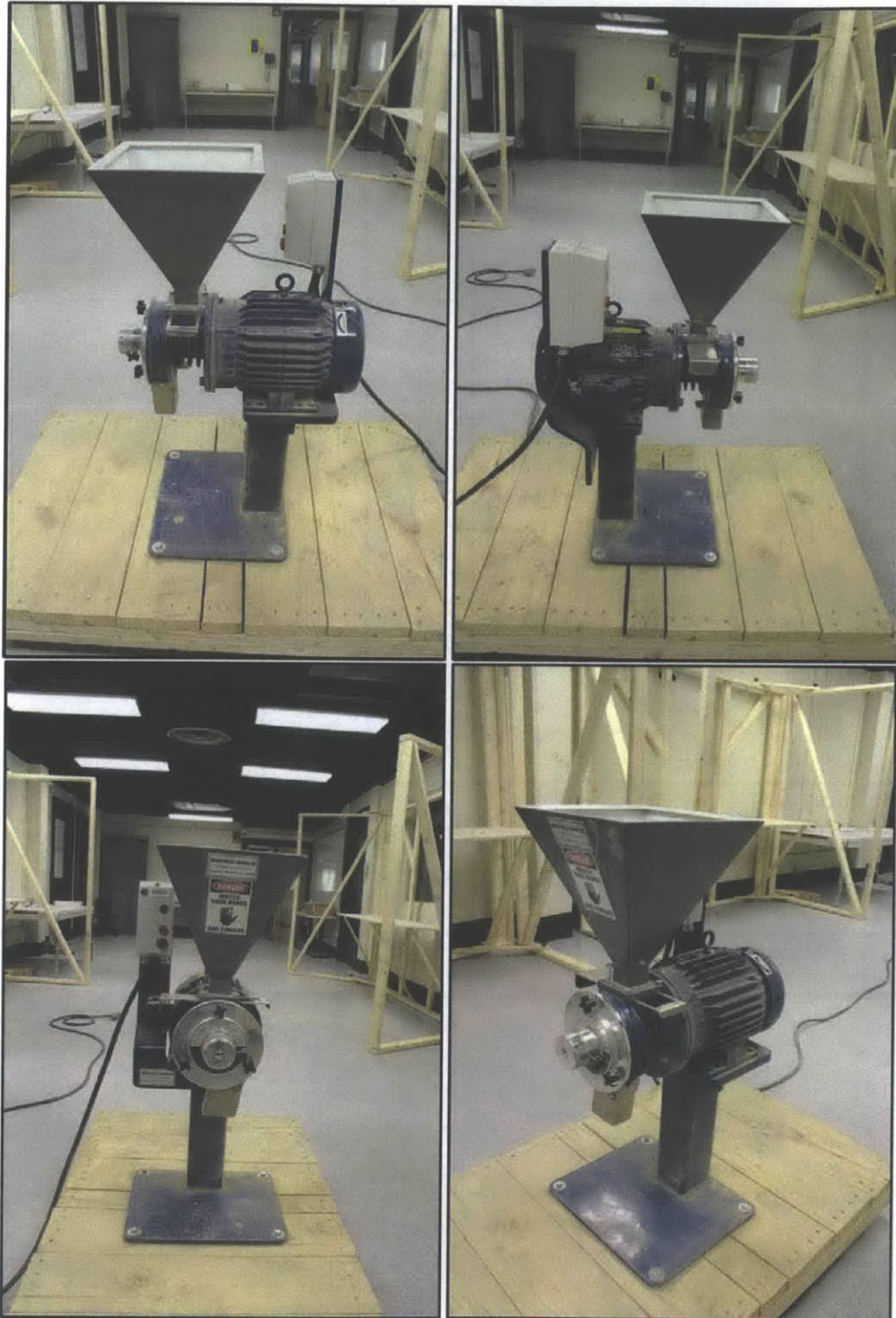


Figure 3-1: GPX Disc Grinder (Horan, 2012)

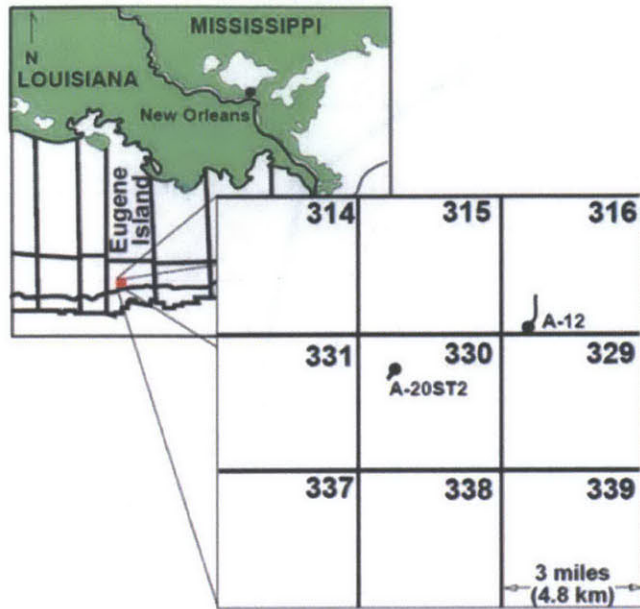


Figure 3-2: Index map showing location of wells A-12 and A-20 (after Stump & Flemings, 2002)



Figure 3-3: Leaching via dialysis tubing

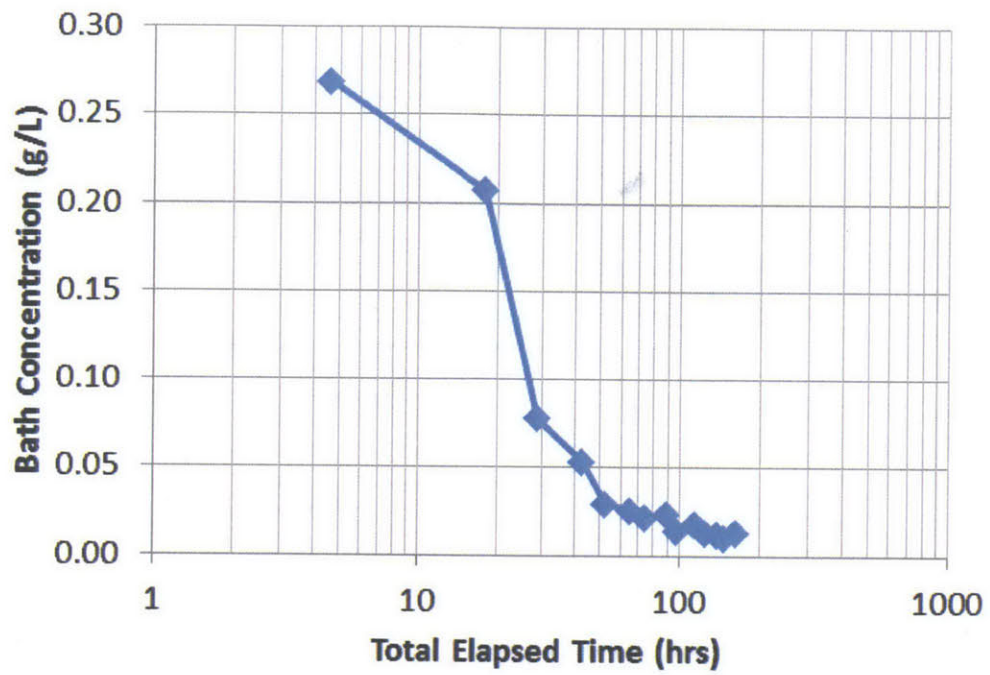


Figure 3-4: Bath concentration vs. time curve during the leaching process for RBBC



Figure 3-5: Resedimentation: Mixing dry soil powder with salt water in an electric mixer



Figure 3-6: Resedimentation: Transferring the sediment slurry to a vacuum cylinder for de-airing



Figure 3-7: Resedimentation: Pouring the sediment slurry into 3" ID settling columns using a funnel method



Figure 3-8: Resedimentation: Configuration of base porous stone and filter paper in sedimentation column

850g kaolinite 1225 g salt soln.
 106 g H₂O + 19 g salt
 16 g/L salt

MIT GEOTECHNICAL LABORATORY

Tested By: ALA
 Start Date: Dec 27/10
 Consolidometer: Pot
 Area (cm²): 3"
 Reference Height (mm): 80 + 0.65 cm
top 0.6 cm

Resedimentation Sample Data Sheet

LVDT Cal Factor (cm/vv): N/A
 Data Acq Channels: LVDT: N/A Vin: N/A

Project: ALAThesRS
 Sample No.: RS166
 Source Material: Kaolinite
 Water Content: 144%
 Salt Conc.: 16 g/L

INC No.	Mass Added (g or kg)	Mass Type	Total Mass (g or kg)	Starting		Ending		Data Acq. File Name	Remarks
				Date	Time	Input (volts)	LVDT (volts)		
s			stone						
1	304 g	2" spacer	304 g	Dec 27/10	11:00	-	-		Pinous stone
2	304 g	2" spacer	608 g	Jan 1/11	13:35	-	-		ref top + 5cm
3	608 g + 1241 g	8" spacer	1241 g	Jan 7/11	11:45	-	-		ref top + 5cm
4	1 Kg	weight	2241 g	Jan 11/11	16:42	-	-		ref top - 10cm + 20.4cm
5	2 Kg	weight	4.2 Kg	Jan 14/11	18:05	-	-		
6	4 Kg	weight	8.2 Kg	Jan 19/11	11:00	-	-		
7	tot = 14 Kg	weight	15.2 Kg	Jan 26/11	17:00	-	-		
8	tot = 30 Kg	weight	31.2 Kg	Jan 31/11	10:20	-	-		
9	tot = 45 Kg	weight	46.2 Kg	Feb 2/11	12:00	-	-		
10	tot = 51.5 Kg	weight	22.7 Kg	Feb 5/11	10:55	-	-		
11	tot = 10 Kg	weight	11.2 Kg	Feb 8/11	11:50	-	-		
12				Feb 11/11	10:30	-	-		
13									
14									
15									

Final Extruded Height (mm): _____

Comments: _____

Figure 3-9: Sample resedimentation log



Figure 3-10: Steel reinforced sedimentation tube (without protective rubber membranes)

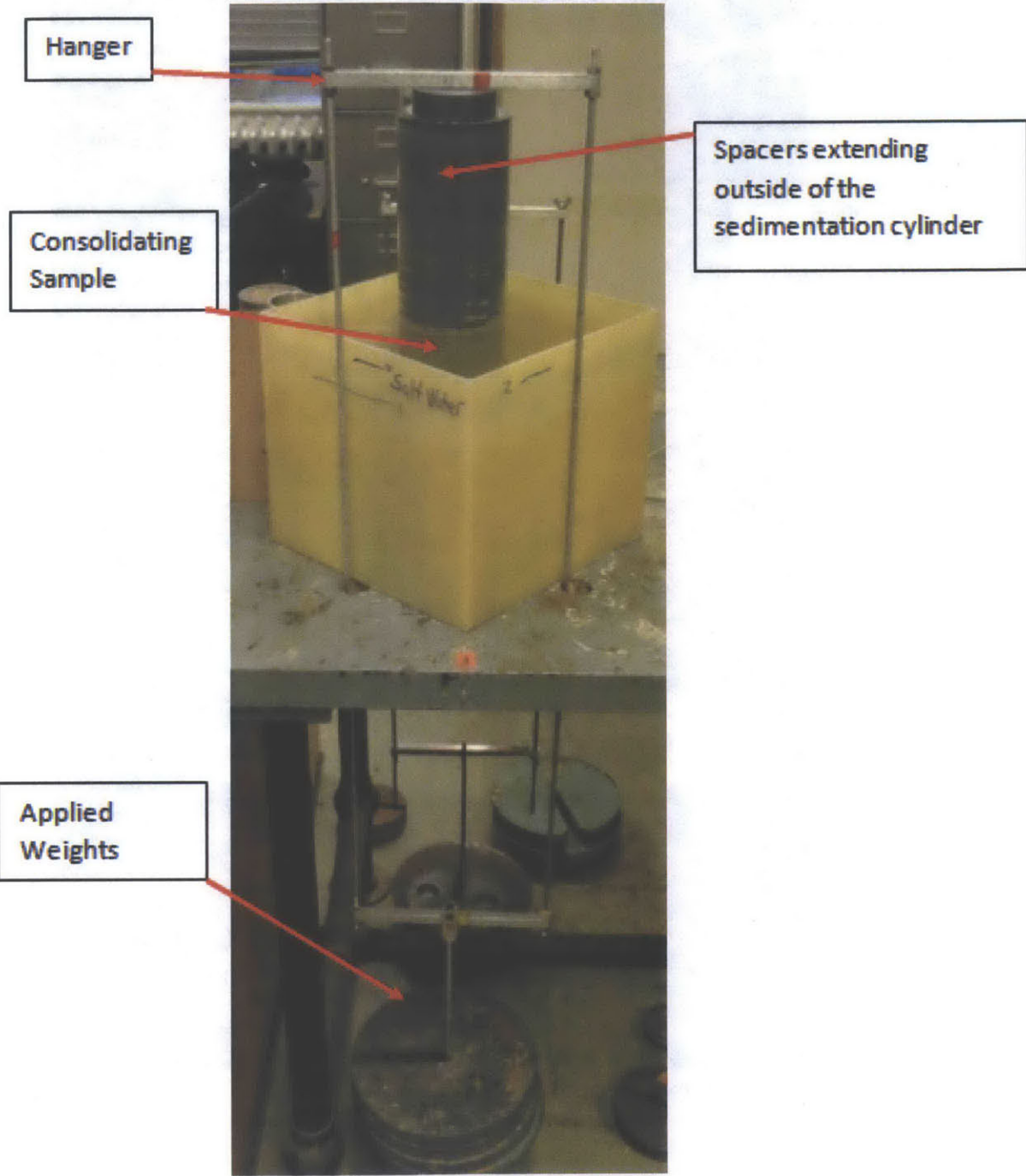


Figure 3-11: Direct loading (gravity) load frame with hanger setup

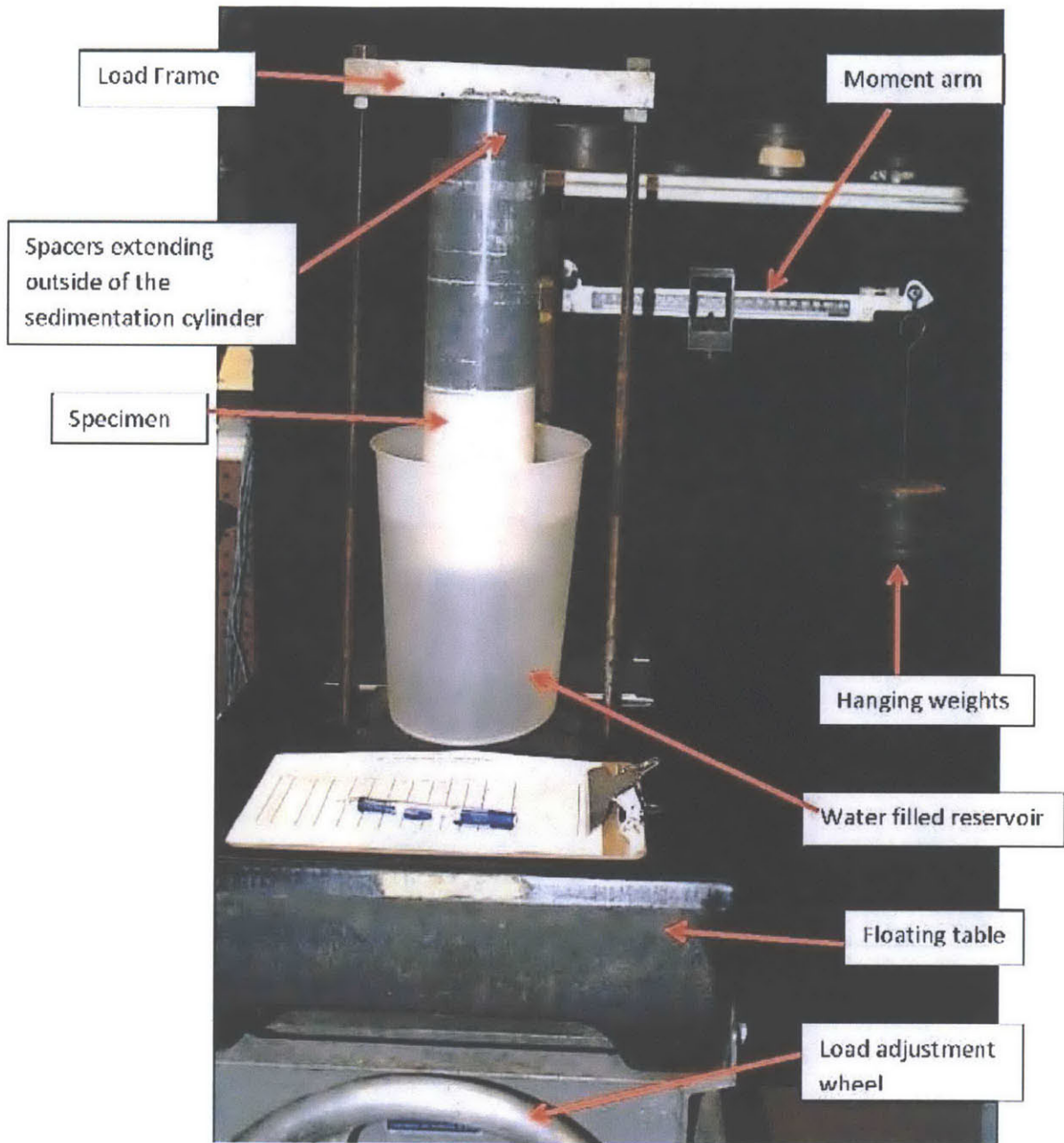


Figure 3-12: Low- medium stress moment arm load frame

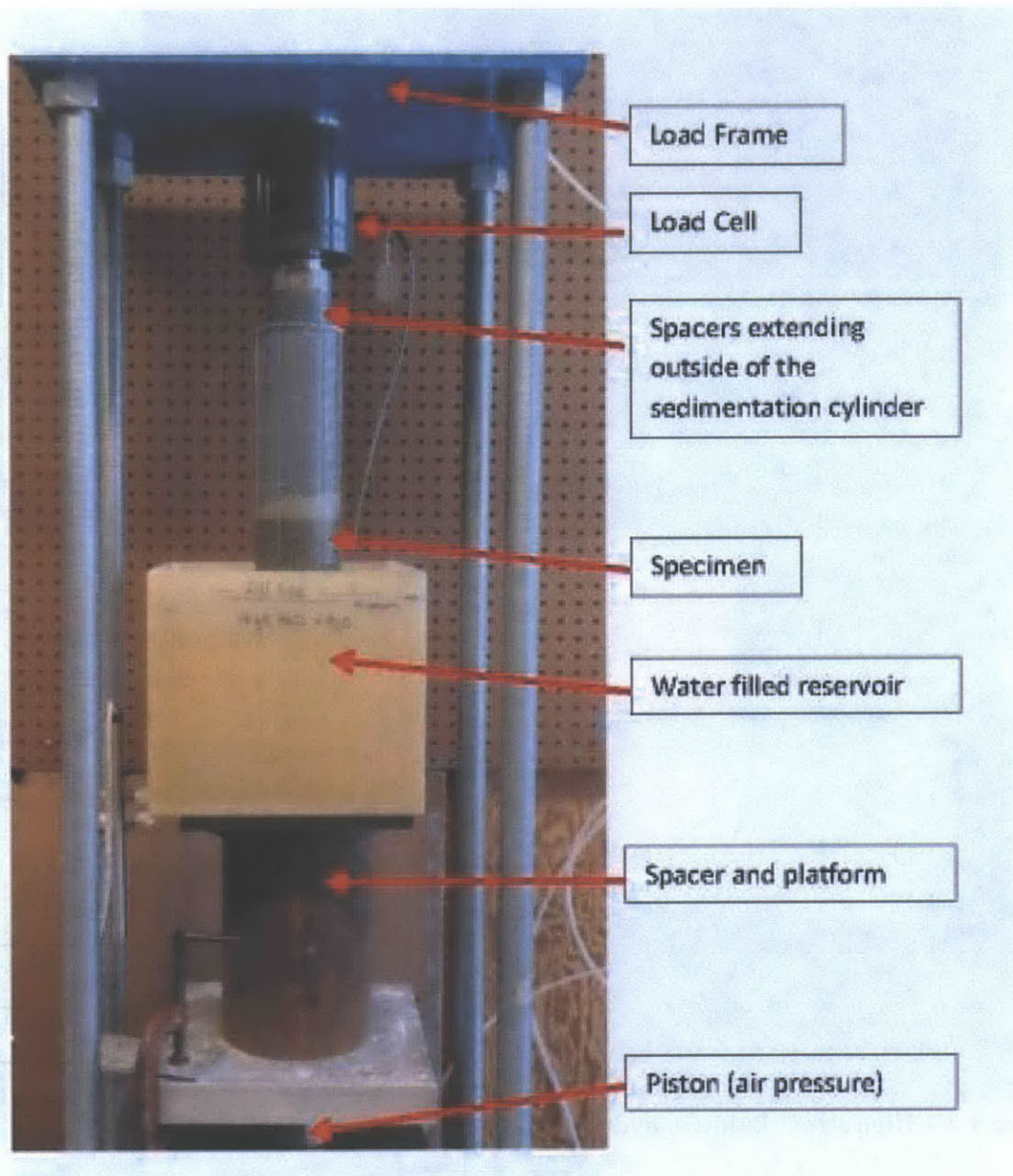


Figure 3-13: Medium - high stress air pressure load frame

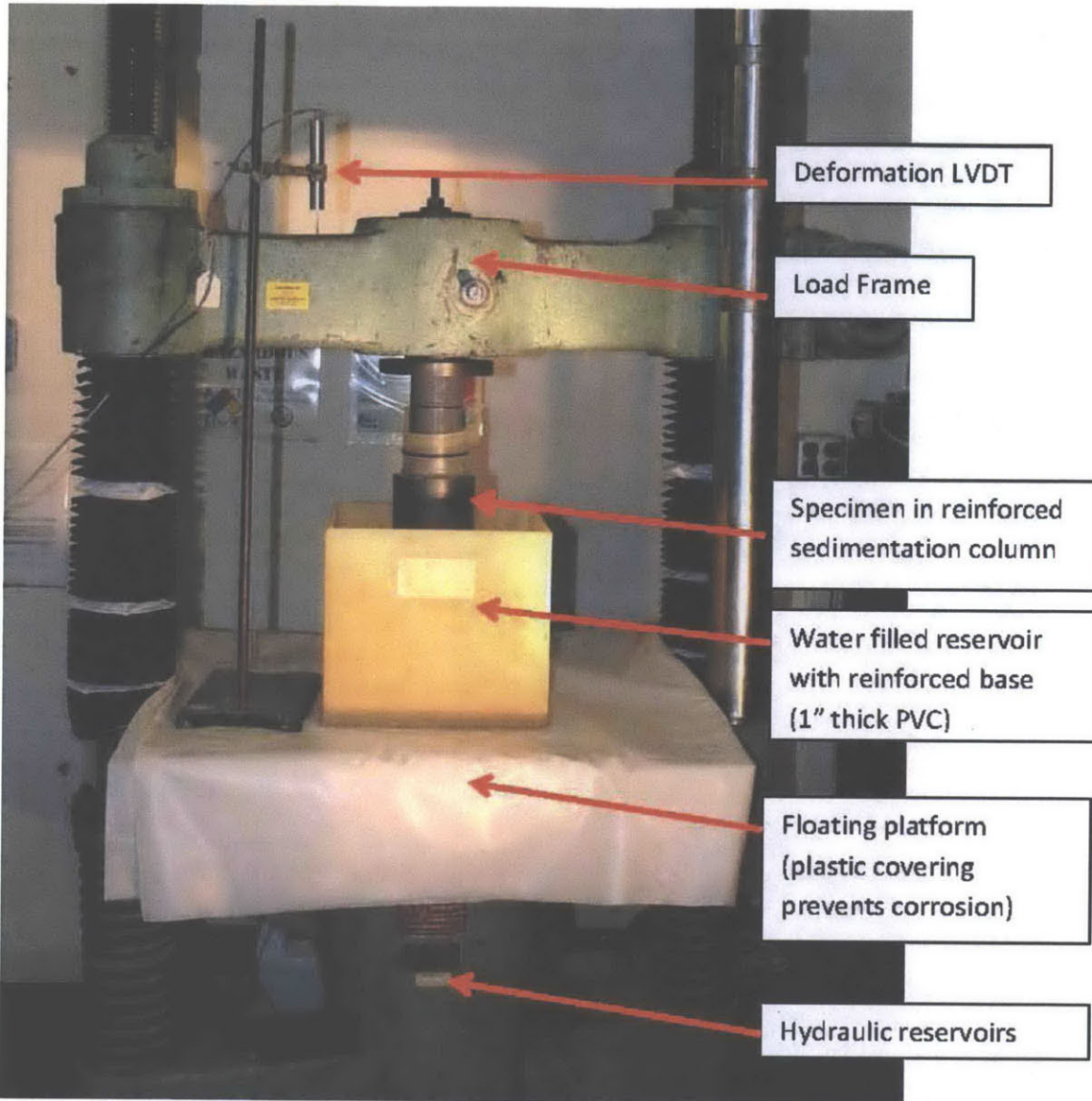


Figure 3-14: High stress Baldwin hydraulic load frame



Figure 3-15: High stress load frame control cart with computer, MAX 100 and PVA

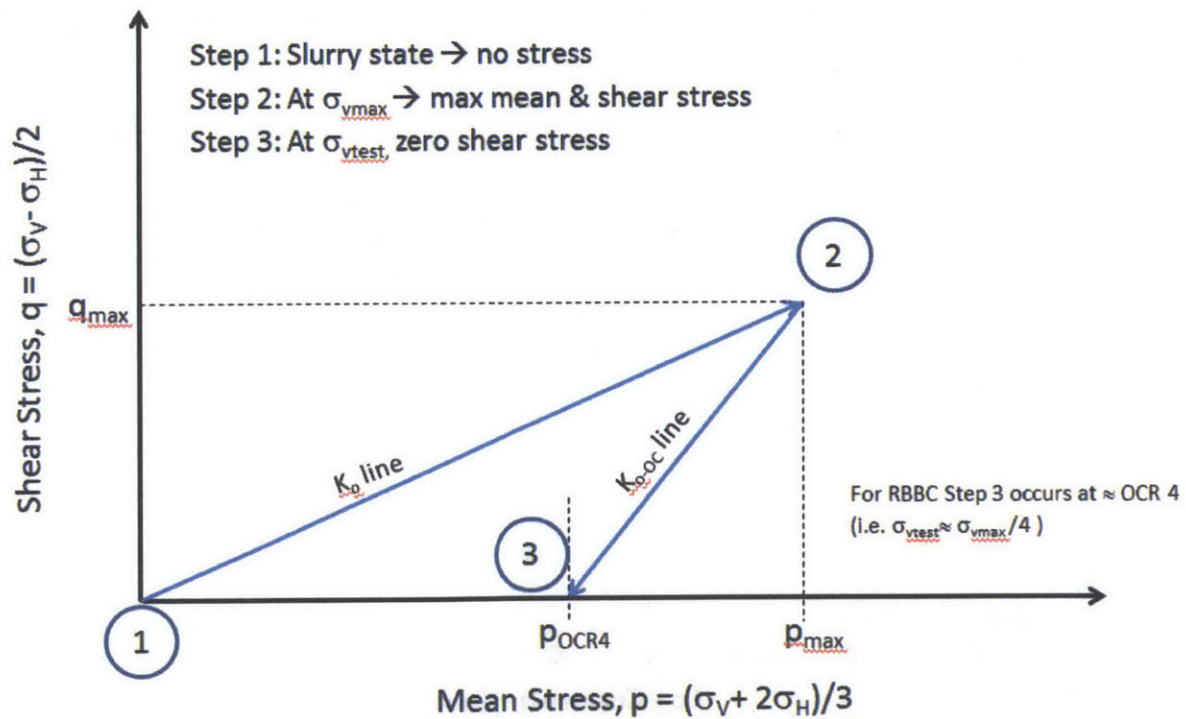


Figure 3-16: Illustrative resedimentation stress path

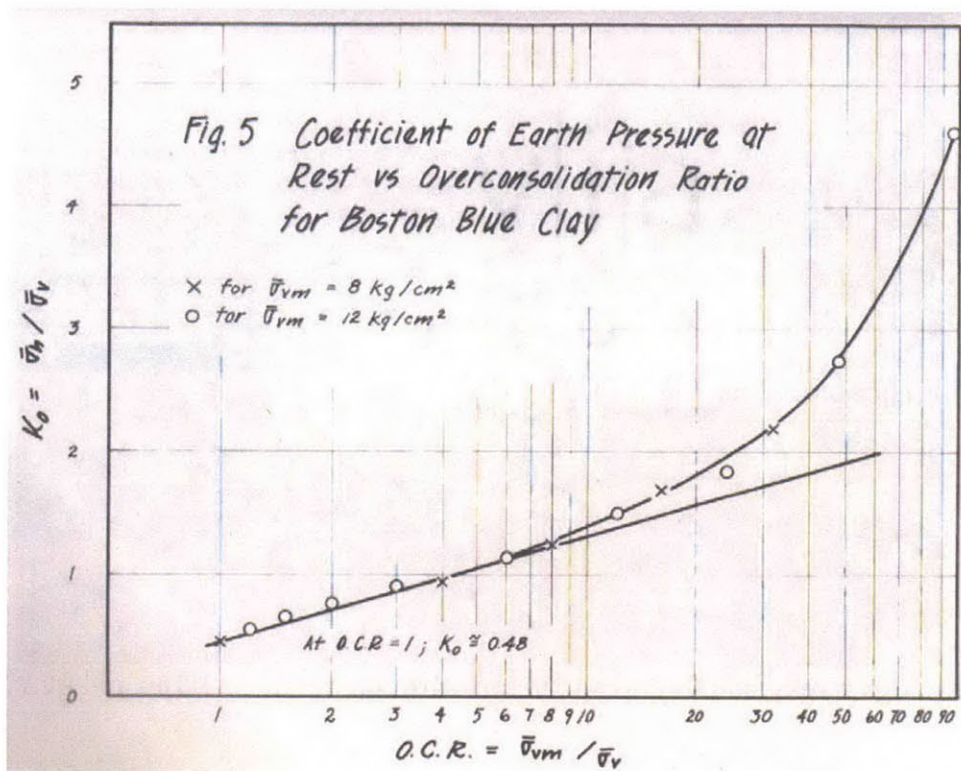


Figure 3-17: Lateral stress ratio, K_o vs. OCR for Boston Blue Clay (Ladd, 1965)

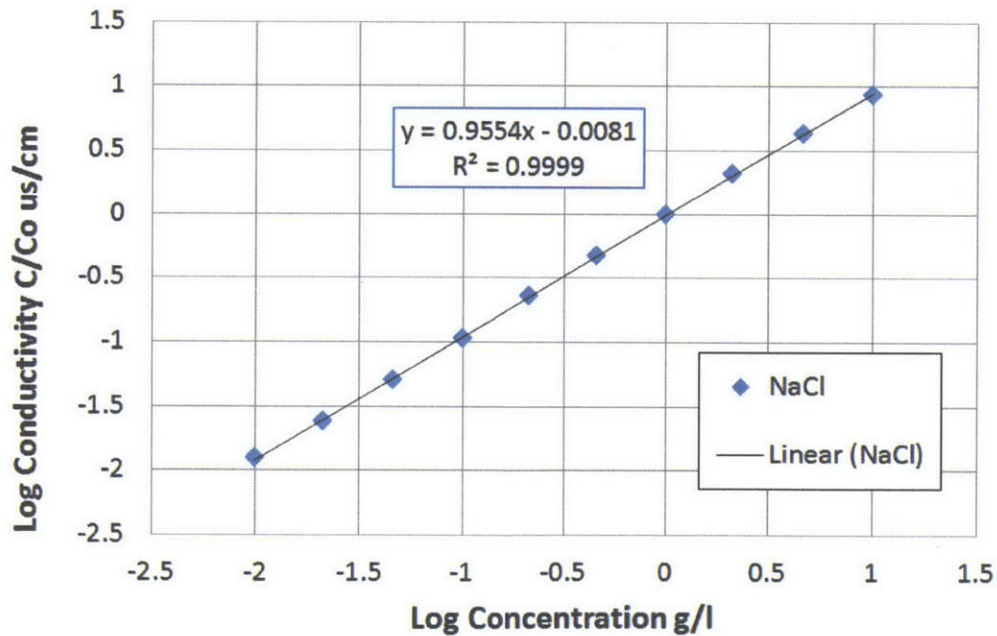


Figure 3-18: NaCl calibration curve for conductivity meter model 23226-505 VWR International. $C_o = 1 \text{ g/L}$ NaCl solution.

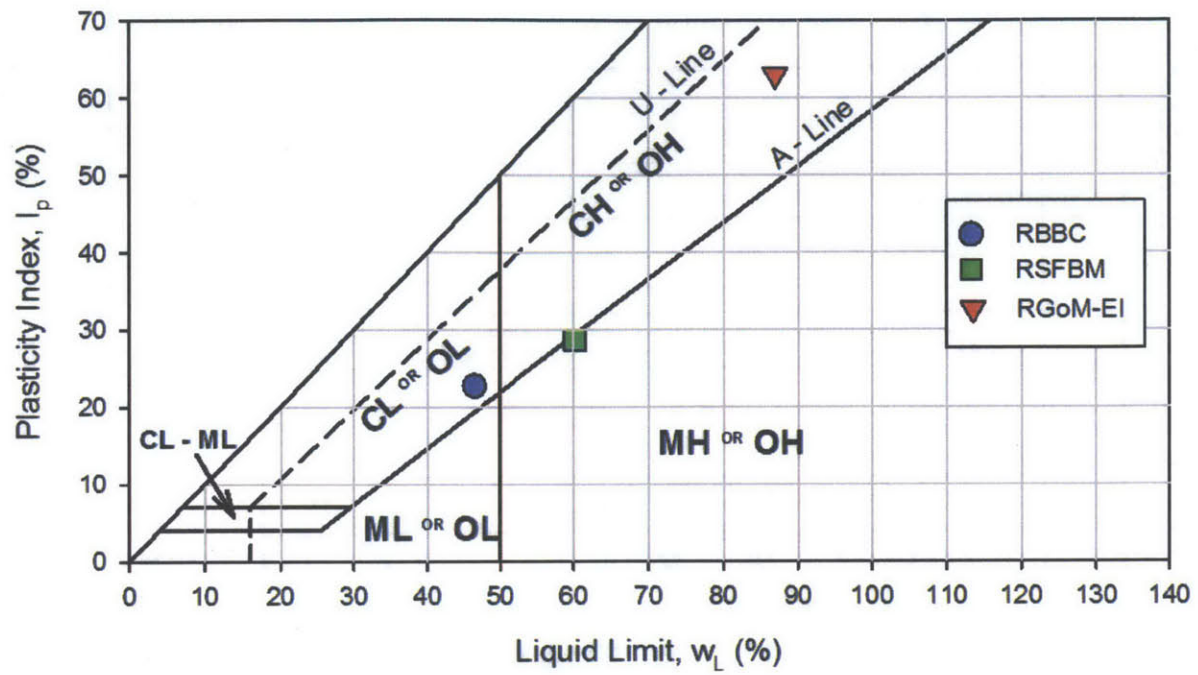


Figure 3-19: Casagrande chart

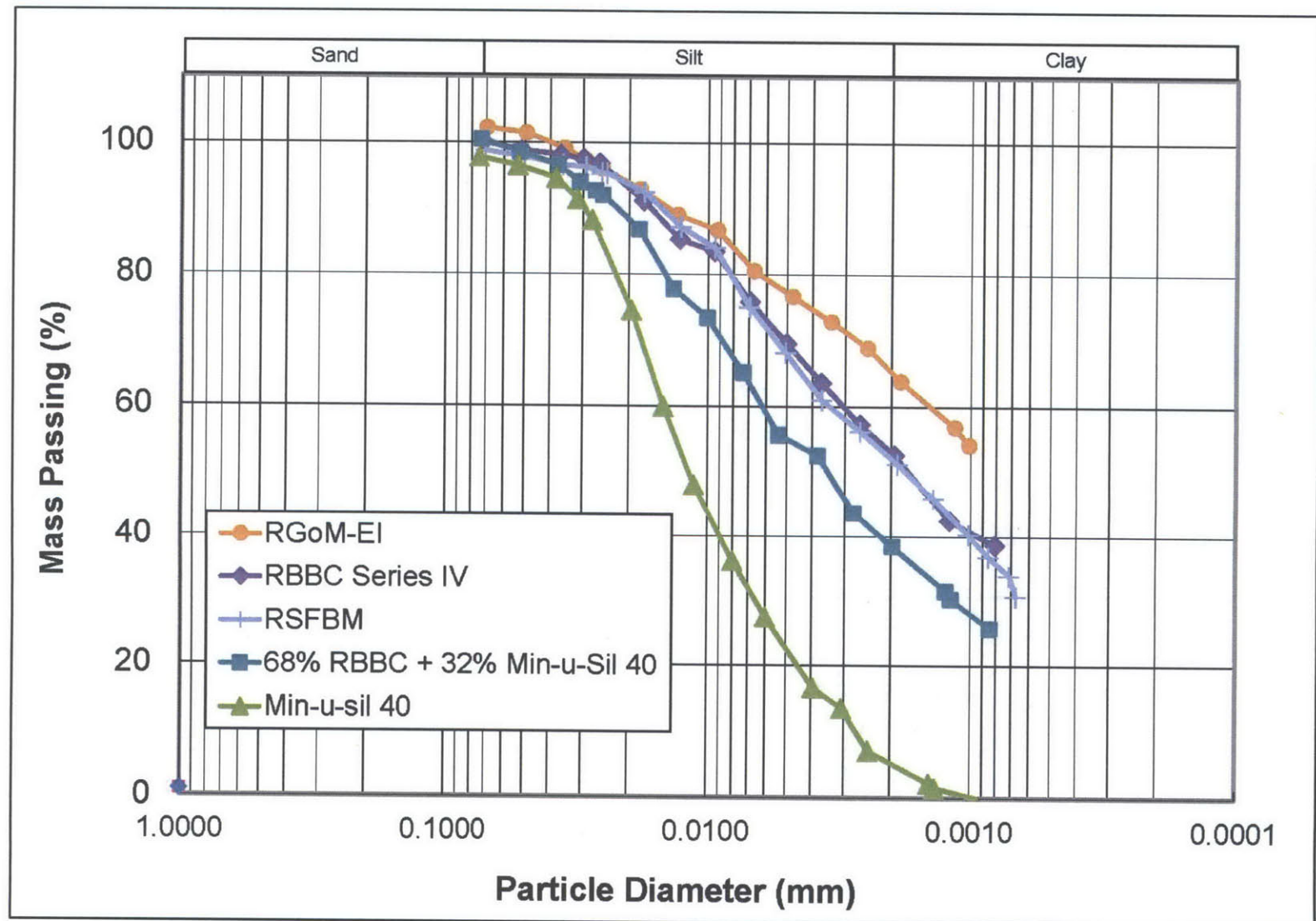


Figure 3-20: Mudrock particle size distribution

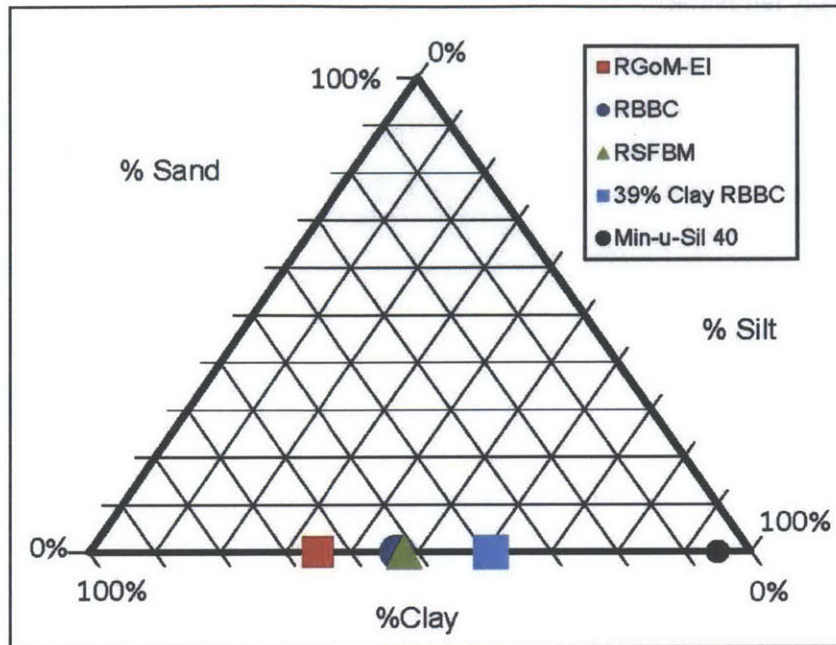


Figure 3-21: Clay Fraction Triangle Plot

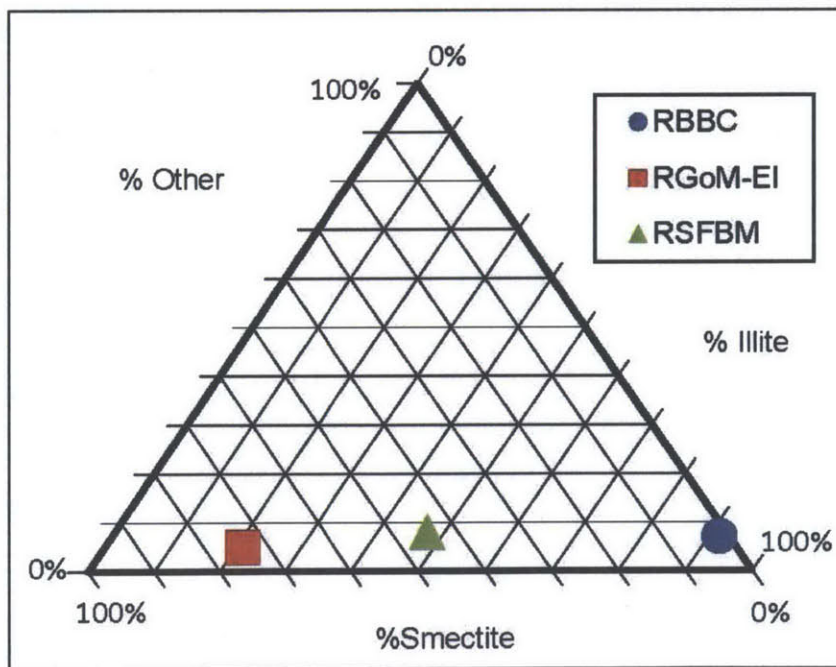


Figure 3-22: Clay Mineralogy Triangle Plot

(Page intentionally left blank)

4 Equipment and Procedures

4	Equipment and Procedures	121
4.1	Specimen Preparation	122
4.2	Permeability and Permeability Anisotropy Measurement	122
4.3	Resistivity and Conductivity Anisotropy Measurement	125
4.4	Measurement Sequence Bias Adjustment.....	127
4.4.1	Global Specimen Method	128
4.4.2	Single Specimen Method.....	130
4.5	Fabric Imaging and Analysis.....	130
4.5.1	Specimen Preparation	130
4.5.2	SEM Imaging Technique	131
4.5.3	Particle Orientation and Aspect Ratio Analysis	132
4.5.4	Sources of Error	133

This chapter summarizes the equipment and procedures used to measure the permeability and resistivity of cubic specimens, as well as the relevant data analysis methods. It also describes in full the methods used to prepare, image and analyze Scanning Electron Microscope images of the fabric structure. This chapter is supported by two appendices. Appendix 2 describes the permeability measurements in detail, including relevant background, equipment description, step by step procedures, and analysis methods. Appendix 3 describes the same for the resistivity measurements.

4.1 Specimen Preparation

Resedimented specimens are extruded from sedimentation tubes and trimmed into 5 cm cubes. Figure 4-1 shows the specimen following resedimentation. Specimens are extruded from the acrylic sedimentation columns using a manual hydraulic jack (Figure 4-2). Extrusion should not significantly alter the specimen stress state or porosity because specimens are rebounded to an OCR of 4 which produces a hydrostatic stress state ($K_o = 1$). Slight uniform expansion of the specimen may occur, but this is found to be insignificant.

Following extrusion, the specimen is then carefully trimmed using a miter box, clamps to form square edges as shown in Figure 4-3. A coarse tree saw is used to trim high stress (>2 MPa) specimens (as shown). A razor blade or wire saw is used to trim low stress (< 2 MPa) specimens. Once trimmed, the specimen is massed and dimensioned using calipers (Figure 4-4).

4.2 Permeability and Permeability Anisotropy Measurement

The permeability of resedimented cubic specimens is measured using the constant head method in a flexible wall permeameter [ASTM International Standard D5084-10, 2010] fitted with square end adapters (isometric view Figure 4-5, dimension section Figure 4-6). A similar method was employed by Chan and Kenney (1973). The measured permeability is then adjusted for measurement sequence bias (described in Section 4.4), a consistent and predictable decrease in the permeability which occurs with successive re-measurement of the same cubic specimen.

Salt water is flowed through the specimen under a constant head gradient in a temperature controlled enclosure stable to $26 \pm 0.1^\circ\text{C}$. The salinity of the salt water is equal to the mudrock pore fluid salinity. The directional permeability is measured by rotating the cubic specimen through three sequential setups measuring each of the vertical (V), first horizontal (H1), and second horizontal (H2) directions. Each sequential measurement requires disassembly and reassembly of the apparatus. Two directional orders are applied: V, H1, and H2 (Vertical order), and H1, V1, and V2 (Horizontal order). This is shown in Figure 4-7 and discussed in more detail in Section 4.4.

Each measurement is composed of the four key steps: pressure up, back pressure, recompression, and permeability measurement.

First, the specimen confining pressure is increased by applying a cell pressure with the drainage lines closed. The applied stress is equal to the final (OCR 4) stress state applied during resedimentation. This allows the specimen to temperature equilibrate and come to a stable sampling effective stress.

Second, the pore pressure is incrementally increased to between 0.35 and 1 MPa to back pressure the specimen while maintaining the sampling effective stress. Back pressure is applied to 1)

pressure saturate the specimen and 2) allow for later permeability testing. No porosity change is expected during back pressure because the mean effective stress remains constant.

Third, the specimen is recompressed to the hydrostatic effective stress corresponding to the OCR 4 stress state for permeability measurement.

Fourth, a constant head gradient is applied by maintaining a differential pore pressure across the specimen, during which both the inflow and outflow volumes are measured over time. Constant head gradients varying from 8 to 280 were applied, with lower gradients applied to higher porosity specimens. A permeability measurement is completed once the inflow and the outflow rates are steady. A minimum of three constant head gradients are applied by increasing the inflow pressure and decreasing the outflow pressure, keeping the mean effective stress in the center of the specimen constant. Constant head gradients are applied in non-sequential order (neither increasing nor decreasing) for quality control. As mentioned in the results section, there is no trend in measured permeability with hydraulic gradient. Further, the measured permeability varied minimally (third significant digit) as the gradient was varied for most specimens.

The hydraulic conductivity is computed using D'Arcy's Law (D'Arcy, 1856; equation 4-1):

$$K = \frac{Q}{iA} = \frac{\Delta V_{in} + \Delta V_{out}}{2\Delta t A} \frac{l\rho g}{\Delta P} \quad 4-1$$

Where K is the hydraulic conductivity, Q is the volumetric flow rate, i the applied gradient, A is the measured area of flow, ΔV_{in} and ΔV_{out} are the increments in inflow and outflow volume, respectively, corrected for measured leaks and secondary compression related volume change, Δt is the time interval of measurement, ΔP is the applied pore pressure differential across the specimen, l is the measured length of flow, ρ is the mass density of the fluid and g is the gravitational constant. The measured inflow is corrected for small leaks and secondary compression volume change by measuring these values separately as a function of time at the same effective stress.

The hydraulic conductivity is converted to permeability using the temperature and salinity dependent density and viscosity (described in Chapter 3) of the permeant according to equation 4-2:

$$k = \frac{K\mu}{\rho g} \quad 4-2$$

Where k is the permeability, ρ and μ are the mass density and the dynamic viscosity, respectively, of the permeant fluid and g is the gravitational constant.

The measured permeability is adjusted for measurement sequence bias (Section 4.4) to account for decreases in permeability associated with handling the specimen between successive re-measurement of the same specimen.

The permeability anisotropy is computed directly as:

$$r_k = \frac{k_{H1} + k_{H2}}{2k_V} \quad 4-3$$

Where r_k is the permeability anisotropy, and k_H and k_V are the adjusted permeabilities in the horizontal and vertical directions, respectively. Equation 2 averages the two horizontal permeability measurements, which are the same, aside from experimental scatter, after correcting for measurement sequence bias (Section 4.4).

The test is automated with a computerized system controlling the cell and pore pressures. Pressure and volume measurements as a function of time are recorded on a central data acquisition system. The electronic measurement, control and data acquisition systems are fully described in Appendix 2.

Constant head permeability tests are known to cause volume change in mudrocks because high hydraulic gradients result in uneven pore pressure distributions across the specimen causing swelling at one end and compression at the other end of the specimen. However, this method results in negligible specimen volume change during the application of hydraulic gradients for two reasons. First, the specimens are over consolidated (OCR 4), yielding a much stiffer volume change response than a normally consolidated mudrock. Secondly, the change in pore pressure at either end of the specimen is small compared to the mean effective stress, further reducing the expected volume change.

Figure 4-8 illustrates the stress and porosity change that the specimen undergoes during application of a hydraulic gradient. A specimen tested with a mean effective stress of 1 MPa has a maximum effective stress (during resedimentation) of 4 MPa. A differential pore pressure varying between 0.04 and 0.1 MPa might be applied to this specimen to measure the permeability. This differential pore pressure is split between the top and bottom of the specimen, meaning the stress change at either end of the specimen varies between 2 and 10% of the mean effective stress. This slight change in stress is not expected to cause significant change in porosity because the specimen is over consolidated and has a stiff stress – porosity response.

The dimensions of each of the three axes of the cubic specimen are measured in four locations to the nearest 0.01 mm both prior to, and after, each directional permeability measurement. These dimensions are averaged for each axis and are used to compute the flow length and flow area for the permeability calculation according to the D'Arcy's law.

The wet mass of the specimen is recorded at the beginning and end of each directional permeability measurement. The dry specimen mass is obtained following completion of all three permeability measurements. The specimen, or a fraction of the specimen, is dried in an oven set to 110 degrees Celsius for a minimum of 24 hours. The porosity is computed using a mass-based approach assuming complete saturation and correcting for the presence of salt in the pore fluid (eq. 4-4):

$$n = \frac{V_v}{V_T} = \frac{V_w + V_{salt}}{V_T} = \frac{\frac{M_w + M_{salt}}{\rho_s}}{\frac{M_s}{G_s \rho_w} + \frac{M_w + M_{salt}}{\rho_s}} \quad 4-4$$

where n is the porosity, V_v , V_w , V_{salt} are the volumes of the voids, the water, and the salt, respectively, V_T is the total specimen volume, M_w , M_{salt} , M_s are the masses of the water, the salt and the solid grains, respectively, G_s is the specific gravity of the grains, ρ_w is the density of distilled water, and ρ_s is the density of pore fluid at the measured salt concentration. With this approach the specimen dimensions and specimen volume are not used to compute porosity, reducing error associated with imperfections in the shape of the cubic specimen. An average porosity is computed for each specimen using the three mass-based porosities corresponding to the end of each directional permeability measurement. Over the course of 3-4 directional measurements on the same specimen, spanning up to one month, the porosity variation using this method was measured to be <0.01 .

All mass measurements are taken after the specimen is removed from the permeameter. During disassembly of the apparatus, the cell pressure is released, inducing negative pore pressures in the specimen. To counteract this, a vacuum is applied to the specimen via the apparatus drainage lines to prevent suction of the free water found in the pore pressure lines. This procedure limits specimen volume change between permeability measurement and massing. The mass is recorded immediately upon removal from the device to prevent drying. Using this approach, errors in porosity measurement related to swelling or drying of the specimen are minimized.

4.3 Resistivity and Conductivity Anisotropy Measurement

The resistivity of resedimented cubic specimens is measured using specialized cubic end adapters in the flexible wall permeameter. The resistivity measurement phase is added as a fifth step onto the permeability measurement sequence: pressure up, back pressure, recompression, permeability measurement and resistivity measurement. The resistivity anisotropy is measured in the same way as the permeability anisotropy: by rotating the cubic specimens to measure the resistivity in different directions. The measured resistivity is also adjusted using the measurement sequence bias technique (described in Section 4.4).

The mudrock resistivity is measured using the 4-probe technique, illustrated in Figure 4-11. Two plate electrodes apply an AC voltage with a fixed frequency to the ends of the specimen with constant area A . Two pin electrodes protrude into the specimen and measure the voltage drop across two points in the specimen separated by length L . The voltage drop across the two pin probes is measured and related to the specimen resistance. Specialized cubic end adapters (Figure 4-12) were designed to incorporate both the plate and pin probes necessary to make the resistivity measurements. Appendix 6 includes CAD drawings for these end adapters.

Using these specialized end adapters, the specimen resistivity is measured between the two pin probes which protrude into the specimen by 5/32 in. Because the pins are conductive for their entire length, the measurement distance is from the midpoint of the upper pin to the midpoint of the lower pin, effectively measuring the majority of the specimen. The measurement assumes that the current field is uniform and oriented perpendicular to the plate probes, which is reasonable considering the cubic geometry.

Resistivity measurements are made using a custom built resistivity measurement system which consists of a custom PCB installed in a user interface box that allows easy connection to the specimen electrodes and power sources. Appendix 3 describes the resistivity measurement system in detail, including a user manual.

In short, the measurement system consists of three sub circuits: a signal generator circuit, a specimen circuit and a measurement circuit. These circuits are described in detail in Appendix 3.

The signal generator circuit creates an alternating current (AC) voltage with a sine wave shape and fixed frequency of approximately 10 kHz and a peak to peak voltage of 24 V. This voltage is fed through the specimen circuit.

The specimen circuit is three resistors in series: a drop resistor, a reference resistor and the specimen itself. The drop resistor is used to set the current in the specimen circuit to within the range of 1 – 6 mA. The reference resistor has a resistance of known value. Measuring the voltage drop across this resistor allows calculation of the current through the specimen using Ohm's Law:

$$i = \frac{V_{ref}}{R_{ref}} \quad 4-5$$

Where i is the current, V_{ref} is the voltage drop over the reference resistor and R_{ref} is the known resistance.

The specimen is the unknown resistor in the series. The voltage drop between two points (the two pin probes) is measured and the resistance is computed by re-arranging Ohm's law (4-6). The current is computed using the reference resistor, as described above.

$$R_{specimen} = \frac{V_{probe}}{i} \quad 4-6$$

Where $R_{specimen}$ is the specimen resistance, V_{probe} is the voltage drop over the specimen measurement probes, and i is the current through the series circuit computed previously (equation 4-5).

The specimen resistivity is computed using equation 4-7:

$$\rho = \frac{RA}{L} \quad 4-7$$

Where ρ is the resistivity, R is the specimen resistance between two pin probes (eq. 4-6), A is the area of voltage application and L is the length separating the measurement pin probes.

The specimen electrical conductivity (σ) is equal to the inverse of its resistivity (ρ):

$$\sigma = \frac{1}{\rho} \quad 4-8$$

Resistivity decreases with increasing pore fluid salinity. As a result, resistivity cannot be used to compare two mudrocks with different pore fluid salinities. The specimen formation factor normalizes the measured resistivity by the pore fluid resistivity:

$$F = \frac{\rho}{\rho_w} \quad 4-9$$

Where F is the formation factor, ρ is the resistivity of the specimen and ρ_w is the resistivity of the pore fluid.

Resistivity measurements can also be made on the bench top, as described in Appendix 3. Measuring the resistivity in the triaxial cell has three key advantages: good saturation via back pressure, good electrical contacts, and measurements are obtained at the representative effective stress. However, resistivity measurements in the triaxial cell take a long time (days to a week per measurement) and are limited to a specific specimen configuration. Bench top measurements are faster and can be performed on any specimen. However, bench top measurements are affected by problems related to specimen saturation and drying during measurement, stress level effects, and poor electrical contacts.

4.4 Measurement Sequence Bias Adjustment

The mudrocks measured for this work are resedimented and uniaxially compressed in the laboratory. They should be cross anisotropic with an isotropic horizontal plane and permeability anisotropy developing in the vertical plane only. However, the permeability results indicate a small but consistent difference between successive horizontal permeability measurements (H1 and H2) that is illustrated in a cross plot as a slope of less than 1 (e.g. Figure 4-9 for RBBC). A similar but opposite trend was noted for the resistivity measurements.

Repeated permeability measurements in the same direction are lower, regardless of the order of measurement as shown in Figure 4-9 and Figure 4-10. Similarly, repeated resistivity measurements are higher. This is likely resultant from handling the specimen between permeability measurements. Slight smearing may occur on the faces which can decrease the measured

permeability. The decrease in permeability due to smearing is consistent and predictable, and is termed the 'measurement sequence bias'.

The measurement sequence bias correction is applied to both permeability and resistivity measurements made on cubic specimens. Only the second and subsequent directional permeability or resistivity measurements require correction. Measurement sequence bias correction, using either the global correction method, or the single specimen method, requires two permeability or resistivity measurements in the same direction. The second permeability direction must be measured twice to correct for measurement sequence bias. Therefore, the optimal measurement sequences are V, H1, H2 (Vertical Order) and H, V1, V2 (Horizontal Order). For Horizontal order, the vertical measurement is repeated to obtain the V2 measurement.

The following sections provide two methods, the global specimen method and the single specimen method, to remove this bias from the data set and correct the measured permeability for the effects of repeated measurement on the same specimen.

4.4.1 Global Specimen Method

The measurement sequence bias, x , is defined as the slope of a cross plot of *successive* permeability measurements made in the same plane (Figure 4-9). Multiple specimens of the same mudrock are required to apply this correction. One measurement per specimen is used to define the measurement sequence bias slope for each plane of interest (e.g. Horizontal bias or Vertical bias). Dividing the H2 permeability measurement by the slope x forces a 1:1 slope with the H1 measurement (see Figure 4-9).

For example, consider a data set consisting of 10 specimens of mudrock A, including five specimens measured using horizontal order and five specimens measured using vertical order. The horizontal measurement sequence is defined by a cross plot of H2 permeability vs. H1 permeability; there are 5 pairs of measurements in the H1 and H2 direction, obtained from those specimens measured using vertical order (see Figure 4-7), that can be used to define the horizontal measurement sequence bias. Similarly, the vertical measurement sequence bias is defined by a cross plot of the V2 vs. the V permeability; in this data set there are 5 pairs of measurements in the vertical direction (V and V2), obtained from those specimens measured using horizontal order (see Figure 4-7), that can be used to define the vertical measurement sequence bias.

To estimate the undisturbed permeability, a global correction is applied based on the number of measurements that have been made on the same specimen:

$$k_1 = \frac{k_n}{x^{(n-1)}} \quad 4-10$$

Where k_1 is the undisturbed permeability, k_n is the measured permeability, x is the measurement sequence bias and n is the measurement number. The undisturbed permeability, k_1 , is the

permeability at measurement number one corrected for permeability decreases associated with n permeability measurements.

A cubic specimen undergoes a minimum of three directional permeability measurements to measure the permeability anisotropy. The first permeability measurement does not require correction and serves as the reference permeability. The second measurement ($n=2$) must be corrected for a permeability decrease associated with the first measurement, regardless of whether the first and second measurements are made in the same direction. The third measurement ($n=3$) must be corrected for permeability decreases associated with the first and second measurements. The exponent ($n-1$) allows superposition of the measurement sequence bias over multiple measurement increments to compute the undisturbed permeability at measurement number one. Equation 4-10 applies for both permeability (k) and hydraulic conductivity (K).

A similar superposition method can be applied to determine the measurement sequence bias, x , in cases where only non-successive measurements in the same direction are available:

$$x = x' \frac{1}{\Delta n} \quad 4-11$$

Where x is the measurement sequence bias between successive permeability measurements, x' is the measurement sequence bias for non-successive permeability measurements, and Δn is the number of measurements separating the non-successive permeability measurements.

In order to correctly apply equation 4-10 to all possible measurement sequences, it is best to convert x' to x (eq. 4-11) which corrects for a single measurement sequence. To illustrate this necessity, consider a series of mudrock specimens measured using Vertical Order where the vertical permeability was re-measured at the end of the test, resulting in measurement sequence of V1, H1, H2, and V2. A cross plot of the V2 permeability vs. the V1 permeability yields a slope x' because V1 and V2 are non-successive. Dividing V2 by x' forces a 1:1 slope with V1, correcting for handling effects over three separate setups. However, applying equation 4-10 with $n = 4$ and x' would erroneously apply the correction factor 3 times. Inspection of equation 4-11 yields that $x' = x^{(n-1)}$ for the case where V1 is the first measurement. In this case, we convert the non-successive bias x' to the successive measurement sequence bias x using equation 4-11 with $\Delta n = 3$.

The global correction method should only be applied to data sets consisting of multiple specimens. Further, there should be a minimum of two specimens on which duplicate measurements were made in each direction that requires correction. For example, if all specimens were measured using vertical order (V, H1, and H2) then the minimum number of specimens is two. If specimens were measured using a combination of vertical and horizontal order (H, V1, and V2), then the minimum number of specimens is four, two each measured using vertical and horizontal order. This requirement results in estimation of the measurement sequence bias, x , in each direction from a minimum of two data points.

4.4.2 Single Specimen Method

An alternative approach, called the single specimen method, is better suited to correct the permeability measurements for single specimens or for small data sets not suitable for correction using the global specimen method. This approach plots directional permeability measurements vs. the measurement number, n (as in Figure 4-10). Sequential permeability measurements in the same direction can be connected and the slope extended to determine the corrected permeability at measurement $n=1$. This approach was first proposed for use in measuring the anisotropy of varved clays to adjust the permeability for noted smearing of the varved layers across the layer boundaries (Chan and Kenney, 1973).

4.5 Fabric Imaging and Analysis

Scanning Electron Microscope (SEM) images of the mudrock fabric were taken of different mudrocks compressed to varying maximum effective stresses during re sedimentation (0.1, 1, 10 and 40 MPa σ'_p). Based on available information, all images were obtained of the resedimented mudrock at OCR 4 which approximates the $K_o = 0$ condition ($\sigma'_H \approx \sigma'_v$, discussed in Chapter 3). The purpose was to study the evolution of the mudrock fabric structure with increasing stress and decreasing porosity. Mudrock fabric is the orientation of the particles, while mudrock texture is the geometry of the particles, including size and aspect ratio. Both mudrock fabric and mudrock texture are quantified through particle based image analysis. This section is divided into four subsections. The first three subsections describe the specimen preparation, imaging and analysis methods, respectively. The final subsection highlights key sources of error that are inherent in such methods and analysis.

4.5.1 Specimen Preparation

Images are taken in either horizontal or vertical planes on oven dried (110 degrees Celsius) specimens. Vertical planes are oriented parallel to the axial loading direction and reveal the particle alignment of particles with respect to the horizontal. Horizontal planes are aligned perpendicular to the direction of axial loading and are parallel to the specimen bedding.

The specimen is prepared for imaging by trimming it into a smaller size and then by removing the water by oven drying. A thin, square cross section of the specimen is cut and the edges are squared for imaging, as shown in Figure 4-13. The square face is a reference face and is normal to the plane that will be imaged. The rectangular face is imaged. The specimen section is cut from a wet specimen or from an oven dried specimen using a combination of a coarse tree saw, a miter box, and a razor blade.

The specimen surfaces are cut as close to perpendicular as possible. The specimen surfaces are squared to the reference face using a squaring block and sand paper. This process creates surfaces that are perpendicular to the reference plane. For the case of imaging the vertical plane, the

reference plane is the horizontal plane and the squaring process enables measurement of particle dip relative to the horizontal.

The viewing surfaces of the oven dried samples are milled using an Argon-ion beam milling technique [Loucks et al, 2009], which uses accelerated Argon ions to polish and smooth a small area of the surface. The ion beam creates a flat viewing surface by milling away the specimen, forming a curved milled boundary as shown in Figure 4-13 in schematic and in Figure 4-14 as an image. This process results in a flat surface with only minor topographic variations. Because this method is not a mechanical polishing process, it does not have the disadvantages of incorporating abrasives into the final surface and does not alter materials that are sensitive to heat (Erdman et al, 2006).

Oven drying is a key source of error in this method because it is known to cause significant volume change and may cause unknown mudrock fabric changes. Modifying and/or replacing this analysis method to reduce this source of error is an active area of research at this time.

4.5.2 SEM Imaging Technique

The Scanning Electron Microscope (SEM) obtains images of mudrock specimens, or any material, by accelerating a beam of electrons towards a flat specimen surface. The beam of electrons interacts with the specimen surface and causes the emission of secondary electrons and backscattered electrons. Special detectors record the electron emission patterns to produce either secondary SEM images (SE images) or backscattered SEM Images (BSE images) that are used to interpret topographic information.

The oven dried specimens measured in this work were polished using the argon ion milling technique and aligned in the microscope such that the base of the image corresponds to either the top or the bottom of the specimen; therefore a vertical line drawn through the image parallels the line of axial loading.

Images were obtained using two different SEM's: a FESEM Supra 55VP SEM in the Center for Nanoscale Systems Lab at Harvard University (Harvard), and a FEI Nova NanoSEM 430 in the Bureau of Economic Geology at the University of Texas at Austin (UT). The types of images and imaging parameters differ between the two institutions.

At Harvard, SE images were obtained using a voltage of 1kV or 2 kV and a working distance varying between 3 to 4 mm. At UT, BSE images were obtained using a fixed voltage of 10 kV and a working distance of 5.9 mm. The voltage and working distance determine the resolution of the image, with lower voltages and closer working distances producing higher resolution images but also narrowing the depth of field.

Images were obtained at different magnifications. Particle orientation analysis was performed primarily on images with magnification varying between 10,000 and 15,000 times for both the Harvard and UT images. This produced images with a width varying between 15 and 30 μM where

the individual clay and silt particles could be individually identified. Additional images were obtained at Harvard University at higher and lower magnifications to separately investigate the clay and silt particle structure and orientation.

4.5.3 Particle Orientation and Aspect Ratio Analysis

JMicroVision (Roudit 2013), a free image analysis software package was used to analyze the particle orientation and aspect ratio of the SEM images. The software is calibrated to convert pixel measurements to length using the image scale bar.

Two different types of particle orientation analyses were compared: 1D and 2D. In 1D analysis, lines are drawn along the particle axis on all platy particles using the 1D measurement tool. Particle length is computed by JMicroVision using this calibration. The measured particle orientation (fabric) and particle length data (texture) are exported for analysis. In 2D analysis all particles are manually traced, including non-platy particles that do not have an obvious dominant orientation. The apparent particle orientation, length and width are computed using JMicrovision and exported for analysis. The particle aspect ratio is computed as the ratio of the particle length to width. Particle length and width are measured in perpendicular orientations.

The manual 1D analysis did not include low aspect ratio particles (aspect ratio close to 1) where the orientation of the long axis was not evident. These particles were, however, included in the 2D analysis for two reasons: First, particles are traced in the 2D analysis and the particle orientation is computed using measured geometry, minimizing the need for the analyst to manually identify the particle orientation. Second, the 2D analysis results were used to further analyze the aspect ratio distribution, and as a result all particles that could be delineated were included in this analysis.

Analysis of images with a field of view of ~15-30 μm considered particles of length ~ 0.2 – 5 μm . Particles less than 0.2 μm are not visible or discernible, and particles greater than 5 μm are disregarded as unrepresentative given the field of view.

JMicroVision uses standard angle measurement notation, measuring angles counter clockwise from quadrant 1 (East). These angles are converted to acute angles referenced to the horizontal according to equation 4-12:

$$\begin{aligned} \theta_{meas} < 90, \quad \theta_{horiz} &= \theta_{meas} \\ \theta_{meas} > 90, \quad \theta_{horiz} &= 180 - \theta_{meas} \end{aligned} \tag{4-12}$$

Where θ_{meas} is the particle angle measured in JMicroVision and θ_{horiz} is the particle angle referenced to the horizontal.

4.5.4 Sources of Error

SEM fabric interpretation is based on the best available technology but imaging mudrocks is still an active topic of research. This section highlights some potential sources of error inherent in this method of fabric analysis.

First, the SEM images are obtained using oven dried specimens. Oven drying is known to cause shrinkage of mudrocks and most likely alters the fabric structure including the particle orientation, in particular when referenced to the horizontal plane.

Second, the measured particle orientation and aspect ratio are apparent values in the plane of measurement. Using the analogy of strike and dip in field mapping, the particle strike may not be perpendicular to the image surface, resulting in the measurement of an apparent dip. There is no way to determine the particle strike using this method and correct the measured apparent particle orientation to find the true particle orientation. As a result, the true particle orientation will likely be higher than the measured particle orientation, and the true particle aspect ratio will be higher than the measured particle aspect ratio. Comparing the particle orientation between specimens with different porosity using this method is a valid exercise. Further, providing that the sample size is sufficiently large, the average particle aspect ratio should not change as a function of stress level or porosity for the same material if the particles are not deformable as is commonly assumed.

Finally, the images are taken on very small sections, approximately 20 μm by 20 μm . It is evident through visual comparisons of images obtained on the same stress level (e.g. see images in Appendix 1) that the fabric is not uniform at this magnification. Particle - particle interactions become very important in the localized particle orientation. Clay particles exhibit locally heterogeneous behavior near larger silt grains, characterized by varying density and orientation distributions. Schneider et al (2011) illustrates this behavior relative to the development of a dual porosity structure at the micro scale in Figure 4-15. Where possible, given the availability of images and time to analyze images, multiple images have been analyzed in an attempt to increase the sample size and account for local heterogeneities in the mudrock fabric.

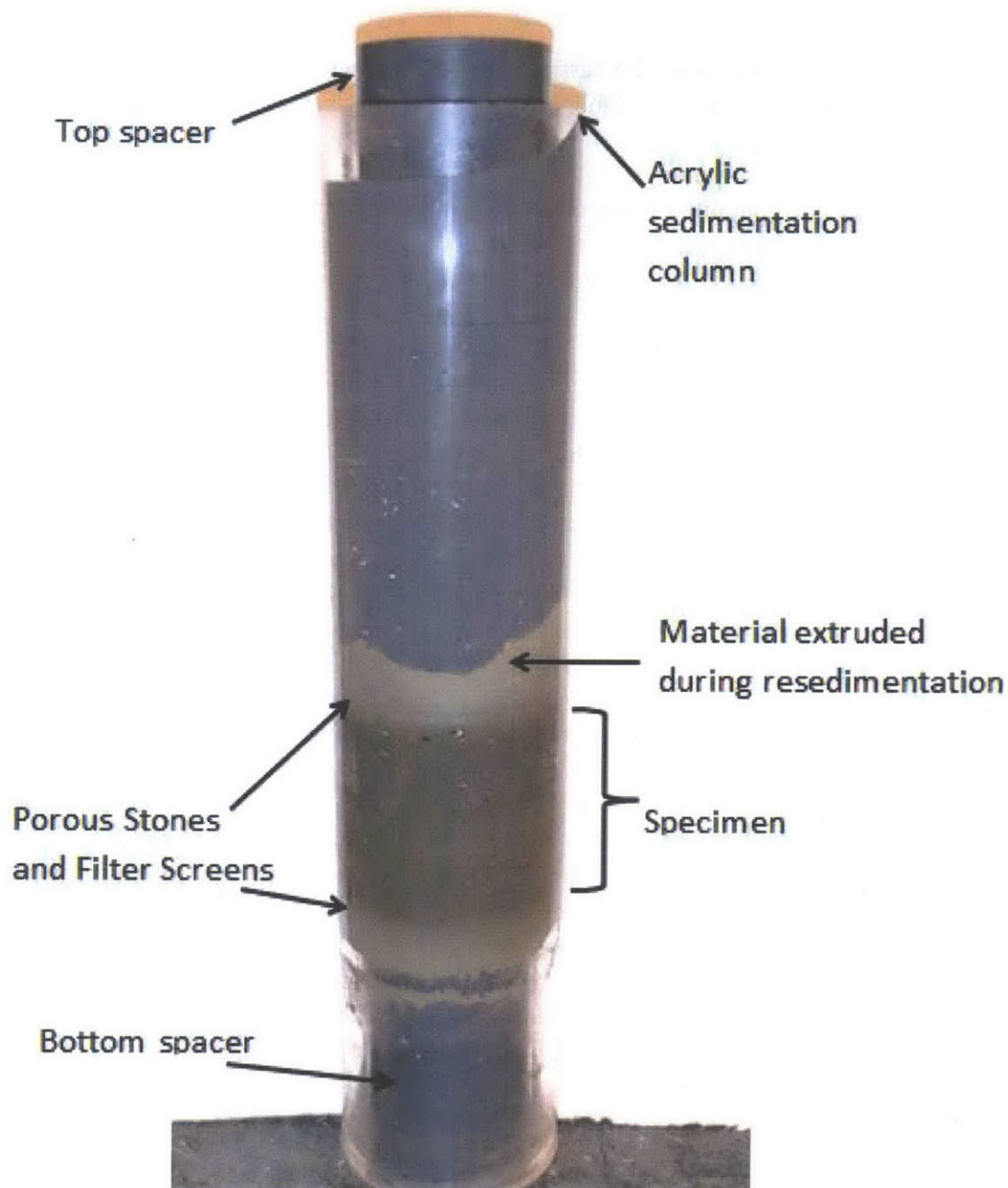


Figure 4-1: Completed resedimented specimen prior to extrusion



Figure 4-2: Extruding a resedimented specimen using the manual hydraulic jack

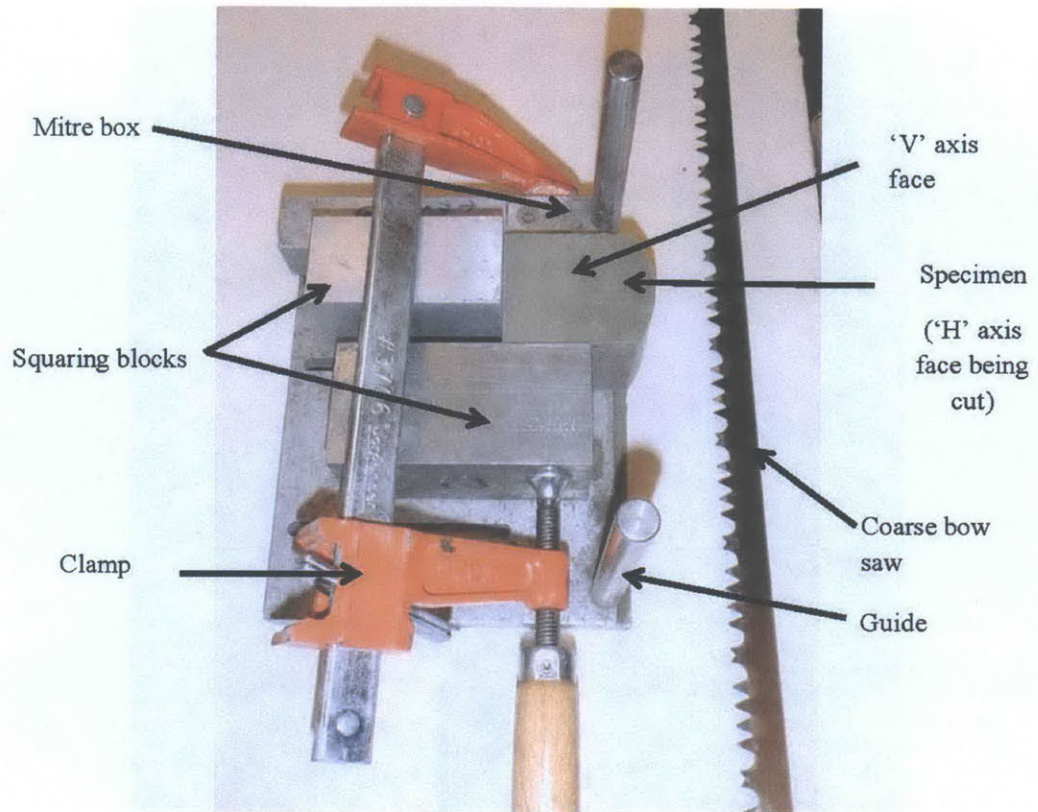


Figure 4-3: Trimming a high stress specimen

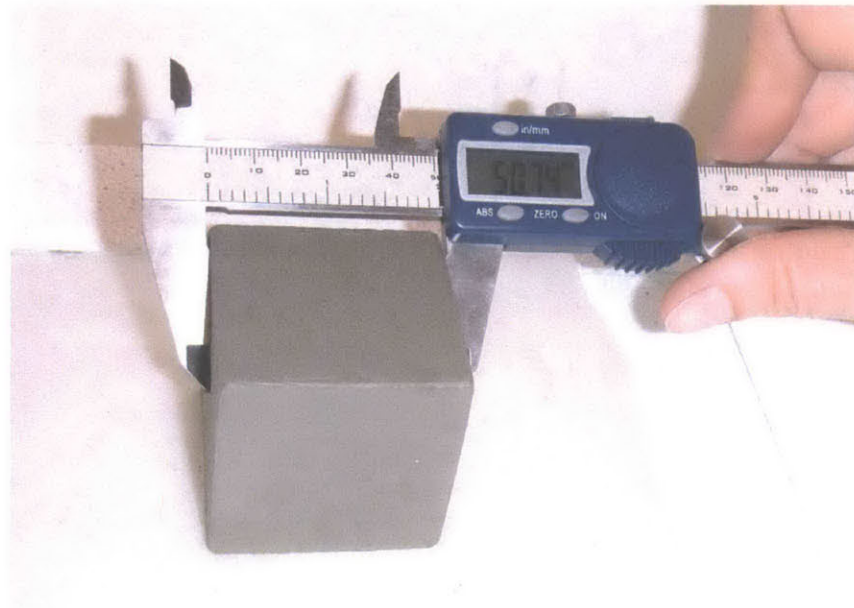
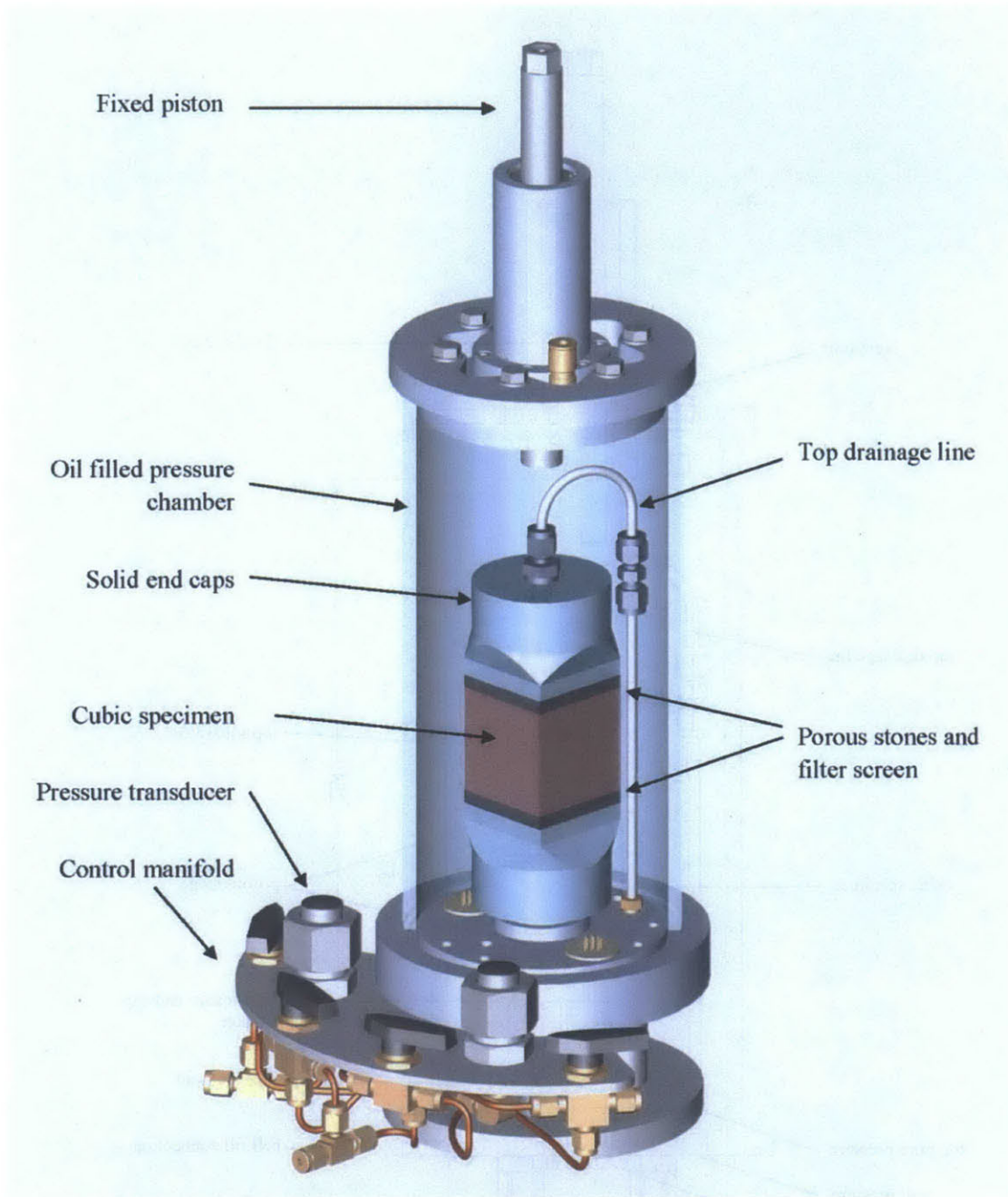


Figure 4-4: Dimensioning the cubic specimen



Not shown: Rubber membrane jacket surrounding specimen and end adapters.

Figure 4-5: Solid view of the low stress triaxial cell (modified for permeability measurement) with manifold and cubic shaped specimen

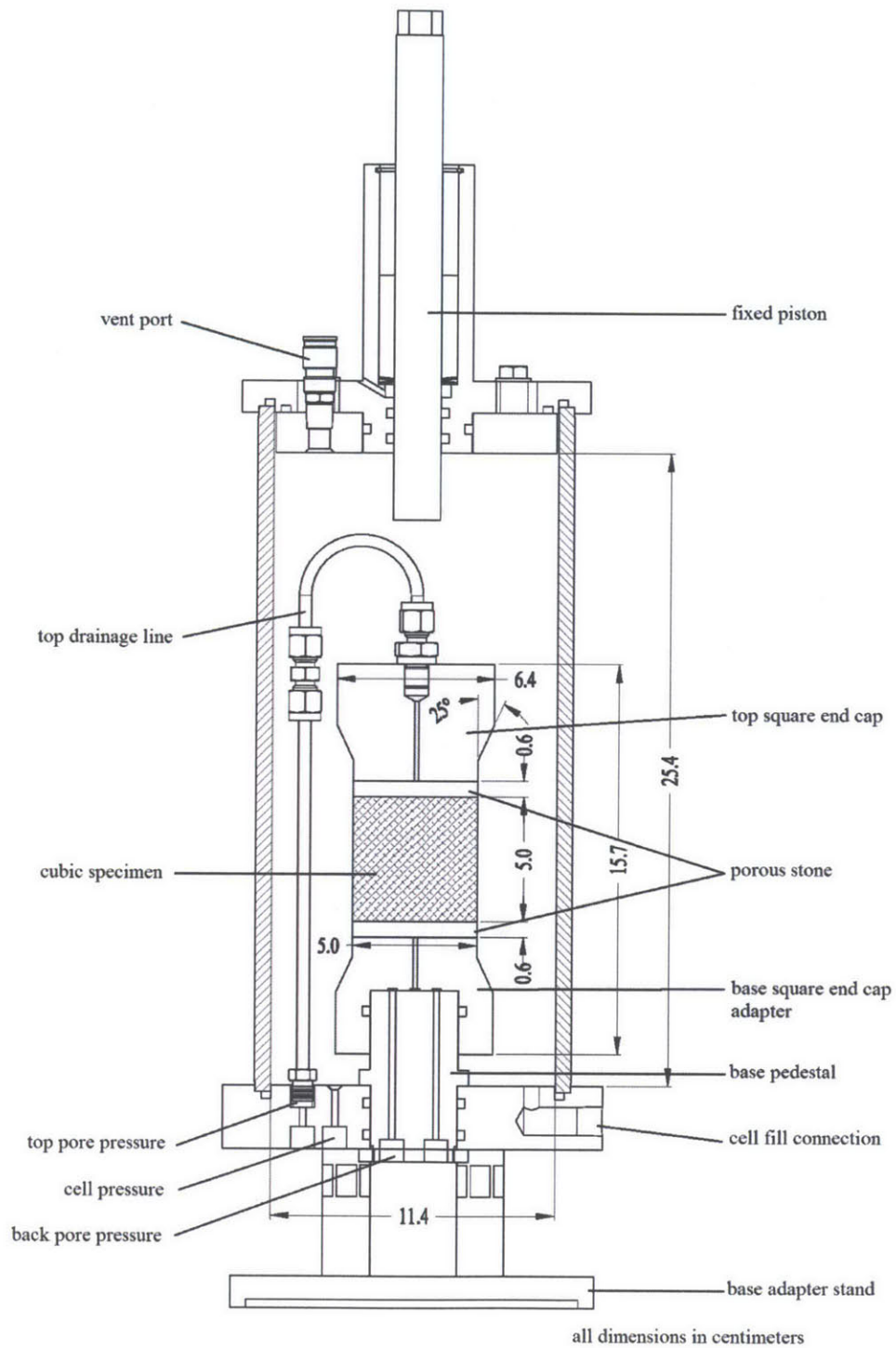


Figure 4-6: Dimensioned section of the low stress triaxial cell (modified for permeability measurement) with cubic specimen

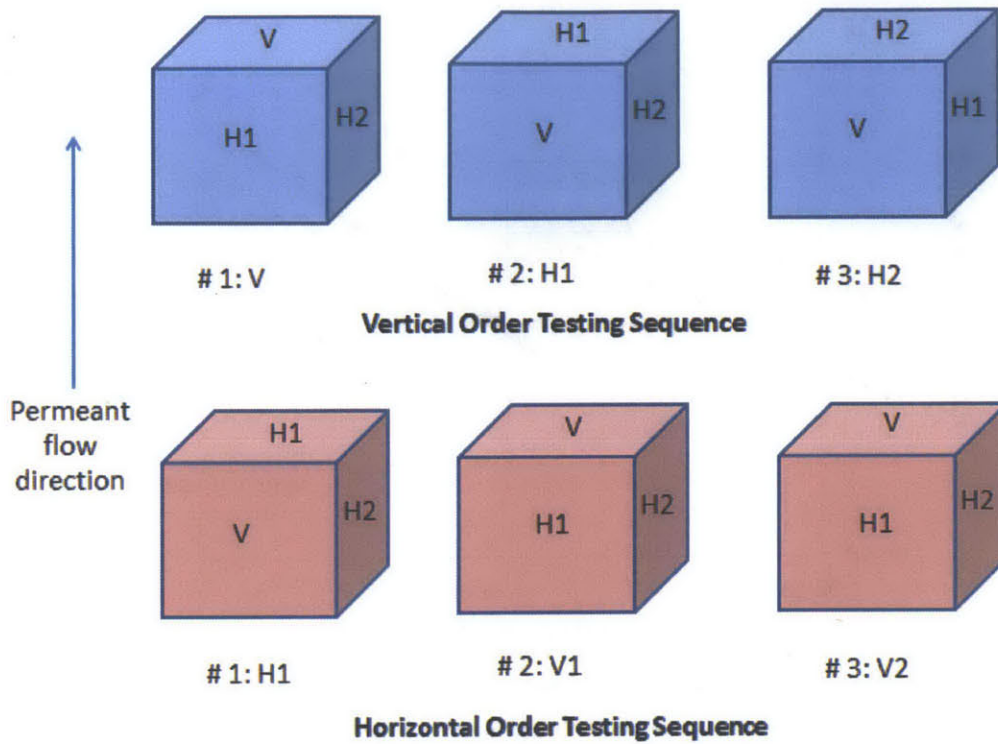


Figure 4-7: Vertical and Horizontal order testing sequences illustrated

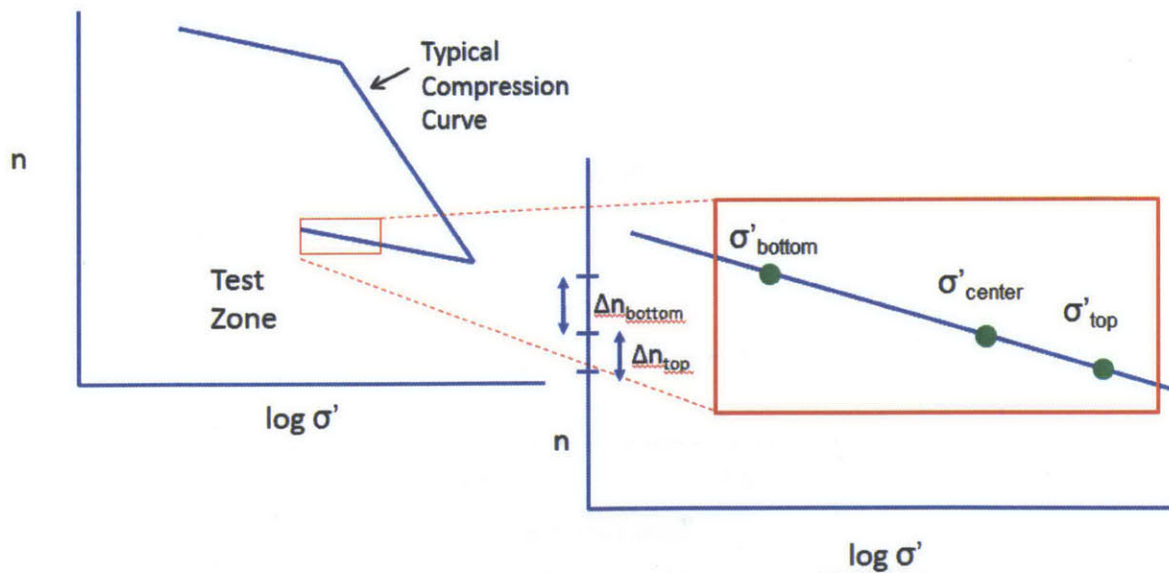


Figure 4-8: Illustration of specimen stress and porosity change during application of a hydraulic gradient

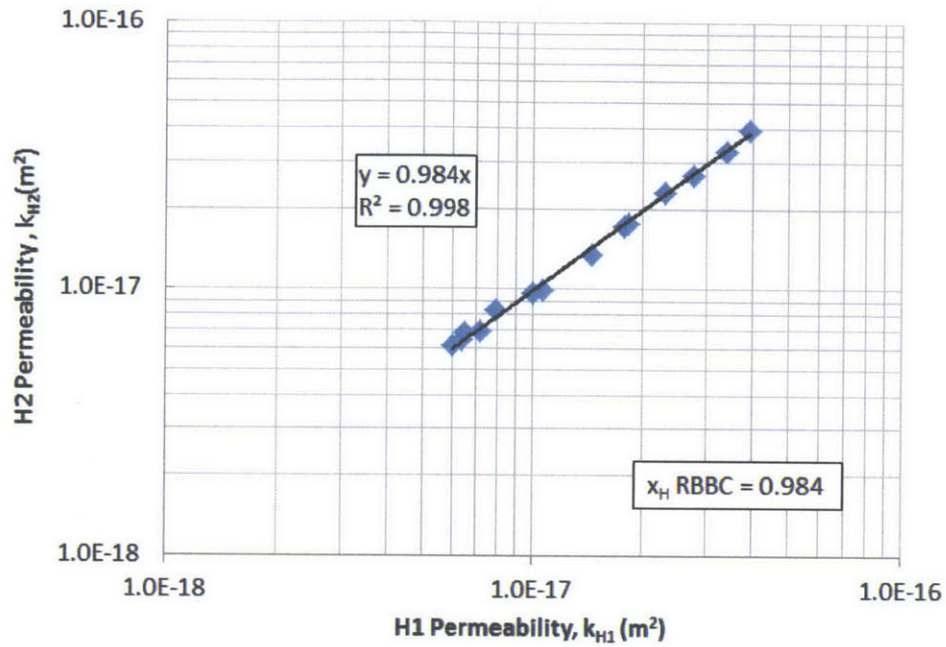


Figure 4-9: Horizontal Measurement Sequence Bias for RBBC

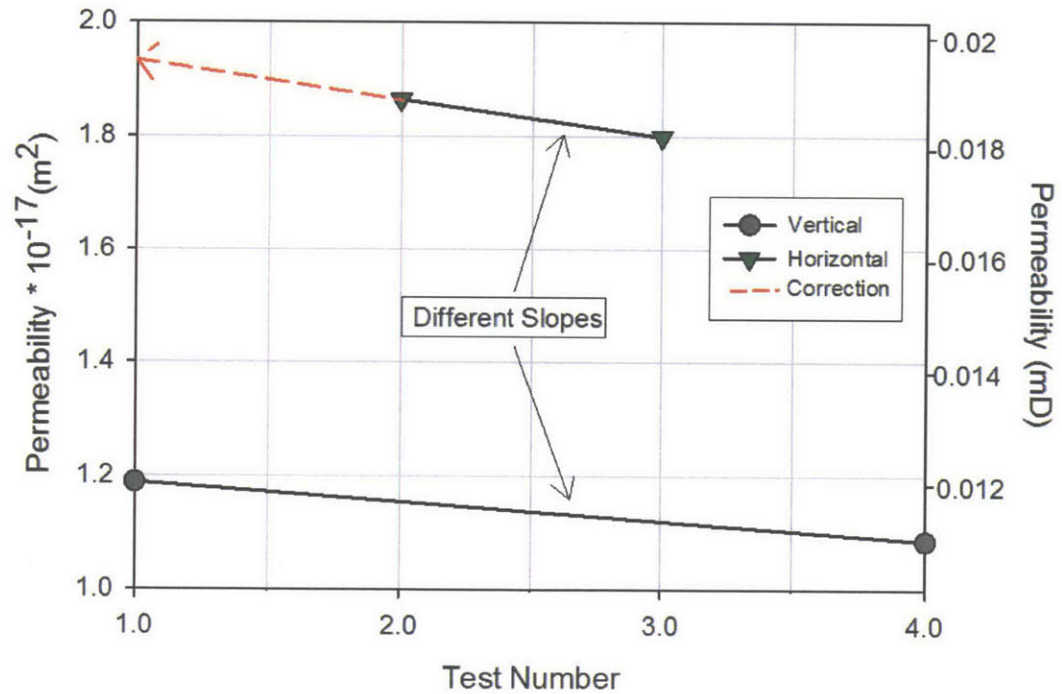


Figure 4-10: Single specimen measurement sequence bias with correction method (after Chan and Kenney, 1973)

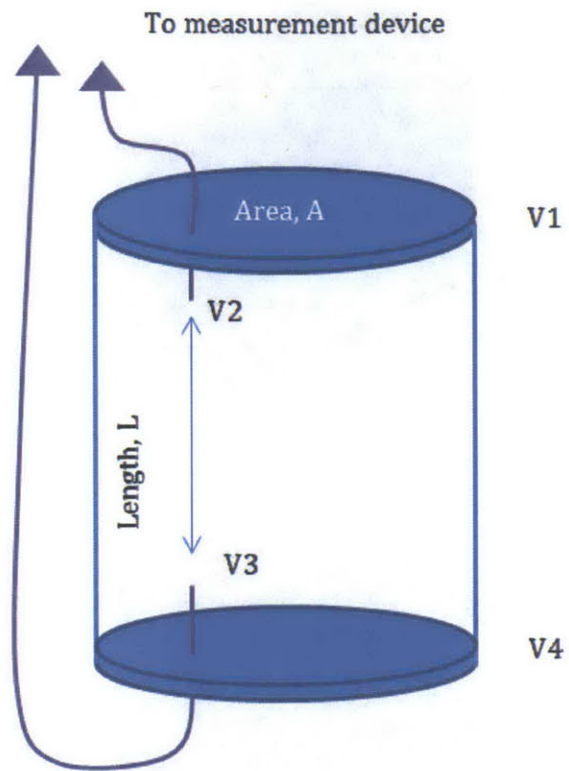


Figure 4-11: 4-Probe resistivity diagram

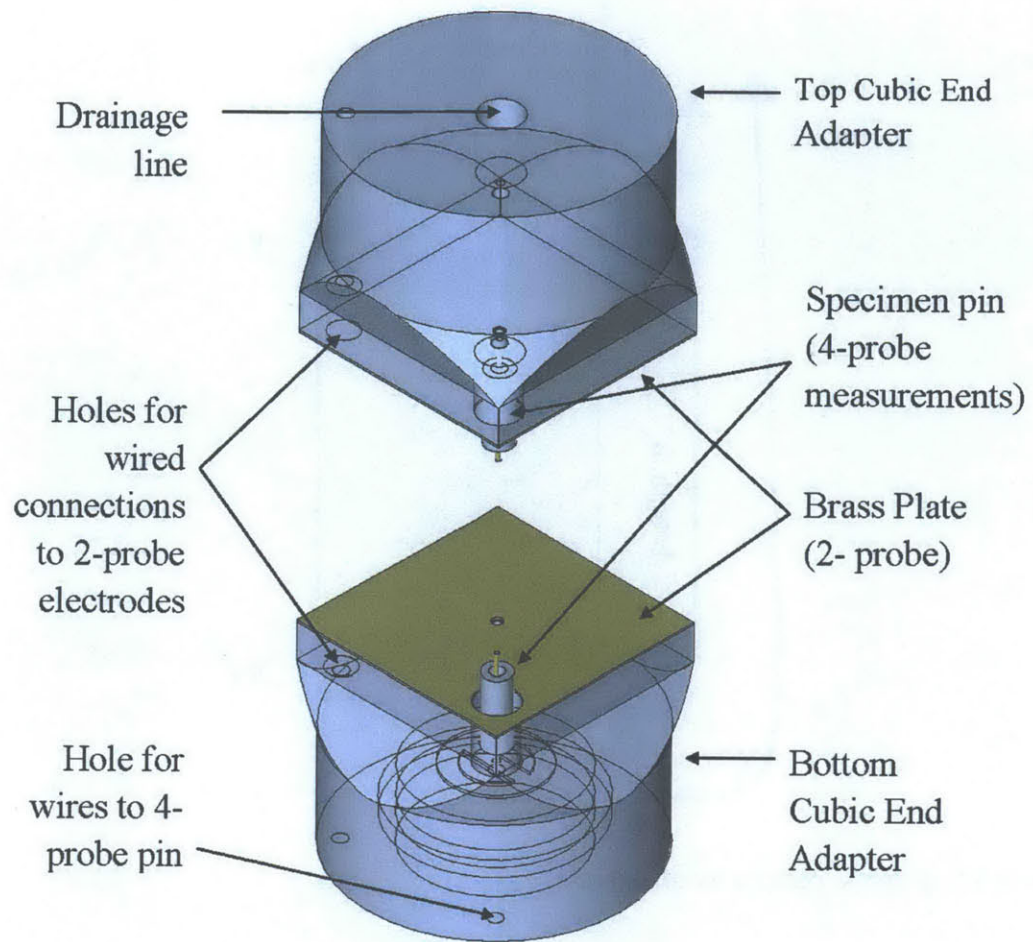


Figure 4-12: Drawing: Cubic end adapters modified for resistivity measurements

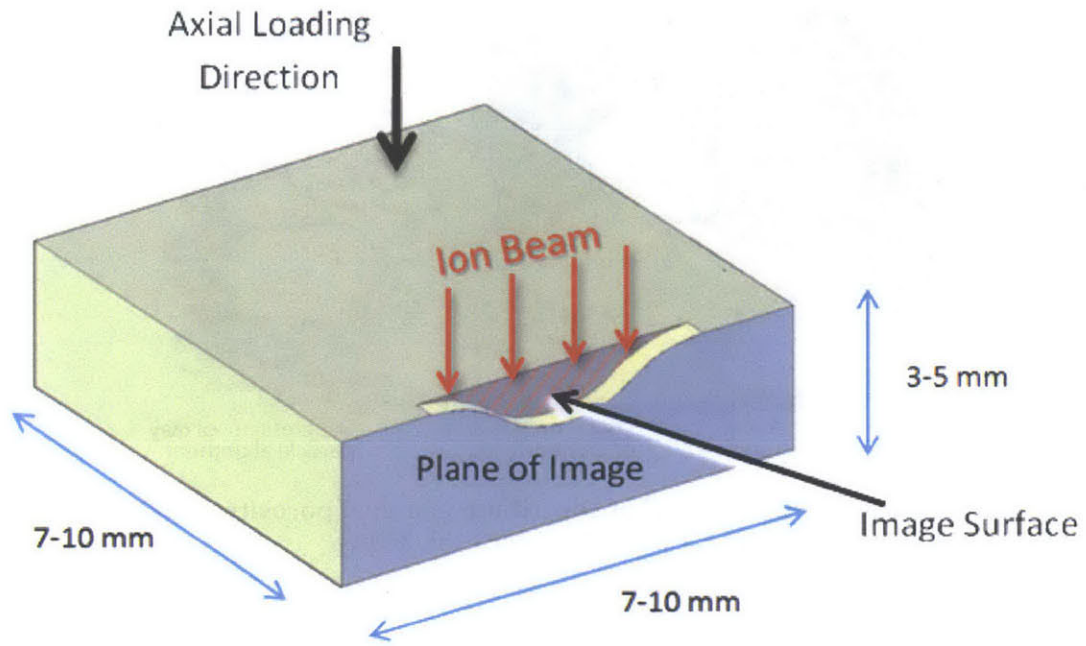


Figure 4-13: Imaging specimen configuration (image courtesy of Amer Deirieh)

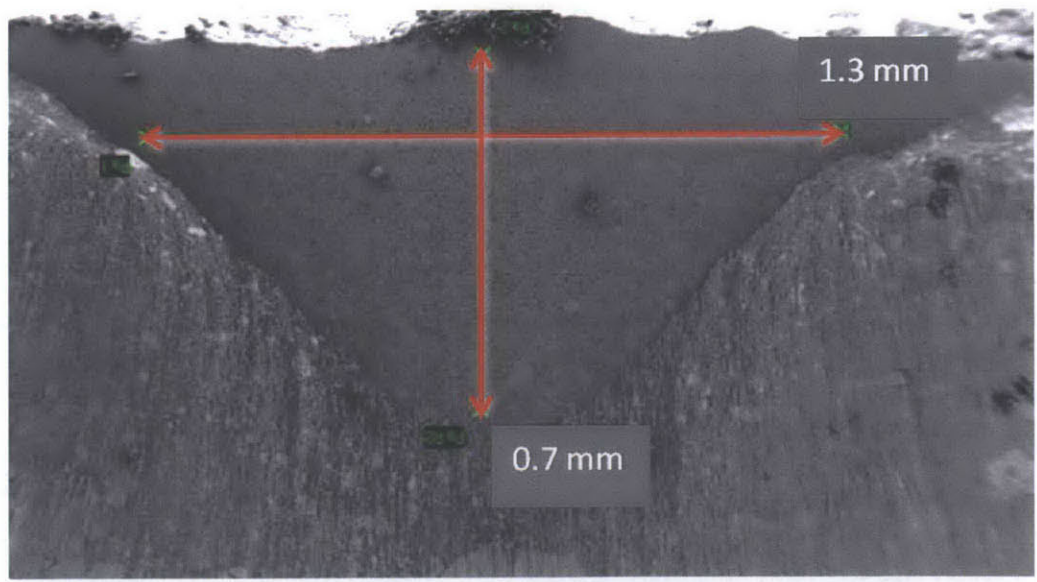


Figure 4-14: SEM image of an ion milled cross section (image courtesy of Amer Deirieh)

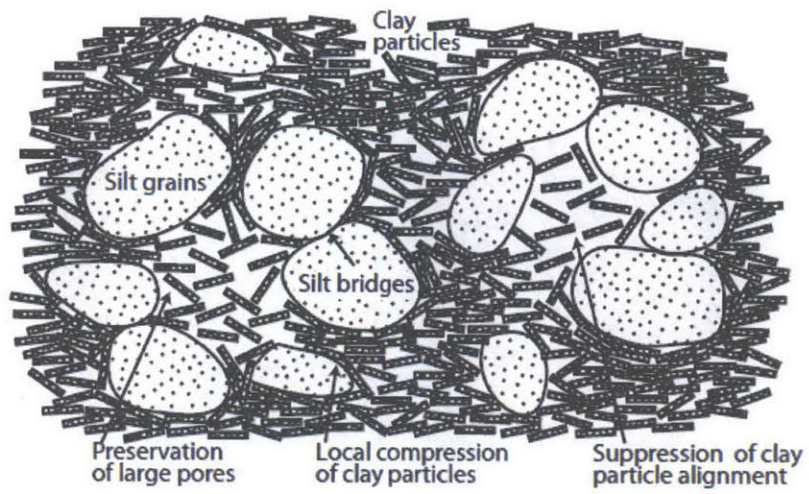


Figure 4-15: Pore scale mechanisms that contribute to a dual porosity structure and lead to heterogeneous fabric at the microscale (Schneider et al, 2011)

5 Results and Analysis

5	Results and Analysis	145
5.1	Resedimentation Results	146
5.1.1	Volume Change.....	147
5.1.2	Salinity	147
5.1.3	Agreement with CRS Compression Curve	149
5.2	Permeability Measurements: Experimental Parameters	151
5.3	Permeability and Permeability Anisotropy Results.....	156
5.3.1	Measurement Sequence Bias	156
5.3.2	RBBC	158
5.3.3	RGoM-EI and RSFBM.....	162
5.3.4	Comparison between mudrocks	163
5.3.5	Effect of Sidewall Friction on Laboratory Anisotropy Measurements	165
5.4	Resistivity Measurements	167
5.4.1	Measurement Sequence Bias	167
5.4.2	RBBC Resistivity.....	168
5.4.3	Comparison between Mudrock Resistivity Anisotropy	170
5.5	Particle Fabric Characterisation	171
5.5.1	UT and MIT Images	173
5.5.2	Mean Particle Orientation	174
5.5.3	Size Dependent Particle Orientation	177
5.5.4	Comparison with X-ray Texture Goniometry.....	179
5.5.5	Aspect Ratio Analysis.....	179
5.6	Summary of Results.....	180

This chapter presents the results of the testing program and discusses the validity of these results. The experimental program included measurement of the permeability and permeability anisotropy of 36 resedimented specimens. A total of 108 good directional permeability measurements were obtained, averaging three measurements per specimen. This includes 24 individual specimens of RBBC, 5 specimens of 39% Clay RBBC, 2 specimens each of RGoM-EI and RSFBM, 2 specimens of Leached RBBC and 1 specimen of Leached RSFBM.

The first section presents the results of the resedimentation program and addresses issues such as volume change, specimen salinity and the obtained stress - porosity relationships. The resedimentation program was very successful, yielding reproducible specimens that underwent minimal volume change during permeability measurement. One hiccup that was noted was a rather high variability in the final specimen salinity.

The second section discusses the details of the permeability measurement program and the third section presents the results of the permeability measurement program. Appendix 1 summarizes the measured permeability for all specimens. The directional permeability measurements were adjusted for measurement sequence bias, described in Chapter 4. These adjusted values were used to compute the permeability anisotropy. Table 5-7 summarizes the adjusted directional permeability and permeability anisotropy measurements for RBBC. The same data are summarized in Table 5-8 for the 39% Clay RBBC, and in Table 5-9 for the remaining mudrocks (RGoM-EI, RSFBM, Leached RBBC, and Leached RSFBM).

Section 4 presents the results of the resistivity measurement program which was initiated partway through this research. The testing program also included measurement of the resistivity and resistivity anisotropy of 18 resedimented specimens. This includes 12 measurements obtained under full saturation, back pressure and loading conditions in the triaxial apparatus: 9 RBBC, 2 Leached RBBC, and 1 Leached RSFBM. In addition, bench top resistivity measurements expanded the resistivity measurement program to include measurements on 14 specimens including: 8 RBBC, 3 39% Clay RBBC, 2 RGoM-EI, and 1 RSFBM. Some specimens were measured using both triaxial cell and bench top methods, allowing for comparison of results.

Section 5 describes the analysis procedure and presents interpreted results for the particle orientation, size and aspect ratio. The particle orientation and aspect ratio was measured using 19 SEM images of RBBC obtained using 6 specimens compressed to different effective stresses. Chapter 4 described the specimen preparation and SEM imaging techniques applied to obtain these images. The images were obtained from two different sources: MIT/ Harvard University (MIT) and the University of Texas at Austin (UT). The repeatability of the image analysis method was analyzed by comparing results obtained by 1) different analysts using the same images, and 2) by the same analyst using similar images obtained at different institutions (MIT vs. UT). Table 5-19 through Table 5-28 summarize the particle orientation and particle aspect ratio measurements. The change in measured particle orientation with decreasing porosity is compared to model predictions, and the effect of particle size on particle orientation is quantified.

Finally, a conclusion section summarizes the key results of the measurement program that will be further analyzed in Chapter 6.

5.1 Resedimentation Results

In total, 36 individually resedimented specimens were fabricated and measured: 24 RBBC, 5 39% Clay RBBC, 2 RSFBM, 2 RGoM-EI, 1 Leached RSFBM, and 2 Leached RBBC. Table 5-1, Table 5-2 and

Table 5-3 summarize the specimen ID, permeability test ID, maximum stress level, test stress level, OCR, void ratio, porosity and porosity variation for each resedimented specimen.

The maximum (peak) stress level (σ'_p) is the highest stress level applied during resedimentation. The test stress level is the stress level after rebound to an OCR of 4 at which all permeability measurements were made. The void ratio and porosity were measured multiple times for each specimen, at the end of each directional permeability measurement using a mass based method (discussed in Chapter 4 and Appendix 2). The average porosity is the average of all porosity measurements made for the same specimen. The variation in porosity is the difference between the maximum porosity and the minimum porosity measured for a single specimen.

The following subsections discuss key parameters on which the resedimented specimens were evaluated, namely degree of volume change, specimen salinity, and the agreement between the cubic specimen stress-porosity measurements with that expected given standard CRS compression curves measured in the laboratory.

5.1.1 Volume Change

One key concern for these experiments was whether or not the specimen volume remains constant or was affected by the successive reassembly process required for each measurement of the same specimen, including re-pressurization, recompression and pressure changes associated with application of the hydraulic gradients. The specimen dimensions were measured at the beginning and end of each directional permeability measurement (set up) using calipers. The volume change during each directional measurement is computed from these dimensions and is reported as a percentage of the total specimen volume at the end of each set up. In total, 108 directional permeability measurements were made.

The results show that both the specimen porosity, measured using mass based methods, and the specimen volume, measured using caliper measurements, did not significantly change through the course of the up to month long permeability measurement sequence. The computed porosity varied by < 0.01 for most specimens, with only three specimens having a larger porosity variation, still < 0.012 (Table 5-1, Table 5-2 and Table 5-3). The variation in porosity is independent of both material type and stress level. The specimen volume change ranged from increasing (swelling) by 5.9% to decreasing (compressing) by -4.8%, with an average increase in volume of only 0.35% (Appendix 1). On average, the specimens underwent minimal volume change during measurement.

5.1.2 Salinity

Table 5-5 summarizes the salinity results for all specimens. The specimen salinity is obtained by first measuring the pore fluid conductivity using a 2 probe conductivity meter and then by converting the measured conductivity to salinity using a calibration curve for sodium chloride (NaCl) solutions.. This measurement process is described in Chapter 3. Point measurements of Sea

salt solutions were used to confirm that the NaCl calibration curve used in the laboratory can be used to estimate the salinity of sea salt based solutions, indicating that the sea salt is NaCl dominant.

The average salinity of the completed RBBC batches is 15.1 g/L, slightly lower than the batched salinity of 16 g/L. The measured salinity is even lower when the total expected salinity of the RBBC mudrock is computed: as discussed in Chapter 3, soil powder with 1.24 g/kg of salt is batched at 100% water content and 16 g/L salinity, yielding a mudrock with a total salinity equal to ~ 17.2 g/L. Further, the salinity of completed RBBC batches varies significantly, ranging from as little as 9 g/L to as much as 23 g/L.

Similarly, the RGoM-EI has a measured average salinity of only 44.7 g/L, nearly half of the 80 g/L batching salinity. If the natural salinity of the mudrock powder is included, the total salinity of RGoM-EI mudrock is expected to be closer to ~ 87 g/L based on the salinity of the mudrock powder and initial water content from Chapter 3. Contrarily, both the 39% Clay RBBC and the RSFBM have higher final average salinities than their batching salinity: 18.4 g/L vs. 10.9 g/L for the 39% Clay RBBC, and 7.7 g/L vs. only 0.4 g/L for the RSFBM. The final salinity of all three leached soils was low, in the 1 g/L range.

There is no trend between measured salinity and increasing maximum applied stress for RBBC (Figure 5-1). Further, the salinity of some specimens was measured both before and after the permeability measurement to determine whether the measurement itself affected the specimen salinity. The salinity measurement was conducted using specimen trimmings before the permeability measurement, and using a portion of the final (wet) specimen following the permeability measurement. Figure 5-2 shows that the permeability measurement does not significantly or consistently affect the measured salinity for all mudrocks measured.

The results describe two concerning trends. First, there is significant scatter in the final specimen salinity for specimens batched using the same initial salinity (e.g. see scatter in Figure 5-1). Second, the average final specimen salinity is lower than the initial salinity. For example, the average salinity of the RGoM-EI specimens is nearly halved during the resedimentation process, while the average RBBC specimen salinity is only ~ 1-2 g/L lower. Research is ongoing to quantify these sources of error, both looking at scatter and the decrease in average salinity.

The source of scatter in the average salinity results is likely attributed to small errors in the salinity measurements and calculations. These can be quantified and corrected over time. There are five key sources of error identified in the results presented herein:

1. Slight loss of salt mass because the supernatant liquid was not re-added to the wet soil and oven dried; the measurement method in Chapter 3 has been updated to avoid this error in the future.
2. Slight error in water content and computed salinity because the dry mass included the mass of salt; this error is expected to be small for the salinities measured in this thesis and can be

corrected in the future by separately calculating the dry mass of soil and the dry mass of salt.

3. Slight error in the mass of salt calculation because the density of the solution was assumed equal to 1000 g/kg when in fact it will vary with the salinity of the solution and exact solutions are known; this may be fixed by computing the density as a function of salinity, however this should not affect the salinity by more than 0.05 g/L.
4. Loss of water and/or salt due to evaporation from the sealed tubes during hydration. When the centrifuge tubes are left overnight, water can evaporate through poorly sealed caps, and further, salt can escape and crystallize on the outside of the tubes, leading to loss of salt errors in the water content which combine to lowering the measured salinity.
5. Incorrect calibration curve. A NaCl calibration curve was used to ascertain the salinity of solutions with unknown or varying salt chemistry. The error associated with assuming NaCl is low, provided the dominant chemistry is NaCl-based; if the salt is CaCl₂ based, for example, another calibration curve would be required, however for the mudrocks studied this is not the case.

The decrease in average salinity poses a different problem and cannot be attributed to the small errors. The most likely cause of the decrease in average salinity decrease is uptake of salt by clay ions, specifically Na⁺ ions by the Smectite minerals though conversion from Ca Smectite to Na Smectite. RBBC has low Smectite content and should experience only a slight decrease in average salinity, whereas RGoM-EI has a high Smectite content and should experience a larger decrease in average salinity. These expected trends are demonstrated by the results, with the RBBC salinity average salinity measuring 15.1 g/L compared to a predicted 17.2 g/L, and RGoM-EI measuring an average of 44.7 g/L compared to a predicted value of ~ 87 g/L (calculations above). Research is ongoing to confirm this hypothesis and quantify this effect.

5.1.3 Agreement with CRS Compression Curve

Results from three Constant Rate of Strain (CRS) measurements were obtained from fellow researchers for comparison with the measured specimen porosity vs. stress relationship. Aiden Horan (MS, '12) provided data for CRS 1219 on RBBC batched at 16 g/L (Figure 5-4 through Figure 5-6, Figure 5-24, Figure 5-28 and Figure 5-31); Brian Fahy (MS '14) provided data for CRS 1364 RGoM-EI batched at 64 g/L (Figure 5-7, Figure 5-8 and Figure 5-34), and Brendan Casey (PhD, '14) provided data for CRS 1333 on RSFBM batched at 0 g/L (Figure 5-9, Figure 5-10 and Figure 5-36).

Compression curves for all mudrocks measured are provided in both e -log σ and n -log σ space in Figure 5-3 through Figure 5-12. In these plots, the resedimented specimen porosity and void ratio are plotted against the final specimen effective stress at OCR 4. This corresponds to the effective stress at which the permeability and resistivity measurements were made. The CRS compression curve, where available, is plotted for comparison. Both the virgin compression line and the OCR 4 line are provided for each CRS measurement. The OCR 4 line is computed by dividing the stress axis of the normally consolidated line of the CRS compression curve by 4, and then by shifting it up by an increment in void ratio defined by the swelling ratio.

Abdulhadi (2009) showed that the swelling index (c_s , slope of the swelling line in void ratio vs. log stress space) is both OCR and stress dependent (Figure 5-13). For RBBC at OCR 4, Abdulhadi (2009) measured the swelling ratio to vary from ~ 0.027 to 0.041 as the maximum applied stress increased from 0.4 MPa to 10 MPa. Similarly, Horan (2012) measured a swelling ratio of 0.028 for RBBC at OCR 4 and 10 MPa effective stress. Table 5-6 summarizes the swelling ratio used to define the OCR 4 line for the various mudrocks studied. The swelling ratio was measured from the noted CRS tests and assumed to be stress independent.

The compression curves are plotted in both e -log σ and n -log σ space. The low plasticity mudrocks (RBBC and 39% clay RBBC) exhibit the most linear compression behaviour in e -log σ space, whereas the higher plasticity mudrocks (RGoM-EI and RSFBM) are most linear in n -log σ space. Changing the clay fraction changes the compressibility of the mudrock; decreasing the clay fraction by adding silt as in the 39% Clay RBBC reduced both the porosity and void ratio for a given stress level (see Figure 5-5 and Figure 5-6).

There is a slight porosity calculation error in the data set. This error most affects the high salinity mudrocks and stems from improper calculation of the salt volume. Initially, the methods to compute the density of salt water described in Chapter 3 were not used; rather a curve fit was used to compute the salt water density as a function of salinity. This curve fit is only valid for pore fluid salinities < 30 g/L and has a higher error than the methods described in Chapter 3 for determining salt water density. Data from over a hundred measurements were reduced using this curve fit to compute salt water density and eventually specimen porosity. Fixing this error would increase the computed porosity of the highest salinity specimens by a maximum of < 0.005 , with all other specimens would see smaller changes in porosity. As a result, this error was deemed negligible and was not corrected.

Overall, all specimens of the same mudrock form a consistent compression curve with decreasing porosity and void ratio with increasing applied effective stress. This supports the repeatability and reproducibility of the resedimentation procedure. A number of RBBC specimens were fabricated with the same stress history; specimens at 0.2 MPa, 0.4 MPa, 1.5 MPa and 2.5 MPa show excellent repeatability in the porosity and void ratio measurements (see Figure 5-3 and Figure 5-4).

The cubic specimen measurements for all mudrocks measured deviate from the computed CRS OCR 4 line. The measured specimen porosity at a given stress level is higher than expected from the CRS measurement (e.g. see Figure 5-3, Figure 5-8 and Figure 5-10). For RBBC this deviation occurs for porosities < 0.41 and stress levels higher than 0.5 MPa; for RGoM-EI and RSFBM the deviation is noticeable for all measurements.

There are two likely causes of the noted porosity deviation: sidewall friction and improper calibration of the load cell in the final stages of resedimentation.

During resedimentation the specimen experiences sidewall friction because of the large contact area with the cylindrical resedimentation tube. Sidewall friction reduces the applied stress felt by the specimen. A specimen that is compressed to 10 MPa and then rebounded to 2.5 MPa during resedimentation has an OCR of 4. However, if sidewall friction supports 5% of the applied load, then the maximum applied stress becomes 9.5 MPa. The rebounded stress will increase, becoming 2.6 MPa. Overall, the specimen will be at OCR 3.65 (9.5 divided by 2.6) instead of OCR 4 as loaded. Sidewall friction results in a lower than expected OCR and may explain some of the noted deviation from the OCR 4 line. The effect of sidewall friction is further discussed in Section 5.3.5.

More than likely, however, the deviation is caused by improper calibration of the load cell on the air pressure load frame. The air pressure load frame is used to compress specimens to maximum effective stresses in excess of ~ 1.8 MPa. The noted porosity deviation (Figure 5-3, Figure 5-8 and Figure 5-10) occurs in specimens with OCR 4 stresses in excess of ~ 0.4 MPa, all of which were resedimented using the air pressure load frame. The air pressure load frame relies on a load cell to measure the applied load; a calibration error in this load cell could lead to a lower than expected applied load and a higher than expected porosity. Figure 5-14 plots the porosity deviation from the CRS OCR 4 line vs. the maximum effective stress for RBBC. This figure illustrates that significant deviation does not occur for those specimens that were resedimented using gravity load frames, and that the deviation increases linearly with maximum applied stress for those specimens resedimented using the air pressure load frame. Affected measurements cannot be back corrected for this error, as the permeability measurement would have been made at an erroneously high testing effective stress and low OCR. Moving forward, the load cell calibration factor on the air pressure load frame should be verified for the full range of applied loads up to 50 kN.

Leaching the soil does not affect the specimen compressibility at high stress levels (>6 MPa). The Leached RSFBM specimen has the same porosity as the natural RSFBM specimen with the same resedimentation stress history (see Figure 5-10), and the leached RBBC specimens fall on the natural RBBC compression curve (see Figure 5-3). This observation is consistent with results reported by Horan (2012).

5.2 Permeability Measurements: Experimental Parameters

A summary of the experimental parameters relating to each individual directional permeability measurement is included in Appendix 1. This summary includes:

1. the sampling effective stress, back pressure, saturation, inflow volume during back pressure, and time between back pressure and the permeability measurement;
2. the correction factors that were applied to the permeability measurement to adjust for measured leaks and secondary compression volume change;
3. all parameters required to compute the hydraulic conductivity, including specimen dimensions (area and length), applied hydraulic gradients, and inflow and outflow volumes; and
4. the computed hydraulic conductivity.

The following paragraphs discuss each of these parameters in detail.

The specimen permeability was measured at the final effective stress following resedimentation, σ' , equal to about $\frac{1}{4}$ (corresponding to OCR 4) of the maximum effective stress, σ'_p . The sampling effective stress, σ'_s , varied from as little as 5% to as much as 100% of σ' . The sample equilibrates to σ'_s during the pressure up phase using an applied hydrostatic stress of σ' . This sampling effective stress is maintained during back pressure to limit specimen volume change prior to the recompression.

The large range of sampling effective stress is due to a change in methodology part way through the measurement program. Initially a wet set up method (pore pressure lines saturated) was used. The disadvantage of this method is that excess water and air become trapped in the pore pressure lines. As the cell pressure is applied and the apparatus warms up to the measurement temperature (about a +6 degree Celsius temperature change), the excess water and air causes a) an increase in pore pressure, b) a decrease in sampling effective stress and c) the need for significant recompression to reset the measurement effective stress, σ' . This process effectively back pressures the specimen during the pressure up phase, which in turn lowers the inflow volume measured during the back pressure phase.

Part way through the measurement program this problem was noticed and a dry set up method was adopted. For the dry set up, the specimen and pore pressure lines were vacuum de-aired until the full cell pressure was applied, and then vacuum saturated, preventing excess water from entering the system and removing entrapped air. . This procedure is described in Appendix 2. Slight pore pressure increases still occur (<0.05 MPa) due to temperature equilibration. Adoption of a dry set up method increased σ'_s/σ' values to between 80% and 100%, indicating good quality specimens.

The back pressure applied to specimens increased over time. Initially low back pressures ranging from 0.2 to 0.35 MPa were applied as the back pressure was limited by low capacity (0.7 MPa) pressure transducers. As the stress level increased and the B value decreased and the pore pressure transducers were changed for higher capacity (1.4 MPa) transducers. The back pressure was increased up to 1 MPa in attempts to increase the B value. The B value ranged from 0.59 to 1.0 (Appendix 1) and increased with decreasing stress level and increasing specimen permeability. The lowest B values were measured for the two high stresses, low permeability RGoM-EI specimens (HC030 and HC031). Increasing the back pressure or leaving the specimen to saturate for long periods of time (multiple days, up to a week) did not increase the B value for these specimens. The low B value was likely a combined result of incomplete saturation and air in the pore pressure lines; consequently the permeability measurements may not be representative.

The inflow volume during back pressure ranged from very little (on the order of 0.1 cm³) to 5 cm³ or higher. The following factors were noted to affect the inflow volume:

- a) Back pressure: An increase in volume is required to increase the back pressure, even for a fully saturated system. This is due to the compliant effect of compressing the existing pore fluid and expanding the pore pressure lines. The increment of volume input required to achieve an increment increase in pressure is not linear; it takes more volume to increase by a fixed increment at low pressures compared to high pressures.
- b) σ'/σ'_s : The lower the sampling effective stress, σ'_s , the higher the back pressure in the specimen following the pressure up phase. For example, if the testing effective stress (equal to the OCR 4 stress following resedimentation) was 10 MPa, but the sampling effective stress was only 9.5 MPa, this means that the specimen pressure is already 0.5 MPa prior to back pressure saturation. Less volume is required to pressurize the lines and specimen from 0.5 to 1 MPa than is required raise the pressure from ~ 0 MPa to 1 MPa (see a).
- c) Time since the permeant filling the pore pressure lines and PVA's was changed: Different specimens are measured at different pore fluid salinities; to do this, the fluid filling the two pore pressure PVA's and all the pore pressure lines must be changed. Despite vacuum saturation techniques, the configuration of the system means that air is inevitability introduced. The pore pressure lines are gradually de-aired over time as the pore pressure system is cyclically pressurized and depressurized. The volume change required to pressurize the pore pressure lines immediately following a pore fluid change is much greater than that after a few months of continual use with the same pore fluid.
- d) Leaks: Leaks affect the measured volume change based on their location and rate. A leak will cause either an uncharacteristically large, or a linearly increasing inflow volume with time.

In general, any inflow volume that is less than $\sim 5 \text{ cm}^3$ and remains constant once the maximum back pressure is reached is indicative of a leak free system. Higher inflow volumes were often indicative of a leak. A common leak location is an external leak through the back pressure pore pressure transducer. A leak in this location is easily identified by 1) an unusually high inflow volume, 2) a constant rate of inflow, and 3) visible leakage at the pore pressure transducer. This is easily corrected and does not affect the specimen. Other medium to large external leaks may not result in large inflow volumes but will appear as a linearly increasing volume at constant pressure. Such medium to large require complete re-setup of the apparatus to fix the leak. Very small external leaks often exist and cannot be located or fixed; these leaks are measured at constant back pressure and effective stress and inflow and outflow volumes are corrected using the measured leak rates.

The time between the beginning of back pressure and the beginning of the hydraulic conductivity measurement varied greatly. A minimum of about 8 hours was required for the back pressure phase, and 8-12 hours for the recompression stage if applicable. The actual time varied mostly based on the operator's schedule.

The secondary compression volume correction adjusts the inflow and outflow volumes recorded during a permeability measurement for creep related volume change. The inflow and outflow

volumes vary linearly with time, and secondary compression volume change varies with the logarithm of time. To handle this rate disparity, the correction factor is applied to the incremental inflow and outflow volumes, typically at 4 minute intervals. Appendix 2 describes this correction factor in more detail.

The rate of secondary compression volume change was only measured for those specimens where $\sigma_s < \sigma'$. The use of the secondary volume correction has varied with time throughout this research program. For most specimens, the rate of secondary compression volume change was low and could only explain small ($<0.04 \text{ cm}^3$) differences between the inflow and outflow volumes. Secondary compression volume change and therefore has a minimal effect on the computed hydraulic conductivity, affecting the third significant digit only. Further, where there is a small leak, it is difficult to correctly determine the rate of secondary compression unless a leak test is performed; such leak tests were not initiated until beyond the halfway point of the research program (beyond HC021). For consistency, secondary compression volume change is only included 1) where recompression was required, allowing measurement of the rate of secondary compression; and 2) where application of the correction factor would affect the second significant digit of the measured hydraulic conductivity.

A minimum of three hydraulic gradients were applied for each directional permeability measurement. The hydraulic gradients were applied for a time period ranging from 6 hours to two weeks, most commonly between 12 to 24 hours. Lower permeability specimens were measured for longer time periods to allow a larger volume of permeant to invade the specimen, reducing the influence of volume change errors on the measurement. The measured hydraulic conductivity did not vary significantly, showing variation only in the third significant digit, between measurements made over short time periods (6 to 24 hours) compared to longer time periods (days to weeks) (e.g. Figure 5-15). The hydraulic gradients applied ranged from 9 to 280, with higher gradients applied to lower porosity and permeability specimens.

Minimal specimen volume change was measured during application of the hydraulic gradients. Because the specimens are measured at an OCR of 4, the stress change response is stiff compared to normally consolidated specimens. The pressure difference was split evenly between the top and the bottom of the specimen, maintaining the effective stress in the middle of the specimen. This method resulted in the volume change at the bottom of the specimen to nearly compensate for the volume change at the top of the specimen. Appendix 1 tabulates the applied pressure differential as a function of effective stress for all measurements. For most specimens the change in pore pressure at either the top or bottom of the specimen was small ($<5\%$) compared to the average effective stress, resulting in a very small stress change and a very small volume change. To account for this small volume change, an equalization period of 3-5 hours of flow was always disregarded in the inflow and outflow volumes used to compute the hydraulic conductivity.

The specimen volume change resulting from application of a hydraulic gradient was computed as the difference between the inflow and outflow volumes corrected for secondary compression and leak associated volume change, where measured. Appendix 1 tabulates the measured volume

change. Additional small volume changes are associated with secondary compression and are small, typically $<0.04 \text{ cm}^3$. The average volume change resulting from application of a hydraulic gradient ranges from 0 to $\pm 0.09\%$ of the specimen volume, and the maximum was 0.14% . Both compression and swelling were equally likely to occur. This indicates that the measurement method did not affect the specimen volume or porosity.

The measured flow volume through the top and bottom of the specimen during measurement of the hydraulic conductivity under a particular hydraulic gradient varied greatly, ranging from as little as 0.03 cm^3 to as much as 10 cm^3 . The lowest flow volumes were recorded on the RGoM-EI specimens with the lowest permeability, and the highest flow volumes were recorded on the higher permeability mudrocks (RBBC and 39% Clay RBBC). Though the flow volumes are very small, distinct linear trends were noted allowing calculation of the hydraulic conductivity. However, the influence of volume errors on the hydraulic conductivity measurement increases as the flow through volume decreases. This results in a high standard deviation in the measured hydraulic conductivity as a function of hydraulic gradient. Volume errors are defined as differences between the inflow and outflow volumes that remain following application of the secondary compression volume correction and correcting for any measured leaks.

The volume errors are tabulated in Appendix 1. The volume error, equal to the difference between the inflow and outflow volumes, is computed as a percentage of the average flow volume for each hydraulic gradient applied to each specimen. The average volume error is $< 10\%$ of the measured average flow volume. Lower permeability specimens such as the RGoM-EI and RSFBM have much higher volume errors, as high as 34% for some hydraulic gradients. Still, a volume error of 34% translates into a potential error in the hydraulic conductivity of one half that, or only 17% , because the inflow and outflow volumes are averaged. For the RGoM-EI specimens with hydraulic conductivity in the range of $2 \times 10^{-10} \text{ cm/s}$ (See Appendix 1, HC031 V) the true value likely ranges from $1.66 \times 10^{-10} \text{ cm/s}$ to $2.34 \times 10^{-10} \text{ cm/s}$. In terms of permeability measurement, this is still a very small range, and is acceptable given the low permeability and difficulty encountered in measuring the permeability of the RGoM-EI specimens in particular (discussed later). However, small changes in the measured directional permeability translate into large changes in the permeability anisotropy. As a result, the permeability anisotropy for RGoM-EI may be greatly affected by volume inflow errors.

One difficulty associated with the constant head method is that small flow volumes used to measure the permeability translate into very shallow pore fluid replacement depths. This is especially true for very low permeability specimens such as the RGoM-EI specimens measured. Considering an average area of 25 cm^2 and assuming a porosity of 0.4 , it would take 1 cm^3 of permeant to invade the specimen and replace the pore fluid for an average depth of 1 mm . The pore fluid originally occupying the 1 mm portion of the specimen is displaced through the specimen, and eventually an equivalent depth of 1 mm of pore fluid is expelled from the specimen. The depth of pore fluid replacement varies with porosity and the inflow volume which is related to the permeability and the length of measurement. Surface smearing can affect the surface layer permeability of the specimen. The average specimen permeability can still be measured using a sensitive measurement

system because the inflow and outflow volumes are constant functions of time. The results indicate that the measured permeability is repeatable and forms linear trend lines, proving the robustness of the method despite the above issues.

5.3 Permeability and Permeability Anisotropy Results

The measured directional hydraulic conductivity for each specimen is summarized in Appendix 1. These values are converted to permeability using the pore fluid salinity, density, viscosity and temperature. The permeability is computed using the salinity of the permeant, and not the measured specimen salinity (Table 5-5), mainly for simplicity because small variations in pore fluid salinity do not significantly affect the permeability. The permeability measurements are corrected for measurement sequence bias, using either the global specimen method or the single specimen method. These analysis methods are described in detail in Chapter 4 and Appendix 2.

Subsection 1 analyzes the effect of the measurement sequence bias correction and proves that it is useful. Subsection 2 discusses the permeability behaviour of RBBC and includes an analysis of the effect of both leaching and clay fraction. Subsection 3 does the same for RGoM-EI and RSFBM, and the behaviour of all mudrocks studied is compared in subsection 4. The permeability behaviour of different mudrocks is discussed and compared using plots of the logarithm of the vertical and horizontal permeability, k_v and k_H , vs. porosity and the logarithm of the maximum effective stress applied during resedimentation, σ'_p . The permeability is plotted as a function σ'_p and not the measurement effective stress, σ' , as was used for the compression plots. Finally, sidewall friction was discussed as a source of error in the resedimented specimens in Section 5.1.3; the last subsection uses a model to demonstrate that even significant sidewall friction would have little effect on the permeability anisotropy measurements.

It is important to note that the permeability – stress plots are provided for qualitative evaluation only. The slopes of the permeability – stress line are influenced by the noted deviation between the measured cubic specimen porosity and the OCR 4 line. As a result, the focus is placed on discussing trends in both permeability and permeability anisotropy with porosity.

5.3.1 Measurement Sequence Bias

All permeability measurements were adjusted for measurement sequence bias. This is a purely empirical correction factor that is applied to account for the noted change in measured permeability with repeated setups. The global adjustment method was applied to RBBC and 39% clay RBBC to reduce scatter. The single specimen adjustment method was applied to all other mudrocks.

Table 5-10 summarizes the measured directional permeability for RBBC in each of the H1, H2, V and V2 directions. Table 5-11 gives the same for the 39% Clay RBBC. The number of permeability measurements separating permeability measurements in the horizontal (H1 and H2) or vertical (V1

and V2) directions (Δn) is included in each table. These data are used to obtain the horizontal and vertical measurement sequence bias, x_H and x_V , respectively, as described in Chapter 4 and Appendix 2. Figure 5-16 and Figure 5-17 give cross plots of the horizontal and vertical permeability used to define x_H and x_V for RBBC. Figure 5-18 and Figure 5-19 give the same for 39% Clay RBBC. Table 5-12 summarizes the measurement sequence bias parameters for RBBC and 39% Clay RBBC.

The measurement sequence bias is found to be direction independent. The measurement sequence bias for RBBC is direction independent. For 39% Clay RBBC, the measurement sequence bias varies with measurement direction; this is likely due to a small data set rather than true material behaviour. For 39% Clay RBBC, only one measurement was performed using the measurement sequence of H1, V, V2 required to determine the value of x_V . Ideally, two or more measurements are required to determine the global measurement sequence bias factors x_H and x_V . However, because the research was in its infancy at the time, some measurements were made using the directional order H1, H2, V. These measurements could not be adjusted using the specimen adjustment method. Consequently the global adjustment parameters required definition; in the case of the vertical direction, this was achieved using one specimen before it was decided to steer the research program in a more interesting direction.

The measurement sequence bias parameters x_H and x_V were determined using measurements on specimens with porosity > 0.36 for both RBBC and 39% Clay RBBC. The permeability anisotropy increases linearly with decreasing porosity for porosities < 0.36 , and then drops off below a porosity of 0.36. This phenomenon is noted for both RBBC and 39% RBBC mudrocks; the cause of this drop off is discussed in Chapter 6.

In order to compare the two measurement sequence bias adjustment methods, global and specimen, both methods were applied to adjust the permeability and permeability anisotropy of RBBC. All specimens with porosity > 0.36 were adjusted using the global adjustment method. Specimens measured using sequences of V, H1, H2 and H, V1, V2 enabled use of the single specimen method. Figure 5-20 and Figure 5-21 compare the horizontal and vertical permeability, respectively, obtained using both methods. Figure 5-22 compares the resultant permeability anisotropy adjusted using the two methods.

There is very good agreement between the two adjustment methods. The single specimen method predicts a slightly higher permeability than the global specimen method for both the horizontal and vertical directions; however the difference is in the third significant digit and is deemed negligible. In terms of permeability anisotropy, the data are scattered about the 1:1 line indicating that any differences in permeability anisotropy are associated with variations in the experimental measurements and not the adjustment methods themselves. For the specimens considered, the specimen adjustment method produces slightly higher permeability anisotropy, with a slope of 0.985, but the difference is again in the third significant digit for permeability anisotropy. Given a sufficiently large data set as was available for RBBC, the two adjustment methods (global and specimen) produce the same result.

Figure 5-23 compares the permeability anisotropy of RBBC computed using the measured directional permeability (open symbols) to that computed using the directional permeability adjusted for measurement sequence bias (closed symbols). Specimens measured using vertical order (circles) adjust to a higher anisotropy and those measured using horizontal order (squares) adjust to a lower anisotropy. This is the expected result of substituting the adjusted, increased permeability value into the permeability anisotropy equation. The permeability anisotropy adjustment is small, +/- 3% for RBBC. Though the test sequence bias correction does not significantly alter the trend of permeability anisotropy with porosity for RBBC (Figure 5-23), it does significantly reduce scatter in the directional permeability data set (Figure 5-24).

Depending on the testing program, one adjustment method may be more applicable or easier to use than the other. The single specimen method is applicable to most measurements where the second direction that is measured is repeated. The single specimen method is the only method available when a limited number of specimens of the same mudrock are measured, preventing calculation of the global correction factors x_v and x_h . On the other hand, where applicable, the global specimen method minimizes experimental noise by applying the same correction factor for all specimens of the same mudrock. It has the advantage of being applicable to specimens where one directional measurement fails, as in the case of HC044 discussed above, or to specimens where the second directional measurement was not repeated, for example measurement sequences of H1, H2, and V as was applied at the onset of the research program.

5.3.2 RBBC

During the research, the permeability was measured on 24 individually resedimented RBBC specimens. Table 5-7 summarizes the permeability and permeability anisotropy ($r_k = k_H/k_V$) measurements adjusted using the interpreted measurement sequence bias for RBBC. The individual specimen characteristics are given in Table 5-1. Figure 5-24 and Figure 5-25 plot the permeability of RBBC as a function of porosity and maximum effective stress, respectively.

As the porosity decreases from 0.49 to 0.30, the horizontal permeability decreases from $6.8 \times 10^{-17} \text{ m}^2$ to $1.6 \times 10^{-18} \text{ m}^2$ and the vertical permeability decreases from $5.7 \times 10^{-17} \text{ m}^2$ to $8.1 \times 10^{-19} \text{ m}^2$. The vertical permeability – porosity trend agrees well with that measured using the CRS device (Figure 5-24). Both the vertical and horizontal permeability form distinct trend lines showing decreasing permeability with decreasing porosity and increasing stress level.

The permeability measurements for specimens with $\sigma'_p > 10 \text{ MPa}$ and $n < 0.36$ do not follow the trends predicted by the lower stress, higher porosity measurements. Trend lines for both the horizontal and vertical permeability were generated using 21 measurements on specimens with $n > 0.36$; Figure 5-26 overlays these trend lines on permeability measurements. This figure shows that the horizontal permeability decreases faster than predicted by the trend line for porosities < 0.36 (see solid black line, Figure 5-26). In addition, the vertical permeability may be elevated compared to the trend line prediction (see dashed black line, Figure 5-26).

Figure 5-27 gives the adjusted permeability anisotropy as a function of porosity. Error bars represent +/-1 standard deviation of variation in the permeability anisotropy. The error bars are calculated using the standard deviation in directional permeability (horizontal and vertical) that was obtained by measuring the permeability at different hydraulic gradients.

The permeability anisotropy of RBBC increases linearly with decreasing porosity for porosities > 0.36. The permeability anisotropy increases from ~ 1.1 at porosity 0.49 to 1.9 at porosity 0.36. For porosities < 0.36 (corresponding to $\sigma'_p > 10$ MPa) the permeability anisotropy of RBBC decreases to as low as 1.4 and does not follow the high porosity trend. The permeability anisotropy is very sensitive to small changes in either the horizontal or vertical permeability because it is a ratio of these two values. The decrease in permeability anisotropy below porosity 0.36 is due to the divergence in slope in permeability measurement with porosity, shown in Figure 5-26. A change in the slope of the horizontal permeability with decreasing porosity is especially evident in this figure. Below porosity 0.36, the horizontal permeability varies in the 2nd significant digit from the predicted trend line (e.g. 1.57×10^{-18} m² for the adjusted measurement vs. 1.93×10^{-18} m² for the trend line).

All permeability measurements presented in Figure 5-24, Figure 5-25, and Figure 5-26 are adjusted for measurement sequence bias. Specimens with porosity > 0.36 were adjusted using the global correction method. The parameters x_H and x_V were determined using only those specimens with porosity > 0.36. Though the noted divergence affects only the 2nd significant digit of the permeability, the permeability anisotropy ratio is very sensitive to small changes in the directional permeability. The adjustment factors were computed as described to ensure that the differences in behaviour above and below a porosity of 0.36 were representative of true material behavior and were not averaged out through the measurement sequence bias adjustment process.

Three specimens were measured with porosity < 0.36; of these three specimens, two specimens with porosity 0.30 and 0.31 were adjusted using the specimen adjustment method. The third specimen with porosity 0.33 (HC044) was adjusted using the global adjustment method and the parameters x_H and x_V obtained using the higher porosity specimens. The specimen adjustment method could not be applied to this third specimen, measured with directional order H, V1, V2, because measurement errors occurred during measurement of the V1 permeability. The specimen analysis is discussed in detail in Appendix 1.

The repeatability of the entire permeability measurement process was evaluated using a total of six specimens compressed to 10 MPa maximum effective stress. The porosity of all six specimens was measured to range from 0.366 to 0.372 with an average porosity of 0.369 (see Table 5-1). Five measurements were made on specimens fabricated in acrylic resedimentation cylinders; the vertical permeability of these five specimens varied from 3.51×10^{-18} m² to 3.77×10^{-18} m² and the horizontal permeability varied from 6.22×10^{-18} m² to 6.75×10^{-18} m² (see Table 5-7). The permeability anisotropy of these five specimens varied from 1.74 to 1.92. The sixth specimen (HC048) was fabricated in a steel reinforced resedimentation cylinder (described in Chapter 3) to determine the effects of the resedimentation boundary conditions on

the measured permeability. The vertical and horizontal permeability of this sixth specimen were higher than the other five specimens, measuring $4.28 \times 10^{-18} \text{ m}^2$ and $7.26 \times 10^{-18} \text{ m}^2$, respectively. The permeability anisotropy was 1.70.

Resedimentation using a steel reinforced acrylic cylinder appears to produce slightly higher permeability and lower permeability anisotropy. This may be because the porosity of the specimen was slightly higher (Table 5-1) with the variability in the 3rd significant digit only. A Grubbs outlier statistical test for the measured permeability and permeability anisotropy determined that the measurements made in the steel cylinder statistically similar to those made in plain acrylic cylinders despite the slightly different permeability and permeability anisotropy.

The effect of adding resistivity measurements following the permeability results was assessed by measuring two specimens compressed to 10 MPa (porosity 0.37), including one specimen compressed in an acrylic resedimentation cylinder (HC036), and one specimen compressed in a steel reinforced resedimentation cylinder (HC048). The permeability and permeability anisotropy of these specimens is described above. Addition of resistivity measurement into the experimental sequence, including electrifying the specimen and the insertion of the pin probes, did not significantly affect the measured permeability, permeability anisotropy or porosity.

There is no significant difference between the permeability measured for specimens 1) resedimented in different cylinders (acrylic vs. steel reinforced acrylic) or 2) where the resistivity is measured following the permeability in the same set up. As a result, the measurement method is deemed to be repeatable.

Effect of Leaching

Two specimens of Leached RBBC were resedimented. Leaching was undertaken according to the procedure described in Chapter 3. Table 5-9 summaries the adjusted permeability and permeability anisotropy measurements for Leached RBBC. The individual specimen characteristics are given in Table 5-3. Figure 5-28 and Figure 5-29 compare the permeability of RBBC and Leached RBBC. Figure 5-30 compares the permeability anisotropy.

The both the horizontal and vertical permeability of the leached RBBC are slightly lower than that of the natural RBBC. This effect is most pronounced for the low stress specimen at porosity 0.44. However, the permeability difference between the RBBC and the Leached RBBC, shown in Figure 5-28, is not significantly larger than the experimental scatter for RBBC. This scatter is most evident in Figure 5-26 when individual specimen permeability measurements are compared to the trend line. Finally, the anisotropy of the Leached RBBC is in agreement with the measurements on natural RBBC. The process of leaching did not significantly change either the permeability or the permeability anisotropy of RBBC.

Further, leaching did not alter either the compression behaviour (Figure 5-11 and Figure 5-12) or the vertical permeability (Figure 5-28) compare to the CRS measurements. This finding is in agreement with results reported by Horan (2012).

A similar result was obtained by comparing RSFBM to Leached RSFBM, discussed in Section 5.3.3.

Effect of Clay Fraction

To study the effect of clay fraction on the permeability of RBBC, Min-u-Sil 40 was added to BBC powder to create a mudrock with 39% clay fraction. The permeability of five individually resedimented specimens of 39% Clay RBBC was measured. These specimens spanned a maximum applied stress range from 1.2 to 9.8 MPa. Table 5-8 summaries the adjusted permeability and permeability anisotropy measurements for 39% Clay RBBC. The individual specimen characteristics are given in Table 5-2. Figure 5-31 and Figure 5-32 compare the vertical and horizontal permeability of 39% clay RBBC (clay fraction = 39%) to that of natural RBBC (clay fraction = 53%). Figure 5-33 compares the permeability anisotropy measured for the two mudrocks.

As the porosity decreases from 0.42 to 0.35, the horizontal permeability decreases from $7.7 \times 10^{-17} \text{ m}^2$ to $1.5 \times 10^{-17} \text{ m}^2$ and the vertical permeability decreases from $5.2 \times 10^{-17} \text{ m}^2$ to $1.1 \times 10^{-17} \text{ m}^2$. Both the vertical and horizontal permeability of 39% Clay RBBC are higher than that of RBBC by nearly one half order of magnitude (Figure 5-31). The vertical and horizontal permeability form log-linear trends showing decreasing permeability with decreasing porosity (Figure 5-31) and increasing maximum effective stress (Figure 5-32). The permeability anisotropy of 39% Clay RBBC is lower than that of RBBC, and increases linearly with decreasing porosity, increasing from 1.4 to 1.6 as the porosity decreases from 0.42 to 0.36.

Similar to RBBC, the permeability anisotropy of 39% Clay RBBC decreases below a porosity of 0.36, corresponding to between 6 and 7 MPa maximum effective stress. All specimens of 39% Clay RBBC were resedimented in acrylic resedimentation cylinders and are therefore the results are not affected by different resedimentation equipment or procedures. This further supports the idea that the decrease in permeability anisotropy below porosity 0.36 is true material behaviour. However, more measurements are required to determine if a similar change in the horizontal permeability trend occurs for porosities < 0.36 , as was noted for RBBC. Further, because the 39% clay RBBC has a higher permeability than the RBBC, additional measurements will also confirm whether the permeability anisotropy decrease is related to an increase in experimental error associated with decreasing specimen permeability. As the specimen permeability decreases, so too does the flow through volume used to measure the specimen permeability; at some point, as is discussed in the following section, the flow measurement errors become significant compared to the total flow volume.

The permeability of 39% Clay RBBC was adjusted using the global adjustment method, as discussed above. From experience with RBBC, this decrease in permeability anisotropy is thought to be due to

a break in slope of the permeability vs. porosity plot at a porosity of 0.35; insufficient data are available to prove this hypothesis. As a result, the highest stress specimen with porosity 0.35 (HC024) was not used in the determination of x_H or x_V because of the noted decrease in permeability anisotropy. Nevertheless, the permeability of this high stress specimen was adjusted using the global adjustment method because the measurement sequence (H1, H2, and V) did not permit use of the single specimen method.

From these results, decreasing the clay fraction of mudrocks by adding silt sized silica both increases the permeability and slightly decreases the permeability anisotropy.

5.3.3 RGoM-EI and RSFBM

Two specimens each of RGoM-EI and RSFBM mudrock and one specimen of Leached RSFBM were individually resedimented and measured. The permeability was adjusted using the single specimen adjustment method. Table 5-9 summarizes the adjusted permeability and permeability anisotropy measurements for RGoM-EI, and RSFBM. The individual specimen characteristics are given in Table 5-3.

Figure 5-34 and Figure 5-35 give the permeability and permeability anisotropy as a function of porosity for RGoM-EI, respectively. Figure 5-36 and Figure 5-37 give the same for RSFBM and Leached RSFBM.

For RGoM-EI, as the porosity decreases from 0.38 to 0.34, the horizontal permeability decreases from $3.0 \times 10^{-19} \text{ m}^2$ to $1.2 \times 10^{-19} \text{ m}^2$ and the vertical permeability decreases from $2.5 \times 10^{-19} \text{ m}^2$ to $8.2 \times 10^{-20} \text{ m}^2$. The permeability anisotropy varies from 1.2 to 1.4 over this porosity range. For RSFBM, as the porosity decreases from 0.39 to 0.36, the horizontal permeability decreases from $1.0 \times 10^{-18} \text{ m}^2$ to $3.7 \times 10^{-19} \text{ m}^2$ and the vertical permeability decreases from $1.0 \times 10^{-18} \text{ m}^2$ to $4.0 \times 10^{-19} \text{ m}^2$. RSFBM is isotropic, with a permeability anisotropy of just under 1 that does not vary with porosity based on the specimens measured. The permeability and porosity of the leached RSFBM is in the same range as that of the natural SFBM compressed to the same stress level (10 MPa). However the permeability anisotropy of the Leached RSFBM is higher, measuring 1.4, indicating the sensitivity of the permeability ratio to small changes in the measured permeability.

Both the RGoM-EI and RSFBM vertical permeability measurements are lower than measured by the CRS device. Adams (2011) showed that for a constant porosity, the permeability of a mudrock measured using the constant head technique and the CRS technique by the same researcher should be within 11% of each other. Using the results of an ASTM interlaboratory study of constant head measurements for the flexible wall permeameter, the hydraulic conductivity of one specimen measure by one lab should be within 20% of that measured for an identical specimen by a different lab (Adams, 2011). However, for both the RGoM-EI and the RSFBM the constant head permeability is roughly one half that measured by the CRS device. Numerous CRS tests have been run by different researchers at MIT with comparable results; therefore the difference is more likely associated with the constant head measurements conducted for this research. These errors may be

more significant for lower permeability specimens such as RGoM-EI and RSFBM, especially since the RBBC results show good agreement between the cubic specimen and CRS measurements.

The RGoM-EI permeability anisotropy has a higher standard deviation, given by the error bars on Figure 5-35, than all other specimens. This is because the directional permeability varied more significantly with hydraulic gradient, varying in the second significant digit as opposed to the third as was the case for all other mudrocks. The variation in permeability, which is too small to be seen in Figure 5-34, translates into a visually large uncertainty in the permeability anisotropy when plotted with a narrow anisotropy scale as shown in Figure 5-35. However, the permeability anisotropy is still low, < 2 , and a variation between 1.2 and 1.65 is not large given the extremely low permeability of the material and measurement problems that were experienced with this particular mudrock.

First, the permeability of the RGoM-EI specimens is very low. Very low inflow and outflow volumes were used to measure the permeability, increasing the influence of small undetectable leaks and creep related volume change. The difference in the inflow volume and outflow volume for flow through measurements at low permeabilities is a higher percentage of the average flow volume; this causes relatively large standard deviations (see Appendix 1). This is a key limitation of the constant head method, where both the measurement time and the measurement error increase with decreasing permeability. Nevertheless, good quality control reduced the volume errors significantly such that constant flow rates were achieved through the specimen and the permeability could be measured.

Second, the RGoM-EI specimens experienced horizontal cracking during the month long permeability measurement process. The cracking initiated after only slight (~ 20 minute) exposure to the air during specimen trimming, and was oriented in the horizontal plane perpendicular to the direction of axial loading (see Figure 5-38). The cracks appeared to be caused by uneven drying. A bench top test was conducted to evaluate the cracking as a function of time on specimen trimmings. Horizontal cracks were noted within ~ 10 minutes of air exposure, and grew over up to two hours of exposure. Long term exposure to the air (overnight) resulted in bulk specimen shrinkage and the closure of all cracks.

The cracks were likely closed when the specimen was recompressed to the measurement effective stress in the flexible wall permeameter. However, the effect of cracking on the measured permeability and permeability anisotropy is unknown.

5.3.4 Comparison between mudrocks

Figure 5-39 and Figure 5-40 compare the directional permeability of the mudrocks studied in k vs. n and k vs. $\log \sigma'_p$ space, respectively. Table 5-1, Table 5-2, and Table 5-3 list the specimen characteristics, and Table 5-7, Table 5-8, and Table 5-9 tabulate the measured permeability and permeability anisotropy.

The horizontal permeability is higher than the vertical permeability for all mudrocks except RSFBM, where the two are nearly equal but the vertical permeability is slightly higher. For a given porosity or maximum axial effective stress σ'_p , 39% Clay RBBC has the highest permeability, followed by RBBC, RSFBM and RGoM in order of decreasing permeability. At a given porosity, the RSFBM is approximately one half of an order of magnitude less permeable than RBBC (Figure 5-39). Similarly, the RGoM-EI is approximately one order of magnitude less permeability than RBBC at the same porosity. Accounting for differences in the mudrock compressibility, Figure 5-40 shows that the RSFBM is one order of magnitude less permeable than RBBC compressed to the same maximum effective stress. Similarly, the RGoM-EI is nearly two orders of magnitude less permeable than RBBC with the same stress history.

Figure 5-41 compares the permeability anisotropy of the mudrock measurements. Despite the large variation in measured permeability, by over two orders of magnitude, the permeability anisotropy does not exceed 2. RBBC has the highest permeability anisotropy, followed by 39% Clay RBBC, RGoM-EI and RSFBM in order of decreasing permeability anisotropy. Note that lower permeability anisotropy does not correspond to lower permeability; RGoM-EI has lower permeability than RSFBM but higher permeability anisotropy. Similarly, 39% Clay has higher permeability than RBBC but lower permeability anisotropy.

Both the RBBC and 39% Clay RBBC show an increase in permeability anisotropy with decreasing porosity, followed by a sudden decrease in permeability anisotropy around porosity 0.36. This decrease is not noted for either RSFBM or RGoM-EI, though extensive measurement of these mudrocks was not conducted.

RGoM-EI has the highest standard deviation (error bars), followed by RSFBM, RBBC and 39% Clay RBBC. The standard deviation in the permeability anisotropy increases with decreasing permeability; this trend occurs because lower permeability specimens are measured using lower flow through volumes increasing the influence of small volume errors and increasing the variation in permeability with hydraulic gradient.

To investigate the influence of errors at low flow volumes (low permeabilities), the coefficient of variation was plotted as a function of porosity, permeability and permeability anisotropy for all mudrocks tested in Figure 5-42 and Figure 5-43. The coefficient of variation is equal to the standard deviation divided by the mean (given in Table 5-7, Table 5-8, and Table 5-9). The coefficient of variation ranges from 0 to 0.02 for most mudrocks, and reaches values in the range of 0.06 to 0.16 for some measurements. The highest value, 0.16, was computed for an RGoM-EI specimen with known measurement challenges.

The coefficient of variation is independent of specimen porosity (Figure 5-42) but is highly dependent on the specimen permeability (Figure 5-43). This observation may be somewhat skewed by the RGoM-EI measurements that had additional sources of error associated with specimen cracking that may not necessarily be associated with low permeability. Figure 5-43 shows that the cubic specimen method produces permeability results with low variability for a wide range of

mudrocks, and in particular specimens with permeability greater than $1 \times 10^{-18} \text{ m}^2$. Below this permeability the error increases; more work is required to identify the lower bound permeability that can be reasonably and accurately measured using the cubic specimen measurement technique.

5.3.5 Effect of Sidewall Friction on Laboratory Anisotropy Measurements

Chapter 6 develops a layered anisotropy model that computes the permeability anisotropy of an equivalent 2-layer system based on the individual layer permeability, permeability anisotropy and compression characteristics. This model is applied here to investigate the effect that sidewall friction might have on the laboratory permeability anisotropy measurements. The model, including all equations, is developed and described in detail in Section 4 of Chapter 6.

Sidewall friction is unavoidable; it occurs along the edges of resedimented specimens in contact with sedimentation columns. Sidewall friction opposes the applied load and reduces the load applied to the specimen. Sidewall friction is difficult to measure, and varies as a function of surface treatment of the sedimentation column, the height-to-diameter ratio of the specimen, and the loading method (floating vs. fixed tube). Resedimented specimens measured in this research were prepared to reduce sidewall friction via the following techniques:

1. The settling column was coated with a thin layer of silicone oil;
2. The height to diameter ratio at the end of compression (maximum friction) was kept as close to 1.5 as possible;
3. A floating tube set up was applied. This method applies load at both the top and bottom of the specimen and allows the sedimentation column to move freely in the vertical direction.

Through reduction of the applied load, sidewall friction affects the porosity and permeability of the resedimented specimen. Mudrock specimens that are resedimented using a floating tube set up should experience maximum friction and hence load reduction in the middle of the tube; the specimens measured for this research were cut as symmetrically close to the middle of the tube as possible. Therefore, any layering should be symmetric about the center of the specimen. The permeability anisotropy contribution of sidewall friction can therefore be computed by assuming an equivalent two layer system with anisotropic sub layers with a thickness contrast of unity, as shown in Figure 5-44.

A simple model is assumed to simulate the effects of sidewall friction: A specimen that is compressed to 10 MPa and then rebounded to 2.5 MPa during resedimentation has an OCR of 4. However, if sidewall friction supports 5% of the applied load, then the maximum applied stress becomes 9.5 MPa. Because sidewall friction opposes motion, the direction reverses when the load is decreased to over consolidate the specimen. Therefore, the actual rebounded stress will increase, becoming 2.6 MPa. Overall, the specimen will be at OCR 3.65 (9.5 divided by 2.6) instead of OCR 4 as loaded. Sidewall friction causes a reduction in maximum applied load, an increase in load in the over consolidated state, and an increase in the OCR.

This model is expressed in mathematical terms by modifying the void ratio equation (presented in Section 6.4) to incorporate sidewall friction (SF, %) into the specimen void ratio calculation (eq. 5-1).

$$e = e_o - c_c [\log(\sigma'_p * (1 - SF)) - \log(0.1)] + c_s \left[\log \left(\sigma'_p - \left(\sigma'_p - \frac{\sigma'_p}{OCR} \right) (1 - SF) \right) - \log(\sigma'_p) \right] \quad 5-1$$

The compressing permeability anisotropy model can be applied to model the effects of sidewall friction on the specimen permeability. Sidewall friction is assumed to affect the middle layer and not the outer layer of the specimen.

Figure 5-45 is a screen shot of the Microsoft Excel model for RBBC. This model uses two layers of equal thickness with the same material properties. The outer layer is frictionless and the inner layer has friction. The model is configured such that the stress level, OCR and sidewall friction can be varied.

Table 5-13 summarizes the specimen permeability anisotropy assuming a 2 layer system and anisotropic layers for three stress levels (0.1 MPa, 1 MPa and 10 MPa) and varying degrees of sidewall friction ranging from 0 to 40% for RBBC specimens at OCR 4. .

For sidewall friction values up to 40%, the difference in permeability anisotropy is small, reaching a maximum of 0.07 at 40% sidewall friction and 10 MPa effective stress. Increasing the stress level and increasing the sidewall friction increases the difference between the apparent permeability anisotropy predicted by the model and the actual permeability anisotropy for the case of zero sidewall friction. Sidewall friction increases the permeability anisotropy that would be measured; however this increase is negligible when compared to the scatter in the permeability anisotropy data set for RBBC (Figure 5-27).

The model, and in particular eq. 5-1, can also be used to estimate the degree of sidewall friction in the cubic specimens. Table 5-14 summarizes the porosity prediction for RBBC at OCR 4 for three maximum effective stresses (0.1, 1 and 10 MPa) and sidewall friction ranging from 0 to 40% assuming a uniform specimen (no layers). The average specimen porosity across six specimens compressed to a maximum effective stress of 10 MPa was 0.369 and varied from 0.366 to 0.372 (see Table 5-1). Approximately 30% sidewall friction is required to produce a specimen porosity of 0.369. This estimate is likely high, because it is based on the assumption that the compression indices are constant over a large stress range. Further, slightly variations in CRS measurements may shift the initial void ratio (and initial porosity slightly).

Therefore, sidewall friction is not likely to exceed 30% and will not significantly affect the permeability anisotropy results.

5.4 Resistivity Measurements

Appendix 1 summarizes the directional resistivity measurements for each specimen. Similar to the permeability measurements, measuring the resistivity multiple times in the same direction causes an increase in the measured resistivity. As a result, the measurement sequence bias correction, originally devised for the permeability measurement, is applied to the resistivity measurement. These values are converted to formation factor using the specimen pore fluid salinity (Section 5.1.2). The pore fluid resistivity is computed using the relationship between the resistivity of sea salt water as a function of salinity (Appendix 4).

Unlike permeability, the formation factor is computed using the specimen salinity (Table 5-5) rather than the salinity of the pore fluid system. For RBBC, the salinity of the pore fluid system is fixed at 16 g/L but the specimen salinity measurements range from 9 g/L to 23 g/L with an average salinity of 15.1 g/L (discussed in Section 5.1.2). Small changes in specimen salinity have a greater impact on the formation factor than the permeability; consequently, computing the formation factor using the measured vs. assumed pore fluid salinity was found to reduce scatter in the formation factor vs. porosity plot (e.g. Figure 5-52, discussed in Section 5.4.2).

The following subsections describe the effect of the measurement sequence bias adjustment, the resistivity behaviour of RBBC, and compare the resistivity anisotropy of different mudrocks measured using the triaxial cell and the bench top measurement method. This discussion is supplemented by Appendix 4 which discusses the bench top measurement method and results.

5.4.1 Measurement Sequence Bias

The resistivity measured in the triaxial cell is corrected for measurement sequence bias using either the global specimen method or the single specimen method. These analysis methods are described in detail in Chapter 4 and Appendix 2 for the permeability and the exact same methodology is applied for resistivity.

Table 5-15 summarizes the measured directional resistivity for RBBC in each of the H1, H2, V and V2 directions. The total number of permeability measurements separating permeability measurements in the horizontal (H1 and H2) or vertical (V1 and V2) directions, equal to the Δn value in the measurement sequence bias equations, is included in this table. These data are used to obtain the horizontal and vertical measurement sequence bias, x_{HP} and x_{VP} , respectively, as described in Chapter 4 and Appendix 2. Figure 5-46 and Figure 5-47 give cross plots of the horizontal and vertical resistivity used to define x_{HP} and x_{VP} for RBBC. Table 5-16 summarizes the measurement sequence bias parameters for RBBC.

Similar to the permeability measurements, a decrease in the conductivity anisotropy for porosities < 0.36 was noted (discussed later). As a result, measurements for porosities < 0.36 are not included in the global measurement sequence bias determination.

Similar to the permeability measurement sequence bias, the resistivity measurement sequence bias is independent of measurement direction, equal to 1.051 in both the horizontal and vertical directions for resistivity measurements on RBBC.

Both measurement sequence bias adjustment methods, global and specimen, were applied to adjust the resistivity of RBBC. All specimens with porosity > 0.36 were adjusted using the global adjustment method. Specimens with porosity < 0.36 were adjusted using the specimen adjustment method where the measurement sequence permitted. HC044 (n = 0.33) was adjusted using the global specimen method because the first vertical measurement failed. Figure 5-48 and Figure 5-49 compare the horizontal and vertical resistivity, respectively, obtained using both methods. Figure 5-50 compares the resultant conductivity anisotropy adjusted using the two methods. Measurements on one specimen (Test ID HC036) were not included in these comparisons because the measurements were not corrected for current losses through the apparatus, and therefore include errors of at minimum 2-3 % and deviate from all predicted trends. The fact that such small errors cause such deviation from the measured trends suggests that the measurement procedure is highly repeatable when performed correctly.

There is very good agreement between the two adjustment methods. The single specimen method predicts a slightly lower resistivity than the global specimen method in the horizontal direction and a slightly higher resistivity in the vertical direction. This direction dependence is likely an artefact of a small sample size (6 specimens) and indicates that there is no significant difference between the predictions of the two methods. In terms of conductivity anisotropy, similar to permeability anisotropy, the data are scattered about the 1:1 line, indicating that any differences in permeability anisotropy are associated with variations in the experimental measurements and not the adjustment methods themselves.

5.4.2 RBBC Resistivity

The directional resistivity of nine specimens of RBBC was measured in the triaxial cell. Table 5-17 summarizes the adjusted resistivity, apparent formation factor, and resistivity and conductivity anisotropy for these measurements. McNeill (1980) suggested the resistivity of clay rich mudrocks typically varies from ~1 to ~100 Ωm or more; the resistivity of RBBC falls within the low end of this range. The apparent formation factor is computed as described in Chapter 4 and Appendix 3 using the measured specimen salinity. The standard deviation of the apparent formation factor is not computed because the accuracy of the salinity measurement is not as quantitatively constrained as that of the resistivity measurements. However, the standard deviation in apparent formation factor is expected to be higher than that measured for the resistivity because of the large (> 2-3 g/L) variations in the measured salinity before and after the permeability measurement (see Table 5-5).

The resistivity and apparent formation factor measurements are not corrected for clay surface conductivity. As a result, all measurements are apparent. Chapter 2 describes the difference between apparent and intrinsic formation factor.

Figure 5-51 plots the measured resistivity, adjusted for measurement sequence bias, as a function of porosity; Figure 5-52 does the same for the apparent formation factor. Both resistivity and apparent formation factor are direction dependent parameters, with the vertical resistivity and apparent formation factor being higher than the horizontal.

The resistivity of RBBC increases with decreasing porosity and ranges from 1.1 to 2.8 in the horizontal direction and 1.4 to 3.7 in the vertical direction as the porosity decreases from 0.47 to 0.31. There is no distinct linear trend in increasing resistivity with decreasing porosity, with the resistivity increasing initially as the porosity decreases to 0.44, then decreasing slightly until a porosity of 0.36, then increasing again for porosities below 0.36. The apparent formation factor vs. porosity plot is much more linear, likely because the data are normalized for variations in the specimen pore fluid salinity. The apparent formation factor increases from 2.0 to 6.0 in the horizontal direction and from 2.5 to 8.3 in the vertical direction as the porosity decreases from 0.47 to 0.31. This increase appears linear on a log-linear plot as shown in Figure 5-52.

As was noted for the permeability measurements, the trend in apparent formation factor in both the vertical and horizontal directions differs below porosity 0.36. It should be noted however that there are fewer measurements of the apparent formation factor than permeability; because the apparent formation factor follows a power law curve, this conclusion may vary depending on how the power law curve is interpreted. It is possible to obtain a power law curve that fits all measurements and shows no deviation in apparent formation factor below porosity 0.36; however this interpretation is not in agreement with the measured conductivity anisotropy data. This concept is further discussed in Chapter 6 in regards to Archie's law.

Figure 5-53 plots the resistivity anisotropy as a function of porosity. Similarly, Figure 5-54 plots the conductivity anisotropy as a function of porosity.

The resistivity anisotropy decreases with decreasing porosity, starting initially at 0.82 at porosity 0.47 and reaching a plateau at around 0.55 in the porosity range 0.43 to 0.36. Below porosity 0.36, the resistivity anisotropy rises again, reaching a value of 0.74 at porosity 0.31. Error bars represent +/- 1 standard deviation and are computed using the standard deviation of the horizontal and vertical resistivity used to compute the resistivity anisotropy.

The conductivity anisotropy is the inverse of the resistivity anisotropy. The conductivity anisotropy is around 1.2 at porosity 0.47, and increases linearly until it reaches a plateau in the range of 1.75 – 1.85 between porosity 0.43 and 0.36. Below porosity 0.36 the conductivity anisotropy decreases. This decrease is similar to that seen in the permeability anisotropy measurements.

The resistivity anisotropy of RBBC decreases with decreasing porosity. The conductivity anisotropy, equal to the inverse of the resistivity anisotropy, increases with decreasing porosity. Comparison of the conductivity anisotropy and the permeability anisotropy (Section 5.3.2) is easy because both measures increase with decreasing porosity. For simplicity, the conductivity anisotropy will be used for all analyses henceforth.

Effect of Leaching

The resistivity of two specimens of Leached RBBC was measured. The resistivity was adjusted using the single specimen measurement sequence bias adjustment method. The adjusted resistivity, apparent formation factor, resistivity and conductivity anisotropy are provided in Table 5-17.

Figure 5-55 compares the resistivity of Leached RBBC to that of natural RBBC. Leached RBBC is more than one order of magnitude more resistive than natural RBBC. This is due to the low salt concentration of the pore fluid rather than a change in mudrock fabric.

Figure 5-56 compares the apparent formation factor of Leached RBBC to that of natural RBBC. The apparent formation factor for Leached RBBC is within the same order of magnitude as that of natural RBBC. For the leached RBBC, the apparent formation factor remains constant or may even decrease with decreasing porosity. More data is required to determine whether this observation is representative of true material behaviour.

Figure 5-57 compares the conductivity anisotropy of Leached RBBC to that of natural RBBC. The anisotropy of the Leached RBBC is slightly lower than that of the natural RBBC at porosity 0.44 and slightly higher than that of the natural RBBC at porosity 0.36, but overall is still within the range of 1.2 - 2.5 over the porosity range measured. This similarity implies that the fabric structure of the leached RBBC is similar to the natural RBBC.

Leaching does not significantly affect the apparent formation factor or conductivity anisotropy of RBBC, though it does significantly increase the directional resistivity.

5.4.3 Comparison between Mudrock Resistivity Anisotropy

The directional resistivity of 39% Clay RBBC, RGoM-EI and RSFBM was measured using the bench top measurement method. The directional resistivity of Leached RSFBM was measured in the flexible wall permeameter.

Appendix 4 compares the resistivity and conductivity anisotropy measured using the bench top configuration to that measured using the cubic resistivity end adapters in the flexible wall permeameter (triaxial configuration) for RBBC and leached RBBC. The resistivity measured using the bench top method is higher than that measured using the triaxial configuration because of differences in specimen stress state & pore pressure, temperature, specimen size, specimen saturation, and goodness of the electrical contacts. However, the conductivity anisotropy measured using these two methods is essentially the same.

Table 5-18 summarizes the bench top resistivity measurements made on three specimens of 39% Clay RBBC, two specimens of RGoM-EI and one specimen of RSFBM. Though these measurements were not made immediately following permeability testing, every attempt was made to maintain

the specimen water content during storage. The specimens were stored in double Ziploc bags with a moist paper towel in between the Ziploc bags, and placed in coolers.

Two versions of the bench top resistivity electrodes have been tested and used for measurements. The first version, shown in Figure 5-58, uses larger specimens and relies on the specimen self-weight for stability. The second version, described in Appendix 3, uses smaller specimens and a load frame to stabilize the specimen during measurement. For this research, the specimen resistivity was measured using the first version of the bench top resistivity measurement technique. Though it has not been explicitly studied, minimal differences are expected between the resistivity measured using the two electrode configurations, and any differences should be primarily associated with specimen size.

Figure 5-59 compares the conductivity anisotropy of 39% Clay RBBC, RGoM-EI and SFBM and Leached RSFBM with that of RBBC and Leached RBBC. Similar to the permeability anisotropy, the conductivity anisotropy is restricted to a small range, <2.5 for all mudrocks despite a wide range of measured resistivity. Many parallels are noted between the conductivity anisotropy and the permeability anisotropy; these parallels will be further developed in the next chapter. The conductivity anisotropy of RBBC increases as the porosity decreases until a porosity of 0.36 and then decreases again, as was noted for the permeability anisotropy. The conductivity anisotropy of the RGoM-EI is the highest, reaching a value of 2.9 at a porosity of 0.34. The permeability anisotropy of RGoM-EI was much lower, but measurement difficulties including specimen cracking (discussed in Section 5.3.3) cause the measurements to be questionable. The RSFBM is relatively isotropic in terms of permeability, and differs from all other specimens in that it has a resistivity that is lower in the vertical direction than the horizontal direction. Leaching did not significantly affect the apparent formation factor or conductivity anisotropy of RBBC, but did noticeably increase the conductivity anisotropy of RBSFM, essentially inverting it (0.66 for natural RSFBM vs. 1.51 for leached RSFBM). More work is needed to determine if this result is actual material behaviour, or if the measurement directions were incorrectly reversed.

5.5 Particle Fabric Characterisation

Backscattered SEM images of RBBC fabric were obtained from Emmanuel and Day-Stirrat (2012). Figure 5-60 compares three images of the vertical plane of RBBC at stress levels of 0.1, 1 and 10 MPa. These images reveal that visually evident changes in the mudrock structure occur as the applied stress increases. Platy particles rotate to become more horizontally aligned and the pore space (identified by black in these images) becomes more compact as particles are vertically compressed. At low effective stresses (0.1 MPa, see inset A Figure 5-60) the particle fabric appears to be somewhat random, with some particles (e.g. near the centre of the image) being oriented ~ 45 degrees to the horizontal. Smaller platy particles have less obvious alignment, and blocky, low aspect ratio silt sized particles (e.g. right of inset A) have indiscernible alignment. As the stress increases to 10 MPa (inset C, Figure 5-60), long platy particles have rotated so the dominant alignment is sub horizontal. Some particles show signs of folding (see bottom of inset C).

Image analysis was performed as a means to quantify the change in particle orientation with increasing stress level and decreasing porosity. Additionally the particle aspect ratio was quantified using this technique. The methods used to quantitatively analyze these images are described in Chapter 4. This section summarizes the analyses that were undertaken to measure the particle orientation and particle aspect ratio of 2D SEM images of oven dried mudrock specimens. Images of RBBC mudrocks were analyzed. The purpose of this study was many fold:

- 1) To measure the change in particle orientation as a function of porosity;
- 2) To determine if particle orientation was a repeatable quantification base on varying a) analyst and b) material handling;
- 3) To determine if the particle aspect ratio could be estimated using image analysis techniques;
- 4) To compare available particle quantification techniques (1D and 2D);

The image analysis summarized in this report were performed by Amy Adams (author), Mun Ngha Cheong, a UROP in the MIT Geotechnical Laboratory from September 2012 – May 2013 and Keiron Durant, an MIT Summer Research Program Student from June – August 2013.

All images that were analyzed are provided in Appendix 1. Table 5-19 summarizes the file name, mudrock, stress level, porosity and types of analysis performed (1D, 2D) for each image analyzed. Table 5-20 summaries the orientation results for each particular image analyzed including the number of measurements, the particle orientation, and the aspect ratio, where applicable.

Image analysis was focused on images of two magnifications. The primary focus was on images with magnification in the range of 10,000 X to 15,000 X were analyzed to obtain the orientation of the mudrock fabric including clay and silt sized particles ranging from 0.2 μm to 5 μm . Additionally, two lower magnification images ranging from 5000 X to 6000 X were analyzed to quantify the fabric and orientation of the larger sized particles only. Only the particles that were visually differentiable (particles of length 0.5 to 21 μm) were included in this analysis.

This section is divided into five subsections. The first subsection discusses the different image sources and addresses issues such as repeatability between images obtained from different sources and analyzed by different analysts. The second subsection summarizes the mean particle orientation as a function of stress level and porosity for the selected images. The third subsection takes this analysis one step farther and examines particle orientation as a function of size in addition to stress level and porosity. Subsection four compares the results of the image analysis method to another commonly applied method that was applied to the same specimens and finds that the two methods produce significantly different particle orientation estimates. Finally, subsection 5 discusses the measurements of particle aspect ratio as a function of particle size and specimen porosity.

5.5.1 UT and MIT Images

Images analyzed in this research were derived from two different sources:

- 1) Images that were resedimented at MIT but processed and imaged at the University of Texas (UT) at Austin are called “UT Images”. Dr. John T. Germaine of MIT, and Ruarri Day-Stirrat (formerly of UT) and Rob Reed of UT were instrumental in preparing and imaging these specimens.
- 2) Images that were similarly resedimented and processed at MIT and imaged using an SEM at Harvard University are called “MIT Images”. Amy Adams and Amer Deirieh of MIT were instrumental in preparing and imaging these specimens.

First, an extensive effort was concentrated on analysis the UT images which spanned stress levels of 0.1, 1 and 10 MPa. Only high magnification images (10,000 to 15000 X) were analyzed. Three images of each stress level were analyzed by Cheong using the 1D analysis. Additionally, 1 image at each stress level was analyzed by Durant using the 1D analysis method. This re-analysis was performed to assess the repeatability of the image analysis method. Finally, 2 images at each stress level were analyzed by Durant using the 2D analysis method. This allowed comparison between the 1D and 2D analysis methods. The results of the individual analyses, including mean and standard deviation particle orientation, mean and standard deviation aspect ratio (2D only), and number of particles analyzed are included in Table 5-20.

A similar effort was focused on analyzing images of specimens prepared and imaged at MIT / Harvard (termed “MIT Images”). Images spanning four stress levels were analyzed: 1, 10, 20, and 40 MPa. Images of two magnifications were obtained; high magnification, similar to that of the UT images (10,000 to 15000 X) and low magnification (5,000 to 6,000 X). The high magnification images were analyzed by Durant and Adams using the 1D analysis method to evaluate the clay and silt fabric for comparison with the UT images. The low magnification images were analyzed by Durant using the 2D analysis method to evaluate the larger particle (silt) fabric only; this analysis was done for stress levels of 10 and 40 MPa only.

The repeatability of the image analysis method was assessed by comparing the particle orientation for the same image measured by 1) different operators using the same technique, and 2) different techniques performed by the same operator. Three images of RBBC obtained from UT were analyzed, one each at 0.1, 1 and 10 MPa effective stress. The images analyzed were: SEM0020_BSE_001, SEM0021_BSE_001, and SEM0022_BSE_001.

Figure 5-61 compares the particle orientation as a function of porosity for these UT images. The average orientation of the particles measured using the 1D analysis is always higher (less horizontally oriented) than that measured using the 2D analysis. The 2D analysis includes low aspect ratio particles with non-obvious long axis; this result indicates that the low aspect ratio particles have dominantly horizontal alignment. There is no definitive trend in the 1D analysis between users. For some images one user measures a higher particle orientation, and for others a lower particle orientation.

It is important to note that this comparison is performed using one image only for three specimens; the measured particle orientation is not used in the final analysis, rather the purpose of this analysis was to compare the particle orientation obtained by different users using different techniques in a controlled manner. The use of only one image incorporates a large degree of sampling bias into the measurements, on top of bias already included due to the use of oven dried specimens and the measurement of apparent vs. true orientations as discussed in Chapter 4.

The results obtained by Cheong using 3 images at each stress level provide the most continuous data set and are likely the most representative of the material behaviour because of the larger sample size. At higher porosities and lower stress levels there is more difference in the results predicted by the two researchers using the 1D and 2D analysis methods; these differences are most likely attributed to differences in the number of images analyzed and thus the representativeness of the results. The variation in orientation measured 1) by different researchers, 2) using specimens prepared at different institutions, and 3) using data sets consisting of a different number of images can be as high as 5-10 degrees. Overall, the particle orientation measurements indicate a nearly linear decrease in orientation with decreasing porosity, from around 45 degrees at porosity 0.57 to 28 degrees at porosity 0.35.

Overall, the image analysis method is repeatable to +/- 4 degrees. The 2D analysis removes the subjectivity required to determine the particle axis. However, it is sometimes difficult to trace very small elongate particles in 2D analysis, whereas the human eye can easily identify the long axis and draw a line through the particle in 1D analysis. For the images measured, the 2D analysis results in a slightly lower measured particle orientation than the 1D analysis. The 2D analysis is biased towards larger particles with lower aspect ratios that are easier to trace, whereas the 1D analysis is biased towards elongated particles with high aspect ratios, regardless of particle size. The 2D analysis takes significantly more time (2-4 times as long) than 1D analysis to perform. Since it is not known which orientation exerts the most control on mudrock fluid flow properties, these factors must be gauged in determining the type of analysis to be performed.

5.5.2 Mean Particle Orientation

To quantify the change in particle orientation with increasing stress and decreasing porosity, particle orientation measurements were averaged across multiple images with the same analysis characteristics (same specimen, same image type, operator, and analysis method) where possible to increase the representativeness of the analysis. This section defines the particle orientation vs. porosity trend for RBBC using data obtained from UT and MIT images, and using the 1D and 2D measurement techniques.

As discussed previously, Cheong performed 1D analysis on three UT images each at three different stress levels, 0.1, 1.0 and 10 MPa, all processed at the University of Texas. The measurements for all three images analyzed at each stress level were combined to form a larger data set, and analysis was performed on this larger data set. Similarly, Durant performed 2D analysis on two images each

at the three stress levels obtained from UT. The images analyzed by Durant were the same as those analyzed by Cheong; the only difference is that Cheong performed 1D analysis and analyzed 1 additional image. Finally, Durant performed 1D analysis of the UT images using single image at each stress level. Table 5-21 summarizes the particle orientation and particle size measurements for the combined data sets for the UT images only. Figure 5-62 shows that the particle orientation measured using each set of combined images is similar, with up to +/- 4 degrees of difference at low stresses (high porosities).

A quality control check was performed on the data using the line length, interpreted as the long axis of the particle in the 2D plane of the image; line length is analogous to particle size. In actuality this line length is an apparent particle size as seen in a 2D cross section. Across all analysis the average particle size is constant, around 1.0 μm, with a constant standard deviation around 0.6 μm. This indicates that the particle size does not change with increasing stress level, or with different users or image analysis techniques, validating both the resedimentation procedure and the image analysis technique.

The particle orientation of MIT Images was analyzed by Durant and Adams. Four specimens of RBBC resedimented to maximum effective stresses of 1, 10, 20, and 40 MPa were analyzed. 1D measurements from two or three images were combined to compute the average orientation for each stress level and porosity. Figure 5-63 compares the average particle orientation for the MIT RBBC images with that measured for the UT RBBC images by Cheong. Both sets of measurements (UT and MIT) were obtained using the 1D analysis technique using images of similar magnification. The March model prediction is provided for reference.

The porosity of the MIT specimens does not compare exactly to that of the UT specimens at similar stress level due to varying degrees of sidewall friction experienced by the specimens during resedimentation (see discussion in section 5.1.3). The mean particle orientation measured for the MIT specimens is much lower than that measured using the UT specimens. This may be due in part to biases incorporated by the measurement procedure. Further, the MIT specimens cover a larger stress range. The permeability anisotropy and resistivity measurements (Figure 5-27 and Figure 5-54) indicate a change in behaviour below porosity 0.36 corresponding to stresses above 10 MPa. Therefore, the orientation trend for the 20, 30 and 40 MPa specimens may not agree with that measured for lower stress specimens.

Finally, Figure 5-64 adds a best fit line to the orientation data; this best fit line is fit using data obtained from MIT and UT images analyzed by different researchers. Figure 5-64 plots data include in tables Table 5-23 and Table 5-24. The particle orientation (θ) as a function of porosity (n) of RBBC is given by:

$$\theta = 16.8e^{1.8n} \tag{5-2}$$

The particle orientation measurements in both Figure 5-62 and Figure 5-63 and summary Figure 5-64 are compared with the particle orientation predicted by the March [1932] model for RBBC.

The March [1932] Model assumes that every increment of uniaxial strain translates into an increment in rotation, defined by:

$$\theta_{\epsilon_v} = \tan^{-1}[(1 - \epsilon_v)\tan\theta_o] \quad 5-3$$

Where ϵ_v is the volumetric (uniaxial) strain and θ is the mean particle orientation relative to the horizontal. The orientation of RBBC is assumed to be initially random ($\theta_o = 45$ degrees) at the beginning of resedimentation (zero effective stress). Strain is computed using the compression curve (Figure 5-3) and the relationship linking strain to void ratio:

$$\epsilon = \frac{\Delta e}{1 + e_o} \quad 5-4$$

Where ϵ is the strain at the current void ratio, e_o is the initial void ratio (equal to 2.78 for RBBC slurry), and Δe is the difference between the current void ratio and the initial void ratio.

March Theory effectively models the rotation of a single particle under the influence of a uniaxial strain field and conceptually maps the change in angle of the hypotenuse of a right angle triangle, representative of a rotating particle, whose vertical axis is being shortened. The March rotation of RBBC particles is computed using (eq. 2-1) and assuming that the particles are initially randomly oriented (i.e. the mean orientation is 45 degrees) when the sediment slurry is mixed for resedimentation (porosity 0.73, strain 0) and that there is uniaxial strain. This assumption could not be explicitly proven in this work, either through fabric analysis or permeability anisotropy measurements at very low effective stresses. However, it is reasonable to assume that dominate fabric alignment will not develop in the sediment slurry prior to placement in the sedimentation cylinders.

This model is far from perfect, and is affected by two significant shortcomings. First, this model implies that particles are compressible or must be able to slip past one another. The hypotenuse of a right angle must shorten in order for the vertical axis to shorten while the horizontal axis remains constant, as is mathematically implied by eq. 2-1. Therefore, the model should only be applied for small strains. Second, the model assumes that axial strain occurs solely through particle rotation. The model does not include strain via particle translation, double layer compression, etc.

There is significant difference between the particle orientations predicted by the March (1932) model and that measured using the image analysis technique for all porosities (Figure 5-62, Figure 5-63, and Figure 5-63). Curiously the best fit particle orientation curve (Figure 5-64) has nearly the same shape as that predicted by the March (1932) model; it is merely translated towards lower porosities.

The model prediction and experimental measurements differ most significantly in where particle rotation initiates. The March model assumes that particle rotation occurs for every increment of strain beginning from the slurry state whereas the fabric measurements suggest that significant

particle orientation may not begin until the specimen porosity is in the range of 0.6 to 0.5 (corresponding to ~ 0.1 MPa axial effective stress) is reached. This finding is based on only one measurement at porosity 0.57 and contradicts the findings of Martin and Ladd (1975) and McCarter et al (2005) who find that particle rotation is most significant at very low effective stresses in resedimented kaolinites. The measurement method should be further analyzed to investigate the effects of oven drying, image size and particle size on measured orientation to confirm that particle rotation is insignificant at low axial effective stresses for RBBC.

Though the trend line in Figure 5-64 suggests that particle orientation will continue with decreasing porosity, the low porosity data in the range of 0.4 to 0.3 suggests that limited particle orientation occurs with decreasing porosity and increasing stress beyond a certain point. This may indicate development of an asymptote, which is suggested by the March [1932] model where the rate of rotation decreases with decreasing porosity. In both cases, using the MIT and UT images, the measured particle orientation is significantly higher than that predicted using the March [1932] model.

Finally, two low resolution (5,000 – 6,000 X) MIT images each at stress levels of 10 and 40 MPa were analyzed by Durant using the 2D analysis method. The purpose of this analysis was to help gauge whether the particle orientation measurements for particles of size 0.2 – 5 μm were representative of the mudrock as a whole. Particles with long axis varying from 0.5 to 21 μm were considered in these lower resolution images. Table 5-22 summarizes the larger particle orientation results.

The larger particles have mean particle size of 2.9 μm which is constant with stress level. The average orientation varies from 32 degrees to the horizontal at 10 MPa to 25 degrees to the horizontal at 40 MPa effective stress. These particle orientations are similar in magnitude and trend as the small particle orientation measurements. Further, the standard deviation in the measured orientations are similar to those measured using the higher magnification images capturing smaller particles up to 5 μm in length.

In summary, the mean particle orientation of RBBC decreases from ~ 45 -50 degrees at porosity 0.57 to as little as ~ 28 degrees at porosity 0.30. This differs significantly from that predicted by the March [1932] model.

5.5.3 Size Dependent Particle Orientation

The effect of particle size on particle orientation was analyzed using the two 1D data sets compared in Figure 5-63: Three UT images each at three stress levels analyzed by Cheong, and two MIT images each at three stress levels (1, 10 and 40 MPa) analyzed by Durant, and three MIT images at one stress level (20 MPa) analyzed by Adams.

Three particle size bins were defined for each data set: particles between 0.2 and 0.6 μm , particles between 0.6 and 1.0 μm , and particles between 1.0 and 5.0 μm . The bins were arbitrarily defined so

that no less than 20% of the particles fell within a single bin. This criterion was satisfied for all but one bin: 1.0 to 5.0 μm sized particles in the 40 MPa MIT specimen.

Histograms were generated to show the particle orientation as a function of particle size and stress level. Figure 5-65 gives histograms for the three particle size bins at each stress level measured for the UT images. Figure 5-66 gives the same for the MIT images analyzed by Durant, and Figure 5-67 for the MIT images analyzed by Adams.

Table 5-23 summarizes the mean and standard deviation particle orientation as a function of particle size and stress level for the UT Images. Table 5-24 summarizes the same for the MIT images.

The UT and MIT images show different trends in orientation as a function of particle size as the stress level increases. However, both images indicate that at 1) the particle orientation decreases with increasing applied stress, indicating rotation to the horizontal, and 2) larger particles undergo more rotation and become more uniformly orientated than small particles. This is true for all but the 20 MPa image (corresponding to porosity 0.33) where the permeability anisotropy and resistivity anisotropy measurements are noted to fall outside of the measured trend (see Figure 5-27 and Figure 5-54).

For the UT Images, at low stress (0.1 MPa), the particle orientation has a relatively uniform distribution between 0 and 90 degrees to the horizontal for all particle sizes (Figure 5-65). A slight peak is seen in the range of 35 to 60 degrees to the horizontal. As the stress level increases, the particle orientation distribution shifts towards decreasing orientation indicating rotation to the horizontal. However, this shift is more evident for the larger (1.0 – 5.0 μm) sized particles. At 10 MPa the smallest particles have a mean particle orientation of 33 degrees to the horizontal, whereas the largest particles have a mean orientation of 24 degrees to the horizontal. The larger particles are 11 degrees more horizontally aligned, on average, than the smaller particles.

An image at the lowest stress level of 0.1 MPa was not available in the MIT image suite. By 1 MPa effective stress, the orientation of the smallest particles is still uniformly distributed, however the orientation of the largest particles is already shifting towards the horizontal (lower orientations). The measured orientations are lower than those measured for the same particle size and effective stress using the UT images. Particles continue to rotate to the horizontal as the applied stress increases to 10 MPa and then to 40 MPa. There is not a significant difference in the orientation distribution of the particles for the two lowest particle size bins (0.2 to 0.6 μm and 0.6 to 1.0 μm) between 10 and 40 MPa. However, the MIT images show that the largest particles undergo the most significant rotation as the stress increases from 10 to 40 MPa, changing orientation from 29 to 24 degrees. This contradicts the finding of the UT images, where significant particle rotation of the largest particles is seen as the stress increases from 1 to 10 MPa. It is interesting to note that the orientation for each particle size at 40 MPa for the MIT images is exactly the same as that measured at 10 MPa for the UT images. This is not a calculation error.

The 20 MPa is anomalous in all aspects of particle orientation. The mean particle orientation is slightly higher than that measured for the 10 MPa specimen, and the particle orientation is independent of size. The particle orientation in the 20 MPa specimen does not follow the above noted trend of increasing alignment with increasing stress level. As mentioned previously, this specimen was also anomalous in terms of permeability and resistivity anisotropy. The anisotropy anomaly may be linked to the fabric anomalies.

5.5.4 Comparison with X-ray Texture Goniometry

Commonly, particle orientation is measured using X-ray texture goniometry (XRD); this section compares the particle orientation measurements obtained via image analysis to those obtained via XRD.

Day-Stirrat et al [2011] measure the Mica preferred orientation of specimens imaged at UT (UT Images) using XRD. They report an increase in orientation from 4.6 m.r.d (multiples of a random distribution, after Wenk [1985]) to 4.9 m.r.d over an applied stress range of 0.1 to 10 MPa. The m.r.d preferred orientation measurements are converted to particle orientation in degrees by relating maximum pole density (ρ_{max}) in m.r.d. to strain (ϵ_v) using equation 8 [Kanitpanyacharoen et al, 2011] and then computing orientation (θ) as a function of strain using March's [1932] theory (eq. 2-1):

$$\epsilon_v = -(\rho_{max}^{-1/2} - 1) \tag{5-5}$$

An m.r.d. of 1 is equal to 45 degrees orientation. For RBBC, the XRD preferred orientation results indicate that the mean particle orientation decreases from 24.9 to 24.3 degrees, only ~ 1 degree change, as the applied stress increases from 0.1 to 10 MPa. There is significant disagreement between particle orientations obtained via image analysis (up to 22 degree particle rotation) and those computed using XRD preferred orientation (~1 degree orientation).

The micas present in RBBC are uncharacteristically large compared to the rest of the RBBC fabric. Image analysis results indicate that large particles experience more rotation at lower effective stresses and become more aligned to the horizontal than smaller particles (Table 5-23, Table 5-24, Figure 5-65, and Figure 5-66). The orientation of the large mica particles may not be representative of the mean particle orientation. The image analysis technique cannot be applied to measure the mica orientation because the field of view of the available images is on the order of the size of a single large mica particle.

5.5.5 Aspect Ratio Analysis

The aspect ratio of the particles was analyzed by Durant using 2D analysis on the UT Images. Two images at each stress level (0.1, 1.0 and 10 MPa) were combined to compute the average aspect ratio as a function of stress; Table 5-25 summarizes these measurements. Aspect ratio in the 2D

plane of measurement is defined as the ratio of the particle length to the particle height in the projected plane of the image.

The effect of 1) particle size on particle aspect ratio and 2) particle aspect ratio on particle orientation were evaluated using a similar analysis method as was used to study the effect of size on particle orientation (Section 5.5.3).

First, the data were divided into three size bins particles between 0.2 and 0.6 μm , particles between 0.6 and 1.0 μm , and particles between 1.0 and 5.0 μm . Table 5-26 summarizes the particle aspect ratio as a function of particle size for each of the three stress levels investigated. Next, these same data were divided into three aspect ratio bins: particles with aspect ratio 1 to 2.3, 2.3 to 4, and > 4 . In both cases, the bins were chosen so that at least 20 percent of the particles within any particular image sat within each bin. Table 5-27 summarizes the particle orientation as a function of aspect ratio and stress level. Finally,

Table 5-28 summarizes the mean aspect ratio and the area fraction of particles falling in each aspect ratio bin by combining data for all three stress levels. These data are used as inputs for later analysis.

The analysis presented in Section 5.5.3 revealed that larger particles undergo more rotation and become more uniformly orientated than small particles. Table 5-26 and Table 5-27 show that this trend is linked with aspect ratio. Larger particles have higher aspect ratios (Table 5-26) and higher aspect ratio particles become more horizontally aligned than lower aspect ratio particles as the applied stress increases. These trends are illustrated in Figure 5-68 and Figure 5-69. There is a slight trend showing increasing particle aspect ratio with increasing stress level, especially for higher aspect ratio particles (Table 5-26, Figure 5-68), however similar to line length, the mean aspect ratio does not vary significantly with stress level. Combining data for all stress levels, the mean aspect ratio is 3.74 ± 2.40 .

5.6 Summary of Results

The permeability, resistivity and fabric measurement programs have been very successful. Resedimentation is an excellent means of producing repeatable specimens with properties that vary based on changes in controlled parameters, in the case of these results, with increasing stress level, decreasing porosity and varying pore fluid salinity.

The specimen porosity follows the predicted OCR 4 line closely, and is affected by sidewall friction which reduces the effective stress felt by the specimen during resedimentation, increasing the final specimen porosity at a given stress level. The average salinity of the specimens is equal to the batching salinity, with considerable scatter, and there is no consistent increase or decrease in specimen salinity during long term constant head permeability measurements.

The permeability decreases with decreasing porosity in both the vertical and horizontal directions for all mudrocks measured. This decrease forms a linear trend in log permeability vs. porosity space. The permeability of the mudrocks measured for this research varies by nearly two orders of magnitude. Despite the large variation in permeability, the permeability anisotropy is restricted to a small range, <2.5.

The permeability anisotropy of RBBC and 39% Clay RBBC increases linearly with decreasing porosity until porosity 0.36, beyond which the permeability anisotropy drops. The permeability of RSFBM is nearly isotropic and does not vary with porosity. Finally, the RGoM-EI experienced cracking, making the permeability difficult to measure, but still yielded consistent results with permeability anisotropy < 2.5.

The resistivity increases with decreasing porosity for RBBC, and the apparent formation factor increases. Many parallels are noted between the conductivity anisotropy and the permeability anisotropy results. Both the permeability anisotropy and conductivity anisotropy are < 2.5 for all mudrocks measured, and follow similar trends. Chapter 6 will compare these two measurements and discuss theoretical models linking the two measures of anisotropy.

Leaching does not significantly affect the mudrock fabric, as interpreted from little change in the permeability, apparent formation factor, permeability anisotropy or conductivity anisotropy measurements for RBBC and RSFBM.

Finally, image analysis reveals that particles rotate to the horizontal with increasing effective stress and decreasing porosity. Particle rotation is size dependent, with larger particles bearing more load and becoming more uniformly aligned to the horizontal than smaller particles. Particle aspect ratio is independent of porosity, indicating particles are shifting and moving instead of breaking, however image analysis is not necessarily a good method to measure the absolute particle orientation or particle aspect ratio; these parameters are 3D features and image analysis is a 2D measurement technique.

Table 5-1: Summary of specimen characteristics: RBBC

Test ID:	Spec. ID:	Mudrock	Max. effective stress,	Meas. effective stress,	OCR	Test Sequence	e	n	Δn
			σ'_p	σ'_{test}					
			MPa	MPa					
HC003	B01	RBBC	0.39	0.10	4	V	0.973	0.493	0.004
HC004	B02	RBBC	0.78	0.20	4	H	0.890	0.471	0.005
HC005	B03	RBBC	1.18	0.29	4	V	0.815	0.449	0.007
HC006	B04	RBBC	1.96	0.49	4	H	0.751	0.429	0.000
HC007	B05	RBBC	1.57	0.39	4	V	0.814	0.449	0.001
HC008	B06	RBBC	3.14	0.78	4	V	0.714	0.416	0.004
HC009	B08	RBBC	4.32	1.08	4	H	0.679	0.404	0.005
HC011	B09	RBBC	5.88	1.47	4	V	0.651	0.394	0.011
HC016	B12	RBBC	5.88	1.47	4	V	0.643	0.391	0.003
HC018	B14	RBBC	9.81	2.45	4	V	0.582	0.368	0.011
HC019	RS160	RBBC	9.81	2.45	4	H	0.576	0.366	0.007
HC020	RS161	RBBC	9.81	2.45	4	V	0.584	0.369	0.003
HC021	RS170	RBBC	9.81	2.45	4	H	0.587	0.370	0.008
HC022	RS173	RBBC	7.85	1.96	4	H	0.613	0.380	0.010
HC034	RS241	RBBC	39.23	9.81	4	V	0.433	0.302	0.005
HC036	RS260	RBBC	9.81	2.45	4	H	0.593	0.372	0.005
HC037	RS235	RBBC	1.57	0.39	4	H	0.801	0.445	0.006
HC038	RS242	RBBC	0.98	0.25	4	V	0.862	0.463	0.002
HC040	RS303	RBBC	30.21	7.55	4	H	0.458	0.314	0.002
HC042	RS302	RBBC	0.78	0.20	4	V	0.877	0.467	0.003
HC044	RS308	RBBC	19.61	4.90	4	H	0.496	0.332	--
HC048	RS334	RBBC	9.81	2.45	4	V	0.592	0.372	--
HC049	RS258	RBBC	2.35	0.59	4	V	0.719	0.418	--
HC050	RS344	RBBC	5.88	1.47	4	H	0.637	0.389	--

Notes:

- 1) e = void ratio, n = porosity, Δn is the variation in porosity (maximum porosity - minimum porosity) across all measurements made on a single specimen. The porosity of each specimen is measured at the end of each directional permeability measurement yielding an average of three porosity measurements per specimen.
- 2) '--' indicates that the porosity was measured only once. Incorporation of resistivity measurement results in small loss of soil particles when holes are drilled for the pin probes. The porosity is measured only following completion of all directional permeability measurements.
- 3) Normal salt concentration for RBBC is 16 g/L.

Table 5-2: Summary of specimen characteristics: 39% Clay RBBC

Test ID:	Spec. ID:	Mudrock	Max. effective stress, σ'_p	Meas. effective stress, σ'_{test}	OCR	Test Dir.	e	n	Δn
			MPa	MPa					
HC024	RS186	39% Clay RBBC	9.81	2.45	4	V	0.534	0.348	0.008
HC025	RS185	39% Clay RBBC	6.28	1.57	4	H	0.565	0.361	0.002
HC026	RS189	39% Clay RBBC	3.14	0.78	4	V	0.653	0.395	0.003
HC027	RS188	39% Clay RBBC	1.96	0.49	4	H	0.671	0.401	0.006
HC029	RS218	39% Clay RBBC	1.18	0.29	4	V	0.738	0.425	0.004

Notes:

- 1) e = void ratio, n = porosity, Δn is the variation in porosity (maximum porosity – minimum porosity) across all measurements made on a single specimen. The porosity of each specimen is measured at the end of each directional permeability measurement yielding an average of three porosity measurements per specimen.
- 2) Normal salt concentration for 39% Clay RBBC is 16 g/L.

Table 5-3: Summary of specimen characteristics: RGoM-EI, RSFBM, Leached RBBC & Leached RSFBM

Test ID:	Spec. ID:	Mudrock	Max. effective stress, σ'_p	Meas. effective stress, σ'_{test}	OCR	Test Dir.	e	n	Δn
			MPa	MPa					
HC030	RS214	RGoM-EI	9.81	2.45	4	V	0.509	0.337	0.006
HC031	RS233	RGoM-EI	5.88	1.47	4	H	0.625	0.385	0.004
HC032	RS223	RSFBM	9.81	2.45	4	V	0.555	0.357	0.007
HC033	RS259	RSFBM	5.88	1.47	4	H	0.641	0.391	0.001
HC045	RS313	Leached RBBC	9.81	2.45	4	V	0.572	0.364	0.000
HC047	RS331	Leached RBBC	1.96	0.49	4	H	0.771	0.435	0.000
HC046	RS319	Leached RSFBM	9.81	2.45	4	V	0.556	0.357	0.000

Notes:

- 1) e = void ratio, n = porosity, Δn is the variation in porosity (maximum porosity – minimum porosity) across all measurements made on a single specimen. The porosity of each specimen is measured at the end of each directional permeability measurement yielding an average of three porosity measurements per specimen.
- 3) Normal salt concentration for RGoM-EI is 80 g/L, for RSFBM was 0.4 g/L (but should have been 16 g/L) and for Leached mudrocks was 0 g/L (distilled water).

Table 5-4: Specimen metrics: stress and volume change (1 of 4)

Test ID	Material	$\sigma'_s / \sigma'_{test}$	$\Delta V_t / V_t$	Hydraulic Gradient Metrics		
				Avg. ΔV	Max ΔV	$\Delta P / \sigma'$
				% of V_{total}	% of V_{total}	%
HC003	RBBC	14%	1.0%	0.06%	0.09%	26% -55%
HC003	RBBC	21%	-0.7%	0.05%	0.09%	23% -58%
HC004	RBBC	5%	1.2%	0.09%	0.13%	13% -22%
HC004	RBBC	14%	-1.2%	0.05%	0.09%	13% -28%
HC004	RBBC	5%	-0.4%	0.04%	0.07%	12% -27%
HC005	RBBC	28%	2.1%	0.02%	0.04%	10% -20%
HC005	RBBC	15%	-0.7%	0.02%	0.04%	10% -20%
HC005	RBBC	42%	-0.3%	0.00%	0.01%	10% -20%
HC006	RBBC	70%	1.0%	0.02%	0.03%	6% -12%
HC006	RBBC	56%	0.5%	0.01%	0.02%	6% -12%
HC006	RBBC	49%	-0.6%	0.02%	0.04%	6% -12%
HC007	RBBC	56%	1.8%	0.02%	0.03%	8% -15%
HC007	RBBC	58%	0.0%	0.01%	0.01%	7% -15%
HC007	RBBC	50%	0.3%	0.03%	0.04%	7% -15%
HC008	RBBC	61%	2.1%	0.03%	0.05%	4% -8%
HC008	RBBC	67%	0.1%	0.03%	0.06%	4% -7%
HC008	RBBC	58%	0.1%	0.04%	0.07%	4% -7%
HC008	RBBC	50%	-0.4%	0.01%	0.02%	4% -7%
HC009	RBBC	73%	2.6%	0.04%	0.07%	4% -9%
HC009	RBBC	43%	0.3%	0.01%	0.02%	4% -7%
HC009	RBBC	27%	-1.3%	0.03%	0.04%	4% -7%
HC011	RBBC	32%	3.1%	0.02%	0.02%	3% -5%
HC011	RBBC	17%	0.3%	0.01%	0.01%	3% -5%
HC011	RBBC	18%	-0.1%	0.01%	0.02%	3% -5%
HC011	RBBC	16%	-1.2%	0.03%	0.06%	3% -5%
HC016	RBBC	53%	3.4%	0.04%	0.04%	3% -5%
HC016	RBBC	51%	-0.6%	0.02%	0.03%	3% -5%
HC016	RBBC	31%	0.4%	0.02%	0.04%	3% -5%
HC018	RBBC	53%	2.2%	0.02%	0.03%	2% -3%
HC018	RBBC	39%	1.5%	0.01%	0.02%	2% -3%
HC018	RBBC	27%	-0.9%	0.01%	0.02%	2% -3%
HC019	RBBC	59%	3.1%	0.04%	0.07%	2% -3%
HC019	RBBC	28%	0.1%	0.09%	0.12%	2% -3%
HC019	RBBC	29%	-1.3%	0.05%	0.08%	2% -3%

Table 5-4: Specimen metrics: stress and volume change (2 of 4)

Test ID	Material	σ'_s/σ'_{test}	$\Delta V_t / V_t$	Hydraulic Gradient Metrics		
				Avg ΔV	Max ΔV	$\Delta P / \sigma'$
				% of V_{total}	% of V_{total}	%
HC020	RBBC	47%	1.3%	0.04%	0.07%	2% -2.8%
HC020	RBBC	28%	1.3%	0.03%	0.06%	2% -3%
HC020	RBBC	20%	-0.2%	0.03%	0.07%	2% -3%
HC021	RBBC	60%	2.6%	0.02%	0.03%	2% -3%
HC021	RBBC	22%	-2.3%	0.02%	0.05%	2% -3%
HC022	RBBC	75%	4.2%	0.02%	0.03%	2% -3%
HC022	RBBC	51%	-0.1%	0.05%	0.07%	2% -3%
HC022	RBBC	23%	-1.5%	0.06%	0.09%	2% -3%
HC024	39% Clay RBBC	81%	0.2%	0.05%	0.08%	2% -2%
HC024	39% Clay RBBC	61%	-0.9%	0.02%	0.06%	2% -2%
HC024	39% Clay RBBC	65%	2.0%	0.01%	0.03%	2% -2%
HC025	39% Clay RBBC	85%	1.1%	0.02%	0.03%	2% -3%
HC025	39% Clay RBBC	76%	-0.4%	0.01%	0.02%	2% -3%
HC025	39% Clay RBBC	73%	-0.2%	0.02%	0.03%	2% -3%
HC026	39% Clay RBBC	93%	0.4%	0.02%	0.04%	2% -4%
HC026	39% Clay RBBC	84%	-0.1%	0.05%	0.06%	2% -4%
HC026	39% Clay RBBC	79%	0.2%	0.02%	0.02%	2% -4%
HC027	39% Clay RBBC	86%	-0.1%	0.02%	0.02%	2% -4%
HC027	39% Clay RBBC	74%	-0.9%	0.01%	0.02%	2% -4%
HC027	39% Clay RBBC	48%	0.5%	0.04%	0.07%	1% -3%
HC029	39% Clay RBBC	70%	0.7%	0.04%	0.05%	3% -7%
HC029	39% Clay RBBC	73%	-0.5%	0.03%	0.04%	4% -7%
HC029	39% Clay RBBC	77%	-0.5%	0.08%	0.14%	1% -5%
HC030	RGoM-EI	100%	2.4%	0.01%	0.02%	2% -5%
HC030	RGoM-EI	97%	0.9%	0.02%	0.03%	3% -5%
HC030	RGoM-EI	69%	0.2%	0.02%	0.04%	3% -5%
HC031	RGoM-EI	97%	2.5%	0.02%	0.02%	5% -8%
HC031	RGoM-EI	77%	0.3%	0.03%	0.04%	5% -8%
HC031	RGoM-EI	93%	-0.2%	0.01%	0.02%	5% -8%
HC032	RSFBM	99%	1.3%	0.02%	0.02%	3% -4%
HC032	RSFBM	72%	0.4%	0.01%	0.03%	3% -5%
HC032	RSFBM	60%	0.5%	0.03%	0.04%	3% -5%

Table 5-4: Specimen metrics: stress and volume change (3 of 4)

Test ID	Material	$\sigma'_s / \sigma'_{test}$	$\Delta V_t / V_t$	Hydraulic Gradient Metrics		
				Avg ΔV	Max ΔV	$\Delta P / \sigma'$
				% of V_{total}	% of V_{total}	%
HC033	RSFBM	93%	1.6%	0.02%	0.03%	4% -7%
HC033	RSFBM	81%	-0.2%	0.01%	0.02%	4% -7%
HC033	RSFBM	87%	0.2%	0.01%	0.01%	4% -7%
HC034	RBBC	78%	5.9%	0.04%	0.10%	0.6% -1%
HC034	RBBC	80%	-4.4%	0.01%	0.02%	0.6% -1%
HC034	RBBC	80%	0.1%	0.02%	0.03%	0.6% -1%
HC036	RBBC	100%	N/A	0.01%	0.01%	2% -3%
HC036	RBBC	60%	-4.8%	0.01%	0.02%	2% -3%
HC036	RBBC	81%	-0.7%	0.01%	0.03%	2% -3%
HC037	RBBC	100%	-0.1%	0.03%	0.05%	3% -6%
HC037	RBBC	100%	0.2%	0.02%	0.03%	3% -5%
HC037	RBBC	60%	-0.3%	0.01%	0.02%	3% -5%
HC038	RBBC	60%	0.2%	0.02%	0.04%	4% -8%
HC038	RBBC	61%	0.2%	0.01%	0.02%	4% -8%
HC038	RBBC	64%	-0.1%	0.02%	0.03%	4% -8%
HC040	RBBC	97%	2.0%	0.01%	0.01%	0.5% -1.3%
HC040	RBBC	97%	0.2%	0.01%	0.01%	0.8% -1.3%
HC040	RBBC	97%	-1.7%	0.01%	0.02%	0.8% -1.3%
HC042	RBBC	70%	0.4%	0.03%	0.08%	9% -19%
HC042	RBBC	60%	-0.2%	0.04%	0.06%	9% -19%
HC042	RBBC	100%	-1.1%	0.03%	0.05%	9% -19%
HC042	RBBC	100%	0.2%	0.04%	0.05%	9% -19%
HC044	RBBC	100%	-0.4%	0.01%	0.01%	0.8% -1.2%
HC044	RBBC	100%	0.1%	0.01%	0.01%	0.8% -1.2%
HC045	Leached RBBC	100%	2.5%	0.04%	0.06%	2% -3%
HC045	Leached RBBC	100%	0.5%	0.05%	0.06%	2% -2%
HC045	Leached RBBC	100%	-1.0%	0.02%	0.03%	2% -2%
HC046	Leached RSFBM	100%	1.3%	0.00%	0.00%	4% -6%
HC046	Leached RSFBM	100%	0.1%	0.02%	0.03%	3% -5%
HC046	Leached RSFBM	100%	0.4%	0.01%	0.01%	3% -5%
HC047	Leached RBBC	100%	-0.2%	0.04%	0.07%	6% -10%
HC047	Leached RBBC	56%	-0.1%	0.01%	0.03%	7% -11%
HC047	Leached RBBC	46%	0.3%	0.02%	0.05%	8% -12%

Table 5-4: Specimen metrics: stress and volume change (4 of 4)

Test ID	Material	σ'_s/σ'_{test}	$\Delta V_t / V_t$	Hydraulic Gradient Metrics		
				Avg ΔV	Max ΔV	$\Delta P / \sigma'$
				% of V_{total}	% of V_{total}	%
HC048	RBBC	100%	2.3%	0.02%	0.02%	2% -3%
HC048	RBBC	100%	0.1%	0.01%	0.01%	2% -3%
HC048	RBBC	100%	-0.5%	0.03%	0.06%	2% -3%
HC049	RBBC	100%	1.6%	0.06%	0.11%	6% -10%
HC049	RBBC	100%	0.6%	0.01%	0.02%	5% -8%
HC049	RBBC	100%	-0.7%	0.02%	0.03%	5% -8%
HC050	RBBC	100%	2.4%	0.01%	0.02%	2% -3%
HC050	RBBC	100%	-1.4%	0.01%	0.01%	2% -3%
HC050	RBBC	100%	-0.6%	0.02%	0.04%	2% -3%
Average		67%	0.35%	0.02%	0.04%	
Maximum		100%	5.88%	0.09%	0.14%	
Minimum		5%	-4.83%	0.00%	0.00%	

Notes:

- 1) σ'_s is the sampling effective stress equal to the effective stress measured after temperature and pressure equilibration during the pressure up phase of the permeability measurement (see Chapter 4 or Appendix 2).
- 2) $\Delta V_t / V_t$ is a measure of the change in specimen volume, computed using the specimen dimensions between the beginning and end of the directional permeability measurement, divided by the specimen volume, computed using the specimen dimensions measured at the end of the directional permeability measurement. It is a potential measure of the specimen volume change associated with one directional permeability measurement.
- 3) ΔV is the difference in volume between the specimen inflow and outflow measured throughout the duration of the application of the hydraulic gradient. This volume measure includes volume change associated with pressure equalization and is corrected for small leaks and creep associated volume change.
- 4) ΔP is the pressure differential applied to the specimen to initiate the hydraulic gradient. σ' is the mean effective stress in the middle of the specimen, equal to the final effective stress following resedimentation to OCR 4.
- 5) The average, maximum and minimum values are computed across all 108 directional measurements, spanning 4 tables.

Table 5-5: Salinity measurements (1 of 2)

Sample ID	Test ID	Mudrock	σ'_p	Porosity n	Moisture Content, w	Salinity			
						Resed	Before Perm	After perm	Avg.
			MPa		%	g/L	g/L	g/L	g/L
B03	HC005	RBBC	1.18	0.45	0.29	16.0	16.5		16.5
B04	HC006	RBBC	1.96	0.43	0.27	16.0	15.7		15.7
B05	HC007	RBBC	1.57	0.74	0.29	16.0	9.4		9.4
B06	HC008	RBBC	3.14	0.42	0.25	16.0	18.2		18.2
B08	HC009	RBBC	4.32	0.40	0.23	16.0	14.1		14.1
B09	HC011	RBBC	5.88	0.39	0.22	16.0	11.1		11.1
B10	HC014	RBBC	7.85	0.36	0.23	16.0	15.3		15.3
B12	HC016	RBBC	5.88	0.39	0.23	16.0	9.2		9.2
B14	HC018	RBBC	9.81	0.37	0.21	16.0	14.8		14.8
RS160	HC019	RBBC	9.81	0.37	0.21	16.0	15.8		15.8
RS161	HC020	RBBC	9.81	0.37	0.21	16.0	13.9		13.9
RS170	HC021	RBBC	9.81	0.37	0.21	16.0	18.3		18.3
RS173	HC022	RBBC	7.85	0.38	0.22	16.0	18.9		18.9
RS186	HC024	39% Clay RBBC	9.81	0.35	0.20	10.9	20.0		20.0
RS185	HC025	39% Clay RBBC	6.28	0.36	0.20	10.9	15.5		15.5
RS189	HC026	39% Clay RBBC	3.14	0.40	0.23	10.9	18.1		18.1
RS188	HC027	39% Clay RBBC	1.96	0.40	0.25	10.9	16.7		16.7
RS218	HC029	39% Clay RBBC	1.18	0.42	0.27	10.9	21.9		21.9
RS214	HC030	RGoM	9.81	0.34	0.18	80.0	49.7		49.7
RS233	HC031	RGoM	5.88	0.38	0.20	80.0	39.8		39.8
RS223	HC032	SFBM	9.81	0.36	0.20	0.4	5.8		5.8
RS259	HC033	SFBM	5.88	0.39	0.24	0.4	9.6		9.6
RS241	HC034	RBBC	39.23	0.30	0.15	16.0	18.8		18.8
RS260	HC036	RBBC	9.81	0.37	0.21	16.0	18.5	14.5	16.5
RS235	HC037	RBBC	1.57	0.45	0.29	16.0	11.2	10.2	10.7
RS242	HC038	RBBC	0.98	0.46	0.31	16.0	22.7	15.6	19.1
RS303	HC040	RBBC	30.21	0.31	0.16	16.0	19.9	14.5	17.2
RS302	HC042	RBBC	0.78	0.47	0.31	16.0	12.5	14.2	13.3
RS308	HC044	RBBC	19.61	0.33	0.18	16.0	18.7	14.1	16.4

Table 5-5: Salinity measurements (2 of 2)

Sample ID	Test ID	Mudrock	σ'_p	Porosity n	Moisture Content, w	Salinity			
						Resed	Before Perm	After perm	Avg.
			MPa		%	g/L	g/L	g/L	g/L
RS313	HC045	Leached RBBC	9.81	0.36	0.21	0.0	0.5	1.1	0.8
RS319	HC046	Leached SFBM	9.81	0.36	0.21	0.0	1.4	1.7	1.5
RS331	HC047	Leached RBBC	1.96	0.44	0.28	0.0	0.5	1.4	0.9
RS334	HC048	RBBC	9.81	0.37	0.21	16.0	17.0	17.9	17.5
RS258	HC049	RBBC	2.35	0.42	0.26	16.0	7.6	11.6	9.6
RS344	HC050	RBBC	5.88	0.39	0.23	16.0	18.8	15.4	17.1

Notes:

- 1) 'Resed' Salinity is the salinity at which the mudrock specimen was resedimented or batched.
- 2) The salinity before permeability measurement is measured using trimmings.
- 3) The salinity after permeability measurement is measured using a portion of the specimen itself.

Table 5-6: Compression index (c_c) and swelling index (c_s) for RBBC, RGoM-EI and RSFBM

Mudrock	Compression Index, c_c		Swelling Index, c_s		Stress Level (MPa)	Source / Reference
	Void Ratio Space, c_{ce}	Porosity Space, c_{cn}	Void Ratio Space, c_{se}	Porosity Space, c_{sn}		
RBBC	0.325	0.102	0.028	0.012	10	CRS 1219 (Horan, 2012)
RGoM-EI	0.459	0.152	0.081	0.040	9 MPa	CRS109 - UT (Betts, 2014)
RSFBM	0.474	0.170	0.082	0.053	40 MPa	CRS 1142 (Kontopoulos, 2012)

Notes:

- 1) The compression index is defined as the slope of the virgin compression line in either void ratio space (e-log stress) or porosity space (n-log stress)
- 2) The swelling index (c_s) is defined as the slope of the swelling line in either void ratio space (e-log stress) or porosity space (n-log stress)

Table 5-7: RBBC permeability summary

Test ID:	Mud-rock	Adjusted using Global Measurement Sequence Bias Method						Anisotropy, r_k Using Individual Specimen Adjustment Method
		Horizontal Permeability, k_H (m ²)		Vertical Permeability, k_V (m ²)		Permeability Anisotropy, r_k		
		Avg.	Stdev.	Avg.	Stdev.	Avg.	Stdev.	
HC003	RBBC	6.77E-17	5.97E-19	5.68E-17	1.28E-18	1.19	0.03	
HC004	RBBC	4.18E-17	4.84E-19	3.00E-17	4.36E-19	1.40	0.03	
HC005	RBBC	3.43E-17	5.22E-19	2.54E-17	1.72E-19	1.35	0.02	1.36
HC006	RBBC	2.33E-17	2.70E-19	1.69E-17	1.79E-19	1.38	0.02	
HC007	RBBC	2.78E-17	4.03E-19	1.76E-17	1.68E-19	1.58	0.03	1.62
HC008	RBBC	1.84E-17	2.81E-19	1.14E-17	1.99E-19	1.61	0.04	1.61
HC009	RBBC	1.41E-17	1.94E-19	8.26E-18	1.57E-19	1.71	0.04	
HC011	RBBC	1.05E-17	1.46E-19	6.40E-18	1.01E-19	1.64	0.03	1.69
HC016	RBBC	1.01E-17	9.99E-20	5.53E-18	7.79E-20	1.82	0.03	1.89
HC018	RBBC	6.56E-18	1.01E-19	3.77E-18	3.89E-20	1.74	0.03	1.69
HC019	RBBC	6.74E-18	3.89E-19	3.55E-18	1.27E-20	1.90	0.11	
HC020	RBBC	6.22E-18	8.98E-20	3.56E-18	8.32E-20	1.75	0.05	1.68
HC021	RBBC	6.83E-18	8.78E-20	3.65E-18	7.61E-20	1.87	0.05	
HC022	RBBC	8.22E-18	1.34E-19	4.71E-18	1.17E-19	1.75	0.05	
HC034*	RBBC	1.57E-18	2.15E-20	8.12E-19	1.78E-20		0.05	1.94
HC036	RBBC	6.74E-18	5.29E-20	3.51E-18	2.69E-20	1.92	0.02	1.72
HC037	RBBC	2.79E-17	7.93E-19	1.63E-17	2.79E-19	1.72	0.06	1.75
HC038	RBBC	4.03E-17	4.96E-19	2.63E-17	3.16E-19	1.54	0.03	1.48
HC040*	RBBC	1.92E-18	1.16E-20	1.37E-18	1.49E-20		0.02	1.40
HC042	RBBC	3.90E-17	4.34E-19	3.32E-17	6.19E-19	1.17	0.03	
HC044	RBBC	2.69E-18	1.02E-19	1.87E-18	2.05E-20	1.44	0.06	
HC048	RBBC	7.26E-18	9.17E-20	4.28E-18	6.61E-20	1.70	0.03	1.74
HC049	RBBC	1.79E-17	3.23E-19	1.12E-17	8.94E-20	1.60	0.03	1.65
HC050	RBBC	1.04E-17	1.15E-19	5.67E-18	5.78E-20	1.84	0.03	1.85

Note:

1) * indicates that the measurement sequence bias correction is applied using the specimen method because of differing behaviour > 10 MPa.

Table 5-8: 39% Clay RBBC permeability summary

Test ID:	Mudrock	Adjusted using Global Measurement Sequence Bias Method						Anisotropy, r_k Using Individual Specimen Adjustment Method
		Horizontal Permeability, k_H (m^2)		Vertical Permeability, k_V (m^2)		Permeability Anisotropy, r_k		
		Avg.	Stdev.	Avg.	Stdev.	Avg.	Stdev.	
HC024	39% Clay RBBC	1.52E-17	8.45E-20	1.10E-17	5.58E-20	1.39	0.01	
HC025	39% Clay RBBC	2.16E-17	2.44E-19	1.31E-17	7.03E-20	1.64	0.02	
HC026	39% Clay RBBC	3.73E-17	9.21E-19	2.40E-17	2.63E-19	1.55	0.04	1.62
HC027	39% Clay RBBC	4.75E-17	2.53E-19	3.32E-17	3.51E-19	1.43	0.02	1.43
HC029	39% Clay RBBC	7.73E-17	1.35E-18	5.22E-17	3.86E-19	1.48	0.03	1.47

Table 5-9: RGoM-EI, RSFBM, Leached RBBC & Leached RSFBM permeability summary

Test ID:	Mudrock	Adjusted using Individual Specimen Measurement Sequence Bias Method					
		Horizontal Permeability, k_H (m^2)		Vertical Permeability, k_V (m^2)		Anisotropy, r_k	
		Avg.	Stdev.	Avg.	Stdev.	Avg.	Stdev.
HC030	RGoM-EI	1.17E-19	1.91E-20	8.19E-20	1.69E-21	1.43	0.24
HC031	RGoM-EI	2.99E-19	4.69E-21	2.53E-19	1.55E-20	1.18	0.07
HC032	RSFBM	3.73E-19	3.19E-20	3.97E-19	2.03E-20	0.94	0.09
HC033	RSFBM	1.01E-18	1.36E-20	1.06E-18	2.62E-20	0.96	0.03
HC045	Leached RBBC	5.75E-18	2.39E-20	2.91E-18	2.65E-20	1.97	0.02
HC046	Leached RSFBM	4.74E-19	2.95E-20	3.62E-19	7.14E-21	1.31	0.09
HC047	Leached RBBC	1.66E-17	1.54E-19	1.30E-17	1.39E-19	1.28	0.02

Table 5-10: RBBC measured permeability for measurement sequence bias determination

Test ID:	Mudrock	Measured Data					
		Horizontal Direction			Vertical Direction		
		K_{H1}	K_{H2}	# Meas. Increments (Δn)	K_{V1}	K_{V2}	# Meas. Increments (Δn)
	m^2	m^2		m^2	m^2		
HC003	RBBC	6.66E-17			5.68E-17		
HC004*	RBBC	4.32E-17	3.92E-17	2	2.95E-17		
HC005	RBBC	3.39E-17	3.32E-17	1	2.54E-17		
HC006	RBBC	2.32E-17	2.30E-17	1	1.64E-17		
HC007	RBBC	2.76E-17	2.67E-17	1	1.76E-17		
HC008	RBBC	1.83E-17	1.77E-17	1	1.17E-17	1.07E-17	3
HC009	RBBC	1.45E-17	1.35E-17	1	8.03E-18		
HC011	RBBC	1.06E-17	9.95E-18	1	6.69E-18	5.87E-18	3
HC016	RBBC	1.00E-17	9.61E-18	1	5.53E-18		0
HC018	RBBC	6.40E-18	6.41E-18	1	3.77E-18		
HC019	RBBC	6.52E-18	6.85E-18	1	3.45E-18		
HC020	RBBC	6.04E-18	6.11E-18	1	3.56E-18		
HC021	RBBC	6.83E-18			3.55E-18		
HC022	RBBC	7.96E-18	8.35E-18	1	4.58E-18		
HC034*	RBBC	1.49E-18	1.42E-18	1	8.12E-19		
HC036	RBBC	6.74E-18			3.60E-18	3.28E-18	1
HC037	RBBC	2.79E-17			1.59E-17	1.59E-17	1
HC038	RBBC	3.92E-17	3.95E-17	1	2.63E-17		
HC040	RBBC	1.92E-18			1.27E-18	1.18E-18	1
HC042**	RBBC	3.77E-17			3.54E-17	2.97E-17	N/A
HC044	RBBC	2.69E-18				1.81E-18	
HC048	RBBC	7.20E-18	6.96E-18	1	4.28E-18		
HC049	RBBC	1.78E-17	1.71E-17	1	1.12E-17		
HC050	RBBC	1.04E-17			5.58E-18	5.53E-18	1

Notes:

- 1) * indicates that the horizontal permeability was not included in the bias measurement ($\Delta n > 1$ or $\sigma > 10$ MPa)
- 2) ** indicates that the vertical permeability was not included in the bias measurement
- 3) Pertinent specimen data including specimen ID, stress level, void ratio and porosity can be found in Table 5-1.

Table 5-11: 39% Clay RBBC measured permeability for Measurement Sequence Bias Determination

		Measured Data					
		Horizontal Direction			Vertical Direction		
Test ID:	Mudrock	K_{H1}	K_{H2}	# Meas. Increments (Δn)	K_{V1}	K_{V2}	# Meas. Increments (Δn)
		m^2	m^2		m^2	m^2	
HC024	39% Clay RBBC	1.51E-17	1.42E-17	1	1.01E-17		
HC025	39% Clay RBBC	2.10E-17	2.05E-17	1	1.21E-17		
HC026	39% Clay RBBC	3.53E-17	3.17E-17	1	2.40E-17		
HC027	39% Clay RBBC	4.75E-17			3.19E-17	3.07E-17	1
HC029	39% Clay RBBC	7.17E-17	6.70E-17	1	5.22E-17		

Notes:

1) Pertinent specimen data including specimen ID, stress level, void ratio and porosity can be found in Table 5-2.

Table 5-12: Measurement Sequence Bias summary for Permeability

Mudrock	Stress / Porosity Range of Measurement	Horizontal Measurement Sequence Bias, x_H	Vertical Measurement Sequence Bias, x_V
RBBC	x_H : 0.4 - 10 MPa, 0.36 < n < 0.5 x_V : 0.4 - 40 MPa, 0.31 < n < 0.5	0.984	0.986
39% Clay RBBC	x_H, x_V : 1.2 - 10 MPa, 0.35 < n < 0.42	0.930	0.962

Table 5-13: Permeability anisotropy as a function of maximum effective stress and sidewall friction for RBBC OCR 4

Stress Level (MPa)	Sidewall Friction (%)				
	0	10	20	30	40
0.1	1.02	1.02	1.01	1.01	1.01
1	1.39	1.39	1.38	1.38	1.39
10	1.92	1.91	1.91	1.94	1.99

Table 5-14: Porosity as a function of stress level and sidewall friction for RBBC at OCR 4

Stress Level (MPa)	Sidewall Friction (%)				
	0	10	20	30	40
0.1	0.54	0.55	0.55	0.55	0.56
1	0.46	0.47	0.47	0.48	0.48
10	0.35	0.36	0.36	0.37	0.38

Table 5-15: RBBC measured resistivity for Measurement Sequence Bias Determination

Test ID:	Material	Measured Data					
		Horizontal Direction			Vertical Direction		
		ρ_{H1}	ρ_{H2}	# Meas. Increments (Δn)	ρ_{V1}	ρ_{V2}	# Meas. Increments (Δn)
		Ωm	Ωm		Ωm	Ωm	
**HC036	RBBC	1.67			3.12	3.46	1
HC037	RBBC	1.86			3.24	3.40	1
HC038	RBBC	1.14	1.22	1	1.61		
*HC040	RBBC	2.78			4.24	4.79	1
HC042	RBBC	1.30			1.78	1.82	1
*HC044	RBBC	2.37				4.12	
HC048	RBBC	1.50	1.56	1	2.68		
HC049	RBBC	1.82	1.91	1	3.17		
HC050	RBBC	1.59			3.01	3.20	1

Notes:

- 1) * indicates that the permeability was not included in the bias measurement ($n < 0.36, \sigma > 10$ MPa)
- 2) ** indicates that the permeability was not included in the bias measurement (not corrected for current loss in measurement apparatus)

Table 5-16: Measurement Sequence Bias summary for Resistivity

Mudrock	Stress / Porosity Range of Measurement	Horizontal Measurement Sequence Bias, $x_{H\rho}$	Vertical Measurement Sequence Bias, $x_{V\rho}$
RBBC	0.8 – 10 MPa, 0.36 < n < 0.47	1.051	1.051

Table 5-17: Resistivity Measurements Summary (Triaxial Cell Measurements)

Test ID:	Mudrock	Resistivity						Formation Factor			Anisotropy				Adjustment Method	I _c Specimen Correction Method
		Horizontal, ρ _H			Vertical, ρ _V			Horizontal F _H	Vertical F _V	Resistivity, ρ _p		Conductivity, I _c				
		Avg.	Stdev.	Ωm	Avg.	Stdev.	Ωm	Avg.	Avg.	Avg.	Stdev	Avg.	Stdev			
		Ωm	Ωm	Ωm	Ωm	Ωm	Ωm									
HC036	RBBC	1.67	0.11	2.93	0.23	3.58	6.30	0.57	0.06	1.76	0.13	Global	1.56			
HC037	RBBC	1.86	0.07	3.01	0.16	2.68	4.34	0.62	0.04	1.62	0.10	Global	1.65			
HC038	RBBC	1.09	0.06	1.61	0.04	2.69	3.95	0.68	0.04	1.47	0.08	Global	1.53			
HC040	RBBC	2.78	0.01	3.70	0.03	6.19	8.24	0.75	0.01	1.33	0.01	Specimen				
HC042	RBBC	1.17	0.02	1.43	0.01	2.07	2.51	0.82	0.01	1.22	0.02	Global	N/A			
HC044	RBBC	2.37	0.01	3.61	0.01	5.05	7.69	0.66	0.00	1.52	0.01	Global	N/A			
HC048	RBBC	1.42	0.03	2.68	0.03	3.21	6.06	0.53	0.01	1.89	0.04	Global	1.86			
HC049	RBBC	1.73	0.02	3.17	0.03	2.26	4.14	0.55	0.01	1.83	0.03	Global	1.84			
HC050	RBBC	1.59	0.02	2.81	0.04	3.53	6.23	0.57	0.01	1.76	0.03	Global	1.77			
HC046	Leached RSFBM	7.67	0.06	11.77	0.00	1.85	2.83	0.65	0.00	1.53	0.01	Specimen				
HC045	Leached RBBC	18.27	0.30	44.45	0.00	2.35	5.72	0.41	0.01	2.43	0.04	Specimen				
HC047	Leached RBBC	30.14	0.00	36.84	0.36	4.56	5.57	0.82	0.01	1.22	0.03	Specimen				

Table 5-18: Summary of Bench top conductivity measurements for 39% Clay RBBC, RGoM-EI and RSFBM

Test ID	Mudrock	Method	Bench top Measurements												Conductivity Anisotropy, I_{σ}		
			Vertical			Horizontal						$\rho_{H,AVG}$					
			Avg. Ωm	Stdev. Ωm	ρ_{V1}	ρ_{H1}		ρ_{H2}		Avg. Ωm	Stdev. Ωm	Avg. Ωm	Stdev. Ωm	Avg. Ωm		Stdev. Ωm	
						Avg. Ωm	Stdev. Ωm	Avg. Ωm	Stdev. Ωm								
HC026	39% Clay RBBC	Protruding, Old	7.90			3.95						4.24	0.00			1.86	
HC027	39% Clay RBBC	Protruding, Old	5.61			3.10						3.34	0.00			1.68	
HC029	39% Clay RBBC	Protruding, Old	4.07			2.48						2.31	0.00			1.77	
HC030	RGoM-EI	Protruding, Old	4.49			1.52						1.54	0.00			2.91	
HC031	RGoM-EI	Protruding, Old	1.70	0.01		0.82	0.04				0.70	0.05	0.76	0.06			2.23
HC032	RSFBM	Protruding, Old	4.57	0.37		6.67	0.02				7.08	0.29	6.88	0.30			0.66

Table 5-19: Summary of image analysis

Image File Name	Mudrock	Institution	Image Type	Magnification X	Maximum Effective Stress, σ'_p MPa	Porosity, n	1D Analysis			2D Analysis	
							Adams	Durant ¹	Cheong ²	Durant ¹	Analysis
SEM0020_BSE_001	RBBC	UT	SE	14000	0.1	0.57		✓			✓
SEM0020_BSE_002	RBBC	UT	SE	14000	0.1	0.57				✓	✓
SEM0020_BSE_004	RBBC	UT	SE	14000	0.1	0.57				✓	
SEM0021_BSE_001	RBBC	UT	SE	14000	1	0.45		✓			✓
SEM0021_BSE_002	RBBC	UT	SE	14000	1	0.45				✓	✓
SEM0021_BSE_004	RBBC	UT	SE	14000	1	0.45				✓	
SEM0022_BSE_001	RBBC	UT	SE	14000	10	0.35		✓			✓
SEM0022_BSE_002	RBBC	UT	SE	14000	10	0.35				✓	✓
SEM0022_BSE_004	RBBC	UT	SE	14000	10	0.35				✓	
HC034 V-018	RBBC	MIT	BSE	15020	40	0.30		✓			✓
HC034 V-022	RBBC	MIT	BSE	5950	40	0.30					
HC034 V-034	RBBC	MIT	BSE	14860	40	0.30		✓			
HC034 V-038	RBBC	MIT	BSE	6010	40	0.30					✓
HC036 V-021	RBBC	MIT	BSE	15020	10	0.37		✓			
HC036 V-025	RBBC	MIT	BSE	5960	10	0.37					✓
HC036 V-036	RBBC	MIT	BSE	10020	10	0.37		✓			
HC036 V-037	RBBC	MIT	BSE	6020	10	0.37					✓
RS242 H-10	RBBC	MIT	BSE	11880	1	0.46		✓			
RS242 H-20	RBBC	MIT	BSE	12000	1	0.46				✓	
HC044-095	RBBC	MIT	BSE	12000	20	0.33			✓		
HC044-096	RBBC	MIT	BSE	12000	20	0.33			✓		
HC044-112	RBBC	MIT	BSE	12000	20	0.33		✓			

Notes:

- 1) Keiron Durant, MIT Summer Research Intern Student in the MIT Geotechnical Laboratory for Summer 2013.
- 2) Mun Ngha Cheong, UROP in the MIT Geotechnical Laboratory from September 2012 – May 2013

Table 5-20: Image analysis results: particle orientation and aspect ratio for each image

Image	1D Analysis			2D Analysis				
	Particle Orientation		# Particles	Particle Orientation		Particle Aspect Ratio		# Particles
	Avg.	Stdev.		Avg.	Stdev.	Avg.	Stdev.	
	Deg.	Deg.	Deg.	Deg.				
Image Analysis by Durant & Adams								
SEM0020_BSE_001	41	21	502	40	24	3.4	2.0	523
SEM0020_BSE_002				47	23	3.3	1.9	353
SEM0021_BSE_001	43	23	341	38	24	3.7	2.3	415
SEM0021_BSE_002				39	23	3.7	2.5	519
SEM0022_BSE_001	28	21	776	26	21	3.9	2.5	649
SEM0022_BSE_002				28	22	4.0	2.4	659
HC034 V-018	30	22	741					
HC034 V-022				27	23	3.0	1.1	224
HC034 V-034	31	26	477					
HC034 V-038				22	21	3.0	2.1	161
HC036 V-021	33	24	838					
HC036 V-025				31	24	2.9	2	210
HC036 V-036	33	23	786					
HC036 V-037				33	23	3.1	2.5	210
RS242 H- 10	39	25	629					
RS242 H- 20	31	23	803					
Image Analysis by Cheong & Adams								
SEM0020_BSE_001	44	24	407					
SEM0020_BSE_002	53	24	825					
SEM0020_BSE_004	51	24	617					
SEM0021_BSE_001	40	24	383					
SEM0021_BSE_002	41	23	530					
SEM0021_BSE_004	33.7	23	305					
SEM0022_BSE_001	27	22	599					
SEM0022_BSE_002	29	22	813					
SEM0022_BSE_004	28.2	20	653					
Image Analysis by Adams								
HC044 -095	34	24	454					
HC044 -096	33	25	416					
HC044 -112	32	24	611					

Table 5-21: Particle orientation measurements for RBBC (UT Images)

Maximum Effective Stress, σ_p	Porosity, n	Orientation ¹	Line Length ¹	Number of Measurements
MPa		degrees	μm	
1D Analysis - Cheong - Combined data from 3 images				
0.1	0.57	50+/-24	0.9+/-0.6	1845
1	0.45	39+/-24	1.1+/-0.7	1211
10	0.35	28+/-21	1.0+/-0.6	2052
1D Analysis - Durant - Combined data from 1 image				
0.1	0.57	41+/-21	1.0+/-0.6	502
1	0.45	43+/-23	1.1+/-0.7	343
10	0.35	28+/-21	0.9+/-0.6	779
2D Analysis - Durant - Combined data from 2 images				
0.1	0.57	43+/-24	1.1+/-0.7	877
1	0.45	39+/-23	1.2+/-0.8	946
10	0.35	27+/-21	1.0+/-0.7	1317

Note:

- 1) Reported as the mean +/- 1 standard deviation.

Table 5-22: Particle orientation measurements for RBBC (MIT Images)

Maximum Effective Stress, σ_p	Porosity, n	Orientation ¹	Line Length ¹	Number of Measurements
MPa		degrees	μm	
1D Analysis - Durant - Combined data from 2 images				
1	0.46	34+/-24	0.9+/-0.7	1442
10	0.37	33+/-23	0.8+/-0.8	1658
40	0.30	30+/-24	0.7+/-0.6	1256
1D Analysis - Adams - Combined data from 3 images				
20	0.33	33+/-24	0.9+/-0.7	1474
2D Analysis - Durant - Combined data from 2 images - Lower Magnification Images				
10	0.37	32+/-24	2.8+/-2.2	404
40	0.30	25+/-22	2.9+/-2.4	385

Note:

- 1) Reported as the mean +/- 1 standard deviation.

Table 5-23: Particle orientation as a function of size and stress level for RBBC (UT Images, 1D analysis, Cheong)

Porosity	Stress (MPa)	Particle Orientation (degrees) ¹		
		0.2 - 0.6 μm	0.6 - 1.0 μm	1.0 - 5.0 μm
0.57	0.1	49+/-24	50+/-24	51+/-25
0.45	1	39+/-25	40+/-25	37+/-22
0.35	10	33+/-22	28+/-21	24+/-19

Note:

- 1) Reported as the mean +/- 1 standard deviation.
- 2) Data combined from analysis of 3 images

Table 5-24: Particle orientation as a function of size and stress level for RBBC (MIT Images, 1D analysis, Durant)

Porosity	Stress (MPa)	Particle Orientation (degrees) ¹			Analyst and # of Images analyzed
		0.2 - 0.6 μm	0.6 - 1.0 μm	1.0 - 5.0 μm	
0.46	1	38+/-25	32+/-23	31+/-23	Durant / 2
0.37	10	35+/-24	31+/-23	29+/-22	Durant / 2
0.33	20	32+/-24	33+/-24	33+/-24	Adams / 3
0.30	40	33+/-24	28+/-24	24+/-22	Durant / 2

Note:

- 1) Reported as the mean +/- 1 standard deviation.
- 2) Data combined from analysis of 2 images

Table 5-25: Aspect ratio measurements for RBBC (UT Images)

Maximum Effective Stress, σ'_p MPa	Porosity, n	Aspect Ratio		Number of Measurements
		Avg.	Stdev.	
0.1 ^a	0.57	3.4	2.0	877
1 ^a	0.45	3.8	2.6	946
10 ^a	0.35	3.9	2.5	1317
All combined	N/A	3.74	2.4	3140

Note:

- a) Combined data from 2 images

Table 5-26: Particle aspect ratio as a function of particle size for RBBC (UT Images)

Particle Size Bin	Particle Aspect Ratio ¹		
	0.1 MPa	1 MPa	10 MPa
0.2 - 0.6 μm	2.2 +/- 0.8	2.2 +/- 0.9	2.4 +/- 0.9
0.6 - 1.0 μm	2.9 +/- 1.3	3.1 +/- 1.5	3.5 +/- 1.4
1.0 - 5.0 μm	4.2 +/- 2.3	4.7 +/- 2.8	5.3 +/- 2.9

Note:

- 1) Combined total over six images, two each spanning three stress levels (0.1, 1 and 10 MPa); Reported as the mean +/- 1 standard deviation.

Table 5-27: Particle orientation as a function of aspect ratio and stress level for UT Images

Aspect Ratio Bin	Particle Orientation ¹		
	0.1 MPa	1 MPa	10 MPa
1-2.3	43 +/- 25	41 +/- 26	35 +/- 25
2.3-4	44 +/- 25	38 +/- 24	28 +/- 21
>4	43 +/- 23	37 +/- 21	22 +/- 18

Note:

- 1) Combined total over six images, two each spanning three stress levels (0.1, 1 and 10 MPa); Reported as the mean +/- 1 standard deviation.

Table 5-28: Aspect ratio as a function of size for RBBC (UT Images)

Aspect Ratio Bin	# Measurements ¹	Mean Aspect Ratio ²	Total Particle Area (μm^2)	Particle Area Fraction
1 - 2.3	967	1.69 +/- 0.34	413	38%
2.3 - 4	1093	3.11 +/- 0.49	291	27%
> 4	1081	6.23 +/- 2.46	374	35%

Note:

- 1) Combined total over six images, two each spanning three stress levels (0.1, 1 and 10 MPa).
- 2) Reported as the mean +/- 1 standard deviation.

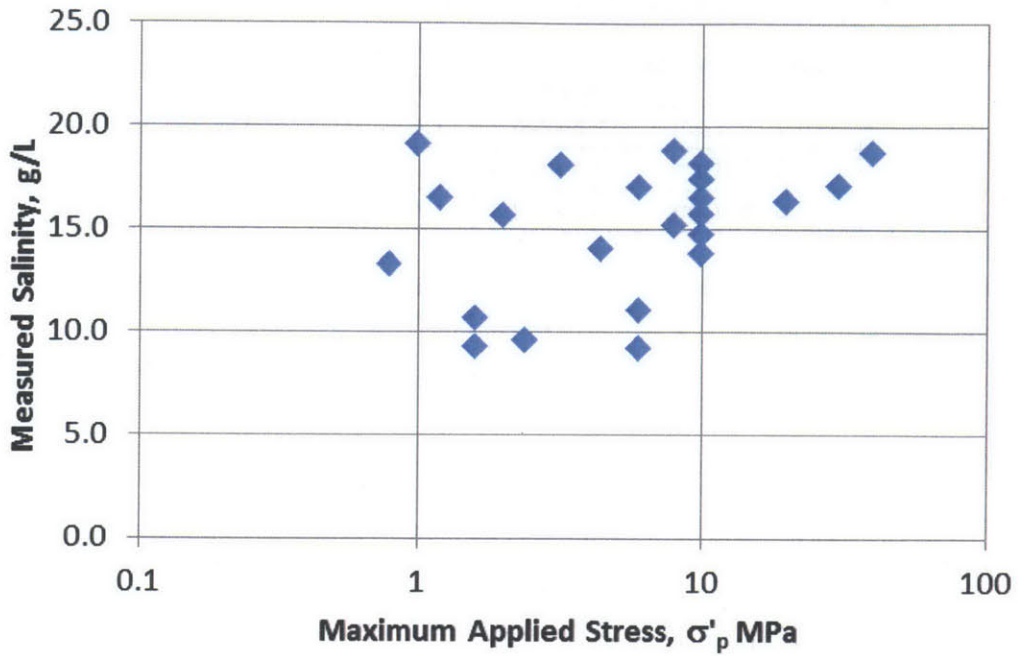


Figure 5-1: Salinity vs. maximum effective stress for RBBC

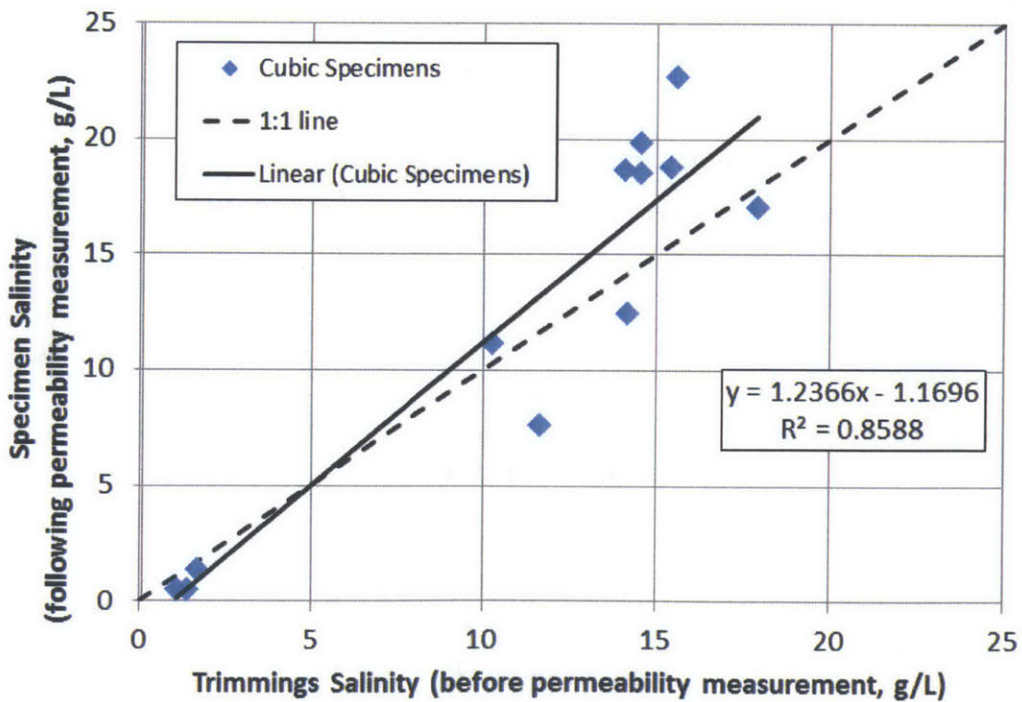


Figure 5-2: Comparison between trimmings salinity and specimen salinity (before vs. after permeability measurement, all mudrocks)

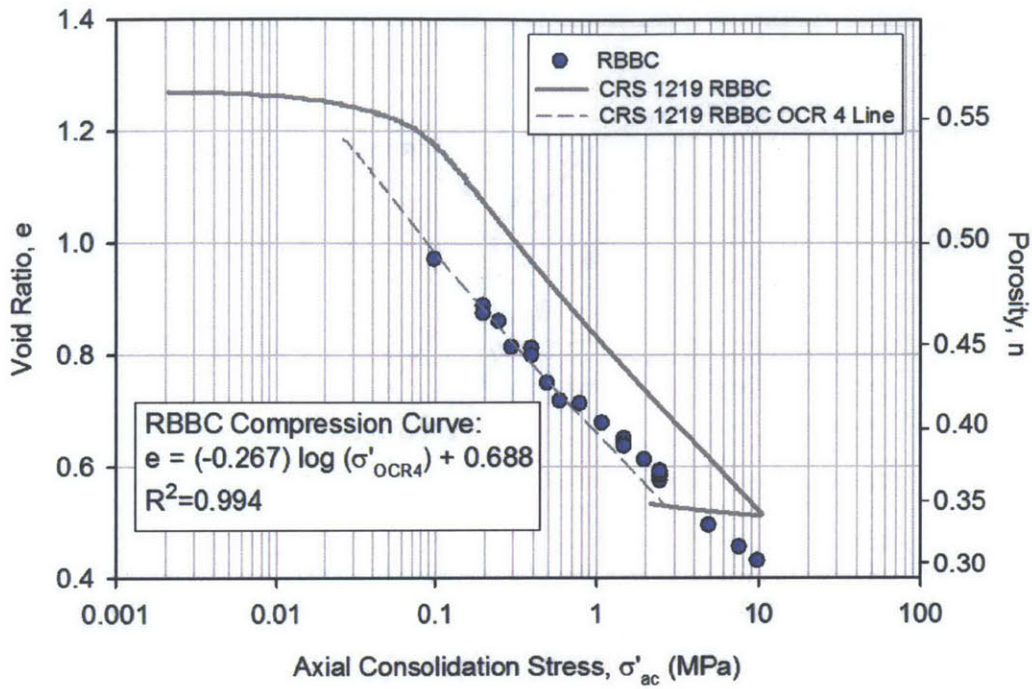


Figure 5-3: Void ratio vs. log axial consolidation stress compression curve: RBBC

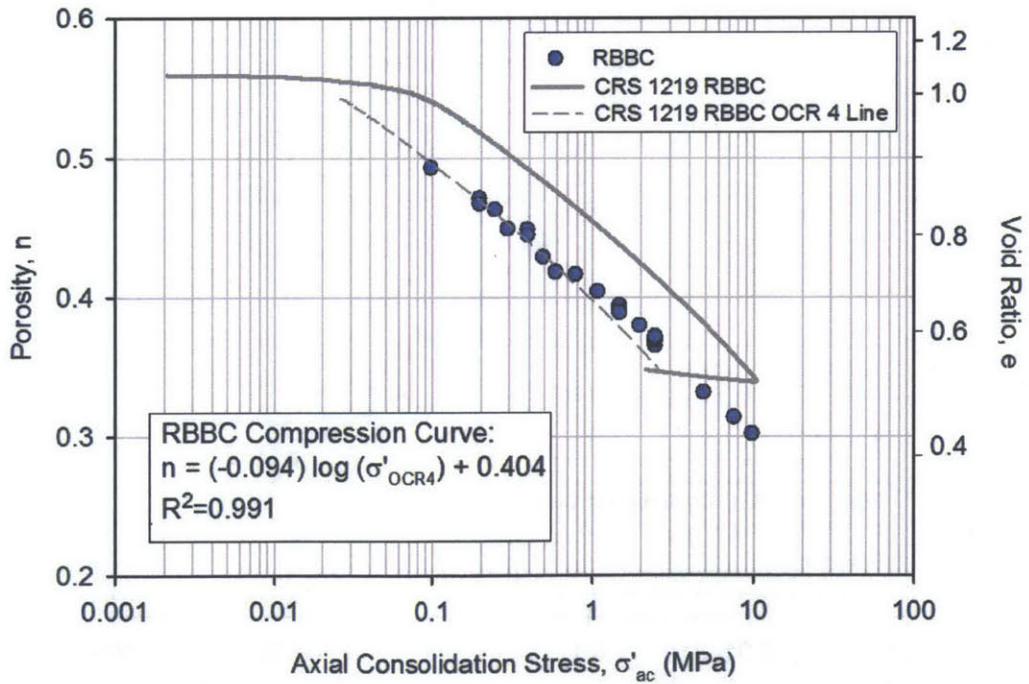


Figure 5-4: Porosity vs. log axial consolidation stress compression curve: RBBC

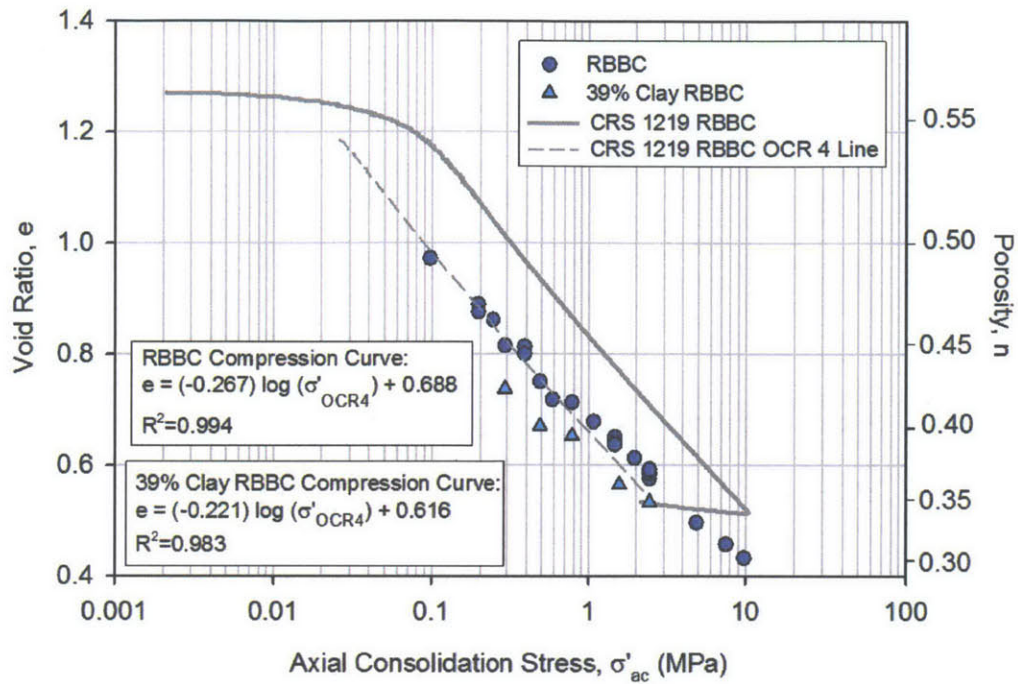


Figure 5-5: Void Ratio vs. log axial consolidation stress compression curve: RBBC & 39% Clay RBBC - effect of clay fraction

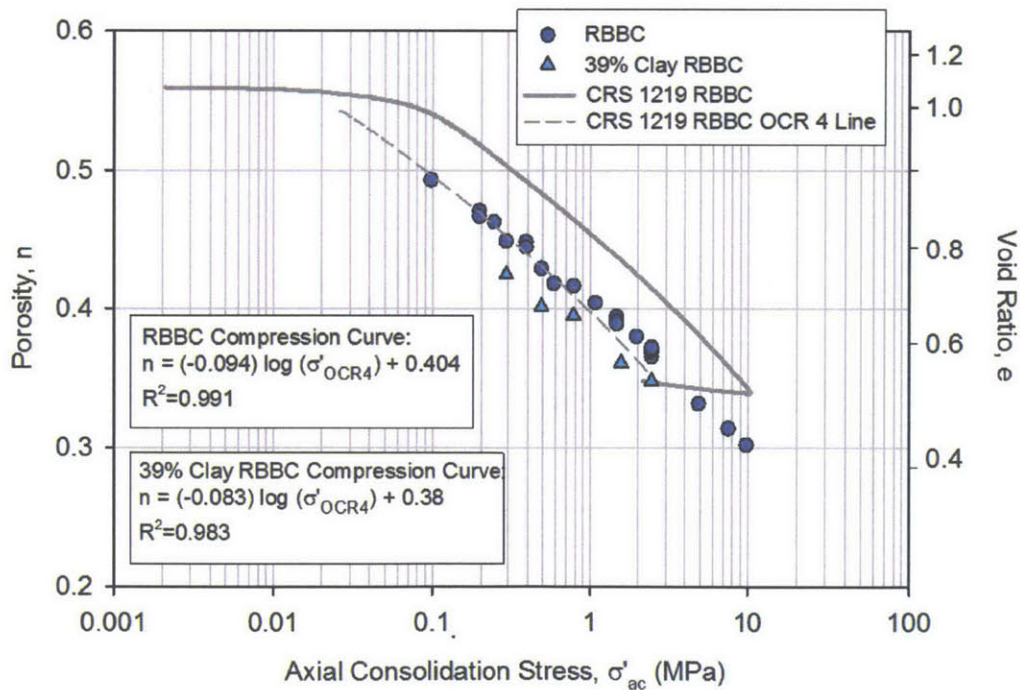


Figure 5-6: Porosity vs. log axial consolidation stress compression curve: RBBC & 39% Clay RBBC - effect of clay fraction

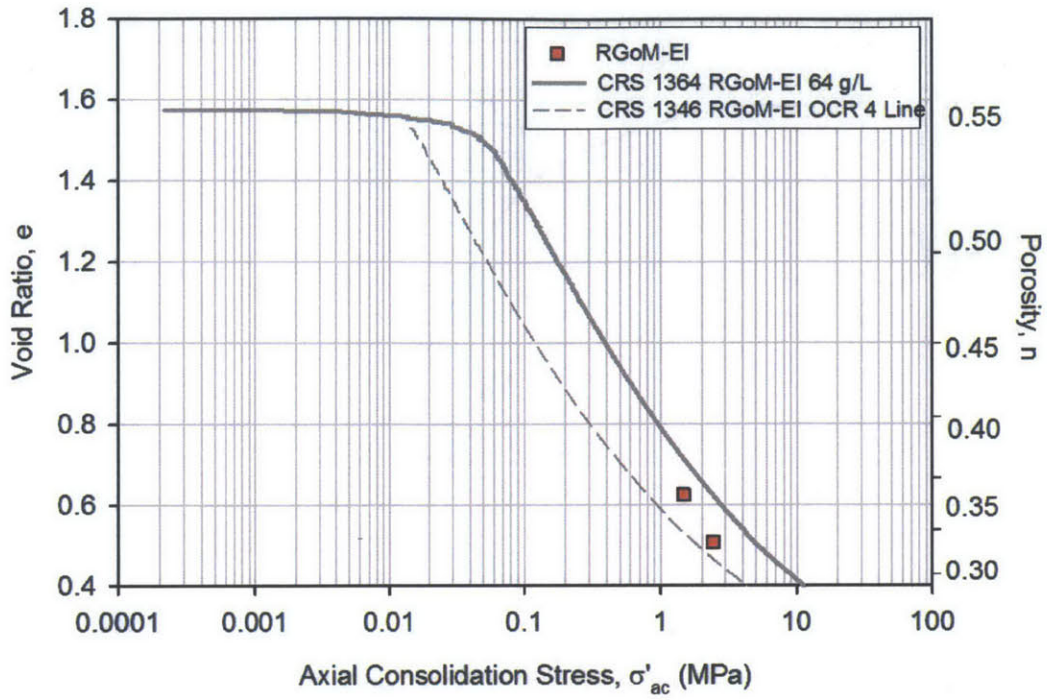


Figure 5-7: Void Ratio vs. log axial consolidation stress compression curve: RGoM-EI

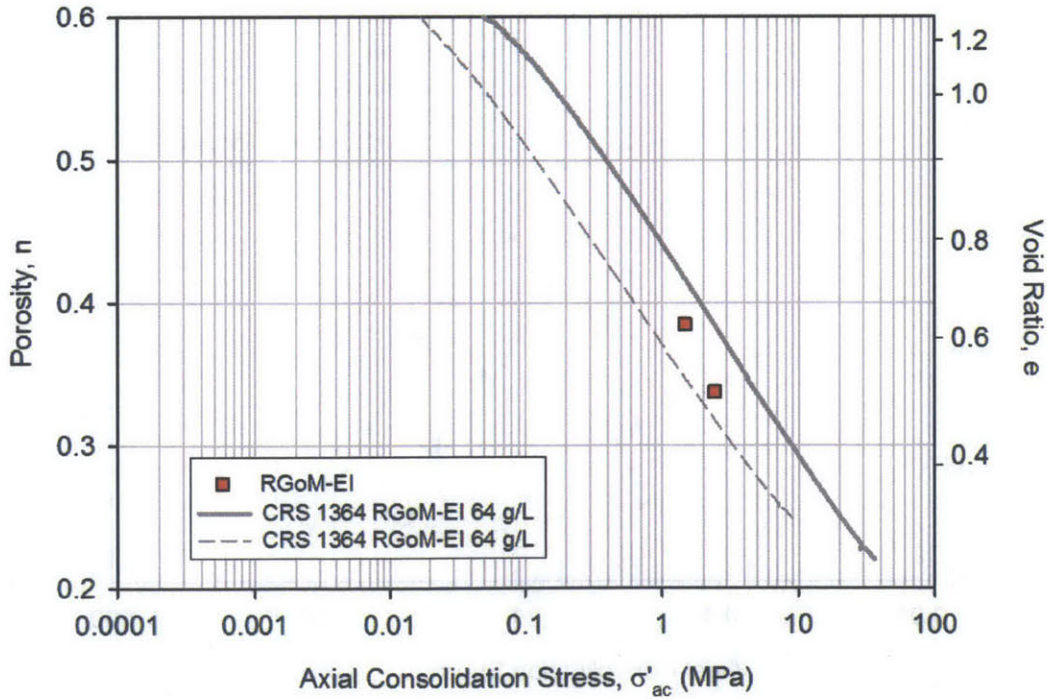


Figure 5-8: Porosity vs. log axial consolidation stress compression curve: RGoM-EI

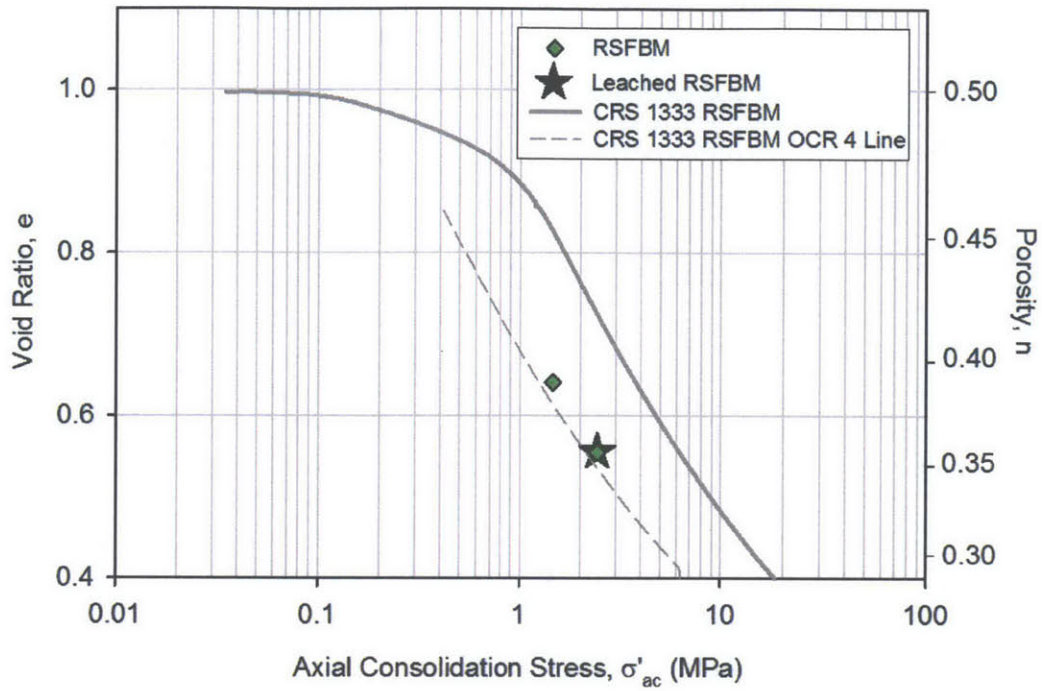


Figure 5-9: Void Ratio vs. log axial consolidation stress compression curve: RSFBM

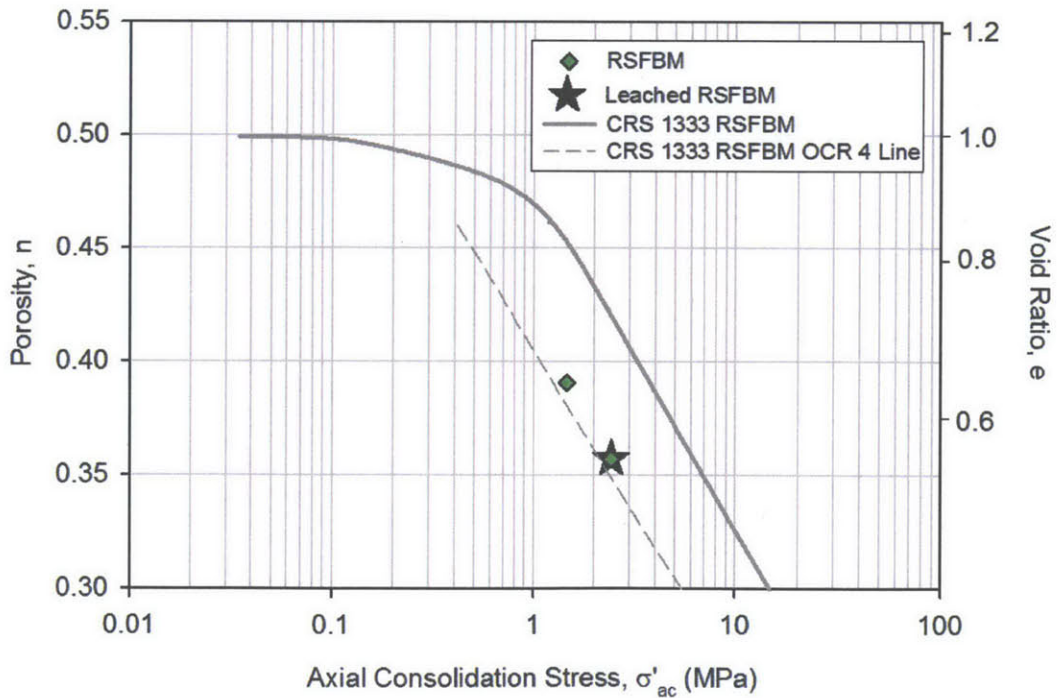


Figure 5-10: Porosity vs. log axial consolidation stress compression curve: RSFBM

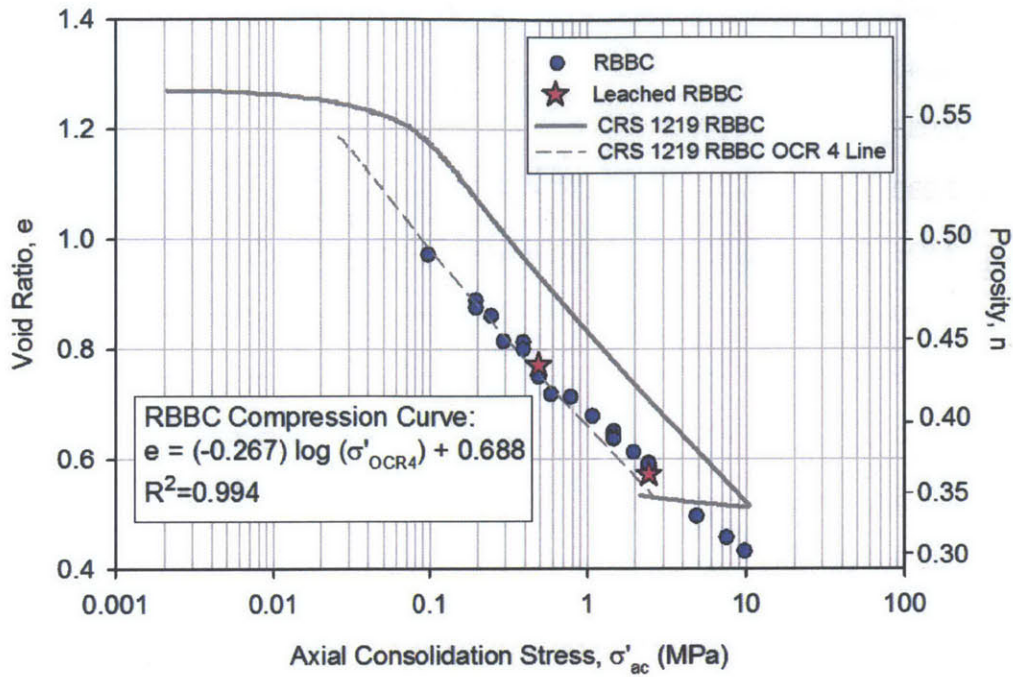


Figure 5-11: Void Ratio vs. log axial consolidation stress compression curve: RBBC - effect of leaching

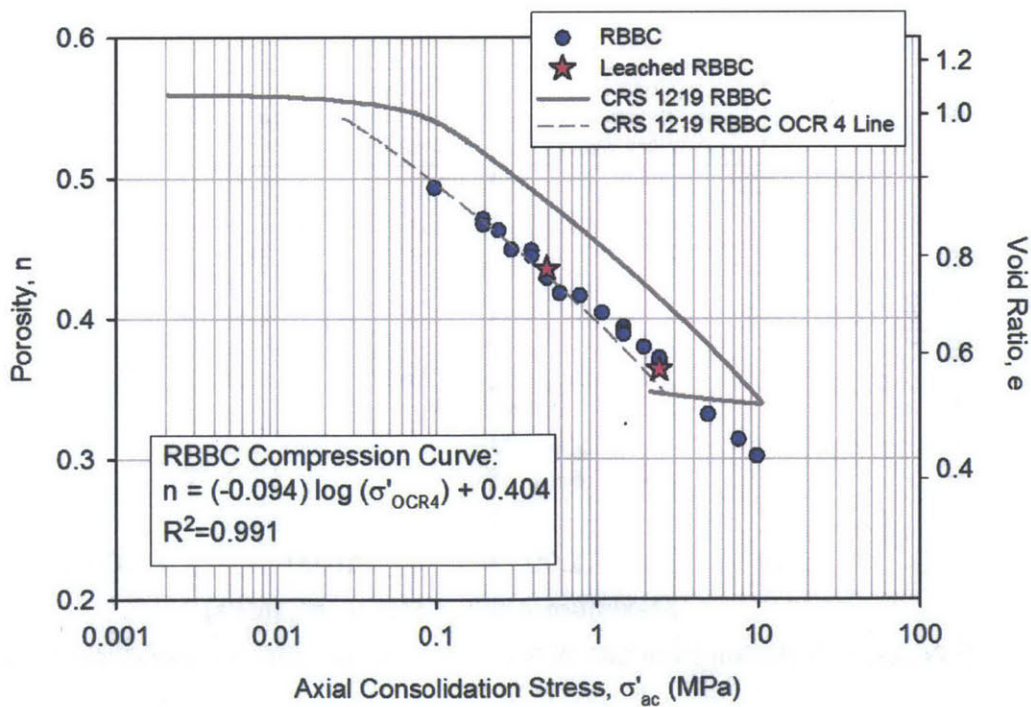


Figure 5-12: Porosity vs. log axial consolidation stress compression curve: RBBC - effect of leaching

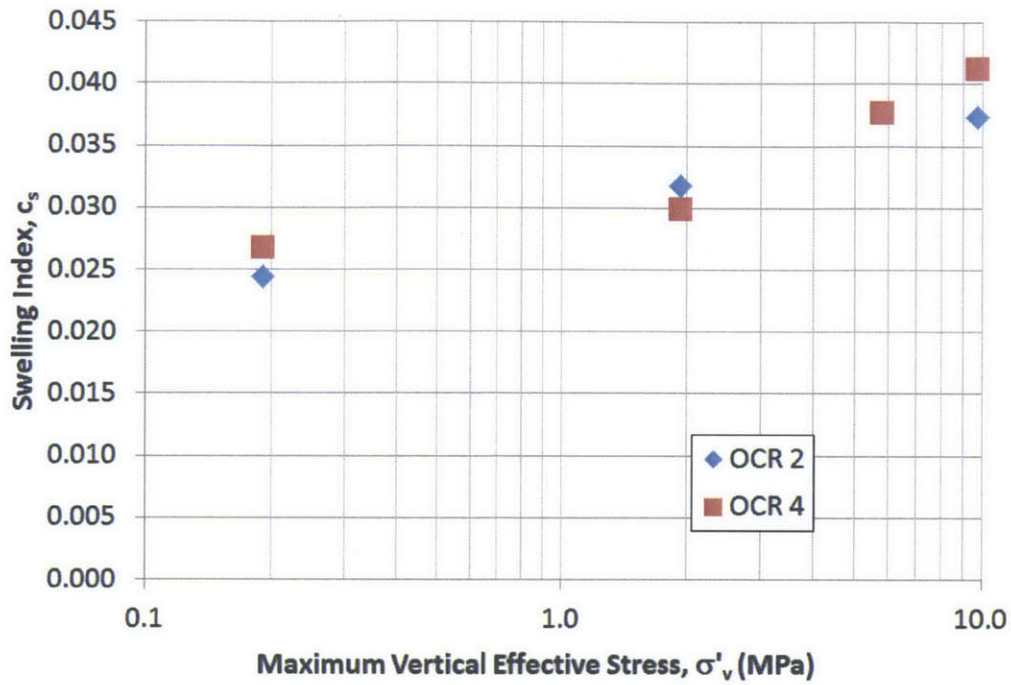


Figure 5-13: Swelling index vs. maximum vertical effective stress as a function of OCR for RBBC K_0 Consolidated in the triaxial cell (data from Abdulhadi, 2009)

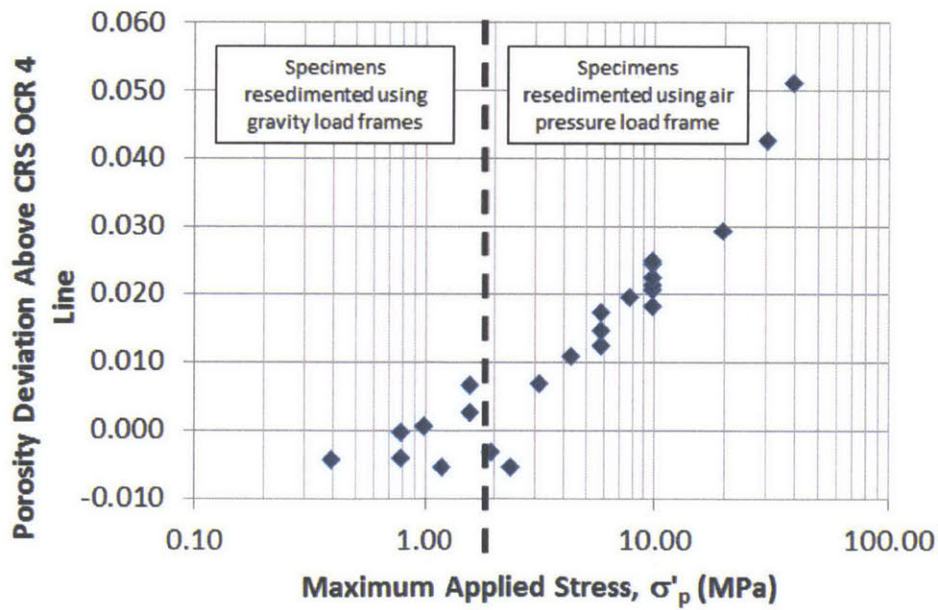


Figure 5-14: Porosity deviation from CRS OCR 4 line vs. maximum effective stress for RBBC

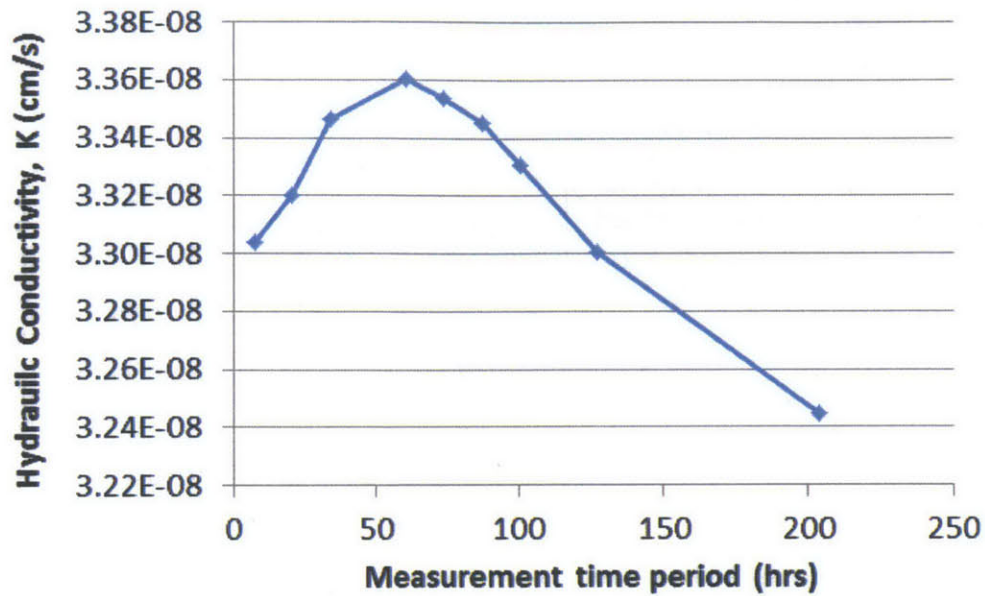


Figure 5-15: Plot of hydraulic conductivity vs. time for a constant hydraulic gradient (HC027, 39% Clay RBBC)

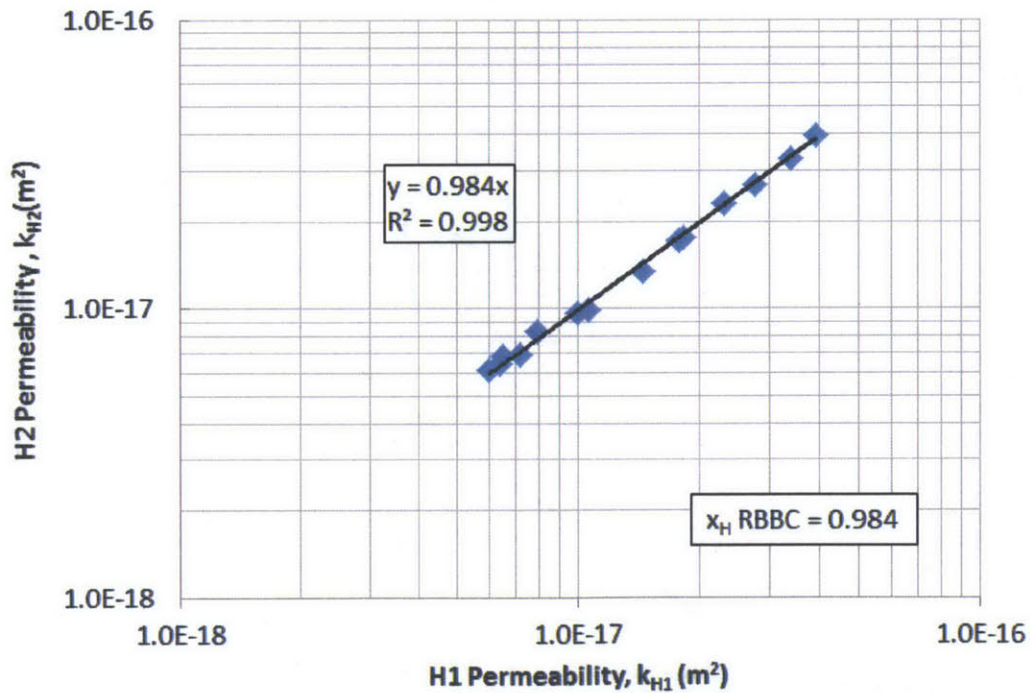


Figure 5-16: Horizontal permeability cross plot to determine measurement sequence bias, x_H , for RBBC

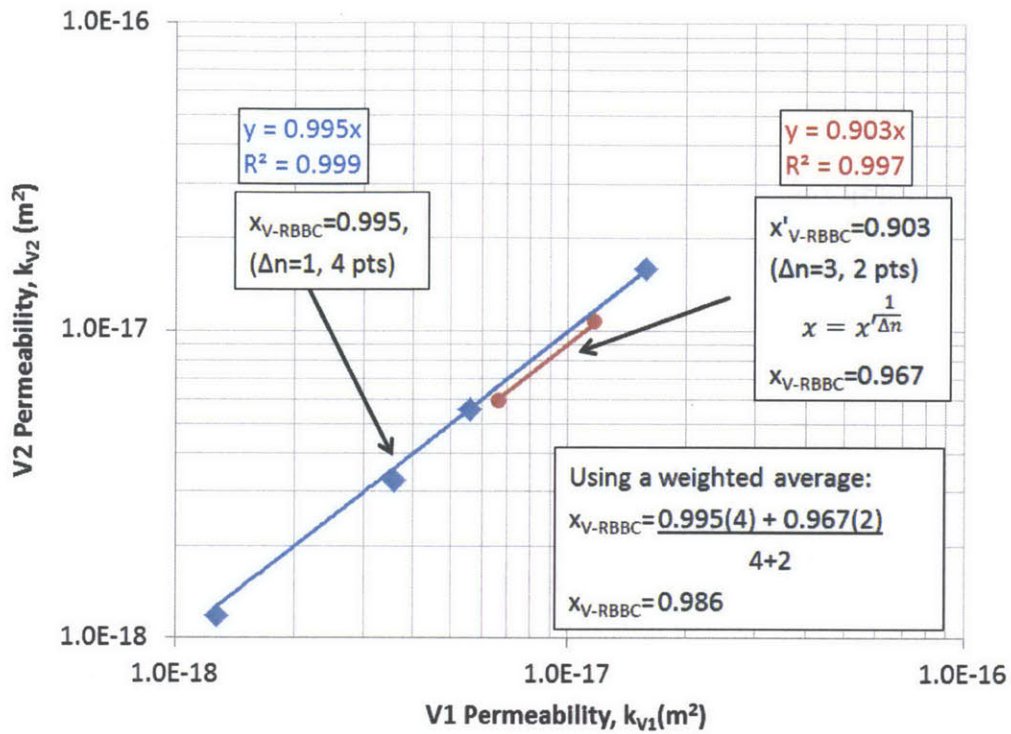


Figure 5-17: Vertical permeability cross plot to determine measurement sequence bias, x_v , for RBBC

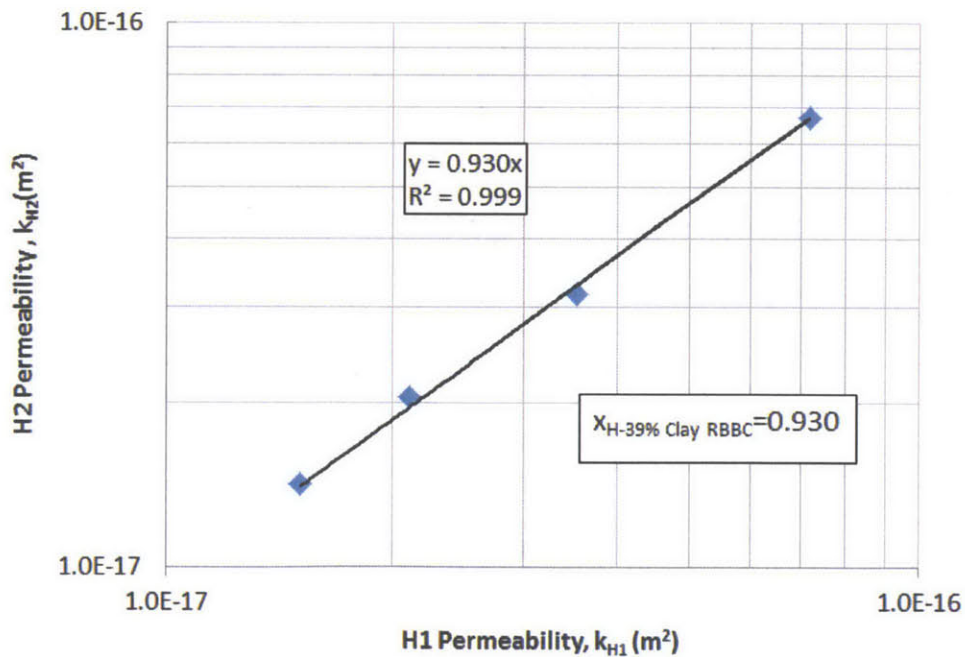


Figure 5-18: Horizontal permeability cross plot to determine measurement sequence bias, x_H , for 39% Clay RBBC

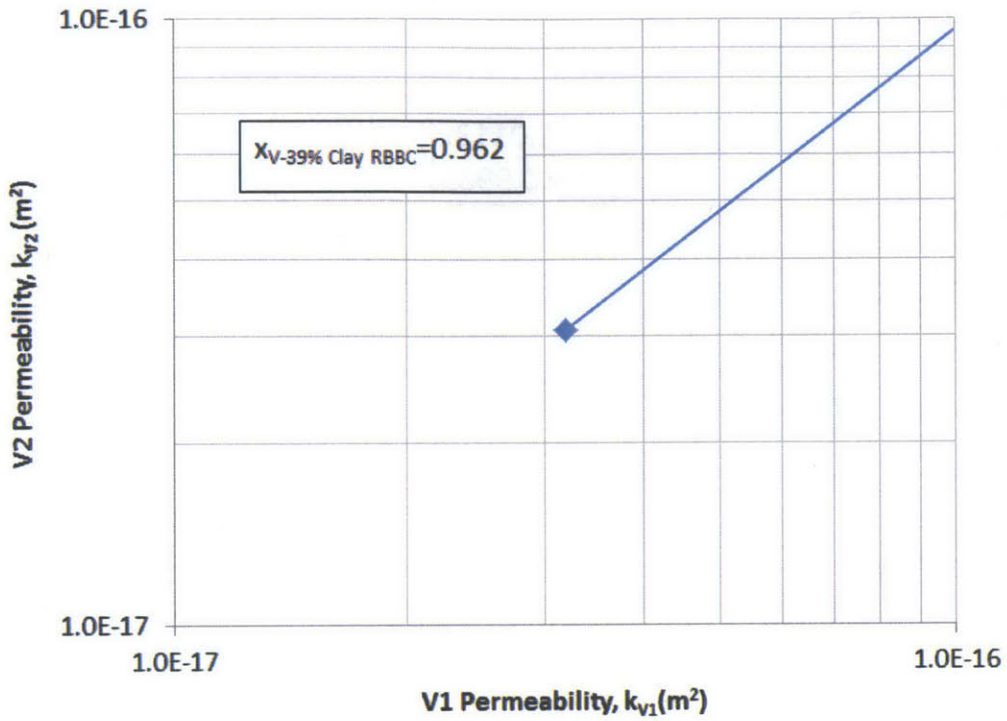


Figure 5-19: Vertical permeability cross plot to determine measurement sequence bias, x_v , for 39% Clay RBBC

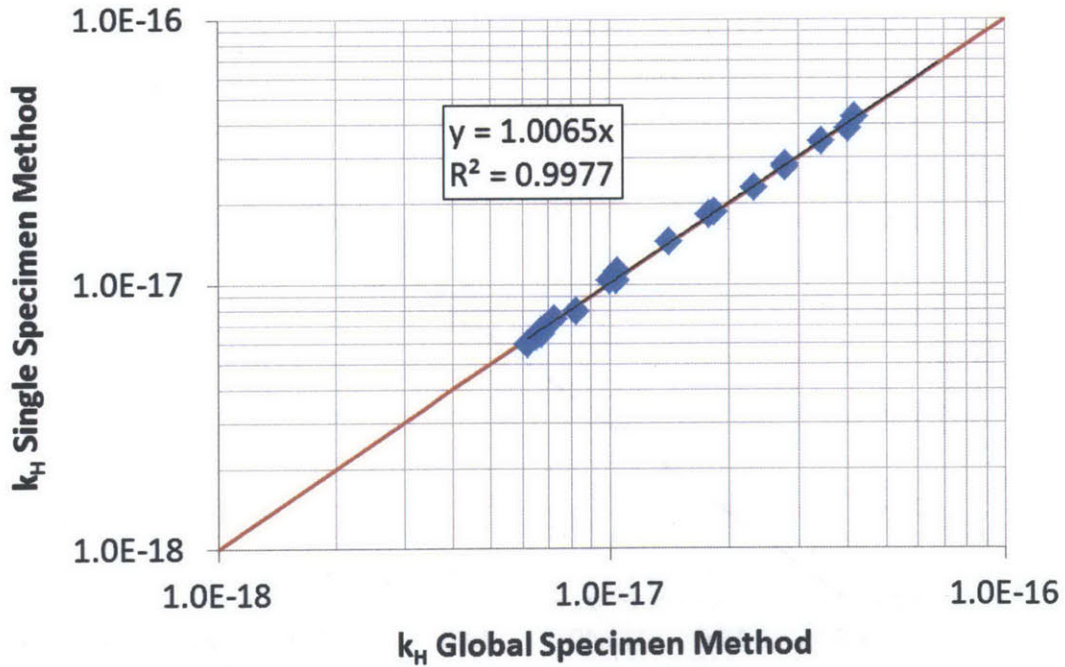


Figure 5-20: Comparison of horizontal permeability adjusted using the global and single specimen methods for RBBC

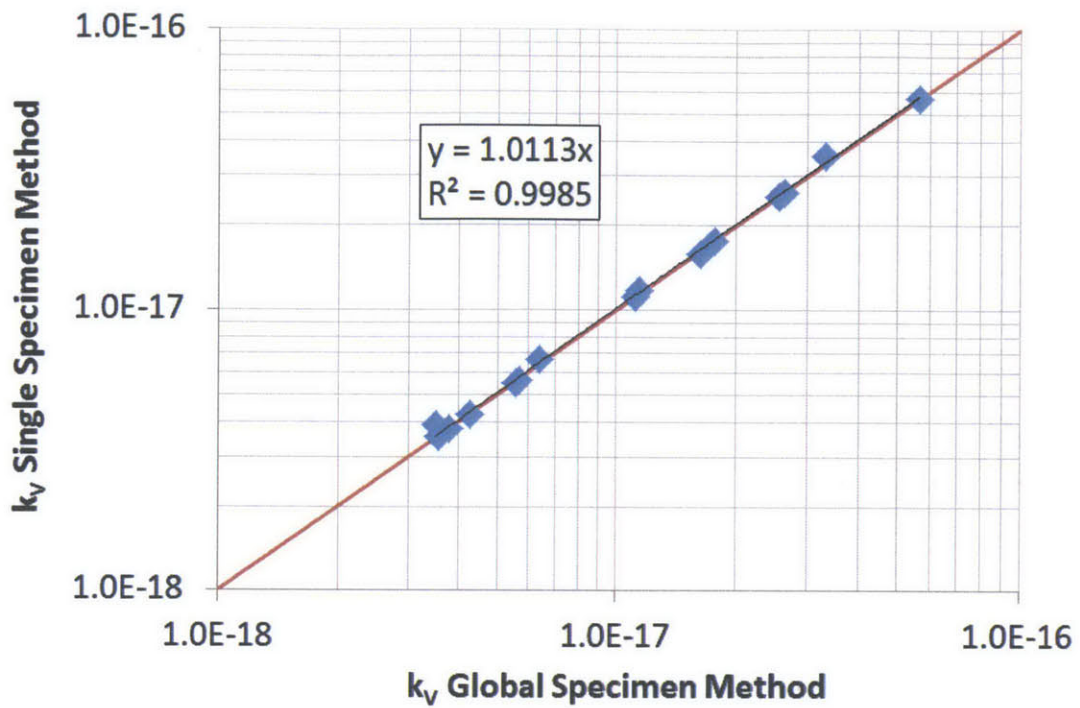


Figure 5-21: Comparison of vertical permeability adjusted using the global and single specimen methods for RBBC

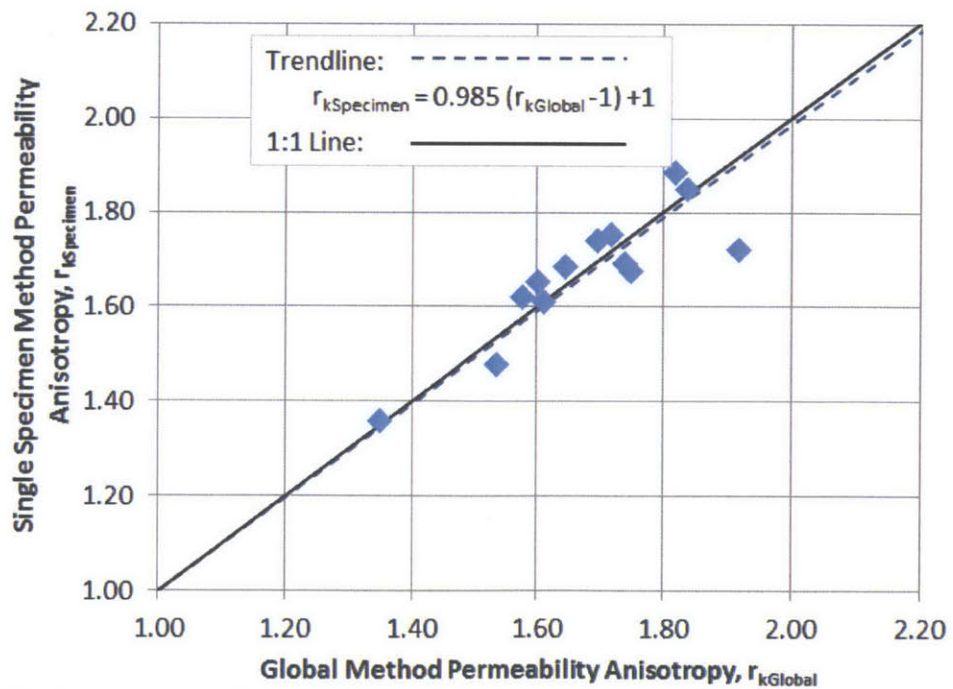


Figure 5-22: Comparison of permeability anisotropy computed using permeability adjusted using the global and single specimen methods for RBBC

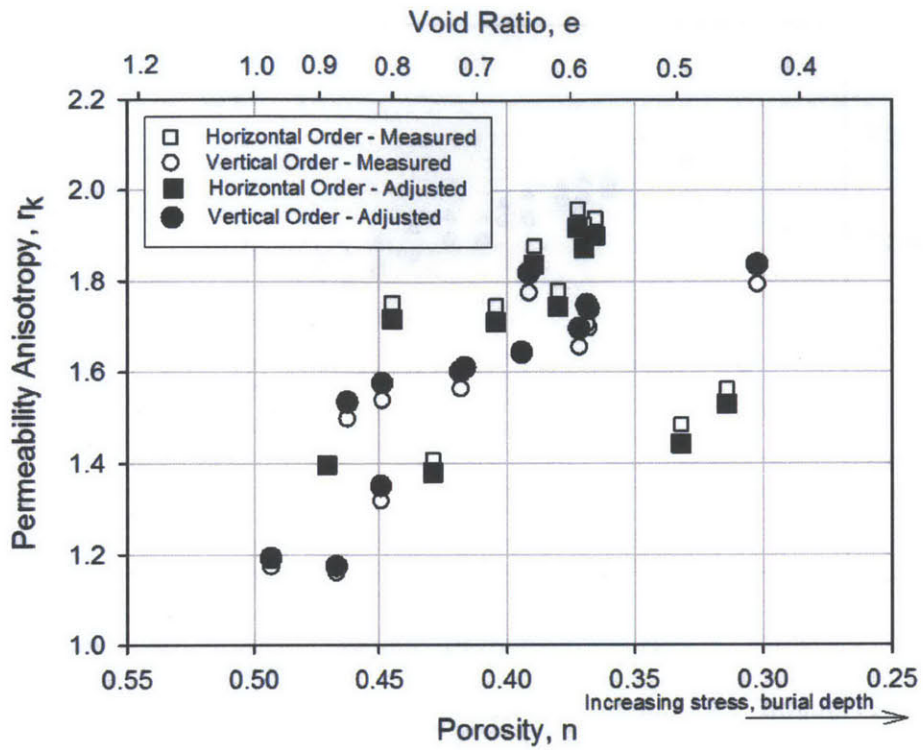


Figure 5-23: Effect of measurement sequence bias adjustment on the permeability anisotropy of RBBC

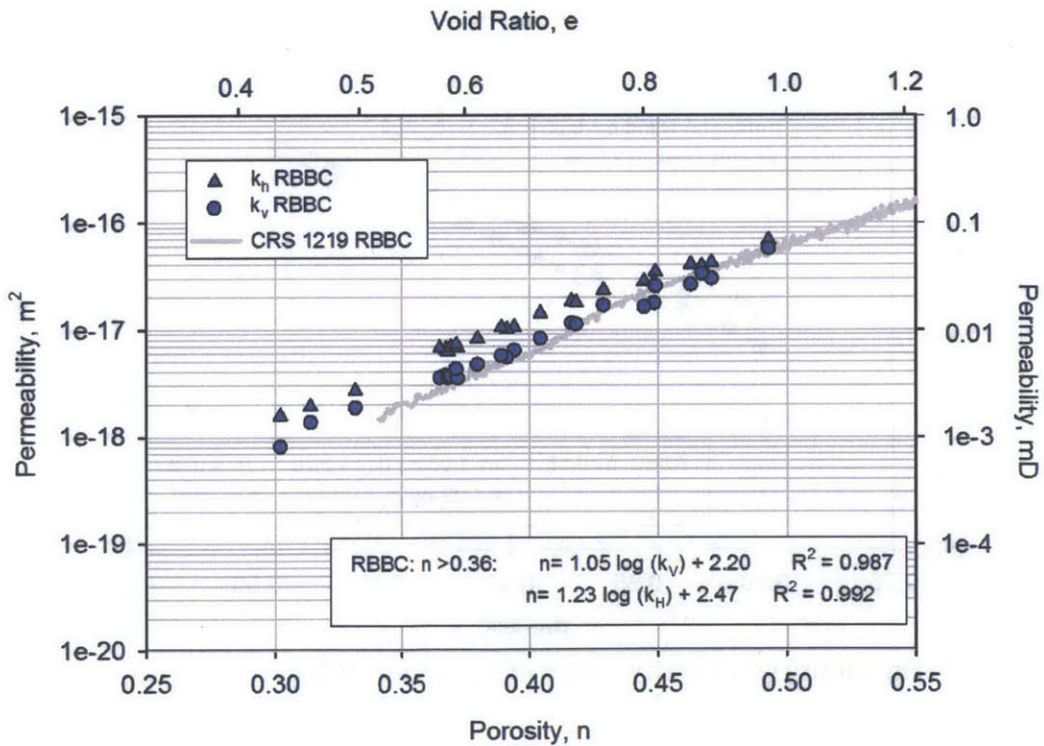


Figure 5-24: Permeability vs. porosity for RBBC

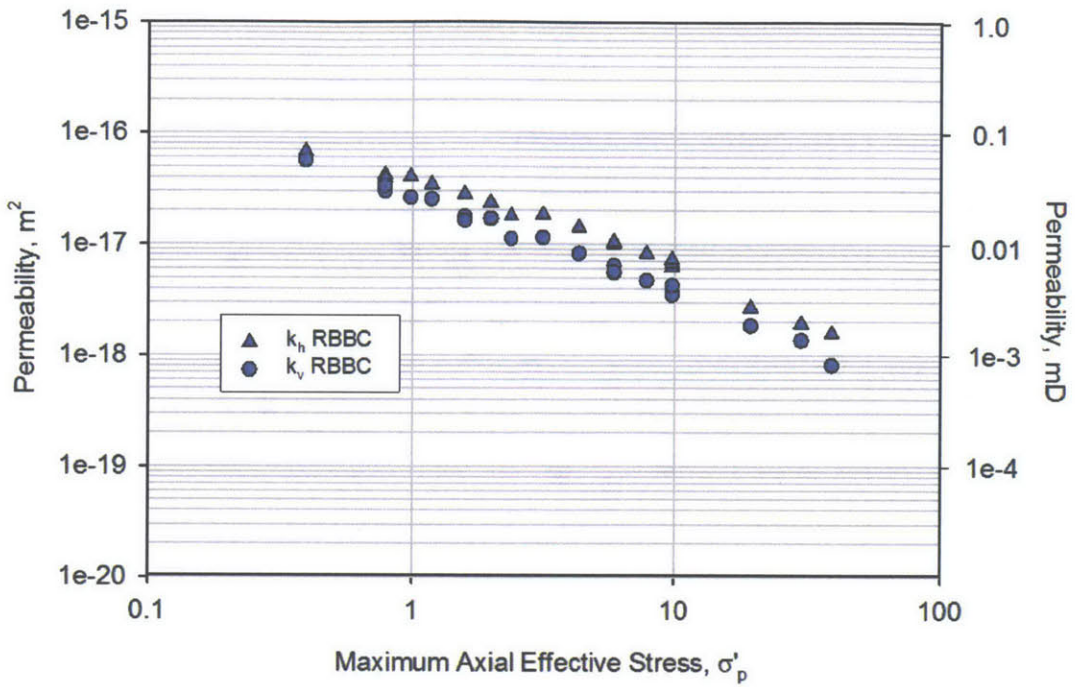


Figure 5-25: Permeability vs. maximum axial effective stress for RBBC

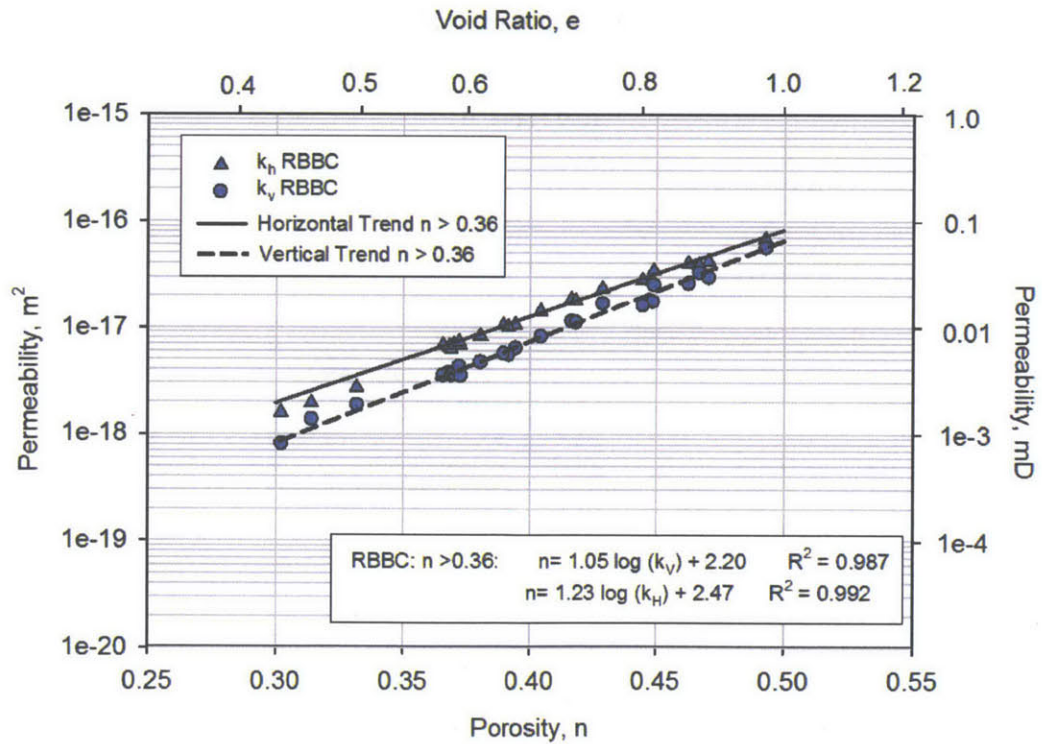


Figure 5-26: Permeability vs. porosity with trend lines for RBBC

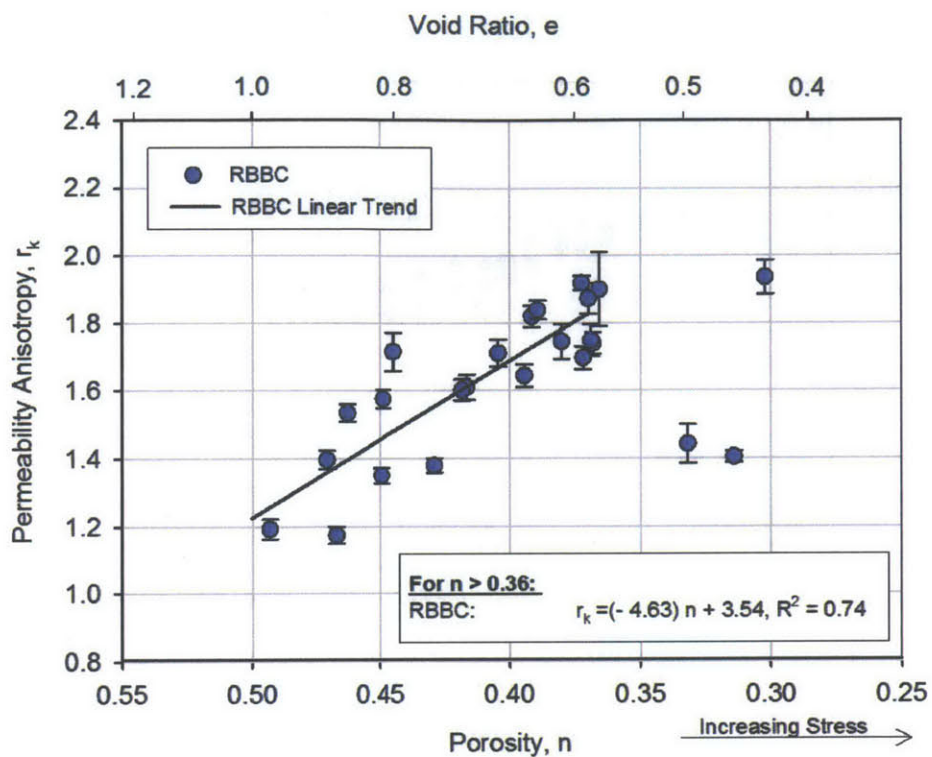


Figure 5-27: Permeability anisotropy vs. porosity for RBBC

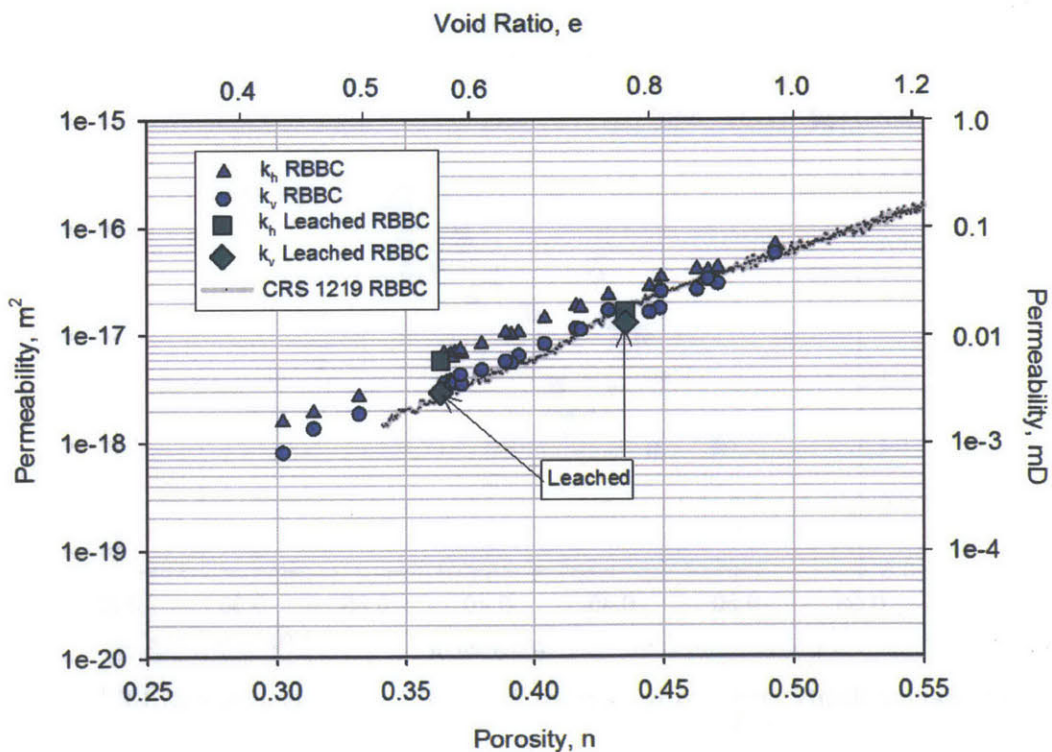


Figure 5-28: Permeability vs. porosity for RBBC and Leached RBBC

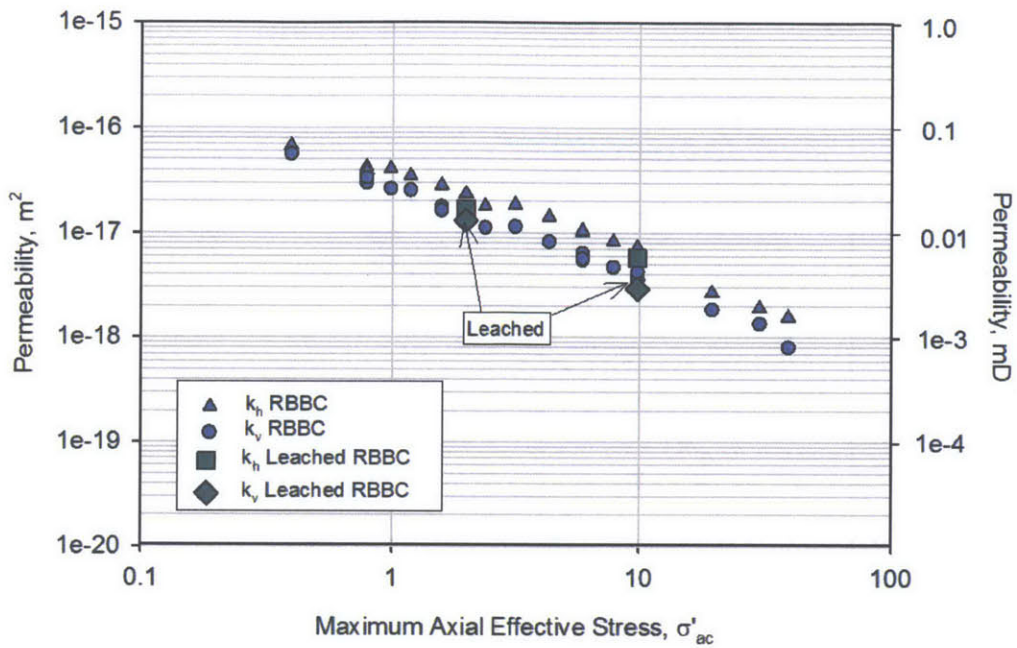


Figure 5-29: Permeability vs. maximum axial effective stress for RBBC and Leached RBBC

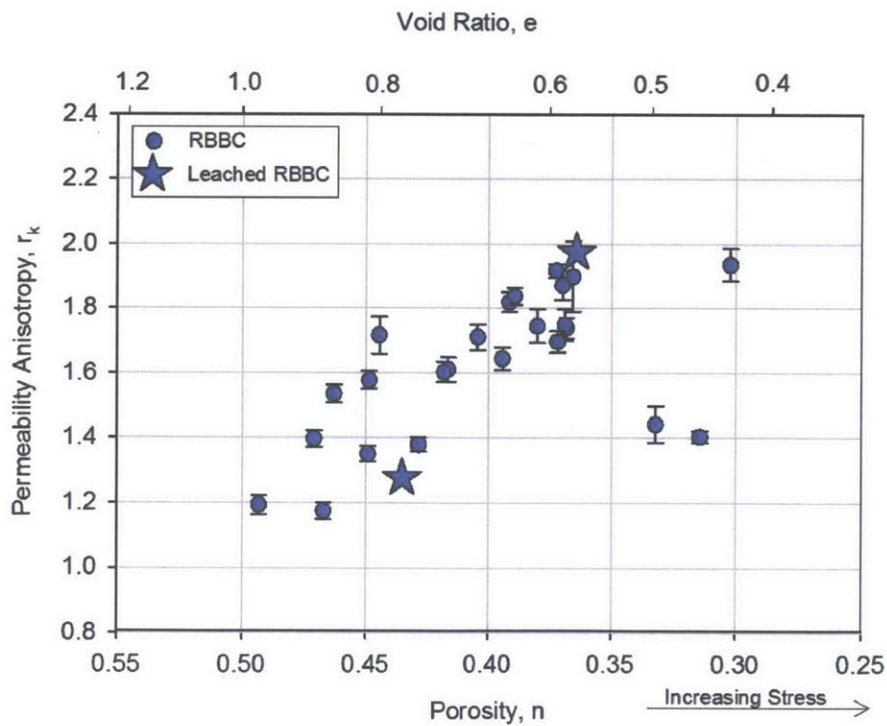


Figure 5-30: Permeability anisotropy vs. porosity for RBBC and Leached RBBC

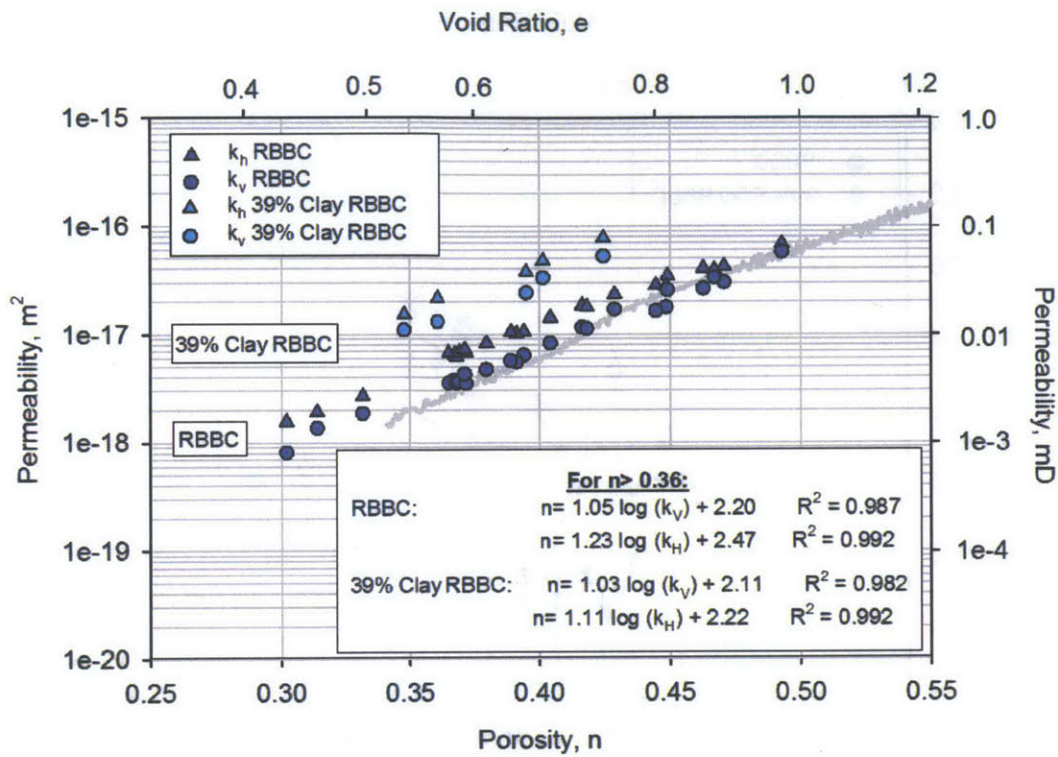


Figure 5-31: Permeability vs. porosity for RBBC and 39% Clay RBBC

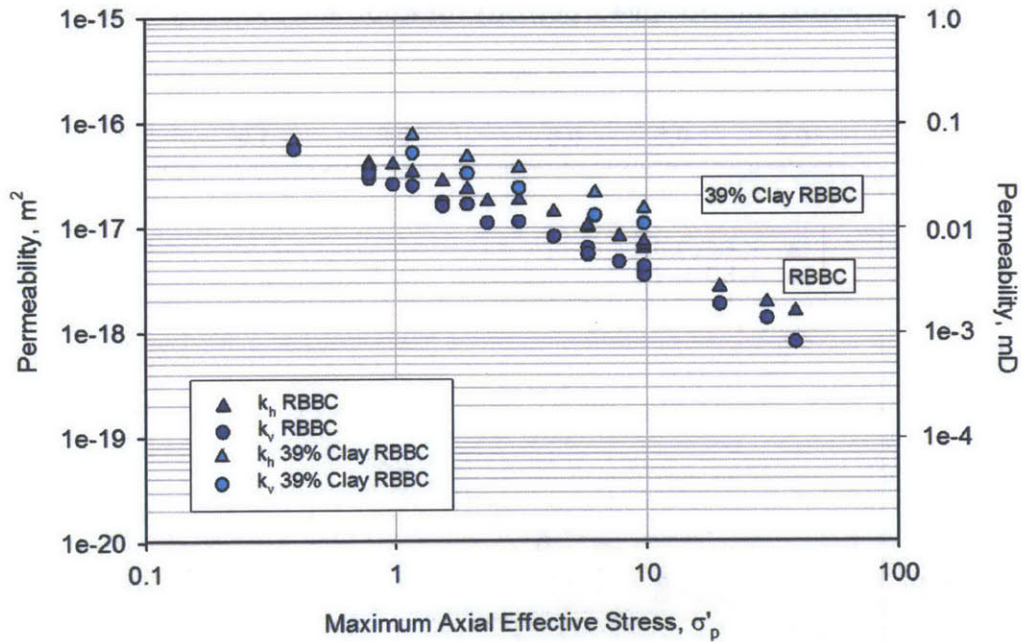


Figure 5-32: Permeability vs. maximum axial effective stress for RBBC and 39% Clay RBBC

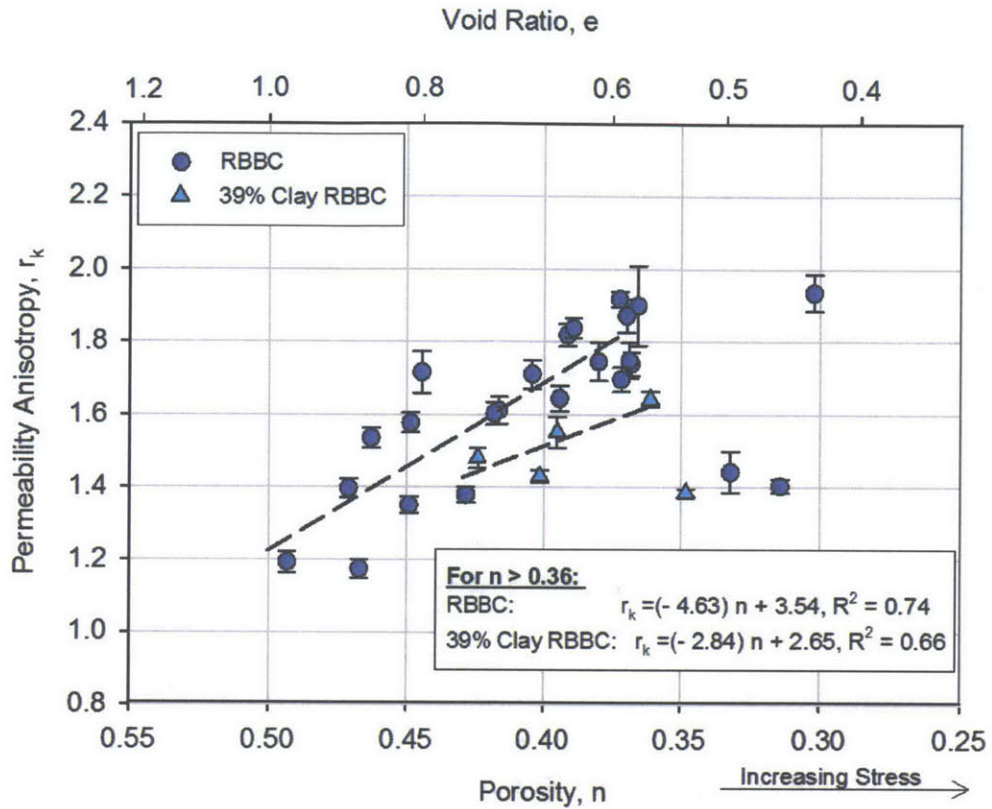


Figure 5-33: Permeability anisotropy vs. porosity for RBBC and 39% Clay RBBC

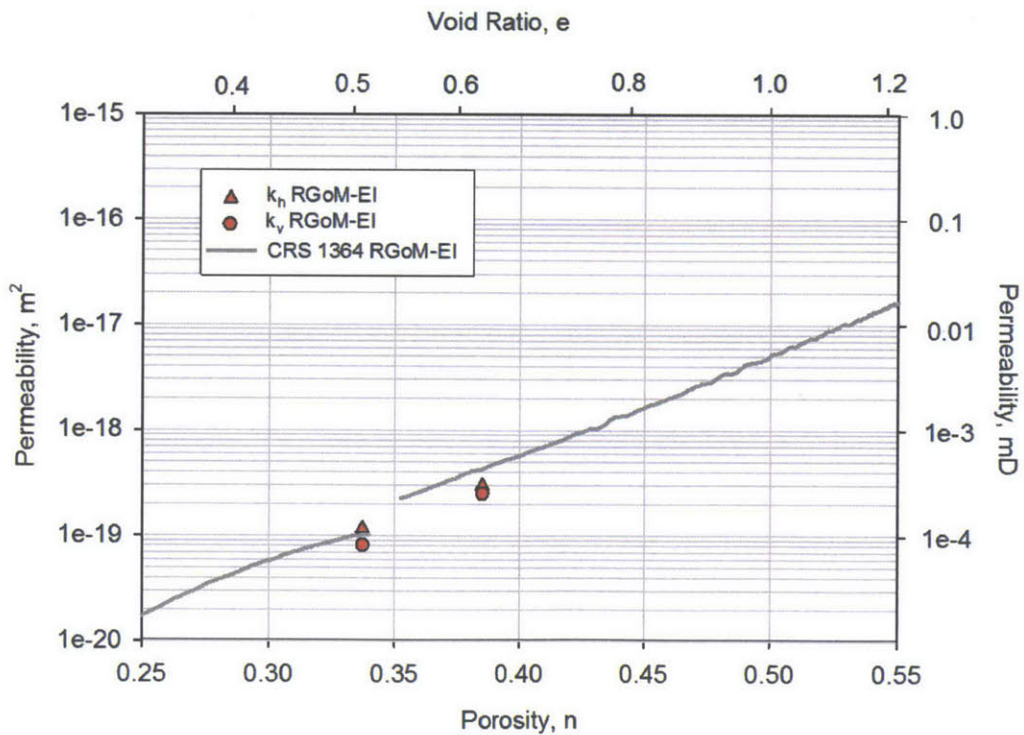


Figure 5-34: Permeability vs. porosity for RGoM-EI

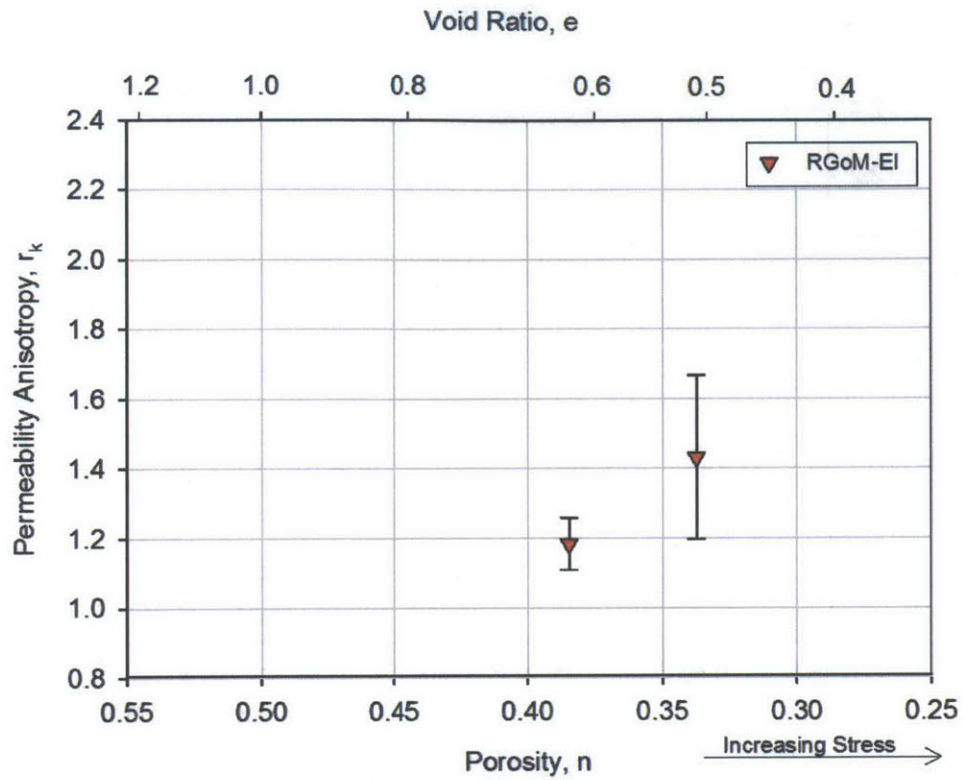


Figure 5-35: Permeability anisotropy vs. porosity for RGoM-EI

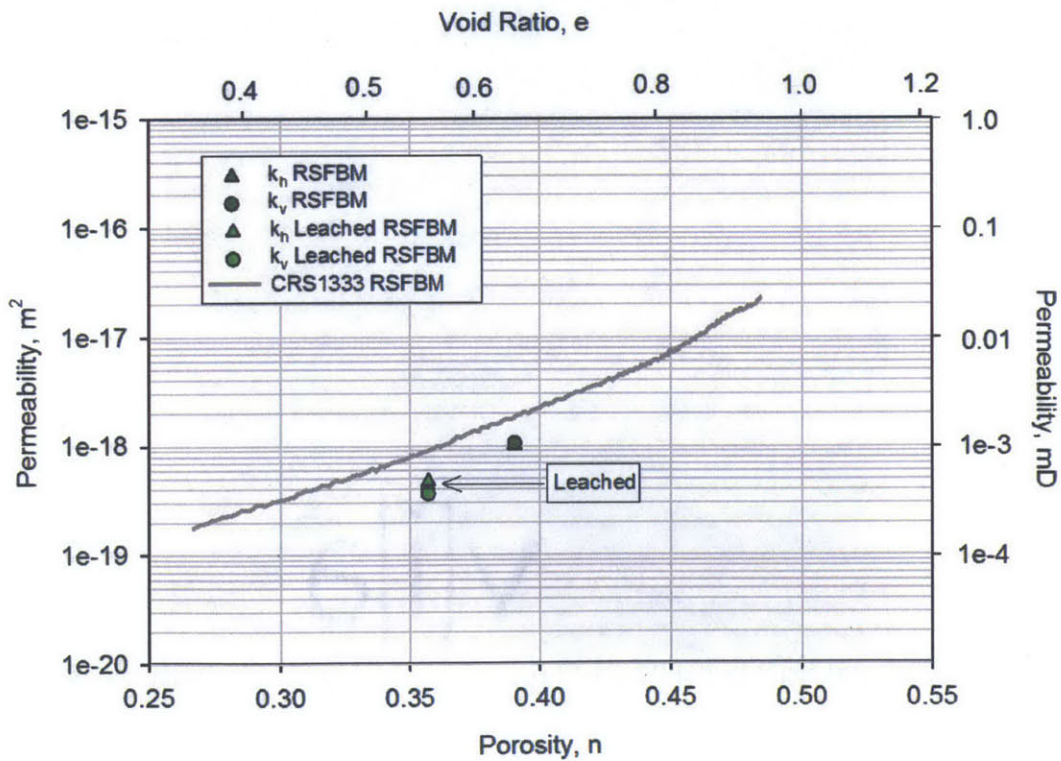


Figure 5-36: Permeability vs. porosity for RSFBM

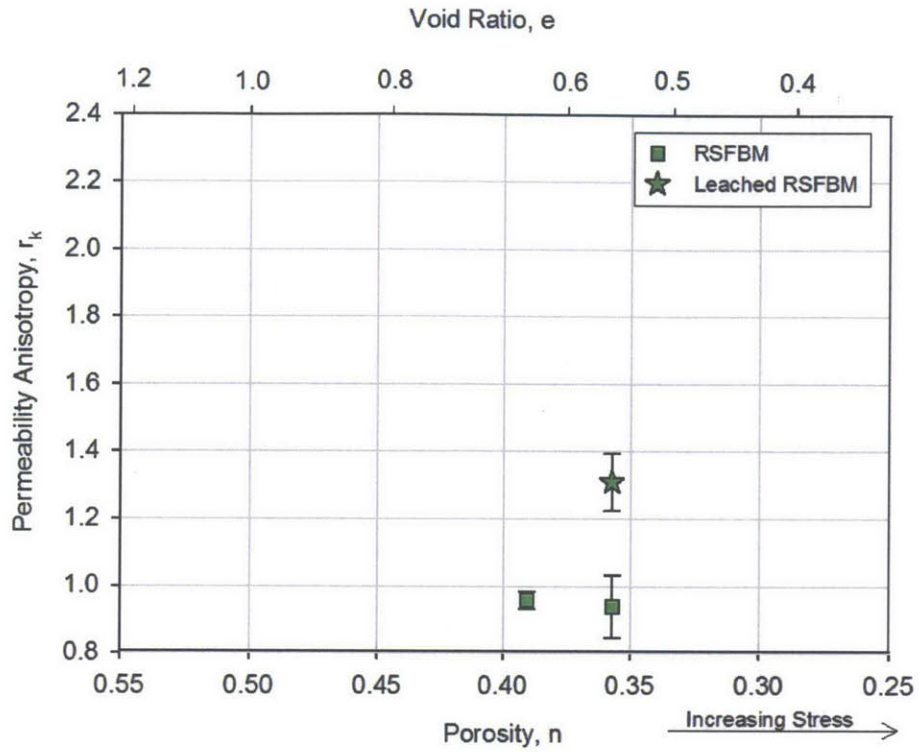


Figure 5-37: Permeability anisotropy vs. porosity for RSFBM

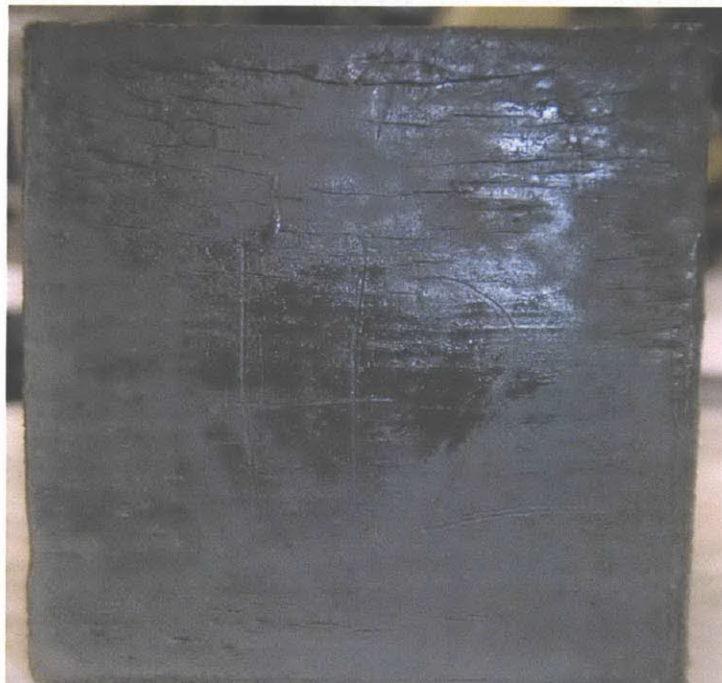


Figure 5-38: Horizontal cracking of RGoM-EI specimens during permeability measurement

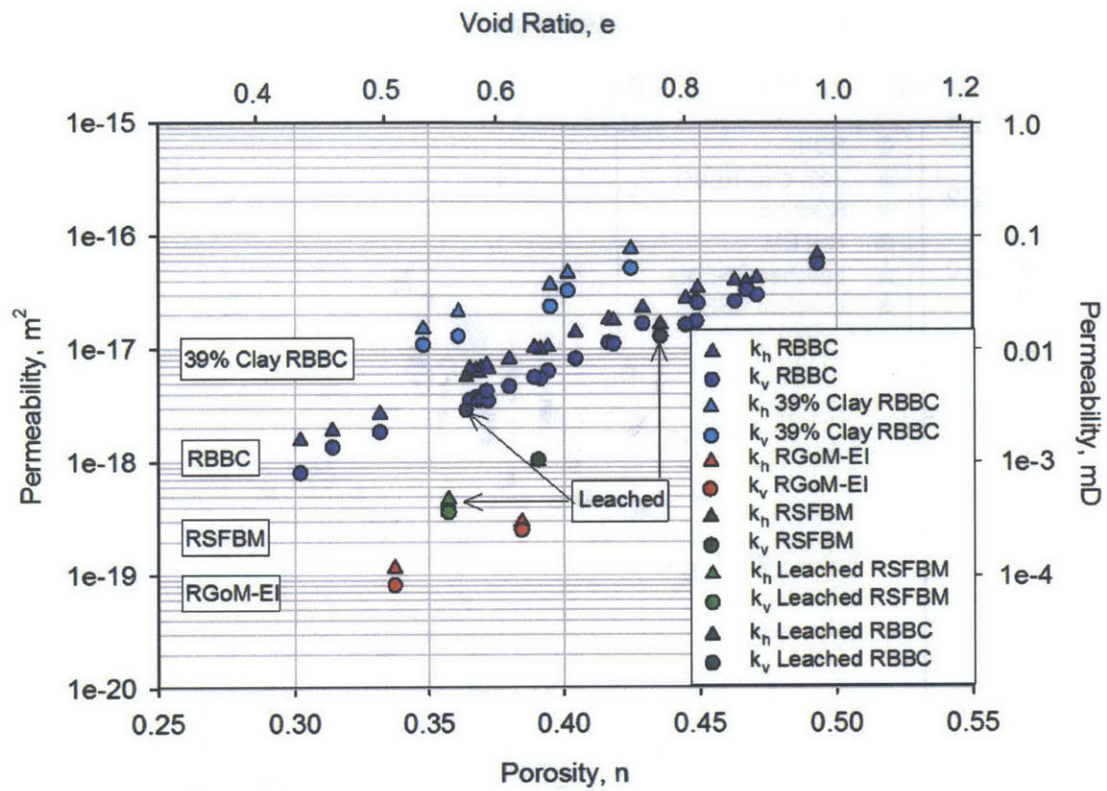


Figure 5-39: Permeability vs. porosity: Comparison between RBBC, RGoM-EI and RSFBM

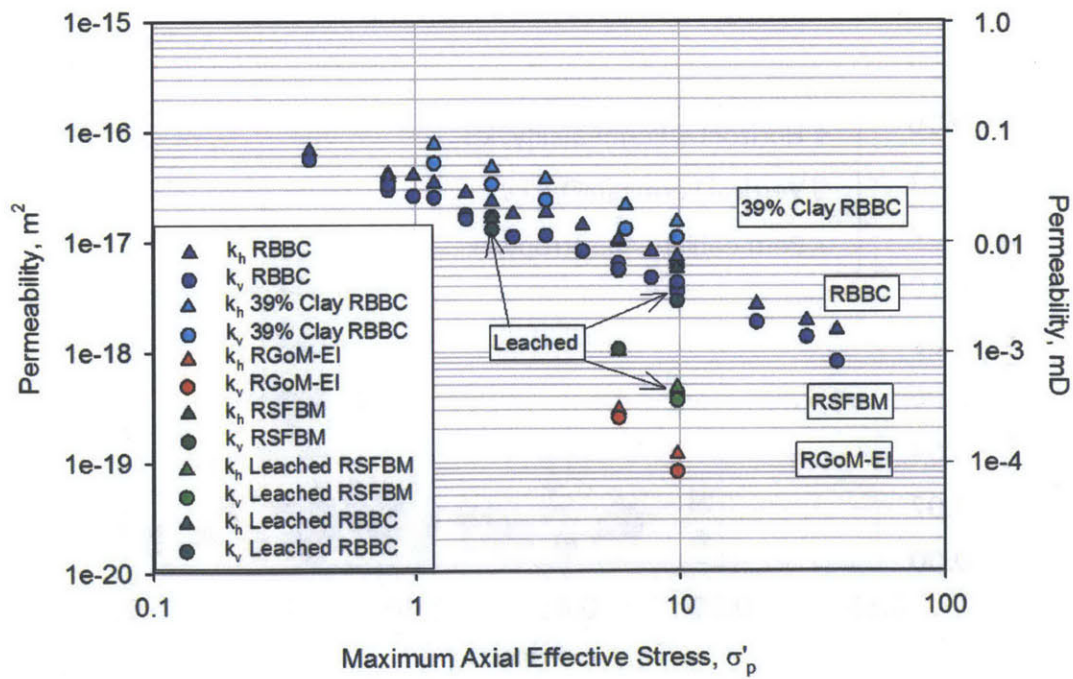


Figure 5-40: Permeability vs. maximum axial effective stress: Comparison between RBBC, RGoM-EI and RSFBM

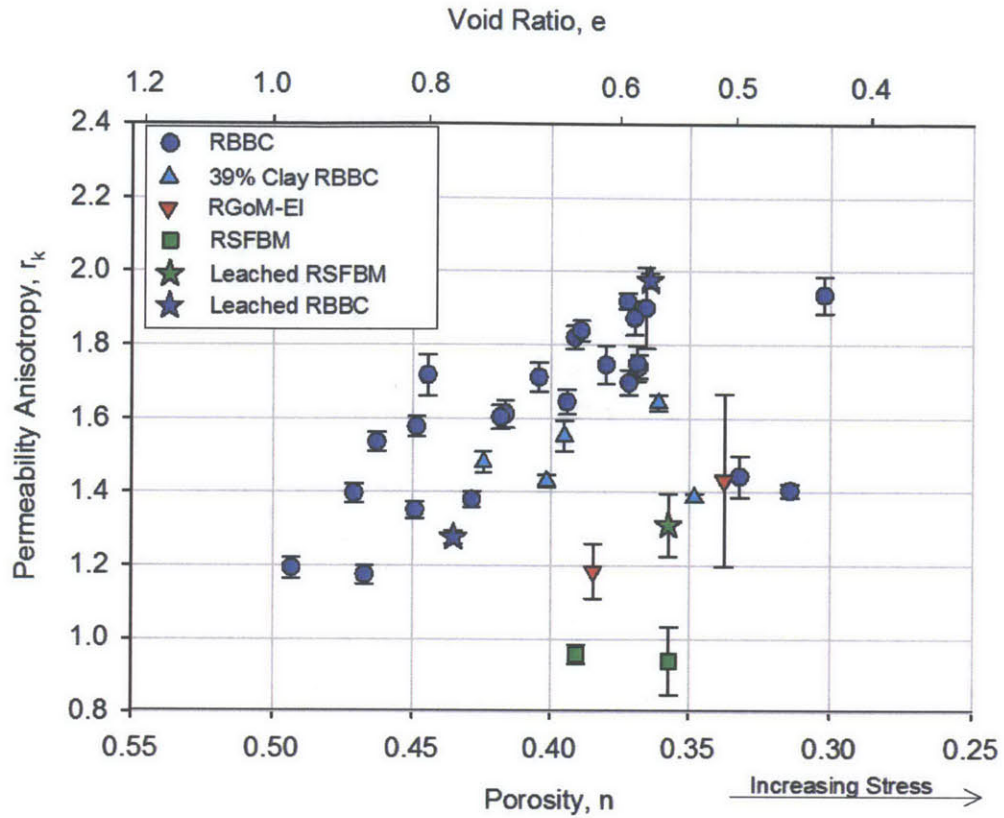


Figure 5-41: Permeability anisotropy vs. porosity: Comparison between RBBC, RGoM-EI and RSFBM

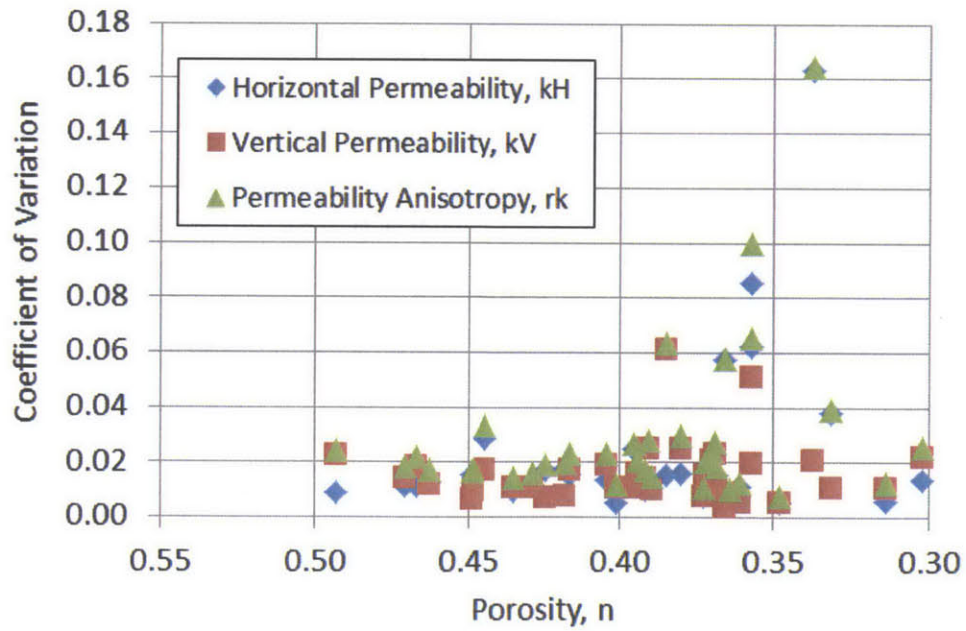


Figure 5-42: Coefficient of Variation as a function of porosity for all mudrocks measured

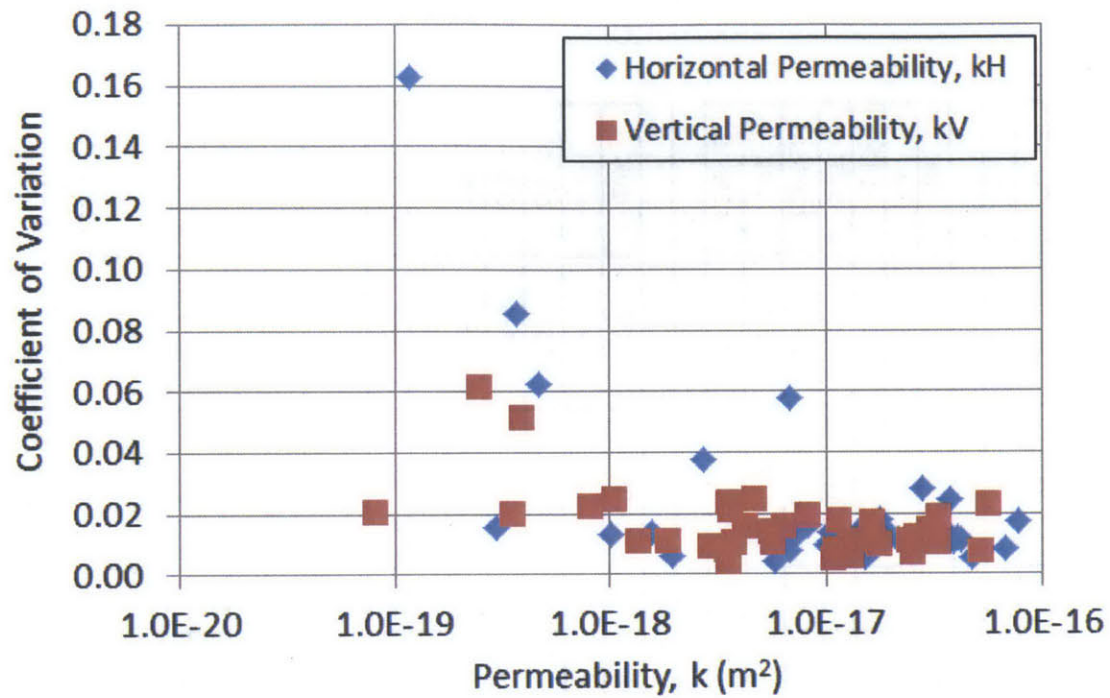


Figure 5-43: Coefficient of variation as a function of permeability for all mudrocks measured

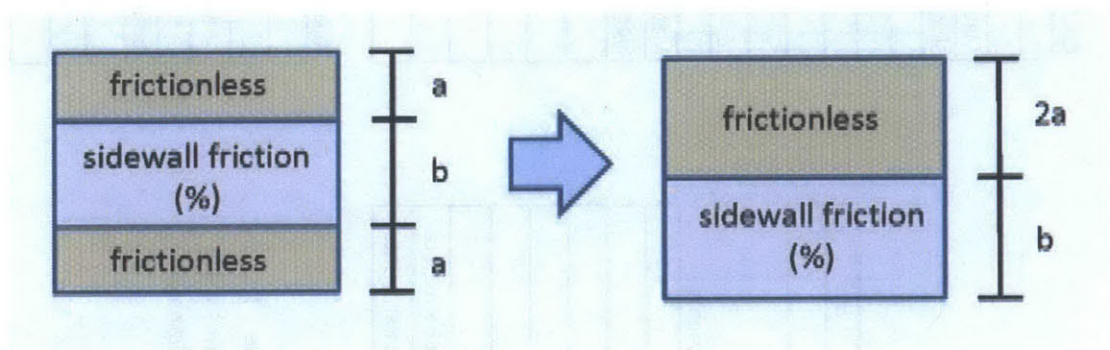


Figure 5-44: Layering due to sidewall friction

2_Layer Sidewall Friction Model

Legend:

Fill in data
Calculations
Results

CONSTANTS:

Box Size:	5	cm
Initial # Layers	2	

Material Properties

	Material #1	Comments
Name	RBBC	
e_o (@ 0.1 Mpa)	1.174	CRS
c_c	0.325	CRS
c_r	0.028	CRS
k_{vo} (@ e_o)	1.42E-16	CRS
$c_{(m), V}$ direction	9.47	CRS
r_k @ e_o	1.04	Cubic Perm Data
dr_{fd}/dn	-4.63	Cubic Perm Data

Notes:

- 1) c_{rn} = slope of $\log k_v$ vs. n plot
- 2) c_c = slope of VCL in e vs. \log stress space
- 3) c_r = slope of swelling line in e vs. \log stress space
- 4) model assumes uniform initial layer thickness

CALCULATIONS:

Stress	Mpa	10	10	10
--------	-----	----	----	----

Material #1

Sidewall Friction:		0%	0%	0%
OCR		4	4	4
$e1$		0.540	0.540	0.540
$n1$		0.351	0.351	0.351
$kv1$	m^2	2.29E-18	2.29E-18	2.29E-18
r_k		1.92	1.92	1.92
$kh1$	m^2	4.39E-18	4.39E-18	4.39E-18

Material #2

Sidewall Friction:		0%	10%	20%
OCR		4	4	4
$e2$		0.540	0.552	0.566
$n2$		0.351	0.356	0.361
$kv2$	m^2	2.29E-18	2.55E-18	2.90E-18
r_k		1.92	1.89	1.87
$kh2$	m^2	4.39E-18	4.83E-18	5.40E-18

Layered Permeability Calculation

Stress	Mpa	10	10	10
# Layers		2.0	2.0	2.0
Material #1 H	cm	2.5	2.5	2.5
Material #2 H	cm	2.5	2.5	2.5
Assuming Anisotropic Layer Permeability				
k Parallel	m^2	4.39E-18	4.61E-18	4.90E-18
k Perpendicular	m^2	2.29E-18	2.41E-18	2.56E-18
r_k		1.92	1.91	1.91

Figure 5-45: Model: Permeability anisotropy of compressing anisotropic mudrock layers: sidewall friction analysis

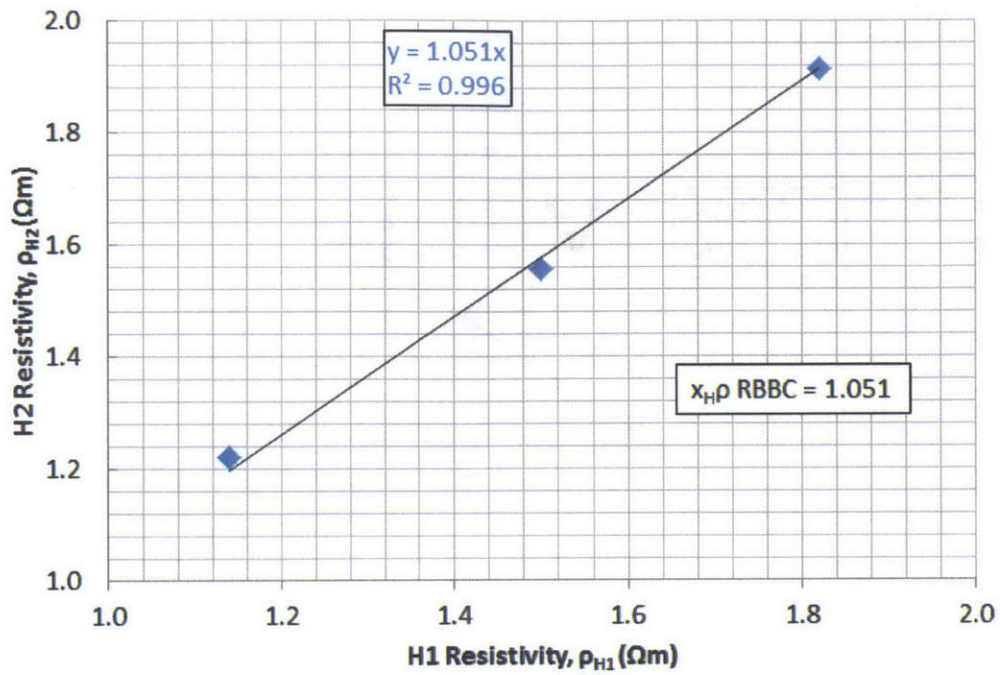


Figure 5-46: Horizontal resistivity cross plot to determine measurement sequence bias, $x_{H\rho}$, for RBBC ($\Delta n = 1$ for all points)

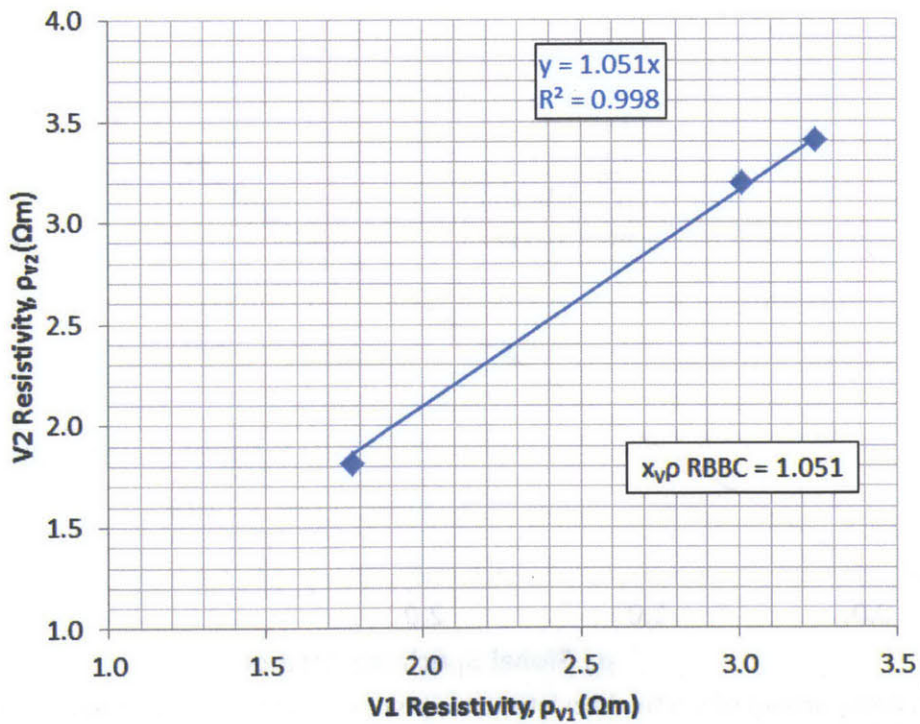


Figure 5-47: Vertical resistivity cross plot to determine measurement sequence bias, $x_{V\rho}$, for RBBC

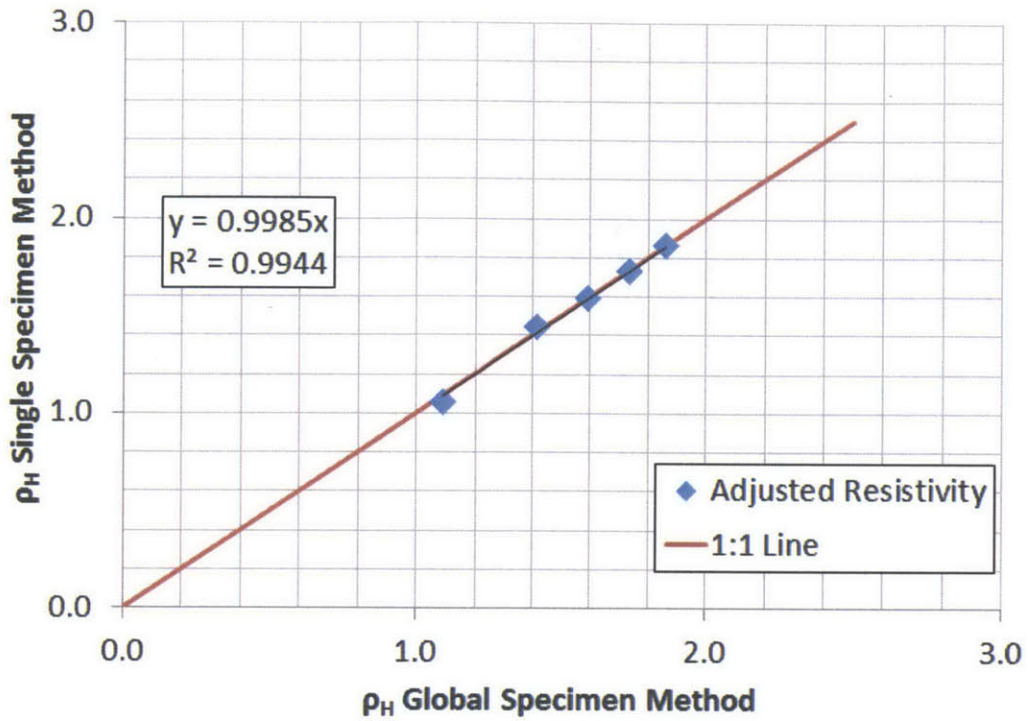


Figure 5-48: Comparison of horizontal resistivity adjusted using the global and single specimen methods for RBBC

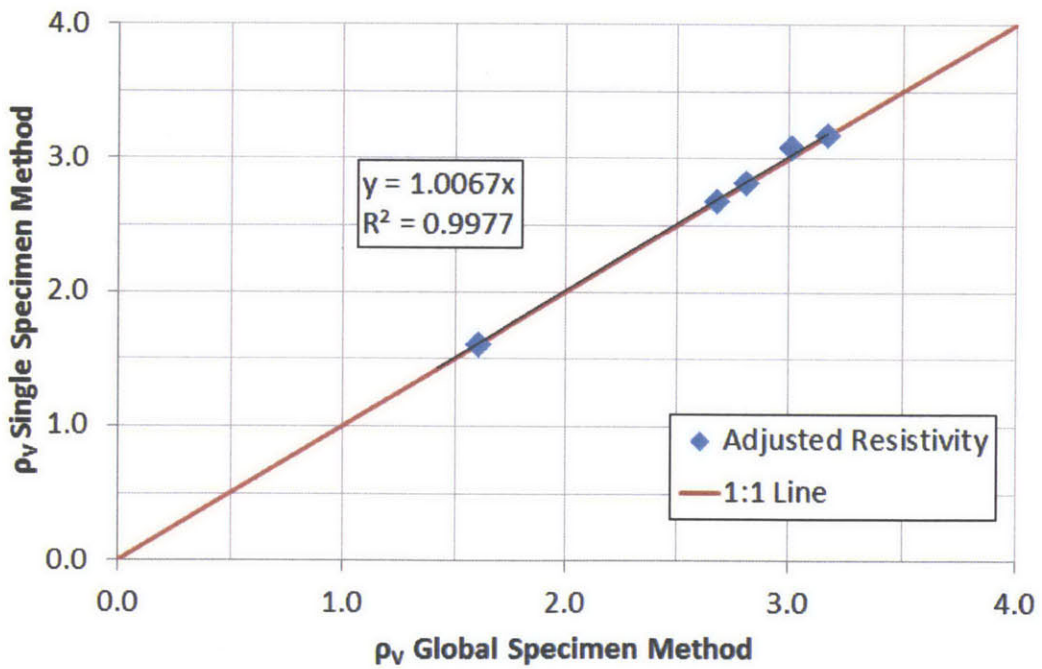


Figure 5-49: Comparison of vertical resistivity adjusted using the global and single specimen methods for RBBC

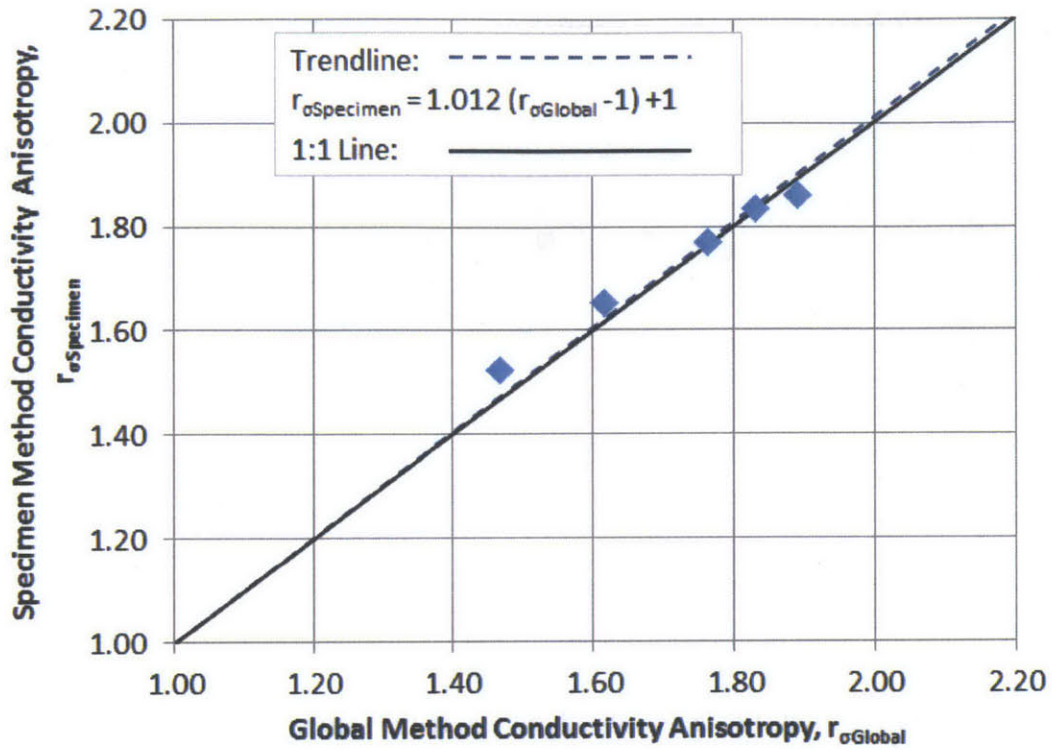


Figure 5-50: Comparison of conductivity anisotropy computed using resistivity adjusted using the global and single specimen methods for RBBC

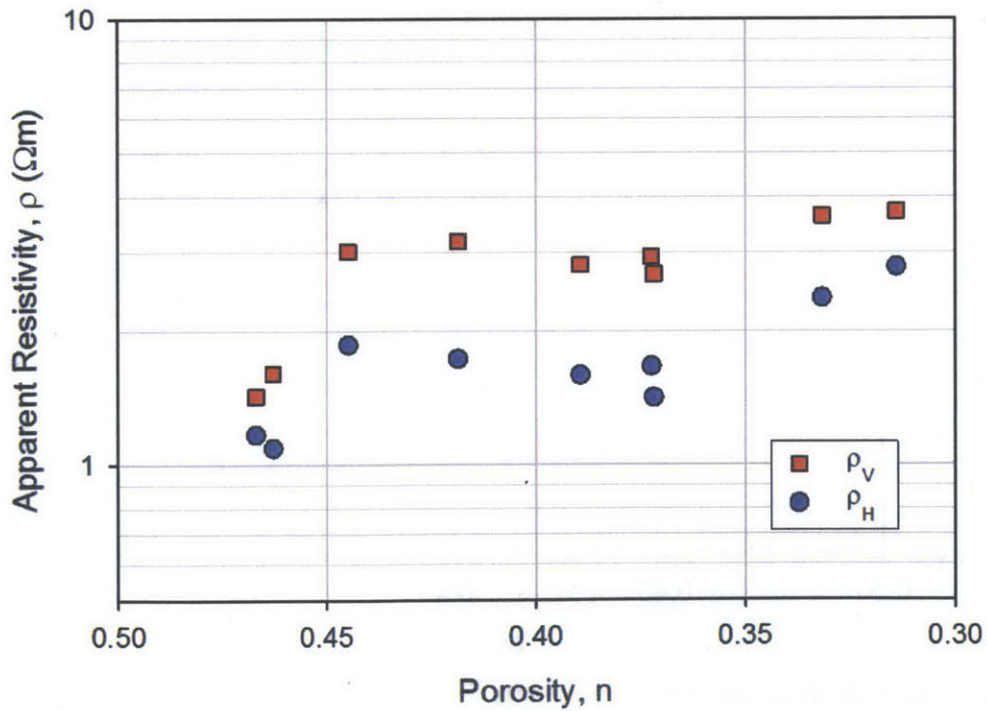


Figure 5-51: Resistivity vs. porosity for RBBC

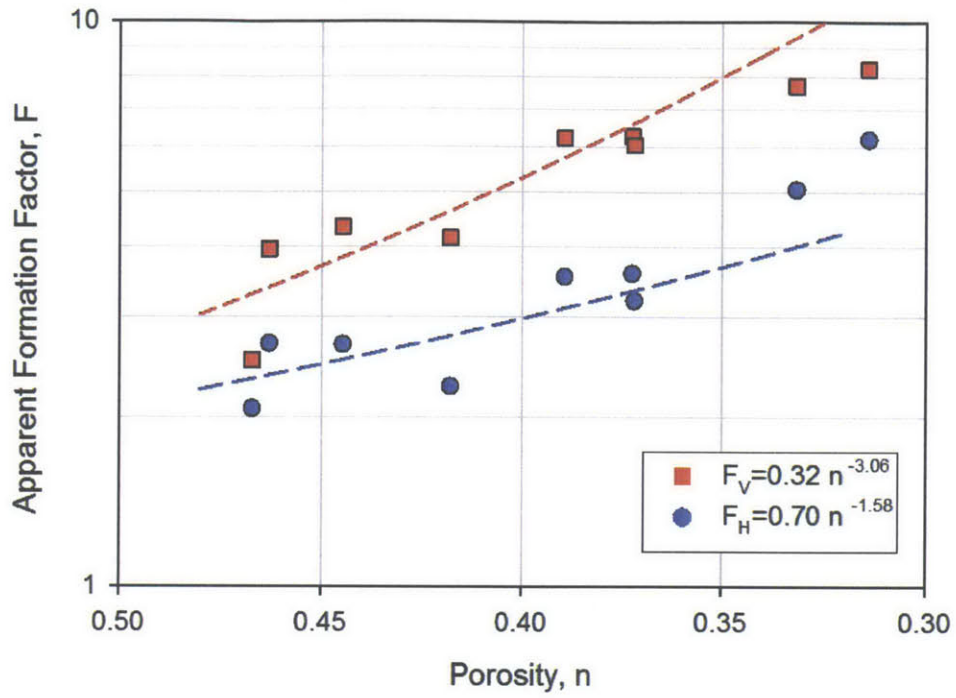


Figure 5-52: Log of apparent formation factor vs. porosity for RBBC. Trend lines are fit for the porosity > 0.36 data.

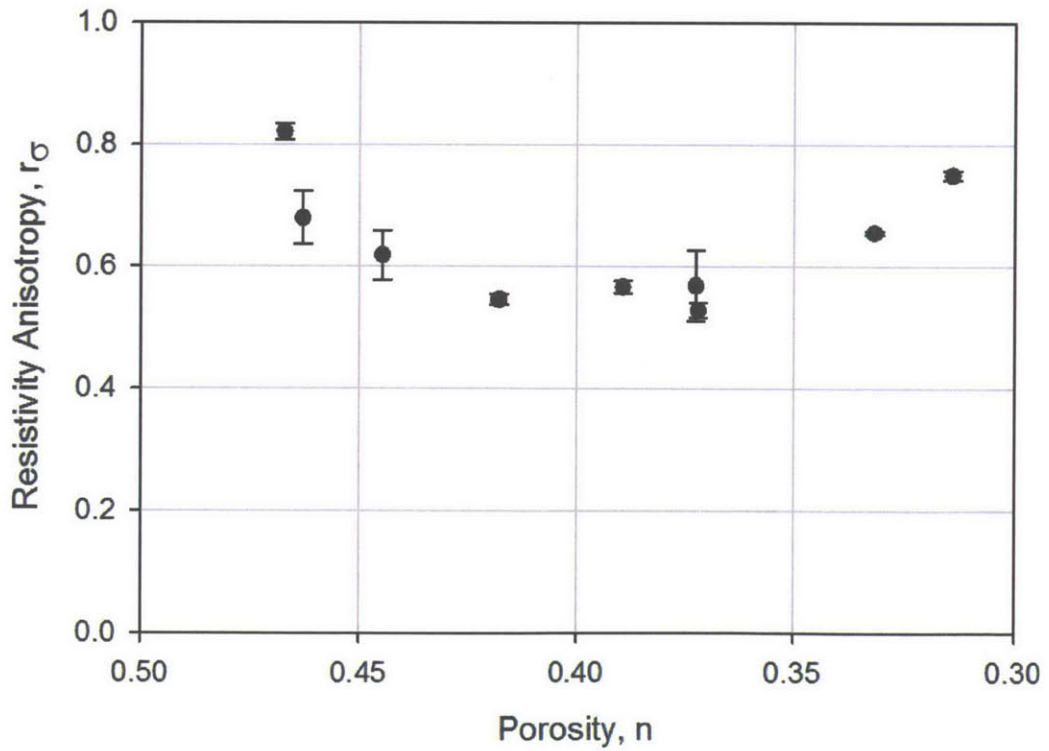


Figure 5-53: Resistivity anisotropy vs. porosity for RBBC

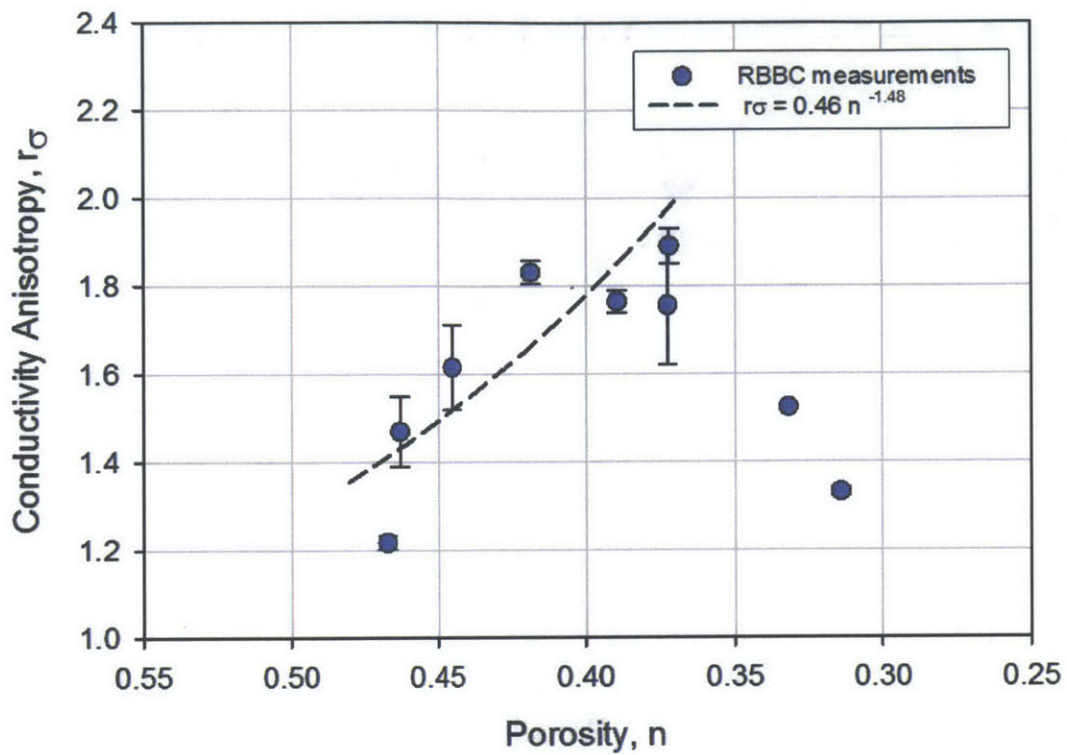


Figure 5-54: Conductivity anisotropy vs. porosity for RBBC

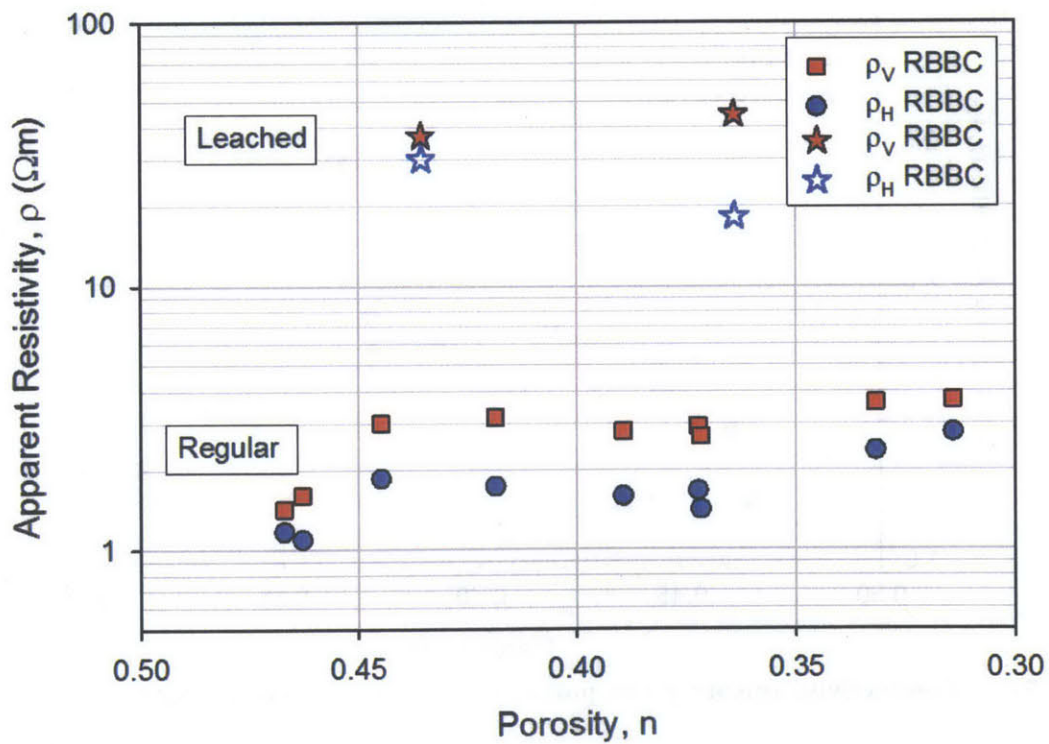


Figure 5-55: Resistivity vs. porosity for RBBC and Leached RBBC

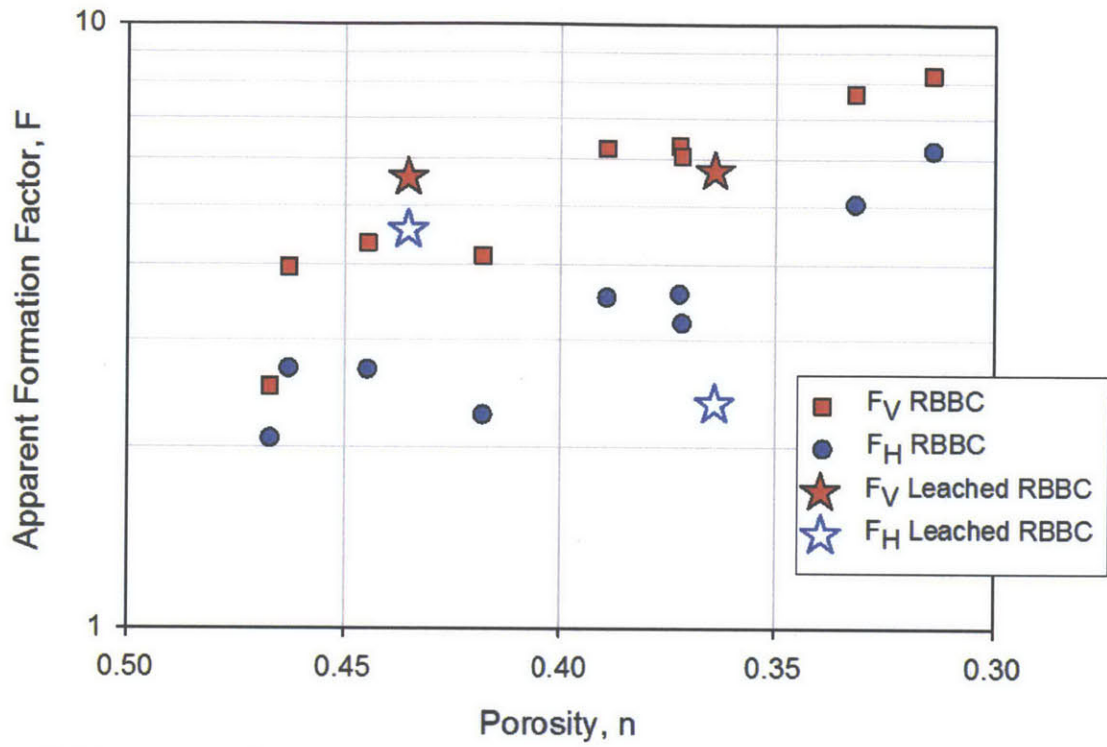


Figure 5-56: Apparent formation factor vs. porosity for RBBC and Leached RBBC

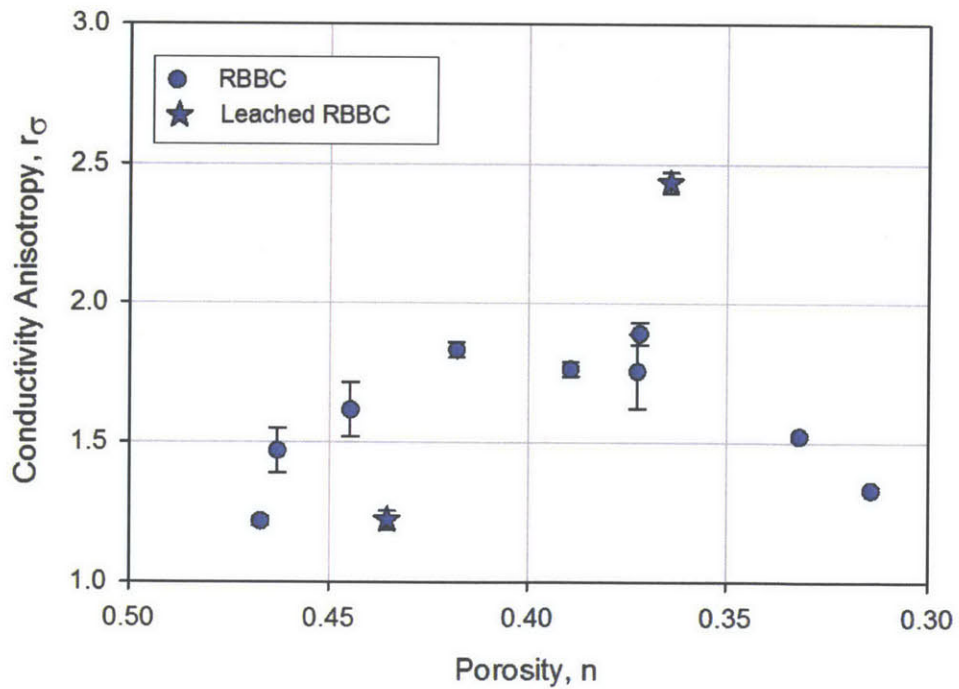


Figure 5-57: Conductivity anisotropy vs. porosity for RBBC and Leached RBBC

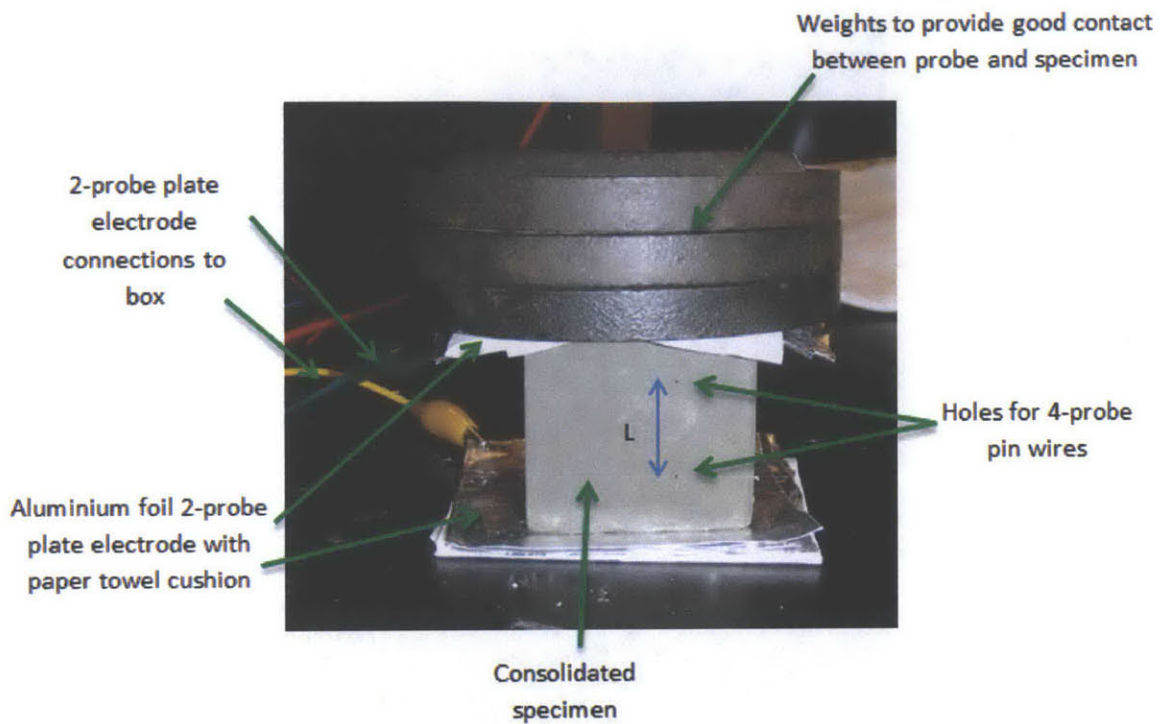


Figure 5-58: First version bench top resistivity measurement set up used to measure the conductivity anisotropy of larger specimens

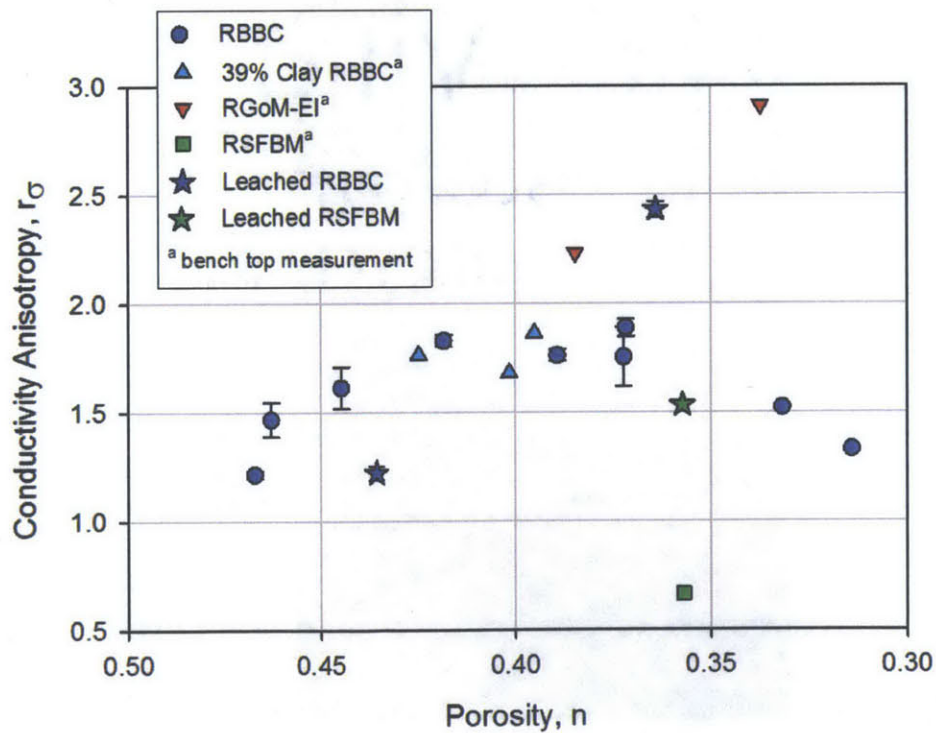


Figure 5-59: Conductivity anisotropy vs. porosity: Comparison between RBBC, 39% Clay RBBC, RGoM-EI, RSFBM, Leached RBBC and Leached RSFBM

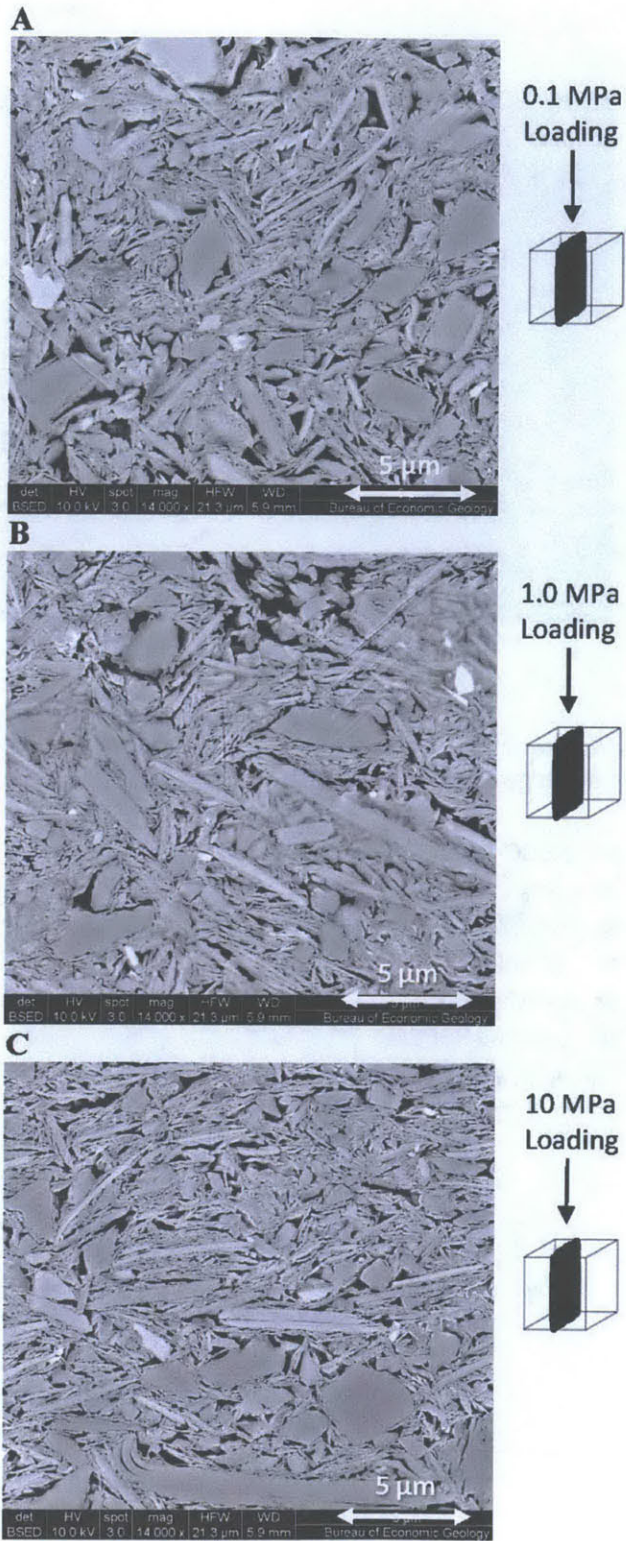


Figure 5-60: BSEM images of the vertical plane of RBBC at (a) 0.1 MPa (b) 1.0 MPa, and (c) 10 MPa [Emmanuel and Day-Stirrat, 2011]

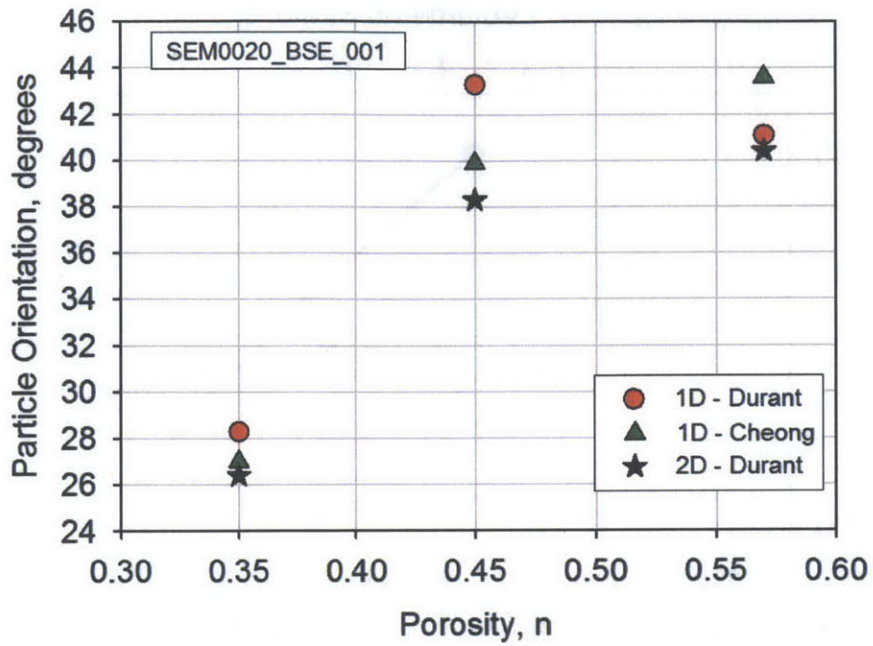


Figure 5-61: Repeatability of Image Analysis for a single RBBC image analyzed by different users and using different techniques

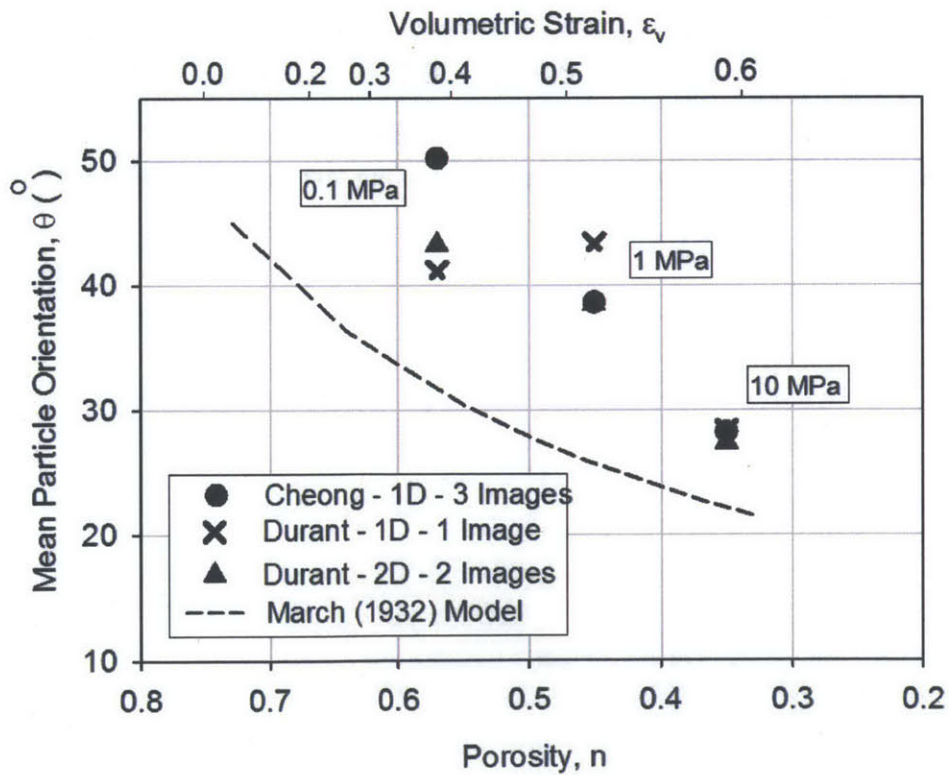


Figure 5-62: Particle orientation vs. porosity for RBBC measured using UT Images

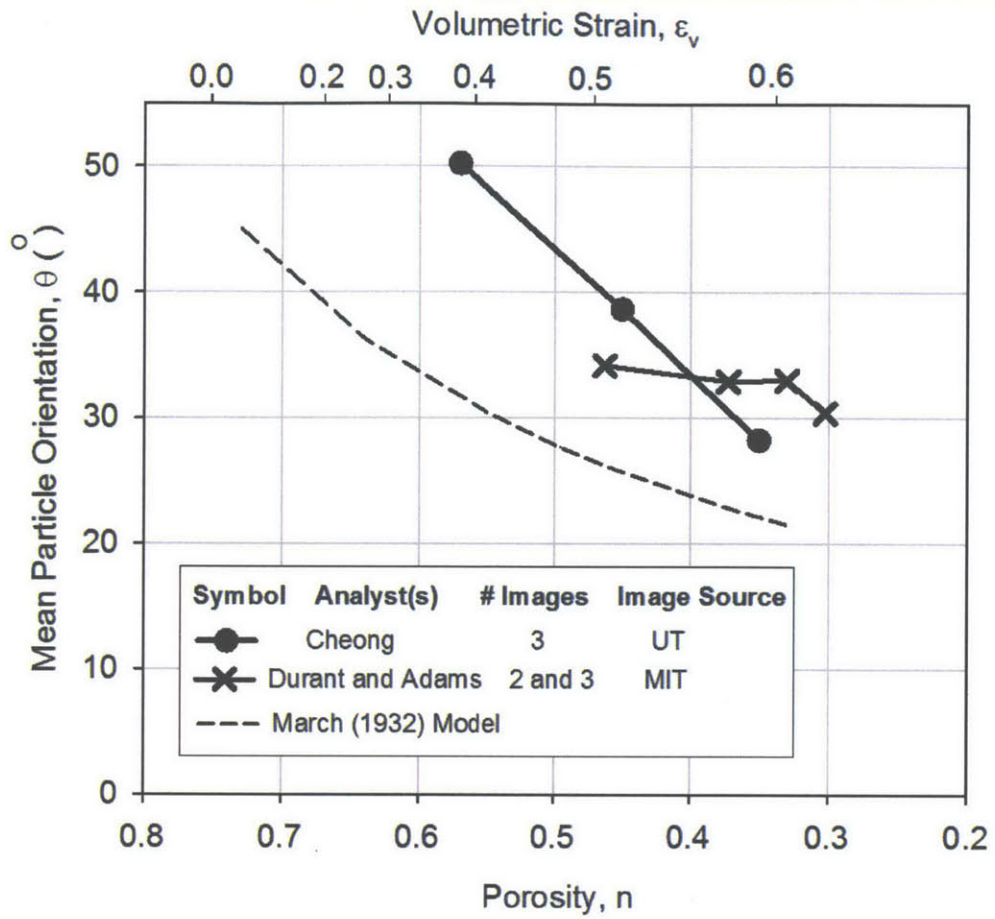


Figure 5-63: RBBC Particle orientation measured using MIT and UT Images (1D Analysis)

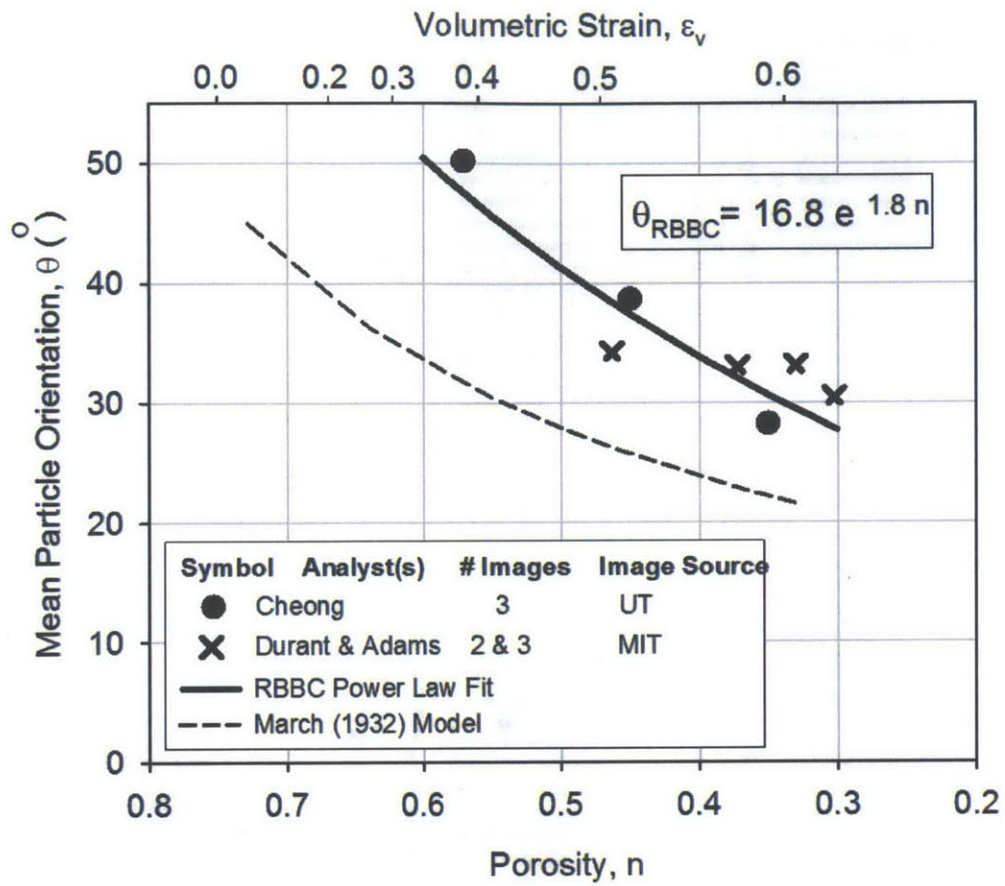


Figure 5-64: Particle Orientation measured using 1D analysis for RBBBC prepared at MIT compared with March 1932 Model

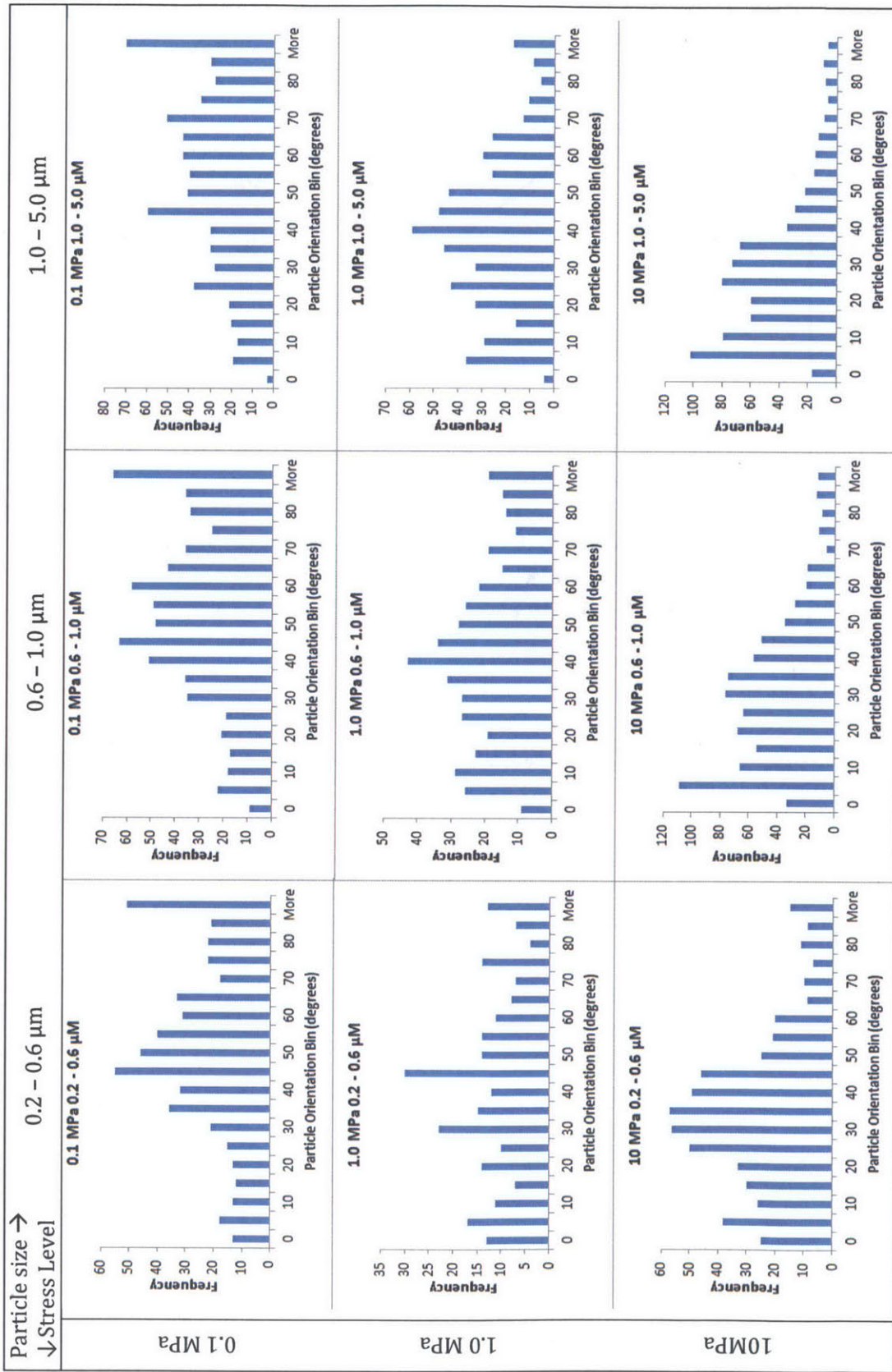


Figure 5-65: Histograms showing particle orientation as a function of particle size for images of RBBC obtained at UT, analyzed using the 1D technique by Cheong

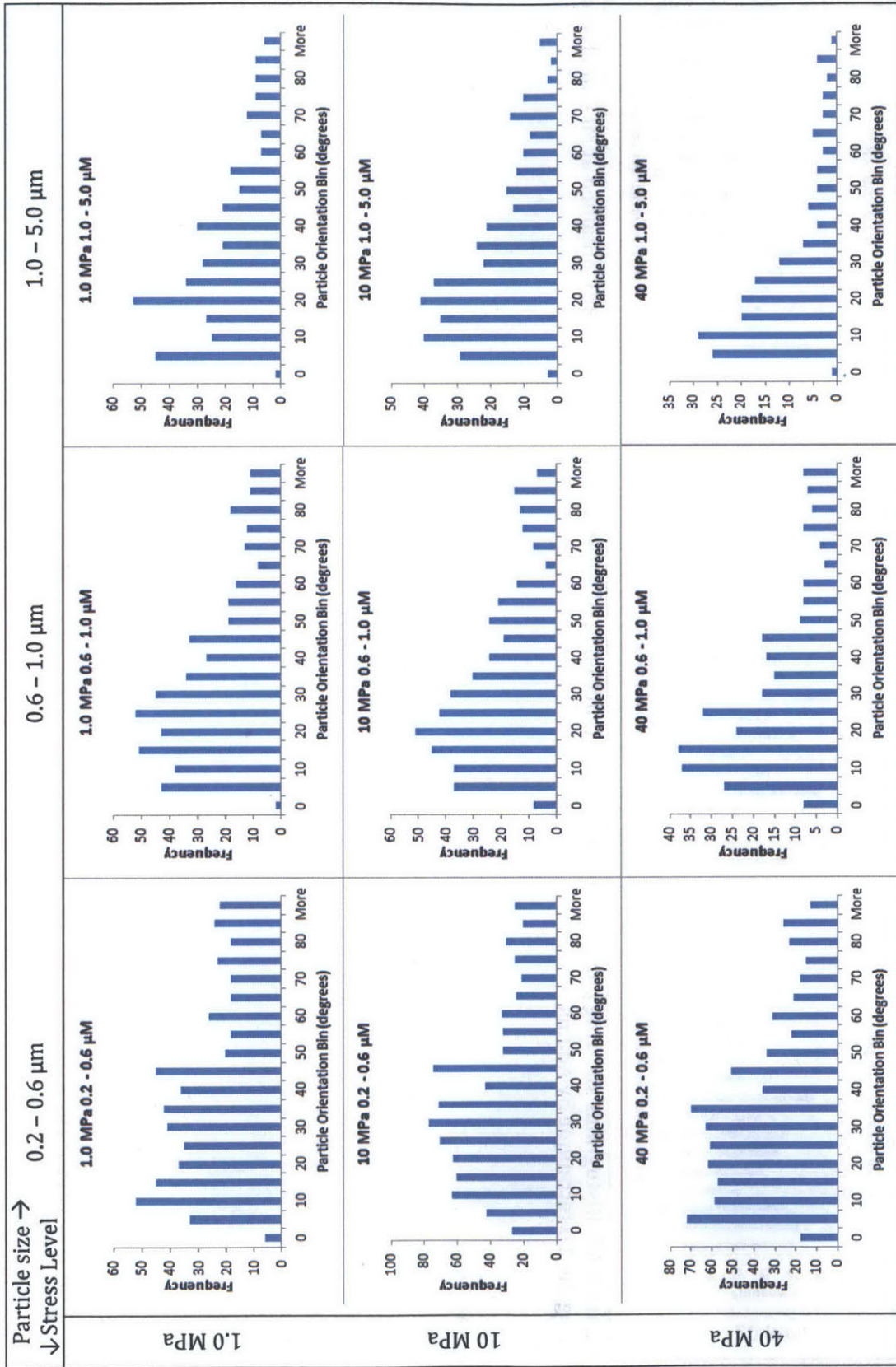


Figure 5-66: Histograms showing particle orientation as a function of particle size for images of RBBC obtained at MIT, analyzed using the 1D technique by Durant

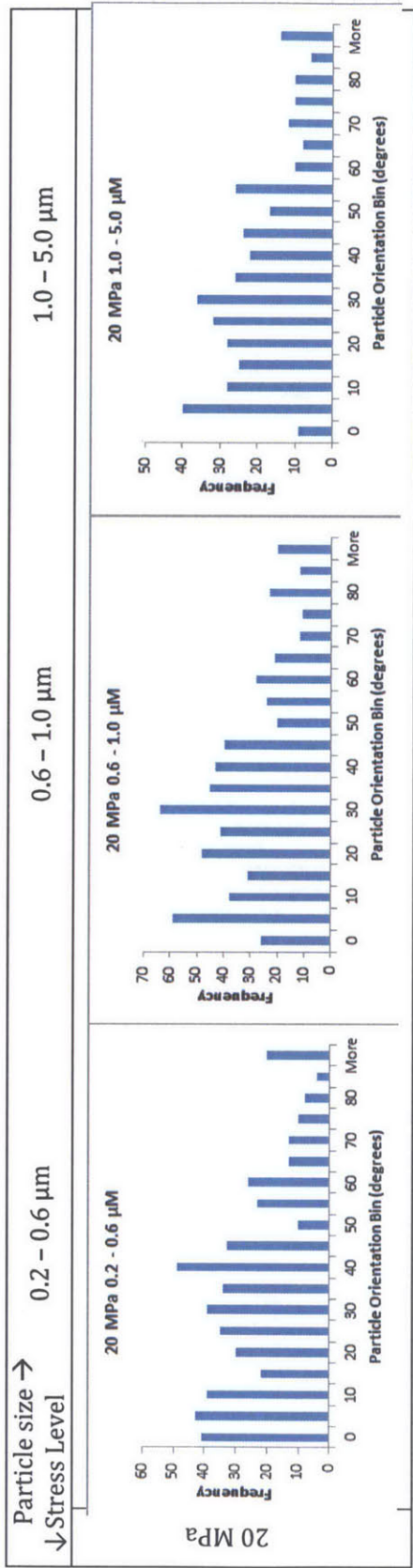


Figure 5-67: Histograms showing particle orientation as a function of particle size for images of RBBC obtained at MIT, analyzed using the 1D technique by Adams

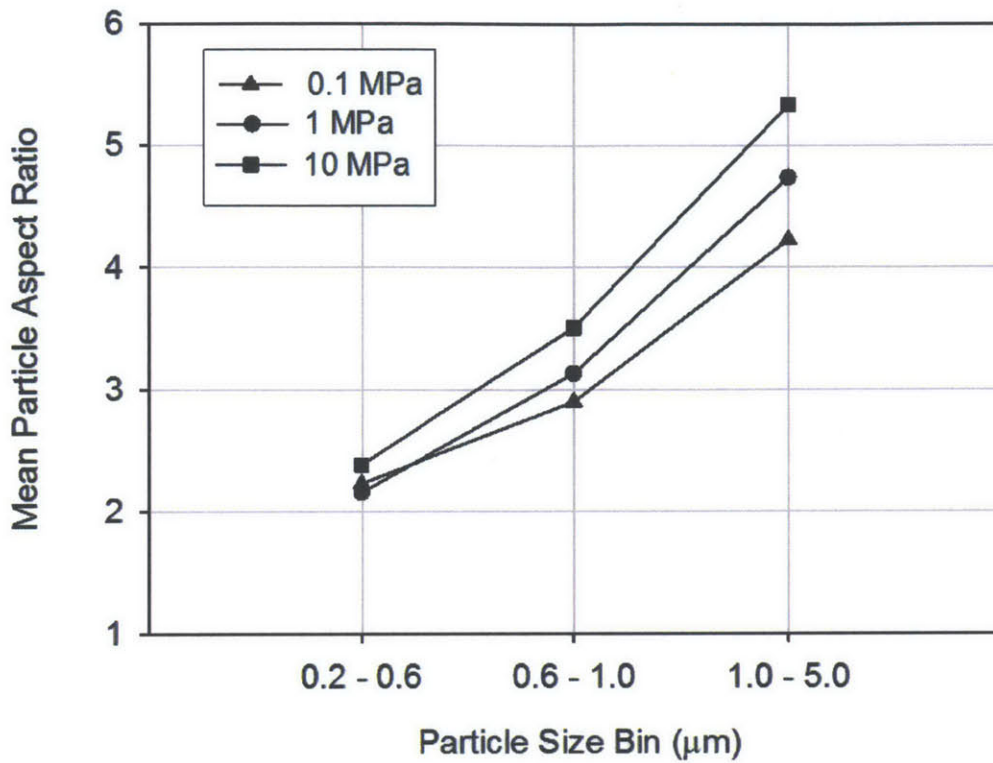


Figure 5-68: Particle aspect ratio as a function of size for 2D analysis of UT Images

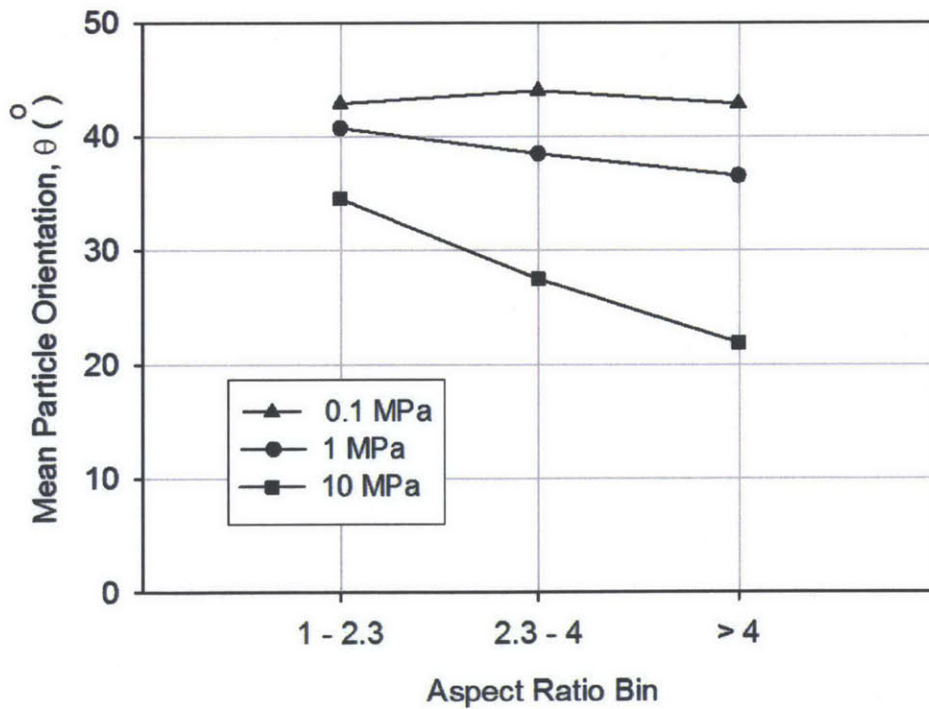


Figure 5-69: Particle orientation as a function of particle aspect ratio for 2D analysis of UT Images

(Page intentionally left blank)

6 Interpretation

6	Interpretation.....	241
6.1	Permeability Anisotropy Development in Uniform Mudrocks	242
6.1.1	Permeability Anisotropy Due to Particle Rotation	243
6.1.2	High Stress Permeability Anisotropy Decrease	245
6.1.3	Magnitude of Permeability Anisotropy: Extrapolation to Basin Effective Stresses... ..	248
6.1.4	Extension to other studied mudrocks.....	249
6.1.5	Summary	251
6.2	Permeability Anisotropy vs. Conductivity Anisotropy in Uniform Mudrocks	252
6.2.1	Theoretical Analogies	252
6.2.2	Archie's Law Applied to RBBC.....	253
6.2.3	Conductivity Anisotropy as a Predictor of Permeability Anisotropy.....	255
6.3	Extension to Layered Systems.....	258
6.3.1	Permeability Anisotropy of Layered Isotropic Mudrocks	258
6.3.2	Permeability Anisotropy of Layered Anisotropic Mudrocks: A Model.....	259
6.3.3	Conductivity Anisotropy of Layered Anisotropic Mudrocks: A Model.....	263
6.4	Summary and Field Extension	267

This chapter further discusses the experimental results presented in chapter 5 and analyzes the data using a variety of existing models and theoretical concepts. This chapter is divided into four sections. The first section summarizes the permeability anisotropy results, discusses interesting behaviour, and compares findings to predictions made using particle based permeability anisotropy models. This comparison highlights the importance of the fabric heterogeneity and the fabric influence on the development of permeability anisotropy in uniform mudrocks. The second section discusses the relationship between conductivity anisotropy and permeability anisotropy using experimental results and a theoretical framework based on analogies between fluid flow and electric circuit equations. The third section applies the experimental findings to a practical case of layered systems that is commonly encountered in the field. An analytic model is developed using concepts of mudrock compression, permeability and resistivity. This model reveals that, though the permeability anisotropy of uniform mudrocks does not exceed ~ 2 , the permeability anisotropy of a system of layered anisotropic mudrocks is significantly higher than that of a similar system consisting of layered isotropic mudrocks. Finally, the fourth section summarizes the experimental interpretation and discusses how the results may be adapted for use in the field.

6.1 Permeability Anisotropy Development in Uniform Mudrocks

The permeability anisotropy of RBBC was extensively measured to study the development of permeability anisotropy in mechanically compressed mudrocks. A total of 24 individually resedimented specimens of RBBC were measured covering a maximum effective stress (σ'_p) range varying from 0.4 to nearly 40 MPa. Additionally, the particle orientation and particle aspect ratio RBBC were analyzed using image analysis; these parameters are inputs for particle based permeability anisotropy models.

The permeability anisotropy of RBBC was measured for the porosity range of 0.5 to 0.30. The permeability anisotropy measurements can be roughly divided into three zones: those for porosity > 0.5 , those for porosity between 0.5 and 0.36, and those for porosity below 0.36 (Figure 6-1). The permeability anisotropy of specimens with porosity higher than 0.5 (maximum effective stress lower than 0.4 MPa) could not be measured because the mudrock is too soft to be trimmed and handled as required for the cubic permeability measurement technique. Similarly, lower porosity specimens ($n < 0.30$) could not be measured due to stress limitations imposed by the available equipment. From porosity 0.5 to porosity 0.36 the permeability anisotropy of RBBC increases monotonically from 1.2 to ~ 1.9 (Figure 5-27). In this region compression occurs via particle rotation, which drives permeability anisotropy development. This analysis is discussed in Section 6.1.1. Below porosity 0.36 (corresponding to about 10 MPa maximum effective stress) the permeability anisotropy drops and no clear trend is apparent, with the permeability anisotropy varying between 1.4 and 1.9. Section 6.1.2 highlights how this decrease is associated with a decrease in the horizontal permeability which may be related to a change in mode of compression from particle orientation to compression related to the strength of the material.

Resistivity measurements for RBBC (Figure 5-54) show that the conductivity anisotropy follows a similar trend as the permeability anisotropy; the conductivity anisotropy increases from 1.2 to 1.9 as the porosity decreases from 0.5 to 0.36 for RBBC and then decreases below porosity 0.36. The link between permeability anisotropy and conductivity anisotropy is further explored in Section 6.2.

In addition to the RBBC measurements, five other mudrocks were briefly studied. Five specimens of 39% Clay RBBC and two specimens of leached RBBC were measured to study the effects of clay fraction and pore fluid salinity, respectively, on fabric formation and permeability anisotropy. Finally, two specimens each of RGOM-EI and RSFBM were measured to study the effects of varying mineralogy and plasticity, and one specimen of leached RSFBM was measured to extend the study of the effect of pore fluid salinity to a mudrock other than RBBC.

The 39% Clay RBBC (cyan triangles, Figure 5-27) behaves similarly to the RBBC; the permeability anisotropy increases from 1.4 to 1.6 as the porosity decreases from 0.43 to 0.36. Below porosity

0.36, corresponding to ~ 6.3 MPa σ'_p , the permeability anisotropy decreases to 1.39. For 39% Clay RBBC, this decrease is suggested by only one measurement with porosity < 0.36 .

The following subsections explore the causes of permeability anisotropy. The first subsection analyzes zone 2 (Figure 6-1) where the permeability anisotropy increases monotonically. Good agreement is shown between experimental measurements and predictions from particle based permeability anisotropy models. Subsection 2 examines zone 3 (Figure 6-1) where the permeability anisotropy suddenly begins to decrease; a change in horizontal permeability trend is found to be the cause, indicating that horizontal flow path continuity changes as stress levels increases. Subsection 3 discusses how these findings can be applied to interpret the behaviour of other mudrocks, and subsection 4 summarizes the key conclusions drawn from the experimental program interpretation relative to the magnitude and causes of permeability anisotropy development in mudrocks.

6.1.1 Permeability Anisotropy Due to Particle Rotation

A common but simplistic conceptual view of mudrock evolution is that mudrocks are composed of randomly oriented platy particles at the seafloor. With increasing burial, particle rotation occurs and a horizontally aligned fabric develops (e.g. O'Brien and Slatt, 1990). As discussed in Chapter 2, permeability anisotropy development is believed to be related to increasing platy particle alignment with increasing compression. Daigle and Dugan [2011] modeled the permeability anisotropy (k_H/k_V) of assemblages of uniform, disk shaped particles as a function of particle angle (θ), particle aspect ratio (m) and porosity (n) (eq. 6). In their model, particles are not in contact with one another and flow paths are continuous. Particle aspect ratio is defined as the ratio of the particle diameter to particle thickness. The model computes the flow path tortuosity in both the horizontal and vertical directions, and relates the tortuosity to the permeability anisotropy according to equation 6-1 (Witt and Brauns, 1983; Scholes et al, 2007):

$$r_k = \frac{k_H}{k_V} = \frac{\tau_V^2}{\tau_H^2} = \frac{\left[1 + \frac{\left[\frac{8m}{9} \cos(\theta) + \frac{2}{\pi} \sin(\theta) \right]}{\left[\frac{3\pi}{8(1-n)} - \frac{1}{2} \right]} \right]^2}{\left[1 + \frac{\left[\frac{8m}{9} \sin(\theta) + \frac{2}{\pi} \cos(\theta) \right]}{\left[\frac{3\pi}{8(1-n)} - \frac{1}{2} \right]} \right]^2} \quad 6-1$$

For mudrocks comprised of particles with varying aspect ratio, Daigle and Dugan [2011] suggest that the equivalent aspect ratio (m_{eq}) (eq. 6-2) dominates anisotropy development:

$$\frac{1}{m_{eq}^2} = \sum_{i=1}^n \frac{f_i}{m_i^2} \quad 6-2$$

Where f_i is the volume fraction of particles with aspect ratio m_i . The aspect ratio of RBBC was analyzed in Chapter 5 using 2D image analysis. The measured aspect ratios were divided into three aspect ratio size bins and the particle area fraction of each aspect ratio bin was computed. Based on this analysis, the equivalent aspect ratio of RBBC is estimated to be 2.41. This equivalent aspect ratio is lower than the mean aspect ratio of 3.74 (Chapter 5). As discussed, aspect ratio analysis is plagued by errors associated with measurement of 3D oriented features in fixed 2D planes using oven dried specimens. As such, the measured aspect ratios are interpreted to provide lower estimates.

The permeability anisotropy of RBBC is modeled using the Daigle and Dugan (2011) relation. This model requires two inputs: 1) the particle orientation as a function of porosity, and 2) the particle aspect ratio. Chapter 5 presents multiple analyses that were performed to investigate the effects of analyst and institution. A power law curve has been fit through all 1D data measurements in order to estimate a smooth particle orientation vs. porosity trend for RBBC for input into the permeability anisotropy model. This fit is shown in Figure 5-64 and used to model the permeability anisotropy. The equivalent aspect ratio of 2.41 is used as an initial input for the permeability anisotropy model.

Four variations of the model prediction are compared to the measured permeability anisotropy of RBBC in Figure 6-5 and Figure 6-6. Two aspect ratios and two particle orientation curves are considered, as described below. For simplicity, this analysis addresses permeability anisotropy at porosities of 0.36 and greater only; as has been noted, the permeability anisotropy trend does not continue past this point and this topic is addressed in Section 6.1.2. The particle orientation measurements for the full porosity range are included in this analysis.

First, Figure 6-5 compares the modeled permeability computed using the measured particle orientation (solid line Figure 5-64) and the computed equivalent aspect ratio. The result under predicts the permeability anisotropy of RBBC at all porosities. Interestingly, the measured permeability anisotropy could be exactly replicated by the model using the measured particle orientations and a particle aspect ratio of 8, higher than both the equivalent and mean aspect ratios ($m_{eq} = 2.41$, $m_{avg} = 3.75$, see Figure 6-5).

A particle aspect ratio of 8 suggests that particles with high aspect ratios dominate flow anisotropy. In RBBC, less than 35% of the 2D particle area fraction has an aspect ratio of > 4 . The idea that high aspect ratio particles dominate flow anisotropy contradicts the idea of equivalent aspect ratio (eq. 6-2) which suggests that the inclusion of even small fractions of low aspect ratio particles will significantly reduce the permeability anisotropy. The Daigle and Dugan (2011) model relies on the interplay between particle orientation and equivalent aspect ratio to predict the permeability anisotropy of a mudrock. However, image analysis results (Chapter 5) suggest that high aspect ratio particles are both larger in size and undergo more significant rotation with increasing applied stress than lower aspect ratio particles. This behavior is not captured in the Daigle and Dugan model. The RBBC permeability anisotropy measurements and model prediction using measured particle orientations (Figure 5-27, Figure 5-64 and Figure 6-5) suggest that 1) particle rotation is not as significant as predicted by idealized models such as March 1932, and 2) the particle aspect

ratio that controls flow anisotropy is much higher than described by the equivalent aspect ratio concept.

Next, the permeability was predicted using the particle orientation predicted by March (1932) model for RBBC (dashed line, Figure 5-64). The March model is described in Chapter 5. For comparison, the same two aspect ratios, the equivalent aspect ratio of 2.41 and the calibrated aspect ratio of 8 were used as inputs. Figure 6-6 compares the model predictions using these inputs with the measured permeability anisotropy. The March (1932) model either over-predicts or under-predicts the permeability anisotropy for an equivalent aspect ratio of 2.41, and over predicts the permeability anisotropy for a particle aspect ratio of 8. No single aspect ratio value was found to produce a curve that captures the measured permeability anisotropy behavior using the particle orientations predicted by the March (1932) model.

The difference between the measured anisotropy and the model prediction computed using the measured equivalent aspect may be related to a combination of the model assumptions and the measurement methods. The model assumes that permeability anisotropy development is related to the equivalent aspect ratio of an assemblage of circular disk-shaped particles that are not in contact with each other. However, it is unknown whether equation 6-1 holds for assemblages of irregular-shaped particles with size and aspect ratio spanning multiple orders of magnitude. Further, as noted, the aspect ratio of angled 3D particles is measured in a fixed 2D plane in a limited field of view. Sample size is relied upon to reduce bias, resulting in a lower bound estimate for both the mean and equivalent aspect ratio. Given these limitations, the agreement between the measured data and the model prediction suggests that particle rotation drives permeability anisotropy development in fine grained homogeneous mudrocks comprised of platy particles (aspect ratio > 1).

It is important to note that, despite the differences between the modeled and the measured permeability anisotropy, all permutations of the modeled permeability anisotropy predicted relatively low anisotropies. The permeability anisotropy of RBBC is <2-3 for compressive stresses up to 10 MPa and porosity greater than 0.37. Despite observed platy particle rotation, RBBC does not develop significant permeability anisotropy.

6.1.2 High Stress Permeability Anisotropy Decrease

Both RBBC and 39% Clay RBBC show monotonic increases in permeability anisotropy with decreasing porosity for porosities above 0.36; below porosity 0.36 the permeability anisotropy decreases. Below porosity 0.36 the horizontal permeability decreases at a faster rate, causing the decrease in permeability anisotropy (Figure 5-26). There is not a noticeable difference in the rate of vertical permeability decreases above and below porosity 0.36. Insufficient measurements were made for 19% clay RBBC to determine if the permeability trend in either the vertical or horizontal direction changes below porosity 0.36.

The conductivity anisotropy measurements on RBBC also show a decrease in anisotropy below porosity 0.36. Similar to the permeability measurements, both the horizontal and vertical apparent formation factor deviate from the predicted trend for RBBC for porosities < 0.36 . This deviation is noted despite the increased sensitivity in these two measured to small variations in the specimen pore fluid salinity. This increased sensitivity leads to more scatter in the directional resistivity vs. porosity (Figure 5-51) and apparent formation factor vs. porosity (Figure 5-52) compared with the directional permeability vs. porosity trends (Figure 5-26). The specimen conductivity anisotropy is the ratio of the vertical and horizontal resistivity measured using the same specimen; therefore the conductivity anisotropy vs. porosity trend is not affected by variations in the pore fluid salinity between specimens.

The permeability anisotropy decrease below 0.36 is repeatable and systematic. The noted changes in the slope of the permeability, resistivity and formation factor vs. porosity trends are indicative of changes in the fabric structure below porosity 0.36. Despite this evidence, there was speculation that varying experimental conditions may have caused this apparent change in behaviour.

Specimen fabrication was initially suggested as a potential cause of the permeability anisotropy decrease. RBBC specimens with porosities below 0.36 are fabricated in steel reinforced sedimentation columns whereas lower stress, higher porosity specimens are resedimented in acrylic sedimentation columns. All 39% clay RBBC specimens were resedimented in acrylic sedimentation columns, which suggested that noted decrease was true material behaviour. Nevertheless, to determine whether the specimen resedimentation equipment and process affected the results, a RBBC specimen was resedimented in a steel reinforced sedimentation column to only 10 MPa σ'_p , corresponding to porosity ~ 0.37 . The resultant permeability anisotropy agreed with that measured using specimens resedimented in acrylic sedimentation columns. Differences in the specimen fabrication procedure are not the cause of the permeability anisotropy decrease below porosity 0.36.

A thorough error check and error analysis was also conducted to identify errors in permeability, porosity and resistivity. A calculation error is not a likely cause because the decrease in anisotropy is systematic, appearing in both the permeability and resistivity measurements for RBBC, and additionally in the permeability measurement for 39% clay RBBC.

The anisotropy decrease at high stresses (porosity < 0.36 for RBBC) is most likely resultant from a fabric change that occurs \sim porosity 0.36 (corresponding to 10 MPa) for RBBC. There is little change in the particle orientation between porosity 0.36 and porosity 0.30 (corresponding to 10 and 40 MPa, respectively). The 20 MPa specimen (porosity 0.33) has particle orientation is slightly higher than that measured at 10 MPa, though this difference is well within the error band of the analysis method. This variation in particle orientation (< 1 degree) is not sufficient to explain the large difference in permeability anisotropy (compare 1.9 to 1.4, Figure 5-27) across this porosity range.

Results in Chapter 5 revealed that above porosity 0.36 larger particles were more horizontally oriented than smaller particles. The difference in orientation between large particles and small particles increased with decreasing porosity and increasing stress level. This may not be true below porosity 0.36. The 20 MPa (porosity 0.33) specimen has particle orientation that is independent of particle size and has low anisotropy, while the 40 MPa (porosity 0.30) specimen has particle orientation that is size dependent and better agrees with the results for porosities > 0.36.

Three of the four measurements below porosity 0.36 shown in Figure 5-27 show a decrease in permeability anisotropy; one measurement maintains a permeability anisotropy equivalent to that at porosity 0.36. This measurement does not show an increase in permeability anisotropy and may be the result of experimental error or variation. More work is required to prove the consistency of the noted changes in fabric and anisotropy trends. Overall, the permeability anisotropy of RBBC is limited to a range <2.

Experiments by Grande and Mondol (2013) support this hypothesis. They measured the permeability anisotropy of ten mechanically consolidated mudrocks with varying percentages of silt, Illite, Kaolinite and Smectite (Figure 6-11). The mudrocks were resedimented to 3 MPa and then installed in a specially designed triaxial cell where they were K_0 consolidated up to maximum effective stresses of 50 MPa. It is not clear if 1) permeability was measured in both direction on the same specimen, or using two specimens, or 2) if permeability was measured at discrete intervals or continuously.

The permeability anisotropy results reported by Grande and Mondol (2013, Figure 6-11) show a similar behavior at high stresses as those measured for RBBC and 39% Clay RBBC over the same stress range. The permeability anisotropy starts relatively high at 3 MPa effective stress and increases to a maximum value that varies based on the mudrock mineralogy. After the maximum permeability has been reached, the permeability anisotropy either remains constant or decreases. This is exemplified by the 50 - 50 Illite-Kaolinite mixture which starts with a permeability anisotropy ~ 2 at 3 MPa, increases to a maximum permeability anisotropy ~3.2 at 30 MPa and then decreases in permeability anisotropy with increasing applied stress to 50 MPa. Overall, the permeability anisotropy measured by Grande and Mondol (2013) for mudrocks compressed up to 50 MPa does not exceed 3.5.

Particle packing theory can be used to further explore the hypothesis that pore space continuity becomes limited with decreasing porosity, limiting permeability anisotropy. The mudrock porosity is equal to the product of the clay porosity and the silt porosity. The clay and silt fraction porosities are defined as:

$$n_{silt} = \frac{V_t - V_{silt}}{V_t} \quad 6-3$$

$$n_{clay} = \frac{V_t - V_c - V_{silt}}{V_t - V_{silt}} \quad 6-4$$

$$n = n_{clay} * n_{silt}$$

6-5

Where n is the total porosity, n_{silt} is the silt fraction porosity, n_{clay} is the clay fraction porosity, V_t is the total volume, V_{silt} is the volume of the silt, and V_c is the volume of the clay. The silt fraction porosity (n_{silt}) is the porosity assuming that the mudrock contained only the silt in the existing structure, essentially counting the clay as voids. The clay fraction porosity, on the other hand, is the porosity of just the clay structure as if it was a mudrock on its own. Table 6-2 gives silt and clay porosities for RBBC and 39% Clay RBBC over the total porosity range studied. The values given in Table 6-2 are computed assuming the clay and silt have the same specific gravity. The clay fraction was used to determine the volume of silt and the volume of clay knowing the volume of solids.

The porosity of uniform spheres ranges from 0.470 – 0.260. Square packing yields the loosest packing state and a porosity of 0.470. Regular close packing (either hexagonal or face centered cubic) yields the densest packing and a porosity of 0.260 (Scott and Kilgour, 1969). Random close packing yields a slightly higher porosity, ~ 0.36.

Comparison of the data in Table 6-2 with the porosities associated with different spherical packing densities offers insight into the clay behaviour. First, for both RBBC and 39% Clay RBBC, the silt porosity (n_{silt}) is much greater than 0.47, the loosest porosity for uniform spheres. This indicates that the mudrocks are not silt supported, and that the clay particles play a dominant role in the fabric structure. Further, for both mudrocks the clay porosity is quite high. Even at a low total porosity of 0.30, the clay porosity is still at or above 0.47, representative of the maximum porosity of uniform spheres. This indicates that there is still room for bulk compression of the clay fabric.

Curiously, the permeability anisotropy of RBBC and 39% Clay RBBC drops off below porosities of 0.36. This porosity is equal to the random close packing porosity for uniform spheres. This fact is likely a mere coincidence, but should be further investigated by measuring the permeability anisotropy of different materials to identify the porosity at which the permeability anisotropy deviates from a linear trend, if any.

6.1.3 Magnitude of Permeability Anisotropy: Extrapolation to Basin Effective Stresses

In sedimentary basins, effective stress ranges from 0.1 MPa at the near surface, to 5 MPa at ~600 mbsf in overpressured offshore basins such as the Ursa basin (Long et al., 2011; Day-Stirrat et al., 2011), and can reach ~27 MPa (2.4 km) before processes other than mechanical compression begin to dominate pore evolution (Day-Stirrat et al., 2008). Naturally, local geothermal gradients will dictate the depth at which chemical alteration takes over from purely mechanical processes.

At 27 MPa (porosity 0.33), reflective of the position in a generic basin where mechanical processes are succeeded by chemical processes, the mean particle orientation is 29° (Figure 5-64) and the permeability anisotropy is predicted to be 2.1 using the Daigle and Dugan model and a calibrated

particle aspect ratio of 8. This extrapolation ignores the measured decrease in permeability anisotropy for porosities lower than 0.36 for RBBC which will be discussed later.

Intense platy particle alignment is not likely to result from mechanical compression alone; the permeability anisotropy of homogeneous mechanically compressed mudrocks with platy particles similar to that of RBBC is limited to <2 .

6.1.4 Extension to other studied mudrocks

Figure 5-41 illustrates the variation in permeability anisotropy with decreasing porosity for all mudrocks studied in this research, including RBBC, Leached RBBC, 39% Clay RBBC, RGoM-EI, RSFBM and Leached RSFBM. Figure 5-59 summarizes the conductivity anisotropy measurements for these mudrocks including bench top measurements. Chapter 5 discusses the permeability and resistivity measurements in detail.

The mudrocks studied in this research cover a wide range of plasticity, clay fraction and clay mineralogy as shown in Figure 3-19, Figure 3-21 and Figure 3-22. The wide variation in these properties is reflected in the large variation in mudrock permeabilities, shown in Figure 5-39. However, despite the wide variation in mudrock plasticity, clay fraction and clay mineralogy, the permeability anisotropy does not vary significantly, obtaining a maximum value of ~ 2.0 (Figure 5-41). The conductivity anisotropy supports this finding, exhibiting little variation across the mudrocks studied and obtaining a maximum value of ~ 3.0 .

Sufficient measurements were not made for RSFBM or RGoM-EI to identify if the permeability anisotropy increases linearly with decreasing porosity as was identified for RBBC. However, curious behaviours were identified.

Two measurements on RSFBM at porosities of 0.39 (6 MPa σ'_p) and 0.36 (10 MPa σ'_p) resulted in isotropic permeability anisotropy. If particles become increasingly aligned with compression, the permeability anisotropy should be greater than 1. A number of explanations are offered for this behaviour.

First, if the RSFBM behaves similarly to RBBC, in that the anisotropy increases with decreasing porosity and then drops off as horizontal flow paths become blocked, it is possible that one measurement was obtained on either side of the drop off point. For example, had measurements of RBBC been made at porosities of 0.45 and 0.33 only, it would appear that the permeability anisotropy has a constant value of ~ 1.4 irrespective of porosity (see Figure 5-27). Additional measurements made for RBBC prove this is not the case.

However, the above explanation is not likely, especially since the two RSFBM measurements were made with a much smaller porosity interval. Further, the RSFBM does not show any permeability anisotropy, whereas even at high porosities the RBBC did show some anisotropy ($r_k > 1$). A more likely theory is that the RSFBM has an initially uniform fabric that does not undergo particle

rotation with compression. This may be due to a dominance of low anisotropy particles, the presence of organics, a tendency towards particle breaking, or other mechanisms. Figure 6-5 shows that as the particle aspect ratio decreases, so too does the permeability anisotropy despite significant measured particle rotation. Further measurements are required to confirm the exact causes of the RSBFM isotropy.

The RGoM-EI mudrock appears to follow the trend of increasing permeability anisotropy with decreasing porosity. Particle based permeability anisotropy models suggest that increasing particle aspect ratio increases permeability anisotropy (see Section 6.1.1); therefore, the permeability anisotropy of RGoM-EI was expected to be higher than that of RBBC because of the high Smectite content with higher particle aspect ratio compared to Illite rich RBBC. Figure 5-41 shows that the permeability anisotropy of RGoM-EI is in fact lower than RBBC despite having higher conductivity anisotropy (Figure 5-59).

As noted in Chapter 5, it was difficult to measure the permeability of the RGoM-EI mudrock due to horizontal cracking that developed with exposure to the air during trimming, and set up of the experiments. A high standard deviation was recorded for the permeability anisotropy (Figure 5-41) compared to the other mudrocks analyzed. As a result, the permeability measurements for RGoM-EI are deemed questionable; the conductivity anisotropy measurements may be more representative of the specimen anisotropy through relations between the conductivity anisotropy and permeability anisotropy that will be discussed in Section 6.2.

Finally, Basak (1972) showed that dispersed fabrics develop permeability anisotropy with increasing compression, whereas flocculated fabrics remain isotropic (discussed in Chapter 2). To investigate this, leaching was undertaken in an attempt to create a dispersed fabric structure using RBBC and compare the anisotropy development between fabric structures.

Leaching was able to reduce the BBC mudrock powder salt content by nearly 15 times relative to the intact salt content, such that leached RBBC was batched at 0.16 g/L at 100% water content compared to regular RBBC which is batched at 16 g/L and 100% water content. Similarly, the salinity of the SBFM mudrock powder was reduced nearly 28 times, such that leached RSBFM was batched at 0.3 g/L and 90.5% water content compared to regular RSBFM which has a natural salt content resulting in 8.5 g/L at 90.5% water content during batching.

It was expected that the change in salinity due to leaching would alter the slurry deposited fabric structure, and that this would be reflected in the permeability and conductivity anisotropy measurements. The permeability, and permeability anisotropy and conductivity anisotropy of leached RBBC specimens do not differ from that measured for regular RBBC specimens at the same porosity and maximum effective stress. The resistivity is significantly different (see Chapter 5) because these properties are very sensitive to changes in the pore fluid salinity, as discussed in Chapter 2.

Similarly, the permeability of leached RSFBM did not differ significantly from that measured for regular RSFBM. However the permeability anisotropy was somewhat higher (1.3 vs. ~ 1.0) because the anisotropy measurement is very sensitive to slight variations in the measured permeability.

Overall, leaching did not alter the measured specimen porosity, permeability or permeability anisotropy at a given consolidation stress. This conclusion is in agreement with the findings of Horan (2012) for high stress mudrocks. However, Leaching does seem to alter the low stress mudrock permeability, compressibility and compression curve, as reported by Horan (2012) and Fahy (2104). This may be due to the alteration of the Debye length, t_D (Ladd, 1996). The Debye length is given by:

$$t_D = \frac{0.020}{v} \sqrt{\frac{DT}{C_o}} \quad 6-6$$

Where v is the cation valence, D is the dielectric constant (equal to the relative permittivity), T is the temperature and C_o is the cation concentration.

Leaching decreases the cation concentration which increases the Debye length and may affect particle spacing at low applied stresses. However, experimental results indicate leaching is insufficient to cause a fabric structural change (i.e. a flocculated fabric is still formed, despite a large Debye length).

6.1.5 Summary

This section summarized the measured permeability anisotropy results for RBBC, 39% Clay RBBC, RGoM-EI and RSFBM. Key outcomes of this discussion are that:

- The permeability anisotropy of RBBC increases linearly with decreasing porosity in the range 0.5 – 0.36. This increase is related to particle rotation.
- The measured particle orientation of RBBC does not agree with that predicted by the March (1932) model, especially for high porosities (>0.5). RBBC may maintain a random particle orientation up to effective stresses in the range of 0.1 MPa before particle rotation plays an important role in mudrock compression.
- For low porosities (<0.36), the permeability anisotropy of RBBC is unpredictable, but is limited by a maximum value dictated by the particle orientation. Deviation from a linear trend in permeability anisotropy with porosity may be related to a change in fabric which alters particle orientation and thus permeability anisotropy.
- The permeability anisotropy does not exceed 2, and the conductivity anisotropy does not exceed 3.0 for the mudrocks studied. These mudrocks cover a wide range of plasticity, mineralogy and clay fraction.
- Leaching does not significantly alter the permeability, permeability anisotropy or conductivity anisotropy of mudrocks.

- More work is required to investigate the transition point between a permeability anisotropy that increases with particle rotation to the horizontal and permeability anisotropy that decreases suddenly with little change in particle orientation.
- However, because significant permeability anisotropy does not develop in mechanically compressed mudrocks, the applications of this work will dictate whether a factor of 2-3 increase in permeability anisotropy merits significant additional work.

6.2 Permeability Anisotropy vs. Conductivity Anisotropy in Uniform Mudrocks

A comparison between the permeability anisotropy and conductivity anisotropy of RBBC indicates that the two measures follow the same trend and fall within the same range: both have values ~ 1.2 at porosity 0.5, and both increase linearly with decreasing porosity to maximum values in the range of 1.9 to 2.0. Further, both the permeability and conductivity anisotropy of RBBC decrease below porosity 0.36. This section discusses the relationship between the permeability and conductivity anisotropy from a theoretical standpoint and describes the experimental evidence linking the two values in uniform mudrocks.

6.2.1 Theoretical Analogies

In soil mechanics, students are often taught concepts of hydraulic conductivity or permeability, summarized in Table 6-3. The hydraulic conductivity of a soil is measured using a variety of fluid flow experiments applying D'Arcy's law. Permeability is a property of the medium and is equal to the hydraulic conductivity normalized by the fluid density and viscosity. The Kozeny Carmen equation is a poor but commonly used relation that is often used to model mudrock permeability. The permeability anisotropy is equal to the ratio of the horizontal permeability divided by the vertical permeability. The permeability anisotropy has been shown to be equal to the ratio of the square of the vertical tortuosity divided by the horizontal tortuosity (e.g. Witt and Brauns, 1983). This result can also be obtained by dividing the horizontal and vertical permeability modelled using the Kozeny Carmen relation. This method assumes that all parameters in the Kozeny Carmen relation, such as specific surface area, specific gravity, porosity and tortuosity factor are isotropic and cancel when divided.

For each equation described above for the permeability, a similar equation exists for resistivity, also included in Table 6-3. These equations are commonly taught in courses of electrical engineering and connection between the two quantities is not often intuitive. Hydraulic conductivity is analogous to electrical conductivity. Though the hydraulic resistivity is rarely mentioned in the literature, the electrical resistivity is more commonly referenced, especially with respect to electrical circuits. Archie's law is the standard model to convert physical characteristic to electrical resistivity in mudrocks and as such is analogous to the Kozeny Carmen relation. Finally, the conductivity anisotropy is the ratio of conductive elements and is analogous to the permeability anisotropy.

6.2.2 Archie's Law Applied to RBBC

Archie's Law (Table 6-3, eq. 6-7) is commonly applied in practice and in the literature to interpret the electrical behaviour of mudrocks in the field yet it was developed for coarser grained, non-conductive materials.

$$\rho = \frac{a \rho_w}{n^m S_w^N} \quad 6-7$$

More rigorously, Archie's law is defined in terms of Formation factor which normalizes for variations in pore fluid salinity:

$$F = \frac{a}{n^m S_w^N} \quad 6-8$$

For a mudrock with 100% brine saturation, Archie's law reduces to:

$$F = a n^{-m} \quad 6-9$$

Where ρ is the resistivity, F is the formation factor, m is the cementation exponent, S_w is the water saturation, N is the saturation exponent, n is the porosity, and a is a fitting parameter sometimes termed the tortuosity parameter.

The cementation exponent m is the slope of the log formation factor vs. porosity curve. The literature suggests the minimum value of m is 1, and m increases >1 as the porosity decreases (Ransom, 2011). The cementation exponent is typically in the range of 1.3 to 2. Unconsolidated sands have a cementation exponent closer to 1.3 and consolidated sandstones have a cementation exponent in the range of 1.8 to 2.0 (Archie, 1942). Clay bearing rocks have higher cementation exponents (Atkins and Smith, 1961).

The parameter a is not formally discussed, but is sometimes called the tortuosity factor or cementation intercept. Many authors assume that $a = 1$ (e.g. Bourlange et al, 2003, Archie, 1942), however some authors suggest that ' a ' can range from 0.5 to 1.5 (e.g. Crain, 2013).

Given the literature values of a and m , and a porosity range from 0.5 to 0.3, the formation factor can range from as little as 1.7 to > 55 depending on what combination of a and m are assumed (Table 6-4).

Archie's law is typically applied as an isotropic law; direction rarely addressed. The majority of downhole field resistivity measurements are in the horizontal direction, and may be influenced by the vertical resistivity depending on the measurement technique applied. Further, once resistivity measurements are made, much time, energy and money is expended to correct field resistivity measurements for clay surface conductivity. Since clay particles are charged, they affect the electrical measurements dependent on the pore fluid salinity and chemistry, the type of clay, the

fabric structure etc. Field resistivity measurements are corrected so that measurements from one location can be compared with measurements from another location, and so that physical parameters such as porosity and saturation can be interpreted from the resistivity measurements.

The apparent formation factor is adjusted to obtain the true or intrinsic formation factor using parallel resistor models available in the literature. Parallel resistor models consider the mudrock fabric as an electrical circuit with series and parallel elements; most often the clay surface conductivity is in parallel with the pore fluid conductivity. Chapter 2 discusses parallel resistor models in detail. Numerous equations have been developed to estimate the clay surface conductivity (e.g. Waxman and Smits 1968, Clavier et al 1984). Further, various laboratory methods are available to measure the clay surface conductivity.

Figure 6-18 gives the Archie interpretation of the apparent F vs. n measurements for RBBC, previously presented in Chapter 5. A power law curve was fit to the vertical and horizontal apparent formation factor vs. porosity data measured for RBBC to determine the vertical and horizontal a and m parameters. Only those apparent formation factor measurements for porosities > 0.36 were included in the fit because of the noted conductivity anisotropy decrease below this point. One measurement at porosity 0.37 (HC036) was not included in the fit because of noted current errors affecting the resistivity measurement (Appendix 1).

Table 6-5 summarizes the Archie parameters for RBBC and predicts the conductivity anisotropy trend based on these parameters and equation 6-10. The Archie a parameters are low based on the above literature values, ranging from 0.32 in the vertical direction to 0.7 in the horizontal direction. However, the literature often deals with horizontal resistivity, so 0.7 is in range. There is no good comparison for the vertical a parameter.

The horizontal m parameter (1.58) is lower than expected for mudrocks, but the vertical m parameter (3.06) is in the expected ranges. The discrepancies between the measured values and the suggested ranges may be due to a number of reasons. First, direction is defined in this study is often undefined or confused in the literature. Second, the literature studies are dominated by coarser grained, non-conductive materials. Mudrocks consist of charged particles that have opposite edge and face charges. Differing particle orientation would thus lead to direction dependent behaviour that is different than that of non-conductive particles. Third, the fit provided in Table 6-5 is provided MS Excel for consistency with the other fits presented in this research; it has been shown that other more sophisticated fitting methods, such as a least squares manual fit, can provide different parameters with a similar trend line result. This final point suffices to call into question the validity of Archie's law as a two parameter law where the definition of each parameter is highly scrutinized.

The conductivity anisotropy can be reformulated using Archie's Law. Archie's law written in the vertical direction is divided by that written in the horizontal direction:

$$r_{\sigma} = \frac{\left(\frac{a}{n^m} \frac{\rho_w}{S_w^N}\right)_V}{\left(\frac{a}{n^m} \frac{\rho_w}{S_w^N}\right)_H} = \frac{a_v}{a_h} n^{m_H - m_V} = a_{\sigma} n^{m_{\sigma}} \quad 6-10$$

The directionality of this equation (vertical divided by horizontal) is reversed because Archie's law describes the specimen resistivity, and the conductivity anisotropy is defined in terms of conductive elements. The equations in Table 6-3 provide further explanation.

Figure 5-54 gave the conductivity anisotropy vs. porosity plot for RBBC. A power law fit was applied to the conductivity anisotropy measurements for porosities > 0.36. The empirical parameters from this power law fit (Figure 5-54) nearly exactly match those predicted by equation 6-10 using the apparent formation factor measurements (Figure 6-18) as inputs. This comparison is shown in Table 6-5. In this case, *uncorrected* directional formation factor (apparent formation factor) Archie parameters can be used to predict the uncorrected conductivity anisotropy. This implies that correction factors designed to remove the conductive effects of the clay particles from the resistivity and formation factor may be isotropic. This concept will be further explored in the next section where the conductivity anisotropy is compared to the permeability anisotropy.

6.2.3 Conductivity Anisotropy as a Predictor of Permeability Anisotropy

This subsection further evaluates the need to apply complex and time consuming clay surface conductivity correction factors to the measured resistivity and formation factor when investigating anisotropy.

Figure 6-19 compares the measured permeability and conductivity anisotropy, measured in the triaxial cell, for RBBC. This plot includes all measurements where both the permeability and conductivity anisotropy were measured, including those for $n < 0.36$ where the anisotropy decreases. Error bars for both anisotropy measurements are included in this plot, along with a 1:1 line. For RBBC, the conductivity anisotropy is equal to the permeability anisotropy within +/- 15 %. Therefore, the permeability anisotropy of RBBC can be estimated via a quick measurement of the electrical conductivity anisotropy.

It would be convenient if this simple equality between the permeability anisotropy and the conductivity anisotropy held true for all mudrocks. Newly developed downhole tools are capable of measuring the resistivity anisotropy by obtaining measurements of both the vertical and horizontal resistivity relative to a borehole axis (e.g. Schlumberger's RT Scanner tool). Resistivity anisotropy data can now be rapidly obtained in the field with limited additional cost or effort.

However, the relation between the conductivity and the permeability anisotropy is not immediately intuitive, and it is curious that the two quantities are equal for RBBC. Aside from being related to particle orientation, fluid and electric current flow are controlled by fundamentally different

processes. Flow flows from regions of high hydraulic head to regions of low hydraulic head through the pore space only. Head loss occurs via boundary contacts with the pore walls. Contrarily, electrical current flows from regions of high voltage to regions of low voltage through a combination of fluid filled pores and along grain surfaces. Electric potential loss is the result of the resistance of the flow path itself, not the flow path boundary. David (1993) shows that for a given pore radius r , the permeability in mudrocks varies inversely with r^4 while electrical resistivity varies with r^2 .

Witt and Brauns (1983) show that both horizontal and vertical fluid flow occurs through the same pore network; thus the boundary conditions do not vary by direction and cancel from the anisotropy equation. The permeability anisotropy is equal to the square of the ratio of the vertical to horizontal tortuosity, as described by equation 2-8.

$$r_k = \frac{\tau_v^2}{\tau_H^2} \quad 6-11$$

Where τ_v is the vertical tortuosity and τ_H is the horizontal tortuosity. The tortuosity is given by:

$$\tau = l/l_o \quad 6-12$$

Where l is the tortuous path actually traversed by a fluid particle and l_o is the direct, uninterrupted path.

The permeability anisotropy has been shown to be equal to the ratio of the vertical to horizontal hydraulic tortuosity (Witt and Brauns, 1983, shown in Table 6-3). This relation can be loosely obtained by writing the permeability anisotropy as the ratio of the horizontal permeability divided by the vertical permeability where permeability is modelled using the Kozeny Carmen relation, as shown by equation 6-13:

$$r_k = \frac{\left(\frac{n^3}{v\tau^2(1-n)^2 G_s^2 S_a^2} \right)_H}{\left(\frac{n^3}{v\tau^2(1-n)^2 G_s^2 S_a^2} \right)_v} = \frac{\tau_v^2}{\tau_H^2} \quad 6-13$$

Witt and Brauns (1983) also equate the electrical resistivity anisotropy to the permeability anisotropy in coarse grained (non-conductive) materials. Whether this relation holds true in mudrocks with conductive grains has not yet been explored in the literature.

Unlike fluid flow, electric current flows through many paths, with the dominant path representing the path of least resistance. In mudrocks, the path of least resistance varies with pore fluid salinity; in fact, this behaviour is exploited to measure the surface conductivity of sandstones using the methods of Waxman and Smits (1968) or Patnode and Wyllie (1950) (discussed in Chapter 2 and Appendix 4).

Using a series circuit analogy, the electrical tortuosity can be defined as:

$$\tau_e = \frac{1}{L_o R_{eq}} \sum_{i=1}^n LR \quad 6-14$$

Where τ_e is the electrical tortuosity, L is the length of each component with resistance R , and electrical flow path encounters n components of varying resistance to form a net flow path with length l_o with resistance R_o . This concept of resistance normalized tortuosity is illustrated in Figure 6-20 for flow in the vertical direction through a fluid filled pore that contacts a solid grain. The electrical tortuosity for this path is given by:

$$\tau_e = \frac{L_1 \rho_w + L_2 \rho_s + L_3 \rho_w}{L \rho_w} \quad 6-15$$

Where ρ_w is the resistivity of the pore fluid and ρ_s is the surface resistivity of the clay particle. The numerator is the resistivity normalized length of flow. In the case of equation 6-15, the resistivity normalization may not be isotropic and thus may not cancel in the anisotropy calculation.

Therefore, the hydraulic tortuosity is not equal to the electric tortuosity. As such, a direct theoretical analogy between eq. 6-10 and eq. 6-13 is not obvious. Experiments, however, indicate that proportionally between the permeability anisotropy and conductivity anisotropy may be simpler than expected.

Figure 6-21 plots the conductivity anisotropy vs. the permeability anisotropy for measurements made on RBBC, RGoM-EI and RSFBM. It should be noted that this plot includes both conductivity anisotropy measurements made in the triaxial cell and those made using bench top measurement methods. The error band on the bench top measurements is unknown but expected to be higher than for the triaxial cell.

RBBC is the only mudrock to follow the 1:1 line, indicating that the conductivity anisotropy is a good measure of the permeability anisotropy of uniform mudrocks, with a small degree of error. Measurements on RBBC, 39% Clay RBBC, and Leached RBBC and Leached RSFBM fall within the +/- 20% error band from the 1:1 line. This means that the measured conductivity anisotropy is within 20% of the permeability anisotropy.

There are three measurements which are clear outliers to this trend: Two RGoM-EI measurements fall well outside of the 20% error band, likely due to errors encountered in the permeability measurements as discussed in Chapter 5. The permeability anisotropy of RGoM-EI is expected to be higher than measured, which would put it closer to the range of +/- 20 % of the conductivity anisotropy. Secondly one RSFBM falls very close to the 20% error band but has a very odd, nearly isotropic permeability.

For most field applications, a 20% error in permeability anisotropy is very good. This is especially true if the permeability anisotropy can be measured quickly using cost effective methods, such as offered by the electrical resistivity technique and the conductivity anisotropy. Further, because the permeability anisotropy of uniform mudrocks is expected to vary by so little, such a low error band is encouraging for the use of empirical relations vs. complex theoretical models.

The measured relationship between the conductivity anisotropy and the permeability anisotropy is only valid for the porosity and applied stress range measured for mechanically compressed mudrocks. Extrapolation of this relationship is not recommended without further research.

6.3 Extension to Layered Systems

The previous two sections of this chapter have discussed the development of permeability anisotropy, as well as the relationship between permeability anisotropy and conductivity anisotropy in uniform (non-layered) mechanically compressed mudrocks. However, the mudrocks that engineers deal with in nature are often layered or non-uniform. This section considers how the above conclusions apply to layered, non-uniform systems and how the results presented in this thesis might be applied by field engineers to study real mudrocks. The models developed in this section show that even low level permeability anisotropy of uniform mudrocks can significantly affect the permeability anisotropy of larger scale systems, and that permeability anisotropy can be estimated using resistivity anisotropy only in uniform mudrocks.

6.3.1 Permeability Anisotropy of Layered Isotropic Mudrocks

The permeability of layered systems can be computed by applying circuit concepts to hydraulic flow. For flow perpendicular to layers, analogous to a series circuit, the flow through each layer is constant and the gradient varies. For the case of flow parallel to the layers, analogous to a parallel circuit, the gradient is constant and the flow through each layer varies.

Using these concepts, the vertical permeability of a layered system is given by:

$$k_v = \frac{\sum_{i=1}^n L_i}{\sum_{i=1}^n L_i / k_{vi}} \quad 6-16$$

Where k_v is the vertical permeability of the system of i layers, L is the thickness, and k_{vi} is the vertical permeability of each individual layer.

The horizontal permeability of a layered system is given by:

$$k_H = \frac{\sum_{i=1}^n k_{Hi} L_i}{\sum_{i=1}^n L_i} \quad 6-17$$

Where k_H is the horizontal permeability of the system of i layers, L is the thickness [L], and $k_{H,i}$ is the horizontal permeability of each individual layer.

The permeability anisotropy, r_k , of a layered system is given by:

$$r_k = \frac{k_H}{k_V} = \frac{\sum_{i=1}^n k_{Hi} L_i \sum_{i=1}^n L_i / k_{Vi}}{(\sum_{i=1}^n L_i)^2} \quad 6-18$$

Equation 6-18 may be further simplified for a two-mudrock system. Consider a vertical column consisting of repeated sequences of two mudrocks with varying layer thickness, e.g. varved clay. This sequence can be reduced to an equivalent two layer system where the thickness of each mudrock layer is equal to the sum of the thicknesses of all layers of the same permeability (Figure 6-22).

Assuming isotropic intra-layer permeability ($k_{vi}=k_{Hi}$), the permeability anisotropy of a two layer system is a function of the permeability contrast (k_1/k_2) and the thickness contrast (L_1/L_2) between layers. Figure 6-23 gives the permeability anisotropy for a two layer system for permeability contrasts varying from 1 to 20. Figure 6-24 gives the same for permeability contrasts up to 100.

The maximum permeability anisotropy in a two layer system with isotropic layers is achieved when half of the mudrock has one permeability and half of the mudrock has another permeability ($L_1/L_2 = 1$). Figure 6-25 plots the permeability anisotropy as a function of the permeability contrast (k_1/k_2) for this case. For a thickness contrast of unity, a unique solution for the permeability anisotropy as a function of the permeability contrast, given by equation 6-19:

$$r_k = \frac{1}{2} + \frac{1}{4} \left(\frac{k_1}{k_2} + \frac{k_2}{k_1} \right) \quad 6-19$$

Equation 6-19 is obtained assuming a 2 layer system and by substituting $L_1=L_2$ and $k_H=k_V$ (isotropic assumption) into equation 6-18. A similar result is obtained for a 2 layer system assuming anisotropic layers by substituting $L_1=L_2$ into equation 6-18:

$$r_k = \frac{1}{4} \left[r_{k1} \left(1 + \frac{k_{v1}}{k_{v2}} \right) + r_{k2} \left(1 + \frac{k_{v2}}{k_{v1}} \right) \right] \quad 6-20$$

Where r_{k1} and r_{k2} are the permeability anisotropy of layer 1 and layer 2, respectively and k_{v1} and k_{v2} are the vertical permeability of layer 1 and layer 2, respectively.

6.3.2 Permeability Anisotropy of Layered Anisotropic Mudrocks: A Model

Natural soil systems consist of layering at various scales, from small scale seasonally-induced layers such as varved clays, to larger scales where depositional regimes change over time forming features such as interbedded shales and even large mass transport deposits such as sandstones found in the

Gulf of Mexico. Layering in itself causes permeability anisotropy due to the high permeability contrast between layers, as demonstrated in Figure 6-22. Experiments performed for this thesis show that permeability anisotropy also develops within uniform layers as a result of orientation of platy particles. These two sources of permeability anisotropy can be superimposed using equation 6-18.

An analytic model is used to simulate the development of permeability anisotropy in a compressing layered system. This model combines three key concepts which contribute to the development of anisotropy in layered systems. First, different layers compress at different rates dependent on their unique compression behaviour. Second, changes in mudrock permeability with compression vary for different layers. Third, the development of permeability anisotropy will vary for different layers and is linked to varying layer compression.

Figure 6-26 gives a schematic of a compressing layered system. As the stress increases, each layer compresses differentially because each mudrock has a different compression curve. Similarly, the vertical permeability of each layer decreases at a different rate. Through knowledge of the permeability anisotropy, the horizontal permeability can also be modelled.

A geologically realistic system of a silt rich mudrock layered with a clay rich mudrock is simulated by layering RBBC (silt rich) and RGoM-EI (clay rich) analogue mudrocks. Two constant rate of strain (CRS) measurements of the compressibility and vertical permeability were obtained for RBBC and RGoM-EI from Aiden Horan and Brian Fahy, respectively. The RBBC CRS curve is compared with the cubic specimen measurements in Chapter 5. Figure 6-27 plots the compression curve in void ratio space for RBBC and RGoM-EI. Figure 6-28 gives the same in porosity space, and Figure 6-30 gives the vertical permeability in porosity space for RBBC and RGoM-EI; the permeability curve is plotted in porosity space because it provides a straighter relation. Table 6-6 summaries the relevant engineering parameters including the void ratio (e_o) and permeability (k_o) at a reference stress level of 0.1 MPa, the compression index (c_c), the swelling index (c_s), and the permeability index (c_{km}) in porosity space for RBBC, RGoM-EI. Data were also available for 39% Clay RBBC and are included in this table for reference purposes.

The model initially begins at 0.1 MPa with equal layer thicknesses of each RBBC and RGoM-EI. This initial condition is arbitrarily set. As the stress increases, each layer compresses based on parameters describing the compression curve.

Chapter 5 presents the compression curves for all mudrocks studied in both void ratio and porosity space and notes that higher plasticity mudrocks (such as RSFBM and RGoM-EI) may behave more linearly in porosity vs. log stress space.

As a result, two equations are developed to model mudrock compression. The first equation computes the void ratio as a function of effective stress (eq. 6-21). This equation is developed for low plasticity mudrocks using the compression indices defined in void ratio space (compression index c_{ce} and swelling index c_{se}). The second equation computes the porosity as a function of

effective stress (eq. 6-22). This equation is developed for high plasticity mudrocks using the compression indices defined in porosity space (compression index c_{cn} and swelling index c_{sn}). Both equations are functions of OCR.

$$e = 1.0 - c_c [\log(\sigma'_p) - \log(\sigma'_o)] + c_s \left[\log\left(\frac{\sigma'_p}{OCR}\right) - \log(\sigma'_p) \right] \quad 6-21$$

$$n = 0.5 - c_{cn} [\log(\sigma'_p) - \log(\sigma'_o)] + c_{sn} \left[\log\left(\frac{\sigma'_p}{OCR}\right) - \log(\sigma'_p) \right] \quad 6-22$$

$$e = \frac{n}{(1-n)} \quad 6-23$$

$$n = \frac{e}{(1+e)} \quad 6-24$$

Both equations 6-21 and 6-22 use a stress intercept σ'_o defined at a fixed porosity of 0.5, equal to void ratio 1.0. The slope of the virgin compression line compression curve is defined by the compression index c_{ce} in void ratio space, and c_{cn} in porosity space. Similarly, the slope of the swelling line is defined by the swelling index c_{se} in void ratio space or c_{sn} in porosity space. The final stress level is defined using the maximum effective stress σ'_p and the OCR. Figure 6-29 illustrates these parameters graphically for RBBC in void ratio space.

The void ratio computed using eq. 6-21 can be converted to porosity using eq. 6-24; similarly the porosity computed using eq. 6-22 can be converted to void ratio using eq. 6-23. Finally, the strain (ϵ_v) is a function of the current (e) and initial (e_o) void ratio:

$$\epsilon_v = \frac{\Delta e}{(1+e_o)} \quad 6-25$$

The following equations are derived only in terms of porosity, n . This is done to match the standard presentation of the relevant data.

The slope of the permeability curve is used to model changes in vertical permeability as a function of porosity using equation 6-26:

$$k_{v,n} = k_{v,n_o} / 10^{c_k(n-0.5)} \quad 6-26$$

Where k_{v,n_o} is the permeability at the fixed porosity of 0.5 (corresponds to e_o 1.0), k is the permeability at the current porosity n , and c_k is the slope of the log permeability vs. porosity curve. Figure 6-31 graphically illustrates these parameters.

The permeability anisotropy is computed using intercept and the slope of the permeability anisotropy – porosity curve dr_k/dn . Figure 6-32 graphically illustrates these parameters that were determined experimentally in Chapter 5. Similar to the compression and permeability parameters, the intercept is defined as the permeability anisotropy at a porosity of 0.5 or void ratio of 1.0:

$$r_{k,n} = \frac{dr_k}{dn}(n - 0.5) + r_{k0} \quad 6-27$$

Finally, the permeability anisotropy is then used to compute the horizontal permeability:

$$k_H = r_{k,n}k_{v,n} \quad 6-28$$

I present the model for normally compressed mudrocks (OCR 1). The model simulates a box view that initially contains 10 layers of interbedded RBBC and RGoM-EI with an initial layer thickness equal to 0.5 cm at 0.1 MPa effective stress. The box view is therefore 5 cm tall. The width of this box view is irrelevant for the model computations and behaviour.

The model has two key simplifying assumptions:

1. The compression indices C_c and C_s are stress independent
2. Vertical permeability and permeability anisotropy are dependent only on porosity and not OCR except through the indirect linkage between OCR and porosity.

Figure 6-33 is a screen shot of the Model programmed in Microsoft Excel that computes the anisotropy of a compressing layered system of RBBC and RGoM-EI. Table 6-7 summarizes key model outcomes.

As the layered system compresses, the different compression characteristics cause the layer thicknesses to decrease at different rates. The RBBC layers compress less than the RGoM-EI layer. As the stress increases more layers fit within the 5 cm box size. At 10 MPa there are 15.6 layers in the box view vs. the original 10 layers. At 0.1 MPa, the layer thickness is set to be uniform at 0.5 cm. With compression from this point to 10 MPa, the RBBC layers are reduced to 0.350 cm thick, whereas the more compressible RGoM-EI layers are now only 0.292 cm thick. This thickness disparity affects the permeability anisotropy development; as was seen in Section 6.3.1, the maximum permeability anisotropy occurs when the thickness contrast is unity.

If the layers are considered isotropic, as evaluated in Section 6.3.1, the system anisotropy increases from 1.8 to 20.8 as the stress increases from 0.1 to 10 MPa (Figure 6-34 and Table 6-7). The permeability anisotropy increase is non-linear because of differential layer compression. In contrast, if each uniform layer is assumed to be independently anisotropic, the permeability anisotropy of the system is higher at all stress levels, increasing from 1.9 to 40.6 over the same stress range. Again, the permeability anisotropy increase is non-linear because of differential layer compression.

These results indicate two key findings. First, the permeability anisotropy of a layered system is higher when each individual, uniform layer has anisotropic permeability. By assuming that the individual layers are isotropic, the permeability anisotropy of the system may be significantly underestimated.

Second, the permeability anisotropy of an anisotropic layered system is not equal to either the sum of or the multiple of the two component anisotropies: the uniform layer anisotropy, and the anisotropy due to layering. For example, at 10 MPa the system permeability anisotropy is 20.8 assuming isotropic layers and 40.6 assuming anisotropic layers. The RBBC layer has permeability anisotropy 1.95 and the RGoM-EI has permeability anisotropy 2.41. The average layer permeability anisotropy is 2.2. The system permeability anisotropy with anisotropic layers (40.6) is greater than the permeability anisotropy generated by layering isotropic layers plus the average layer permeability anisotropy (20.8 + 2.2 = 23.0), and is lower than the multiple of these two values (20.8 * 2.2 = 45.8). This complexity is introduced because each layer has unique compression characteristics which in turn define the thickness contrast between layers and control the layer porosity which in turn dictates the layer permeability characteristics. Therefore, the unique behaviour of individual layers adds complexity to the system behaviour. The permeability of layered systems and should be carefully considered.

6.3.3 Conductivity Anisotropy of Layered Anisotropic Mudrocks: A Model

In a similar manner as was done for the permeability anisotropy, the conductivity anisotropy of layered systems can also be computed using variations of equations 6-16 to 6-18. The equations are essentially the same when formulated in terms of electrical conductivity (σ), and are the inverse when in formulated in terms of either the electrical resistivity (ρ) or formation factor (F).

The vertical conductivity, resistivity and formation factor of a layered system are given by:

$$\sigma_V = \frac{\sum_{i=1}^n L_i}{\sum_{i=1}^n L_i / \sigma_{Vi}} \quad 6-29$$

$$\rho_V = \frac{\sum_{i=1}^n \rho_{Vi} L_i}{\sum_{i=1}^n L_i} \quad 6-30$$

$$F_V = \frac{\sum_{i=1}^n F_{Vi} L_i}{\sum_{i=1}^n L_i} \quad 6-31$$

Where σ_v , ρ_v , and F_v are the vertical electrical conductivity, resistivity and formation factor of the system of i layers, respectively, L is the thickness, and σ_{vi} , ρ_{vi} , and F_v are the vertical conductivity, resistivity and formation factor of each individual layer, respectively.

Similarly, the horizontal conductivity, resistivity and formation factor of a layered system are given by:

$$\sigma_H = \frac{\sum_{i=1}^n \sigma_{Hi} L_i}{\sum_{i=1}^n L_i} \quad 6-32$$

$$\rho_H = \frac{\sum_{i=1}^n L_i}{\sum_{i=1}^n L_i / \rho_{Hi}} \quad 6-33$$

$$F_H = \frac{\sum_{i=1}^n L_i}{\sum_{i=1}^n L_i / F_{Hi}} \quad 6-34$$

Where σ_H , ρ_H , and F_H are the horizontal electrical conductivity, resistivity and formation factor of the system of i layers, respectively, L is the thickness, and σ_{Hi} , ρ_{Hi} , and F_{Hi} are the horizontal conductivity, resistivity and formation factor of each individual layer, respectively.

Finally, the conductivity anisotropy, r_σ , of a layered system in terms of formation factor is given by:

$$r_\sigma = \frac{F_V}{F_H} = \frac{\sum_{i=1}^n F_{Vi} L_i \sum_{i=1}^n L_i / F_{Hi}}{(\sum_{i=1}^n L_i)^2} \quad 6-35$$

The model is extended using the above equations to investigate the agreement between the permeability anisotropy and the conductivity anisotropy for layered mudrocks. The vertical and horizontal formation factors are computed using equation 6-9.

Due to the limited resistivity data that was measured in the triaxial cell spanning different mudrocks, the model computes the anisotropy of interbedded normally compressed (OCR 1) RBBC. Each layer is compressed to different maximum effective stress, as shown in Figure 6-35, to mathematically simulate realistic permeability and formation factor contrasts between layers. Although geologically unrealistic, this model is a mathematical trick that produces a layered system with geologically realistic material property contrasts between layers.

Three scenarios are considered:

1. Case A (Uniform case) layers only 10 MPa RBBC;
2. Case B (Intermediate case) layers RBBC compressed to 10 MPa effective stress with RBBC compressed to 1 MPa effective stress; and
3. Case C (Maximum case) layers RBBC c

The above model cases use RBBC with well-defined compression, permeability and resistivity trends to achieve realistic porosity, permeability and formation factor contrasts between layers. This method contrasts the model described in Section 6.3.2 which layers RBBC and RGoM-EI to achieve a system with different layer properties.

Figure 6-36 is a screen shot of the model in Microsoft Excel adapted to compute the permeability for each scenario described in Figure 6-35. The permeability anisotropy vs. layering scenario is graphed in Figure 6-37. For the isotropic case ($k_v=k_H$ in each layer) the permeability anisotropy increases from 1 in the uniform case to as high as 18.7 when RBBC at 10 MPa is layered with RBBC at 0.1 MPa with a thickness contrast of unity. If the layers are assumed to be ideally isotropic ($k_H = r_k * k_v$ in each layer) the maximum permeability anisotropy increases marginally to 19.6. In this case, the individual layer permeability anisotropy does not significantly increase the permeability anisotropy of the system because of the unrealistic porosity contrast between layers for the selected scenarios.

Next, the model is modified to compute the conductivity anisotropy for each layering scenario. Formation factor is used in place of permeability to compute the conductivity anisotropy of the layered system. Formation factor is chosen over resistivity because the formation factor is independent of pore fluid salinity. Further, the Archie parameters have previously been defined for RBBC (Table 6-5 and Figure 6-18).

Figure 6-38 gives a screen shot of the model modified to predict the conductivity anisotropy for each layered mudrock described in Figure 6-35. The conductivity anisotropy (inverse of resistivity anisotropy) vs. layering scenario is graphed in Figure 6-39 . For the isotropic case ($F_v=F_H$ in each layer) the conductivity anisotropy increases from 1 in the uniform case to 1.6 when RBBC at 10 MPa is layered with RBBC at 0.1 MPa with a thickness contrast of unity. If the layers are assumed to be ideally isotropic ($F_H = r_\sigma * F_v$ in each layer) the permeability anisotropy of the layered mudrock system is nearly constant ~ 2 .

Table 6-8 summarizes the permeability, apparent formation factor, permeability anisotropy and conductivity anisotropy for RBBC using this model.

The model yields interesting results relating to how conductivity and permeability anisotropy develop in layered mudrocks.

The permeability and conductivity anisotropy do not follow similar trends despite being computed using similar equations (Figure 6-40). As the stress level in the second layer decreases, increasing the permeability contrast between layers, the permeability anisotropy of the system increases (Table 6-8). This is true whether the uniform layers are assumed to be isotropic or anisotropic. The permeability anisotropy varies significantly, ranging from 1 in the uniform isotropic case to as high as 19, and is lowest when the two layers have the same stress level and porosity.

The conductivity anisotropy behaves very differently. Most noticeably, it does not vary nearly as much as the permeability anisotropy, ranging only from 1.0 to 1.6 for isotropic layers and being relatively constant ~ 2 for anisotropic layers. For isotropic layers, the conductivity is isotropic for the uniform mudrock as expected and increases as the stress level decreases in the second layer. However, Table 6-8 and Figure 6-40 reveal that the conductivity anisotropy of the layered system

neither increases nor decreases monotonically as the stress level of the second layer decreases. This is due to the fact that the formation factor varies only slightly with porosity whereas the permeability varies significantly. The conductivity anisotropy of the uniform mudrock (both layers compressed to 10 MPa) is correctly predicted to equal that measured by the experiments (2.22).

The key observation from Figure 6-40 and Table 6-8 is that the permeability anisotropy is only equal (within +/- 20%, as predicted in Figure 6-21) to the conductivity anisotropy for the special case of a uniform mudrock. As soon as layering develops, the conductivity anisotropy diverges from the permeability anisotropy. This result was also reported by Georgi et al (2011). This divergence is due to the difference between the permeability and the formation factor values. The permeability varies logarithmically with porosity and can span orders of magnitude while the formation factor of the same mudrock varies only slightly. For RBBC, the permeability varies from $\sim 1.4 \times 10^{-16} \text{ m}^2$ at 0.1 MPa to between $2 \times 10^{-18} \text{ m}^2$ and $4 \times 10^{-18} \text{ m}^2$, depending on direction, at 10 MPa. The apparent formation factor varies from $\sim 2 \text{ } \Omega\text{m}$ at 0.1 MPa to between 4 and 8.5 at 10 MPa. A large permeability variation translates to only a very small variation in apparent formation factor.

The formation factor used in these correlations is the apparent formation factor and is uncorrected for the effects of clay surface conductivity. Applying this correction would be time and energy intensive at best, if the correct methods could be identified. Still, application of this correction factor would not significantly increase the formation factor or significantly alter the variation in formation factor with porosity to be more similar to the variation in permeability with porosity. Therefore, the use of apparent formation factor in this analysis is appropriate.

To cause the permeability anisotropy and conductivity anisotropy of a layered system to be more similar, the variation in permeability and resistivity must be similar over the same porosity range. The chart produced in the isotropic case analysis (Figure 6-23) showed that permeability anisotropy increases with increasing permeability contrast (k_1/k_2) between layers. This figure also showed that maximum permeability anisotropy occurs when the layer thickness ratios are near unity ($l_1 \sim l_2$), as is the case for these simulations. In this model the contrast in horizontal permeability is high between layers, varying from 1 to >10 with increasing stress level while the formation factor contrast varies only by a factor of 1 to 2 with stress level. Horizontal fluid flow dominates one layer where horizontal electric current flow is more evenly portioned between layers (Figure 6-41), mimicking a uniform mudrock despite significant differences in layer properties. Including the anisotropy of the individual layers based on the laboratory results increases increasing the net horizontal permeabilities thus increasing the permeability anisotropy of the system. In the case of electrical conductivity, the contrast in formation factor between layers is small making the layered mudrock appear uniform in terms of formation factor. Including the anisotropy of individual layers cannot change this fact, since both layers will have nearly equal anisotropy and the formation factor contrast will not change significantly.

This disparity between the variation in permeability (~ 2 orders of magnitude) and formation factor (factor of 3) with decreasing porosity and increasing effective stress is also cited as a main reason for the lack of useful correlation between the formation factor and the permeability of sands

and mudrocks. Such correlation would require site specific calibration of the permeability – porosity and formation factor – porosity relation. Even if such a site specific calibration were performed, Huntley (1986) shows that the relation between hydraulic conductivity and formation factor for a uniform clean sand materials is sufficiently steep to render it useless (Figure 2-20).

6.4 Summary and Field Extension

The previous sections have discussed the development of permeability anisotropy, the range of permeability anisotropy expected from uniform mudrocks, the link between the electrical conductivity anisotropy and the permeability anisotropy, and how the results might be extended to layered mudrocks that are accounted in nature.

First, the permeability anisotropy of mechanically compressed uniform mudrocks is not expected to be high, and will be limited to the range of 1-2 or 3 depending on the mudrock. Particle orientation drives permeability anisotropy development to a point beyond which changes in fabric structure are noted to correspond with significant decreases in permeability anisotropy.

There are many analogies linking fluid and electrical current flow in mudrocks. Using these analogies, one can see that both the permeability anisotropy and electrical resistivity anisotropy are governed by many of the same physical factors and thus should be related in some predictable way.

Such a predictable trend between the two quantities was measured in the laboratory using uniform specimens. The conductivity anisotropy is equal to +/- 20% of the permeability anisotropy for six studied mudrocks. This can be useful knowledge for field engineers because downhole measurements of the conductivity anisotropy can yield good estimates of the mudrock permeability anisotropy. These data can in turn be used for input into basin models and engineering calculations.

However, the analysis of the permeability anisotropy and conductivity anisotropy of layered systems from a theoretical point of view has shed light on two very important realities. First, permeability anisotropy in layered systems develops as a combined effect of 1) the permeability anisotropy of individual uniform layers, and 2) the layering of uniform anisotropy units. The latter causes much more substantial permeability anisotropy development when the layered units have high permeability contrast. Experimental results show that the permeability anisotropy of uniform mudrocks is relatively low, in the range of 1 – 2 or potentially 1 – 3 depending on electrical predictions. As a result, the difference in permeability anisotropy that results from assuming a layered system is comprised of anisotropic vs. isotropic layers is minimal.

Further, for layered systems, the relationship between the permeability anisotropy and the conductivity anisotropy no longer holds. The permeability contrast between layers may be very high, but the corresponding resistivity contrast is significantly lower, leading to a large discrepancy between the theoretical conductivity anisotropy and permeability anisotropy. This result should be further confirmed using field data.

Nevertheless, all is not lost. Downhole electrical resistivity and resistivity anisotropy measurements (the inverse of conductivity anisotropy) are made continuously at short depth intervals. The uniform mudrock assumption may in fact hold true for many of the mudrocks studied in the field, making the relationship between conductivity anisotropy and permeability anisotropy useful in many cases. This relationship is even more useful because it is based on measured data that is uncorrected for clay surface conductivity. This means that complex measurements of clay surface conductivity and pore fluid chemistry are not required. In fact, the error bar on this relationship shown in Figure 6-21 is likely less than the error associated with making all the required measurements to correct the data set. Therefore, the relationships measured in this work remain a useful result when carefully applied.

Table 6-1: Summary of 1D Particle Orientation Analysis for RBBC

Maximum Effective Stress, σ'_p	Porosity, n	Axial Strain, ϵ_v^1	Orientation ²	Line Length ²	Number of Measurements
MPa			degrees	μm	
1D Analysis - Cheong - UT Images - Combined data from 3 images					
0.1	0.57	0.38	50+/-24	0.9+/-0.6	1845
1	0.45	0.52	39+/-24	1.1+/-0.7	1211
10	0.35	0.59	28+/-21	1.0+/-0.6	2052
1D Analysis - Durant - MIT Images - Combined data from 2 images					
1	0.46	0.51	34+/-24	0.9+/-0.7	1442
10	0.37	0.58	33+/-23	0.8+/-0.8	1658
40	0.30	0.62	30+/-24	0.7+/-0.6	1256

Note:

1. For 1D compression, axial strain is equal to volumetric strain.
2. Reported as the mean +/- 1 standard deviation.

Table 6-2: Clay and Silt Porosities for RBBC and 39% Clay RBBC

n	RBBC		39% Clay RBBC	
	n _{silt}	n _{clay}	n _{silt}	n _{clay}
0.75	0.88	0.85	0.85	0.88
0.70	0.86	0.81	0.82	0.86
0.65	0.84	0.78	0.79	0.83
0.60	0.81	0.74	0.76	0.79
0.55	0.79	0.70	0.73	0.76
0.50	0.77	0.65	0.70	0.72
0.45	0.74	0.61	0.66	0.68
0.40	0.72	0.56	0.63	0.63
0.38	0.71	0.54	0.62	0.61
0.36	0.70	0.51	0.61	0.59
0.34	0.69	0.49	0.60	0.57
0.32	0.68	0.47	0.60	0.57
0.30	0.67	0.45	0.60	0.57

Table 6-3: Permeability and Resistivity Equation Analogies

Permeability (Hydraulic Property)	Resistivity (Electrical Property)
Hydraulic Conductivity: $K = \frac{Q}{iA}$	Conductivity: $\sigma = \frac{1}{\rho}$
Hydraulic Resistivity: not really used, 1/K	Resistivity: $\rho = \frac{RA}{L}$
Permeability: $k = \frac{K\mu}{pg}$	Formation Factor: $F_a = \frac{\rho_r}{\rho_w}$
Kozeny Carmen: $k = \frac{n^3}{v\tau^2(1-n)^2G_s^2S_a^2}$	Archie's Law: $\rho = \frac{a \rho_w}{n^m S_w^N}$
Anisotropy of conductive elements: $r_k = \frac{K_H}{K_V} = \frac{k_H}{k_V}$	Anisotropy of conductive elements: $r_\sigma = \frac{1}{r_\rho} = \frac{\sigma_H}{\sigma_V} = \frac{\rho_V}{\rho_H}$
Anisotropy model analogy: $r_k = \frac{\left(\frac{n^3}{v\tau^2(1-n)^2G_s^2S_a^2}\right)_H}{\left(\frac{n^3}{v\tau^2(1-n)^2G_s^2S_a^2}\right)_V} = \frac{\tau_V^2}{\tau_H^2}$	Anisotropy model analogy: $r_\sigma = \frac{\left(\frac{a \rho_w}{n^m S_w^N}\right)_V}{\left(\frac{a \rho_w}{n^m S_w^N}\right)_H} = \frac{a_V}{a_H} n^{m_H - m_V} = a_\sigma n^{m_\sigma}$
<p>Symbol Legend: K: Hydraulic conductivity k: permeability Q: volumetric flow rate i: hydraulic gradient A: area of flow μ: dynamic viscosity ρ: mass density of fluid g: gravitational constant n: porosity v: tortuosity factor τ: flow tortuosity G_s: specific gravity S_a: specific surface area r_k: permeability anisotropy and the subscript V or H denotes direction</p>	<p>Symbol Legend: ρ: resistivity (ρ_w: fluid resistivity, ρ_r: rock resistivity) σ: conductivity R: resistance A: area L: length F_a: apparent formation factor a: tortuosity parameter m: cementation exponent N: saturation exponent S_w: water saturation r_ρ: resistivity anisotropy r_σ: conductivity anisotropy and the subscript V or H denotes direction</p>

Table 6-4: Formation factor as a function of a and m using literature bounds

m=	1.8	1.8	2.2	2.2	3	3
a=	0.5	1.5	0.5	1.5	0.5	1.5
Porosity	Formation Factor					
0.5	1.7	5.2	2.3	6.9	4.0	12.0
0.3	4.4	13.1	7.1	21.2	18.5	55.6

Table 6-5: Archie parameters for RBBC

	a	m
Horizontal (H)	0.70	1.58
Vertical (V)	0.32	3.06
Anisotropy (σ) Computed	0.46	-1.48
Anisotropy (σ) Measured	0.46	-1.48

Table 6-6: RGoM-EI and RBBC compression and permeability parameters for layered permeability anisotropy and resistivity models

Parameter	RBBC (Silt Rich Analogue)	RGoM-EI (Clay Rich Analogue)	Source
σ_o (@ n = 0.5) (MPa)	0.342	0.309	CRS
c_{c-e} space	0.325		CRS
c_{s-e} space	0.028		CRS
c_{c-n} space		0.152	CRS
c_{s-n} space		0.040	CRS
k_{vo} (@ n = 0.5)	6.15E-17	5.20E-18	CRS
c_{kn}	9.47	10.12	CRS
$r_k = r_\sigma$ (@ n = 0.5)	1.23	1.23	Cubic specimens
dr_k/dn	-4.63	-4.63	Cubic specimens
a_v	0.32	N/A	Cubic specimens
m_v	3.06	N/A	Cubic specimens

Notes:

- 1) Permeability anisotropy data (r_k @ e_o (OCR 4) and dr_k/dn) for RGoM-EI assumed equal to that of RBBC based on similarity in conductivity anisotropy trend.
- 2) Conductivity anisotropy trend assumed equal to permeability anisotropy trend based on experimental results.

Table 6-7: Compressing layer permeability anisotropy model results summary for layered RBBC and RGoM-EI at OCR 1

Stress (MPa)	# Layers in Box	Layer Thickness Contrast (RBBC : RGoM-EI)	System Permeability Anisotropy	
			Isotropic Layers	Anisotropic Layers
0.1	10.0	1.000	1.8	1.9
1	12.6	1.154	7.8	11.1
10	15.6	1.201	20.8	40.6

Table 6-8: Comparison of permeability and resistivity for a layered RBBC at OCR 1 with thickness contrast of unity

Maximum Effective Stress (MPa)		Permeability (m ²)			Formation Factor			r _k /r _σ
Layer 1	Layer 2	k _H	k _V	r _k	F _H	F _V	r _σ	
Isotropic layer permeability								
10	10	2.02E-18	2.02E-18	1.00	8.42	8.42	1.00	1.00
10	1	1.36E-17	3.75E-18	3.63	4.91	5.94	1.21	3.00
10	0	7.45E-17	3.99E-18	18.66	3.37	5.26	1.56	11.96
Anisotropic layer permeability								
10	10	3.95E-18	2.02E-18	1.95	4.32	8.42	1.95	1.00
10	1	1.98E-17	3.75E-18	5.28	3.13	5.94	1.90	2.78
10	0	7.84E-17	3.99E-18	19.64	2.76	5.26	1.91	10.30

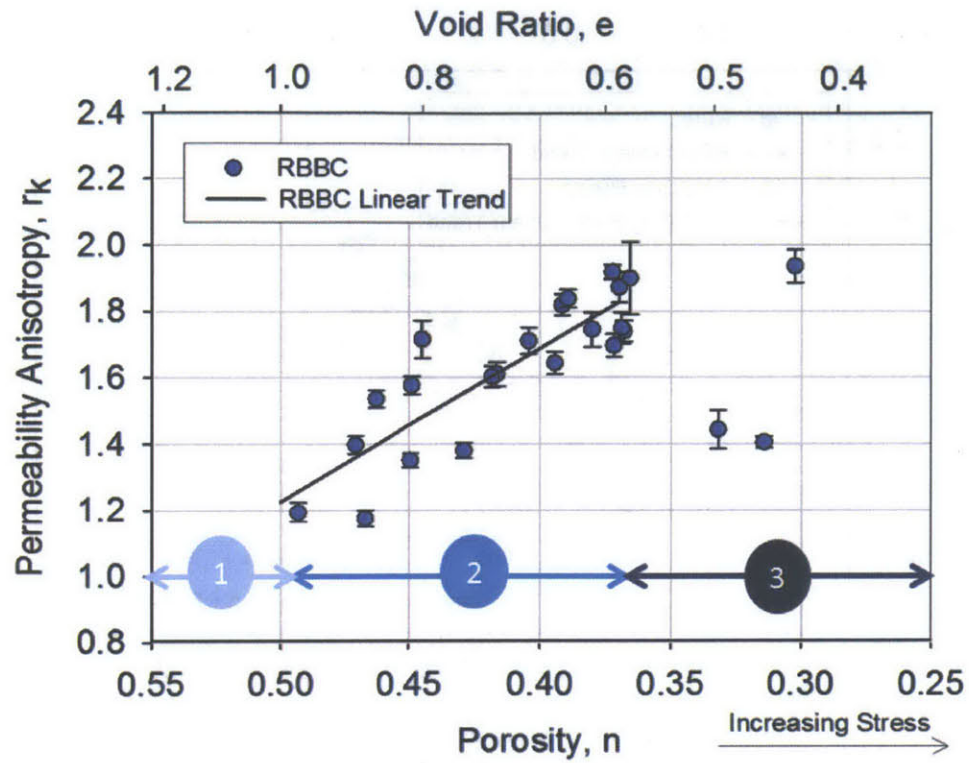


Figure 6-1: Three zones of distinct permeability anisotropy behaviour noted RBBC are related to different deformation mechanisms

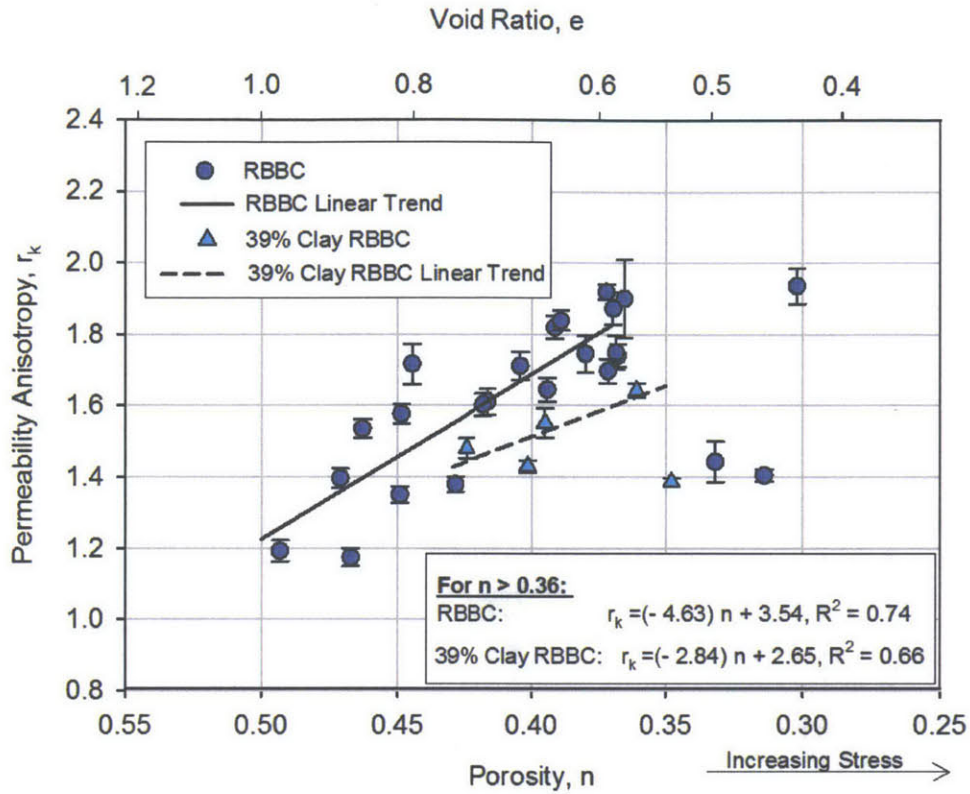


Figure 6-2: Permeability anisotropy vs. porosity for RBBC and 39% Clay RBBC

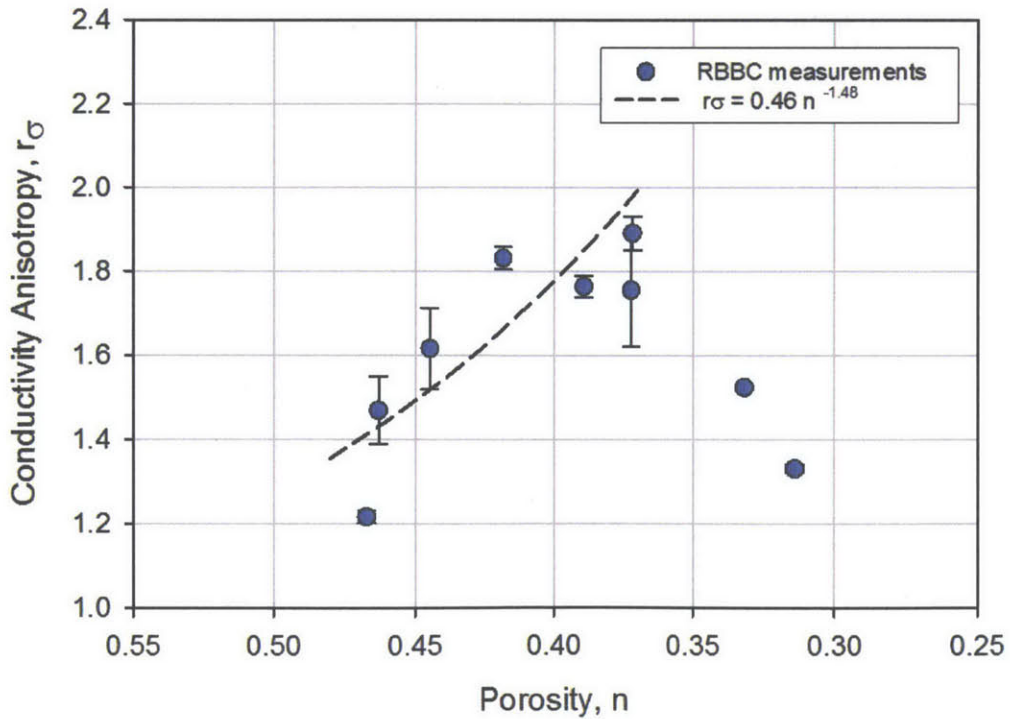


Figure 6-3: Conductivity anisotropy vs. porosity for RBBC

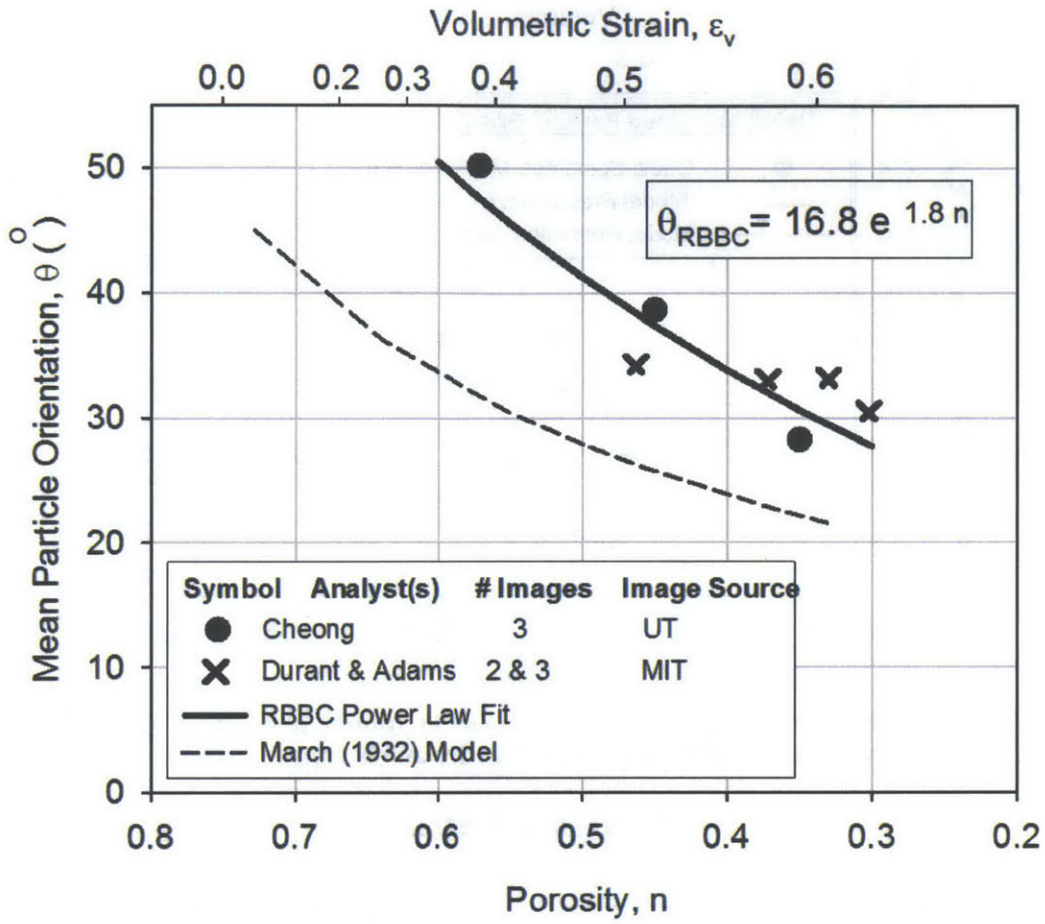


Figure 6-4: Particle Orientation for RBBC prepared at MIT compared with March 1932 Model

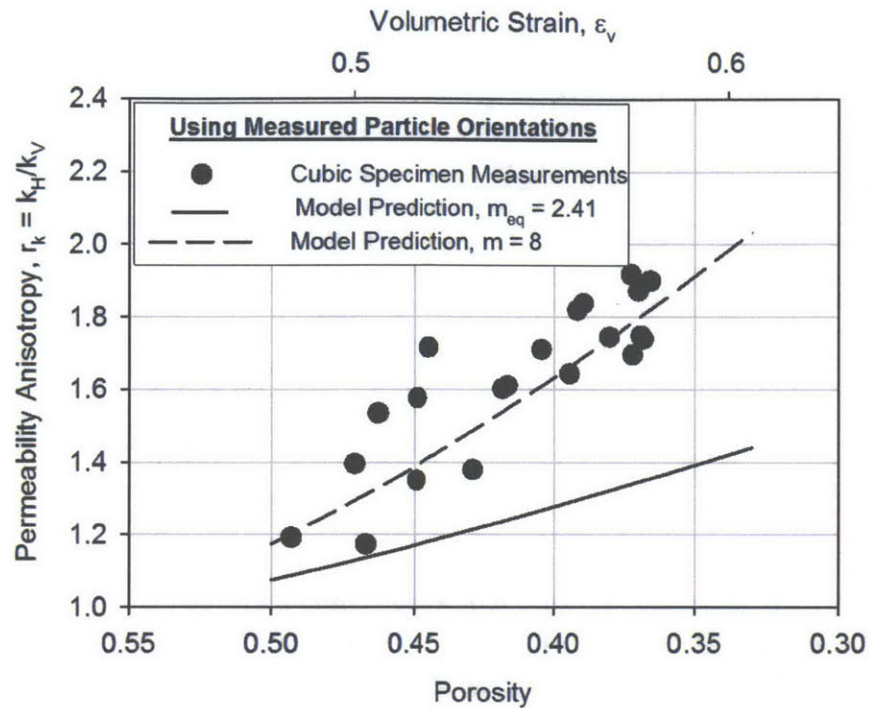


Figure 6-5: Comparison of Daigle and Dugan (2011) model prediction using measured particle orientation with measured RBBC permeability anisotropy

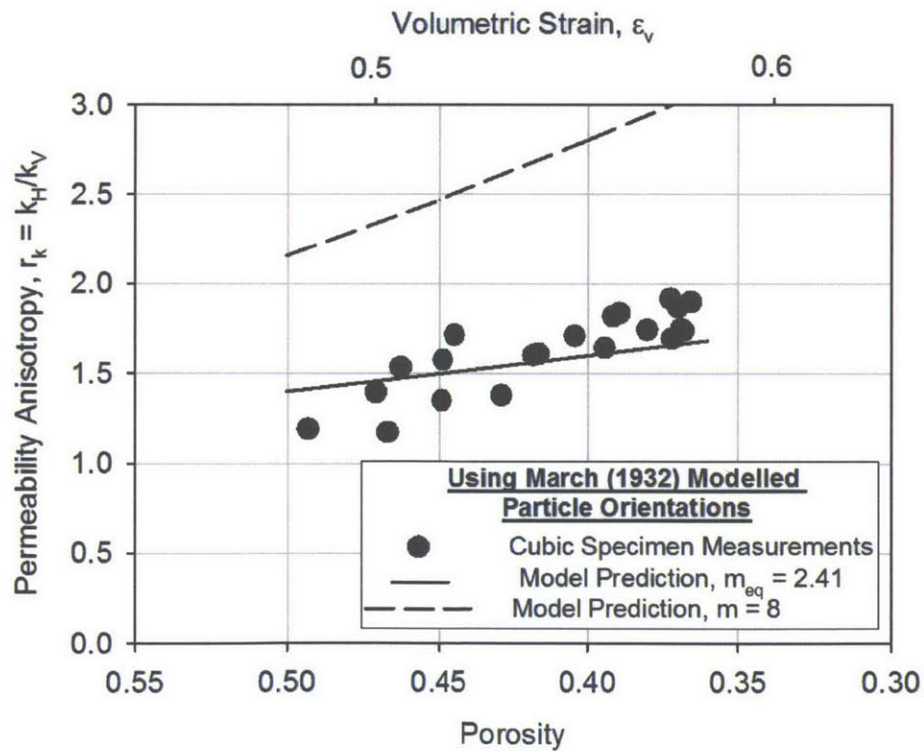


Figure 6-6: Comparison of Daigle and Dugan (2011) model prediction computed using March (1932) modelled particle orientation with measured RBBC permeability anisotropy

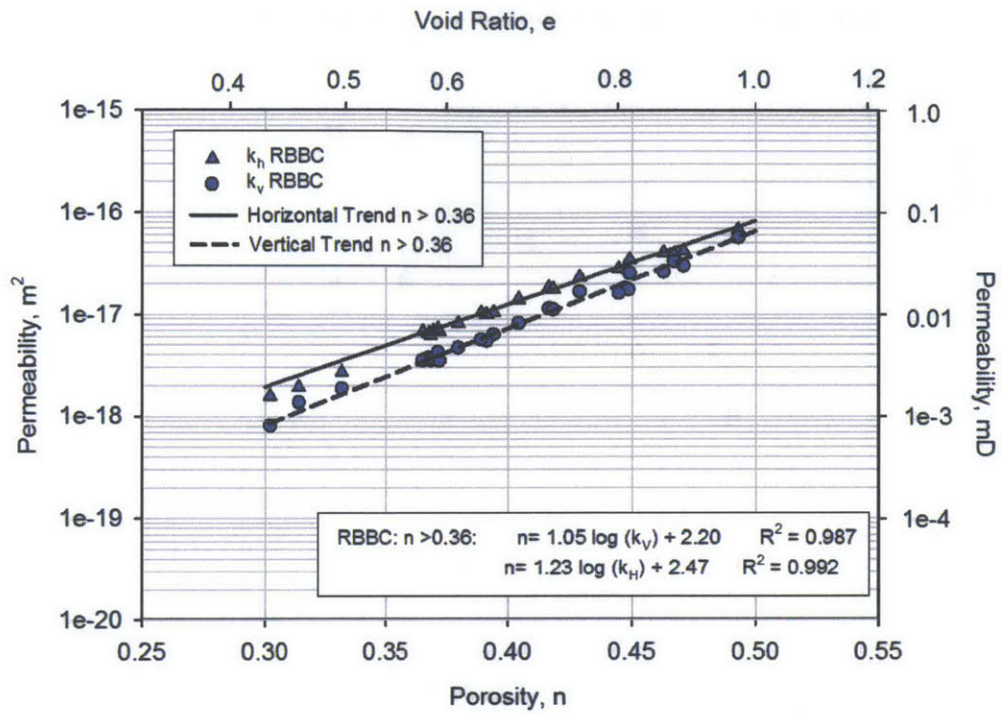


Figure 6-7: Permeability vs. porosity with trend lines for RBBC

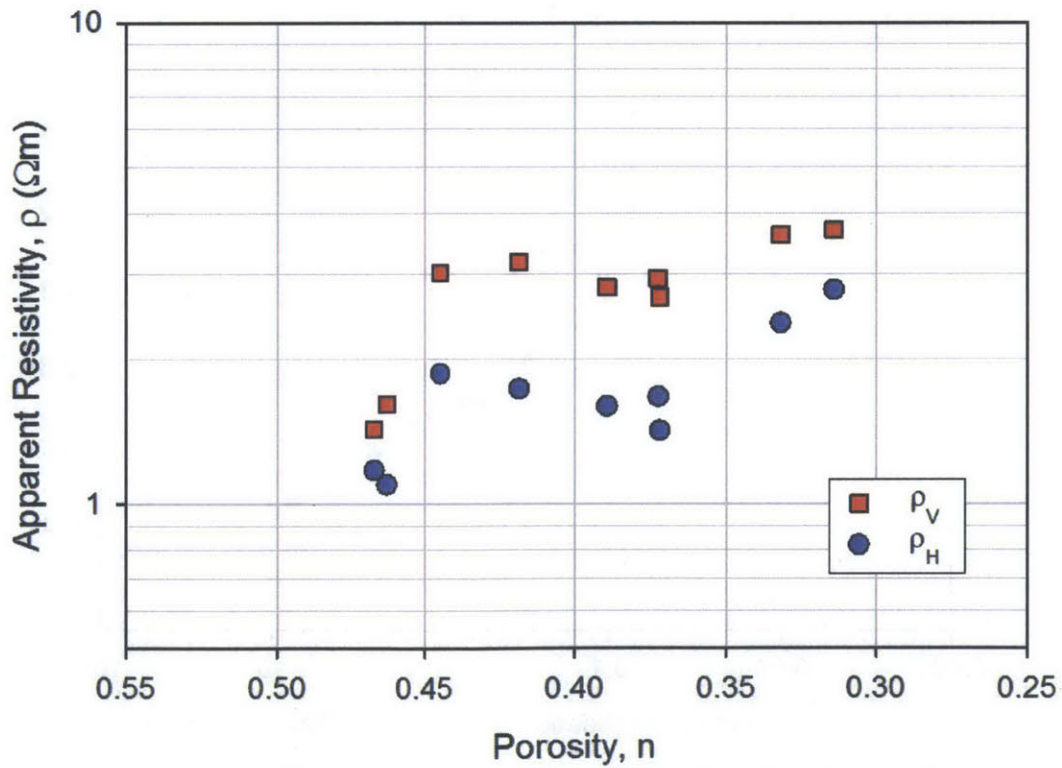


Figure 6-8: Resistivity vs. porosity for RBBC

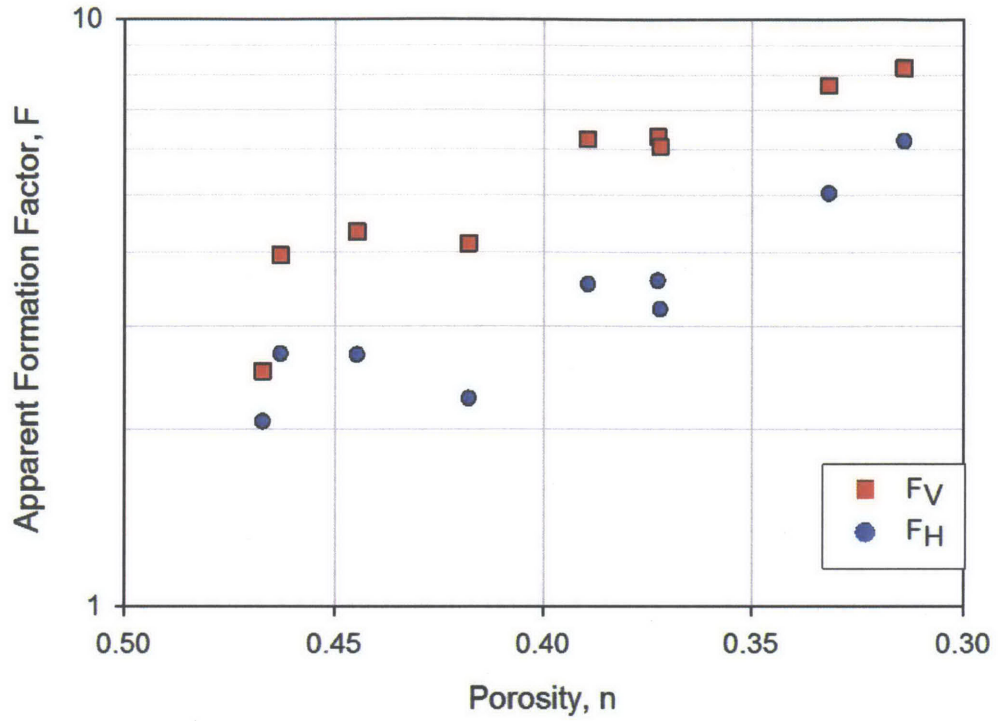


Figure 6-9: Formation factor vs. porosity for RBBC

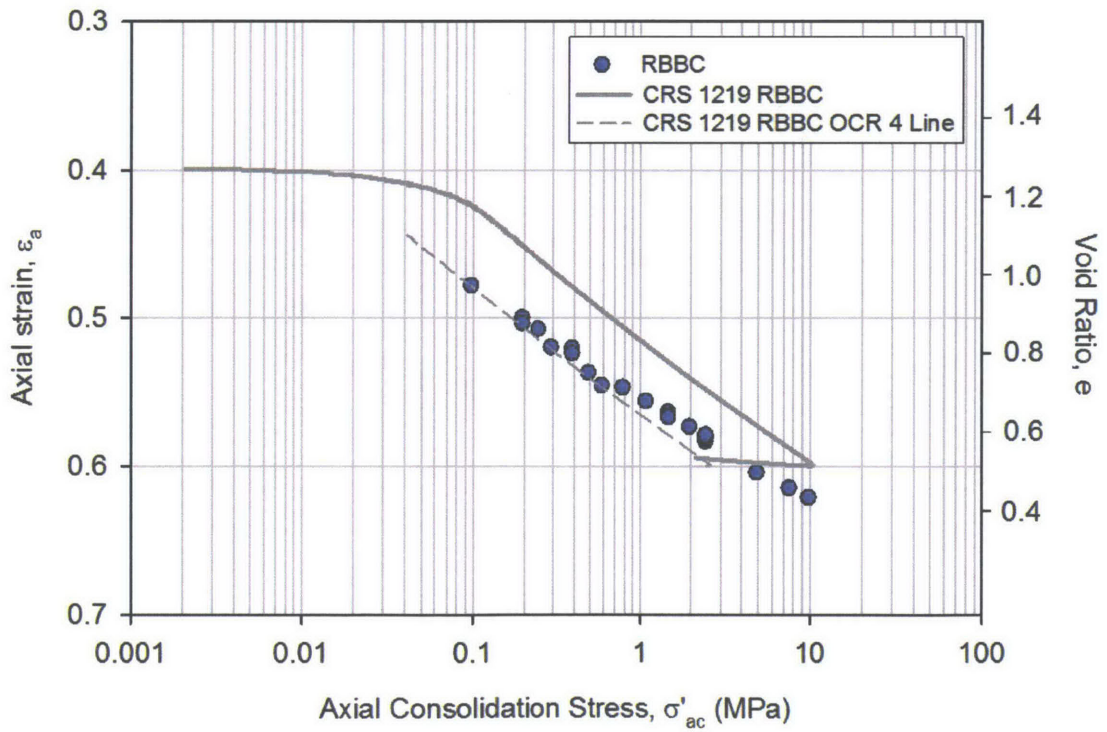


Figure 6-10: Axial strain vs. log of axial consolidation stress for RBBC

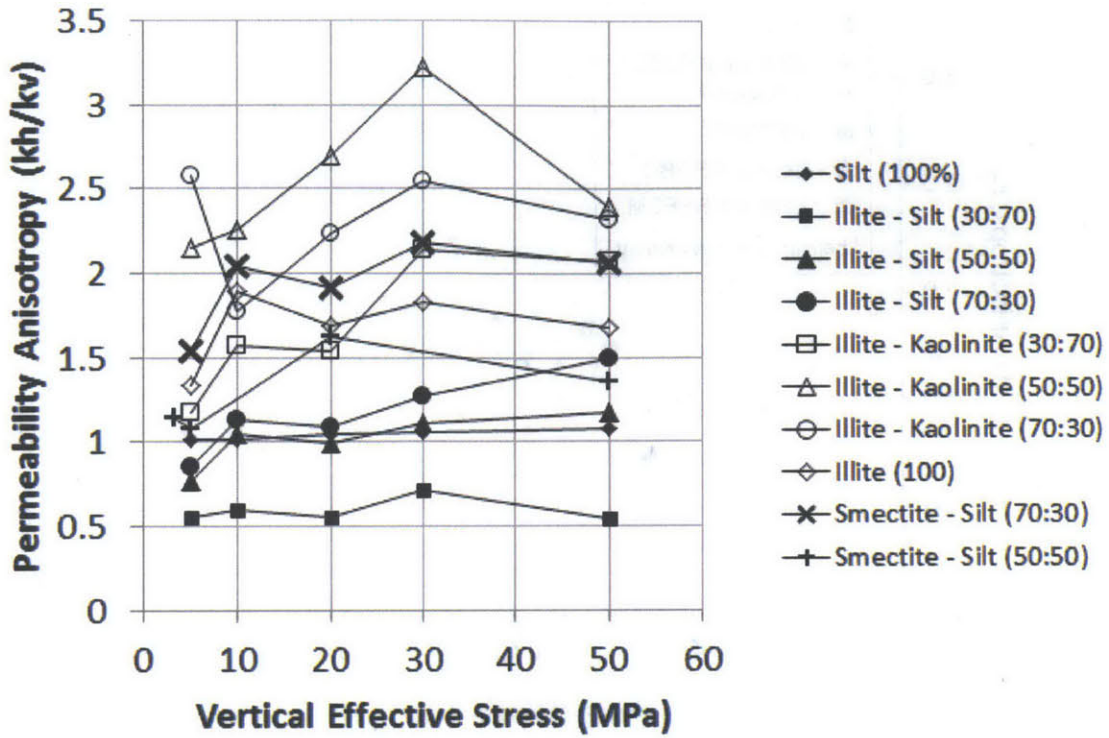


Figure 6-11: Permeability anisotropy vs. vertical effective stress for various mudrocks (Grande and Mondol, 2013)

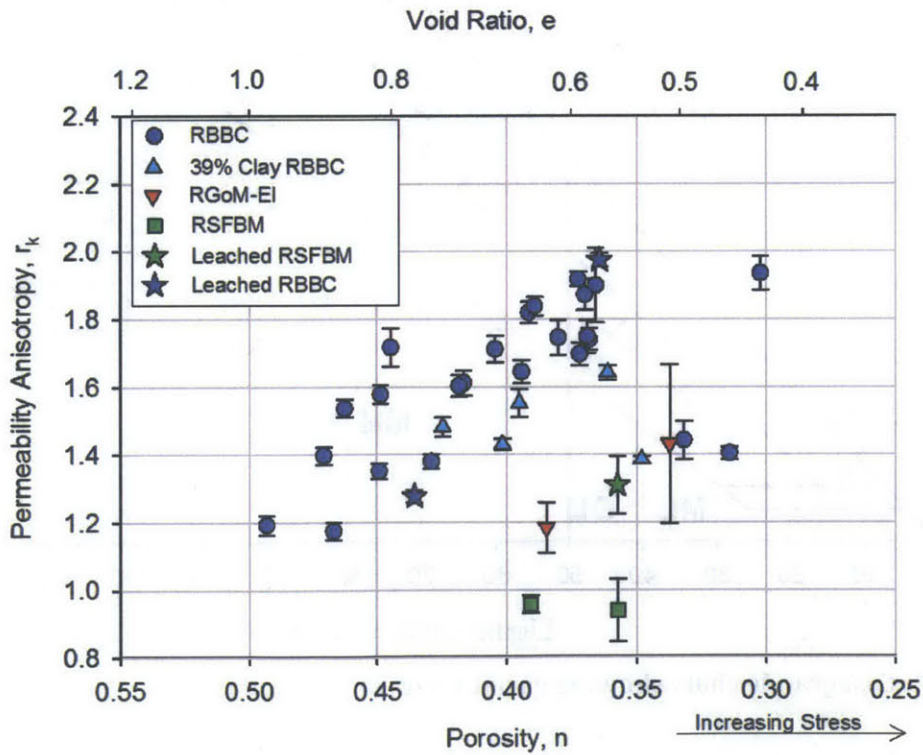


Figure 6-12: Permeability anisotropy vs. porosity for RBBC, RGoM-EI and RSFBM

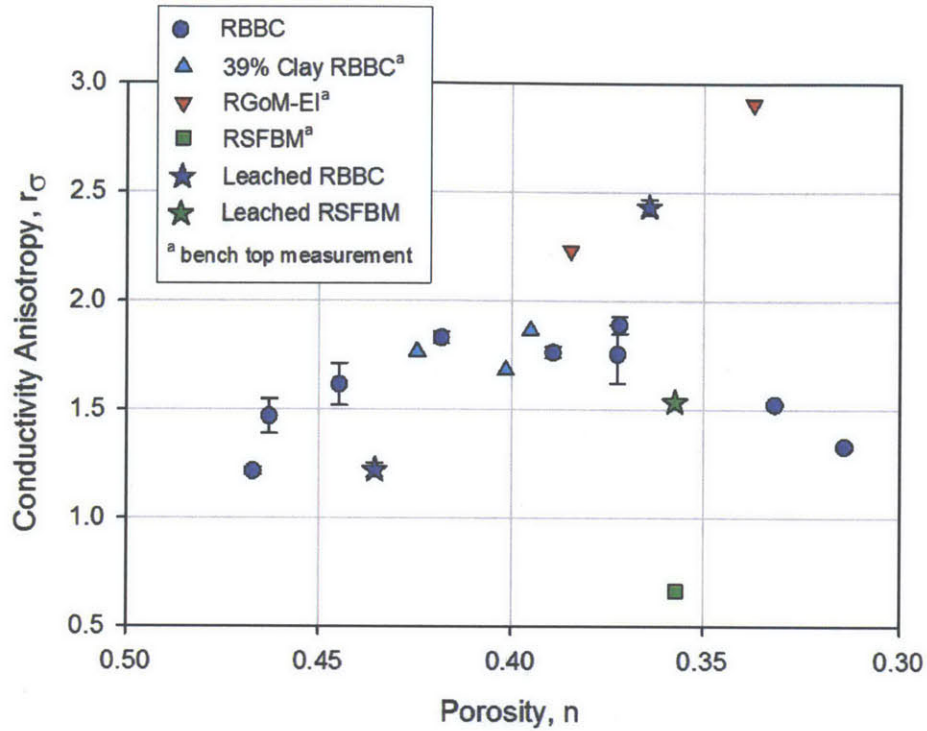


Figure 6-13: Conductivity anisotropy vs. porosity: Comparison between RBBC, 39% Clay RBBC, RGoM-EI, RSFBM, Leached RBBC and Leached RSFBM

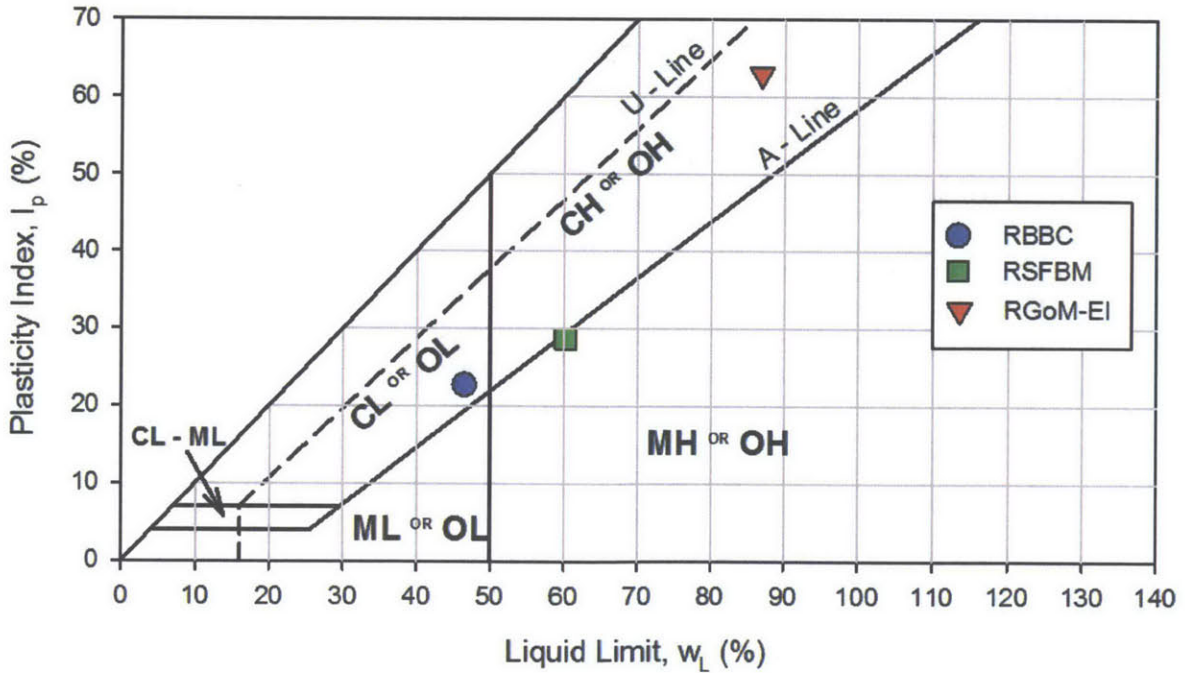


Figure 6-14: Casagrande chart showing variation in mudrock plasticity

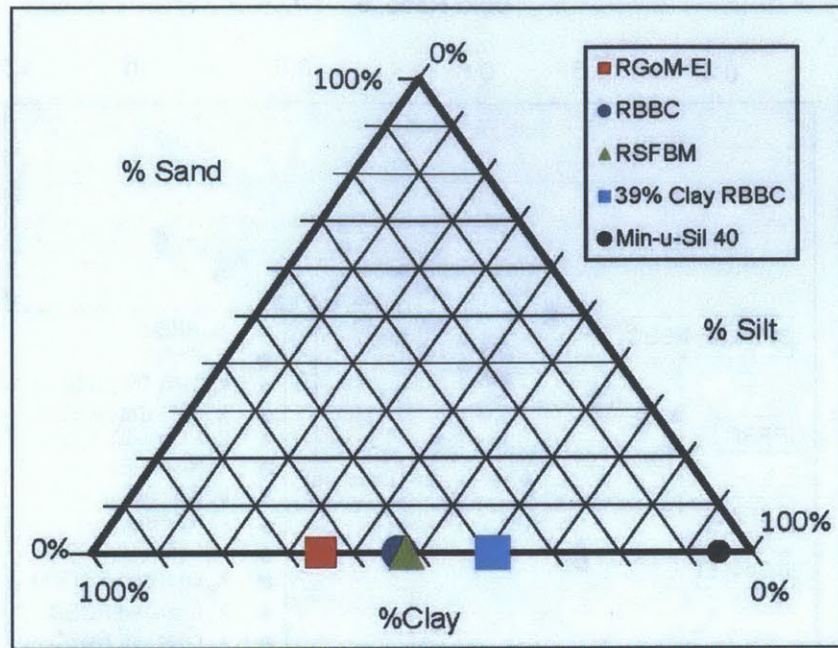


Figure 6-15: Clay Fraction Triangle Plot

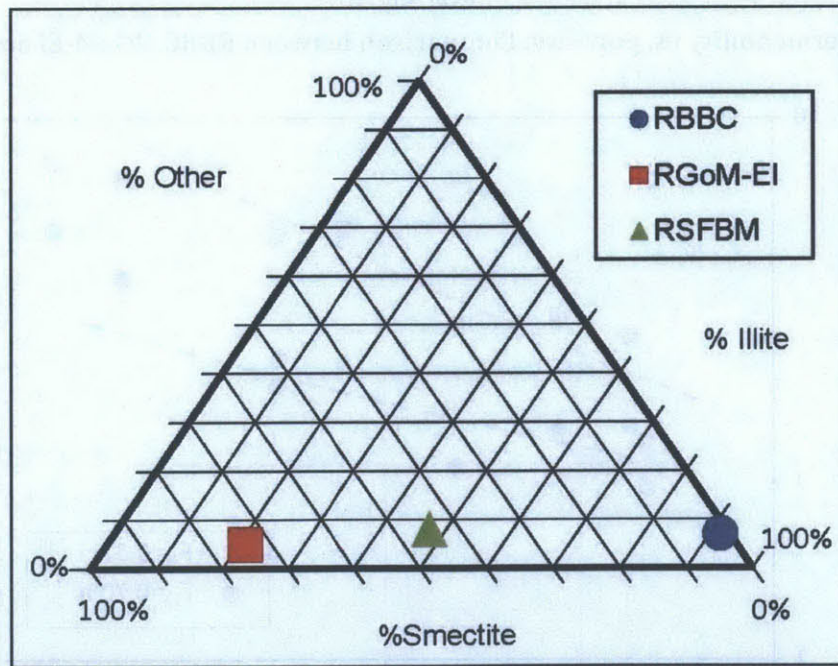


Figure 6-16: Clay Mineralogy Triangle Plot

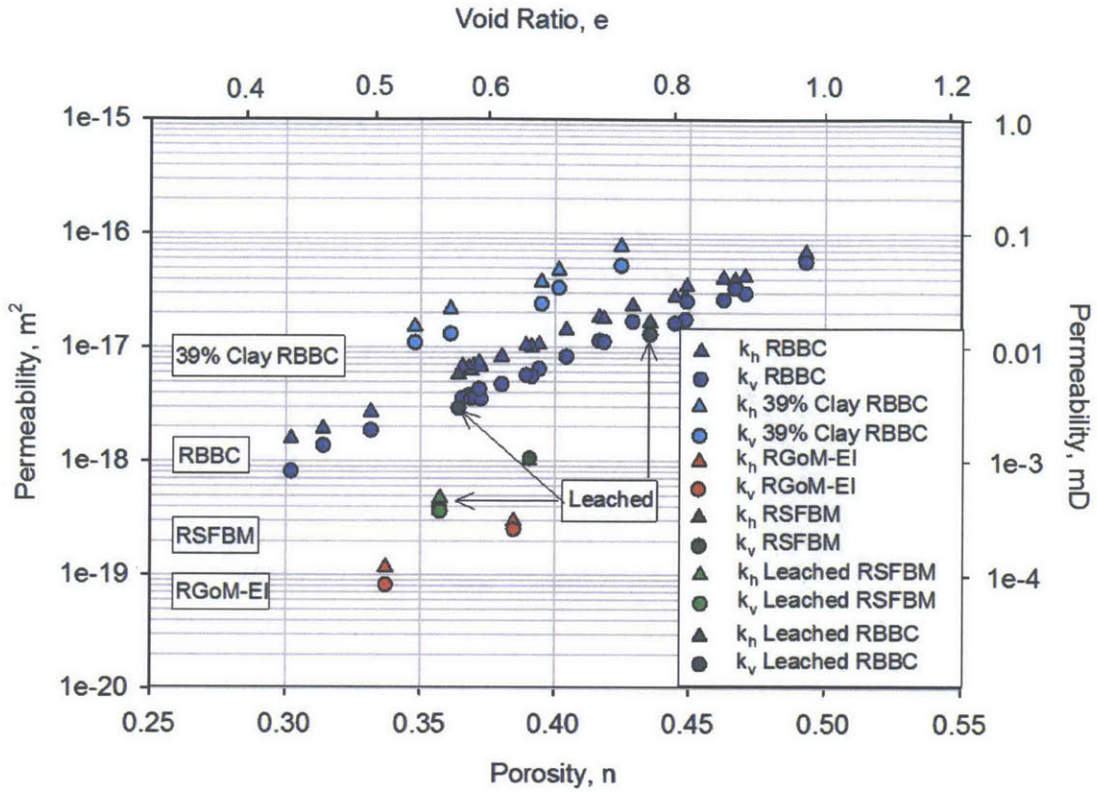


Figure 6-17: Permeability vs. porosity: Comparison between RBBC, RGoM-EI and RSFBM

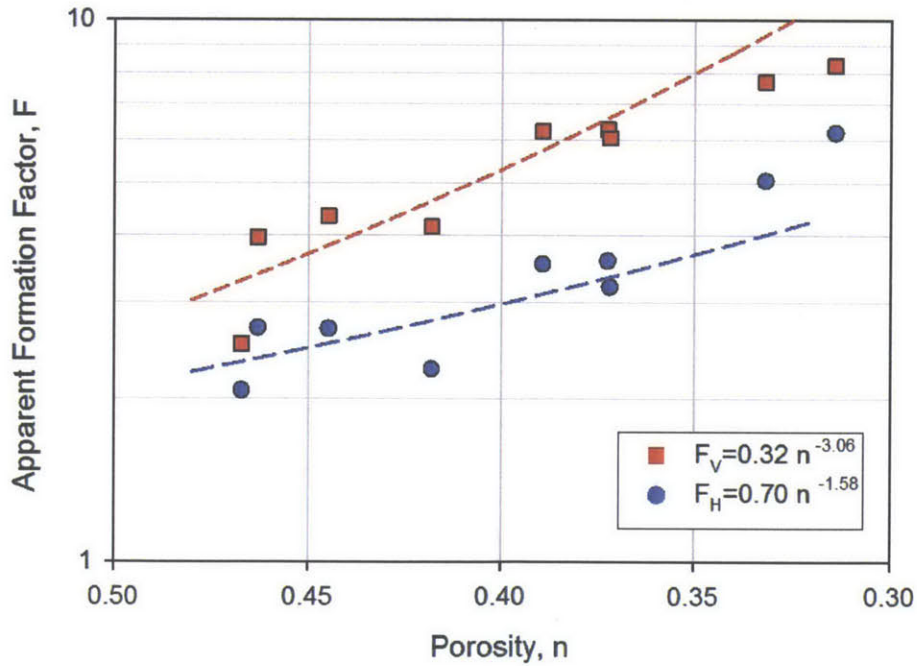


Figure 6-18: Log of apparent formation factor vs. porosity for RBBC (fit does not include data for porosity <0.36)

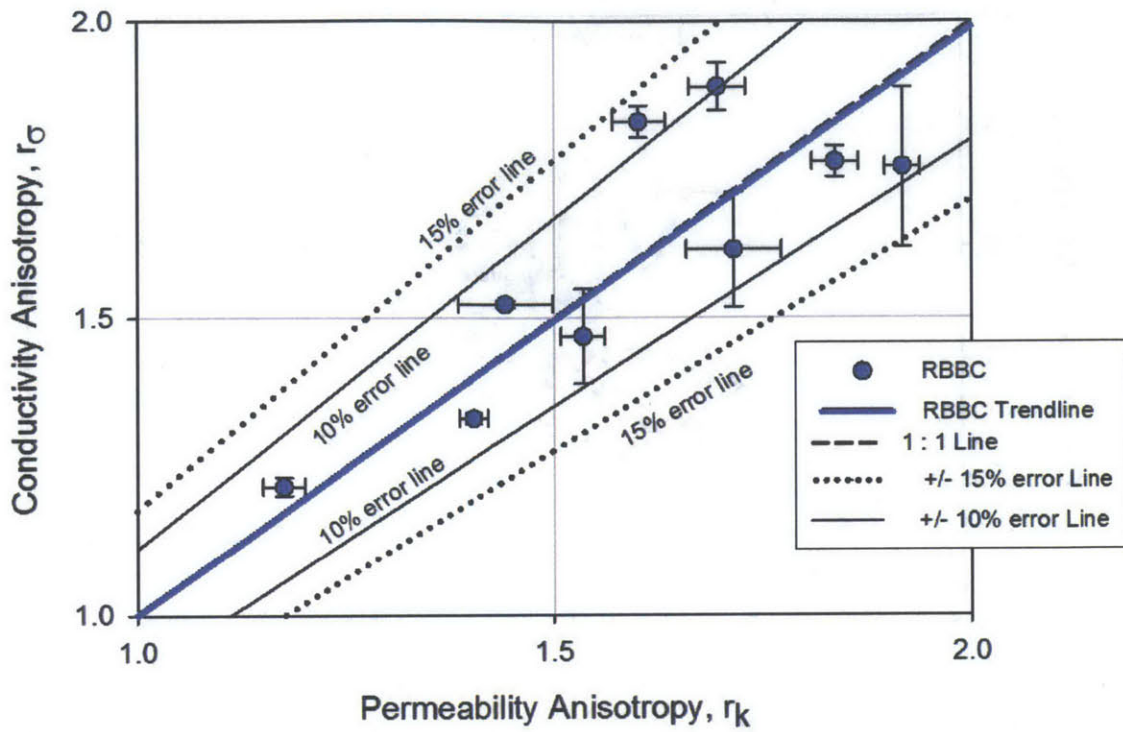


Figure 6-19: Cross plot of conductivity anisotropy vs. permeability anisotropy for RBBC

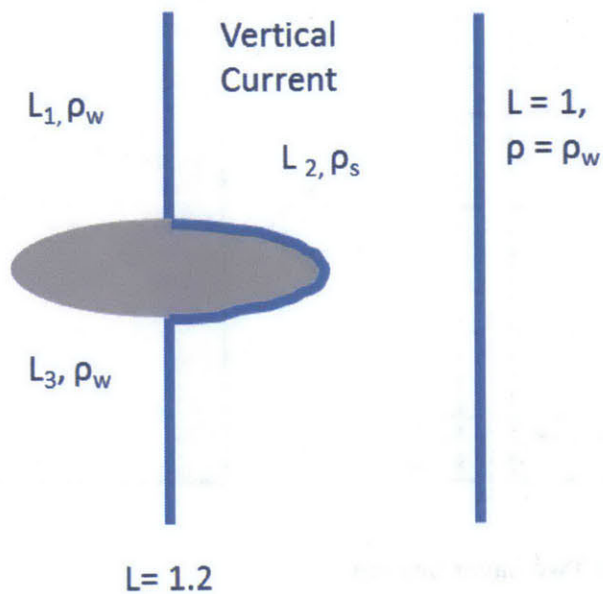


Figure 6-20: Illustration of electrical tortuosity concept

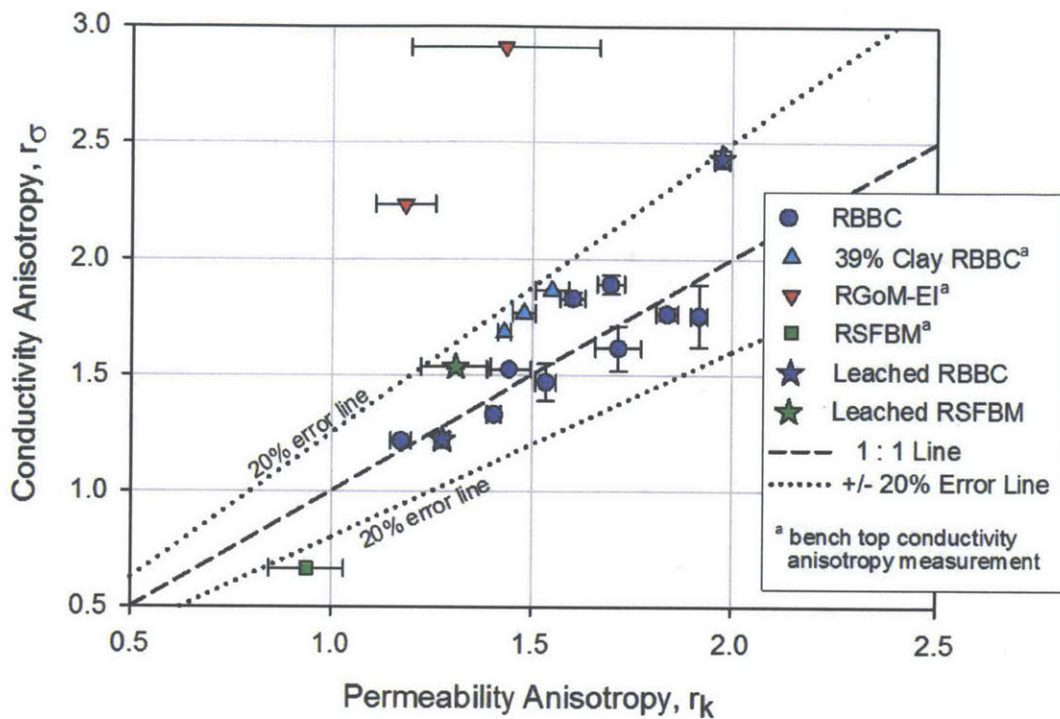


Figure 6-21: Cross plot of conductivity anisotropy vs. permeability anisotropy for RBBC, RGoM-EI and RSFBM

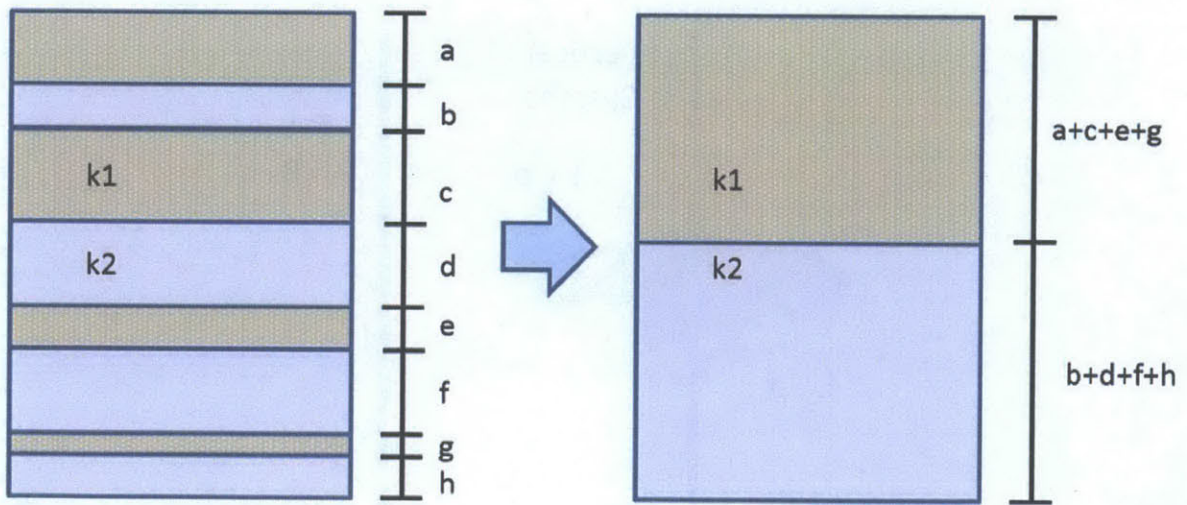


Figure 6-22: Equivalent Two Layer System

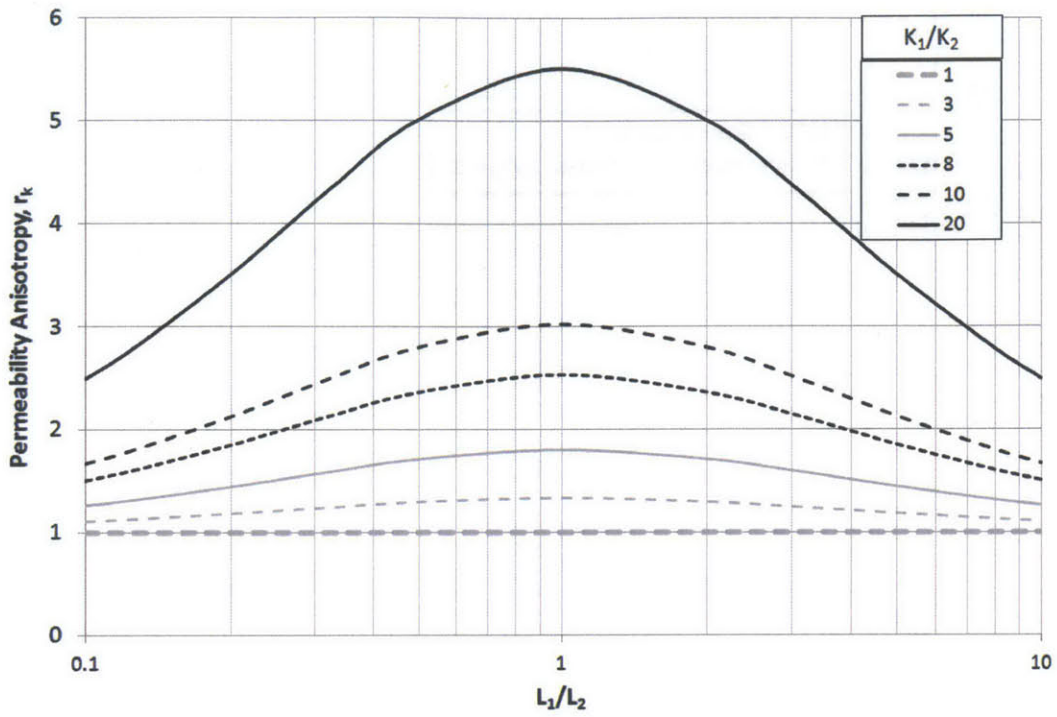


Figure 6-23: 2 Layer system permeability anisotropy, permeability contrast 1 to 20

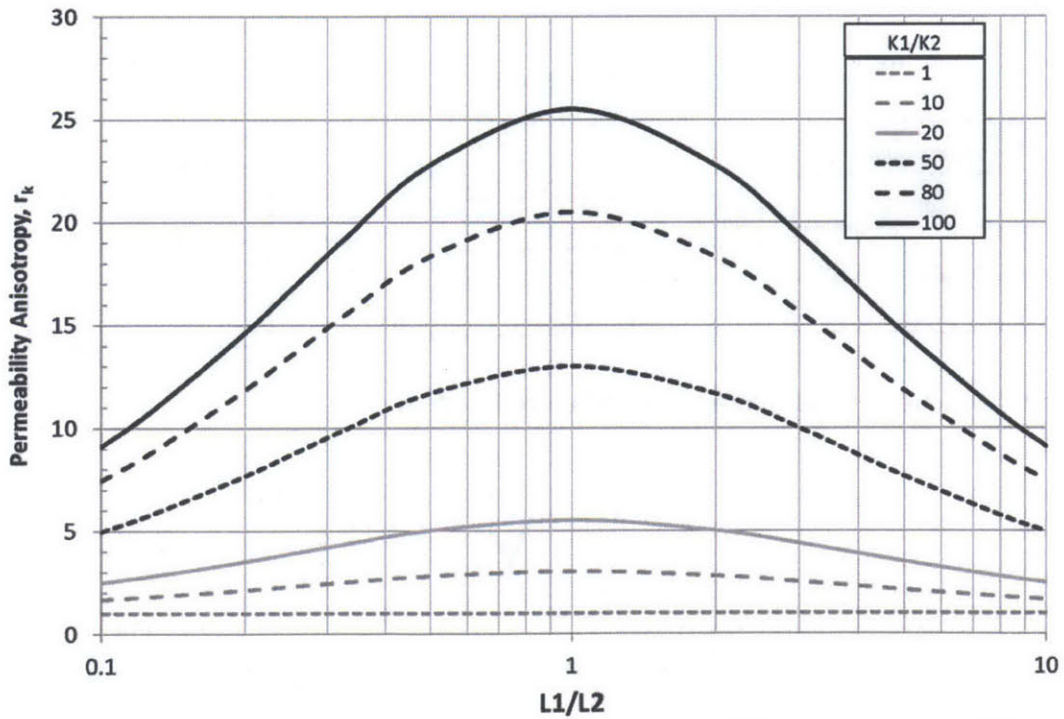


Figure 6-24: 2 Layer system permeability anisotropy, permeability contrast 1 to 100

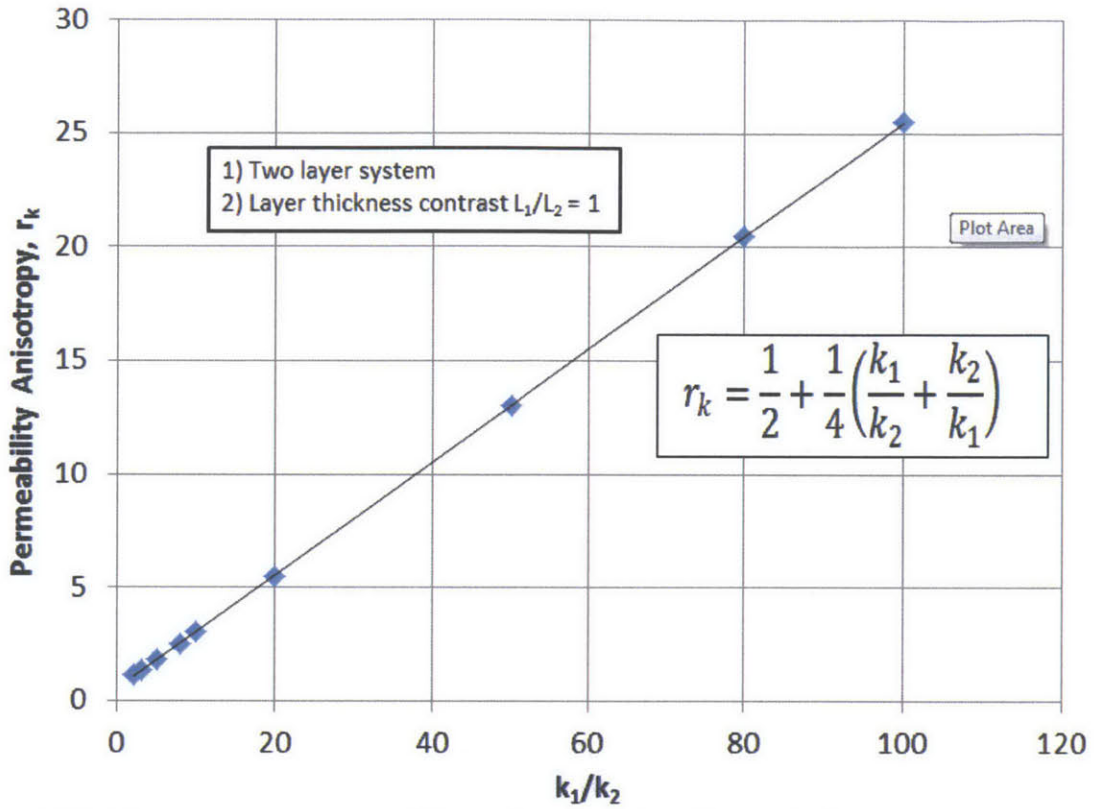


Figure 6-25: 2 Layer system permeability anisotropy, fixed layer thickness contrast = 1

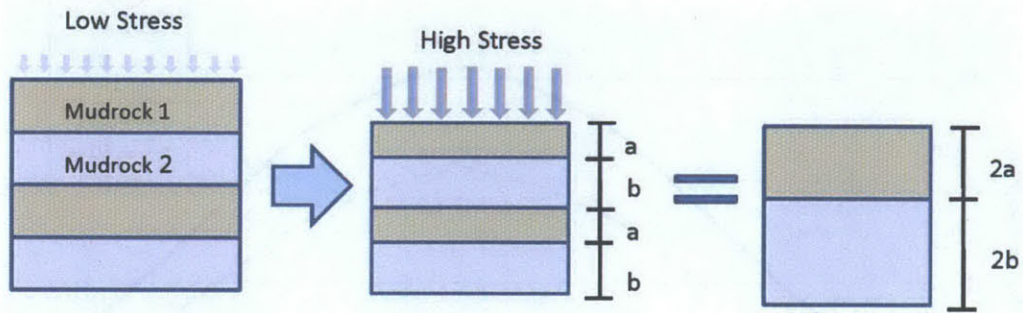


Figure 6-26: Schematic of a compressing layered system

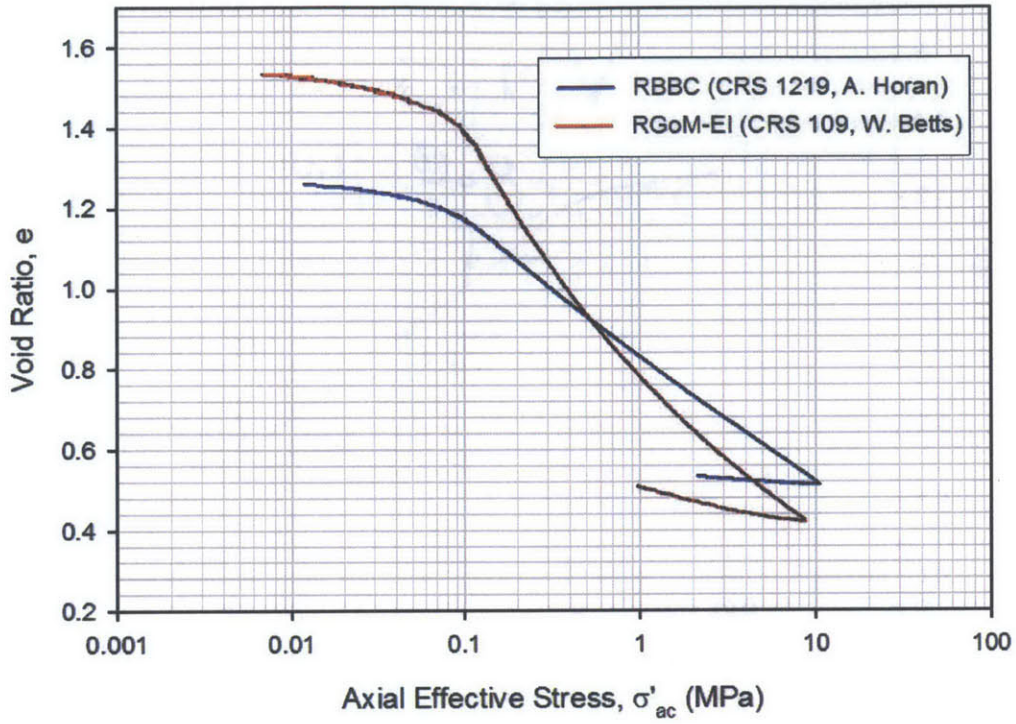


Figure 6-27: CRS compression curve in void ratio-log stress space for RBBC (CRS 1219) and RGoM-EI (CRS 109)

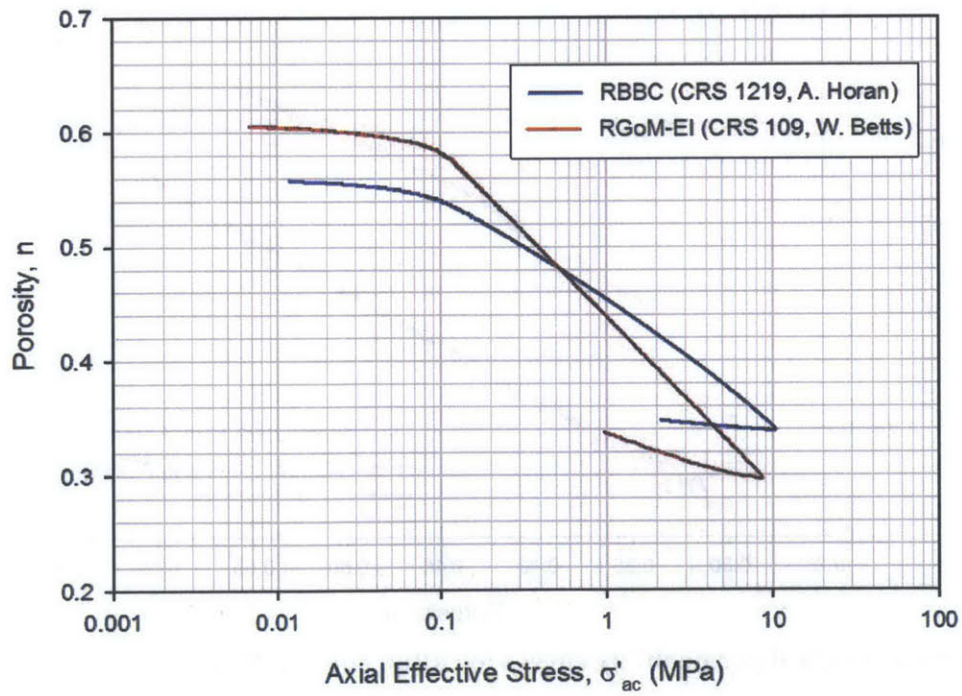


Figure 6-28: CRS compression curves in porosity - log stress space for RBBC (CRS 1219) and RGoM-EI (CRS 109)

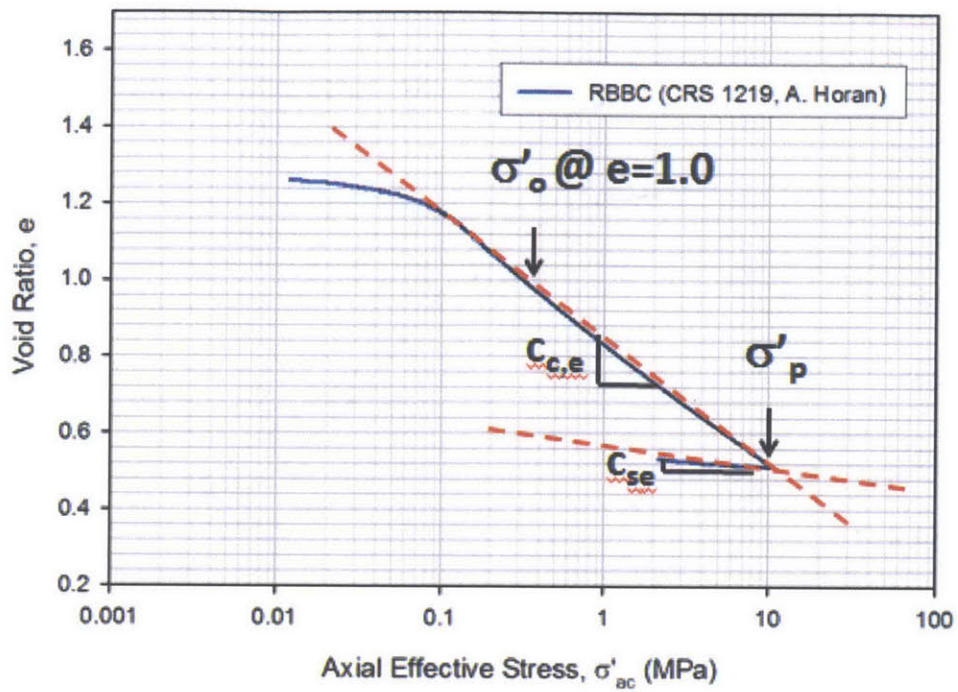


Figure 6-29: Graphic illustration of model compression parameters for RBBC (CRS 1219)

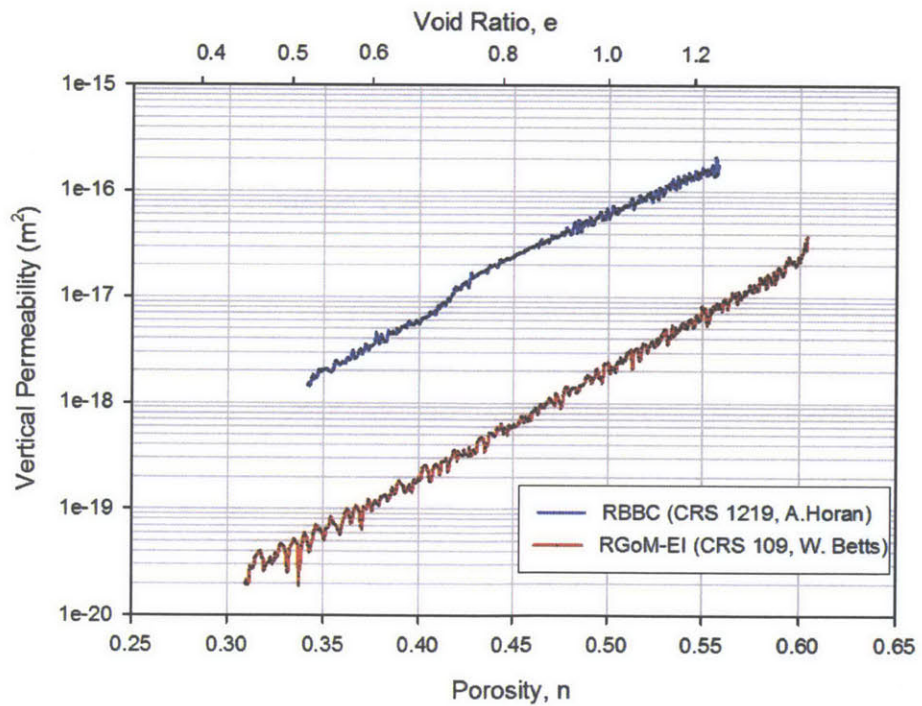


Figure 6-30: CRS vertical permeability curves for RBBC and RGoM-EI

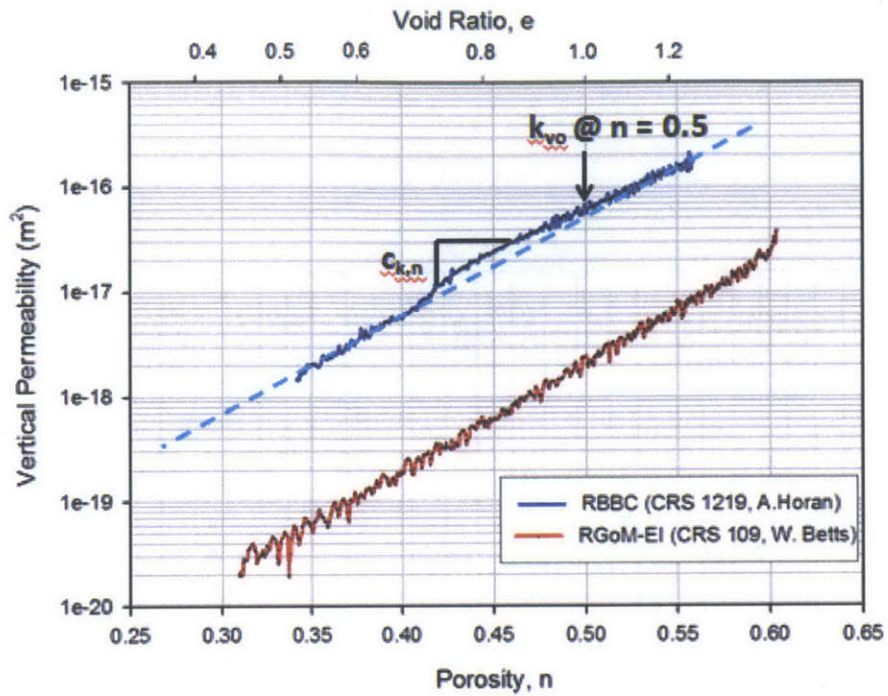


Figure 6-31: Graphic illustration of model permeability parameters

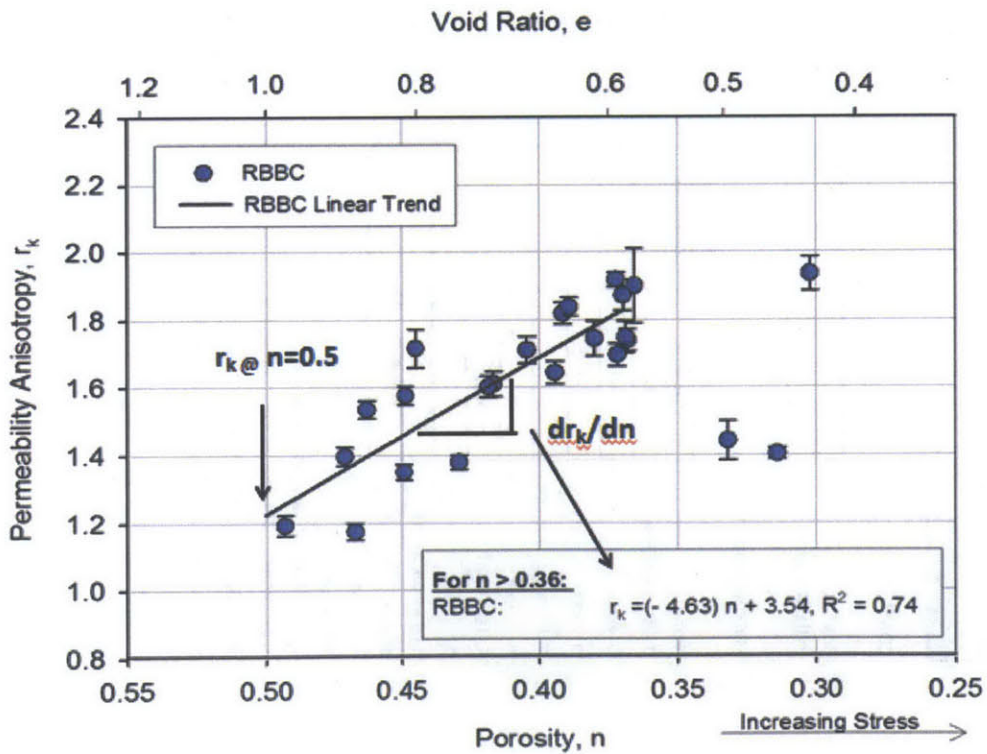


Figure 6-32: Graphic illustration of model permeability anisotropy parameters

Compressing Anisotropic Equivalent 2 Layer Model

Legend:

Fill in data
Calculations
Results

CONSTANTS:

Box Size:	5	cm
Initial # Layers	10	

Material Properties

	Material #1	Material #2
Name	RBBC	RGoM-EI
σ_o (@ n = 0.5) (Mpa)	0.342	0.309
c_c - e space	0.325	
c_s - e space	0.028	
c_c - n space		0.152
c_s - n space		0.040
k_{vo} (@ n = 0.5)	6.15E-17	5.20E-18
c_{en}	9.47	10.12
r_k (@ n = 0.5, OCR4)	1.23	1.23
dr_k/dn	-4.63	-4.63

Notes:

- 1) c_{en} = slope of log k_v vs. n plot
- 2) c_c = slope of VCL in e vs. log stress space
- 3) c_s = slope of swelling line in e vs. log stress space
- 4) model assumes uniform initial layer thickness

CALCULATIONS:
Material Properties

OCR	1	1	1
Stress	Mpa	0.1	1
			10

Material #1	RBBC		
e1	1.174	0.848	0.523
ϵ_1	0.000	-0.150	-0.299
n1	0.540	0.459	0.343
kv1	m ² 1.47E-16	2.52E-17	2.02E-18
r_k	1.04	1.41	1.95
kh1	m ² 1.53E-16	3.56E-17	3.95E-18
Material #2	RGoM-EI		
e2	1.350	0.732	0.371
ϵ_2	0.000	-0.263	-0.417
n2	0.574	0.422	0.270
kv2	m ² 2.95E-17	8.54E-19	2.47E-20
r_k	0.88	1.58	2.29
kh2	m ² 2.60E-17	1.35E-18	5.65E-20

Permeability - Assuming isotropic elemental permeabilities

Stress	Mpa	0.1	1	10
# Layers		10.0	12.6	15.6
Material #1 H	cm	0.5	0.425	0.350
Material #2 H	cm	0.5	0.368	0.292
Isotropic Layers				
k Parallel	m ²	8.83E-17	1.39E-17	1.12E-18
k Perpendicular	m ²	4.91E-17	1.77E-18	5.36E-20
r_k		1.80	7.84	20.80
Anisotropic Layers				
k Parallel	m ²	8.94E-17	1.97E-17	2.18E-18
k Perpendicular	m ²	4.91E-17	1.77E-18	5.36E-20
r_k		1.82	11.13	40.62

Figure 6-33: Model: Permeability anisotropy of compressing layered RBBC and RGoM-EI mudrock

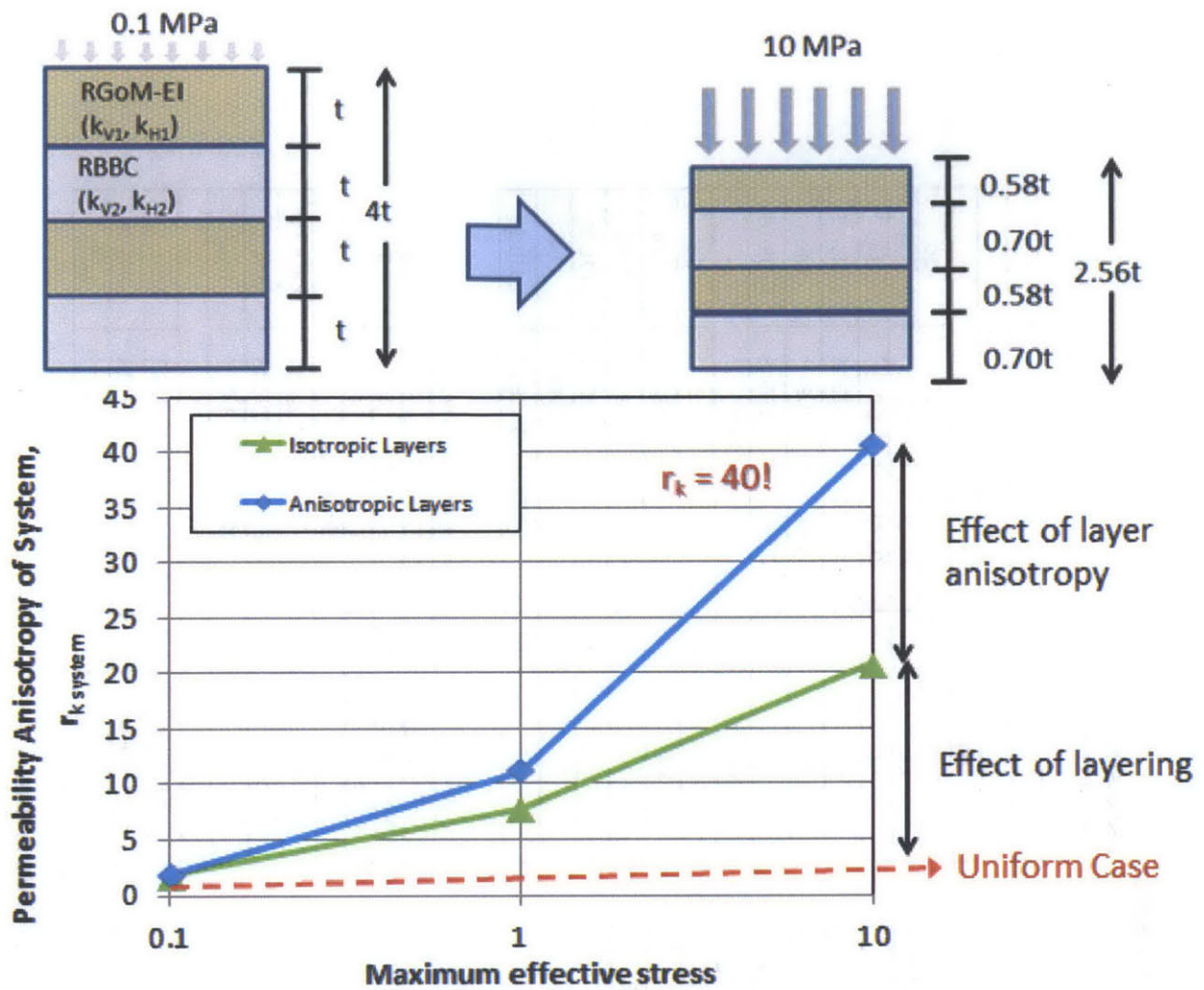


Figure 6-34: Permeability anisotropy of a layered system vs. maximum effective stress

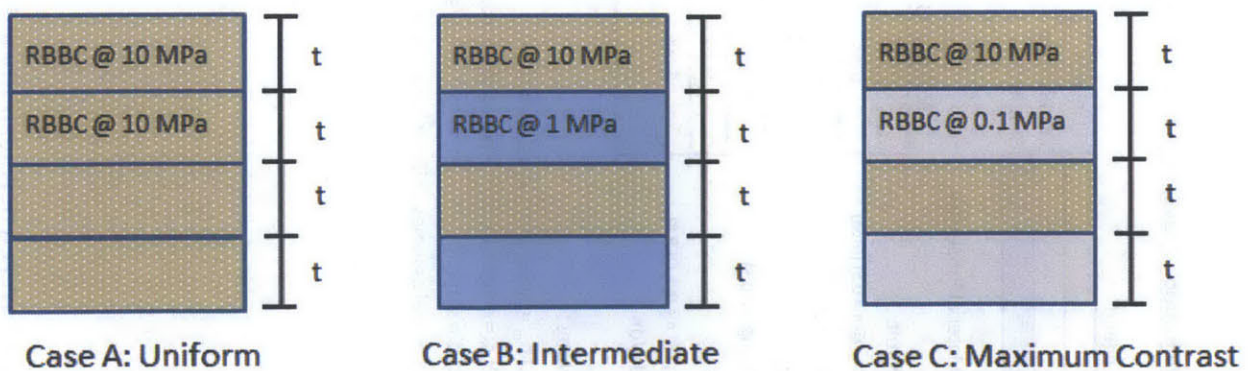


Figure 6-35: Permeability anisotropy and resistivity anisotropy model scenarios

Anisotropic 2 Layer Model - Fixed Layer Thickness - Permeability

Legend:

Fill in data
Calculations
Results

Material Properties:

	Material #1	Material #2
Name	RBBC	RBBC
σ_o (@ n = 0.5) (Mpa)	0.342	0.342
c_c	0.325	0.325
c_s	0.028	0.028
k_{vo} (@ n = 0.5)	6.15E-17	6.15E-17
c_{kn}	9.47	9.47
r_k (@ n = 0.5, OCR 4)	1.23	1.23
dr/dn	-4.63	-4.63

Notes:

- 1) c_{kn} = slope of log k_v vs. n plot
- 2) c_c = slope of VCL in e vs. log stress space
- 3) c_s = slope of swelling line in e vs. log stress space
- 4) model assumes uniform initial layer thickness

CALCULATIONS:
Material Properties

OCR	1	1	1
Material #1	RBBC		
Stress	Mpa	10	10
e1		0.523	0.523
n1		0.343	0.343
kv1	m ²	2.02E-18	2.02E-18
r_k		1.95	1.95
kh1	m ²	3.95E-18	3.95E-18
Material #2	RBBC		
Stress	Mpa	10	1
e2		0.523	0.848
n2		0.343	0.459
kv2	m ²	2.02E-18	2.52E-17
r_k		1.95	1.41
kh2	m ²	3.95E-18	3.56E-17

Permeability - Assuming isotropic elemental permeabilities

# Layers	2	2	2
Material #1 H	cm	5	5
Material #2 H	cm	5	5
Isotropic Layers			
k Parallel	m ²	2.02E-18	1.36E-17
k Perpendicular	m ²	2.02E-18	3.75E-18
r_k		1.00	3.63
Anisotropic Layers			
k Parallel	m ²	3.95E-18	1.98E-17
k Perpendicular	m ²	2.02E-18	3.75E-18
r_k		1.95	5.28

Figure 6-36: Layered permeability anisotropy model: RBBC layers

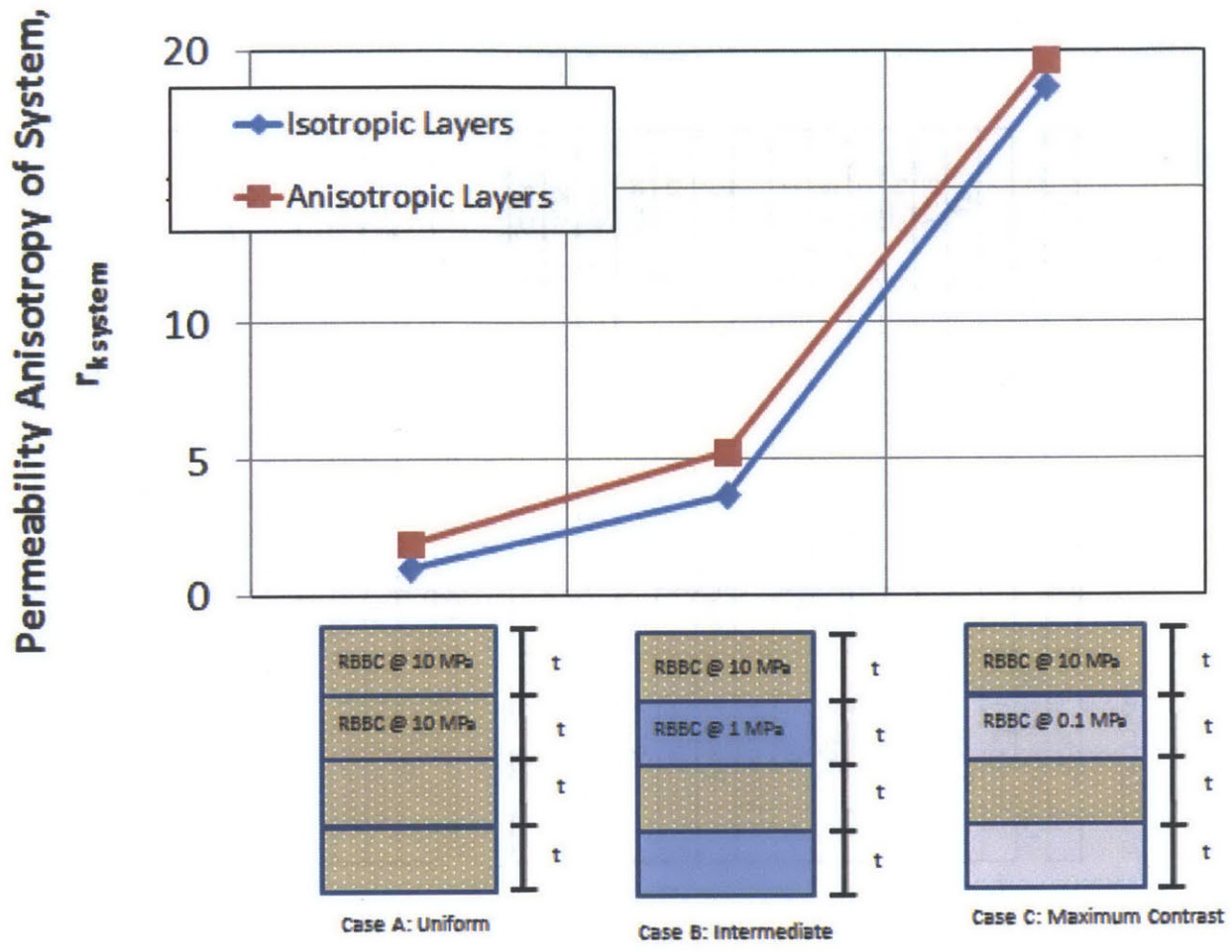


Figure 6-37: Permeability anisotropy of different model scenarios

Anisotropic 2 Layer Model - Fixed Layer Thickness - Resistivity

Legend:

Fill in data
Calculations
Results

Material Properties:

	Material #1	Material #2
Name	RBBC	RBBC
e_0 (@ 0.1 MPa)	1.17	1.17
c_c	0.325	0.325
c_s	0.028	0.028
a_v	0.32	0.32
a_H	0.70	0.70
m_v	3.06	3.06
m_H	1.58	1.58

Notes:

- 1) c_{kn} = slope of $\log k_v$ vs. n plot
- 2) c_c = slope of VCL in e vs. \log stress space
- 3) c_r = slope of swelling line in e vs. \log stress space
- 4) model assumes uniform initial layer thickness

CALCULATIONS:

OCR	1	1	1
Material Properties			
Material #1	RBBC		
Stress	Mpa	10	10
e_1		0.523	0.523
n_1		0.344	0.344
Fv1		8.41	8.41
Fh1		3.79	3.79
r_σ		2.22	2.22
Material #2	RBBC		
Stress	Mpa	0.1	10
e_2		1.174	0.849
n_2		0.540	0.459
Fv1		2.11	3.47
Fh1		1.85	2.40
r_σ		1.14	1.45

Resistivity - Assuming isotropic elemental resistivity

# Layers	2	2	2
Material #1 H	cm	5.0	5.0
Material #2 H	cm	5.0	5.0
Isotropic Layers			
F Parallel		3.37	4.91
F Perpendicular		5.26	5.94
r_σ		1.56	1.21
Anisotropic Layers			
F Parallel		2.49	2.93
F Perpendicular		5.26	5.94
r_σ		2.11	2.02

Figure 6-38: Layered resistivity and conductivity anisotropy model: RBBC layers

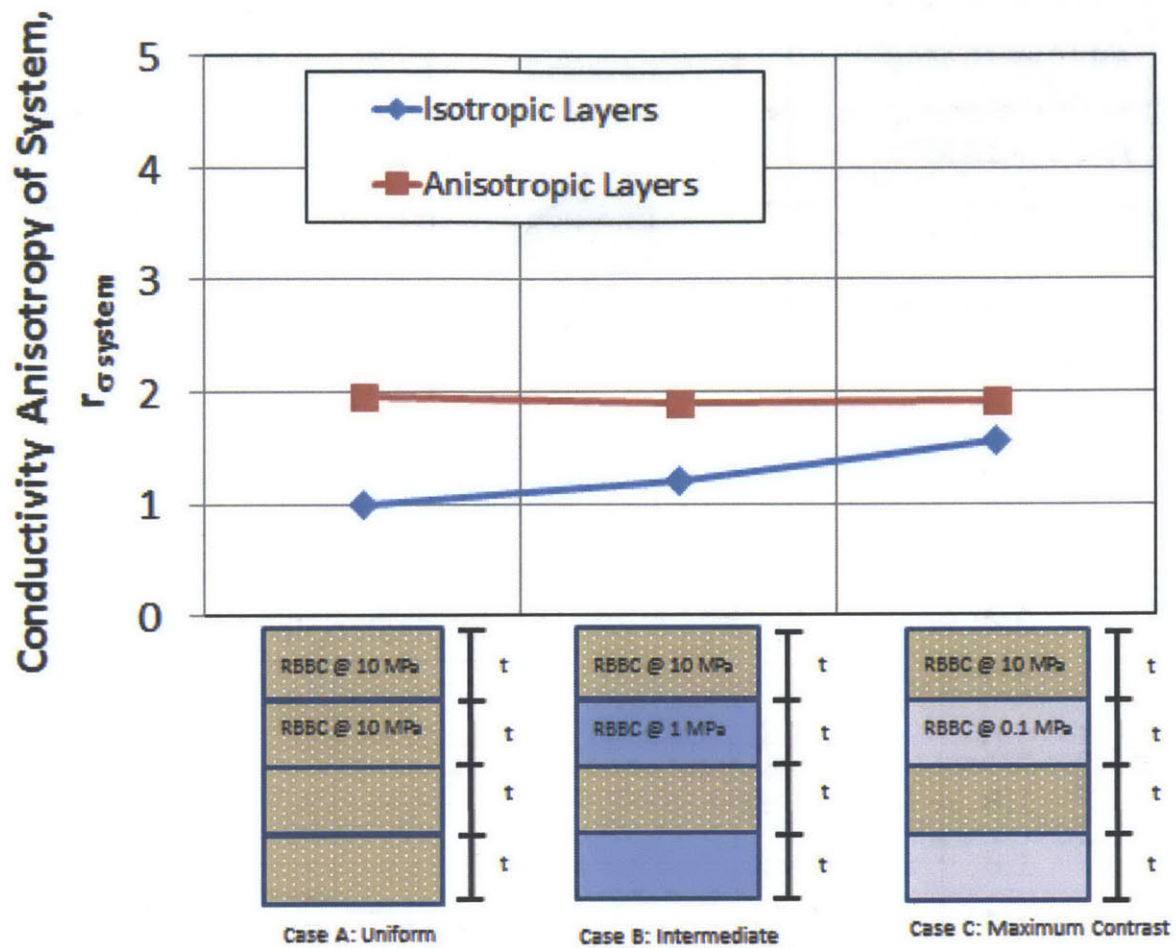


Figure 6-39: Conductivity anisotropy of different model scenarios

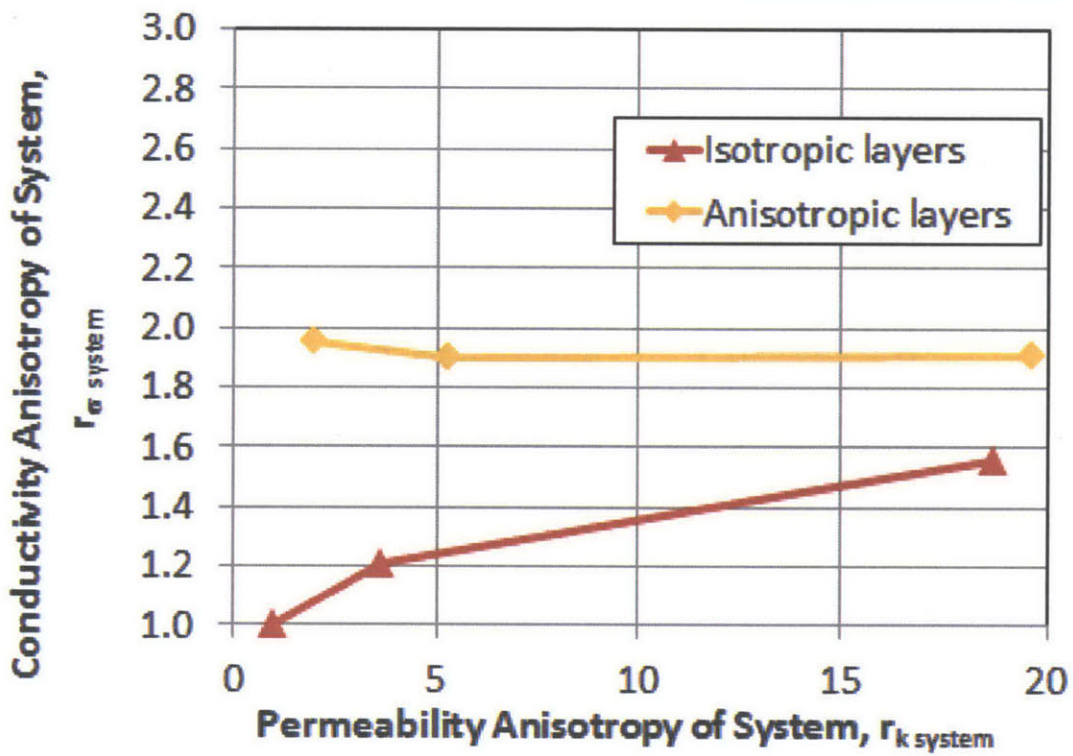
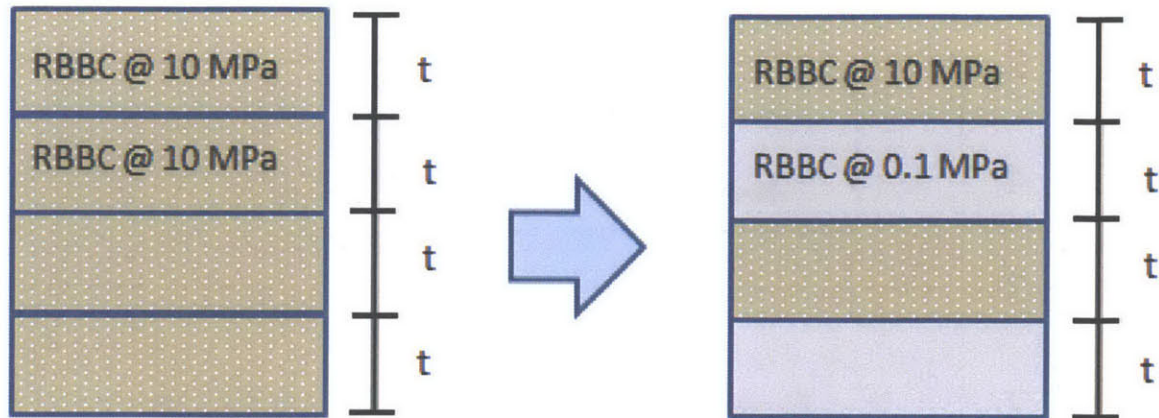


Figure 6-40: Conductivity anisotropy vs. permeability anisotropy for a layered system of RBBC at OCR 1 (layers compressed to different maximum effective stresses)

Permeability Case: $K1/K2 = 10+$



Resistivity Case: $F1/F2 = 2$



Figure 6-41: Partitioning of horizontal fluid and electric flow in layered systems

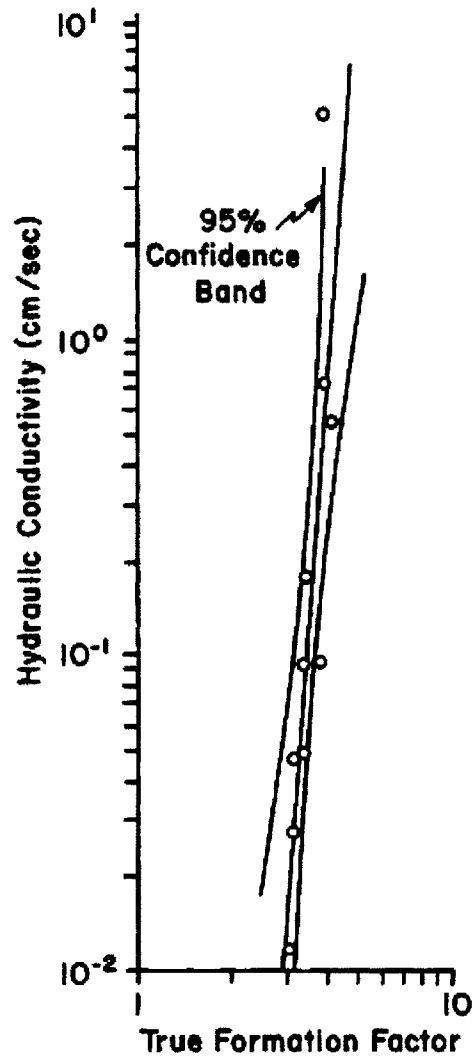


Figure 6-42: Relation between hydraulic conductivity and formation factor for a well sorted clay free sand (Huntley, 1986)

7 Conclusions and Recommendations

7	Conclusions and Recommendations	299
7.1	Overview	300
7.2	Key Findings and Conclusions	301
7.2.1	Range of Permeability Anisotropy in Mechanically Compressed Mudrocks	301
7.2.2	Particle Rotation drives Permeability Anisotropy Development	301
7.2.3	High Stress Permeability Anisotropy Decrease	302
7.2.4	Archie's Law Interpretation of RBBC	302
7.2.5	Relationship between Permeability Anisotropy and Resistivity Anisotropy	302
7.2.6	Extension to Layered Systems	303
7.3	Summary of Experimental Program Results.....	304
7.3.1	Compression & Salinity Measurements	304
7.3.2	Measurement Sequence Bias	304
7.3.3	Permeability & Permeability Anisotropy Measurements.....	305
7.3.4	Resistivity, Formation Factor & Resistivity Anisotropy Measurements.....	306
7.3.5	Mudrock Fabric and Texture Measurements.....	307
7.4	Recommendations for Future Research	308
7.4.1	New equipment development	308
7.4.2	Stress Level Dependence & Effect of OCR.....	309
7.4.3	Effect of Initial Fabric & Salinity.....	310
7.4.4	Effect of Mineralogy and Clay Fraction.....	311
7.4.5	Effect of Cementation or Temperature.....	311

This chapter is divided into four sections. The second section provides the key findings addressing subjects such as the limits and causes of permeability anisotropy, the relationship between permeability anisotropy and resistivity anisotropy, and the applicability of the measurements to field situations. The third section provides a global overview of the research program including the findings of individual experimental programs including the permeability, resistivity and fabric measurements. Finally the fourth section recommends a future research path based on the findings of and difficulties encountered in this research.

7.1 Overview

This thesis experimentally studied the evolution of permeability anisotropy and resistivity anisotropy in mechanically compressed mudrocks. Resedimented mudrocks were used to systematically study the magnitude and evolution of permeability anisotropy of elemental (uniform) mudrocks. The studied mudrocks were mechanically compressed to maximum effective stresses ranging from 0.4 to 40 MPa. In total, 36 resedimented specimens were analyzed. An extensive study was conducted using 24 specimens of Resedimented Boston Blue Clay (RBBC). Additional measurements were made using 2 specimens of Resedimented Gulf of Mexico Clay from the Eugene Island Block (RGOM-EI) and 2 specimens of Resedimented San Francisco Bay Mud (RSFBM). Variations of these mudrocks were also studied, including five specimens of RBBC with added Min-u-Sil 40 to reduce the clay fraction (called "39% Clay RBBC"), and 3 specimens that were leached to remove the natural salts from the mudrock powder.

Specimens were compressed and unloaded to an overconsolidation ratio (OCR) 4 during the resedimentation process, and then unloaded, extruded and trimmed into 5 cm cubes for permeability measurement under hydrostatic effective stress. The permeability anisotropy was measured by sequentially measuring the permeability along each axis of the cubic specimen using the constant head permeability measurement technique in a flexible wall permeameter. Each permeability measurement required the permeameter apparatus to be assembled & disassembled, with the specimen being rotated between setups to measure the different flow direction. The second and subsequent permeability measurements on the same specimen were adjusted for measurement sequence bias. Measurement sequence bias adjusts for the systematic decrease in measurement permeability that occurs when a specimen is re-measured multiple times in the same direction. This decrease in permeability results from handling the specimen between permeability measurements.

Partway through the research program, resistivity measurement was incorporated into the measurement sequence. The resistivity of cubic specimens was measured using a 4-probe resistivity technique, with 4 electrodes built into the cubic end adapters used in the flexible wall permeameter. The resistivity anisotropy was measured in parallel with the permeability measurement. The specimen resistivity was measured following each directional permeability measurement, before the apparatus was disassembled and the specimen rotated prior to reassembly for measurement in a different direction. In this way the permeability and resistivity anisotropy were measured simultaneously. Measurement sequence bias adjustments were applied to both the permeability and resistivity measurements to account for the effects of multiple measurements on the same specimen.

Finally, high quality SEM images of RBBC were obtained at various stress levels and porosities. Manual analysis of the particle orientation, length and aspect ratio was used to identify trends in particle orientation, particle length and particle aspect ratio as a function of applied stress and porosity. Measurements were also conducted to assess the repeatability of the manual analysis

method comparing the effects of varying analysts, specimen preparation and specimen imaging locations.

The results of the permeability, resistivity and image analysis tests were combined to analyze different aspects of anisotropy development, including the magnitude of permeability anisotropy development in uniform mudrocks, the potential causes of anisotropy development and the link between permeability anisotropy and resistivity anisotropy. The following sections summarize the experimental results and interpretations in detail.

7.2 Key Findings and Conclusions

The following sections summarize the key findings and conclusions related to the development of permeability and resistivity anisotropy in mechanically compressed mudrocks and the relevance of these experimental findings to larger scale systems.

7.2.1 Range of Permeability Anisotropy in Mechanically Compressed Mudrocks

The permeability anisotropy varies from ~ 1 to ~ 2 in the mudrocks studied. Permeability anisotropy increases linearly with decreasing porosity for RBBC, with a change in behaviour at low porosity (>0.36). Some mudrocks are isotropic, such as RSFBM. Leaching increases the permeability anisotropy in RSBFB but does not significantly change the permeability anisotropy in RBBC. RGoM-EI has lower permeability anisotropy than RBBC, though this may be the result of difficulties in measurement.

7.2.2 Particle Rotation drives Permeability Anisotropy Development

Permeability anisotropy predicted using a particle rotation model was compared to experimental results to show that particle rotation drives permeability anisotropy development.

The permeability anisotropy of RBBC was predicted using a particle based permeability anisotropy model based on particle orientation, aspect ratio and porosity. These parameters are used to define the geometry of the assemblage, compute of the horizontal and vertical tortuosity, and compute the permeability anisotropy as the ratio of the horizontal to vertical tortuosity.

Typically, particle based permeability anisotropy models apply the March (1932) Model or other similar model to predict the particle orientation and define either the mean or weighted average aspect ratio based on available information. These values can roughly capture the permeability anisotropy of RBBC (Figure 6-6) for porosities > 0.36 . However, use of the measured particle orientation combined with a high aspect ratio more similar to the aspect ratios of the larger particles better predicts the permeability anisotropy magnitude and trend of RBBC (Figure 6-5).

Both particle orientation and particle aspect ratio play key roles in permeability anisotropy development in mechanically compressed mudrocks. Permeability anisotropy is most influenced by the higher aspect ratio particles that undergo more rotation with compression.

7.2.3 High Stress Permeability Anisotropy Decrease

The preceding section argued that permeability anisotropy development is related to particle orientation as suggested by theoretical models. However, permeability anisotropy models predict rapid increases in permeability anisotropy as the mean particle orientation decreases. Permeability anisotropy measurements indicate that the permeability anisotropy of RBBC reaches a maximum of ~ 2 at porosity 0.36 and then decreases with increasing compression (Figure 6-1). A similar trend is seen in the conductivity anisotropy of RBBC (Figure 6-3).

This decrease in permeability anisotropy is linked to a change in fabric evidenced by a change in permeability behavior and a change in particle orientation. Below porosity 0.36 the horizontal permeability decreases faster than the vertical permeability (Figure 6-7). There is no significant change in mean particle orientation with decreasing porosity; however the particle orientation becomes increasingly particle size independent.

7.2.4 Archie's Law Interpretation of RBBC

Archie's Law is commonly applied in the oil industry to interpret the porosity or saturation of mudrocks. The apparent formation factor of RBBC was interpreted using Archie's Law and assuming directional dependence. The 'a' parameter is interpreted to be 0.32 in the vertical direction and 0.70 in the horizontal direction. Similarly, the m parameter is interpreted to be 3.06 in the vertical direction and 1.58 in the horizontal direction (Figure 6-18)

Applying an Archie's Law interpretation to the conductivity anisotropy, the 'a' parameter for the anisotropy is interpreted to be 0.46 and the m parameter for the anisotropy is 1.48 (Figure 6-3). These results can be achieved 1) by dividing the vertical formation factor written in terms of Archie's law by the horizontal formation factor written in terms of Archie's Law; or 2) by regressing the conductivity anisotropy vs. porosity measurements using a power law relationship.

These results demonstrate that Archie's law is a direction dependent relationship, and more importantly that the 'a' and 'm' parameters are direction dependent.

7.2.5 Relationship between Permeability Anisotropy and Resistivity Anisotropy

Permeability and resistivity are shown to be governed by similar equations in soils; for every permeability related equation there is a resistivity analog (Table 6-3). However fluid flow and electric current flow occur via fundamentally different mechanisms through mudrocks. However,

in high salinity mudrocks the dominant flow path for both fluid flow and electric flow should be through the fluid filled pore space, suggesting a non-trivial relationship between the permeability anisotropy and conductivity anisotropy.

Despite this theoretical incongruity, experiments reveal that the conductivity anisotropy can be used to estimate the permeability anisotropy of uniform mudrocks within +/- 20% error. The permeability anisotropy of RBBC is directly proportional to the conductivity anisotropy (inverse of the resistivity anisotropy) of RBBC within +/- 15% error (Figure 6-19). Similarly, the permeability anisotropy of all mudrocks studied falls within +/- 20% of the conductivity anisotropy (Figure 6-21). RGoM-EI is the exception to this rule. Further work is required to determine if this exception is due to inaccuracies in the permeability measurement, or if in fact it represents real soil behaviour. In the latter case the relationship between permeability anisotropy and conductivity anisotropy may be a family of curves whose slope is related to a material property. More work is needed to quantify this.

Apparent formation factor values are used to define the conductivity anisotropy. In practice, the measured resistivity and formation factor are typically adjusted to account for the surface conductivity of the clay particles which varies as a function of clay mineralogy and pore fluid conductivity. However, because these relationships are defined using unadjusted values (ignoring clay surface conductivity), this implies that correction factors designed to remove the conductive effects of the clay particles from the resistivity and formation factor may be isotropic.

7.2.6 Extension to Layered Systems

The permeability anisotropy of a system of layered isotropic mudrocks can be computed using a closed form solution that is a function of the thickness and permeability of each layer. The maximum permeability anisotropy for a system of layered isotropic mudrocks is achieved when half of the mudrock has one permeability and half of the mudrock has a different permeability. Permeability anisotropy increases as the permeability contrast between layers (k_1/k_2) increases.

For a compressing system of anisotropic layered mudrocks, the permeability anisotropy is computed using an analytic model. Including the anisotropy of the individual layers can significantly increase the permeability anisotropy of the system. For RBBC layered with RGoM-EI, the permeability anisotropy generated due to only layering and differential compression of the individual layers (isotropic assumption) increased from 1.8 to 13.2 as the stress increased from 0.1 to 10 MPa. However, when each layer is assumed to be individually anisotropic per the experimental measurements in this research, the permeability anisotropy of the system increases from 1.9 to 25.8 over the same stress range. The permeability anisotropy of the system is nearly doubled by assuming that each uniform layer has permeability anisotropy of as little as 2.

However, the same is not true for the conductivity anisotropy. The conductivity anisotropy is only equal to the permeability anisotropy for the special case of uniform mudrocks. The permeability contrast between layers is much larger than the formation factor contrast between layers. This is

because permeability varies logarithmically over many orders of magnitude for commonly seen mudrocks (e.g. Figure 6-17) whereas the formation factor does not vary significantly between mudrocks despite a large variation in permeability. In layered systems, the permeability anisotropy can vary significantly with increasing stress while the conductivity anisotropy may remain relatively constant.

7.3 Summary of Experimental Program Results

This section summarizes the compressibility, permeability, resistivity, and fabric measurements for the different mudrocks in detail.

7.3.1 Compression & Salinity Measurements

The resedimented specimens were compressed to a maximum effective stress during resedimentation, rebounded to an OCR of 4, and then trimmed into a cube. The cubic specimen void ratio and log stress measurements follow the OCR 4 line derived from CRS measurements for void ratios > 0.7 and porosities > 0.42 (Figure 5-3 through Figure 5-12). Below void ratio 0.7 and porosity 0.42 the cubic specimen void ratio and stress measurements deviate from the OCR 4 line. This deviation is likely a combination of 1) sidewall friction that reduces the applied load during resedimentation; and 2) an incorrect calibration factor on the medium – high stress air pressure load frame leading to inaccurate stress application.

Adding silt to reduce the clay fraction shifts the compression curve towards lower void ratios (Figure 5-5). Further, leaching does not affect the compression behaviour for either RBBC (Figure 5-11) or RSFBM (Figure 5-10).

The salinity of resedimented specimens does not correlate with the batching salinity. Two factors are noted: First, the average value of the measured salinity is lower than the predicted value based on the salt content of the mudrock powder and the known mass of salt added during batching. Second, there is scatter in the measured salinity about this average value. More work is needed to quantify the sources of this error, however at this time the decrease in average value is thought to be associated with the transformation of Ca Smectite to Na Smectite, and the scatter is thought to be associated with small, measurable errors inherent in the measurement method and associated calculations.

7.3.2 Measurement Sequence Bias

Both the measured permeability and measured resistivity were adjusted for measurement sequence bias. Measurement sequence bias is a systematic decrease in permeability or increase in resistivity that results from successive re-assembly the cubic specimen apparatus. Two methods of measurement sequence bias were applied: The global method developed two directional correction factors, x_H and x_V , that were derived based on the entire data set for a particular mudrock. This approach aimed to reduce scatter in the correction factors and was applied to the RBBC and 39%

Clay RBBC data sets. The single specimen method adjusted the measured permeability or resistivity using the noted decreases for a particular specimen. This method was applied to the smaller RGoM-EI, RSFBM, Leached RBBC, Leached RSFBM data sets.

The global measurement sequence bias factors for the permeability, x_H and x_V , were 0.984 and 0.986 for RBBC, respectively, and 0.930 and 0.962 for 39% Clay RBBC, respectively. For the resistivity, the factors $x_{H\rho}$ and $x_{V\rho}$ were both equal to 1.051 for RBBC. The measurement sequence bias is likely direction independent, with any apparent directional dependency related to experimental error.

A comparison of the global specimen method and the single specimen method for RBBC revealed that they produce essentially the same results for cases where sufficient data are available to apply both methods.

7.3.3 Permeability & Permeability Anisotropy Measurements

The cubic specimen permeability vs. porosity measurements forms linear trends in log permeability vs. porosity space (Figure 5-39). The permeability in the horizontal direction is higher than that in the vertical direction for most specimens. The permeability of RBBC ranges from $6.8 \times 10^{-17} \text{ m}^2$ in horizontal direction and $5.7 \times 10^{-17} \text{ m}^2$ in the vertical direction at porosity 0.49 to $1.6 \times 10^{-18} \text{ m}^2$ in horizontal direction and $8.1 \times 10^{-19} \text{ m}^2$ in the vertical direction at porosity 0.30 (Figure 5-26). There is a break in slope of the log horizontal permeability vs. porosity curve that occurs at porosity 0.36 (Figure 5-26).

The permeability of 39% clay RBBC, with lower clay fraction, is ~ 3 times higher than that of RBBC at the same porosity (Figure 5-39). Similarly, the RSFBM is one half of an order of magnitude less permeable, and the RGoM-EI is one order of magnitude less permeable than RBBC at the same porosity (Figure 5-39).

Overall, the permeability anisotropy of the studied mudrocks does not exceed 2.0 (Figure 5-41). The mudrocks studied span a wide range of plasticity (Figure 6-14), clay fraction (Figure 6-15) and mineralogical composition (Figure 6-16).

The permeability anisotropy of RBBC increases monotonically from 1.2 at porosity 0.50 to 1.9 at porosity 0.36 (Figure 5-27). Below porosity 0.36 the permeability anisotropy of RBBC decreases. Similarly, the permeability anisotropy of 39% clay RBBC increases monotonically from 1.4 at porosity 0.43 to 1.6 at porosity 0.36; below porosity 0.36 the permeability anisotropy of 39% clay RBBC also decreases (Figure 5-33). This decrease in permeability anisotropy is linked with a break in slope in the log permeability vs. porosity data for RBBC (Figure 5-26) and particle orientation that remains relatively constant with decreasing porosity (Figure 5-64) and is independent of particle size (Table 5-24).

RSFBM has nearly isotropic permeability at porosity 0.39 and 0.36 (Figure 5-41). The permeability anisotropy of RGoM-EI ranges from 1.2 at porosity 0.34 to 1.4 at porosity 0.385 (Figure 5-41). However, the permeability of RGoM-EI was difficult to measure because the specimen dried and developed horizontal cracks during trimming; therefore the permeability and permeability anisotropy results may not be representative.

Finally, leaching the soil to remove the salt does not alter the permeability anisotropy of either RBBC or RSFBM (Figure 5-41) in the stress range studied.

7.3.4 Resistivity, Formation Factor & Resistivity Anisotropy Measurements

The apparent resistivity of RBBC increases monotonically from 1.09 Ωm in the horizontal direction and 1.43 Ωm in the vertical direction at porosity ~ 0.46 to 2.78 Ωm in the horizontal direction and 3.70 Ωm in the vertical direction at porosity 0.31 (Figure 5-51, Table 5-17). Similarly, the apparent formation factor for RBBC increases monotonically from 2.07 in the horizontal direction and 2.51 in the vertical direction at porosity 0.46 to 6.19 in the horizontal direction and 8.24 in the vertical direction at porosity 0.31 (Figure 5-52, Table 5-17).

The resistivity of Leached RBBC is approximately one order of magnitude higher than that of RBBC (Figure 5-55); however the formation factor of Leached RBBC is similar to that of RBBC (Figure 5-56). This further suggests that leaching does not affect the fabric structure; rather the differences in resistivity between Leached RBBC and RBBC result primarily from differences in pore fluid salinity.

Finally, the resistivity and formation factor of RBBC measured using bench top methods agree well with those measured in the triaxial cell (Appendix 4). Limited measurements of the resistivity and formation factor of RGoM-EI, RSFBM, and 39% Clay RBBC were made using bench top measurements only. Therefore the trends in resistivity and formation factor for these mudrocks were not compared.

The resistivity anisotropy of RBBC decreases monotonically from 0.8 to 0.53 as the porosity decreases from 0.47 to 0.36; the resistivity anisotropy then increases to 0.75 as the porosity further decreases to 0.31 (Figure 5-53). The inverse trend is noted for the conductivity anisotropy which increases monotonically from 1.2 to 1.9 as the porosity decrease from 0.47 to 0.36 and then decreases to 1.3 as the porosity further decreases to 0.31 (Figure 5-54). The conductivity anisotropy measurements are similar in both trend and magnitude to the permeability anisotropy measurements (Figure 5-27).

The conductivity anisotropy of all mudrocks studied indicates a monotonic increase in conductivity anisotropy with decreasing porosity (Figure 5-59). Similar to the permeability anisotropy results, both high stress, low porosity ($n < 0.36$) RBBC mudrocks and RSFBM diverge from this trend. However, unlike the permeability anisotropy results, RGoM-EI follows the general trend with high conductivity anisotropy.

Finally, leaching does not significantly alter the conductivity anisotropy of RBBC (Figure 5-57).

7.3.5 Mudrock Fabric and Texture Measurements

SEM images approximately 20 μm square were manually analyzed to determine the orientation, length and aspect ratio of individual particles discernable within the image. This manual technique produces results that are independent of the analyst, yielding mean particle orientations within ± 4 degrees for a given set of images of the same specimen. Both 1D analysis and 2D analysis was studied. The 1D analysis method requires the user to self-select the long axis of the particle to determine orientation, and results in measurements of particle length and particle orientation. Conversely, 2D analysis method requires the user to trace the particle perimeter; the particle geometry is used to compute the particle orientation, length and aspect ratio.

Though the 2D analysis allows the inclusion of lower aspect ratio particles, no significant difference in mean particle orientation was noted from the 1D analysis.

The mean particle orientation for RBBC decreases monotonically from ~ 50 degrees to the horizontal at 0.1 MPa and porosity 0.57 to as low as 28 degrees to the horizontal at 40 MPa and porosity 0.30 (Figure 6-4). These results contrast measurements from X-Ray Texture goniometry, which suggest a mean particle orientation varying from 25 to 24 degrees over this stress range. This difference is likely due to scale differences between the two techniques; the image analysis technique focuses on small scale particle orientation whereas the X-Ray goniometry technique captures the behaviour of larger particles, in this case larger Mica particles which may not be representative of the mean behaviour.

The particle orientation is both a function of particle size and particle aspect ratio. At 0.1 MPa and porosity 0.57, the mean particle orientation of RBBC mudrock is independent of particle size. However, with compression, larger particles ($> 1 \mu\text{m}$) undergo significantly more rotation than smaller particles (0.2 – 0.6 μm) (Figure 5-64 and Figure 5-65). At 10 MPa larger particles have a mean orientation of 24 degrees to the horizontal, while smaller particles have a mean orientation of only 33 degrees to the horizontal. Increasing the stress level and decreasing the porosity reduces the size dependence of the particle orientation and without significantly changing the mean particle orientation.

Larger particles also have higher aspect mean aspect ratios > 4 , whereas smaller particles have lower mean aspect ratios ~ 2.3 (Figure 5-66). Further, particles with low aspect ratio (varying between 1 and 2.3) undergo less rotation than higher aspect ratio particles (>4). Low aspect ratio RBBC particles experienced only 8 degrees rotation, from 43 to 35 degrees to the horizontal. High aspect ratio particles rotated more, rotating 21 degrees from 43 to 22 degrees to the horizontal, as the applied stress increases from 0.1 to 10 MPa (Figure 5-68 and Table 5-27).

Finally, the mean aspect ratio for RBBC is 3.74 ± 2.40 . This value is independent of stress level, indicating that particle breaking is not significant within the stress levels investigated.

7.4 Recommendations for Future Research

More measurements covering a wider stress range and wider range of mudrocks are required to better quantify the behaviours noted in this thesis. Specifically, more work should be done to systematically investigate the high stress permeability anisotropy, as well as the relationship between permeability anisotropy and conductivity anisotropy for a wide range of mudrocks. Special focus should be placed on mudrocks with varying Smectite content because of the issues encountered measuring Smectite rich RGoM-EI. Finally, the test method developed herein using cubic specimens yields trends with very low scatter at the expense of time; a new method should be developed to expedite the process and allow more rapid exploratory testing that will be validated with point measurements made using the cubic specimen method.

7.4.1 New equipment development

New equipment should be developed to investigate the permeability anisotropy of specimens compressed to effective stresses lower than 0.4 MPa and higher than 40 MPa. The development of a new method and new equipment could also speed up the permeability and resistivity anisotropy measurement process and allow a more thorough investigation of additional factors (described below) within the graduate student lifespan.

Using the cubic specimen method, the minimum stress of 0.4 MPa is constrained by the specimen's ability to maintain a cubic shape without disturbance during the testing timespan. The maximum stress is currently constrained by 3 factors: the maximum capacity of the highest stress load frame combined with the specimen size (~60 MPa), the required OCR of 4 (yields a maximum of 15 MPa measurement effective stress) and the maximum capacity of the flexible wall permeameter (10 MPa). To increase the stress range of the experiments using the cubic specimen method, both the capacity of the resedimentation load frame and the flexible wall permeameter must be significantly increased. The sedimentation cylinders will also need to be strengthened accordingly.

A better solution may be to develop a completely new set of equipment that uses a different measurement technique. Such a new technique might be developed by modifying current techniques that are used in the literature to measure the permeability anisotropy of specimens. One method is to measure the permeability anisotropy of a mudrock by measuring the permeability in the vertical and horizontal direction using two different specimens. Each specimen is loaded using either CRS or incremental oedometer methods to sequentially increasing vertical effective stresses. Constant head or constant flow tests are performed following stabilization at each stress level to measure the permeability. The permeability anisotropy is computed by dividing the horizontal permeability measured on one specimen by the vertical permeability measured on another specimen. These techniques require the use of two specimens and measurements are never obtained at exactly the same porosity and effective stress. Because the permeability anisotropy

ratio is very sensitive to small changes in permeability, this leads to scatter in the permeability anisotropy vs. porosity trend. The cubic specimen method provides results with less scatter within the stress range 0.4 to 40 MPa.

However, a new solution by Yune and Jung (2011) provides a radial CRS solution. This, combined with the solution for vertical CRS, would provide continuous measurement of both the vertical and horizontal permeability as function of porosity using two different specimens: one to measure the vertical permeability using the standard CRS solution, and one to measure the horizontal permeability using a radial CRS solution. This would solve the problem of measuring the horizontal permeability at one porosity and the vertical permeability at a slightly different porosity. Additionally, this approach would not require handling the specimen multiple times. Further, the technology already exists at MIT to perform vertical CRS tests up to 100 MPa. This technology could be adapted to measure lower stress specimens as well. This method would only work for uniform materials, such as the resedimented mudrocks used in this study.

Finally, the resistivity measurement could be easily incorporated into the CRS by adding electrodes to the top and bottom of the specimen as was done for the cubic specimen method. However, currently, the resistivity measurement process is manual and would have to be done incrementally. One option would be to automate this process and have a computer take measurements at fixed intervals; however this would require significant technology development which may not be merited.

7.4.2 Stress Level Dependence & Effect of OCR

The current research program investigated the behaviour of mudrocks compressed to maximum effective stresses ranging from 0.4 to 40 MPa. An extensive study was conducted for RBBC which revealed two potential stress level dependencies. As a result, the stress range of investigation should be extended to include both lower and higher maximum effective stresses. This will require the development of new equipment, as discussed above.

Measuring the permeability anisotropy of lower stress specimens will reveal 1) the stress level and porosity at which anisotropy begins to develop and 2) the porosity and strain level at which particle rotation becomes important.

Measuring the permeability anisotropy of different mudrocks over a larger stress range, including higher effective stresses (up to or exceeding 40 MPa) will confirm whether the trends measured for RBBC are representative of average mudrock behaviour. The RBBC results suggested that there is a transition point at which the pore space continuity becomes an important controlling factor in permeability anisotropy development. Systematically measuring the permeability anisotropy vs. stress for different mudrocks, as was done for RBBC but extended to higher stress levels, will confirm if pore space continuity affects the permeability anisotropy development of all mudrocks. Specifically, this systematic approach could investigate whether or not this behaviour is characteristic of Smectite rich mudrocks found in the Gulf of Mexico.

Finally, this research used the cubic specimen method which required specimens to be rebounded to an OCR ~ 4 to produce a $K_o \sim 1$. This condition allowed specimens to be trimmed into, and to maintain a cubic shape. However, natural mudrocks vary in OCR and many are normally consolidated. Many aspects of soil behaviour are OCR dependent, including mudrock compression behaviour (e.g. compression ratio SR) and mudrock strength. Though the literature has shown that the permeability varies with porosity, the permeability anisotropy has not been explicitly shown to be independent of OCR; measuring the permeability anisotropy at different OCR's will prove or disprove this hypothesis.

7.4.3 Effect of Initial Fabric & Salinity

Marine mudrocks have naturally flocculated fabrics. Soil leaching was performed in an attempt to modify the initial fabric by altering the pore fluid salinity to alter particle aggregation during sedimentation and create a dispersed fabric. Although the method of leaching was able to remove most of the salts, the measurements revealed that leaching was unable to alter the mudrock compressibility, permeability, resistivity or anisotropy. Based on comparison with results reported by Horan (2012), leaching was unable to produce a dispersed initial fabric.

Instead of modifying naturally flocculated marine mudrocks, it might be more productive to obtain a lake sedimented mudrock with a naturally dispersed fabric for re-sedimentation. Permeability and resistivity analysis combined with particle orientation analysis will reveal whether lake sedimented mudrocks have different initial fabrics, and if the initial fabric in turn affects permeability anisotropy development in terms of both magnitude and trend.

Though the pore fluid salinity does not significantly affect the measured permeability aside from potentially altering the mudrock fabric, the salinity significantly impacts the mudrock resistivity. The formation factor normalizes the resistivity by the pore fluid salinity; however mudrocks are comprised of charged particles with surface conductivity that is a function of pore fluid salinity. Measured formation factor values are often adjusted to account for particle surface conductivity.

This research suggests that when comparing the resistivity anisotropy and the permeability anisotropy, the particle surface conductivity is unimportant at the pore fluid salinities measured. However, this work does not explicitly investigate the effects of varying pore fluid salinity on measured formation factor or resistivity anisotropy, and more specifically, the relationship between conductivity anisotropy and permeability anisotropy. Future work might involve measuring a mudrock that is more reactive to changes in pore fluid salinity, such as a Smectite rich mudrock. Specimens could be made at different salinities to compare the anisotropy difference as a function of salinity. The results of such work would prove the dependence or independence of the conductivity anisotropy on salinity, and further, whether the complex correction factors applied to field resistivity in practice are isotropic.

7.4.4 Effect of Mineralogy and Clay Fraction

This research measured the permeability and resistivity of a variety of mudrocks covering a range of plasticity, clay fraction and mineralogy. Comparison between the RBBC and 39% Clay RBBC results showed that adding silt to reduce the clay fraction had a measurable effect on the trend and magnitude of the permeability anisotropy development. A similar study to investigate the effects of increasing the clay fraction, or systematically adjusting the mineralogy might also be worthwhile.

Further, the RGoM-EI Mudrock was difficult to measure because it cracked horizontally. As a result, only two specimens were studied. However, this mudrock is of general interest because it is most representative of the mudrocks encountered in practice. More work is needed to understand how to successfully measure the permeability anisotropy of RGoM-EI mudrock, and to determine why it cracked. This might be combined with the above systematic study of the effects of clay fraction and mineralogy. For example, Smectite might be incrementally added to RBBC to determine at the Smectite percentage that causes specimen cracking, or a significant decrease in permeability.

7.4.5 Effect of Cementation or Temperature

Finally, this research focused on the permeability anisotropy of mechanically compressed mudrocks. However, natural mudrocks are mechanically compressed, cemented and thermally altered. This research could be extended by incorporating either cementation or temperature into the mix to determine if these factors increase, decrease or otherwise alter the permeability anisotropy development, or the observed relationship between resistivity anisotropy and permeability anisotropy.

(Page intentionally left blank)

Bibliography

Abdulhadi, N. O. (2009). "An Experimental Investigation into the Stress-Dependent Mechanical Behavior of Cohesive Soil with Application to Wellbore Instability." Ph.D. Thesis, MIT, Cambridge, MA

Abu-hassanein, B. Z. S., Benson, C. H., and Blotz, L. R. (1996). "Electrical resistivity of compacted clays." *Journal of Geotechnical Engineering*, (MAY), 397–406.

Adams, A. L. (2011), "Laboratory Evaluation of the Constant Rate of Strain and Constant Head Techniques for Measurement of the Hydraulic Conductivity of Fine Grained Soils", MS Thesis, MIT, Cambridge, MA.

Adams, A. L., Germaine, J. T., Flemings, P. B., and Day-Stirrat, R. J. (2013). "Stress induced permeability anisotropy of Resedimented Boston Blue Clay." *Water Resources Research*, 49, p. 1–11.

Allman, M. A., and Atkinson, J. H. (2010). "Mechanical properties of reconstituted Bothkennar soil." *Geotechnique*, 42(2), 289–301.

Anderson, G. R. (1991). "Physical Mechanisms Controlling the Strength and Deformation Behavior of Frozen Sand." MIT, Cambridge, MA.

Archie, G. E. (1942). "The electrical resistivity log as an aid in determining som reservoir characteristics." *Transactions of the American Institute of Mining and Metallurgical Engineers*, 146, 54–62.

ASTM Standard D2435 (2011), "Standard Test Methods for One-Dimensional Consolidation Properties of Soils Using Incremental Loading", ", ASTM International, West Conshohocken, PA, 2003, www.astm.org

ASTM Standard D4186 (2006), "Standard Test Method for One-Dimensional Consolidation Properties of Saturated Cohesive Soils Using Controlled-Strain Loading", ASTM International, West Conshohocken, PA, 2003, www.astm.org

ASTM Standard D854 (2010). "Standard Test Methods for Specific Gravity of Soil Solids by Water Pycnometer." ASTM International, West Conshohocken, PA,

Atkins Jr., E. R., and Smith, G. H. (1961). "The significance of particle shape in formation resistivity factor - porosity relationships." *Journal of Petroleum Technology*, 13(3), 285–291.

Bachrach, R. (2011), "Elastic and resistivity anisotropy of shale during compaction and digenesis : Joint effective medium modeling and field observations", *Geophysics*, 76(6), E175 – E186

- Barosh, P. J., C. A. Kaye, and D. Woodhouse (1989), "Geology of the Boston Basin and vicinity" *Civil Engineering Practice, Journal of the Boston Society of Civil Engineers*, v. 4(1), p. 39 – 52.
- Basak, P. (1972), Soil structure and its effects on hydraulic conductivity, *Soil Science*, 114(6), 417–422.
- Bergaya, F., and Vayer, M. (1997). "CEC of clays: Measurement by adsorption of a copper ethylenediamine complex." *Applied Clay Science*, 12(3), 275–280.
- Bešter-Rogač, M., and D. Habe (2006), "Modern Advances in Electrical Conductivity Measurements of Solutions", *Acta Chimica Slovenica*, 53, 391–395.
- Bethke, B. C. M. (1989). "Modeling subsurface flow in sedimentary basins." *Geologische Rundschau*, 78(1), 129–154.
- Blewett, J., McCarter, W. J., Chrisp, T. M., and Starrs, G. (2001). "Monitoring sedimentation of a clay slurry." *Geotechnique*, 51(8), 723–728.
- Boggs, S. (2006). *Principles of Sedimentology and Stratigraphy* (Fourth Edi., p. 139). Upper Saddle River, NJ: Pearson Education Inc.
- Bourlange, S., Henry, P., Moore, J. C., Mikada, H., and Klaus, A. (2003). "Fracture porosity in the décollement zone of Nankai accretionary wedge using Logging While Drilling resistivity data." *Earth and Planetary Science Letters*, 209, 103–112.
- Brannan, G. O., and Von Gonten, W. D. (1973). "The effect of temperature on the formation resistivity factor of porous media." *Society of Petrophysicists & Well Log Analysts Fourteenth Annual Logging Symposium*.
- Broichhausen, H., Littke, R., and Hantschel, T. (2005). "Mudstone compaction and its influence on overpressure generation, elucidated by a 3D case study in the North Sea." *International Journal of Earth Sciences*, 94, 956–978.
- Brunauer, S., P. H. Emmett, and E. Teller (1938), "Adsorption of Gases in Multi-Molecular Layers", *Journal of the American Chemical Society*, 60, 309–319.
- Burland, J. B. (1990), "On the compressibility and shear strength of natural clays", *Geotechnique*, 40(3), 329–378.
- Carman, P. C. (1937). "Fluid flow through a granular bed." *Trans. Inst. Chem. Eng.*, 15, 150-156.
- Carman, P. C. (1956). *Flow of gasses through porous media*. Butterworth, London.
- Carroll, D. (1959), Ion exchange in clays and other minerals, *Bulletin of the Geological Society of America*, 70, 70–100.

Casey, B. (2011). "The Significance of Specimen End Restraint in High Pressure Triaxial Testing of Cohesive Soil." SM Thesis, MIT, Cambridge, MA.

Casey, B. (2014). "The Consolidation and Strength Behavior of Mechanically Compressed Fine-Grained Sediments ", PhD Thesis, MIT, Cambridge, MA.

Casey, B., and Germaine, J. T. (2013a). "Stress Dependence of Shear Strength in Fine-Grained Soils and Correlations with Liquid Limit." *Journal of Geotechnical and Geoenvironmental Engineering*, 139(10), 1709–1717.

Casey, B., and Germaine, J. T. (2013b). "Variation of Cohesive Sediment Strength with Stress Level." *Multiphysical Testing of Soils and Shales, Springer Series in Geomechanics and Geoengineering*, 1–6.

Casey, B., Germaine, J. T., Flemings, P. B., Reece, J. S., Gao, B., and Betts, W. (2013). "Liquid limit as a predictor of mudrock permeability." *Marine and Petroleum Geology*, Elsevier Ltd, 44, 256–263.

Cauble, D. F. (1996). "An Experimental Investigation of the Behavior of a Model Suction Caisson in a Cohesive Soil." MIT, Cambridge, MA.

Cerato, A. B. (2001). "Influence of specific surface area on geotechnical characteristics of fine-grained soils." M.S. Thesis, University of Massachusetts Amherst, Amherst, MA.

Cerato, A. B., and A. J. Lutenegeger (2004), "Determining Intrinsic Compressibility of Fine-Grained Soils", *Journal of Geotechnical and Geoenvironmental Engineering*, 130(August), 872–877.

Cerato, A. B., and A. J. Lutenegeger (2005), "Activity , Relative Activity and Specific Surface Area of Fine-Grained Soils", in Proceedings of the 16th International Conference on Soil Mechanics and Geotechnical Engineering (ICSMGE), vol. 2, pp. 325–328, Osaka, Japan, Sept. 12-16th.

Chan, H. T., and Kenney, T. C. (1973). "Laboratory Investigation of Permeability Ratio of New Liskeard Varved Soil." *Canadian Geotechnical Journal*, 10, 453–472.

Chapuis, R. P., and D. E. Gill (1989), "Hydraulic anisotropy of homogeneous soils and rocks: influence of the densification process", *Bulletin of the International Association of Engineering Geology*, 39, 75–86.

Clavier, C., Coates, G., and Dumanoir, J. (1984). "The theoretical and experimental bases for the Dual-Water Model for the interpretation of shaly sands." *Society of Petroleum Engineers Journal*, 153–168.

Clennell, M. B., D. N. Dewhurst, K. M. Brown, and G. K. Westbrook (1999), "Permeability anisotropy of consolidated clays", *Muds and Mudstones: Physical and Fluid Flow Properties. Geological Society, London, Special Publications*, 158, 79–96.

Cotecchia, F., and Chandler, R. J. (1997). "The influence of structure on the pre-failure behaviour of a natural clay." *Geotechnique*, 47(3), 523–544.

- Crain, E. R. (2013). "Crain's Petrophysical Handbook - Resistivity Basics." <<http://www.spec2000.net/06-resistivityarchie.htm>>.
- Daigle, H., and B. Dugan (2011), "Permeability anisotropy and fabric development: A mechanistic explanation", *Water Resources Research*, 47, W12517
- Darcy, H. (1856). "Les Fontaines Publiques de la ville de Dijon". Paris.
- Das, B. M. (2008), *Advanced Soil Mechanics*, 3rd ed., Taylor & Francis, New York, USA.
- David, C. (1993). "Geometry of flow paths for fluid transport in rocks." *Journal of Geophysical Research*, 98(B7), 12267–12278.
- Day-Stirrat, R. J., A. M. Schleicher, J. Schneider, P. B. Flemings, J. T. Germaine, and B. A. van der Pluijm (2011), "Preferred orientation of phyllosilicates: Effects of composition and stress on reseedimented mudstone microfabrics", *Journal of Structural Geology*, 33, 1347–1358
- Day-Stirrat, R. J., Aplin, A. C., Srodon, J., and van der Pluijm, B. a. (2008). "Diagenetic reorientation of phyllosilicate minerals in paleogene mudstones of the Podhale Basin, Southern Poland." *Clays and Clay Minerals*, 56(1), 98–109.
- Day-Stirrat, R. J., Flemings, P. B., You, Y., Aplin, A. C., and van der Pluijm, B. a. (2012). "The fabric of consolidation in Gulf of Mexico mudstones." *Marine Geology*, 295-298, 77–85.
- Day-Stirrat, R. J., Schleicher, A. M., Schneider, J., Flemings, P. B., Germaine, J. T., and van der Pluijm, B. A. (2011). "Preferred orientation of phyllosilicates: Effects of composition and stress on reseedimented mudstone microfabrics." *Journal of Structural Geology*, 33, 1347–1358.
- de Lima, O. A. L., and Sharma, M. M. (1990). "A grain conductivity approach to shaly sandstones." *Geophysics*, 55(10), 1347-1356.
- Delage, P., and G. Lefebvre (1984), "Study of the structure of a sensitive Champlain clay and of its evolution during consolidation", *Canadian Geotechnical Journal*, 21, 21–35.
- Denicol, P. S., and X. D. Jing (1998), "Effects of water salinity, saturation and clay content on the complex resistivity of sandstone samples", *Geological Society, London, Special Publications*, 136(1), 147–157, doi:10.1144/GSL.SP.1998.136.01.13.
- Dewhurst, D. N., Aplin, A. C., Sarda, J.-P., and Yang, Y. (1998). "Compaction-driven evolution of porosity and permeability in natural mudstones- An experimental study and at." *Journal of Geophysical Research*, 103(B1), 651–661.
- Dewhurst, D. N., K. Brown, M. B. Clennell, and G. K. Westbrook (1996), "A comparison of the fabric and permeability anisotropy of consolidated and sheared silty clay", *Engineering Geology*, 42, 253–267

Emmanuel, S., and Day-Stirrat, R. J. (2012). "A framework for quantifying size dependent deformation of nano-scale pores in mudrocks." *Journal of Applied Geophysics*, Elsevier B.V., 86, 29–35.

Erdman, N., Campbell, R., and Asahina, S. (2006). "Precise SEM Cross Section Polishing via Argon Beam Milling." *Microscopy Today*, May, 22–25.

Evans, R. L. (2007), "Using CSEM techniques to map the shallow section of seafloor: From the coastline to the edges of the continental slope", *Geophysics*, 72(2), WA105–WA116.

Fahy, B. (2014), "The Influence of Salinity on the Mechanical Behavior of High Plasticity Soils", SM Thesis, MIT, Cambridge, MA.

Georgi, D., A. Bepalov, L. Tabarovsky, and J. Schoen (2002), "On the Relationship between Resistivity and Permeability Anisotropy", *Society of Petroleum Engineers Annual Technical Conference and Exhibition, San Antonio, Texas, SPE 77715*.

Germaine, J. T. (1982). "Development of the Directional Shear Cell for Measuring Cross Anisotropic Clay Properties." ScD Thesis, MIT, Cambridge, MA.

Germaine, J. T. (2009). "1.37 Geotechnical Measurements and Exploration Course Notes". Massachusetts Institute of Technology, Department of Civil and Environmental Engineering, Fall 2009.

Germaine, J. T., and Germaine, A. V. (2009). *Geotechnical Laboratory Measurements for Engineers*. John Wiley & Sons, Inc, Hoboken, New Jersey.

Giao, P. H., Chung, S. G., Kim, D. Y., and Tanaka, H. (2003). "Electric imaging and laboratory resistivity testing for geotechnical investigation of Pusan clay deposits." *Journal of Applied Geophysics*, 52(4), 157–175.

Graham, D. J., and Midgley, N. G. (2000). "Graphical Representation of Particle Shape using Triangular Diagrams: An Excel Spreadsheet Method." *Earth Surface Processes and Landforms*, 25, 1473–1477.

Grande, L., and Mondol, N. H. (2013). "Geomechanical, hydraulic and seismic properties of unconsolidated sediments and their applications to shallow reservoirs." *American Rock Mechanics Association 47th US Rock Mechanics / Geomechanics Symposium*, San Francisco, CA, USA.

Grennan, J. (2010). "Characterization of a Reconstituted Low Plasticity Silt." SM Thesis, MIT, Cambridge, MA.

Horan, A. J. H. (2012), "The mechanical behavior of normally consolidated soils as a function of pore fluid salinity", SM Thesis, MIT, Cambridge, MA.

- Huntley, D. (1986), "Relations between permeability and electrical resistivity in granular aquifers", *Groundwater*, 24(4), 466–474.
- Jones, C. A. (2010). "Engineering Properties of Resedimented Ugnu Clay from the Alaskan North Slope." MIT, Cambridge, MA.
- Kanitpanyacharoen, W., Wenk, H.-R., Kets, F., Lehr, C., and Wirth, R. (2011). "Texture and anisotropy analysis of Qusaiba shales." *Geophysical Prospecting*, 59, 536–556.
- Kontopoulos, N. S. (2012). "The effects of sample disturbance on preconsolidation pressure for normally consolidated and overconsolidated clays." PhD. Thesis, MIT, Cambridge, MA.
- Kozeny, J. (1927). "Über kapillare Leitung des Wassers im Boden." *Sitzungsber Akad. Wiss. Wien*, 136, 271-306.
- Ladd, C. C. (1996). "1.361 Advanced Soil Mechanics Notes." Massachusetts Institute of Technology.
- Ladd, R. S. (1965). "Use of Electrical Pressure Transducers to Measure Soil Pressure". Cambridge, MA, 51.
- Lambe, T. W. (1958), "The engineering behavior of compacted clay", *Proceedings of the American Society of Civil Engineers*, 84(SM.2), 35 pp.
- Lambe, T. W., and R. V. Whitman (1969), *Soil Mechanics*, John Wiley & Sons, Inc, New York.
- Leroueil, S., Bouclin, G., Tavenas, F., Bergeron, L., and Rochelle, P. La. (1990). "Permeability anisotropy of natural clays as a function of strain." *Canadian Geotechnical Journal*, 27, 568–579.
- Lide, D. R. (Ed.). (1994). *CRC Handbook of Chemistry and Physics*. CRC Press Inc.
- Long, H., Flemings, P. B., Germaine, J. T., and Saffer, D. M. (2011). "Consolidation and overpressure near the seafloor in the Ursa Basin, Deepwater Gulf of Mexico." *Earth and Planetary Science Letters*, Elsevier B.V., 305, 11–20.
- Losh, S., Eglinton, L., and Wood, J. (1994). Coring and Inorganic Geochemistry in the Pathfinder Well. In *Results of the Pathfinder drilling program into a major growth fault*. CD-ROM. LDEO Press. Lamont Doherty Earth Observatory, Palisades, NY.
- Losh, S., Walter, L., Meulbroek, P., Martini, A., Cathles, L., and Whelan, J. (2002). "Reservoir fluids and their migration into the South Eugene Island Block 330 reservoirs, Offshore Louisiana." *AAPG Bulletin*, 86(8), 1463–1488.
- Loucks, R. G., Reed, R. M., Ruppel, S. C., and Jarvie, D. M. (2009). "Morphology, genesis, and distribution of nanometer-scale pores in siliceous mudstones of the Mississippian Barnett Shale." *Journal of Sedimentary Research*, 79(12), 848–861.

- Machta, F., K. Eusterhuesa, G. J. Pronkb, and K. U. Totschea (2011), "Specific surface area of clay minerals: Comparison between atomic force microscopy measurements and bulk-gas (N₂) and -liquid (EGME) adsorption methods", *Applied Clay Science*, 53(1), 20–26.
- March, A. (1932), "Mathematische theorie der regelung nach der korngestalt bei affiner deformation", *Zeitschrift für Kristallograph*, 81, 287–297.
- Marjanovic, J. (2012). "The Study of Shear and Longitudinal Velocity Measurements of Sands and Cohesive Soils by." SM Thesis, MIT, Cambridge, MA.
- Martin, R. T. (1982). "Suggested Method of Test for Determination of Soluble Salts in Soil." *ASTM STP 476*, 288–290.
- Martin, R. T., and C. C. Ladd (1975), "Fabric of Consolidated Kaolinite", *Clays and Clay Minerals*, 23, 17–25.
- McCarter, W. J. (1984). "The electrical resistivity characteristics of compacted clays." *Géotechnique*, 34(2), 263–267.
- McCarter, W. J., Blewett, J., Chrisp, T. M., and Starrs, G. (2005). "Electrical property measurements using a modified hydraulic oedometer." *Canadian Geotechnical Journal*, 42, 655–662.
- McNeill, J. D. (1980). Electrical conductivity of soil and rocks. Geonics Limited. Technical Note TN5.
- Meegoda, N. J., I. P. King, and K. Arulanandan (1989), "An expression for the permeability of anisotropic granular media", *International Journal for Numerical and Analytical Methods in Geomechanics*, 13(1989), 575–598.
- Middleton, G. V. (Ed.). (2003). *Encyclopedia of Sediments and Sedimentary Rocks* (pp. 451–459). AA Dordrecht, The Netherlands: Kluwer Academic Publishers.
- Mitchell, J. K. (1956), The importance of structure to the engineering behavior of clay, Sc.D Thesis, MIT, Cambridge, MA.
- Mousseau, R. J., and R. P. Trump (1967), Measurement of Electrical Anisotropy of Clay-like Materials, *Journal of Applied Physics*, 38(11), 4375–4379
- Neuzil, C. E. (1994), How permeable are clays and shales, *Water Resources Research*, 30(2), 145–150.
- Nichols, G. (2009). *Sedimentology and Stratigraphy* (Second Edi., p. 21). Oxford, UK: John Wiley & Sons, Inc.
- O'Brien, N. R., and M. Slatt, R. (1990). *Argillaceous rock atlas*. Springer-Verlag, New York.

- Olsen, H. W. (1962), "Hydraulic flow through saturated clays", *Clays and Clay Minerals*, 9(2), 131-161.
- Ortega, O. J. (1992). "Computer Automation of the Consolidated-Undrained Direct Simple Shear Test." MIT, Cambridge, MA.
- Patnode, H. W., and Wyllie, M. R. J. (1950). "The presence of conductive solids in reservoir rocks as a factor in electric log interpretation." *Journal of Petroleum Technology*, 189, 47-52.
- Queeney, K. M. (2003). "Principles and Hardware of Electrolytic Conductivity Measurements." *Instrumentation, Systems, and Automation Society 48th Analysis Division Symposium*.
- Ransom, R. C. (2011). "Dual-water Archie and the importance of water geometry. A model and discussion." <www.archieparameters.com> (Mar. 22, 2013).
- Revil, A., L. M. Cathles III, S. Losh, and J. A. Nunn (1998), "Electrical conductivity in shaly sands with geophysical applications", *Journal of Geophysical Research*, 103(B10), 23925-23936
- Roduit, N. (2013). "JMicroVision: Image analysis toolbox for measuring and quantifying components of high-definition images. Version 1.2.7. <http://www.jmicrovision.com>."
- Santamarina, J. C., Klein, K. A., Wang, Y. H., and Prencke, E. (2002). "Specific surface : determination and relevance." *Canadian Geotechnical Journal*, 39, 233-241.
- Sawyer, D. E., Flemings, P. B., Dugan, B., & Germaine, J. T. (2009). Retrogressive failures recorded in mass transport deposits in the Ursa Basin, Northern Gulf of Mexico. *Journal of Geophysical Research*, 114(B10102), 1-20. doi:10.1029/2008JB006159
- Schneider, J. (2011). "Compression and permeability behavior of natural mudstones." PhD. Thesis, University of Texas at Austin, Austin, TX.
- Schneider, J., Flemings, P. B., Day-Stirrat, R. J., and Germaine, J. T. (2011). "Insights into pore-scale controls on mudstone permeability through resedimentation experiments." *Geology*, 39(11), 1011-1014.
- Scholes, O. N., Clayton, S. A., Hoadley, A. F. A., and Tiu, C. (2007). "Permeability anisotropy due to consolidation of compressible porous media." *Transport of Porous Media*, 68, 365-387.
- Scott, G. D., and Kilgour, D. M. (1969). "The density of random close packing of spheres." *British Journal of Applied Physics*, 2(2), 863-866.
- Sharqawy, M. H., V, J. H. L., and Zubair, S. M. (2010). "Thermophysical properties of seawater : a review of existing correlations and data." *Desalination and Water Treatment*, 16, 354-380.

Sheahan, T. C. (1991). "An Experimental Study of the Time-Dependent Undrained Shear Behavior of Resedimented Clay Using Automated Stress-Path Triaxial Equipment." MIT, Cambridge, MA.

Sheeran, D. E., and Krizek, R. J. (1971). "Preparation of homogeneous soil samples by slurry consolidation." *Journal of Materials*, 6(2), 356–373.

Skempton, A. W., and Jones, O. T. (1944). "Notes on the compressibility of clays." *Quarterly Journal of the Geological Society*, 100, 119–135.

Smith, R. E., and Wahls, H. E. (1969). "Consolidation under constant rate of strain." *Journal of the Soil Mechanics and Foundations Division*, 95(SM2), 519–539.

Stow, D. a. V. (1981). Fine-grained sediments: Terminology. *Quarterly Journal of Engineering Geology and Hydrogeology*, 14(4), 243–244. doi:10.1144/GSL.QJEG.1981.014.04.02

Stump, B. B., and Flemings, P. B. (2002). "Consolidation state, permeability, and stress ratio as determined from uniaxial strain experiments on mudstone samples from the Eugene Island 330 area, offshore Louisiana." *Pressure regimes in sedimentary basins and their prediction*, A. R. Huffman and G. L. Bowers, eds., American Association of Petroleum Geologists, Tulsa, OK, 131–144.

Tavenas, F., Leblond, P., Jean, P., and Leroueil, S. (1983). "The permeability of natural soft clays. Part 1: Methods of Laboratory Measurement." *Canadian Geotechnical Journal*, 20, 629–644.

Tavenas, F., P. Leblond, P. Jean, and S. Leroueil (1983), "The permeability of natural soft clays. Part 2 Permeability characteristics", *Canadian Geotechnical Journal*, 20, 645–660.

V. Engelhardt, W., and K. H. Gaida (1963), "Concentration changes of pore solutions during the compaction of clay sediments", *Journal of Sedimentary Petrology*, 33(4), 919–930.

Voltolini, M., H.-R. Wenk, N. H. Mondol, K. Bjørlykke, and J. Jahren (2009), "Anisotropy of experimentally compressed kaolinite-illite-quartz mixtures", *Geophysics*, 74(1), D13–D23

Waxman, M. H., and Smits, L. J. M. (1968). "Electrical conductivities in oil-bearing shaly sands." *Society of Petroleum Engineers Journal*, 243, 107–122.

Wenk, H.-R. (1985). "Measurement of Pole Figures." *Preferred orientation in deformed metals and rocks; an introduction to modern texture analysis*, Academic Press, Orlando, FL, 11–47.

Wissa, A. E. Z., Christian, J. T., Davis, E. H., and Heiberg, S. (1971). "Consolidation Testing at Constant Rate of Strain." *ASCE Journal of Soil Mechanics and Foundations Division*, 97(10), 1393–1413.

Witt, K.-J., and Brauns, J. (1984). "Permeability-anisotropy due to particle shape." *Journal of Geotechnical Engineering*, 109, 1181–1187.

Witt, K.-J., and J. Brauns (1981), Durchlassigkeitsanisotropie von Haufwerken infolge Kornplattigkeit und Kornorientierung, *Series of the Institute of Soil and Rock Mechanics, University of Karlsruhe, Karlsruhe, Federal Republic of Germany*, 87.

Yang, Y., and A. C. Aplin (1998), "Influence of lithology and compaction on the pore size distribution and modelled permeability of some mudstones from the Norwegian margin", *Marine and Petroleum Geology*, 15, 163–175.

Yang, Y., and A. C. Aplin (2007), "Permeability and petrophysical properties of 30 natural mudstones", *Journal of Geophysical Research*, 112, B03206

Yune, C., & Jung, Y. (2011). Application of Multi-Directional Flow Consolidometer for a Constant Rate of Strain Consolidation Test Under Various Drainage Conditions. *Geotechnical Testing Journal*, 35(2), 1–11.

Appendices

Appendix 1:	Raw Data	325
Appendix 2:	Permeability Anisotropy Measurement: Equipment, Methods and Analysis	371
Appendix 3:	Resistivity and Conductivity Anisotropy Measurement	419
Appendix 4:	Bench Top Resistivity Measurements: Summary of Results	461
Appendix 5:	Cation Exchange Capacity (CEC) and Specific Surface Area (SSA) Analysis	485
Appendix 6:	Equipment CAD Drawings.....	509
Appendix 7:	Sample Data Sheets	529
Appendix 8:	Constant Head Hydraulic Conductivity Program Code	537

(Page intentionally left blank)

Appendix 1: Raw Data

This appendix summarizes and describes the raw measurements made for this work.

Contents

Appendix 1: Raw Data	323
1 Permeability Measurements	326
2 Resistivity Measurements	327
3 Image Analysis	328

List of Tables

Table A1-1: Flexible Wall Permeameter Permeability and Resistivity Measurement Experimental Parameters (Page 1 of 6)	329
Table A1-2: Summary of Hydraulic Gradient measurements for Hydraulic Conductivity Calculation (1 of 10)	335
Table A1-3: Specimen metrics: stress and volume change (1 of 3)	345

List of Figures

Figure A1-1: 0.1 MPa RBBC UT Image, filename: SEM0020_BSE_001	348
Figure A1-2: 0.1 MPa RBBC UT Image, filename: SEM0020_BSE_002	349
Figure A1-4: 0.1 MPa RBBC UT Image, filename: SEM0020_BSE_004	350
Figure A1-5: 1 MPa RBBC UT Image, filename: SEM0021_BSE_001	351
Figure A1-6: 1 MPa RBBC UT Image, filename: SEM0021_BSE_002	352
Figure A1-7: 1 MPa RBBC UT Image, filename: SEM0021_BSE_004	353
Figure A1-8: 10 MPa RBBC UT Image, filename: SEM0022_BSE_001	354
Figure A1-9: 10 MPa RBBC UT Image, filename: SEM0022_BSE_002	355
Figure A1-10: 10 MPa RBBC UT Image, filename: SEM0022_BSE_004	356
Figure A1-11: 1 MPa RBBC MIT Image filename: RS242 H- 10, from HC038	357
Figure A1-12: 1 MPa RBBC MIT Image filename: RS242 H- 20, from HC038	358
Figure A1-13: 10 MPa RBBC MIT Image filename: HC036 V-036	359
Figure A1-14: 10 MPa RBBC MIT Image filename: HC036 V-021	360
Figure A1-15: 10 MPa RBBC MIT Image filename: HC036 V-025	361
Figure A1-16: 10 MPa RBBC MIT Image filename: HC036 V-037	362
Figure A1-17: 20 MPa RBBC MIT Image filename: HC044-095	363
Figure A1-18: 20 MPa RBBC MIT Image filename: HC044-096	364
Figure A1-19: 20 MPa RBBC MIT Image filename: HC044-112	365
Figure A1-20: 40 MPa RBBC MIT Image filename: HC034 V-034	366
Figure A1-21: 40 MPa RBBC MIT Image filename: HC034 V-018	367
Figure A1-22: 40 MPa RBBC MIT Image filename: HC034 V-022	368
Figure A1-23: 40 MPa RBBC MIT Image filename: HC034 V-038	369

1 Permeability Measurements

Table A1-1 summarizes the experimental parameters for every directional permeability and resistivity measurement conducted in the flexible wall permeameter. Table A1-2 summarizes the measurements used to compute the hydraulic conductivity for each hydraulic gradient applied to each specimen in all directions. Table A1-3 computes some specific metrics based on these parameters related to the stress and volume changes experienced by the specimen during the measurement procedure. The following list describes notes of interest related to specific directional measurements detailed in Table A1-1, Table A1-2, Table A1-3 and the computed porosity, permeability, or permeability anisotropy tabulated in Chapter 5:

- 1) HC004: was measured in an odd order: H1, V, H2. As a result, HC004 is not included in the horizontal measurement sequence bias calculation for RBBC.
- 2) HC007: The porosity seems high but there is no identifiable problem with the measurements.
- 3) HC011V2: A leak was identified and the rate inferred from the recompression data using graphical methods. The leak rate was not directly measured. A similar scenario occurred in HC021V, where the leak was directly measured. In HC021V it was noted that the leak rate inferred from the recompression data is double that measured during a leak test, likely due to variation in the pore pressure system configuration between the two measurements. Since no leak test was available for HC011V2, this logic was used to correct the data set and yielded near equality in the inflow and outflow volumes
- 4) HC021V: A leak was noted and measured. The hydraulic gradient measurements were adjusted for the leak, as was the recompression curve. Secondary compression was still significant even after adjusting for the leak, and was accounted for in the hydraulic conductivity measurement.
- 5) HC042: This specimen was used to determine the effect of resistivity measurement on the permeability. The test sequence was V, 'failed H1 test', H1, V2, V3. Resistivity was measured on H1, V2 and V3. No permeability or resistivity data from this measurement are used to define the measurement sequence bias correction factors, though the measurements can be corrected using these factors.
- 6) HC042H1: There is no BP inflow volume measurement due to loss of data acquisition during this time period.
- 7) HC044 - The second measurement, direction V, failed due to leakage. Leakage occurred via holes that were formed in the membrane from the high cell pressure forcing the membrane into the tiny pin probe holes from the previous direction's resistivity measurement. This problem was rectified in subsequent measurements by filling these holes with rubber plugs (pieces of O-Ring).
- 8) HC036H1: Excessive swelling of the specimen may have occurred during disassembly of the apparatus. The specimen was allowed access to water via the pores pressure lines for more than 5 minutes while attempts were made to remove the cubic end adapter. Therefore, the final specimen dimensions were disregarded and the initial dimensions were used for

length and area determinations. The final mass was disregarded and the specimen porosity was determined using measurements from subsequent directional measurements.

- 9) HC032: There was a leak in the pore pressure transducer. Data relevant to the back pressure phase was deemed irrelevant. Further, the pore pressure transducer was mistakenly overloaded (while disconnected from the specimen) and replaced later during the measurement. Therefore, two different pore pressure transducer zeros and calibration factors are used to reduce the data for this measurement.
- 10) HC030 and HC031: Had very low BP and low B Values. These specimens likely weren't saturated correctly. The BP should have been increased to 1.0 MPa to increase B value.

2 Resistivity Measurements

Two types of resistivity measurements were made for this thesis: measurements in the triaxial cell and measurements on the bench top. Resistivity measured in the triaxial cell was measured on the same specimens, in the same setup following the permeability measurement; data on these measurements are included in Table A1-1. Resistivity measured using the bench top method was also measured on sub specimens (cut portions) of the same specimens as those included in Table A1-1. These measurements were performed at laboratory temperatures (between 20 and 27 degrees Celsius).

The following paragraphs provide comments related to specific specimens listed in Table A1-1:

- 1) HC036 – Resistivity measurements show a current variation. Further, the correction factor accounting for current loss through the apparatus could not be applied to two measurements (H1 and V directions). The V2 measurement was used to estimate that this correction factor lowers the measured resistivity by a minimum of ~ 2-3%. Therefore, the HC036V and HC036H1 resistivity are high by ~ 2-3%; these errors will affect the computed conductivity anisotropy.
- 2) HC036, HC037, HC038 – showed a current trend in measured resistivity, where the resistivity was lowest at a current of 2 mA and highest in the current range of 6 – 10 mA. This error was due to unsteady measurements and likely a grounding problem. A poor connection on the ground wire was discovered on the resistivity measurement box and corrected, causing the current trend to disappear in subsequent measurements. As a result, the standard deviation of these measurements is higher than others.
- 3) HC038 – An internal wire was flattened at one point during the setup of the apparatus (it was caught in the seal between the cell wall and the base of the cell). It is not believed that this affected the resistivity measurements.
- 4) HC048 – The resistivity was measured before and after back pressure to determine the effect of back pressure saturation on the measurements. Before back pressure, resistivity was 2.74 Ωm . After back pressure resistivity was 2.68 Ωm . Saturation decreases the measured resistivity slightly, but the decrease is in the third significant digit and not significant.

3 Image Analysis

Image analysis was performed on images of RBBC obtained from two different sources: 9 images, 3 at each stress level (0.1, 1.0 and 10 MPa) of specimens resedimented and imaged at the Bureau of Economic Geology at the University of Texas at Austin, and 13 images of specimens resedimented at MIT and imaged using a SEM at Harvard University: 2 at 1 MPa, 4 at 10 MPa, 3 at 20 MPa and 4 at 40 MPa. Figure A1-10 to Figure A1-22 present these images.

Table A1-1: Flexible Wall Permeameter Permeability and Resistivity Measurement Experimental Parameters (Page 1 of 6)

Test ID	Material	σ'_s	BP	BP Vol	B	σ'	c_u	Ttime	ΔV Dim.	Meas. #	Dir.	L	A	Leak Rate		ρ
														Top	Bot	
		Mpa	Mpa	cm ³		Mpa	no	hr	cm ³			cm	cm ²	cm ³ /hr	cm ³ /hr	Ωm
HC003	RBBC	0.01	0.20	1.21	N/A	0.10	no	68.6	1.2	1	V	5.04	24.84	N/A	N/A	--
HC003	RBBC	0.02	0.20	0.92	1.00	0.10	no	48.9	-0.9	2	H1	4.94	25.20	N/A	N/A	--
HC004	RBBC	0.01	0.20	1.65	N/A	0.20	no	74.3	1.6	1	H1	4.88	26.04	N/A	N/A	--
HC004	RBBC	0.01	0.20	0.76	1.00	0.20	no	144.8	-1.5	2	V	5.16	24.30	N/A	N/A	--
HC004	RBBC	0.03	0.20	0.45	N/A	0.20	no	61.6	-0.4	3	H2	4.96	25.22	N/A	N/A	--
HC005	RBBC	0.08	0.25	1.22	N/A	0.29	no	48.4	2.6	1	V	5.12	24.67	N/A	N/A	--
HC005	RBBC	0.05	0.25	0.34	1.00	0.29	no	44.6	-0.8	2	H1	4.92	25.50	N/A	N/A	--
HC005	RBBC	0.12	0.25	0.88	N/A	0.29	no	49.2	-0.4	3	H2	4.95	25.29	N/A	N/A	--
HC006	RBBC	0.34	0.25	0.48	N/A	0.49	no	42.1	1.3	1	H1	5.02	25.14	N/A	N/A	--
HC006	RBBC	0.27	0.25	0.35	0.97	0.49	no	62.0	0.6	2	H2	4.94	25.67	N/A	N/A	--
HC006	RBBC	0.24	0.25	0.23	0.97	0.49	no	45.0	-0.8	3	V	5.10	24.70	N/A	N/A	--
HC007	RBBC	0.22	0.25	0.19	0.97	0.39	no	41.7	2.3	1	V	5.06	25.79	N/A	N/A	--
HC007	RBBC	0.23	0.25	0.14	0.97	0.39	no	49.3	0.0	2	H1	5.07	25.71	N/A	N/A	--
HC007	RBBC	0.20	0.25	0.14	0.98	0.39	no	96.5	0.4	3	H2	5.04	25.94	N/A	N/A	--
HC008	RBBC	0.48	0.25	0.03	0.96	0.78	no	30.3	2.7	1	V	5.21	24.60	N/A	N/A	--
HC008	RBBC	0.52	0.25	0.08	0.95	0.78	no	60.1	0.2	2	H1	4.87	26.33	N/A	N/A	--
HC008	RBBC	0.46	0.25	0.10	0.94	0.78	yes	65.9	0.1	3	H2	5.01	25.62	N/A	N/A	--
HC008	RBBC	0.39	0.25	0.06	0.95	0.78	no	25.0	-0.5	4	V2	5.25	24.37	N/A	N/A	--
HC009	RBBC	0.78	0.25	0.32	0.92	1.08	no	40.2	3.4	1	H1	4.98	25.94	N/A	N/A	--
HC009	RBBC	0.46	0.25	0.01	N/A	1.08	no	28.2	0.4	2	H2	5.00	25.92	N/A	N/A	--
HC009	RBBC	0.29	0.25	0.01	0.98	1.08	no	24.1	-1.7	3	V	5.17	24.75	N/A	N/A	--
HC011	RBBC	0.48	0.34	0.28	0.99	1.47	no	85.2	3.9	1	V	5.17	24.69	N/A	N/A	--
HC011	RBBC	0.25	0.34	0.07	0.98	1.47	no	257.5	0.4	2	H1	4.95	25.89	N/A	N/A	--
HC011	RBBC	0.26	0.34	0.08	N/A	1.47	no	40.4	-0.1	3	H2	4.95	25.86	N/A	N/A	--
HC011	RBBC	0.24	0.34	0.05	N/A	1.47	no	50.3	-1.6	4	V2	5.19	24.38	0.007	N/A	--

Table A1-1: Flexible Wall Permeability and Resistivity Measurement Experimental Parameters (Page 2 of 6)

Test ID	Material	σ'_s Mpa	BP Mpa	BP Vol cm ³	B	σ' Mpa	c _c	Time hr	ΔV Dim. cm ³	Meas. #	Dir.	L cm	A cm ²	Leak Rate		ρ Ωm
														Top cm ³ /hr	Bot cm ³ /hr	
HC016	RBBC	0.78	0.34	3.15	N/A	1.47	no	48.3	4.3	1	V	5.14	24.94	N/A	N/A	--
HC016	RBBC	0.76	0.34	1.76	N/A	1.47	no	24.1	-0.8	2	H1	4.90	26.00	N/A	N/A	--
HC016	RBBC	0.46	0.34	0.11	N/A	1.47	no	27.0	0.5	3	H2	5.04	25.40	N/A	N/A	--
HC018	RBBC	1.30	0.34	0.11	N/A	2.45	no	29.5	2.8	1	V	5.16	25.56	N/A	N/A	--
HC018	RBBC	0.95	0.34	0.04	N/A	2.45	no	42.3	2.1	2	H1	5.03	26.63	N/A	N/A	--
HC018	RBBC	0.66	0.34	0.05	N/A	2.45	no	56.0	-1.2	3	H2	5.06	26.19	N/A	N/A	--
HC019	RBBC	1.44	0.34	1.66	N/A	2.45	yes	96.1	4.0	1	H1	5.05	25.11	N/A	N/A	--
HC019	RBBC	0.70	0.34	-0.20	N/A	2.45	no	73.1	0.1	2	H2	4.96	25.58	0.000	0.000	--
HC019	RBBC	0.71	0.34	0.30	N/A	2.45	no	40.3	-1.7	3	V	5.04	24.81	N/A	N/A	--
HC020	RBBC	1.16	0.34	-0.05	N/A	2.45	no	85.9	1.7	1	V	5.16	26.53	0.013	0.000	--
HC020	RBBC	0.70	0.34	0.05	N/A	2.45	yes	64.9	1.8	2	H1	5.12	27.08	N/A	N/A	--
HC020	RBBC	0.48	0.34	0.06	N/A	2.45	no	87.2	-0.3	3	H2	5.12	27.04	N/A	N/A	--
HC021	RBBC	1.47	0.34	5.01	N/A	2.45	no	41.0	3.4	1	H1	5.00	25.45	N/A	N/A	--
HC021	RBBC	0.54	0.34	0.12	N/A	2.45	yes	44.3	-2.9	3	V	5.11	24.57	0.010	0.000	--
HC022	RBBC	1.46	0.34	3.70	N/A	1.96	no	92.1	5.4	1	H1	4.99	25.63	0.000	0.000	--
HC022	RBBC	1.00	0.34	0.62	N/A	1.96	no	25.1	-0.1	2	H2	4.95	25.81	N/A	N/A	--
HC022	RBBC	0.44	0.34	4.99	N/A	1.96	no	49.7	-1.9	3	V	5.14	24.49	N/A	N/A	--
HC024	39% Clay	1.99	0.34	0.76	0.85	2.45	yes	24.9	0.26	1	H1	5.08	26.32	N/A	N/A	--
HC024	39% Clay	1.50	0.39	0.46	0.73	2.45	yes	51.8	-1.21	2	H2	5.03	26.34	N/A	N/A	--
HC024	39% Clay	1.59	0.39	0.03	0.86	2.45	yes	48.1	2.71	3	V	5.17	25.80	N/A	N/A	--
HC025	39% Clay	1.33	0.39	-0.01	0.90	1.57	no	52.0	1.34	1	H1	4.99	25.23	N/A	N/A	--
HC025	39% Clay	1.20	0.39	0.11	0.88	1.57	no	63.2	-0.44	2	H2	4.95	25.32	N/A	N/A	--
HC025	39% Clay	1.14	0.39	0.18	0.88	1.57	no	88.2	-0.25	3	V	5.06	24.72	N/A	N/A	--
HC026	39% Clay	0.73	0.39	1.08	0.94	0.78	no	48.5	0.52	1	V	5.10	25.28	N/A	N/A	--
HC026	39% Clay	0.66	0.49	0.93	0.95	0.78	no	96.9	-0.14	2	H1	4.96	25.98	N/A	N/A	--
HC026	39% Clay	0.62	0.39	0.44	0.94	0.78	no	126.6	0.24	3	H2	5.05	25.54	N/A	N/A	--

Table A1-1: Flexible Wall Permeability and Resistivity Measurement Experimental Parameters (Page 3 of 6)

Test ID	Material	σ'_s	BP	BP Vol	B	σ'	c_u	Time	ΔV Dlim.	Meas. #	Dir.	L	A	Leak Rate		ρ
														Top	Bot	
		Mpa	Mpa	cm ³		Mpa		hr	cm ³			cm	cm ²	cm ³ /hr	cm ³ /hr	Ωm
HC027	39% Clay	0.42	0.44	0.72	0.95	0.49	no	86.4	-0.20	1	H1	5.06	25.87	N/A	N/A	--
HC027	39% Clay	0.36	0.44	0.80	0.95	0.49	no	49.2	-1.21	2	V	5.18	25.07	N/A	N/A	--
HC027	39% Clay	0.24	0.44	0.10	0.98	0.49	no	121.4	0.66	3	V2	5.18	25.19	N/A	N/A	--
HC029	39% Clay	0.21	0.34	0.21	0.99	0.29	no	25.1	0.92	1	V	5.12	24.61	N/A	N/A	--
HC029	39% Clay	0.22	0.34	0.22	0.99	0.29	no	110.6	-0.64	2	H1	4.93	25.39	N/A	N/A	--
HC029	39% Clay	0.23	0.39	0.42	0.99	0.29	no	73.6	-0.61	3	H2	4.93	25.29	N/A	N/A	--
HC030	RGoM-EI	2.45	0.54	10.31	0.59	2.45	no	505.9	3.00	1	V	5.02	25.09	0.000	0.000	--
HC030	RGoM-EI	2.38	0.54	1.36	0.67	2.45	yes	117.0	1.18	2	H1	5.06	25.15	0.001	0.002	--
HC030	RGoM-EI	1.69	0.54	-0.06	0.72	2.45	yes	102.4	0.25	3	H2	5.01	25.42	0.003	0.001	--
HC031	RGoM-EI	1.42	0.49	8.64	0.81	1.47	no	97.0	3.43	1	H1	5.19	26.71	0.000	0.003	--
HC031	RGoM-EI	1.14	0.49	0.56	0.72	1.47	no	68.8	0.43	2	V	5.27	26.40	0.000	0.002	--
HC031	RGoM-EI	1.37	0.49	-4.23	0.72	1.47	no	257.5	-0.30	3	V2	5.27	26.36	0.000	0.001	--
HC032	RSFBM	2.42	0.98	N/A	0.80	2.45	no	204.9	1.66	1	V	5.06	24.98	-0.001	0.000	--
HC032	RSFBM	1.76	0.98	0.40	0.93	2.45	yes	40.6	0.45	2	H1	4.97	25.49	0.001	0.000	--
HC032	RSFBM	1.48	0.98	0.11	0.86	2.45	yes	87.7	0.68	3	H2	5.03	25.32	0.004	0.000	--
HC033	RSFBM	1.37	0.98	2.37	0.93	1.47	no	86.9	2.16	1	H1	5.00	26.47	0.002	0.000	--
HC033	RSFBM	1.20	0.98	1.02	0.91	1.47	no	89.5	-0.24	2	V	5.22	25.29	0.000	0.000	--
HC033	RSFBM	1.27	0.98	1.06	0.96	1.47	no	68.3	0.27	3	V2	5.23	25.30	0.002	0.000	--
HC034	RBBC	7.60	0.97	0.39	0.82	9.81	no	50.8	7.5	1	V	5.25	24.36	0.000	0.000	--
HC034	RBBC	7.83	0.98	2.96	0.80	9.81	no	97.4	-5.4	2	H1	4.97	24.68	0.000	0.000	--
HC034	RBBC	7.86	0.98	3.31	0.79	9.81	no	48.8	0.2	3	H2	4.89	25.09	0.000	0.000	--
HC036	RBBC	2.45	0.98	1.24	0.91	2.45	no	79.1	N/A	1	H1	5.03	25.59	0.000	0.002	1.67
HC036	RBBC	1.47	0.98	0.04	0.96	2.45	yes	39.3	-6.4	2	V	5.32	24.98	0.000	-0.001	3.03
HC036	RBBC	2.00	1.08	4.12	0.90	2.45	yes	88.1	-0.9	3	V2	5.31	24.88	0.000	0.000	3.46

Table A1-1: Flexible Wall Permeability and Resistivity Measurement Experimental Parameters (Page 4 of 6)

Test ID	Material	σ'_s Mpa	BP Mpa	BP Vol cm ³	B	σ' Mpa	c _u	Time hr	ΔV Dilm. cm ³	Meas. #	Dir.	L cm	A cm ²	Leak Rate		ρ Ωm
														Top cm ³ /hr	Bot cm ³ /hr	
HC037	RBBC	0.39	0.79	7.90	0.96	0.39	no	25.8	-0.1	1	H1	5.10	25.67	0.000	0.000	1.86
HC037	RBBC	0.39	0.98	6.96	0.97	0.39	no	16.5	0.2	2	V	5.03	26.08	0.000	0.000	3.24
HC037	RBBC	0.24	0.59	0.20	1.00	0.39	yes	40.7	-0.4	3	V2	5.02	26.04	0.000	0.000	3.40
HC038	RBBC	0.15	0.39	0.18	0.99	0.25	yes	24.6	0.2	1	V	5.01	25.22	0.000	0.000	1.61
HC038	RBBC	0.15	0.39	0.12	1.00	0.25	yes	25.4	0.3	2	H1	4.99	25.34	0.000	0.000	1.14
HC038	RBBC	0.16	0.39	0.14	1.00	0.25	yes	32.5	-0.1	3	H2	5.04	25.07	0.000	0.000	1.22
HC040	RBBC	7.36	0.98	1.04	0.80	7.55	no	97.5	2.6	1	H1	5.06	25.97	0.001	0.000	2.78
HC040	RBBC	7.36	0.98	9.23	0.76	7.55	no	42.6	0.3	2	V	5.18	25.43	0.002	0.000	4.24
HC040	RBBC	7.36	0.98	3.76	0.78	7.55	no	60.6	-2.2	3	V2	5.12	25.32	0.002	0.000	4.79
HC042	RBBC	0.14	0.49	1.25	1.00	0.20	yes	66.5	0.5	1	V	5.06	24.98	0.000	0.000	--
HC042	RBBC	0.12	0.49	N/A	1.00	0.20	yes	28.8	-0.3	3	H1	4.93	25.46	0.000	0.000	1.30
HC042	RBBC	0.20	0.49	1.99	0.99	0.20	no	14.2	-1.4	4	V2	5.05	24.55	0.000	0.000	1.78
HC042	RBBC	0.20	0.49	2.08	0.96	0.20	no	48.9	0.2	5	V3	5.04	24.64	0.000	0.000	1.82
HC044	RBBC	4.90	0.98	2.13	0.85	4.90	no	26.2	-0.5	1	H1	5.00	24.36	0.002	0.000	2.37
HC044	RBBC	4.90	0.98	1.58	0.82	4.90	no	0.4	0.1	3	V2	4.82	25.28	0.000	0.000	4.12
HC045	Leached	2.45	0.98	5.20	0.85	2.45	no	26.7	3.37	1	V	5.19	25.50	0.000	0.000	44.45
HC045	Leached	2.45	0.98	3.50	0.89	2.45	no	25.7	0.61	2	H1	5.01	26.52	0.002	0.000	18.57
HC045	Leached	2.45	0.98	4.25	0.87	2.45	no	38.9	-1.31	3	H2	5.06	26.00	-0.001	0.000	18.87
HC046	Leached	2.45	0.98	3.29	0.90	2.45	no	120.0	1.61	1	V	4.99	25.20	0.002	0.001	11.77
HC046	Leached	2.45	0.98	3.76	0.89	2.45	no	1.6	0.14	2	H1	5.01	25.15	0.002	0.001	8.59
HC046	Leached	2.45	0.98	2.30	0.89	2.45	no	26.9	0.57	3	H2	5.04	25.09	0.001	0.000	9.51
HC047	Leached	0.49	0.69	3.95	0.97	0.49	no	24.9	-0.28	1	H1	5.07	24.66	0.000	0.000	30.14
HC047	Leached	0.27	0.69	0.26	0.99	0.49	yes	36.5	-0.09	2	V	4.91	25.42	0.000	-0.001	29.43
HC047	Leached	0.23	0.69	0.16	1.00	0.49	yes	65.5	0.35	3	V2	4.92	25.45	0.000	0.000	22.02

Table A1-1: Flexible Wall Permeameter Permeability and Resistivity Measurement Experimental Parameters (Page 5 of 6)

Test ID	Material	σ'_s Mpa	BP Mpa	BP Vol cm ³	B	σ' Mpa	c _u	Time hr	ΔV Dim. cm ³	Meas. #	Dir.	L cm	A cm ²	Leak Rate cm ³ /hr		ρ Ωm
														Top	Bot	
HC048	RBBC	2.45	0.98	1.16	0.93	2.45	no	24.0	3.2	1	V	5.23	26.31	0.001	0.000	2.68
HC048	RBBC	2.45	0.98	1.93	0.91	2.45	no	21.7	0.1	2	H1	5.15	26.73	0.000	0.000	1.50
HC048	RBBC	2.45	0.98	9.01	N/A	2.45	no	24.3	-0.7	3	H2	5.08	26.94	0.001	0.000	1.56
HC049	RBBC	0.59	0.69	5.18	0.95	0.59	no	25.6	2.1	1	V	5.01	26.41	0.000	0.001	3.17
HC049	RBBC	0.59	0.69	3.06	1.00	0.59	no	24.3	0.7	2	H1	5.12	26.03	0.000	0.000	1.82
HC049	RBBC	0.59	0.69	2.82	0.95	0.59	no	67.9	-0.9	3	H2	5.15	25.71	0.000	0.000	1.91
HC050	RBBC	1.47	0.98	2.30	0.94	1.47	no	26.5	3.3	1	H1	4.97	27.04	0.000	0.000	1.59
HC050	RBBC	1.47	0.98	2.03	0.94	1.47	no	25.2	-1.8	2	V	5.22	25.42	0.000	0.000	3.01
HC050	RBBC	1.47	0.98	1.80	0.95	1.47	no	20.2	-0.81	3	V2	5.21	25.33	0.000	0.000	3.20

Table A1-1: Flexible Wall Permeameter Permeability and Resistivity Measurement Experimental Parameters (Page 6 of 6)

Notes:

σ'_s	Sampling effective stress after pressure up.
BP	Back pressure (final)
BP Vol	Total volume inflow from the beginning to the end of back pressure. Includes specimen and system pressurization, as
B	B value following back pressure and prior to permeability measurement
σ'	Effective stress of permeability measurement
c_α	Yes / No to indicate if secondary compression correction was applied to measured gradient volumes.
Time	Time between the beginning of Back pressure to the beginning of the first hydraulic gradient. Includes back pressure, hold stress and recompression phases, where applicable.
ΔV Dim.	Change in volume based on dimensional measurements, measured from the beginning (setup) and end (take down) of a directional measurement
Meas #	Measurement number equal to the number of consecutive measurements, including the current measurement, performed on the same specimen; equal to n in the test sequence bias correction.
Direction	Direction of measurement; V = vertical, H1 = first horizontal, H2 = second horizontal, V2 = repeat of vertical
L	Length of flow for permeability measurement
A	Area of flow for permeability measurement; corresponds to the orientation of the cubic specimen for that particular directional measurement
Leak Rate	Measured very small leak rate through the top or bottom of the specimen. Measured by independently controlling the top and bottom pore pressure to the same value.
ρ	Measured resistivity (not adjusted for measurement sequence bias)

Table A1-2: Summary of Hydraulic Gradient measurements for Hydraulic Conductivity Calculation (1 of 10)

Test ID	Grad. #	ΔP	i	Total Flow Volume		K Flow Volume		Meas. Time	K
				Top	Bot	Top	Bot		
		kPa		cm ³	cm ³	cm ³	cm ³	hr	cm/s
HC003	1	25.3	50.8	2.13	2.21	1.75	1.80	6.50	6.01E-08
	2	53.9	108.1	9.55	9.61	8.73	8.81	14.42	6.29E-08
	3	40.7	81.6	2.01	2.12	1.57	1.63	3.50	6.28E-08
	4	25.6	51.4	5.23	5.28	4.96	4.99	17.75	6.10E-08
HC003	1	37.2	76.3	8.08	8.20	7.41	7.47	15.00	7.17E-08
	2	56.4	115.6	3.26	3.23	2.17	2.16	2.83	7.29E-08
	3	22.5	46.1	5.75	5.80	5.45	5.51	18.00	7.27E-08
HC004	1	43.9	91.0	2.21	2.26	1.92	1.95	4.80	4.72E-08
	2	43.9	91.0	2.87	2.98	1.92	1.95	11.25	4.72E-08
	3	25.8	53.6	9.32	9.49	2.58	2.66	18.50	4.64E-08
HC004	1	39.2	76.7	1.33	1.42	1.18	1.25	5.65	3.20E-08
	2	23.6	46.3	0.76	0.79	0.63	0.65	5.00	3.17E-08
	3	52.8	103.4	3.27	3.23	3.03	2.99	10.20	3.26E-08
HC004	1	25.0	50.9	2.54	2.56	2.28	2.30	11.58	4.27E-08
	2	54.0	110.0	2.73	2.77	2.23	2.29	5.33	4.23E-08
	3	40.5	82.6	5.83	5.94	5.59	5.68	17.53	4.29E-08
HC005	1	59.5	117.4	2.02	1.97	1.67	1.72	5.90	2.75E-08
	2	29.9	59.0	2.11	2.14	1.95	1.97	13.60	2.75E-08
	3	45.7	90.2	1.09	1.10	0.90	0.91	4.07	2.79E-08
HC005	1	58.8	120.9	3.94	3.93	3.58	3.59	8.90	3.63E-08
	2	28.9	59.3	2.58	2.54	2.42	2.37	11.80	3.73E-08
	3	45.1	92.6	1.16	1.16	0.97	0.97	3.10	3.69E-08
HC005	1	45.8	93.7	1.37	1.37	1.21	1.24	4.00	3.59E-08
	2	59.8	122.3	1.46	1.46	1.35	1.35	3.33	3.63E-08
	3	30.4	62.2	3.21	3.23	3.16	3.17	15.53	3.59E-08
HC006	1	30.6	61.6	0.68	0.71	0.54	0.55	3.87	2.53E-08
	2	60.0	120.9	0.78	0.77	0.45	0.46	1.67	2.49E-08
	3	46.4	93.6	3.82	3.85	3.65	3.68	17.07	2.53E-08
HC006	1	45.9	94.0	0.57	0.60	0.42	0.43	1.95	2.49E-08
	2	59.7	122.2	0.91	0.91	0.67	0.67	2.35	2.52E-08
	3	30.4	62.3	2.53	2.55	2.42	2.44	17.00	2.48E-08
HC006	1	29.8	59.0	0.64	0.64	0.57	0.57	6.05	1.80E-08
	2	58.3	115.7	3.15	3.16	2.89	2.91	16.00	1.76E-08
	3	44.7	88.7	3.42	3.36	3.31	3.25	23.33	1.78E-08
HC007	1	58.8	117.6	0.56	0.57	0.38	0.39	1.85	1.90E-08
	2	29.5	58.9	2.18	2.22	2.10	2.13	20.25	1.91E-08
	3	44.9	89.9	0.66	0.65	0.56	0.55	3.45	1.94E-08

Table A1-2: Summary of Hydraulic Gradient measurements for Hydraulic Conductivity Calculation (2 of 10)

Test ID	Grad. #	ΔP	i	Total Flow Volume		K Flow Volume		Meas. Time	K
				Top	Bot	Top	Bot		
		kPa		cm ³	cm ³	cm ³	cm ³	hr	cm/s
HC007	1	44.8	89.3	0.89	0.90	0.69	0.70	2.80	3.00E-08
	2	58.3	116.3	1.40	1.39	1.12	1.11	3.45	3.01E-08
	3	28.9	57.6	2.45	2.45	2.33	2.33	14.60	3.00E-08
HC007	1	29.1	58.4	0.50	0.51	0.38	0.38	2.40	2.87E-08
	2	58.6	117.5	1.72	1.69	1.45	1.42	4.55	2.87E-08
	3	44.7	89.7	3.55	3.49	3.34	3.30	13.47	2.95E-08
HC008	1	45.5	88.4	1.24	1.20	1.10	1.07	10.92	1.27E-08
	2	30.0	58.2	0.50	0.48	0.43	0.41	6.40	1.28E-08
	3	59.2	114.8	2.06	2.00	1.92	1.87	14.75	1.27E-08
HC008	1	28.7	59.5	1.28	1.33	1.14	1.18	10.25	2.00E-08
	2	58.4	121.1	1.83	1.84	1.57	1.57	7.00	1.96E-08
	3	44.5	92.4	3.97	3.89	3.80	3.73	21.50	2.00E-08
HC008	1	44.4	89.5	2.58	2.54	2.34	2.34	14.67	1.93E-08
	2	58.2	117.3	1.22	1.24	0.99	1.01	4.87	1.90E-08
	3	28.9	58.4	1.92	1.84	1.83	1.74	17.17	1.93E-08
HC008	1	43.5	83.8	0.69	0.68	0.60	0.58	6.80	1.18E-08
	2	28.1	54.1	1.29	1.28	1.22	1.20	21.83	1.17E-08
	3	58.0	111.8	2.16	2.19	2.05	2.07	18.42	1.14E-08
HC009	1	96.5	195.7	2.88	2.90	2.56	2.58	8.87	1.59E-08
	2	38.0	77.0	1.52	1.62	1.37	1.45	12.33	1.59E-08
	3	57.2	116.1	1.16	1.19	1.02	1.05	6.13	1.56E-08
HC009	1	38.8	78.4	1.79	1.79	1.63	1.65	15.17	1.48E-08
	2	78.6	159.0	1.33	1.33	1.08	1.09	5.00	1.46E-08
	3	58.8	118.9	2.77	2.75	2.60	2.59	15.92	1.47E-08
HC009	1	77.2	151.0	0.78	0.72	0.43	0.40	3.47	8.91E-09
	2	41.0	80.1	0.90	0.92	0.82	0.84	13.33	8.68E-09
	3	60.9	119.2	2.29	2.34	2.19	2.24	24.33	8.58E-09
HC011	1	38.3	74.8	1.79	1.82	1.61	1.65	33.42	7.34E-09
	2	77.7	151.8	1.10	1.13	0.99	1.01	10.27	7.21E-09
	3	58.1	113.6	0.85	0.84	0.78	0.76	10.50	7.25E-09
HC011	1	58.1	118.7	2.26	2.25	1.78	1.80	13.83	1.17E-08
	2	77.9	159.2	1.29	1.27	1.09	1.08	6.40	1.15E-08
	3	38.5	78.7	1.28	1.28	1.19	1.20	14.25	1.14E-08
HC011	1	77.7	158.7	1.60	1.59	1.12	1.13	7.07	1.08E-08
	2	38.2	77.9	1.09	1.08	1.01	0.99	12.73	1.09E-08
	3	57.4	117.3	2.76	2.74	2.66	2.64	22.53	1.08E-08

Table A1-2: Summary of Hydraulic Gradient measurements for Hydraulic Conductivity Calculation (3 of 10)

Test ID	Grad. #	ΔP	i	Total Flow Volume		K Flow Volume		Meas. Time	K
				Top cm ³	Bot cm ³	Top cm ³	Bot cm ³		
		kPa						hr	cm/s
HC011	1	38.2	74.4	0.98	0.97	0.86	0.86	20.40	6.47E-09
	2	77.0	150.2	1.59	1.59	1.51	1.49	17.87	6.37E-09
	3	57.8	112.7	2.94	3.03	2.90	2.98	47.20	6.29E-09
HC016	1	58.8	115.6	1.52	1.57	1.34	1.39	22.07	5.95E-09
	2	45.2	88.9	1.06	1.12	1.01	1.06	21.67	5.98E-09
	3	68.9	135.4	2.16	2.19	2.10	2.12	28.47	6.11E-09
HC016	1	68.8	142.0	1.08	1.10	0.66	0.68	4.60	1.10E-08
	2	45.1	93.1	1.60	1.63	1.50	1.53	16.00	1.09E-08
	3	59.3	122.2	3.06	3.07	2.96	2.97	23.87	1.08E-08
HC016	1	59.0	118.3	1.57	1.52	1.24	1.21	10.73	1.05E-08
	2	68.4	137.2	0.88	0.89	0.73	0.74	5.60	1.05E-08
	3	45.2	90.7	1.59	1.57	1.53	1.51	17.67	1.04E-08
HC018	1	46.5	91.1	0.61	0.57	0.40	0.39	11.47	4.11E-09
	2	65.8	129.1	0.86	0.84	0.81	0.79	16.27	4.13E-09
	3	56.2	110.3	0.87	0.88	0.84	0.84	20.53	4.05E-09
HC018	1	57.9	116.6	0.57	0.58	0.35	0.35	4.47	7.05E-09
	2	49.3	99.2	1.31	1.30	1.24	1.22	18.67	6.93E-09
	3	68.4	137.7	2.62	2.60	2.55	2.52	27.93	6.87E-09
HC018	1	68.4	136.6	0.70	0.68	0.45	0.44	5.00	6.90E-09
	2	48.8	97.4	0.88	0.87	0.81	0.80	12.60	6.97E-09
	3	58.5	116.9	0.55	0.54	0.49	0.47	6.20	7.03E-09
HC019	1	58.4	117.0	1.88	1.79	1.68	1.56	21.33	7.08E-09
	2	68.0	136.2	0.79	0.75	0.69	0.65	7.60	7.11E-09
	3	48.6	97.3	0.95	0.97	0.78	0.79	12.60	7.03E-09
	3	38.7	77.6	1.22	1.16	0.49	0.46	9.47	7.12E-09
HC019	1	48.7	99.4	1.16	1.07	0.55	0.52	7.93	7.40E-09
	2	68.3	139.4	2.32	2.23	1.30	1.26	14.13	7.05E-09
	3	58.4	119.2	2.10	1.96	2.04	1.90	22.73	7.89E-09
HC019	1	68.7	137.8	1.16	1.06	1.02	0.93	21.13	3.75E-09
	2	48.9	98.1	0.80	0.75	0.61	0.57	17.87	3.76E-09
	3	58.6	117.4	0.97	0.92	0.93	0.89	23.27	3.74E-09
HC020	1	58.6	114.9	0.79	0.70	0.46	0.42	10.07	3.97E-09
	2	68.4	134.1	1.09	1.16	1.04	1.10	21.93	3.81E-09
	3	48.9	95.8	0.81	0.79	0.71	0.70	20.07	3.82E-09

Table A1-2: Summary of Hydraulic Gradient measurements for Hydraulic Conductivity Calculation (4 of 10)

Test ID	Grad. #	ΔP	i	Total Flow Volume		K Flow Volume		Meas. Time	K
				Top cm ³	Bot cm ³	Top cm ³	Bot cm ³		
		kPa						hr	cm/s
HC020	1	68.4	135.0	2.14	2.06	1.71	1.59	18.53	6.63E-09
	2	49.0	96.7	0.77	0.73	0.45	0.41	6.87	6.53E-09
	3	58.8	116.1	0.33	0.31	0.33	0.31	4.27	6.52E-09
HC020	1	48.7	96.2	1.12	1.02	0.78	0.73	12.00	6.72E-09
	2	68.5	135.2	0.98	0.97	0.53	0.53	6.13	6.57E-09
	3	58.4	115.3	0.78	0.76	0.40	0.39	5.33	6.63E-09
HC021	1	68.2	137.8	1.13	1.15	0.67	0.69	7.33	7.37E-09
	2	48.5	98.1	0.90	0.93	0.58	0.60	8.87	7.36E-09
	3	58.3	117.9	1.86	1.87	1.45	1.47	17.93	7.53E-09
HC021	1	68.0	134.5	1.34	1.28	0.91	0.87	19.00	3.95E-09
	2	48.4	95.7	0.64	0.65	0.47	0.49	14.87	3.83E-09
	3	58.2	115.1	0.85	0.84	0.65	0.64	16.80	3.79E-09
HC022	1	48.5	98.2	1.88	1.91	1.17	1.19	15.00	8.69E-09
	2	38.6	78.3	1.20	1.24	0.90	0.92	14.67	8.59E-09
	3	58.3	118.1	2.24	2.24	1.77	1.77	18.73	8.67E-09
HC022	1	58.9	120.4	1.19	1.12	0.25	0.23	2.33	9.21E-09
	2	39.3	80.4	0.91	0.82	0.56	0.50	7.80	9.09E-09
	3	49.2	100.4	2.12	2.09	1.69	1.68	20.20	8.94E-09
HC022	1	58.3	114.8	0.67	0.56	0.39	0.34	7.20	5.03E-09
	2	38.8	76.3	0.41	0.36	0.23	0.20	6.27	5.08E-09
	3	48.6	95.6	0.79	0.71	0.56	0.51	13.20	4.84E-09
HC024	1	39.7	79.1	2.97	3.07	2.36	2.45	19.67	1.64E-08
	2	59.4	118.2	1.96	1.98	1.53	1.55	8.33	1.65E-08
	3	49.4	98.4	1.83	1.91	1.06	1.11	7.13	1.64E-08
HC024	1	57.8	116.2	3.89	3.97	1.59	1.63	9.47	1.54E-08
	2	38.3	77.1	1.13	1.14	0.87	0.88	7.73	1.55E-08
	3	48.5	97.4	2.12	2.13	1.01	1.04	7.20	1.54E-08
HC024	1	58.4	114.2	2.53	2.53	2.08	2.09	17.87	1.10E-08
	2	38.9	76.0	0.97	0.93	0.65	0.62	8.07	1.11E-08
	3	48.6	95.0	1.25	1.23	0.85	0.84	8.73	1.10E-08
HC025	1	47.5	96.2	2.86	2.84	1.61	1.61	8.10	2.28E-08
	2	28.3	57.2	1.39	1.37	0.79	0.79	6.67	2.28E-08
	3	38.0	76.9	1.89	1.85	1.07	1.06	6.60	2.31E-08
HC025	1	28.5	58.2	1.74	1.73	0.89	0.92	7.67	2.23E-08
	2	47.9	97.8	2.53	2.53	1.56	1.54	7.87	2.21E-08
	3	37.9	77.4	2.14	2.12	0.90	0.90	5.67	2.25E-08

Table A1-2: Summary of Hydraulic Gradient measurements for Hydraulic Conductivity Calculation (5 of 10)

Test ID	Grad. #	ΔP	i	Total Flow Volume		K Flow Volume		Meas. Time	K
				Top cm^3	Bot cm^3	Top cm^3	Bot cm^3		
		kPa						hr	cm/s
HC025	1	28.7	57.3	1.01	0.97	0.66	0.67	9.87	1.32E-08
	2	48.4	96.7	1.03	1.01	0.45	0.45	4.00	1.31E-08
	3	38.6	77.1	1.38	1.35	0.91	0.90	9.93	1.33E-08
HC026	1	28.6	56.6	3.20	3.24	2.54	2.55	18.73	2.64E-08
	2	12.8	25.4	0.65	0.67	0.36	0.36	5.93	2.62E-08
	3	20.8	41.3	1.32	1.34	0.83	0.85	8.67	2.58E-08
HC026	1	21.2	43.3	3.67	3.75	2.90	2.97	19.07	3.80E-08
	2	29.0	59.1	6.12	6.20	5.05	5.14	23.80	3.88E-08
	3	13.4	27.4	1.94	1.96	1.44	1.46	14.80	3.83E-08
HC026	1	22.5	45.1	1.99	2.02	1.28	1.29	8.87	3.48E-08
	2	14.7	29.4	2.20	2.21	1.74	1.74	19.27	3.34E-08
	3	30.3	60.7	5.41	5.37	4.43	4.39	22.53	3.51E-08
HC027	1	9.3	18.5	1.42	1.44	0.99	1.00	11.27	5.13E-08
	2	19.7	39.2	4.19	4.16	3.28	3.26	17.33	5.17E-08
	3	10.0	20.0	1.14	1.12	0.65	0.65	6.73	5.18E-08
HC027	1	10.0	19.6	1.42	1.45	1.13	1.14	18.33	3.49E-08
	2	19.7	38.5	1.58	1.57	0.57	0.57	4.73	3.48E-08
	3	13.8	27.0	0.91	0.93	0.49	0.51	5.93	3.44E-08
HC027	1	13.8	27.0	2.08	2.04	1.67	1.64	20.40	3.31E-08
	2	6.0	11.7	0.72	0.67	0.53	0.50	14.60	3.34E-08
	3	9.9	19.4	1.61	1.52	1.31	1.24	21.53	3.36E-08
HC029	1	10.3	20.3	2.32	2.39	1.83	1.90	18.40	5.62E-08
	2	20.0	39.6	4.65	4.70	3.65	3.69	18.40	5.69E-08
	3	14.2	28.0	2.24	2.25	1.54	1.54	10.87	5.70E-08
HC029	1	14.5	29.7	3.48	3.52	2.42	2.45	11.53	7.79E-08
	2	20.3	41.6	6.70	6.70	5.19	5.22	17.73	7.73E-08
	3	10.6	21.6	1.62	1.56	1.00	1.00	6.45	7.87E-08
HC029	1	10.0	20.6	3.18	3.22	2.52	2.53	18.60	7.26E-08
	2	4.2	8.5	7.66	7.83	7.61	7.78	0.00	7.16E-08
	3	13.9	28.5	4.77	4.85	3.84	3.88	20.07	7.42E-08
HC030	1	57.3	110.5	0.19	0.19	0.17	0.16	199.96	8.15E-11
	2	116.2	223.9	0.04	0.06	0.02	0.02	11.93	8.21E-11
	3	96.6	186.1	0.03	0.03	0.02	0.03	0.00	7.90E-11
HC030	1	77.6	148.5	0.08	0.12	0.06	0.08	31.93	1.53E-10
	2	116.8	223.6	0.09	0.10	0.05	0.05	17.73	1.43E-10
	3	97.3	186.2	0.12	0.11	0.09	0.07	32.67	1.46E-10

Table A1-2: Summary of Hydraulic Gradient measurements for Hydraulic Conductivity Calculation (6 of 10)

Test ID	Grad. #	ΔP	i	Total Flow Volume		K Flow Volume		Meas. Time	K
				Top cm ³	Bot cm ³	Top cm ³	Bot cm ³		
		kPa						hr	cm/s
HC030	1	98.3	189.7	0.18	0.13	0.13	0.09	31.93	1.99E-10
	2	78.6	151.6	0.06	0.06	0.04	0.03	14.87	1.74E-10
	3	118.1	227.8	0.08	0.08	0.05	0.05	14.47	1.64E-10
HC031	1	78.4	152.7	0.13	0.11	0.11	0.09	22.00	3.01E-10
	2	117.8	229.5	0.16	0.14	0.09	0.08	13.73	2.93E-10
	3	98.1	191.1	0.12	0.09	0.07	0.06	11.67	2.92E-10
HC031	1	98.1	188.3	0.17	0.21	0.08	0.10	23.27	2.09E-10
	2	117.8	226.1	0.07	0.10	0.04	0.05	9.87	2.14E-10
	3	78.5	150.7	0.10	0.16	0.10	0.14	42.47	2.01E-10
HC031	1	79.1	152.0	0.05	0.04	0.04	0.04	14.60	1.82E-10
	2	118.3	227.1	0.15	0.13	0.13	0.11	35.93	1.54E-10
	3	98.7	189.6	0.07	0.07	0.06	0.06	20.27	1.63E-10
HC032	1	61.6	123.2	0.09	0.10	0.06	0.07	13.33	4.66E-10
	2	100.7	201.4	0.15	0.17	0.11	0.13	16.07	4.22E-10
	3	81.3	162.5	0.11	0.13	0.08	0.10	14.00	4.36E-10
HC032	1	98.2	201.6	0.23	0.19	0.18	0.15	18.67	4.72E-10
	2	117.7	241.6	0.28	0.27	0.22	0.22	22.67	4.39E-10
	3	78.4	161.0	0.15	0.16	0.11	0.13	18.80	4.38E-10
HC032	1	98.1	198.9	0.18	0.13	0.12	0.09	11.40	5.11E-10
	2	78.5	159.2	0.19	0.15	0.14	0.12	18.13	4.91E-10
	3	117.6	238.6	0.29	0.28	0.23	0.24	23.53	4.53E-10
HC033	1	78.4	160.2	0.40	0.42	0.31	0.34	18.87	1.13E-09
	2	97.9	200.1	0.24	0.26	0.13	0.14	6.33	1.13E-09
	3	59.2	121.0	0.13	0.16	0.09	0.11	7.60	1.11E-09
HC033	1	78.4	153.3	0.37	0.35	0.29	0.28	18.47	1.10E-09
	2	58.6	114.7	0.18	0.14	0.11	0.10	8.67	1.14E-09
	3	98.2	192.1	0.19	0.19	0.10	0.09	5.13	1.09E-09
HC033	1	59.1	115.4	0.14	0.12	0.09	0.08	7.93	1.05E-09
	2	98.1	191.6	0.23	0.21	0.15	0.14	7.93	1.06E-09
	3	78.6	153.5	0.17	0.16	0.12	0.11	7.73	1.04E-09
HC034	1	58.8	113.0	2.29	2.15	2.08	1.98	226.67	9.04E-10
	2	97.7	187.9	0.23	0.23	0.09	0.16	11.13	8.70E-10
	3	78.4	150.8	0.15	0.14	0.09	0.09	7.73	8.72E-10
HC034	1	78.6	159.8	0.61	0.60	0.50	0.49	21.33	1.63E-09
	2	98.1	199.7	0.47	0.48	0.32	0.33	11.47	1.61E-09
	3	58.8	119.6	1.10	1.12	1.02	1.04	59.53	1.63E-09
HC034	1	98.3	203.1	0.28	0.25	0.17	0.16	5.80	1.55E-09
	2	58.8	121.4	0.24	0.22	0.16	0.14	8.80	1.55E-09
	3	78.6	162.3	0.22	0.21	0.13	0.13	6.00	1.52E-09

Table A1-2: Summary of Hydraulic Gradient measurements for Hydraulic Conductivity Calculation (7 of 10)

Test ID	Grad. #	ΔP	i	Total Flow Volume		K Flow Volume		Meas. Time	K
				Top	Bot	Top	Bot		
		kPa		cm ³	cm ³	cm ³	cm ³	hr	cm/s
HC036	1	49.0	98.3	0.91	0.89	0.57	0.56	8.47	7.38E-09
	2	68.6	137.6	1.40	1.40	0.93	0.93	10.07	7.30E-09
	3	58.6	117.5	0.77	0.76	0.37	0.37	4.67	7.27E-09
HC036	1	77.4	146.8	0.56	0.56	0.31	0.31	6.00	3.90E-09
	2	48.2	91.4	0.43	0.43	0.27	0.28	8.53	3.93E-09
	3	57.9	109.9	0.26	0.28	0.12	0.14	3.33	3.90E-09
HC036	1	48.7	92.6	0.48	0.45	0.32	0.31	10.60	3.59E-09
	2	68.6	130.6	0.32	0.32	0.19	0.20	4.73	3.54E-09
	3	58.6	111.6	0.57	0.57	0.39	0.39	10.93	3.57E-09
HC037	1	22.3	44.2	1.15	1.22	0.57	0.61	4.87	2.96E-08
	2	12.4	24.7	0.76	0.79	0.42	0.44	6.20	3.02E-08
	3	18.0	35.6	0.59	0.61	0.22	0.23	2.20	3.13E-08
HC037	1	20.7	41.6	0.66	0.69	0.42	0.43	6.27	1.74E-08
	2	11.1	22.4	0.44	0.45	0.28	0.29	7.80	1.74E-08
	3	16.9	34.0	0.47	0.50	0.20	0.21	3.80	1.72E-08
HC037	1	10.7	21.6	0.21	0.20	0.10	0.10	2.80	1.76E-08
	2	20.6	41.4	0.87	0.85	0.53	0.51	7.73	1.73E-08
	3	16.7	33.6	1.05	1.04	0.76	0.76	14.20	1.71E-08
HC038	1	20.2	40.9	1.60	1.55	1.04	1.04	9.80	2.86E-08
	2	10.5	21.2	0.49	0.50	0.29	0.29	5.40	2.82E-08
	3	16.2	32.8	1.63	1.66	1.20	1.23	14.13	2.89E-08
HC038	1	16.6	33.7	1.21	1.21	0.72	0.72	5.47	4.31E-08
	2	20.7	41.9	2.44	2.46	1.62	1.63	10.00	4.26E-08
	3	10.9	22.0	1.92	1.92	1.49	1.50	17.73	4.21E-08
HC038	1	10.3	20.6	1.42	1.39	1.01	1.01	12.67	4.28E-08
	2	19.9	40.0	1.81	1.83	1.04	1.05	6.73	4.32E-08
	3	16.1	32.3	1.72	1.69	1.08	1.06	8.53	4.30E-08
HC040	1	98.0	198.0	0.91	0.89	0.71	0.70	18.33	2.08E-09
	2	39.4	79.5	0.36	0.35	0.28	0.28	17.93	2.08E-09
	3	68.4	138.2	0.30	0.30	0.17	0.16	6.13	2.10E-09

Table A1-2: Summary of Hydraulic Gradient measurements for Hydraulic Conductivity Calculation (8 of 10)

Test ID	Grad. #	ΔP	i	Total Flow Volume		K Flow Volume		Meas. Time	K
				Top cm^3	Bot cm^3	Top cm^3	Bot cm^3		
		kPa						hr	cm/s
HC040	1	97.8	190.7	0.56	0.58	0.45	0.46	18.73	1.38E-09
	2	59.0	115.0	0.11	0.12	0.04	0.05	3.00	1.37E-09
	3	78.3	152.6	0.31	0.32	0.21	0.22	11.00	1.40E-09
HC040	1	98.2	193.8	0.32	0.34	0.20	0.22	9.40	1.28E-09
	2	58.9	116.2	0.29	0.30	0.23	0.23	16.73	1.30E-09
	3	78.3	154.5	0.12	0.13	0.08	0.09	4.67	1.28E-09
HC042	1	37.7	75.1	4.24	4.34	2.94	3.02	11.47	3.84E-08
	2	18.2	36.3	1.16	1.15	0.70	0.69	5.47	3.90E-08
	3	27.9	55.7	2.90	2.90	1.94	1.93	10.13	3.81E-08
HC042	1	18.2	37.3	1.69	1.68	0.97	0.98	7.00	4.07E-08
	2	37.7	77.2	3.19	3.26	1.74	1.80	6.13	4.08E-08
	3	27.9	57.2	2.78	2.85	1.70	1.75	7.93	4.16E-08
HC042	1	37.6	75.1	2.18	2.25	1.25	1.30	5.93	3.24E-08
	2	18.1	36.2	1.30	1.32	0.79	0.80	7.80	3.17E-08
	3	27.7	55.4	2.36	2.38	1.56	1.57	9.80	3.26E-08
HC042	1	18.4	36.9	1.23	1.29	0.73	0.75	6.93	3.26E-08
	2	38.1	76.4	2.40	2.43	1.35	1.35	6.20	3.22E-08
	3	28.4	56.9	1.74	1.77	0.94	0.96	5.87	3.21E-08
HC044	1	48.5	98.1	0.38	0.37	0.26	0.26	10.67	2.82E-09
	2	58.5	118.2	0.62	0.60	0.47	0.46	15.33	2.92E-09
	3	38.9	78.7	0.15	0.15	0.09	0.09	4.33	3.04E-09
HC044	1	58.0	121.6	0.22	0.21	0.10	0.10	4.67	1.98E-09
	2	39.3	82.4	0.21	0.20	0.14	0.13	9.07	1.99E-09
	3	49.2	103.0	0.19	0.18	0.09	0.09	5.20	1.95E-09
HC045	1	48.7	94.8	0.63	0.71	0.50	0.56	18.60	3.27E-09
	2	68.4	133.1	1.11	1.17	0.91	0.96	23.80	3.21E-09
	3	58.9	114.7	0.71	0.74	0.54	0.56	16.20	3.22E-09
HC045	1	58.4	119.1	1.84	1.88	1.49	1.52	20.93	6.33E-09
	2	39.1	79.7	1.13	1.18	0.90	0.94	19.20	6.31E-09
	3	48.9	99.8	1.21	1.29	0.92	0.98	15.80	6.31E-09
HC045	1	47.9	96.7	0.98	1.00	0.70	0.71	12.47	6.24E-09
	2	38.7	78.2	0.94	0.97	0.75	0.75	16.40	6.23E-09
	3	58.3	117.8	1.26	1.22	0.91	0.89	13.07	6.27E-09

Table A1-2: Summary of Hydraulic Gradient measurements for Hydraulic Conductivity Calculation (9 of 10)

Test ID	Grad. #	ΔP	i	Total Flow Volume		K Flow Volume		Meas. Time	K
				Top cm ³	Bot cm ³	Top cm ³	Bot cm ³		
		kPa						hr	cm/s
HC046	1	137.1	280.4	0.25	0.24	0.20	0.20	19.87	3.94E-10
	2	117.5	240.3	0.17	0.17	0.12	0.13	14.27	4.02E-10
	3	97.9	200.2	0.18	0.17	0.14	0.14	18.87	4.10E-10
HC046	1	98.4	200.6	0.23	0.27	0.19	0.22	22.67	5.02E-10
	2	118.1	240.8	0.19	0.19	0.14	0.14	12.93	4.83E-10
	3	78.6	160.2	0.15	0.17	0.12	0.13	18.87	4.69E-10
HC046	1	98.2	198.8	0.19	0.20	0.16	0.16	19.33	4.66E-10
	2	78.9	159.8	0.15	0.16	0.12	0.13	19.67	4.52E-10
	3	117.8	238.7	0.10	0.10	0.09	0.09	9.80	4.12E-10
HC047	1	37.9	76.5	3.06	3.15	2.45	2.52	19.87	1.84E-08
	2	28.3	57.1	1.97	2.01	1.51	1.54	16.53	1.83E-08
	3	47.6	96.0	1.73	1.71	0.95	0.93	5.93	1.86E-08
HC047	1	45.3	94.3	2.78	2.78	2.16	2.17	17.73	1.41E-08
	2	35.6	74.1	2.34	2.30	1.87	1.82	19.13	1.42E-08
	3	55.2	114.9	1.61	1.59	0.87	0.84	5.67	1.43E-08
HC047	1	38.3	79.6	1.66	1.68	1.16	1.17	11.47	1.40E-08
	2	57.8	120.0	3.72	3.71	2.94	2.96	19.27	1.39E-08
	3	48.0	99.7	3.28	3.21	2.64	2.57	20.20	1.41E-08
HC048	1	48.8	94.3	0.62	0.65	0.41	0.44	10.33	4.62E-09
	2	68.5	132.3	1.43	1.46	1.14	1.16	19.40	4.73E-09
	3	58.5	113.0	0.54	0.56	0.29	0.30	5.93	4.60E-09
HC048	1	48.6	96.5	0.80	0.79	0.43	0.44	6.00	7.82E-09
	2	67.9	134.7	1.36	1.38	0.86	0.87	8.53	7.80E-09
	3	58.6	116.3	0.61	0.59	0.18	0.17	2.00	7.86E-09
HC048	1	58.0	115.4	2.15	2.24	1.74	1.79	20.53	7.68E-09
	2	48.6	96.5	1.54	1.58	1.20	1.22	17.13	7.52E-09
	3	68.1	135.3	2.23	2.23	1.75	1.74	17.73	7.50E-09
HC049	1	47.7	97.1	2.24	2.32	1.71	1.76	15.53	1.21E-08
	2	38.0	77.3	2.15	2.29	1.72	1.84	20.07	1.20E-08
	3	57.4	117.0	1.62	1.62	0.96	0.95	7.00	1.22E-08
HC049	1	28.5	56.8	1.06	1.07	0.57	0.56	5.47	1.94E-08
	2	47.8	95.5	2.07	2.05	1.19	1.19	6.93	1.92E-08
	3	38.2	76.3	2.26	2.25	1.58	1.56	11.33	1.94E-08
HC049	1	47.7	94.6	2.94	2.97	2.14	2.15	13.07	1.88E-08
	2	28.4	56.3	1.20	1.23	0.72	0.73	7.67	1.82E-08
	3	37.9	75.2	1.45	1.47	0.80	0.81	6.13	1.88E-08

Table A1-2: Summary of Hydraulic Gradient measurements for Hydraulic Conductivity Calculation (10 of 10)

Test ID	Grad. #	ΔP	i	Total Flow Volume		K Flow Volume		Meas. Time	K
				Top	Bot	Top	Bot		
		kPa		cm ³	cm ³	cm ³	cm ³	hr	cm/s
HC050	1	48.7	99.0	2.30	2.28	1.77	1.74	16.13	1.13E-08
	2	29.3	59.5	1.55	1.56	1.22	1.24	18.93	1.12E-08
	3	39.2	79.7	2.11	2.09	1.66	1.65	18.60	1.15E-08
HC050	1	28.9	56.5	1.69	1.67	1.54	1.52	48.27	6.12E-09
	2	48.5	95.0	0.81	0.81	0.54	0.54	10.27	6.07E-09
	3	38.6	75.6	0.53	0.55	0.33	0.33	7.93	6.01E-09
HC050	1	48.4	94.9	1.13	1.13	0.88	0.87	16.93	5.98E-09
	2	29.4	57.6	1.05	1.00	0.89	0.84	27.47	6.03E-09
	3	39.2	77.0	0.50	0.49	0.29	0.28	6.73	6.01E-09

Notes:

Grad #	Number identifying the sequence of hydraulic gradients used to measure the permeability (1 = first, 2 = second, etc)
ΔP	Pressure difference applied initiate the hydraulic gradient; split evenly between top and bottom of specimen.
i	Hydraulic gradient. Computed using L and ΔP .
Total Flow Volume	Total flow volume through either the top or bottom of the specimen during the entire gradient. Corrected for measured leak rate and secondary compression where applicable. Includes flow attributed to stress equalization and slight specimen volume change.
K Flow Volume	Flow volume through either the top or bottom of the specimen used for calculation of the hydraulic conductivity. Corrected for measured leak rate and secondary . Does not include flow attributed to stress equalization. compression where applicable.
Meas. Time	Time for the hydraulic conductivity measurement over which V_{top} and V_{bot} were measured.
K	Computed hydraulic conductivity (measured, not adjusted for measurement sequence bias). Computed using the average of the top and bottom K Flow Volume measurements.

Table A1-3: Specimen metrics: stress and volume change (1 of 3)

Test ID	Material	Meas. #	Direction	$\sigma's/\sigma'$	$\Delta V / V_t$	Hydraulic Gradient Metrics			
						Avg ΔV	Max ΔV	$\Delta V/V_{avg}$	$\Delta P / \sigma'$
						cm^3	% of V_{total}	% of V_{total}	%
HC003	RBBC	1	V	14%	1.0%	0.06%	0.09%	1% -4%	26% -55%
HC003	RBBC	2	H1	21%	-0.7%	0.05%	0.09%	0% -1%	23% -58%
HC004	RBBC	1	H1	5%	1.2%	0.09%	0.13%	1% -3%	13% -22%
HC004	RBBC	2	V	5%	-1.2%	0.04%	0.07%	2% -5%	12% -27%
HC004	RBBC	3	H2	14%	-0.4%	0.05%	0.09%	1% -3%	13% -28%
HC005	RBBC	1	V	28%	2.1%	0.02%	0.04%	1% -3%	10% -20%
HC005	RBBC	2	H1	15%	-0.7%	0.02%	0.04%	0% -2%	10% -20%
HC005	RBBC	3	H2	42%	-0.3%	0.00%	0.01%	0% -3%	10% -20%
HC006	RBBC	1	H1	70%	1.0%	0.02%	0.03%	1% -2%	6% -12%
HC006	RBBC	2	H2	56%	0.5%	0.01%	0.02%	0% -2%	6% -12%
HC006	RBBC	3	V	49%	-0.6%	0.02%	0.04%	0% -2%	6% -12%
HC007	RBBC	1	V	56%	1.8%	0.02%	0.03%	2% -5%	8% -15%
HC007	RBBC	2	H1	58%	0.0%	0.01%	0.01%	0% -1%	7% -15%
HC007	RBBC	3	H2	50%	0.3%	0.03%	0.04%	0% -2%	7% -15%
HC008	RBBC	1	V	61%	2.1%	0.03%	0.05%	3% -5%	4% -8%
HC008	RBBC	2	H1	67%	0.1%	0.03%	0.06%	0% -3%	4% -7%
HC008	RBBC	3	H2	58%	0.1%	0.04%	0.07%	0% -5%	4% -7%
HC008	RBBC	4	V2	50%	-0.4%	0.01%	0.02%	1% -3%	4% -7%
HC009	RBBC	1	H1	73%	2.6%	0.04%	0.07%	1% -6%	4% -9%
HC009	RBBC	2	H2	43%	0.3%	0.01%	0.02%	0% -2%	4% -7%
HC009	RBBC	3	V	27%	-1.3%	0.03%	0.04%	2% -7%	4% -7%
HC011	RBBC	1	V	32%	3.1%	0.02%	0.02%	2% -3%	3% -5%
HC011	RBBC	2	H1	17%	0.3%	0.01%	0.01%	1% -1%	3% -5%
HC011	RBBC	3	H2	18%	-0.1%	0.01%	0.02%	1% -2%	3% -5%
HC011	RBBC	4	V2	16%	-1.2%	0.03%	0.06%	1% -3%	3% -5%
HC016	RBBC	1	V	53%	3.4%	0.04%	0.04%	1% -5%	3% -5%
HC016	RBBC	2	H1	51%	-0.6%	0.02%	0.03%	0% -4%	3% -5%
HC016	RBBC	3	H2	31%	0.4%	0.02%	0.04%	1% -2%	3% -5%
HC018	RBBC	1	V	53%	2.2%	0.02%	0.03%	0% -4%	2% -3%
HC018	RBBC	2	H1	39%	1.5%	0.01%	0.02%	0% -1%	2% -3%
HC018	RBBC	3	H2	27%	-0.9%	0.01%	0.02%	0% -4%	2% -3%
HC019	RBBC	1	H1	59%	3.1%	0.04%	0.07%	1% -7%	2% -3%
HC019	RBBC	2	H2	28%	0.1%	0.09%	0.12%	3% -7%	2% -3%
HC019	RBBC	3	V	29%	-1.3%	0.05%	0.08%	5% -8%	2% -3%
HC020	RBBC	1	V	47%	1.3%	0.04%	0.07%	2% -9%	2% -2.8%
HC020	RBBC	2	H1	28%	1.3%	0.03%	0.06%	5% -10%	2% -3%
HC020	RBBC	3	H2	20%	-0.2%	0.03%	0.07%	0% -7%	2% -3%
HC021	RBBC	1	H1	60%	2.6%	0.02%	0.03%	1% -3%	2% -3%
HC021	RBBC	3	V	22%	-2.3%	0.02%	0.05%	2% -4%	2% -3%
HC022	RBBC	1	H1	75%	4.2%	0.02%	0.03%	0% -3%	2% -3%
HC022	RBBC	2	H2	51%	-0.1%	0.05%	0.07%	1% -11%	2% -3%
HC022	RBBC	3	V	23%	-1.5%	0.06%	0.09%	10% -14%	2% -3%
HC024	39% Clay RBBC	1	H1	81%	0.2%	0.05%	0.08%	2% -5%	2% -2%
HC024	39% Clay RBBC	2	H2	61%	-0.9%	0.02%	0.06%	0% -3%	2% -2%
HC024	39% Clay RBBC	3	V	65%	2.0%	0.01%	0.03%	0% -5%	2% -2%

Table A1-3: Specimen metrics: stress and volume change (2 of 3)

Test ID	Material	Meas. #	Direction	$\sigma's/\sigma'$	$\Delta V / V_t$	Hydraulic Gradient Metrics			
						Avg ΔV	Max ΔV	$\Delta V/V_{avg}$	$\Delta P / \sigma'$
						cm^3	% of V_{total}	% of V_{total}	%
HC025	39% Clay RBBC	1	H1	85%	1.1%	0.02%	0.03%	0% -1%	2% -3%
HC025	39% Clay RBBC	2	H2	76%	-0.4%	0.01%	0.02%	0% -2%	2% -3%
HC025	39% Clay RBBC	3	V	73%	-0.2%	0.02%	0.03%	1% -1%	2% -3%
HC026	39% Clay RBBC	1	V	93%	0.4%	0.02%	0.04%	1% -3%	2% -4%
HC026	39% Clay RBBC	2	H1	84%	-0.1%	0.05%	0.06%	1% -2%	2% -4%
HC026	39% Clay RBBC	3	H2	79%	0.2%	0.02%	0.02%	0% -1%	2% -4%
HC027	39% Clay RBBC	1	H1	86%	-0.1%	0.02%	0.02%	1% -1%	2% -4%
HC027	39% Clay RBBC	2	V	74%	-0.9%	0.01%	0.02%	1% -4%	2% -4%
HC027	39% Clay RBBC	3	V2	48%	0.5%	0.04%	0.07%	2% -7%	1% -3%
HC029	39% Clay RBBC	1	V	70%	0.7%	0.04%	0.05%	0% -3%	3% -7%
HC029	39% Clay RBBC	2	H1	73%	-0.5%	0.03%	0.04%	0% -1%	4% -7%
HC029	39% Clay RBBC	3	H2	77%	-0.5%	0.08%	0.14%	1% -2%	1% -5%
HC030	RGoM-EI	1	V	100%	2.4%	0.01%	0.02%	9% -33%	2% -5%
HC030	RGoM-EI	2	H1	97%	0.9%	0.02%	0.03%	14% -30%	3% -5%
HC030	RGoM-EI	3	H2	69%	0.2%	0.02%	0.04%	8% -29%	3% -5%
HC031	RGoM-EI	1	H1	97%	2.5%	0.02%	0.02%	9% -23%	5% -8%
HC031	RGoM-EI	2	V	77%	0.3%	0.03%	0.04%	23% -34%	5% -8%
HC031	RGoM-EI	3	V2	93%	-0.2%	0.01%	0.02%	4% -20%	5% -8%
HC032	RSFBM	1	V	99%	1.3%	0.02%	0.02%	12% -22%	3% -4%
HC032	RSFBM	2	H1	72%	0.4%	0.01%	0.03%	2% -18%	3% -5%
HC032	RSFBM	3	H2	60%	0.5%	0.03%	0.04%	4% -29%	3% -5%
HC033	RSFBM	1	H1	93%	1.6%	0.02%	0.03%	9% -24%	4% -7%
HC033	RSFBM	2	V	81%	-0.2%	0.01%	0.02%	7% -12%	4% -7%
HC033	RSFBM	3	V2	87%	0.2%	0.01%	0.01%	9% -9%	4% -7%
HC034	RBBC	1	V	78%	5.9%	0.04%	0.10%	1% -55%	0.6% -1%
HC034	RBBC	2	H1	80%	-4.4%	0.01%	0.02%	2% -2%	0.6% -1%
HC034	RBBC	3	H2	80%	0.1%	0.02%	0.03%	1% -9%	0.6% -1%
HC036	RBBC	1	H1	100%		0.01%	0.01%	1% -2%	2% -3%
HC036	RBBC	2	V	60%	-4.8%	0.01%	0.02%	1% -10%	2% -3%
HC036	RBBC	3	V2	81%	-0.7%	0.01%	0.03%	1% -5%	2% -3%
HC037	RBBC	1	H1	100%	-0.1%	0.03%	0.05%	2% -6%	3% -6%
HC037	RBBC	2	V	100%	0.2%	0.02%	0.03%	3% -5%	3% -5%
HC037	RBBC	3	V2	60%	-0.3%	0.01%	0.02%	0% -5%	3% -5%
HC038	RBBC	1	V	60%	0.2%	0.02%	0.04%	0% -2%	4% -8%
HC038	RBBC	2	H1	61%	0.2%	0.01%	0.02%	0% -1%	4% -8%
HC038	RBBC	3	H2	64%	-0.1%	0.02%	0.03%	0% -1%	4% -8%
HC040	RBBC	1	H1	97%	2.0%	0.01%	0.01%	1% -3%	0.5% -1.3%
HC040	RBBC	2	V	97%	0.2%	0.01%	0.01%	3% -11%	0.8% -1.3%
HC040	RBBC	3	V2	97%	-1.7%	0.01%	0.02%	2% -10%	0.8% -1.3%
HC042	RBBC	1	V	70%	0.4%	0.03%	0.08%	0% -3%	9% -19%
HC042	RBBC	3	H1	60%	-0.2%	0.04%	0.06%	1% -3%	9% -19%
HC042	RBBC	4	V2	100%	-1.1%	0.03%	0.05%	1% -3%	9% -19%
HC042	RBBC	5	V3	100%	0.2%	0.04%	0.05%	0% -3%	9% -19%
HC044	RBBC	1	H1	100%	-0.4%	0.01%	0.01%	0% -3%	0.8% -1.2%
HC044	RBBC	3	V2	100%	0.1%	0.01%	0.01%	0% -9%	0.8% -1.2%

Table A1-3: Specimen metrics: stress and volume change (3 of 3)

Test ID	Material	Meas. #	Direction	$\sigma's/\sigma'$	$\Delta V / V_t$	Hydraulic Gradient Metrics			
						Avg ΔV	Max ΔV	$\Delta V/V_{avg}$	$\Delta P / \sigma'$
						cm^3	% of V_{total}	% of V_{total}	%
HC045	Leached RBBC	1	V	100%	2.5%	0.04%	0.06%	4% -10%	2% -3%
HC045	Leached RBBC	2	H1	100%	0.5%	0.05%	0.06%	2% -7%	2% -2%
HC045	Leached RBBC	3	H2	100%	-1.0%	0.02%	0.03%	0% -2%	2% -2%
HC046	Leached RSBFM	1	V	100%	1.3%	0.00%	0.00%	1% -8%	4% -6%
HC046	Leached RSBFM	2	H1	100%	0.1%	0.02%	0.03%	0% -17%	3% -5%
HC046	Leached RSBFM	3	H2	100%	0.4%	0.01%	0.01%	1% -8%	3% -5%
HC047	Leached RBBC	1	H1	100%	-0.2%	0.04%	0.07%	2% -3%	6% -10%
HC047	Leached RBBC	2	V	56%	-0.1%	0.01%	0.03%	0% -3%	7% -11%
HC047	Leached RBBC	3	V2	46%	0.3%	0.02%	0.05%	0% -3%	8% -12%
HC048	RBBC	1	V	100%	2.3%	0.02%	0.02%	2% -5%	2% -3%
HC048	RBBC	2	H1	100%	0.1%	0.01%	0.01%	0% -2%	2% -3%
HC048	RBBC	3	H2	100%	-0.5%	0.03%	0.06%	0% -3%	2% -3%
HC049	RBBC	1	V	100%	1.6%	0.06%	0.11%	1% -7%	6% -10%
HC049	RBBC	2	H1	100%	0.6%	0.01%	0.02%	0% -2%	5% -8%
HC049	RBBC	3	H2	100%	-0.7%	0.02%	0.03%	0% -2%	5% -8%
HC050	RBBC	1	H1	100%	2.4%	0.01%	0.02%	1% -2%	2% -3%
HC050	RBBC	2	V	100%	-1.4%	0.01%	0.01%	0% -2%	2% -3%
HC050	RBBC	3	V2	100%	-0.6%	0.02%	0.04%	2% -6%	2% -3%

Average	67%	0.3%	0.02%	0.04%
Maximum	100%	5.9%	0.09%	0.14%
Minimum	5%	-4.8%	0.00%	0.00%

Notes:

$\sigma's/\sigma'$	Sampling effective stress as a percentage of measurement effective stress at OCR 4
$\Delta V / V_t$	Difference between specimen volume at the beginning and end of the measurement, divided by the total specimen volume at the end of the measurement. Volumes are measured using caliper measurements of specimen dimensions.
Avg ΔV	Average specimen volume change measured during a hydraulic gradient. Equal to the difference in the measured inflow and outflow volumes from the beginning to the end of the pressure differential. Includes volume change associated with pressure equalization, but corrected for small leaks and secondary compression, where applicable.
Max ΔV	Maximum specimen volume change measured during a hydraulic gradient for a given measurement set up. See above.
$\Delta P / \sigma'$	Range of variation in pore pressure applied across the specimen during hydraulic gradients, divided by the specimen effective stress. Pore pressure variation is divided evenly between the top and bottom of the specimen, maintaining effective stress in the center of the specimen.

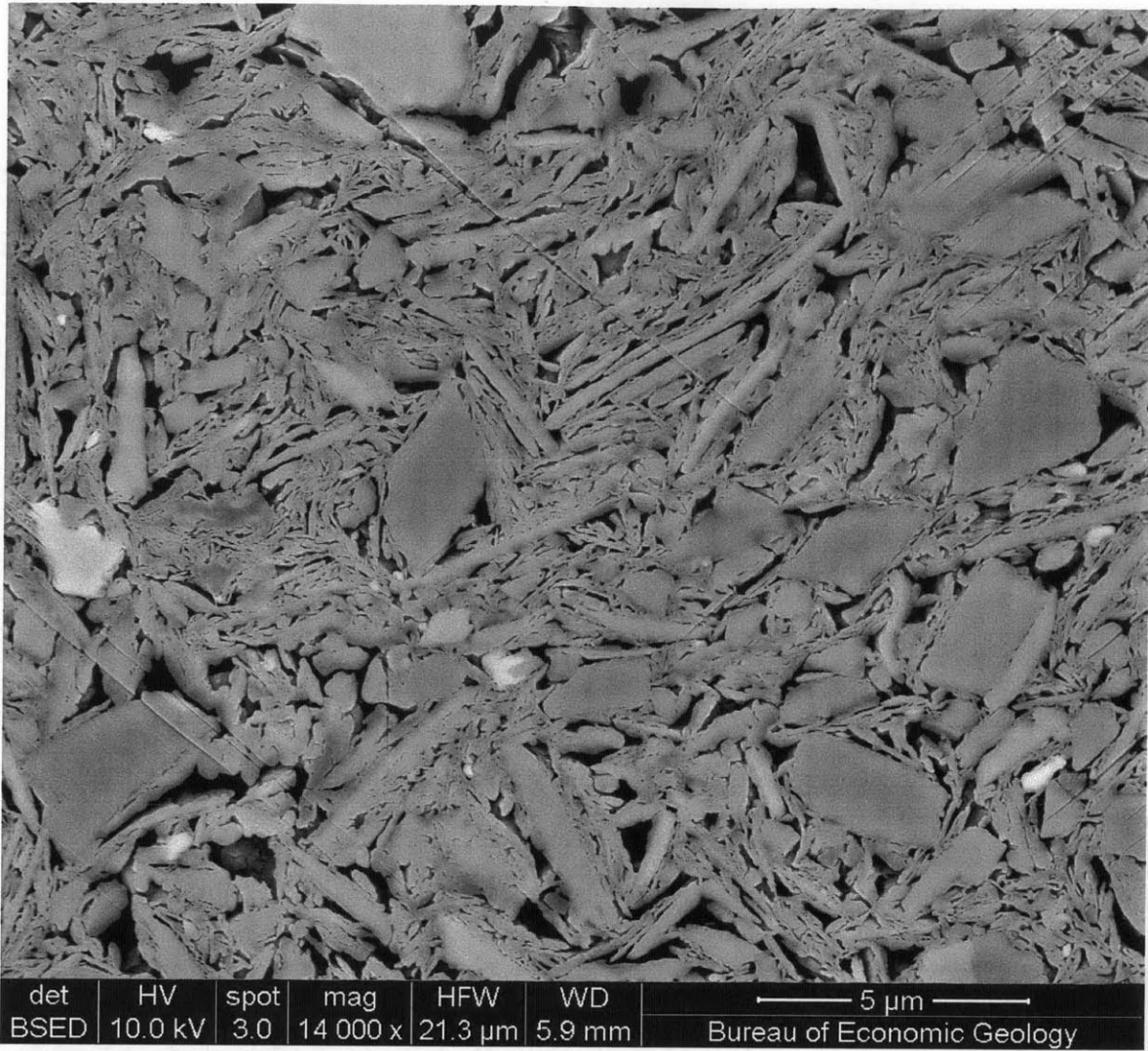


Figure A1-1: 0.1 MPa RBBC UT Image, filename: SEM0020_BSE_001

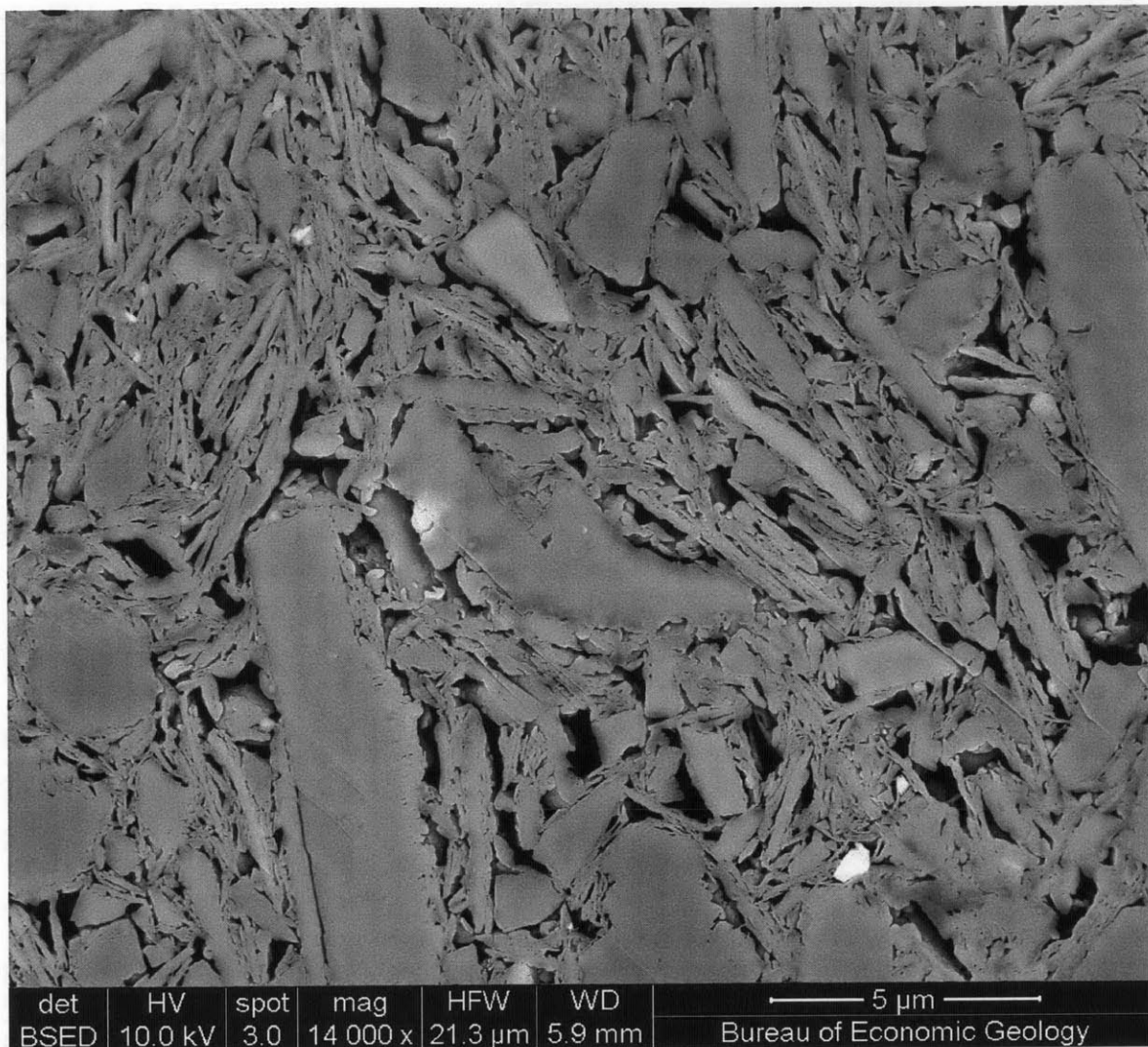


Figure A1-2: 0.1 MPa RBBC UT Image, filename: SEM0020_BSE_002

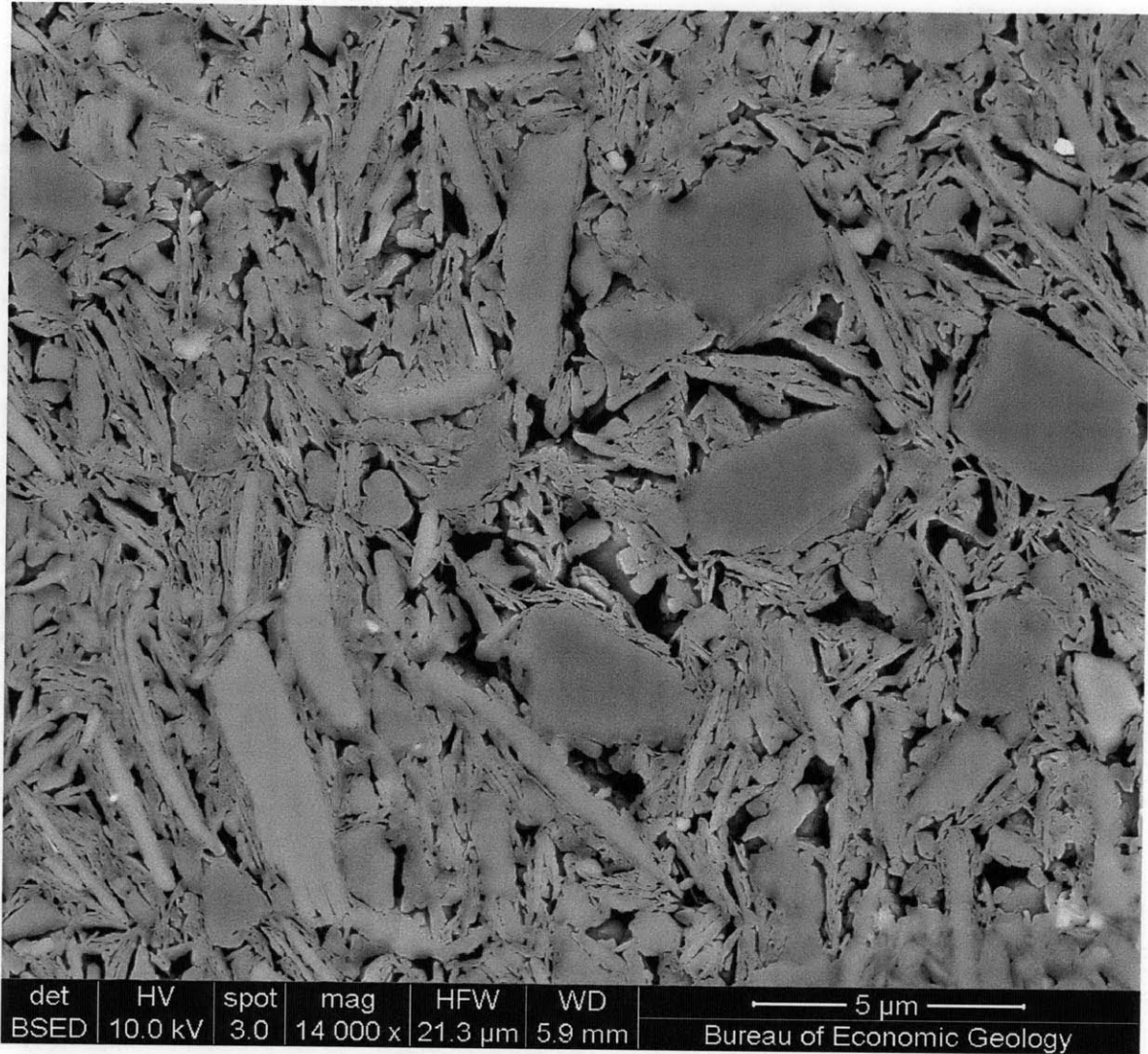


Figure A1-3: 0.1 MPa RBBC UT Image, filename: SEM0020_BSE_004

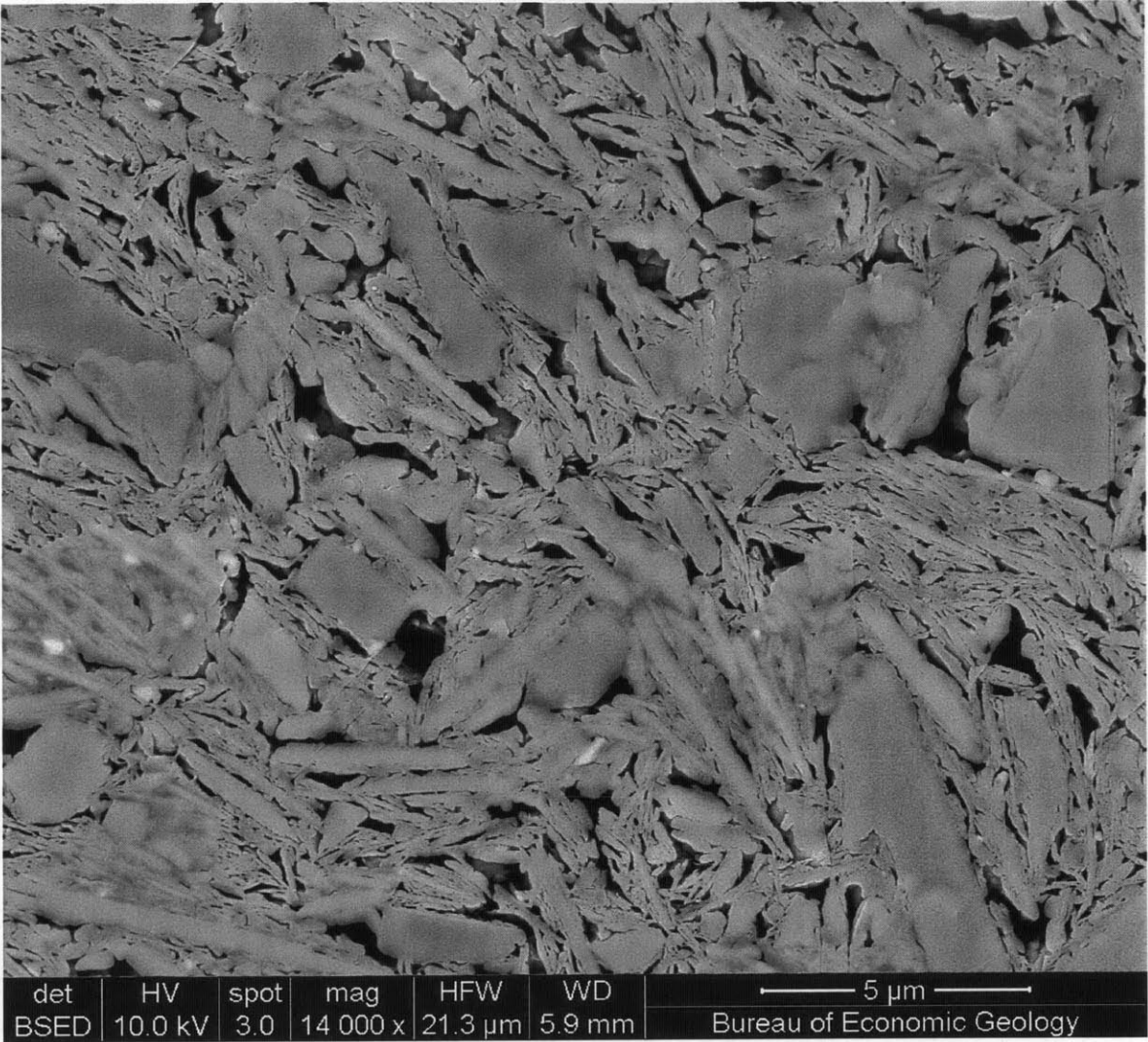


Figure A1-4: 1 MPa RBBC UT Image, filename: SEM0021_BSE_001

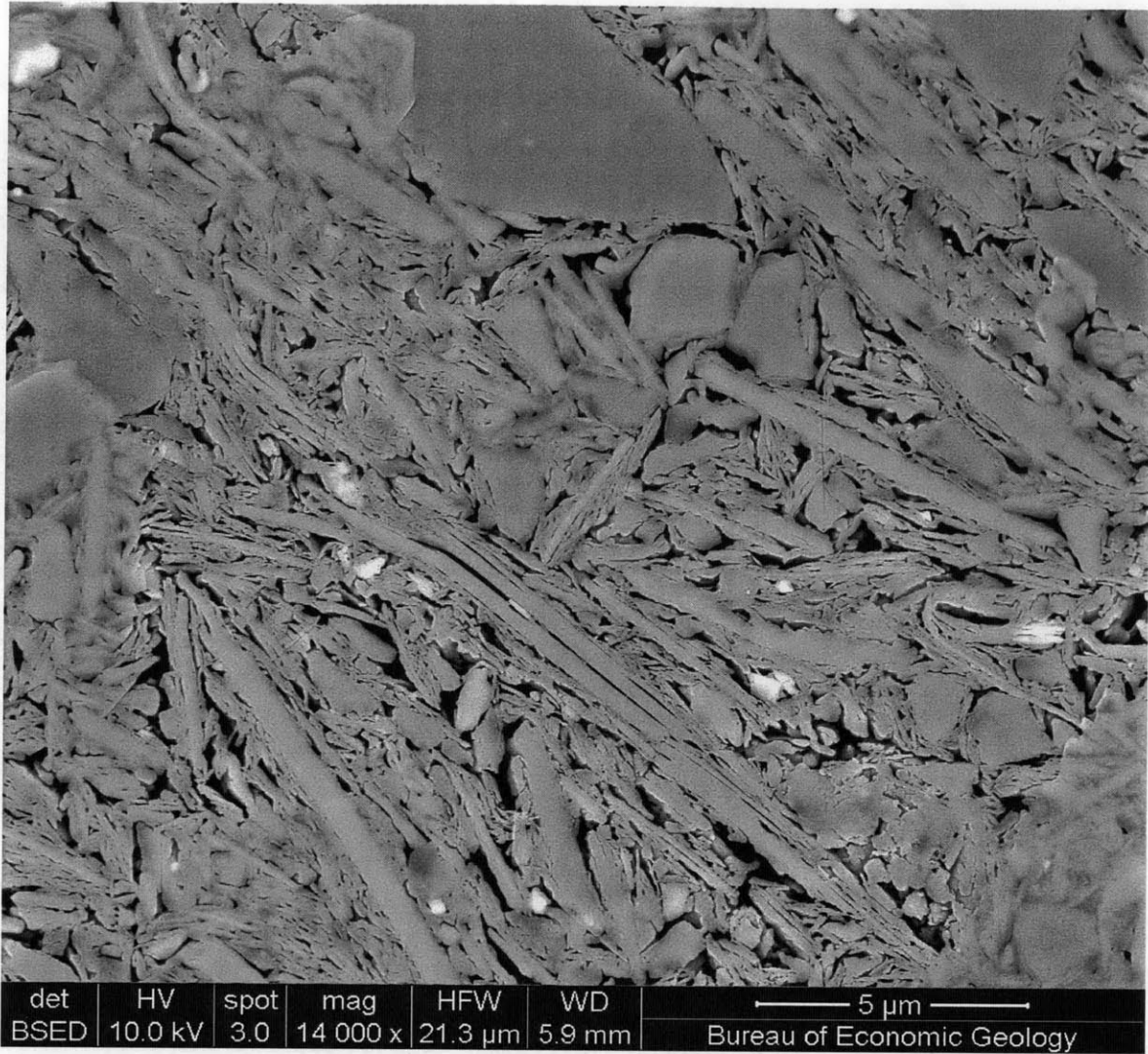


Figure A1-5: 1 MPa RBBC UT Image, filename: SEM0021_BSE_002

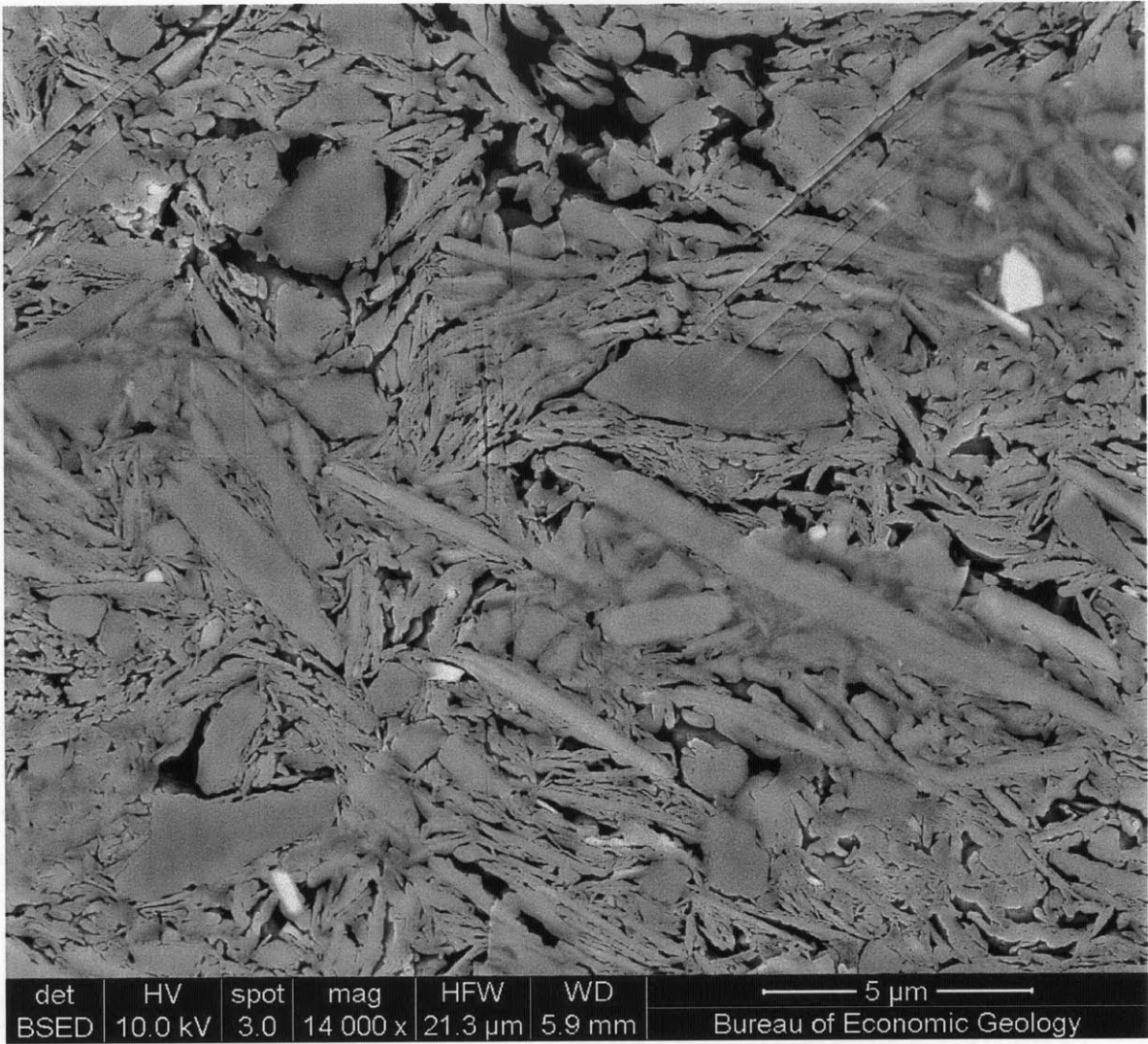


Figure A1-6: 1 MPa RBBC UT Image, filename: SEM0021_BSE_004

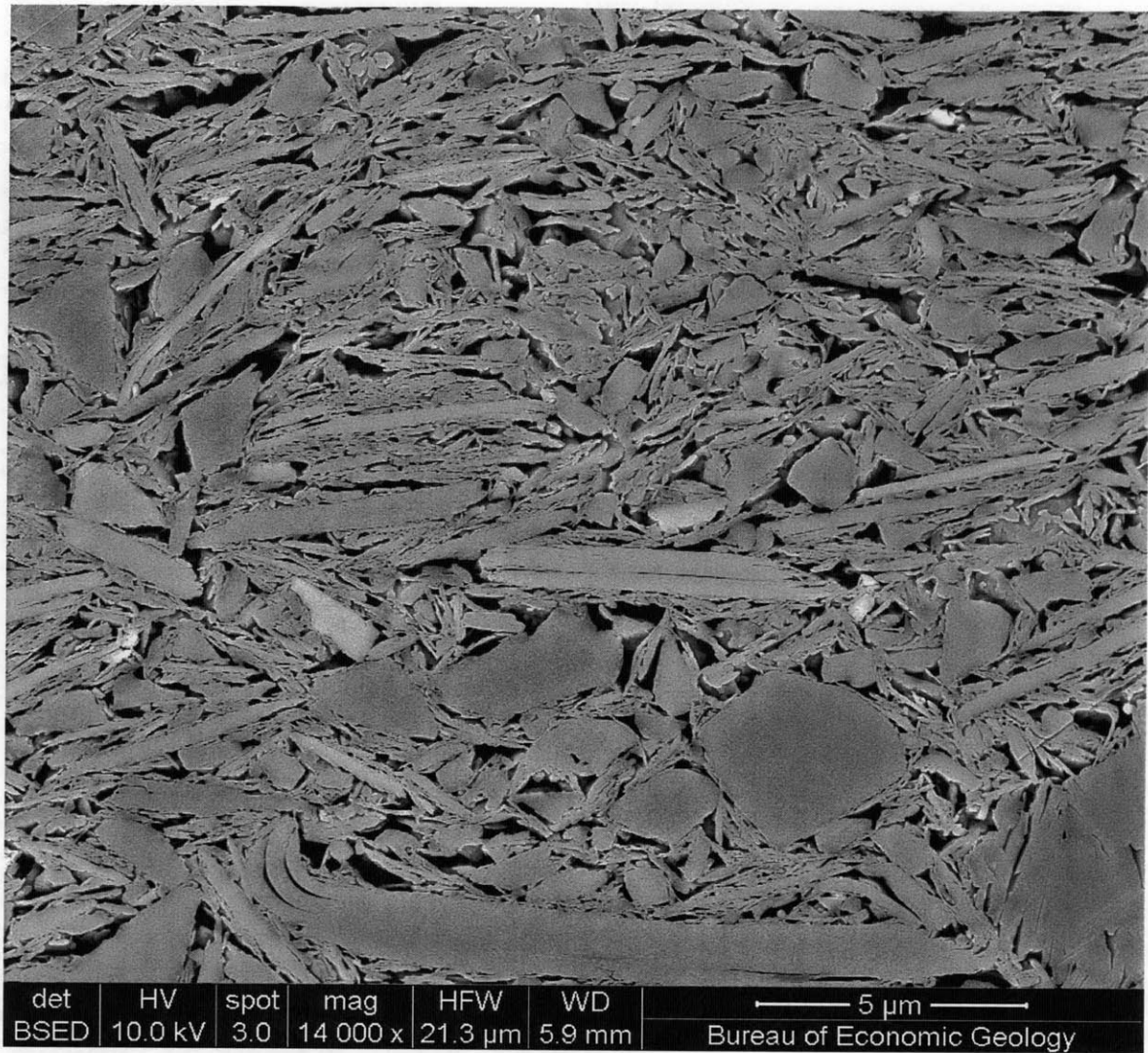


Figure A1-7: 10 MPa RBBC UT Image, filename: SEM0022_BSE_001

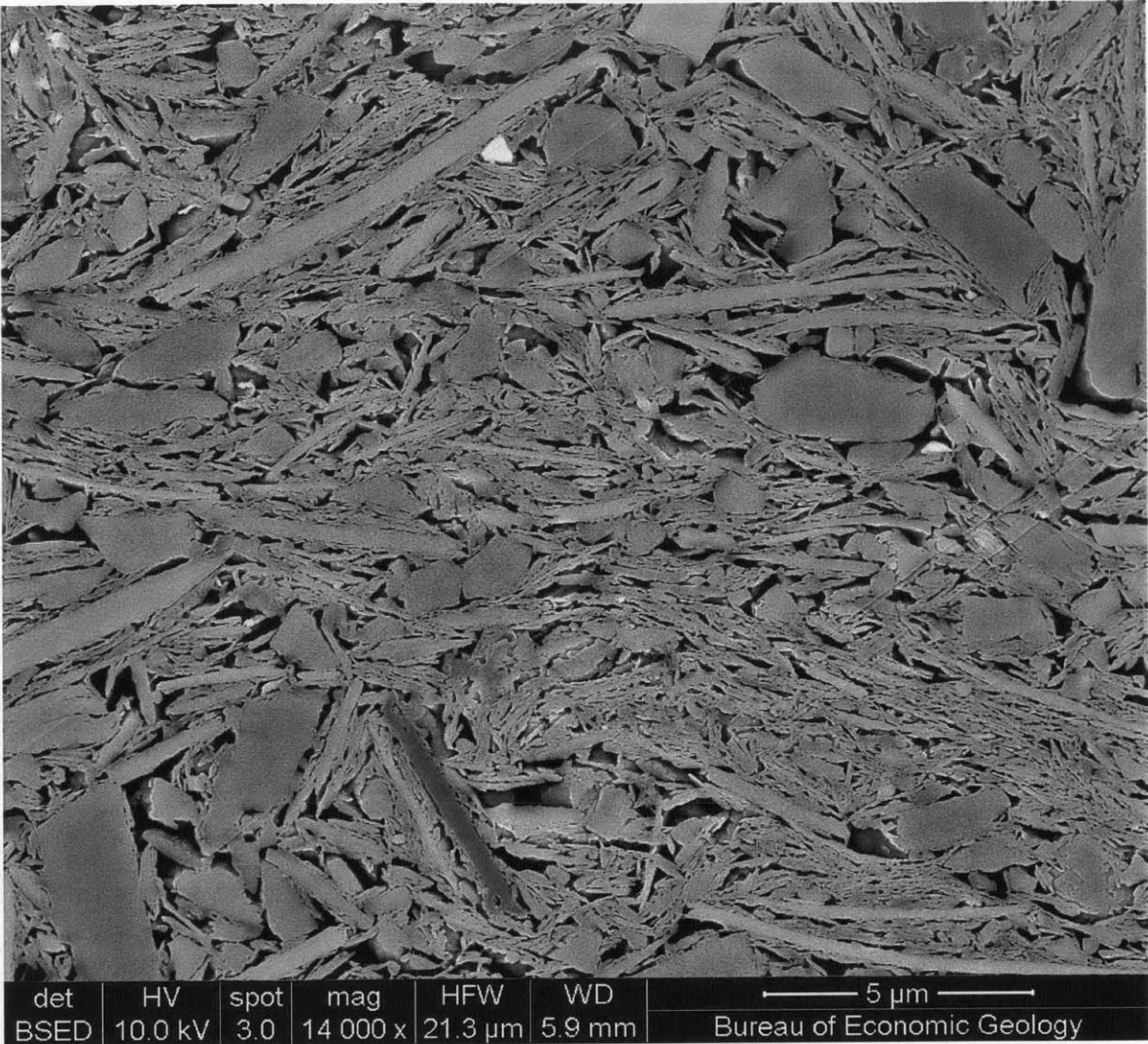


Figure A1-8: 10 MPa RBBC UT Image, filename: SEM0022_BSE_002

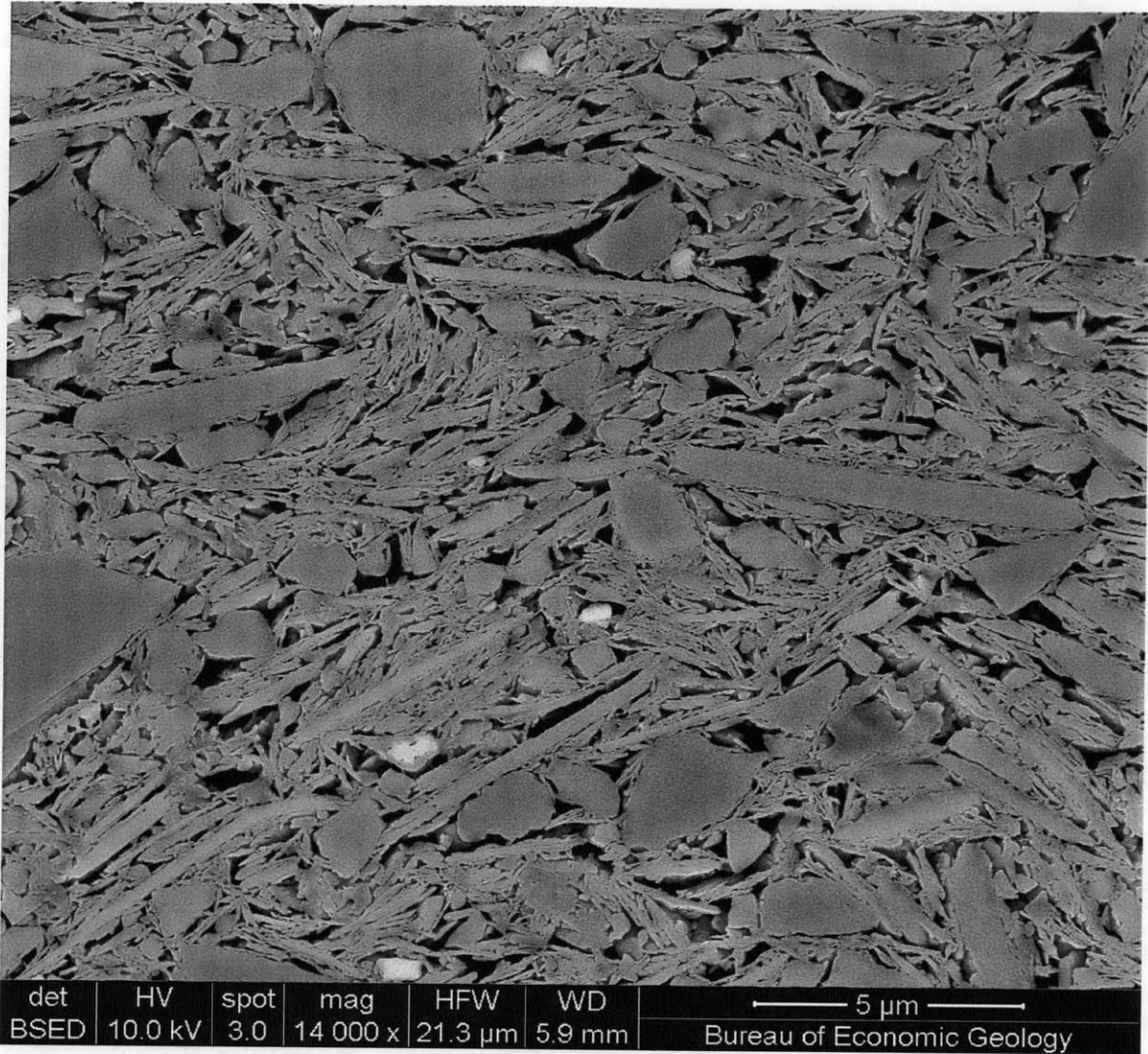


Figure A1-9: 10 MPa RBBC UT Image, filename: SEM0022_BSE_004

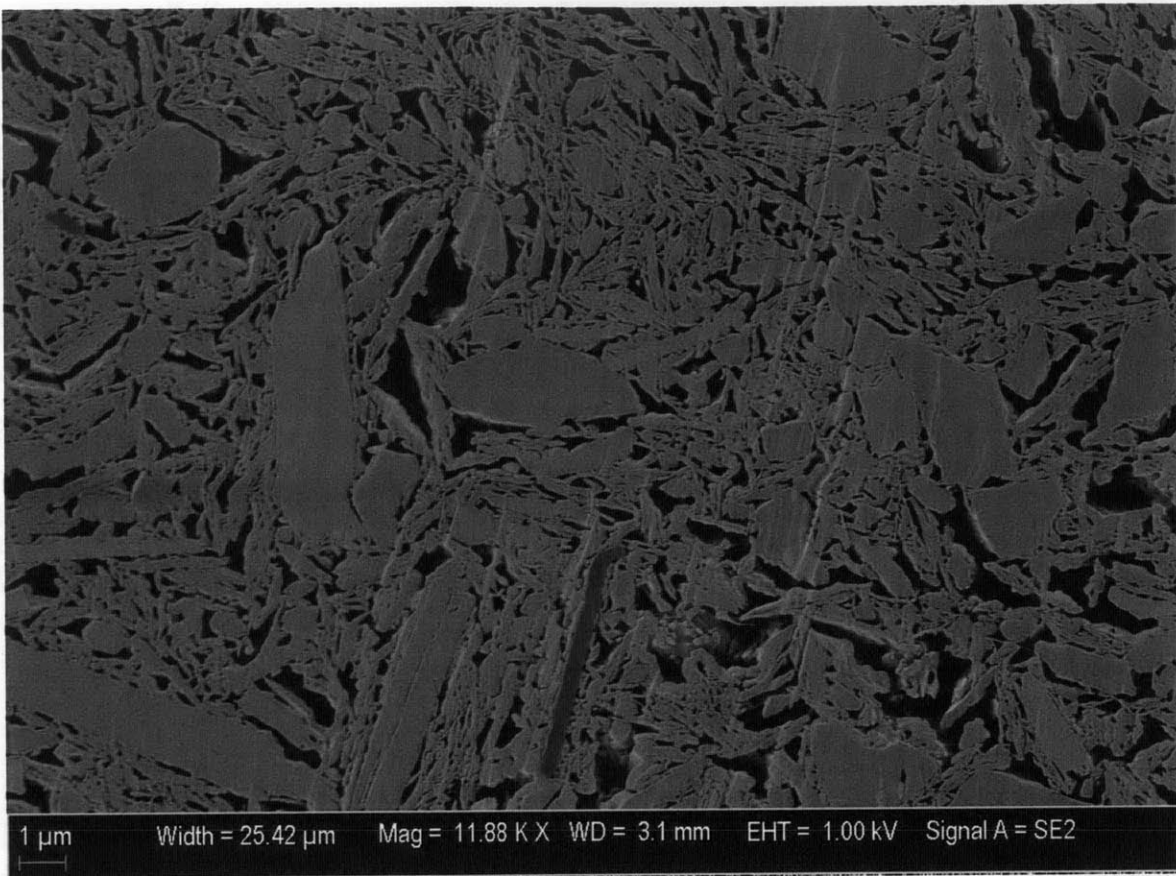


Figure A1-10: 1 MPa RBBC MIT Image filename: RS242 H- 10, from HC038

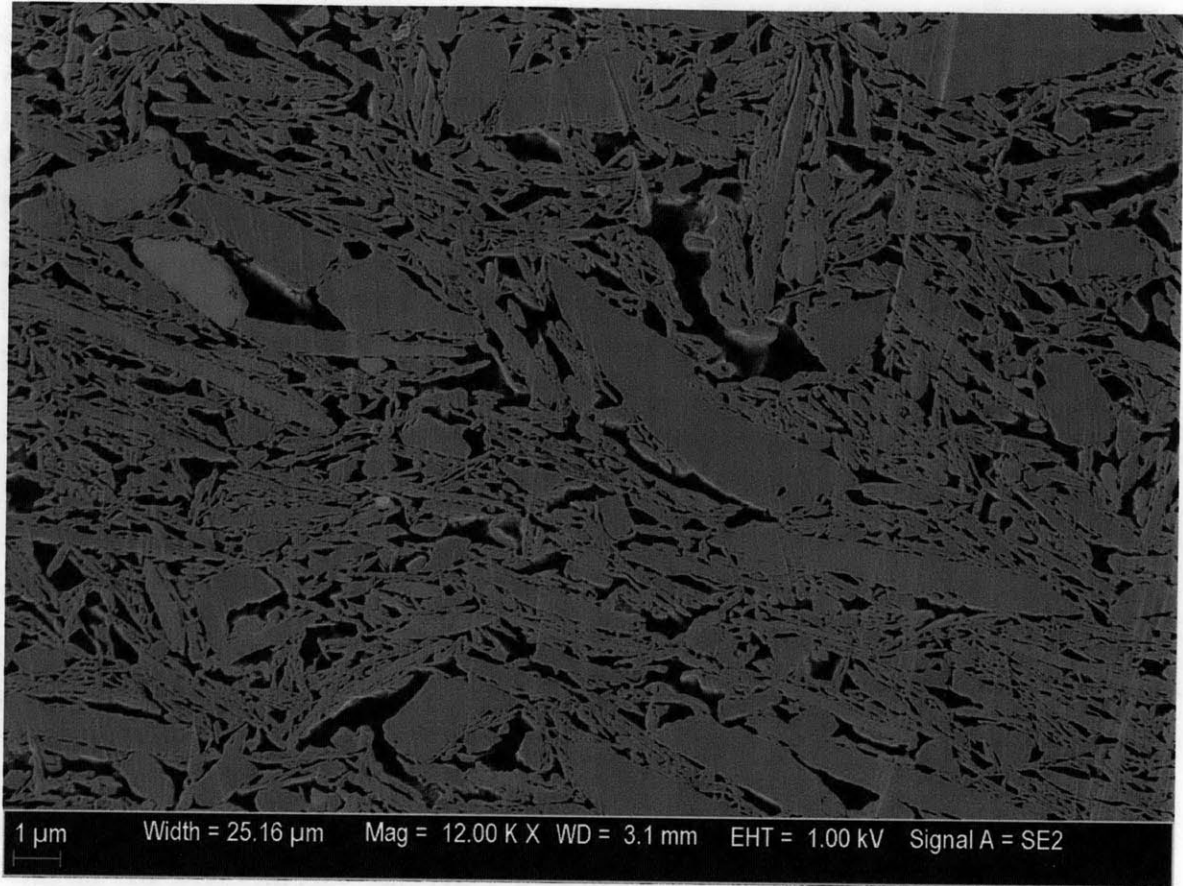


Figure A1-11: 1 MPa RBBC MIT Image filename: RS242 H- 20, from HC038

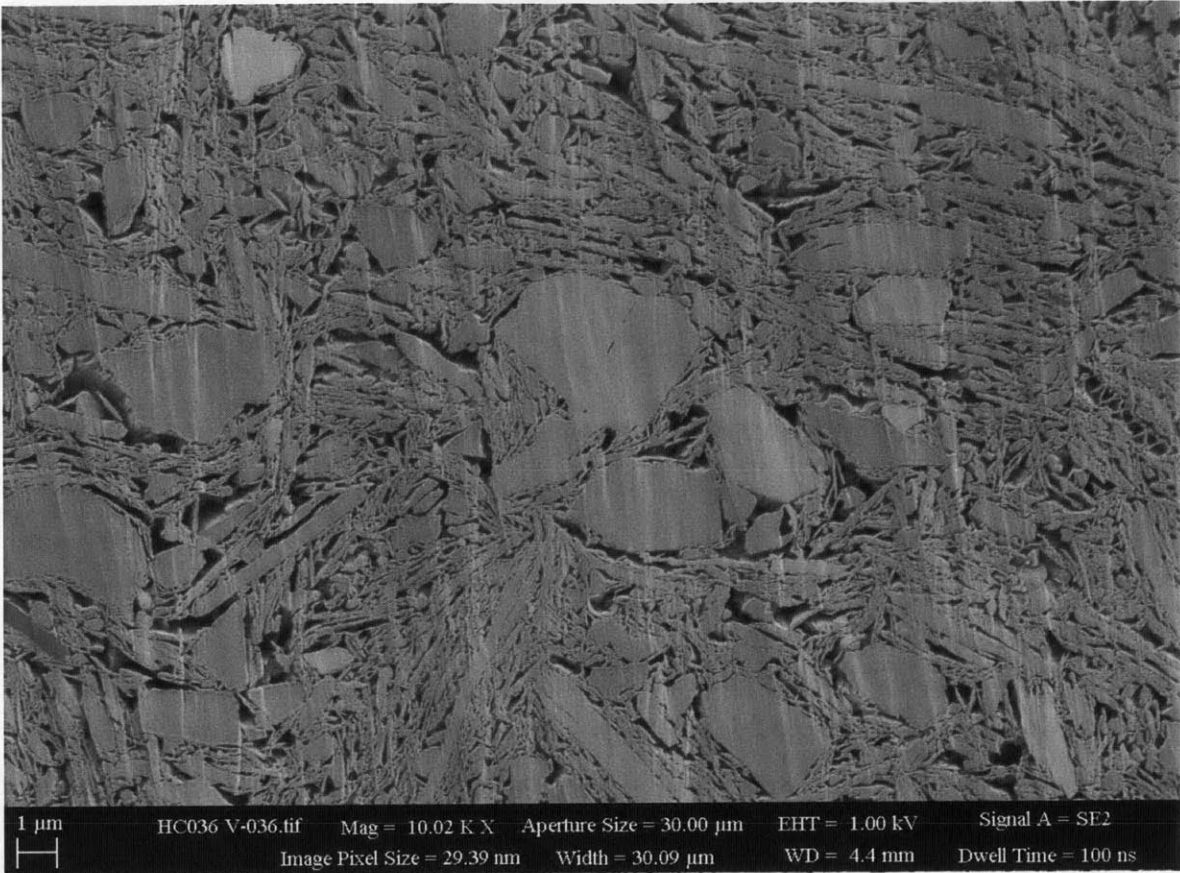


Figure A1-12: 10 MPa RBBC MIT Image filename: HC036 V-036

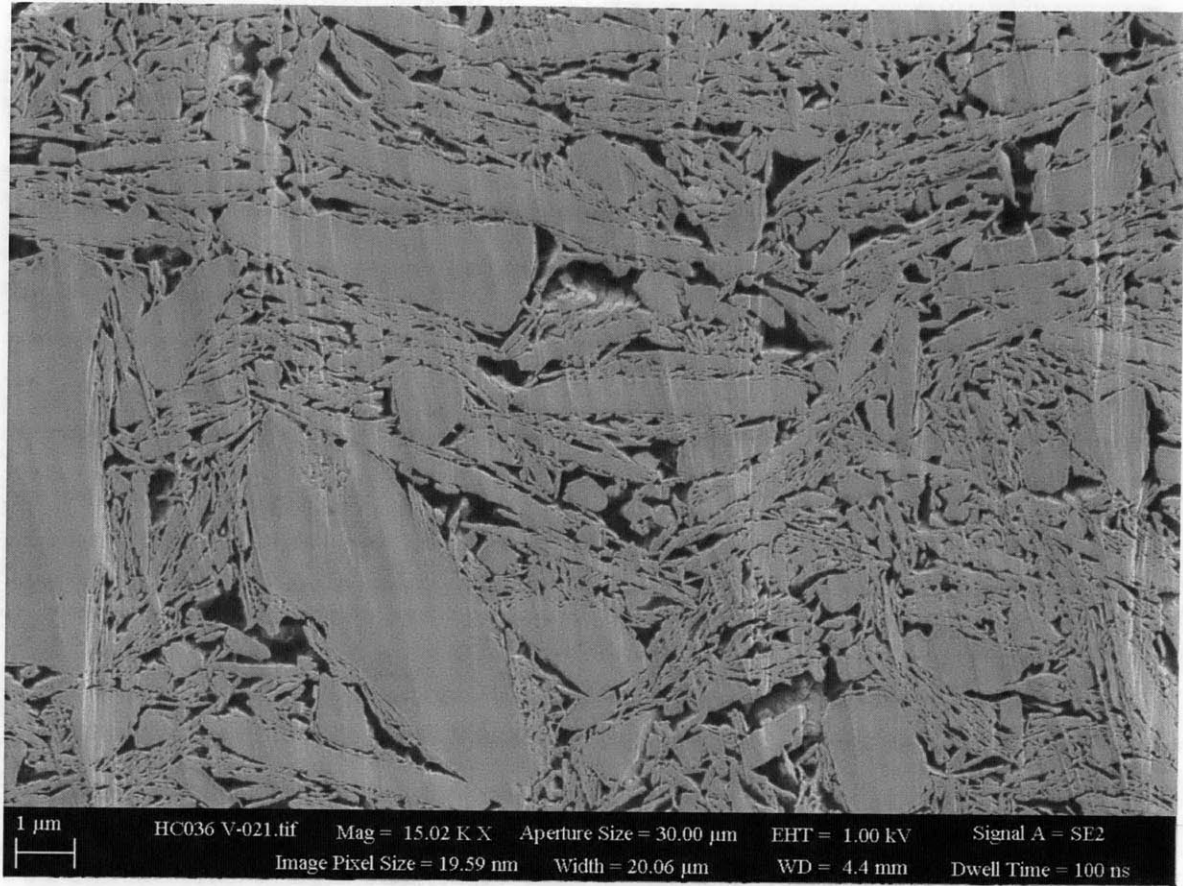


Figure A1-13: 10 MPa RBBC MIT Image filename: HC036 V-021

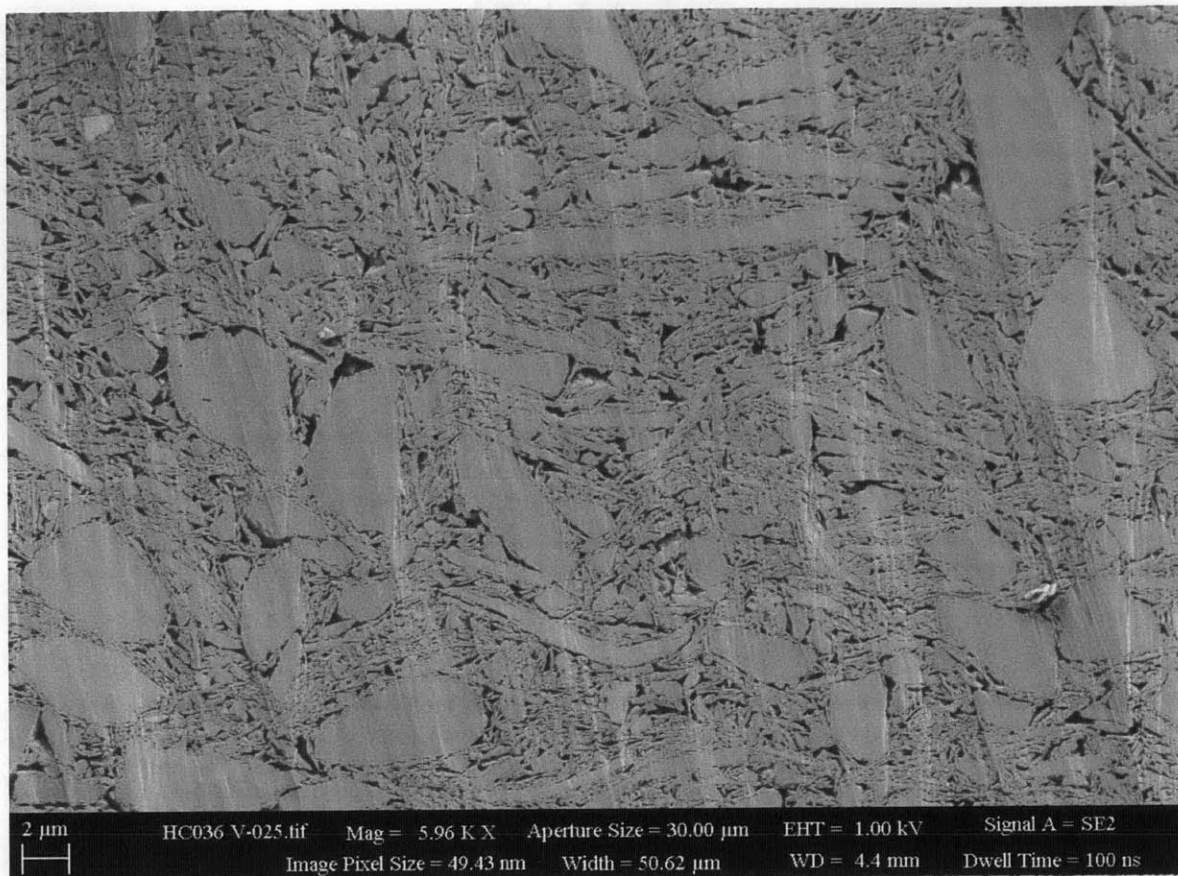


Figure A1-14: 10 MPa RBBC MIT Image filename: HC036 V-025

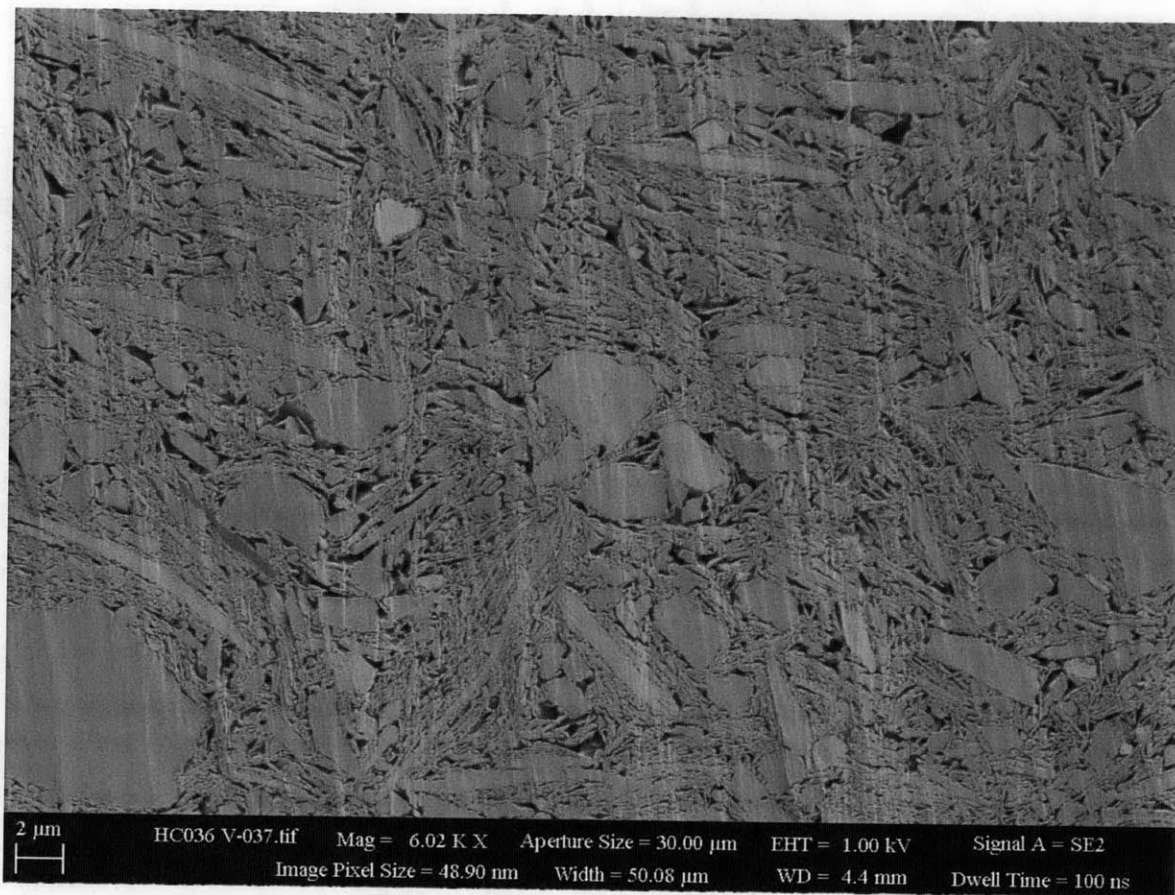


Figure A1-15: 10 MPa RBBC MIT Image filename: HC036 V-037

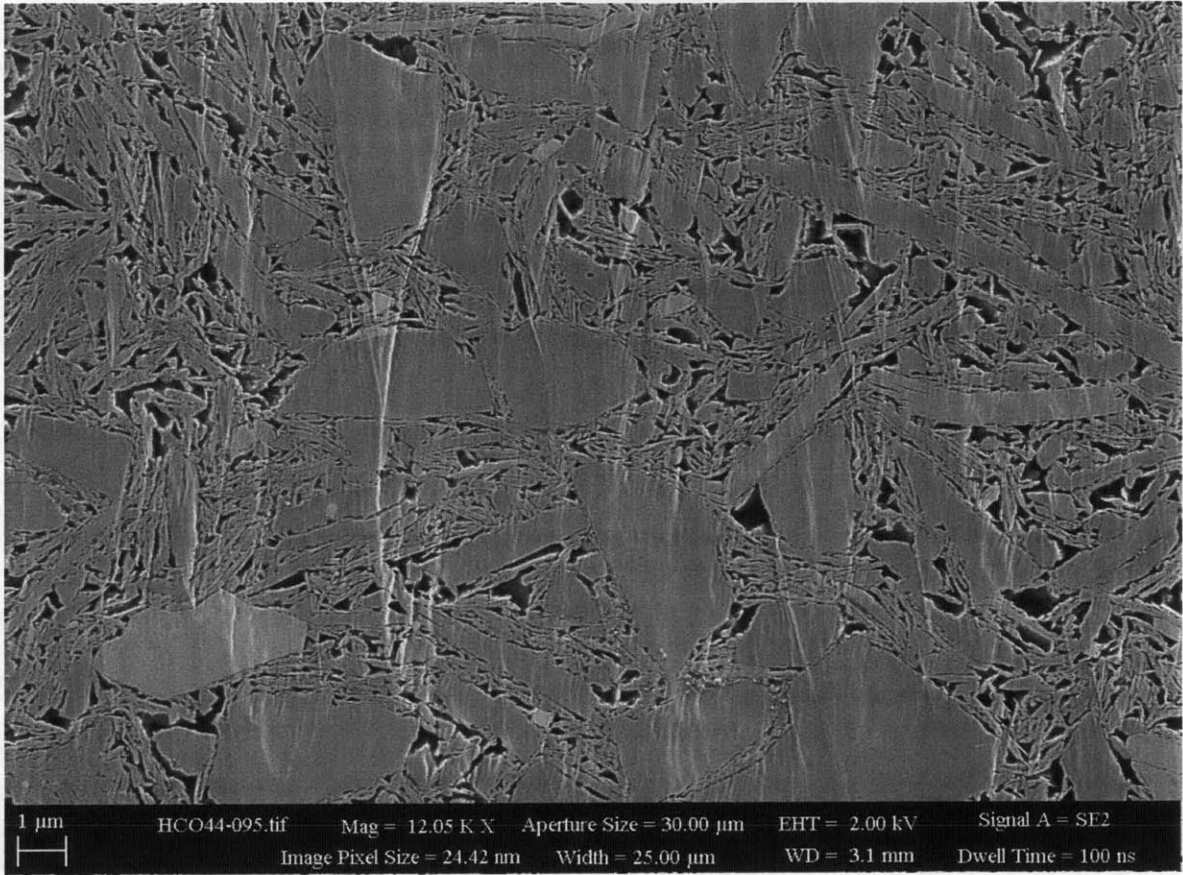


Figure A1-16: 20 MPa RBBC MIT Image filename: HC044-095

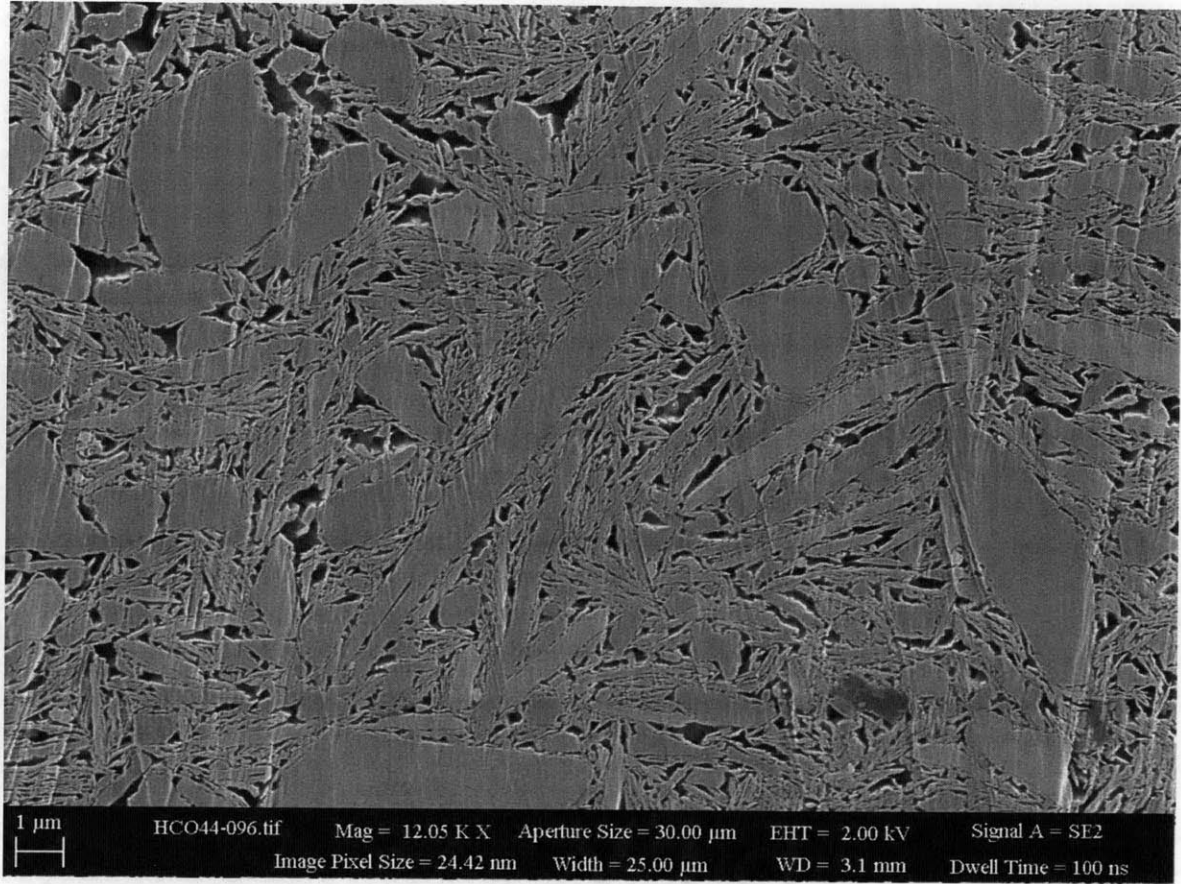


Figure A1-17: 20 MPa RBBC MIT Image filename: HC044-096

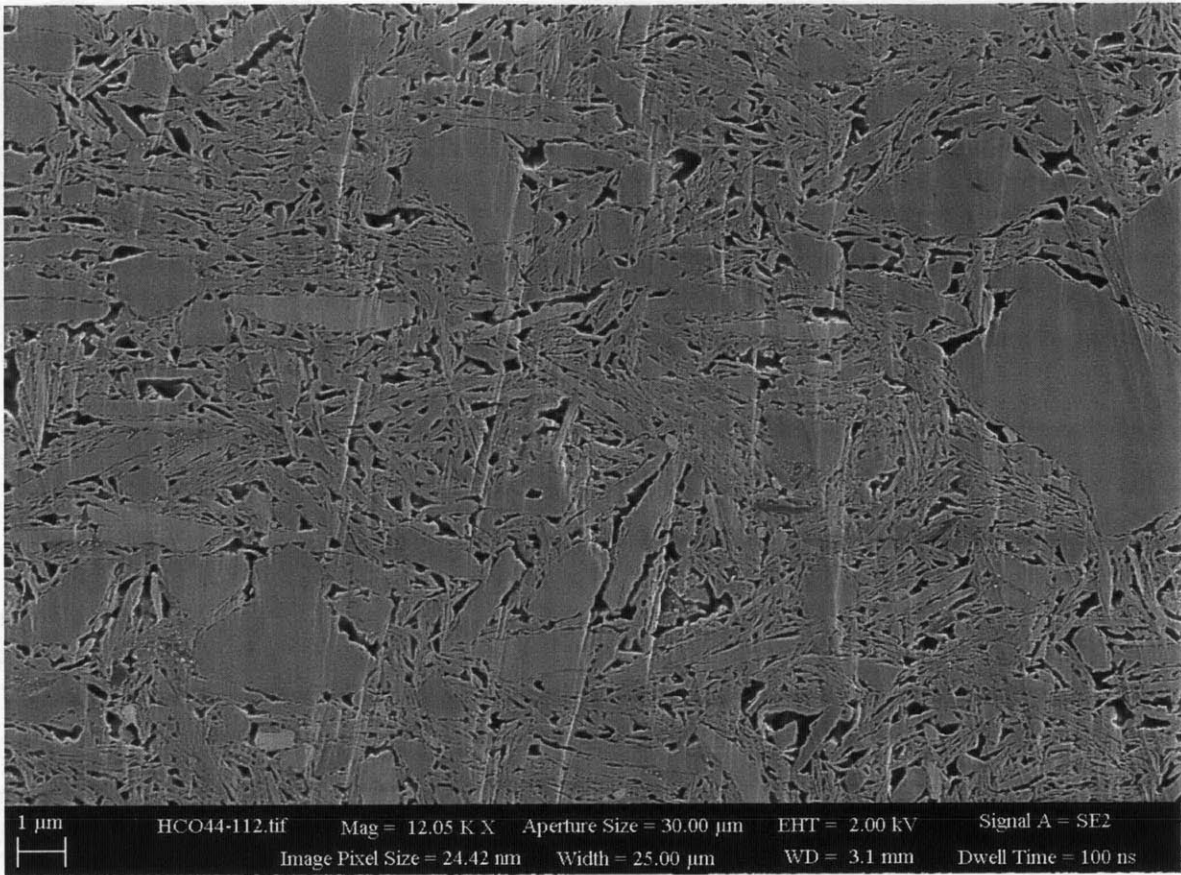


Figure A1-18: 20 MPa RBBC MIT Image filename: HC044-112

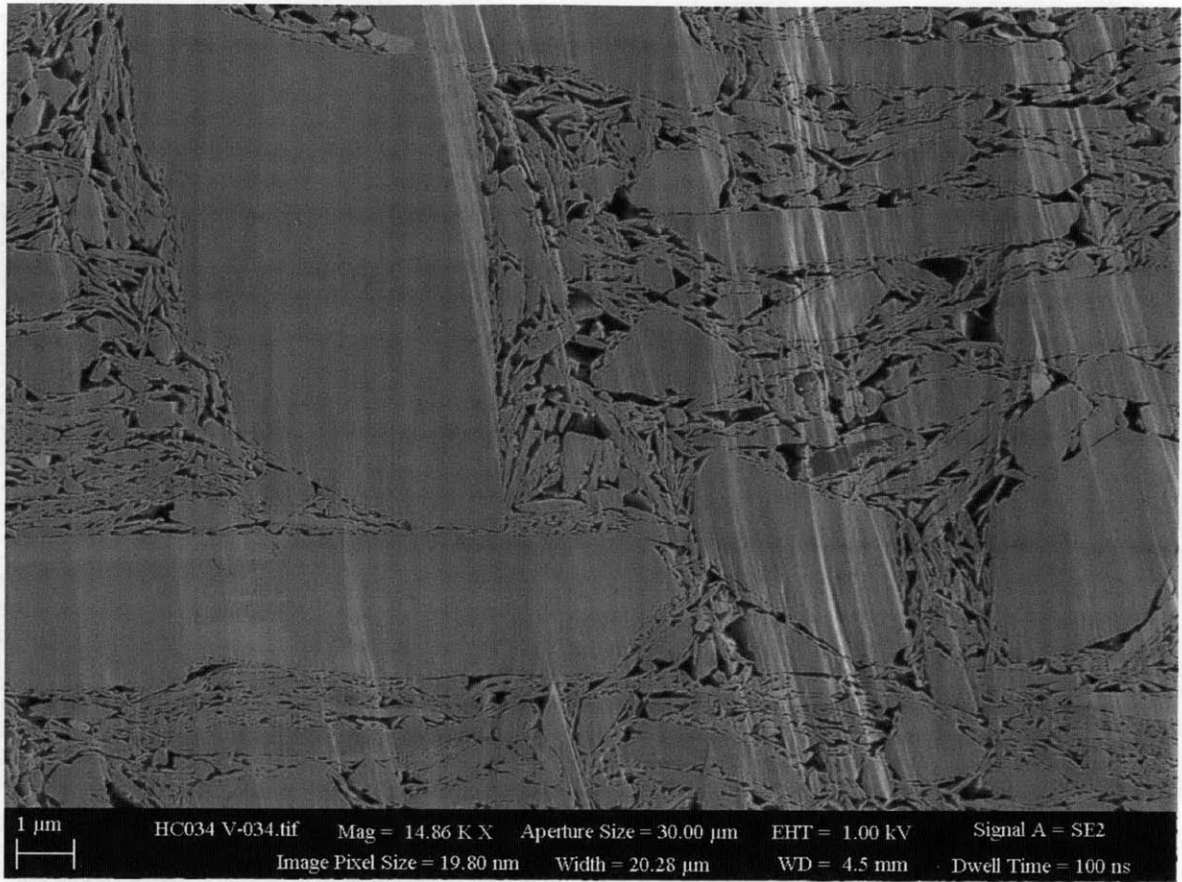


Figure A1-19: 40 MPa RBBC MIT Image filename: HC034 V-034

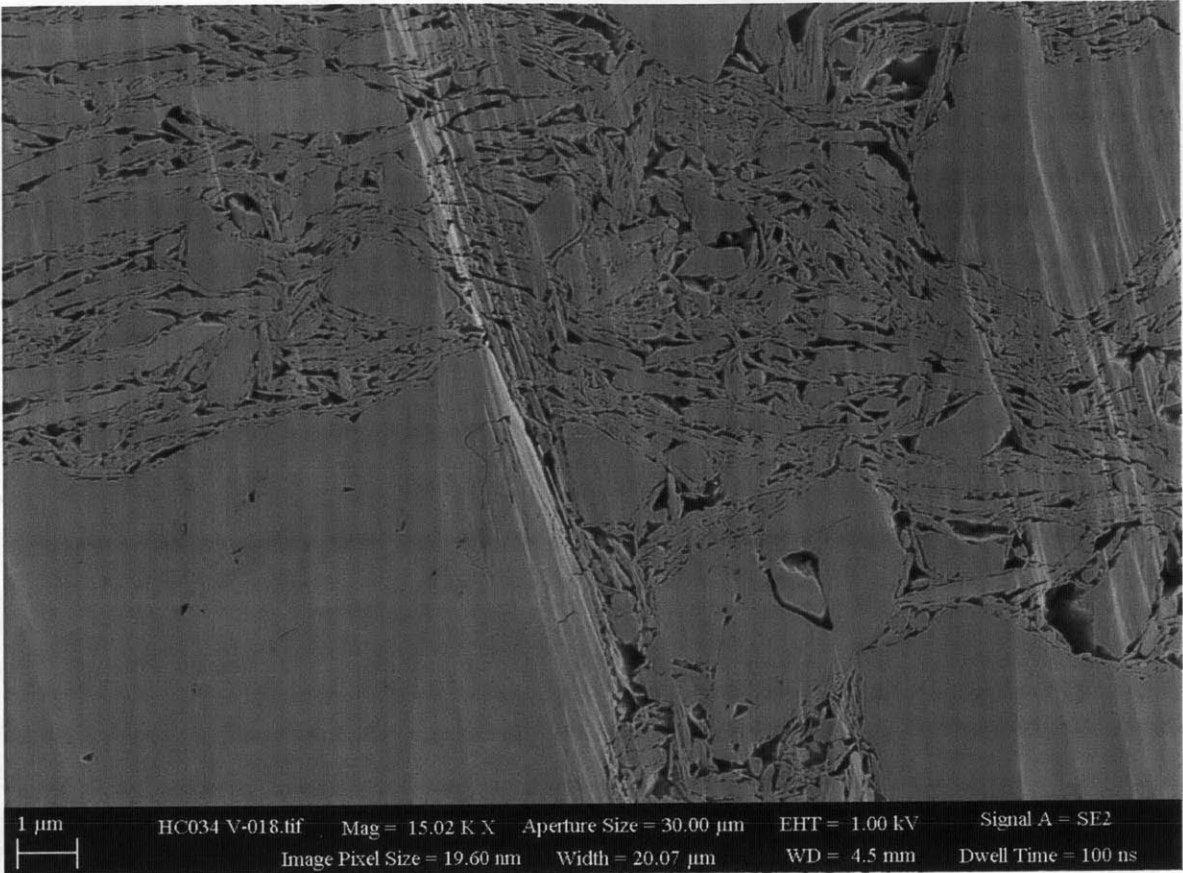


Figure A1-20: 40 MPa RBBC MIT Image filename: HC034 V-018

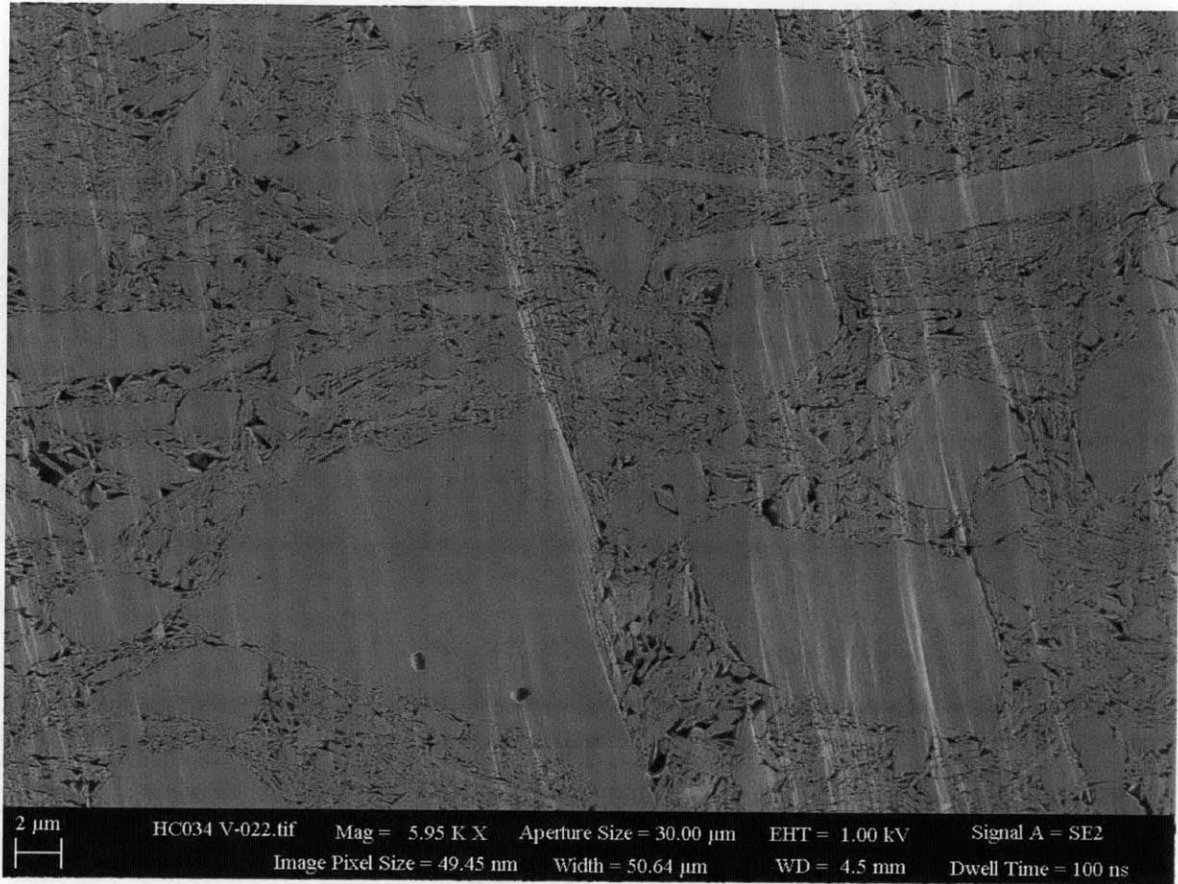


Figure A1-21: 40 MPa RBBC MIT Image filename: HC034 V-022

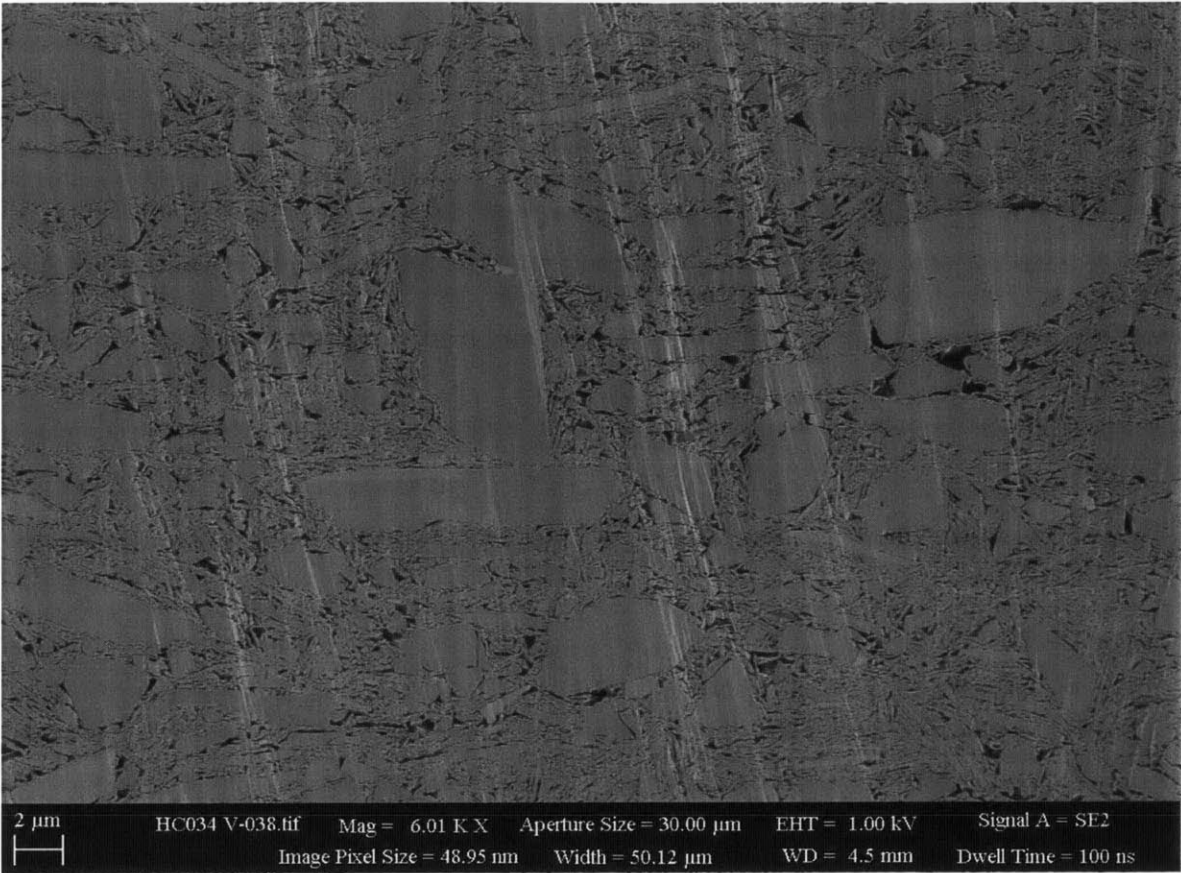


Figure A1-22: 40 MPa RBBC MIT Image filename: HC034 V-038

(Page intentionally left blank)

Appendix 2: Permeability Anisotropy Measurement: Equipment, Methods and Analysis

This appendix serves as a standalone reference manual for cubic permeability measurements. As such, this appendix contains a detailed description of the equipment, methods and analysis required to perform a constant head permeability measurement of a cubic mudrock specimen using the flexible wall permeameter. Step by step instructions on how to set up and run a permeability measurement using the flexible wall permeameter are provided. Additional steps are included for the case of resistivity measurement (further described in Appendix 3).

Contents

Appendix 2: Permeability Anisotropy Measurement: Equipment, Methods and Analysis.....	371
1 Background: Laboratory Permeability Measurement.....	373
1.1 Constant Head Method.....	373
1.2 Falling Head Method	374
1.3 Oedometer Method.....	375
1.4 Constant Rate of Strain (CRS) Method.....	376
2 Measurement Automation	377
2.1 Measurement Instrumentation	377
2.2 Data Acquisition System.....	379
3 Flexible Wall Permeability Measurement	381
3.1 Permeameter Equipment.....	382
3.2 Procedure	383
4 Data Analysis Methods – Permeability	392
4.1 Porosity / Void Ratio Determination	392
4.2 Hydraulic Conductivity Calculation	394
4.3 Leakage Correction.....	394
4.4 Measurement Sequence Bias Correction.....	397
4.5 Permeability Calculation	399
4.6 Permeability Anisotropy Calculation	399

List of Tables

Table A2-1: Transducer data	401
-----------------------------------	-----

List of Figures

Figure A2-1: Schematic diagram showing a constant head test with downward flow through the system. (Germaine and Germaine, 2009).....	402
Figure A2-2: Schematic diagram showing a falling head test (Germaine and Germaine, 2009)	402
Figure A2-3: Typical incremental oedometer setup (Germaine and Germaine, 2009).....	403
Figure A2-4: Example of Log of time and Square Root of time methods for time-deformation curve analysis in the incremental oedometer method (ASTM D2435)	404
Figure A2-5: Schematic of a standard Trautwein CRS apparatus (ASTM D4186).....	405
Figure A2-6: Schematic drawing of a centralized data acquisition system (Germaine and Germaine, 2009)	406
Figure A2-7: Schematic diagram of control system hardware components (Grennan, 2010).....	407
Figure A2-8: Solid view of the low stress triaxial cell (modified for permeability measurement) with manifold and cubic shaped specimen	408
Figure A2-9: Dimensioned section of the low stress triaxial cell (modified for permeability measurement) with cubic specimen	409
Figure A2-10: Photograph of pressure volume actuators (PVA's) used to control cell and pore pressures in triaxial cells.....	410
Figure A2-11: Completed resedimented specimen prior to extrusion	411
Figure A2-12: Extruding a resedimented specimen using the manual hydraulic jack.....	412
Figure A2-13: Trimming a high stress specimen	413
Figure A2-14: Dimensioning the cubic specimen.....	413
Figure A2-15: Specimen assembled with porous stones, filter screens and top end adapter.....	414
Figure A2-16: Specimen with double rubber membrane and O ring seals	414
Figure A2-17: Water trap cylinder configuration used for vacuuming during specimen set up.....	415
Figure A2-18: Effect of loss of temperature control during a hydraulic gradient: volume vs. time.	415
Figure A2-19: Effect of loss of temperature control during a hydraulic gradient: flow rate vs. time	416
Figure A2-20: Secondary compression volume change determination for test HC019H1	416
Figure A2-21: Leak rate determination method.....	417
Figure A2-22: Horizontal Measurement Sequence Bias for RBBC	418
Figure A2-23: Single specimen measurement sequence bias with correction method (after Chan and Kenney, 1973).....	418

1 Background: Laboratory Permeability Measurement

There are many different permeability measurement techniques that are suited to different types of soils, testing time scales, and laboratory or field setups. The most common methods include constant and falling head boundary conditions, as well as the constant rate of strain technique. Permeability may also be back calculated from compression measurements using the standard oedometer; these methods are described in detail herein. Other methods that have been developed include constant flow, constant volume variable head, and constant head constant volume tests (Germaine, 2009).

A permeameter is a laboratory device used to measure the permeability of a material; for each permeability test method there are different permeameter schematics that can be used. A permeameter is used to measure the hydraulic conductivity of a material using a particular fluid called a permeant. The permeability of the material is computed from the measured hydraulic conductivity using the previously described relation (Section 2):

$$k = \frac{K\mu}{\rho g} \quad \text{A2-1}$$

Where k is the permeability, K is the hydraulic conductivity, ρ and μ are the mass density and the dynamic viscosity, respectively, of the permeant fluid and g is the gravitational constant.

A given permeameter setup can often only test a limited range of permeabilities (i.e. a few orders of magnitude) due to physical constraints, mostly relating to the application of the hydraulic gradient and/or the flow volume required. Because natural permeability varies by up to 14 orders of magnitude (Germaine, 2009), different permeameters are typically required to measure the permeability of different soils, for example a coarse sand and a clay.

1.1 Constant Head Method

A constant head test is a simple, steady state permeability measurement method that is used to evaluate a specimen at a single and constant void ratio. A hydraulic gradient is applied and maintained across a specimen via a differential head at two points. Figure A2-1 shows a schematic constant head test setup (Germaine and Germaine, 2009).

The flow rate can be measured and the hydraulic conductivity computed according to Darcy's Law:

$$K = \frac{Q}{iA} \quad \text{A2-2}$$

Where K is the hydraulic conductivity, Q is the flow rate through the specimen, i is the dimensionless gradient across the specimen and A is the area of flow. Hydraulic conductivity is then converted to permeability using equation A2-1.

Equation A2-2 applies only once flow has reached steady state; this can be verified by measuring the time variance of flow rate and ensuring that the inflow increment is equal to the outflow increment. Depending on the set up, the gradient i can be measured in different ways; in the permeameter shown in Figure A2-1, manometers measure the change in hydraulic head between two points in the system and the gradient is computed as this change in total head divided by distance between the manometer ports. Another method, applied in this work, uses a back pressured specimen enclosed in a triaxial cell where pore pressure transducers measure the difference in head between two points in the specimen.

1.2 Falling Head Method

The falling head method is another common permeability measurement method. Falling head tests do not require an input tank of constant head, and are applicable to materials over a wide range of permeability, especially those with medium and low hydraulic conductivity. Figure A2-2 shows a schematic drawing of a falling head test setup (Germaine and Germaine, 2009).

The hydraulic conductivity of a soil can be computed in a falling head test by equating the time varying flow rate in the inflow tube to that of the specimen:

$$a \frac{dh}{dt} = KA \frac{h}{L} \quad \text{A2-3}$$

and solving for the hydraulic conductivity, k :

$$K = \frac{aL}{A(t_1 - t_0)} \ln \left(\frac{h_0}{h_1} \right) \quad \text{A2-4}$$

Where K is the hydraulic conductivity, a is the area of the inflow tube, A is the area of the specimen, L is the length of the specimen. h_0 is the initial height of water in the inflow column at t_0 and h_1 is the height of water in the inflow column after some time t_1 . Hydraulic conductivity is then converted to permeability using equation A2-1.

Some limitations of the falling head method include the physical height of the inflow tube (typically limited by the ceiling or availability of materials), as well as the effects of capillarity which can reduce the head applied to the specimen. For fine grained soils, in order to increase the gradient without increasing the volume of flow and hence the time duration of the test, the engineer is tempted to reduce the area of the inflow tube, a . However capillarity effects become important as the area of the inflow column decreases (Germaine and Germaine, 2009) and this effect must be balanced to ensure the measured change in height reflects the change in head applied to the specimen. Unlike the constant head test, where manometers may be used to measure the head difference across a portion of the specimen, there is no method of measuring the actual hydraulic head applied to the specimen as a function of time in a falling head test.

1.3 Oedometer Method

Traditionally, incremental oedometer tests are used to measure the compression characteristics, including the hydraulic conductivity, of cohesive soils. The hydraulic conductivity can be inferred from the computed coefficient of consolidation computed at each load increment.

The incremental oedometer test uses a procedure involving the application of loads using load increment ratios (LIR) of between 0.5 and 1, but more commonly closer to 1, to a specimen trimmed into a rigid ring, placed between two porous stones and submerged in a water bath allowing for double drainage. Figure A2-3 shows a typical incremental oedometer setup (Germaine and Germaine, 2009).

Incremental loads are left for a period of time during which the time deformation curve is measured. Each load increment requires separate analysis to determine the end of primary consolidation strain which is then used to create a compression curve (stress – strain relationship, typically e -log σ' space). Incremental oedometer tests are long in duration and intensive in data analysis, typically requiring at minimum 10 or more load increments to define a suitable compression curve.

There are two common analysis techniques used to reduce the time deformation curves for each load increment: root-time and log time methods. Figure 2-4 gives examples of these two methods (ASTM D2435). Each method can be used to compute the coefficient of consolidation for that increment, C_v . However, there is a disagreement between the C_v values obtained from the two methods. Ladd (1996) estimates, based on numerous case histories, that:

$$C_{v_{\text{root time}}} = 2 \pm 0.5 C_{v_{\text{log time}}} \quad \text{A2-5}$$

Typically the results from each of the two methods are averaged and the average coefficient of consolidation is reported. This discrepancy in coefficient of consolidation from the two methods is especially important, however, because the hydraulic conductivity computed using the incremental oedometer is based on the coefficient of consolidation:

$$C_v = \frac{k}{m_v \gamma_w} \quad \text{A2-6}$$

Where C_v is the coefficient of consolidation, k is the hydraulic conductivity, γ_w is the unit weight of water, and m_v is the coefficient of volume compressibility. Therefore a scatter in the coefficient of consolidation translates into a scatter in the hydraulic conductivity.

ASTM standard D2435 (Method A) prescribes that loads be left for 24 hours and that deformation measurements need only be taken at 0 and 24 hours time. The ASTM standard method significantly reduces the data collection workload. Using the 24 hour increment approach, significant secondary

compression behaviour is included in the compression measurements, and detailed time deformation curves are not obtained for each increment. The maximum past pressure, σ'_p , and the slope of the virgin compression line in e - $\log\sigma'$ space, c_c are underestimated due to the inclusion of secondary compression. More concerning, without detailed time deformation curves the coefficient of consolidation, C_v , used to compute the hydraulic conductivity, k , cannot be determined using either of the methods detailed in Figure A2-4.

1.4 Constant Rate of Strain (CRS) Method

The Constant Rate of Strain (CRS) method is a relatively new way to rapidly and accurately measure both the compression and permeability characteristics of a soil. Contrary to the oedometer method which only provides data at discrete loading intervals, the CRS method produces a continuous data sequence with increasing load. For most soils the CRS technique is much faster than the standard oedometer technique. Only very low permeability soils ($\sim 10^{-20} \text{ m}^2$) require a very low strain rate resulting in very long measurement times comparable to that of the oedometer method.

The CRS method loads a soil specimen at a constant rate of deformation with a constant head boundary condition at the top of the specimen and a no flow boundary condition at the base. Measurements of deformation and excess pore pressure generated at the base of the specimen during loading are used to compute the permeability and compressibility of the soil. Adams (2011) provides an extensive treatment of the background, equipment, methods and analysis relative to the CRS measurement method.

A schematic of a standard Trautwein CRS apparatus is shown in Figure A2-5. The specimen is trimmed into a rigid ring and placed between two porous stones and encased within a pressurized cell. The specimen is singly drained to the pressurized cell and the buildup of pore pressure at the base of the specimen is measured using a small volume measurement system. The apparatus is installed in a load frame that applies load at a constant rate of deformation via a piston in contact with the top of the specimen. As the load increases, the specimen deforms vertically and excess pore pressure develops at the base of the specimen. Data acquisition is used to record deformation and pore pressure as a function of applied stress. The permeability and coefficient of compressibility, c_v , are directly computed from the applied strain rate and excess pore pressure at a given applied load.

The hydraulic conductivity is computed using Wissa's linear theory adjusted for large strains (Wissa et al 1971):

$$K_v = \frac{\dot{\epsilon} H_0 H \gamma_w}{2 \Delta u_b} \quad \text{A2-7}$$

Where K_v is the vertical hydraulic conductivity, $\dot{\epsilon}$ is the strain rate as a function of time t equal to $\frac{\Delta \epsilon}{\Delta t}$, H_0 is the initial height of the specimen, H is the height of the specimen at time t , γ_w is the unit weight of water, and Δu_b is the measured excess pore pressure at the base of the specimen.

2 Measurement Automation

The MIT Geotechnical Laboratory employs many devices to run laboratory tests, most of which are automated. This section describes the elements common to many devices including measurement instrumentation devices, data acquisition and computer control programs.

2.1 Measurement Instrumentation

Geotechnical measurements require precise measurement of the time rate of deformation, force and volume change. These measurements are possible using non automated methods, including stop watches for time, burettes for volumes, dial gauges for deformation, and proving rings for force measurements. However, automation simplifies the measurement process, extends measurement capabilities and allows for a higher frequency of measurements with a reduced labour load. Transducers are used to measure physical quantities that change during a test.

At MIT a central data acquisition system (described in section 2.2) is used to record transducer readings all over the lab based on tasks that are set by the user. The transducers commonly employed in the laboratory can be subdivided into four categories: load cells, axial displacement transducers, pressure transducers, and volume change transducers. All transducers used in the MIT geotechnical laboratory require a common input voltage of 5.5 volts of Direct Current (DC) and output a DC current. Each transducer is calibrated to obtain a calibration factor, and has a characteristic resolution and stability.

Numerous transducers have been utilized for this research; Table A2-1 summarizes the four categories of transducers used to make measurements for this research and specifies the range, resolution and stability for each transducer.

The following sections briefly describe the calibration method and each of the four categories of transducer used in this research.

2.1.1 Load Cells

Load cells are used to measure the applied load during medium-high stress resedimentation and during CRS measurement. The measured load is converted to stress based on a known constant specimen area. The load cells use a shear beam geometry to concentrate strains in an instrumented section. Strains are measured with strain gauges whose output voltage can be related to the applied load using the calibration relationship.

The load cell used in the high stress CRS is a Toledo Transducers Inc. model SS1009-10K load cell with a capacity of 10,000 lb (44.5 kN). The load cell used for Medium-High Stress Resedimentation is a MTS Systems Corporation 661.21 series force transducer with a capacity of 22 000 lb (100 kN).

2.1.2 Axial Displacement Transducers

Axial displacement transducers measure deformation during CRS measurement and sometimes for resedimentation. In the geotechnical laboratory, axial deformation is measured using Linear Variable Differential Transformers (LVDT) manufactured by Trans-Tek Inc. LVDT's with a liner range of 2.5 cm were used for this research and are most commonly used in the laboratory. An LVDT is comprised of three coils including one primary coil in the center and two secondary coils on either side. A current in the primary coil creates a magnetic field which induces a voltage in each of the secondary coils. This voltage is proportional to the mutual inductance with the primary coil. As a ferrous core moves through the center of the coils, the mutual inductance is altered, changing the voltage response. A slight movement of the core produces a nearly linear change in the differential voltage output between the two secondary coils. This differential voltage can be related to the displacement using the calibration factor.

2.1.3 Pressure Transducers

Pressure transducers are used for hydraulic conductivity measurement, CRS measurement, and high stress resedimentation. Pressure transducers are used to accurately measure applied cell pressures and specimen pore pressures at different locations. The high stress resedimentation setup uses a pressure transducer to monitor the applied load instead of a load cell. The pressure transducer measures the pressure in a hydraulic cell which is directly proportional to the applied load.

All pressure transducers used for this research are type AB/HP or AB pressure transducers manufactured by Data Instruments. They measure the gauge pressure by means of deflection of a steel diaphragm instrumented with strain gauges. The pressure transducers are sealed (type PSIS). The Flexible Wall Permeameter uses one 2000 psi (14000 kPa) pressure transducer to measure the cell pressure and two 100 psi (700 kPa) pressure transducers to measure the top and base pore pressures. The CRS device uses two 200 psi (1400 kPa) pressure transducers to measure the cell and pore pressure. The high stress resedimentation setup uses one 2000 psi (14000 kPa) pressure transducer to monitor the load frame hydraulic pressure.

2.1.4 Volume Change Transducers

Volume change transducers are used in the Flexible Wall Permeameter to accurately measure the volume going into or out of the specimen at different locations. Volume change is computed by measuring the displacement of a piston in a Pressure Volume Actuator (PVA) by means of a string pot. The area of the piston is known and remains constant; therefore the volume change is a function of displacement only. String pots are similar to LVDT's in that they measure displacements; however they use a spring loaded spool and a sensor that detects rotation which can be linked to the cable's linear extension or velocity using a time measurement. Unlike an LVDT,

which can be enabled to work using gravity alone, a string pot requires tension to be maintained on the end of the string. The string pot is favoured over the LVDT because it has a much larger range (30 cm vs. 2.5 cm), has a very high output, has a very linear output with little system backlash and has little to no A/C noise associated with the readings (Grennan, 2010). The string pots are manufactured by Celesco and are type SP1. They have a range of 30 cm but are installed on PVA's with a maximum piston stroke length of approximately 17 cm giving a volume range of 48 cm³ with a piston diameter of 3/4 inch (1.905 cm).

2.2 Data Acquisition System

A centralized computer based data acquisition system is used in the MIT Geotechnical laboratory to provide a single location for collection and storage of all transducer measurements; Grennan (2010) describes this system. The computerized system is flexible allowing users to specify customized and sometimes complicated transducer recording schedules based on experimental needs; multiple schedules can be run simultaneously. A centralized data acquisition system is a cost effective and efficient means of recording digital data in large laboratories and is heavily relied upon at MIT.

Figure A2-6 is a schematic drawing of the central data acquisition system (Germaine and Germaine, 2009). The components of the system can be sub divided into 4 categories:

- 1) The laboratory testing device, such as the CRS device, which includes the transducers, power supply, junction box, voltmeter and ground;
- 2) A switching mechanism which allows the data acquisition mechanism to connect to a particular transducer to make a measurement;
- 3) An Analogue to Digital (A/D) converter that converts the voltage output from each transducer and the power supply to a digital word which can be read by a computer; this device is critical to the precision of the final measurement; and
- 4) A computer which controls the process and components and performs all administrative and computational tasks associated with collecting and archiving the measurements associated with all programmed tasks.

The MIT Geotechnical data acquisition system uses a PC equipped with an Intel 486 microprocessor and driven by Microsoft's Windows XP operating system. This computer is interfaced with an expanded channel Hewlett Packard HP3497A data acquisition unit equipped with a very low noise 5.5 digit integrating analog-to-digital converter with auto-ranging amplification capabilities to four voltage scales (0.1, 1, 10 and 100V). The system is currently configured to simultaneously monitor 180 channels distributed throughout the laboratory while providing analog to digital conversion and data storage capabilities at speeds of up to 1 Hertz.

2.2.1 Computer Control System

Many standard testing devices in the MIT Geotechnical Laboratory, including the Flexible Wall Permeameter, CRS and high stress resedimentation used in this study, are automated and computer controlled. Grennan (2010) summarizes the automation history of the MIT Geotechnical laboratory. Modification of existing manual system components was initiated in the early 1990's. Sheahan (1991) first developed an automated stress path triaxial cell; this was followed by automation of the high pressure triaxial cell (Anderson, 1991), the direct simple shear device (Ortega, 1992), and a special Caisson Element test cell (Cauble, 1996).

Sheahan and Germaine developed a series of BASIC control programs beginning in the early 1990's. Continued automation as well as development of the automation system(s) has been ongoing to improve flexibility and quality control as well as to bring automation to new devices. The advantages of automation include a significant reduction in labour requirements with respect to making the actual measurements, as well as a reduction in the potential for incorporating human error into the test progression. Further, computer control increases the flexibility of the test sequence.

Automation is controlled by drive systems using closed loop feedback control. This is employed using the following steps:

- 1) The transducers make measurements of the actual stress-strain state of the specimen;
- 2) The voltage output of the transducer is sent to the computer via an A/D converter and converted to engineering units using a calibration factor and zero value;
- 3) The software compares the engineering units with a prescheduled time history of the specimen state that is set by the user upon initiation of the test or test stage;
- 4) A control algorithm makes a calculation based on step 3 to decide what action needs to be taken by the motors to maintain the prescribed stress-strain state schedule;
- 5) The signal is sent to the motors which then carry out the computed action.

Figure A2-7 (Grennan, 2010) presents the basic hardware components required to undertake this process. An A/D converter converts the analog voltage output of the transducers to a digital word readable by the computer. Multi-channel AD 1170 converters, manufactured by Analog Devices, are used in the MIT Geotechnical Laboratory as they provide high precision with a minimum 18 bit resolution. A computer processes the signals converted by the A/D converter, and computes a new command signal to be sent to the testing device according to the programmed and calibrated algorithm. Either direct proportional control or proportional-integral-derivative (PID) control algorithms are used. The new command signal is sent out through a digital to analog (D/A) converter located in the computer and is converted into a voltage signal readable by the control motors. Strawberry Tree Inc. D/A converters with 12 bit resolution and ± 5 volt range are used. A Max 100 motor controller is used to turn the DC servo motor at a rate that is proportional to the command voltage. A variety of different motors are used in the MIT Geotechnical Laboratory. Electro Craft model E352 and E372 motors were used in this research.

A control program written in QBASIC is used for automated control of laboratory measurement equipment. The program allows the user to set up the system for testing as well as to control the different components of a test. The program consists of two separate modular programs which call each other. The first module is a setup program where the user enters the test specific data including transducer calibration factors, transducer zero values, transducer channel numbers relating to the computer control, and other test specific parameters. This program then calls the second program, the control module, and stores the user specified information in memory for use by the control module. The program was originally developed for triaxial testing, but with continuous updating and expansion of automation through the laboratory, many different versions programs have been developed allowing for task-specific applications. General functions are organized into component modules, including initial pressure up, back pressure saturation, consolidation, shear and hold stress.

For this work, the triaxial control program has been modified for use with the Flexible Wall Permeameter device. This new program is called the hydraulic conductivity control program. Modifications include the addition of a third volume measurement and control system, and the ability to control a second pore pressure. Shear modes were removed as no piston is used in this test method. The output display was also significantly modified to display meaningful data pertaining to a hydraulic conductivity test.

This hydraulic conductivity control program is also used to partially control CRS measurement and high stress resedimentation. For these applications, only one axis of control is used and only the hold stress routine is used to maintain a specified stress state in the system.

Appendix 8 lists the code for the hydraulic conductivity control program for reference.

Despite local computer control, the central data acquisition system is used to record all data for all tests conducted in the laboratory.

3 Flexible Wall Permeability Measurement

The flexible wall permeameter is used to measure the permeability of low permeability materials such as fine grained mudrocks. A cell pressure and pore pressure are applied to the specimen to produce a hydrostatic effective stress state. The flexible wall permeameter gains its name because the specimen is encased in a flexible rubber membrane providing a flexible boundary condition and allows deformation all three dimensions. The constant head method is used to measure the permeability. A differential pore pressure is applied across a specimen and inflow and outflow volumes are monitored as a function of time. Section 5 describes the calculations required to compute the void ratio, porosity, hydraulic conductivity, and permeability of specimens measured using the flexible wall permeameter.

3.1 Permeameter Equipment

The permeameter consists of a modified triaxial cell with a fixed piston that is plumbed to allow control of one cell pressure and two pore pressures. The specimen is encased in a double rubber membrane with O ring seals and sits between a base platen and a top cap with a porous stone and filter screen on each end. The specimen is placed in a pressurized cell fluid that simulates a hydrostatic stress field and holds the membrane onto the specimen. The pore pressure at the top and bottom of the specimen may be independently controlled, or can be hydraulically connected as in a conventional triaxial apparatus to allow double specimen drainage, for example during back pressure and consolidation stages of a test. Independent control of two pore pressures allows for the application of a differential pressure and a constant head gradient, initiating flow for a constant head hydraulic conductivity test.

There exist many versions of the triaxial cell in the Geotechnical Laboratory; variations include maximum cell capacity and slight design improvements are continuously made as new cells are built. Two standard triaxial cells were employed for this research: a low pressure cell and a high pressure cell. The low pressure cell has a clear acrylic cell wall and a maximum allowable cell pressure of 200 psi (1.4 MPa). This cell was used to measure the permeability of specimens up to 0.8 MPa effective stress, assuming a back pressure of 0.4 MPa and leaving a slight safety margin. The high pressure cell has a steel cell wall and a maximum allowable cell pressure of 2000 psi (14 MPa). The high pressure cell is used to measure the permeability of specimens up to 10 MPa effective stress under back pressures up to 1 MPa, leaving a slight safety margin.

Figure A2-8 gives a solid view of low pressure triaxial cell modified for permeability measurement including the plumbed manifold. Figure A2-9 gives a dimensioned section view of the low pressure cell. The high pressure cell has similar design.

For this research, specially designed 5 cm square end cap adapters are used to convert the standard circular end platens to square platens required to measure a 5 cm cubic specimen. The cubic specimen is shown along with the cubic end adapters in Figure A2-8 and Figure A2-9. The cubic end adapters are further modified with electrodes to allow measurement of the specimen resistivity and are described in Appendix 3 with drawings given in Appendix 6. Section 3.2 gives the measurement set up and sequence procedure with the additional steps required for resistivity measurement included where appropriate.

The cell and pore pressures are adjusted using computer controlled pressure volume actuators (PVA's). A PVA is a fluid filled reservoir with a piston (hydraulic jack) whose movement changes the reservoir volume. In a closed system an increase in the reservoir volume results in a decrease in system pressure and vice versa. Computer control drives the piston dependent on the control algorithm. Figure A2-10 is a photograph of two pressure volume actuators with fluid reservoirs on top to allow for refilling. The PVA is plumbed to the triaxial cell via copper tubing with Swagelok connections and valves. Volume change is computed by measuring the inflow or outflow volume of

the PVA's using string pots. In this set up it is not possible to determine the deformation or strain along a particular axis of the specimen; only the volumetric deformation may be measured.

3.2 Procedure

The following procedure is applied to measure the directional permeability of a cubic specimen using cubic end adapters. Additional steps required for the simultaneous measurement of the specimen resistivity are included in this procedure. These additional steps are followed by "(resistivity only)" and are applicable only if using the cubic resistivity end adapters (described in Chapter 5). A sample data sheet is provided in Appendix 7.

1. Prepare the apparatus:
 - Clean and grease the base platen and the cubic end adapters using general purpose vacuum grease (i.e. Dow Corning High vacuum grease). Be careful not to over grease and plug the bottom drainage hole with grease.
 - Snap the square end base adapter onto the base platen.
 - Ensure that all fluid reservoirs are full and all pore pressure lines are full and de-aired.
 - Verify all electrical connections through the 9 pin connectors in the base of the cell (resistivity only).
 - Make sure the apparatus is generally clean and prepare the workspace.
2. Trim a specimen:
 - Obtain a resedimented specimen.
 - Quickly remove the load from the specimen and remove the specimen, in the sedimentation column, from the loading device (Figure A2-11).
 - Remove excess water from the specimen
 - Extrude the specimen using the manual hydraulic jack (Figure A2-12).
 - Measure the final height of the specimen and record on the resedimentation data sheet.
 - Trim the specimen and label the directional axes:
 - a. Using a miter box, trim the specimen into a 5 cm cube (Figure A2-13). Squaring blocks and a clamp are used to hold and square the specimen during trimming. Trim low stress (< 1.5 MPa maximum applied stress) specimens using a wire saw. Trim medium stress specimens (between 1.5 and ~ 3 MPa maximum effective stress) using a razor blade as a knife, slowly slicing and not sawing. Trim high stress specimens (> ~ 3 MPa maximum applied stress) using a coarse toothed bow saw blade, sawing quickly and using the miter box as a guide. The rough cut face is then levelled and squared using a 11" razor blade in a shaving action.
 - b. Trim the ends of the specimen first, and mark the ends with a 'V' for the vertical axis. Next trim the sides of the specimen, and mark the 'H1' and 'H2' axis. Surface markers

(e.g. tin foil) can be used; however it is easiest and most useful to *lightly* etch the direction ('V', 'H1' or 'H2') into the surface. This method maintains the directional marker throughout the test process and does not affect the measurement. Be very careful not to lose knowledge of direction during the trimming process!

- c. If performing a resistivity measurement (using the cubic resistivity end caps), carefully hand drill two holes for the pin probes using a # 62 drill. Check the hole depth using the top cubic resistivity end adapter and ensure the hole is not drilled deeper than the probe is long.

- Measure the dimensions and mass of the specimen and record on the specimen data sheet. Make 4 measurements of the length of each axis of the cube (Figure A2-14).

3. Set the specimen up:

- Determine the axis of permeability measurement V, H1 or H2. Orient the specimen such that the axis of measurement is vertical.
- Arrange a porous stone and filter screen on each end of the specimen along this axis with the filter screen next to the specimen. Place the cubic top cap on top of the specimen assembly. The specimen should look as shown in Figure A2-15. Starting from the bottom, there should be: a porous stone, a filter screen, the specimen, another filter screen, another porous stone, and finally the cubic top cap.
- Place the specimen assembly on the square face of the bottom cubic adapter.
- Expand a 2.5 inch (6.35 cm) diameter, 9 inch long, 0.025" thick rubber membrane (#S-54125 from Durham Geo Slope Indicator) onto a membrane stretcher and place over the specimen.
- Stretch four greased #228 1/8 inch O rings onto an O ring stretcher and apply two each to the O ring surfaces of the base and top caps, leaving a space equal to the width of one O ring between them. Given the specimen size, you may need to apply the O rings on the O ring spacer one at a time.
- Expand another rubber membrane using the membrane stretcher and coat the inside with a light coating of silicone oil to prevent the membranes from fusing due to the cell pressure. Apply over the specimen. Manually remove any trapped air between the membranes.
- Apply two more O rings, one each on the top and bottom caps, filling in the gap left between the two existing O rings. This doubly sealed O ring method has been used at MIT for many years and is found to create an excellent seal.
- Neatly fold over the excess membrane at the base and top of the specimen. This prevents a mess when disassembling the setup.
- Connect the top cap drainage line to the apparatus drainage line extending from the base. Figure A2-16 shows the specimen set up at this point.

- Connect the top and base end adapter electrical wires to those in the base of the cell. Position sections of clear plastic tubing over conductive connections to prevent short circuiting (resistivity only).
4. De-air the pore pressure lines and check for large leaks:
- Remove the base pore pressure transducer
 - Disconnect the pore pressure lines from the PVA's by closing off the required valves.
 - Isolate the specimen by closing all drainage valves on the manifold.
 - Apply a vacuum to the manifold pore pressure lines through a specially made water trap cylinder, shown in Figure A2-17. The cylinder is partially filled with water and plugged with a rubber stopper through which one or more pieces of tubing passes, connecting to the pore pressure lines of the apparatus through the pressure transducer housings. One end of these tubing sections is submerged in water of the appropriate salt concentration (equal to that of the permeant). As the vacuum is applied, air is removed from the pore pressure lines and can be seen as bubbles exiting through the water from the tubing sections. This provides a good means of performing an initial leak check of the pore pressure system prior to complete set up.
 - Monitor the vacuum in the manifold pore pressure lines for a few minutes to ensure there are no leaks in the vacuum set up. A leak is characterized by a continuous stream of bubbles through the water that does not stop or whose rate does not rapidly decrease with time.
 - If no leaks exist, open the manifold valves to hydraulically connect the specimen drainage lines (top and bottom) to the vacuum. Again, wait a few minutes and monitor the system for leaks. A leak is again characterized by a continuous stream of bubbles through the water that does not stop or whose rate does not rapidly decrease with time. Keep the PVA's hydraulically disconnected from the vacuum system at all times.
 - If a leak is found, identify the location of the leak by systematically isolating parts of the connected system. Often large leaks are identified at this step and will require complete disassembly of the specimen and restarting from step 3. Do not proceed until any leaks are located and corrected.
5. Assemble the apparatus:
- Maintain the vacuum on the specimen to prevent swelling from free access to water. To prevent drying, close off the specimen drainage vales, to maintain the vacuum existing in the specimen but disconnect it from the active vacuum pump.
 - Ensure the cell wall O ring is lubricated with vacuum grease and in place.
 - Position the cell wall over the specimen.
 - Tightly bolt the cell wall to the cell base.

- Fill the cell with silicone oil: Open the cell fill valve and cell pressure release valve. Connect and pressurize the fill tank. Monitor filling to minimize spillage of silicone oil. Once full, close the cell fill and pressure release valves. Depressurize the fill tank by opening to the atmosphere.
- Record zero values (voltmeter and computer readings) for all transducers except the pore pressure transducer. Set up the computer program with the normalized computer zero values.

6. Pressure-up the specimen:

- Re-initiate active vacuum on the specimen by reopening the specimen drainage lines to the vacuum pump. Wait for 20 seconds or so after doing this to let any built up air escape and perform another leak check as described above.
- Using manual control, pressurize the cell to the OCR 4 effective stress at the end of resedimentation, or specimen effective stress prior to extrusion. Monitor pressurization using the pressure up routine of the computer program.
- Initiate computer control to maintain the cell pressure for pressure up.
- Release the vacuum and close the pore pressure valves to isolate the specimen (create an undrained case) once the desired cell pressure is reached. This causes saturation of the pore pressure lines and porous stones when water is drawn into the tubing connected to the pore pressure transducer housings.
- Unhook the vacuum. Install and zero the back pressure transducer.
- Adjust the valves so that the base pore pressure transducer reads only the specimen pore pressure and is disconnected from the PVA. Visually monitor the change in specimen pressure using the computer control on-screen report. Excessive, rapid increases in specimen pressure may be indicative of a cell pressure leak. If a leak is suspected, repeat the process for step #6 to verify before disassembling the apparatus to find the leak.
- If not leak is suspected, start a new task on the data acquisition system to monitor all channels at 4 minute intervals.
- Allow the system to pressure up until the pore pressure has stabilized (about 8 hours). Note the sampling effective stress.

7. Backpressure the specimen:

- Set the back pressure routine to 50 kPa increments from 0 to 300 kPa back pressure, and 100 kPa increments beyond this, maintaining the sampling effective stress. Do not start the routine yet.
- Start a new task on the data acquisition system to monitor all channels at 4 minute intervals.
- Close off the base and top pressure PVA free surface reservoirs and adjust the valves to hydraulically connect the PVA's to the base and the top of the specimen, and each other. Turn on computer control for the back pressure and the cell pressure (already on).
- Initiate computer control.

- Record the volume change as a function of back pressure.
- Perform incremental B value measurements to monitor saturation as desired (see next step).

8. Confirm saturation – measure the ‘B’ value:

- The B value is equal to the change in pore pressure of an undrained specimen divided by the change in cell pressure.
- Turn off computer control of the back pressure. Adjust the valves to close off the top and base specimen drainage lines (disconnect from the PVA’s). Monitor the specimen pressure using the base pore pressure transducer.
- Start a new task on the data acquisition system to monitor all channels at 20 second intervals for 10 minutes.
- Apply a cell pressure increment of 100 to 200 kPa depending on the specimen effective stress. Do so either manually or using the hold stress routine.
- Monitor the specimen pressure at 20 second intervals for 10 minutes.
- Reduce the cell pressure to the original value.
- Open the pore pressure lines and set the control program to hold the stress equal to the effective stress (cell pressure and pore pressure) prior to B value measurement.
- Continue with back pressure saturation or recompression as desired.

Unsaturated specimens will have a characteristic specimen pressure vs. time curve that increases, peaks, and then decreases. The pressure vs. time curve for saturated specimens will increase, peak and level off or continue to very slowly increase. Back pressure the specimen until saturation is achieved (B value > ~ 0.98), the B value does not increase with increasing backpressure, or the maximum back pressure (1 MPa) is reached. Due to high pore pressure system compressibility and low stiffness associated with the cubic end adapters, maximum B values in the range of 0.75 to 0.98 have been accepted. These values are in agreement with saturated B values predicted by Casey (2014) based on the increasing stiffness of the soil matrix.

9. Recompression to end of resedimentation effective stress state:

- Start a new task on the data acquisition system to monitor all channels at “C” increment (increasing time step).
- Ensure top and bottom drainage lines are open and hydraulically connected.
- Set the cell pressure and back pressure to computer control.
- Increase the cell pressure and maintain the back pressure using the hold stress routine.
- Maintain this step for at least 12 hours or until the rate of secondary compression can be determined from the data file.

10. Constant head gradients:

- Hydraulically isolate the back pressure and top pressure PVA's. Maintain drainage to the specimen. The top of the specimen is now connected to the top pressure PVA, and the bottom to the back pressure PVA.
- Start a new task on the data acquisition system to monitor all channels at 4 minute increments.
- Use the hold stress routine to set the top, cell and back pressures such that the top pressure is decreased by $\Delta u/2$, the cell pressure is maintained, the base pore pressure is increased $\Delta u/2$, where Δu is the desired differential pore pressure.
- Set the top, cell and back pressure to computer control.
- Maintain the gradient for 12 to 24 hours as required until flow equilibrium is reached between the inflow and outflow increments and an accurate measurement of the specimen hydraulic conductivity is made.
- Repeat for at least 3 different gradients (values of Δu). Make sure to neither consistently increase nor decrease the applied gradient.
- Measure additional gradients as required if significant variability in the measured hydraulic conductivity is noted.
- Perform a leak test by setting the computer to control the base pore pressure equal to the top pore pressure. Maintain hydraulic isolation of the two pore pressures during this process, allowing the computer to independently establish control over each axis. A leak will be evident because the computer will be unable to maintain pressure control over either the top or bottom pore pressure without constant, small volume change.

The differential pore pressure ranged from 4.2 to 137 kPa (corresponding to hydraulic gradients ranging from 8.5 to 281) for this research. Specimens compressed to a high effective stresses were measured using high gradients, and specimens compressed to low effective stresses were measured using low gradients.

11. Resistivity measurement (only if using the cubic resistivity end adapters):

- Connect the resistivity measurement box to the power supply and allow a 10 – 20 minute warm up period. Appendix 3 provides a detailed procedure for connecting & powering the box.
- Connect the 4 electrode wires extending from the base of the cell to the resistivity measurement box.
- Appendix 3 provides a detailed procedure for measuring the resistivity.
- Measure the resistivity of the specimen using multiple combinations of the reference and drop resistor. Ensure that all amplified voltage measurements are in the range of 1.2 to 8.5 volts.
- Disconnect the resistivity measurement box.

12. Disassemble the apparatus

- Turn off computer control.
- Close off the drainage lines.
- Connect the vacuum assembly as in step 4 to apply a vacuum to the top and bottom of the specimen.
- Once vacuum is applied, quickly reduce the cell pressure using manual control of the motors.
- Drain the cell using 35 – 70 kPa (5 – 10 psi) of air pressure connected through the top pressure release valve.
- Close off the pore pressure valves to maintain a vacuum on the specimen, and turn off the vacuum device.
- Unbolt and remove the cell wall.
- Suction any excess silicone oil from the base of the cell using a squirt bottle.
- Disconnect the top drainage line. Adjust the valves to connect the base of the specimen to the back pressure PVA open to the atmosphere, breaking the vacuum seal.
- Remove the specimen from the apparatus.
- Carefully wipe the excess silicone oil from the specimen using Scott 1000 brand toilet paper.
- Remove the O rings. Stretch the ends of the membranes over the membrane stretcher and apply a vacuum to expand and remove them.

13. Measure the specimen dimensions at 4 points along each axis using digital calipers. Mass the specimen.

14. Repeat steps 3 – 11 for each directional measurement. Measure the permeability in either vertical order (V, H1, H2) or horizontal order (H1, V, V2). This procedure repeats the second permeability measurement.

15. If measuring the resistivity, seal the pin probe holes prior to re-measurement of the specimen. Holes will form in the membrane due to the cell pressure over unsealed holes. Obtain a small, thin O ring and cut into pieces the length of the pin probes. Seal the holes by enlarging the hole until the piece of cut O ring fits in the hole. In this case, use only the final wet mass, instead of the average of the wet mass following each directional set up, to compute the specimen porosity. Each time the specimen is re-set up, requiring the drilling of new holes and the plugging of existing holes, some mass is lost. This mass loss is roughly 0.2 – 0.3 grams per set up. This error, which increases with each subsequent set up, will lead to a porosity error if the wet mass used to compute the porosity does not correspond to the same dry mass as the final specimen. To avoid this error, only the final wet mass, immediately prior to oven drying is used to compute specimen porosity. Because the porosity is calculated using a mass based approach, and not a volume based approach, the small mass losses through the testing sequence will not affect the

computed porosity if the final wet mass is combined with the final dry mass to compute the porosity.

16. Final specimen processing:

- Place the specimen in a Ziploc bag, and this bag in another Ziploc bag with a wet paper towel. Allow to equalize overnight.
- Remove the specimen from the bag and re-mass the specimen.
- Clearly etch directional markers ('V', 'H1', 'H2') on each face.
- Cut the specimen in half. Etch the directional markers in to the cut faces.
- Record the wet mass of one half of the specimen and oven dry for 2-3 days. Record the dry mass and compute the whole specimen dry mass and water content using mass ratios. Store the dry specimen in a labelled Ziploc bag for future use.
- Further cut the remaining half into two pieces, one small (1/3 size) and one large (2/3 size) piece. Etch directional markers into the cut faces.
- Perform a salinity measurement on the large piece.
- Retain the small size piece in the moist state for image analysis. Place in a double Ziploc bag with a moist paper towel between the two bags. Properly label the bags with the specimen ID, test ID and other relevant properties. Store in a cooler.

3.2.1 File Name protocol

A standardized protocol is used to name the data acquisition files. Each filename is constructed using the following three part formula:

Filename = Test ID + Direction + Stage

A2-8

The Test ID is the HC test number that is derived from the lab signup sheet. The direction refers to the direction of the test, and is indicated by both a letter (H or V) and a number (1, 2, 3...). The number n indicates that the particular test is the nth measurement in that particular direction. Finally, the stage refers to the stage of the test; these roughly follow the sample data sheet (Appendix 7). Examples of stage number are given as follows:

- Pressure up = S3
- Backpressure = S4
- Recompression = S5
- B value Test = BV1 (1st test), BV2 (2nd test), etc.
- Hydraulic Gradient = G1, G2, G3 etc.
- Leak Test = Leak

Therefore, a data acquisition file titled HC025V2G3 signifies that the file contains data for the third hydraulic gradient of a specimen that 1) is being measured under HC test # 025 (HC025), 2) is

oriented such that the permeability in the vertical direction is being measured; 3) has previously been measured (or measurement has been previously attempted) once in the vertical direction (V2).

3.2.2 Leaks

Permeability measurement in clays is very sensitive to small changes in specimen volume and leaks. It is important to reduce leakage as much as possible and to measure even very small leaks where they exist so as to correct the permeability measurement.

Tavenas et al (1983) found that a minimum of 25 kPa of cell pressure was required to prevent flow along the specimen boundary between the specimen and the membrane; cell pressures many times this minimum are applied in this work. Silicone oil, a viscous fluid, is used to apply cell pressure to the system. Silicone oil is selected for many reasons, most notably because it aids in preventing leaks. It was originally introduced into the MIT lab for use with frozen soils and has been used in many different applications since. Oil does not penetrate the rubber membranes used to seal the specimens in the cell, and it is immiscible with water-based permeant, therefore the use of oil as a cell fluid prevents the initiation of flow through the intact membrane. This setup does not prevent large leaks such as tears in the membrane or inadequate seals in the internal pore pressure plumbing where volumes of cell fluid are introduced into the pore fluid system. Thus far, system leakage has been minor.

Leakage can be gauged using multiple methods. Large leaks are identified by a rapid, large pressure increases during pressure up or by an unsteady time rate of volume change during back pressure. A compression curve that shows increasing specimen volume or does not achieve characteristic secondary compression is indicative of a moderate to slow leak. Leaks may be further identified by testing for pressure dissipation in the pore pressure system under fixed volume and constant cell pressure.

Small leaks in the pore pressure system are very difficult if not impossible to find. All permeability measurements should include a leak measurement stage. Small leaks are identified by setting the top and bottom pore pressure equal to the same calibrated value but controlling the pressure separately. This creates a hydraulic connection through the specimen. Small leaks appear as a linear volume change with time, usually only at one end of the specimen (e.g. Figure A2-21). Where a small leak exists, provided the leak rate is significantly less than the permeability of the soil (<10%), the leak rate is measured, the approximate location is determined (into or out of the specimen), and the measured flow volumes are adjusted prior to permeability calculation. In the case of Figure A2-21, a leak is noted at the top of the specimen. The measured leak rate is $0.04 \text{ cm}^3/20 \text{ hr} = 0.002 \text{ cm}^3/\text{hr}$. This means that to maintain pressure in the specimen, the computer must control the PVA's to remove in $0.002 \text{ cm}^3/\text{hr}$ of fluid. The outflow volume measured during the hydraulic gradient is adjusted to subtract this leakage volume.

3.2.3 Temperature Control

The flexible wall permeameter is installed in a closed temperature controlled enclosure controlled to $\pm 0.1^{\circ}\text{C}$. A temperature control box containing a light bulb and fan heats the enclosure. Temperature is monitored by a mercury sensor switch. When the temperature rises above a certain point, causing the conductive mercury to expand, the circuit is closed and power is cut to the light bulb.

It is very important to maintain temperature control especially during the hydraulic gradient portions of the permeability measurement. Slight changes in temperature cause volumetric changes in the specimen and permeant. Figure A2-18 and Figure A2-19 illustrate the effect of a loss of temperature control on a specimen of RSFBM in terms of both flow volume vs. time and flow rate vs. time.

4 Data Analysis Methods – Permeability

This section describes the full process required to analyze the permeability measurements. First the porosity is calculated. Next the hydraulic conductivity is computed using the measured flow rate and gradient. This value is adjusted for measured leaks and measurement sequence bias. Next, the permeability is computed. Finally, the permeability anisotropy is computed once the permeability is determined in both the horizontal and vertical directions.

4.1 Porosity / Void Ratio Determination

The void ratio and porosity of the specimen is computed using a mass based approach assuming 100% saturation and using the measured specific gravity of grains. This approach is taken because the trimmed cubic specimen is not a perfect cube; slight errors in the volume measurement of the cube lead to large errors in the porosity. Unlike other measurements undertaken in the Geotechnical laboratory, such as the triaxial test on clays, the initial specimen volume is not easily or accurately measured.

A quick sensitivity analysis reveals the errors associated with volume based porosity measurements. Assume a perfect 5 cm cube with volume 125 cm^3 . If the porosity is 0.4 (average for the specimens investigated in this work), the volume of solids would be 75 cm^3 . If a measurement error of $+0.5\text{ mm}$ is made in any one dimension, the measured cubic volume (and hence the volume of voids) would increase by 1.25 cm^3 and the porosity would increase by 0.006 to 0.406. . If this error occurred in two dimensions, the volume error would increase to 2.51 cm^3 , and the porosity would be computed as 0.412. Finally, if a $+0.5\text{ mm}$ measurement error were made in all three dimensions the volume error would be 3.79 cm^3 , and the porosity would be 0.418, or 0.018 higher than the true porosity. Using a mass based approach, the volume of voids is back calculated knowing the total specimen mass, the dry specimen mass, and assuming complete saturation. Chapter 5 shows that the porosity variation measured using the mass based method for all specimens measured for this

research was < 0.01 , indicating that the mass based approach is significantly more accurate than the volume based approach.

The wet mass and dimensions of the specimen are recorded at the beginning and end of each directional permeability measurement. The dry specimen mass is obtained following completion of all permeability measurements, after oven drying. A portion of the specimen is dried in an oven set to 110 degrees Celsius for a minimum of 24 hours. The dry mass of the entire specimen (M_s) is computed by multiplying the dry mass of the portion of the specimen ($M_{s,portion}$) by the ratio of the wet mass of the entire specimen before cutting ($M_{wet,specimen}$) divided by the wet mass of the portion of the specimen that was dried ($M_{wet,portion}$):

$$M_s = M_{s,portion} * \frac{M_{wet,specimen}}{M_{wet,portion}} \quad A2-9$$

The porosity is the computed using a mass-based approach assuming complete saturation and correcting for the presence of salt in the pore fluid:

$$n = \frac{V_v}{V_T} = \frac{V_w + V_{salt}}{V_T} = \frac{\frac{M_w + M_{salt}}{\rho_s}}{\frac{M_s}{G_s \rho_w} + \frac{M_w + M_{salt}}{\rho_s}} \quad A2-10$$

where n is the porosity, V_v , V_w , V_{salt} are the volumes of the voids, the water, and the salt, respectively, V_T is the total specimen volume, M_w , M_{salt} , M_s are the masses of the water, the salt and the solid grains, respectively, G_s is the specific gravity of the grains, ρ_w is the density of distilled water, and ρ_s is the density of pore fluid at the measured salt concentration.

All mass measurements, except for the initial specimen mass following trimming, are taken after the specimen is removed from the permeameter. During disassembly of the apparatus, the cell pressure is released, inducing negative pore pressures in the specimen. To counteract this, a vacuum is applied to the specimen to prevent suction of free water found in the pore pressure lines. This procedure limits specimen volume change between permeability measurement and massing. The mass is recorded immediately upon removal from the device to prevent drying. Using this approach, errors in porosity measurement related to swelling or drying of the specimen are not likely.

Negligible porosity change (<0.01) is measured throughout the up to month-long duration of each specimen permeability anisotropy measurement as a result of minimal specimen mass change. There is no systematic trend in porosity with measurement direction or set up number, indicating that changes in porosity are due to experimental error. An average porosity is computed for each specimen using the three mass-based porosities corresponding to the end of each directional permeability measurement.

Void ratio (e) is computed using the relation:

$$e = \frac{V_v}{V_s} = \frac{n}{1 - n} \quad \text{A2-11}$$

Void ratio is typically only used for compression curves for comparison with standard geotechnical literature. Porosity is used for permeability trends.

4.2 Hydraulic Conductivity Calculation

The hydraulic conductivity is computed using D'Arcy's Law (D'Arcy, 1856; equation A2-12):

$$K = \frac{Q}{iA} = \frac{\Delta V_{in} + \Delta V_{out}}{2\Delta t A} \frac{L\rho g}{\Delta P} \quad \text{A2-12}$$

Where K is the hydraulic conductivity, Q is the volumetric flow rate, i the applied gradient, A is the measured area of flow, ΔV_{in} and ΔV_{out} are the increments in inflow and outflow volume, respectively, Δt is the time interval of measurement, ΔP is the applied pore pressure differential across the specimen, L is the measured length of flow, ρ is the mass density of the fluid and g is the gravitational constant. The measured inflow and outflow volumes are corrected for tiny leaks (<5% flow rate) and secondary compression volume change by measuring these values separately as a function of time at the same effective stress.

4.3 Leakage Correction

Leaks occur in any hydraulic system. For accurate permeability measurement it is essential to minimize pore pressure system leakage as much as possible. Where extremely small leaks exist that cannot be found and sealed, it is necessary to measure the leak rate and correct flow measurements for the leak.

Large leaks sometimes occur and require immediate action to locate and fix the leaking element. Such leaks involve large volume change (>5 cm³) over small periods of time (minutes to a few hours) are easily identifiable. In the flexible wall permeameter most large leaks are cell pressure leaks and occur at one of three points: 1) Into the top pressure drainage line due to an improper Swagelok connection; 2) through the membrane due to either a perforated membrane or an improper Oring seal; or 3) through the base end adapter due to an improper seal onto the bottom circular end platen.

Small leaks are identified by unequal inflow and outflow volumes during a hydraulic gradient or an uncharacteristic compression curve when a recompression stage is undertaken.

Two forms of flow correction are applied: Secondary compression flow correction, which is related more to creep volume change than leakage, and a small leakage flow correction.

4.3.1 Secondary Compression (Creep) Volume Correction

Secondary compression flow, or creep, associated volume change, can sometimes explain the small differences between measured inflow and outflow volumes. Correcting for the very small log time rate of volume change can minimize the scatter in the measure permeability and significantly reduce the standard deviation for the case where small leaks are not present. The Hypothesis A model for secondary compression can be applied to correct for creep associated volume change using the measured log time rate of volume change during the recompression stage. Hypothesis A assumes that secondary compression begins only following primary consolidation whereas Hypothesis B assumes that secondary compression occurs simultaneously with primary consolidation. Hypothesis A was selected for simplicity, however the difference associated with either a Hypothesis A or B assumption is negligible in this case because of the specimen size, the fast rate of primary consolidation (under 1 hour) and the long measurement times (multiple days).

Correction for secondary compression volume change is only undertaken for specimens where the sampling effective stress is lower than the OCR 4 stress during resedimentation, i.e. when the recompression stage is undertaken (Step 9 of Section 3.2). During recompression, the time rate of volume change is recorded and a typical compression curve constructed (see example in Figure A2-20). This stage is held long enough until a measure of the rate log linear time rate of secondary compression is obtained. During hydraulic gradients, the measured inflow and outflows are adjusted using secondary volume change because hydraulic gradients are measured using linear time increments. The data acquisition system provides time stamps to each file during the test. These time stamps are tracked allowing calculation of the absolute time at any point during a constant head gradient referenced to the start of the recompression stage (i.e. Hypothesis A secondary compression). Using these data, the log time difference between the start of a constant head gradient any measure data point is used to predict what component of the volume change is associated with secondary compression:

$$\Delta V_s = c_a \log \left(\frac{t}{t_i} \right) \quad \text{A2-13}$$

Where ΔV_s is the volume change associated with secondary compression referenced to the beginning of the constant head gradient, c_a is rate of secondary compression (see Figure A2-20), t is the absolute time of a given measurement referenced to the start of the recompression stage, and t_i is the absolute time of the first measurement of the constant head gradient referenced to the start of the recompression stage.

To apply the secondary volume flow correction, the secondary volume change is set to zero at the beginning of each gradient. The secondary volume change is computed for each data point to account for the log time nature of the correction. Flow is assumed to be equally distributed between the top and the bottom of the specimen, and always flows out of the specimen. Therefore, one half

of the flow is subtracted from the top flow volume measurement (volume out) and one half is added to the bottom flow measurement (volume in).

4.3.2 Small Leak Volume Correction

Small leaks are present in most permeability experiments. The importance of small leaks increases with decreasing permeability. Small leaks are identified by 1) irreconcilable differences in the measured inflow and outflow volumes over time during a constant head gradient, or 2) unusual recompression volume change vs. log time behavior.

The leak rate varies with pore pressure and gradient, however these do not change significantly over the applied constant head gradients. An average leak rate is computed at the mean effective stress following measurement of the permeability via at least three constant head gradients. At this point the secondary compression volume change is so low that it is negligible. Typical leak rates ranged from 0.001 to 0.002 cm³/hr and are tabulated in Appendix 1.

To measure a leak, the base and top pore pressure are set equal via computer control and the time rate of volume change is measured. A leak is typically characterized by a linear time rate of volume change in either the inflow or outflow over 12 to 24 hours. The leak rate is computed and subtracted from either the inflow or the outflow volume, as appropriate, for all constant head gradients. Figure A2-21 gives an example of a typical leak measurement identifying a leak at the top of the specimen. In this case, the leak rate is measured using a linear approximation of the leak rate as shown. This leak is measured as volume coming out of the specimen and can be explained by a very small cell pressure leak that occurs in the top drainage line beyond the specimen itself but affects measured outflow volumes. To correct for the measured leak, the leak volume is computed as a function of time during each hydraulic gradient and is subtracted from all measured outflows to obtain the true, no leakage outflow representative of the volume outflow from the specimen itself. This corrected outflow volume is used to compute the permeability. Similarly, for the case of leakage measured at the base of the specimen, the leak rate is measured as in a flow rate into the specimen and is also subtracted from the measured flow volumes during a constant head gradient:

$$V' = V_{meas} - V_{leak} \quad \text{A2-14}$$

Where V' is the corrected volume inflow or outflow, V_{meas} is the measured volume inflow or outflow, and V_{leak} is the leak rate measured either into the base of the specimen (volume inflow) or out of the top of the specimen (volume outflow). Equation A2-14 applies for both internal and external leaks because the sign of V_{leak} will change depending on whether the leak is into the specimen (external) or out of the specimen (internal).

4.4 Measurement Sequence Bias Correction

The mudrocks measured for this work are resedimented and uniaxially compressed in the laboratory. They should be cross anisotropic with an isotropic horizontal plane and permeability anisotropy developing in the vertical plane only. However, the permeability results indicate a small but consistent difference between successive horizontal permeability measurements (H1 and H2) that is illustrated in a cross plot as a slope of less than 1 (e.g. Figure A2-22 for RBBC).

Repeated permeability measurements in the same direction are lower, regardless of the order of measurement as shown in Figure A2-22 and Figure A2-23. This is likely resultant from handling the specimen between permeability measurements. Slight smearing may occur on the faces which can decrease the measured permeability. The decrease in permeability due to smearing is consistent and predictable, and is termed the 'measurement sequence bias'. The following sections provide two methods, the global specimen method and the single specimen method, to remove this bias from the data set and correct the measured permeability for the effects of repeated measurement on the same specimen.

Only the second and subsequent directional permeability measurements require correction. Measurement sequence bias correction, using either the global correction method, or the single specimen method, requires two permeability measurements in the same direction. The second permeability direction must be measured twice to correct for measurement sequence bias. Therefore, the optimal measurement sequences are V, H1, H2 (Vertical Order) and H, V1, V2 (Horizontal Order).

4.4.1 Global Specimen Method

The global specimen method can be applied to data sets where there are 1) permeability measurements for multiple specimens of the same mudrock and 2) where the permeability measurements are performed with some consistency in order of measurement, allowing the global measurement bias factors to be accurately determined. The global specimen method is a 'global' method because it combines data from all specimens of the same mudrock to define the measurement sequence bias parameters for the material, which are then applied globally to all measurements made using that material.

The measurement sequence bias, x , is defined as the slope of a cross plot of *successive* permeability measurements made in the same plane (Figure A2-22). Measurements from multiple specimens of the same mudrock are required to define this slope for each plane of interest. Dividing the H2 permeability measurement by the slope x forces a 1:1 slope with the H1 measurement (see Figure A2-22).

To estimate the undisturbed permeability, a global correction is applied based on the number of measurements that have been made on the same specimen:

$$k_1 = \frac{k_n}{x^{(n-1)}} \quad \text{A2-15}$$

Where k_1 is the undisturbed permeability, k_n is the measured permeability, x is the measurement sequence bias and n is the measurement number. The undisturbed permeability, k_1 , is the permeability at measurement number one corrected for permeability decreases associated with n permeability measurements.

A cubic specimen undergoes a minimum of three directional permeability measurements to measure the permeability anisotropy. The first permeability measurement does not require correction. The second measurement ($n=2$) must be corrected for a permeability decrease associated with the first measurement. The third measurement ($n=3$) must be corrected for permeability decreases associated with the first two measurements. The exponent ($n-1$) allows superposition of the measurement sequence bias over multiple measurement increments to compute the undisturbed permeability at measurement number one. Equation A2-15 applies for both permeability (k) and hydraulic conductivity (K).

The measurement sequence bias factor x cannot be directly measured from a permeability cross plot when directional permeability measurements are non-successive, e.g. a measurement sequence V, H1, H2, V2. In this case (i.e. for the vertical direction in the example shown, x may be obtained using the slope of a cross plot of non-successive permeability measurements with fixed test number separation Δn , shown by equation A2-16:

$$x = x' \frac{1}{\Delta n} \quad \text{A2-16}$$

Where x is the measurement sequence bias between successive permeability measurements, x' is the measurement sequence bias for non-successive permeability measurements, and Δn is the number of measurements separating the non-successive permeability measurements.

Consider a series of mudrock specimens where the vertical permeability was re-measured at the end of the test, resulting in measurement sequence of V1,H1,H2,V2. The horizontal measurement sequence bias, x_H is equal to the slope of a cross plot of measured H2 permeability vs. the measured H1 permeability because these permeabilities are measured successively ($\Delta n=1$). Conversely, a cross plot of the measured V2 permeability vs. the measured V1 permeability yields a slope x' because V1 and V2 are non-successive ($\Delta n = 3$). Dividing the V2 permeability by x' forces a 1:1 slope with V1, correcting for handling effects over three separate setups. Applying equation A2-15 with $n = 4$ and x' to adjust the V2 permeability would erroneously correct the V2 permeability for decreases associated with $3 * 3 = 9$ setups. To avoid this error, the non-successive bias x' is first converted to the successive measurement sequence bias x using equation A2-16 with $\Delta n = 3$. Then, equation A2-15 is applied to adjust the measured V2 permeability for permeability decreases associated with 3 separate setups only. Therefore, in order to correctly apply equation A2-15 to all possible measurement sequences, it is necessary to use equation A2-16 convert x' to x .

The global correction method should only be applied to data sets consisting of multiple specimens. Further, there should be a minimum of two specimens on which duplicate measurements were made in each direction that requires correction. For example, if all specimens were measured using vertical order (V, H1, H2) then the minimum number of specimens is two. If specimens were measured using a combination of vertical and horizontal order (H, V1, V2), then the minimum number of specimens is four, two each measured using vertical and horizontal order. This requirement results in estimation of the measurement sequence bias, x , in each direction from a minimum of two data points.

4.4.2 Single Specimen Method

An alternative and simpler approach, called the single specimen method, is better suited to correct the permeability measurements for single specimens or for small data sets. This approach plots directional permeability measurements vs. the measurement number, n (as in Figure A2-23). Sequential permeability measurements in the same direction can be connected and the slope extended to determine the corrected permeability at measurement $n=1$. This approach was first proposed for use in measuring the anisotropy of varved clays to adjust the permeability for noted smearing of the varved layers across the layer boundaries (Chan and Kenney, 1973).

The single specimen method can only be used when the second and subsequent directions of measurement are repeated, allowing connection of two points to form a slope (as in Figure A2-23). Thus, specimens measured using Vertical Order (V, H1, H2) or Horizontal order (H1, V1, V2) can be adjusted using the single specimen method. However, specimens measured using a modified version of Horizontal order (H1, H2, V), as was applied for a number of RBBC specimens, cannot be adjusted using the single specimen method. This is because there is only one measurement of the vertical permeability, so a slope cannot be formed to estimate the vertical permeability at test #1 as in Figure A2-23. As a result, the global specimen method was applied to the RBBC and 39% Clay RBBC specimens.

4.5 Permeability Calculation

The hydraulic conductivity is then converted to permeability based on the permeant density and viscosity according to equation A2-1. The fluid density and viscosity are computed based on the temperature and salinity using standard tables and equations presented in Chapter 3.

4.6 Permeability Anisotropy Calculation

The permeability anisotropy is computed as the ratio of the horizontal to vertical permeability. For this measurement technique, multiple measurements of the permeability in the horizontal or vertical direction are obtained. These measurements should be the same once adjusted for measurement sequence bias. Permeability measurements made in the same direction and adjusted

using the single specimen method adjust to the same value. However, permeability measurements adjusted using the global specimen method are subject to greater specimen variability but less systematic variability. As such, measurements in the same direction are averaged in the permeability anisotropy calculation.

$$r_k = \frac{k_{H_{AVG}}}{k_{V_{AVG}}} \quad \text{A2-17}$$

Where r_k is the permeability anisotropy, $k_{H_{AVG}}$ is the average undisturbed permeability and $k_{V_{AVG}}$ is the average undisturbed vertical permeability.

Table A2-1: Transducer data

Measurement	Device	Range	Resolution	Stability	Device / Quantity
Axial Deformation	LVDT	2.5 cm	±0.0015%	±0.0045%	Resedimentation - axial deformation
			(0.1 mV)	(0.3 mV)	
Axial Force	Load Cell	100 kN	0.1 kN	0.2 kN	Medium - High Stress Resedimentation - load
			(0.001 mV)	(0.002 mV)	
Hydraulic Pressure	Pressure Transducer	700 kPa	0.006 kPa	0.024 kPa	Permeameter - pore pressure
			(0.001 mV)	(0.004 mV)	
Hydraulic Pressure	Pressure Transducer	14000 kPa	0.13 kPa	0.26 kPa	Permeameter - cell pressure
			(0.001 mV)	(0.002 mV)	
Volume Change	String pot	48 cm ³	± 0.004%	± 0.004%	Permeameter
			(0.1 mV)	(0.1 mV)	

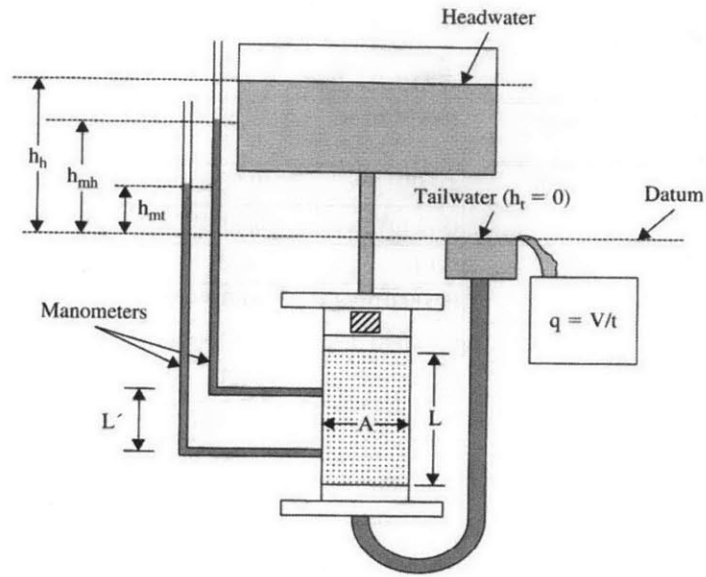


Figure A2-1: Schematic diagram showing a constant head test with downward flow through the system. (Germaine and Germaine, 2009)

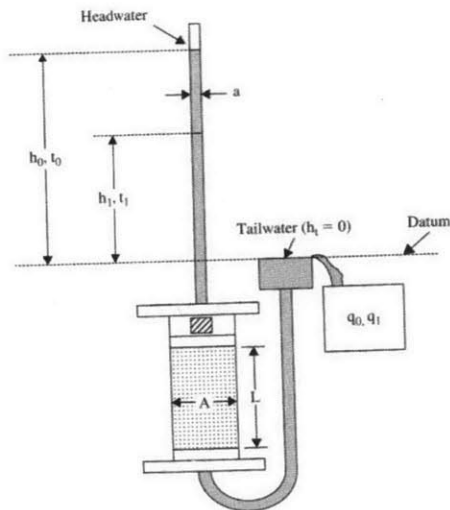
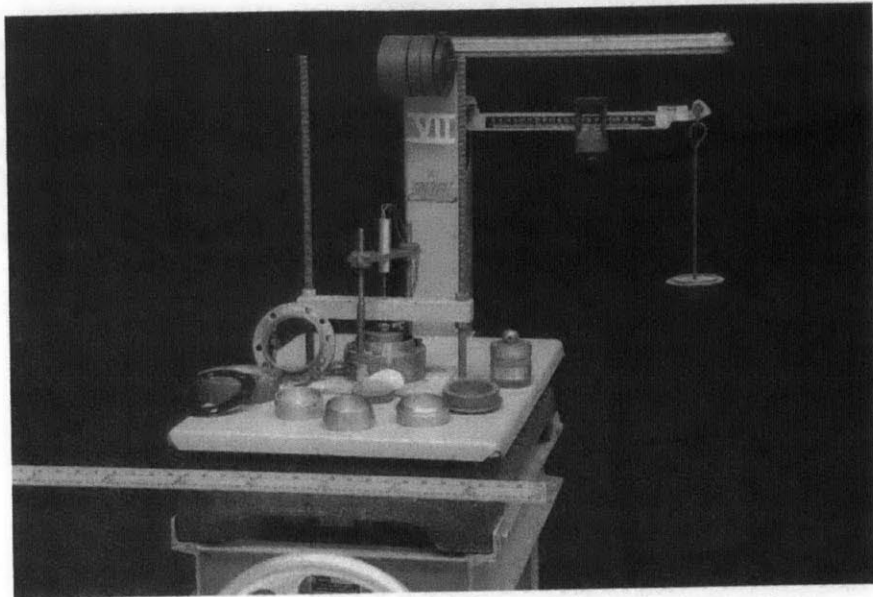
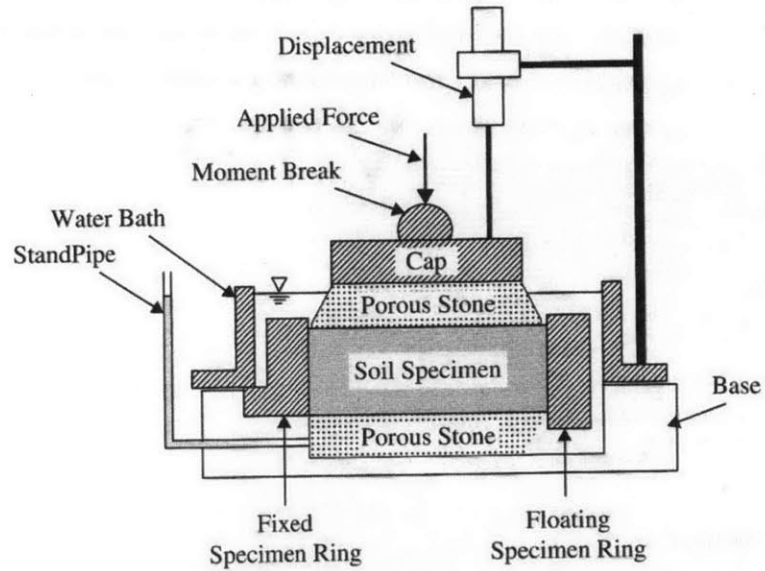


Figure A2-2: Schematic diagram showing a falling head test (Germaine and Germaine, 2009)

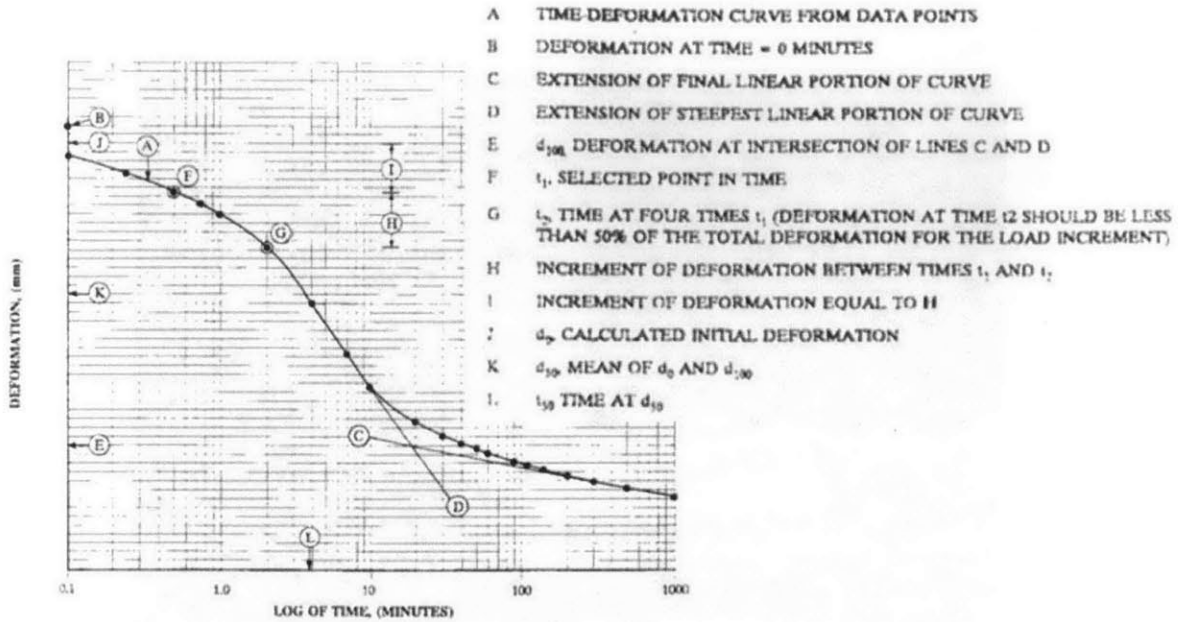


(a) Typical Setup with loading frame and all components

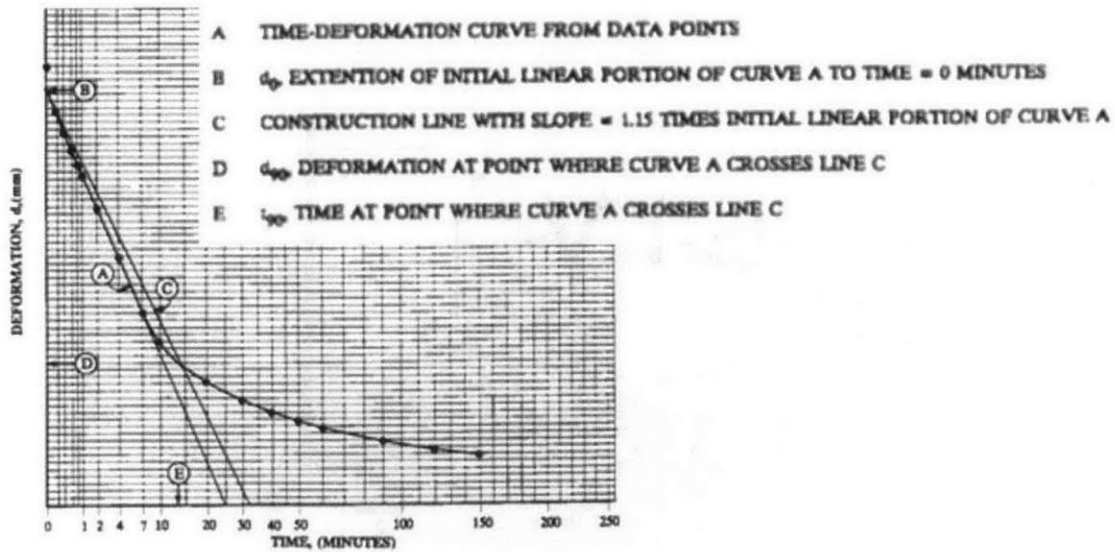


(b) Close up of soil specimen with boundary conditions and applied forces

Figure A2-3: Typical incremental oedometer setup (Germaine and Germaine, 2009)



(a) Log Time Method



(b) Root Time Method

Figure A2-4: Example of Log of time and Square Root of time methods for time-deformation curve analysis in the incremental oedometer method (ASTM D2435)

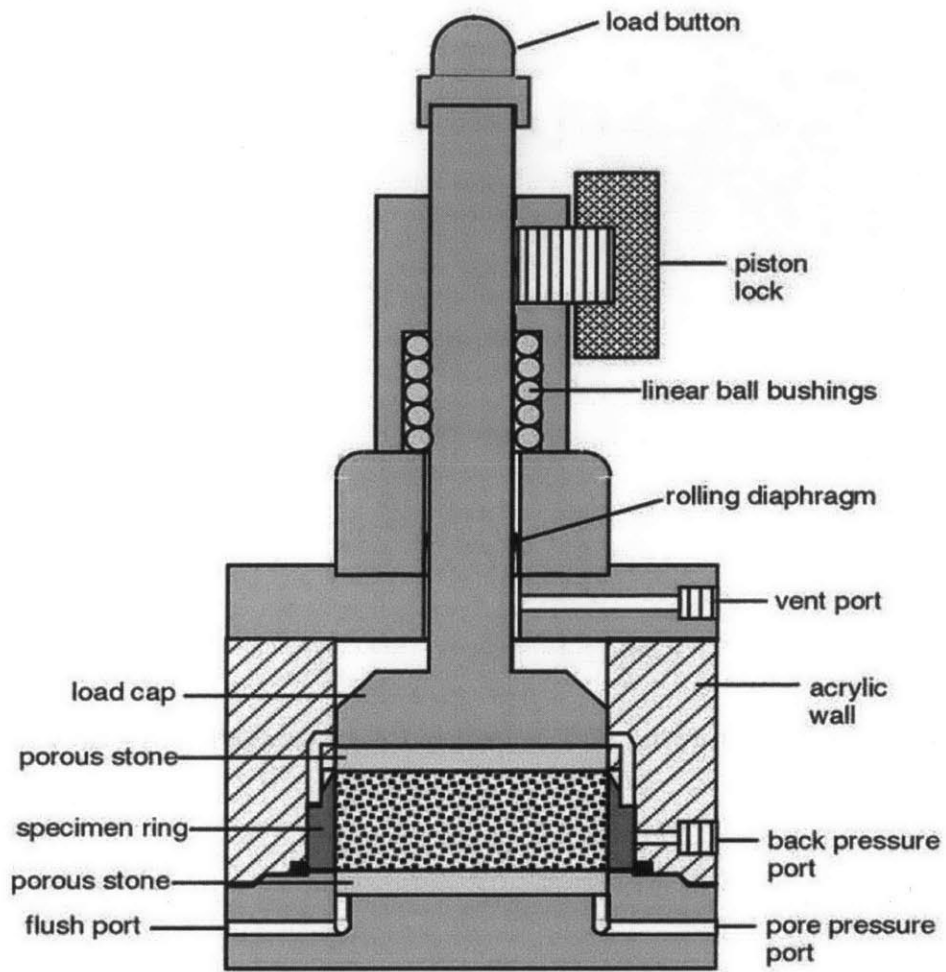


Figure A2-5: Schematic of a standard Trautwein CRS apparatus (ASTM D4186)

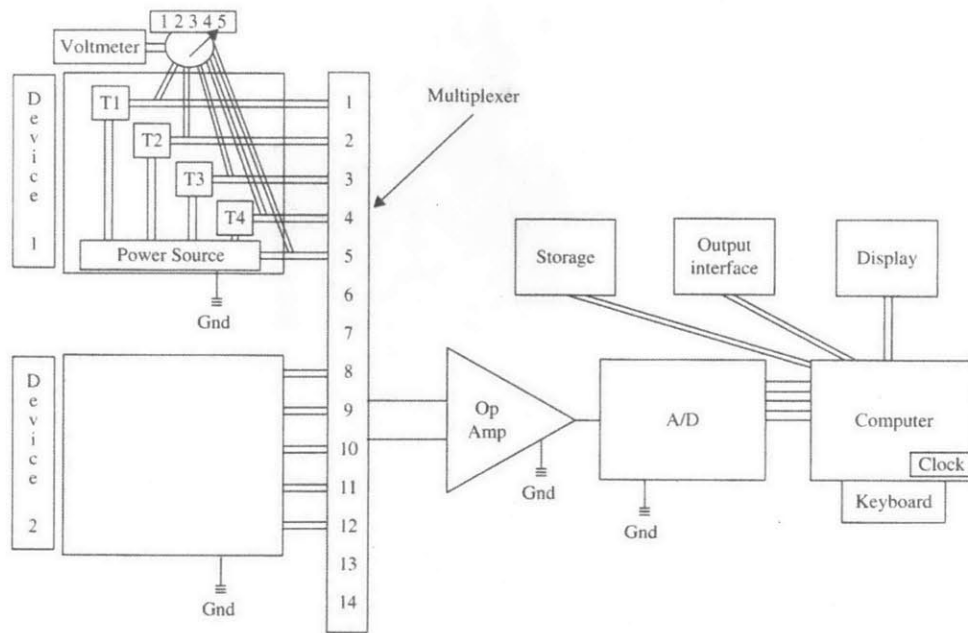


Figure A2-6: Schematic drawing of a centralized data acquisition system (Germaine and Germaine, 2009)

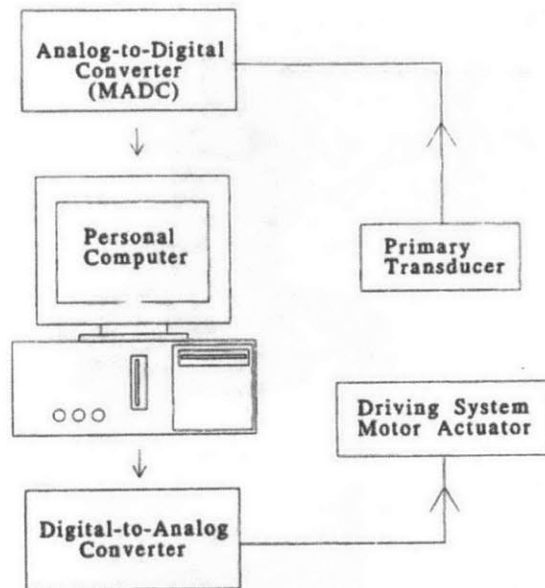
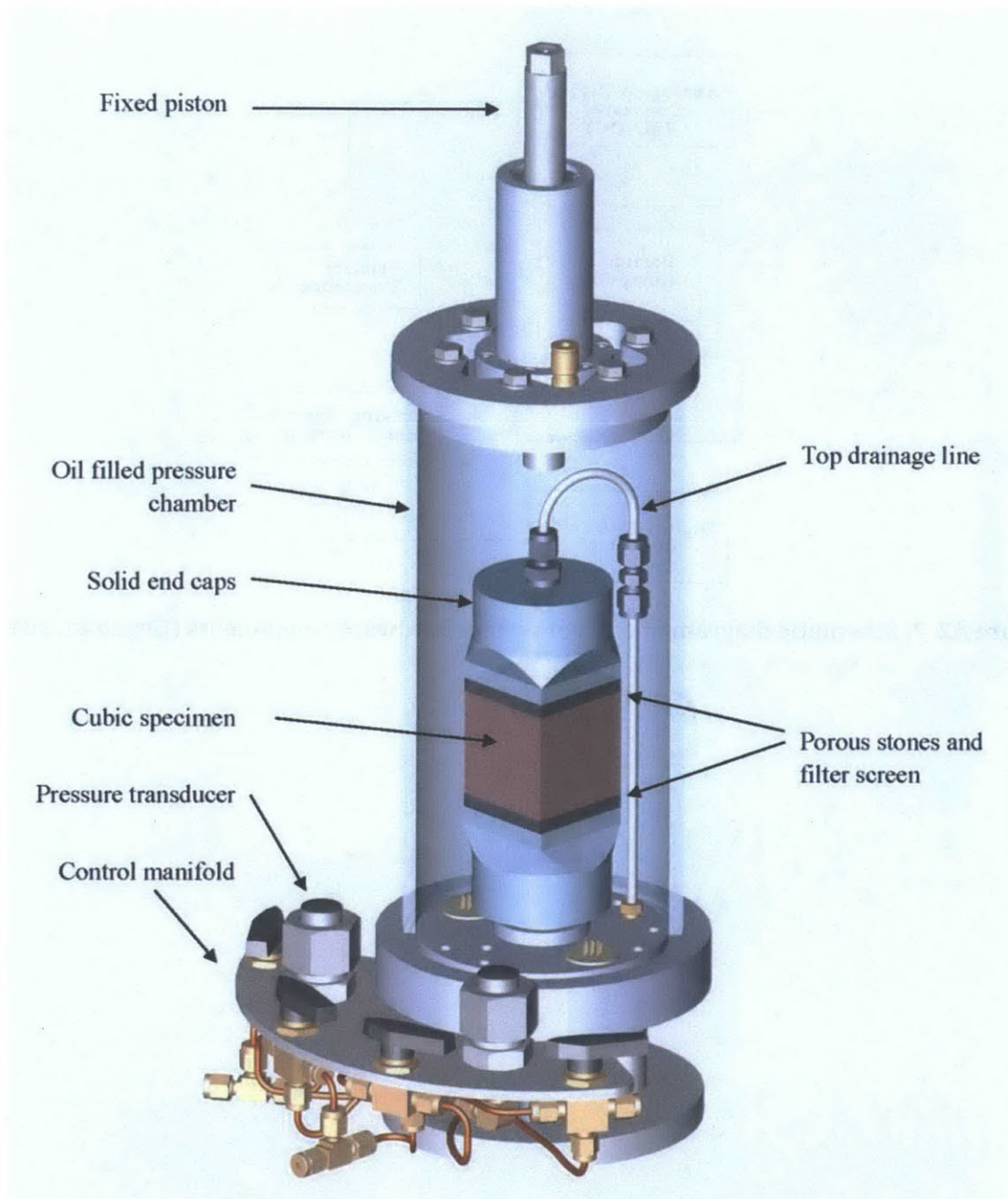


Figure A2-7: Schematic diagram of control system hardware components (Grennan, 2010)



Not shown: Rubber membrane jacket surrounding specimen and end adapters.

Figure A2-8: Solid view of the low stress triaxial cell (modified for permeability measurement) with manifold and cubic shaped specimen

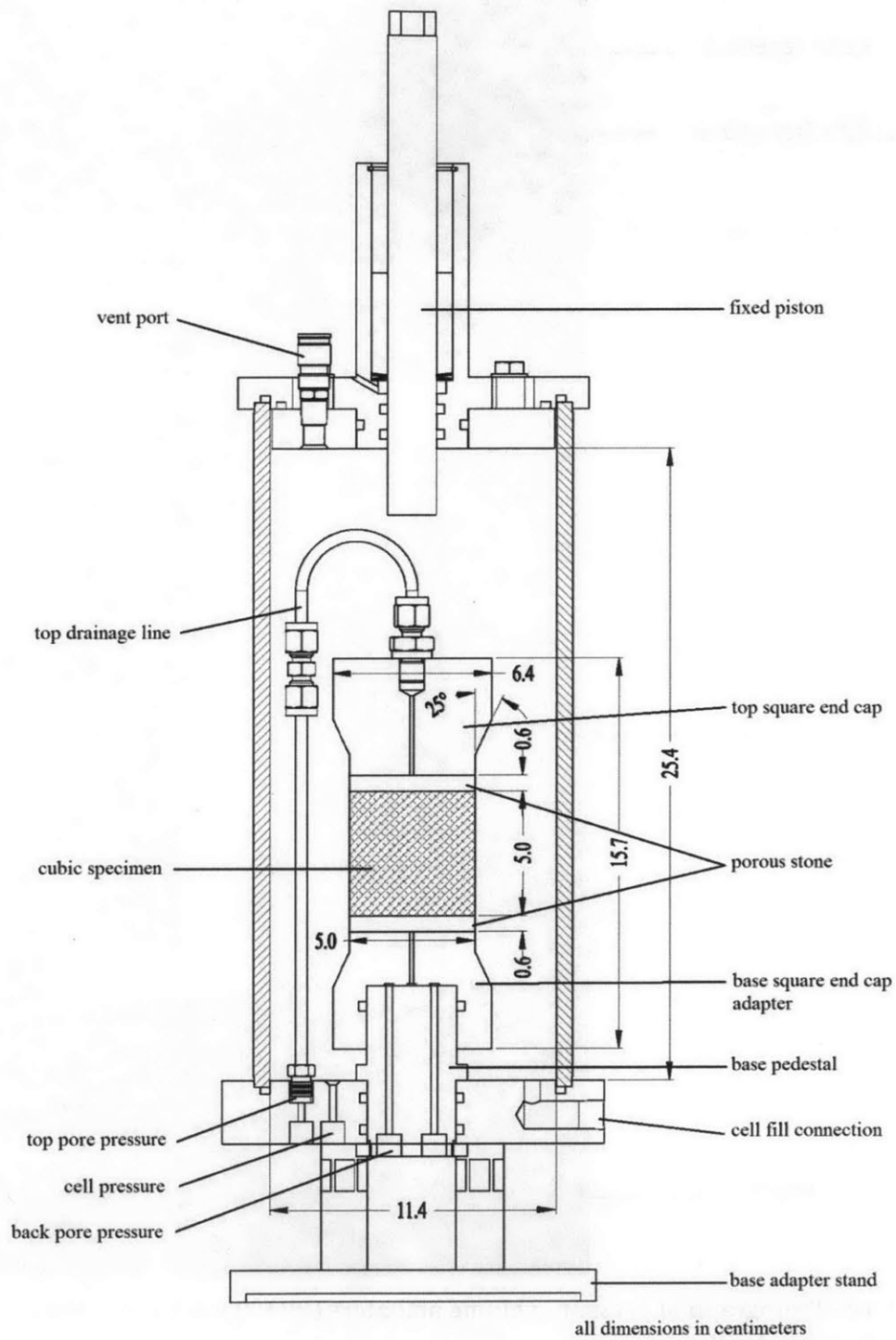


Figure A2-9: Dimensioned section of the low stress triaxial cell (modified for permeability measurement) with cubic specimen

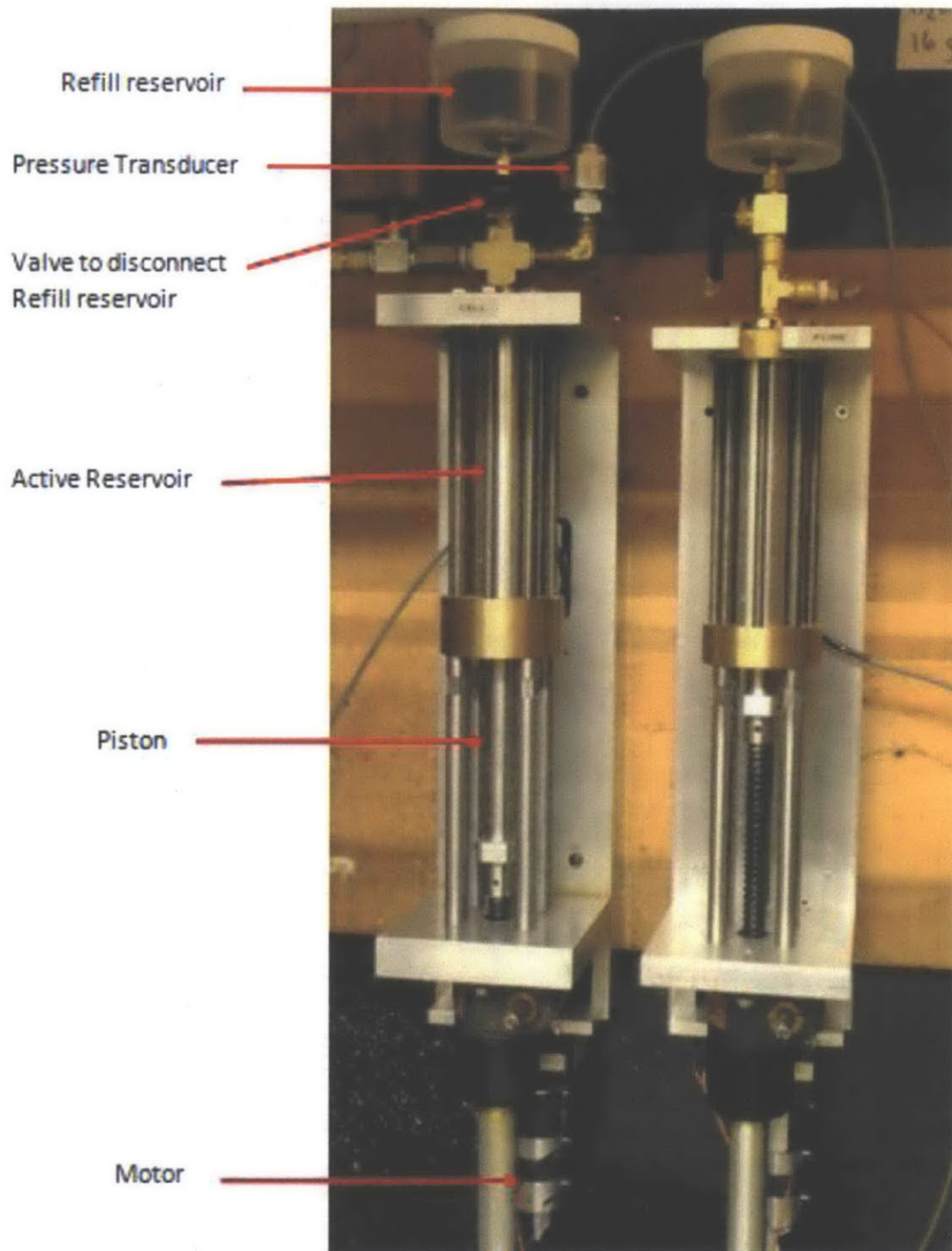


Figure A2-10: Photograph of pressure volume actuators (PVA's) used to control cell and pore pressures in triaxial cells

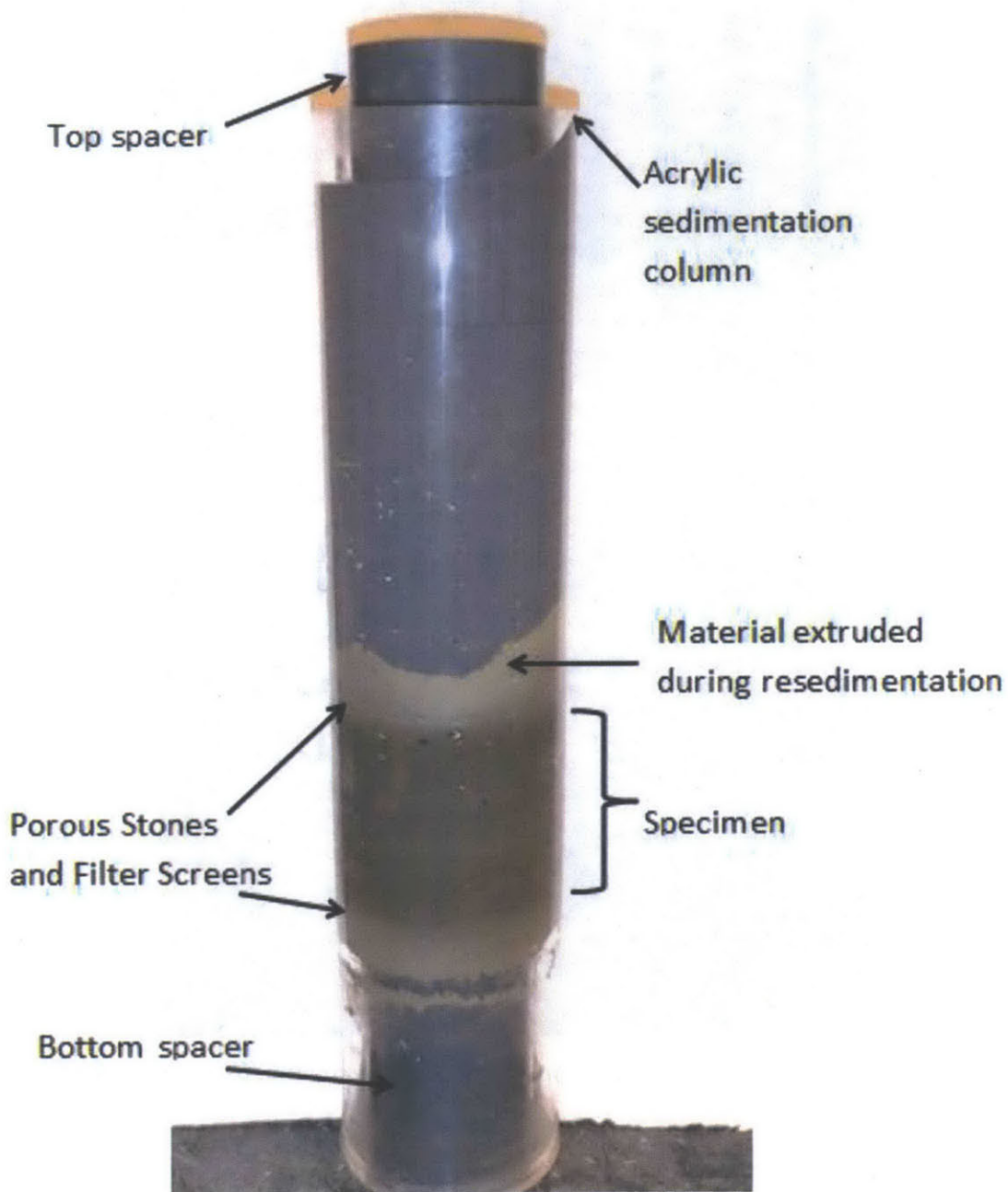


Figure A2-11: Completed resedimented specimen prior to extrusion



Figure A2-12: Extruding a resedimented specimen using the manual hydraulic jack

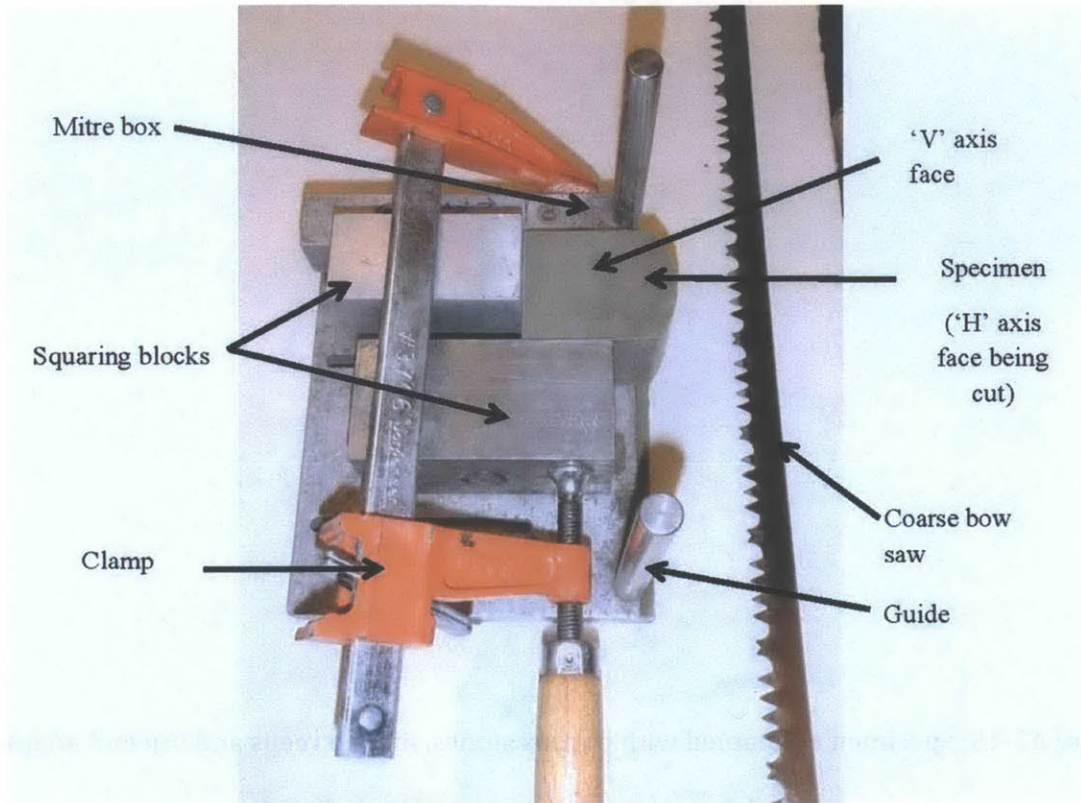


Figure A2-13: Trimming a high stress specimen

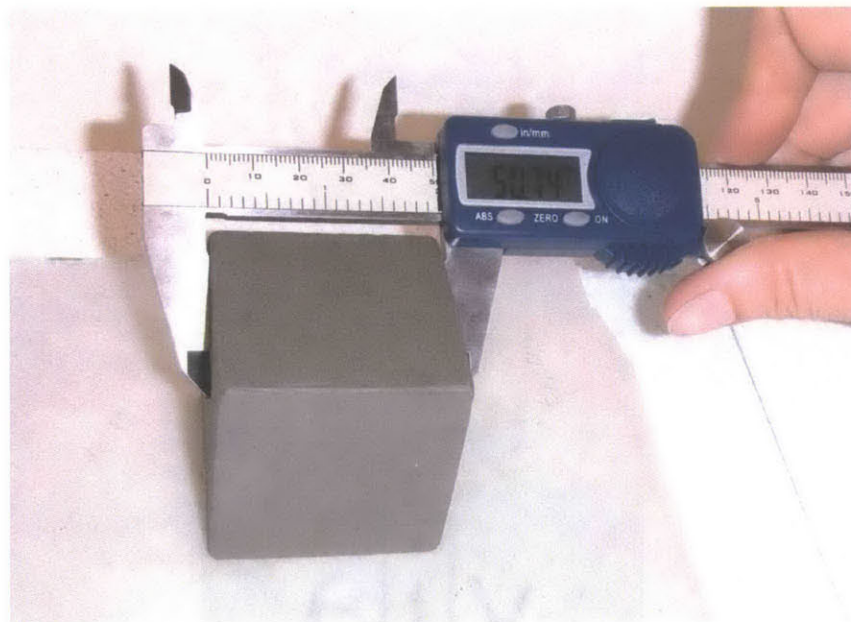


Figure A2-14: Dimensioning the cubic specimen



Figure A2-15: Specimen assembled with porous stones, filter screens and top end adapter



Figure A2-16: Specimen with double rubber membrane and O ring seals

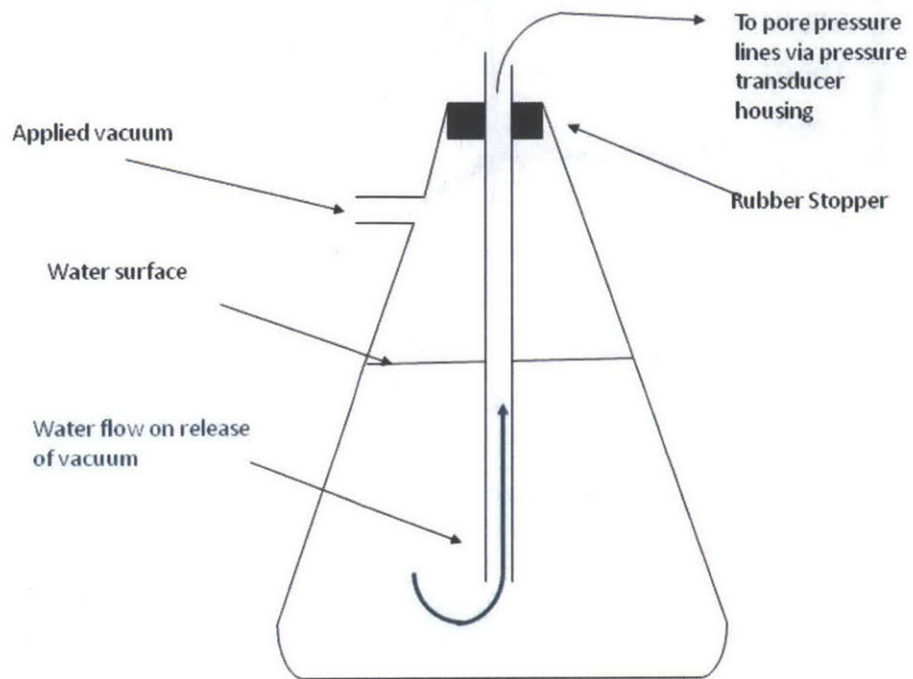


Figure A2-17: Water trap cylinder configuration used for vacuuming during specimen set up

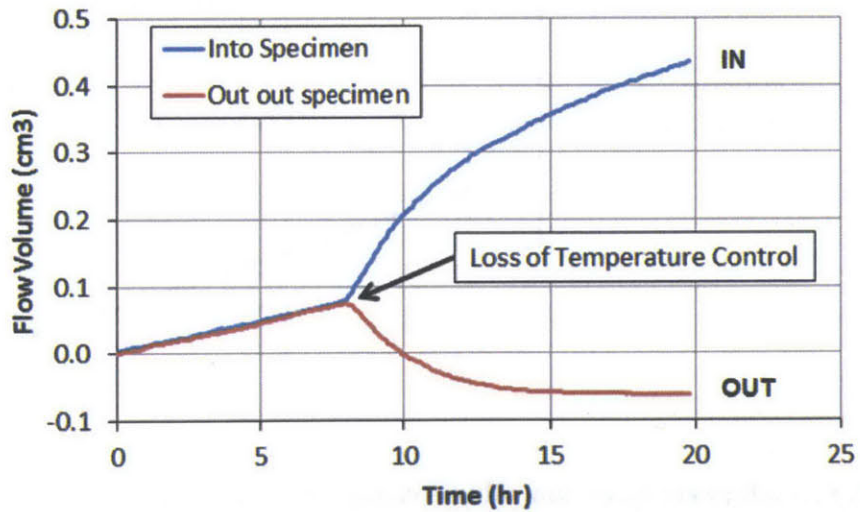


Figure A2-18: Effect of loss of temperature control during a hydraulic gradient: volume vs. time

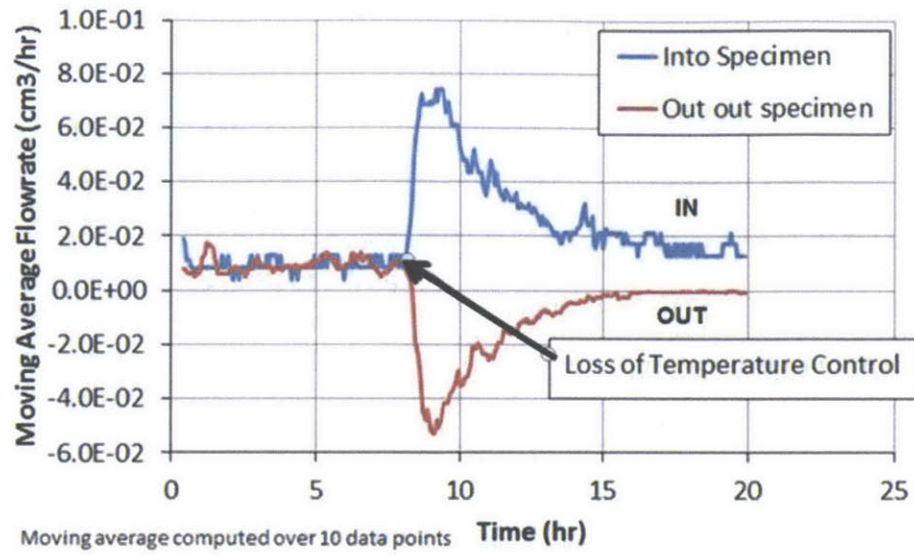


Figure A2-19: Effect of loss of temperature control during a hydraulic gradient: flow rate vs. time

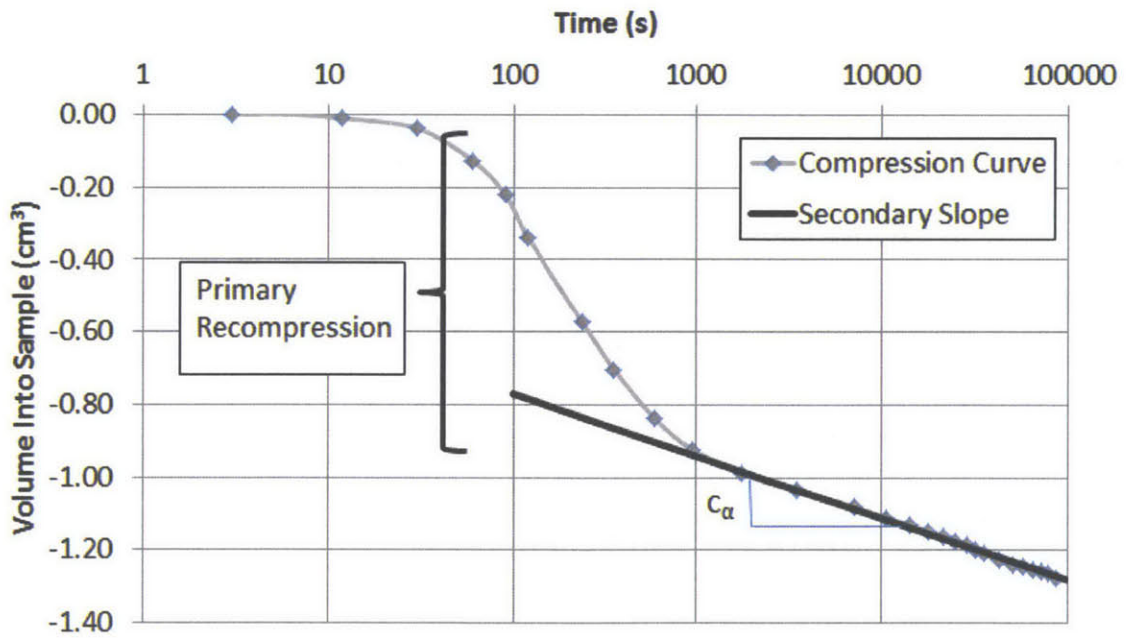


Figure A2-20: Secondary compression volume change determination for test HC019H1

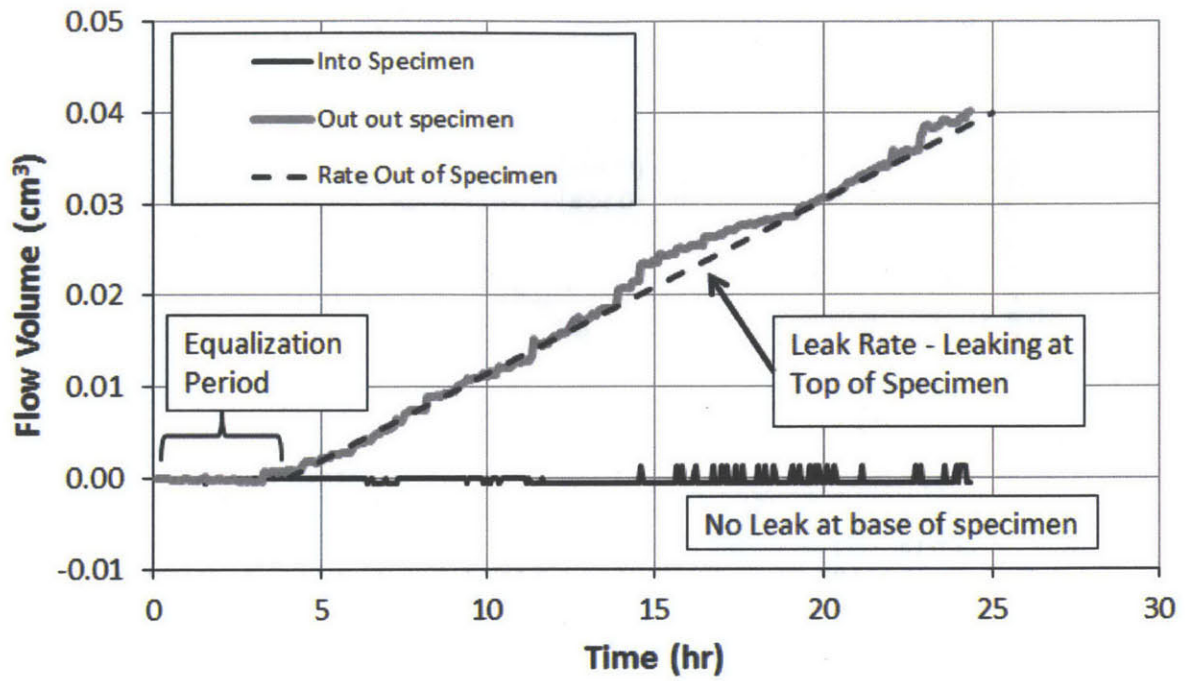


Figure A2-21: Leak rate determination method

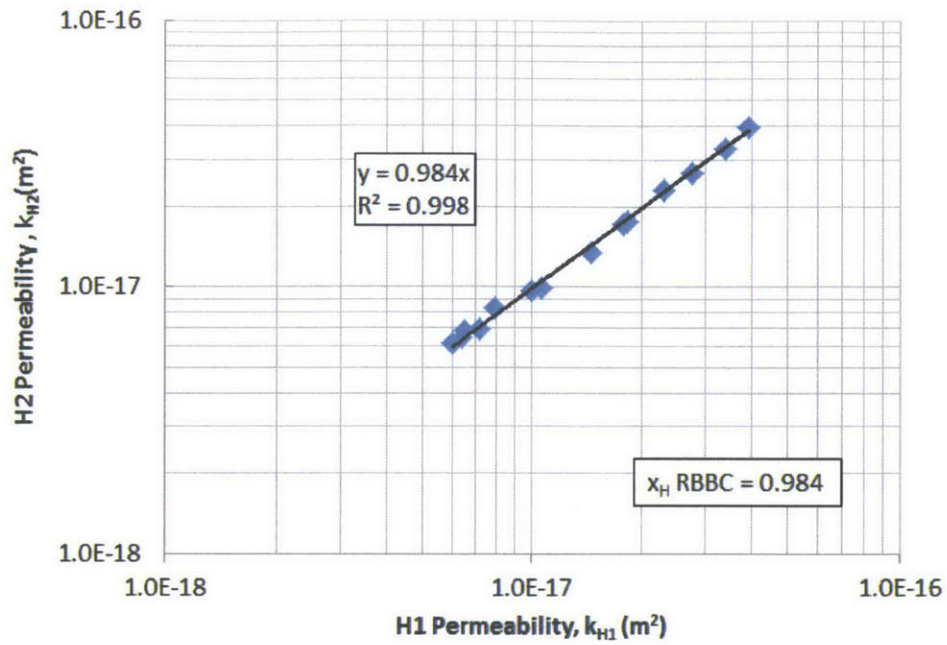


Figure A2-22: Horizontal Measurement Sequence Bias for RBBC

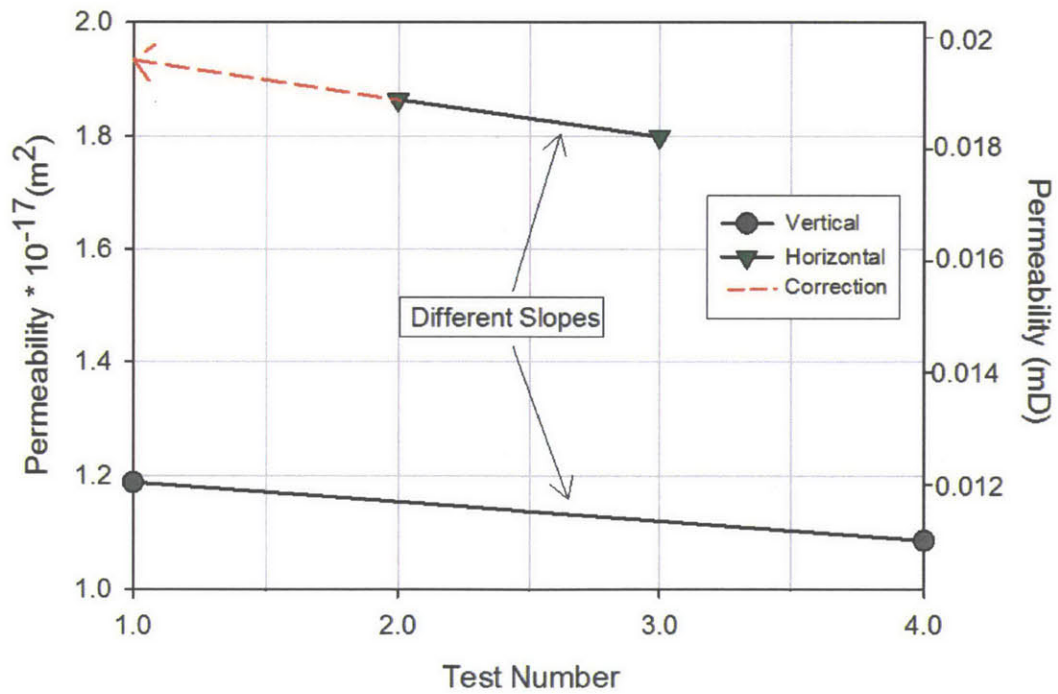


Figure A2-23: Single specimen measurement sequence bias with correction method (after Chan and Kenney, 1973)

Appendix 3: Resistivity and Conductivity Anisotropy Measurement

This appendix serves as a standalone reference manual for the resistivity measurements. It contains a summary of the types of resistivity measurements, a detailed description of the design and components of the resistivity measurement system and the measurement electrodes, and a user manual for making resistivity measurements. Also included is a very useful 'troubleshooting guide' for reference when things go awry. Finally, a data analysis section provides all equations required to compute the resistivity given different electrode configurations.

Contents

Appendix 3:	Resistivity and Conductivity Anisotropy Measurement.....	419
1	Background	421
1.1	Resistivity and Formation Factor	421
1.2	Resistivity Measurement Techniques.....	422
1.3	Frequency	423
2	Resistivity Measurement System.....	424
2.1	PCB Design Summary	425
2.2	Signal Generator Circuit.....	426
2.3	Specimen Circuit.....	428
2.4	Measurement Circuit.....	429
3	Measurement Electrodes.....	431
3.1	Triaxial Configuration	431
3.2	Bench Top Configuration - Unconsolidated specimens.....	434
3.3	Bench top Configuration - Consolidated Specimens.....	434
4	User Manual	437
4.1	Connecting the Box.....	437
4.2	Measuring Resistivity	438
4.3	Troubleshooting and Rules of Thumb	439
5	Data Analysis	439
5.1	Resistivity Calculation.....	439

5.2	Current Effect.....	440
5.3	Frequency effect.....	441

List of Tables

Table A3-1:	Resistivity Measurement System Circuit Components (Page 1 of 2).....	442
Table A3-2:	Wiring Colour Codes for End Cap Adapters.....	444
Table A3-3:	MIT06 Cell Resistance Measurements.....	444

List of Figures

Figure A3-1:	4-Probe resistivity diagram.....	445
Figure A3-2:	Frequency effect for 2-probe resistivity measurements (after Blewett et al, 2001)...	445
Figure A3-3:	Ideal specimen circuit.....	446
Figure A3-4:	Resistivity measurement system user interface.....	446
Figure A3-5:	PCB Artist Schematic resistivity measurement system circuit drawing.....	447
Figure A3-6:	Schematic circuit drawing for resistivity measurement box - signal generator circuit and specimen circuit.....	449
Figure A3-7:	Schematic circuit drawing for resistivity measurement box - measurement circuit..	450
Figure A3-8:	PCB board layout.....	451
Figure A3-9:	Resistivity box wiring diagram	452
Figure A3-10:	Flexible wall permeameter with cubic end adapters	453
Figure A3-11:	Drawing: Cubic end adapters modified for resistivity measurements	454
Figure A3-12:	Construction of cubic resistivity end adapters: plate probe wire connections.....	455
Figure A3-13:	Construction cubic resistivity end adapters: specimen pin probes	455
Figure A3-14:	Specimen Circuit in Flexible Wall Permeameter.....	456
Figure A3-15:	Bench top electrode configuration for unconsolidated materials	456
Figure A3-16:	Consolidated specimen bench top resistivity measurement configuration	457
Figure A3-17:	Close up of specimen configuration for consolidated specimen bench top resistivity measurement	458
Figure A3-18:	Consolidated specimen bench top resistivity electrode equipment.....	459
Figure A3-19:	CRS specimen cracked during 4-probe pin insertion.....	460
Figure A3-20:	Frequency vs. Conductivity Anisotropy for Four Specimens.....	460

1 Background

Electrical measurements in soils can be traced back to the 1930's. Over time, researchers have used electrical measurements to study various soil properties including but not limited to: moisture content, compaction, liquefaction, freezing, microstructure, permeability, salinity, contamination, stress-strain behaviour, porosity, hardening, and chemical diffusion. McCarter et al (2005) provide an excellent summary of different researchers who have used both high- and low-frequency electrical measurements in soil science to study these properties.

In soils, conductance is primarily electrolytic in nature with the flow of ions occurring along the continuous wetted phase for coarse grained soils, and additionally along charged platy particles in fine grained soils. The electric flow path is influenced by soil structure and saturation. Soil structure is in turn controlled by the particle size, shape, orientation, porosity, and electrical properties of the wetting pore fluid and conductive solid grains (McCarter et al, 2005; de Lima and Sharma, 1990)

1.1 Resistivity and Formation Factor

Resistivity is the area and length normalized resistance of a soil or rock. The bulk resistivity sums the effects of all conductance paths including electrolytic and surface conduction, as well as end effects and frequency effects. Bulk resistivity is computed using equation A3-1.

$$\rho = \frac{RA}{L} \quad \text{A3-1}$$

Where ρ is the resistivity, R is the measured resistance, A is the area of voltage application and L is the length of probe separation. The length parameter is the parameter most susceptible to error and must be carefully measured and controlled to obtain a good measurement of the resistivity. For example, consider a specimen with constant area of 10 cm² measured with a probe separation length of 2.0 cm that results in a measured resistance of 40 Ω . This equates to a resistivity of 2.0 Ωm . However, if the measured length is 2.1 cm, corresponding to a measurement error of +1 mm or 5% of the total length, the computed resistivity, 1.9 Ωm , is reduced by 5%.

Electrical conductivity (σ) is the inverse of the electrical resistivity (ρ):

$$\sigma = \frac{1}{\rho} \quad \text{A3-2}$$

Resistivity decreases with increasing pore fluid salinity. As a result, resistivity cannot be used to compare two mudrocks with different pore fluid salinities. Formation factor normalizes the soil resistivity by the pore fluid resistivity and is a measure of the pore geometry:

$$F = \frac{\rho}{\rho_w} \quad \text{A3-3}$$

Where F is the formation factor, ρ is the resistivity of the mudrock and ρ_w is the resistivity of the pore fluid. As described in Section 2, the apparent formation factor is computed using the measured resistivity. For all mudrocks, and even some Archie type rocks (with non-conductive grains), the formation factor itself varies with pore fluid salinity, ion content and sometimes mudrock mineralogy. Various correction factors (discussed in Section 2) are applied to extract the intrinsic formation factor from the measured or apparent formation factor and obtain a true measure of pore geometry.

1.2 Resistivity Measurement Techniques

Bulk soil resistivity is commonly measured using one of three techniques: 2-probe, 4-probe or inductive. The Resistivity Measurement System can perform measurements using both 2- and 4-probe techniques, described herein. Queeney (2003) provides a detailed description of the inductive technique.

The basic principle for both the 2-probe and the 4-probe techniques is the same. A differential voltage is applied through two electrodes. The current used to apply this differential voltage can be either alternative current (AC) or direct current (DC). A specimen is placed between the two electrodes, generating an electric field is generated across the specimen. Ions in the specimen flow from the high voltage electrode to the low voltage electrode. The specimen electrical conductivity is a function of the ions available for flow and the resistance of the flow path.

In the MIT Geotechnical laboratory, we use prismatic specimens with a known geometry to create a uniform electric field through the specimen. Though electrodes are typically made of or coated with platinum, brass electrodes are used here. An Alternating current (AC) is applied to prevent polarization of the electrodes. Polarization occurs when an "ion cloud" builds up at one electrode, preventing the further migration of other ions (Queeney, 2003). Further, the power is not kept on for continuous time periods to prevent electroplating and coating of the electrodes. Electrodes are cleaned and polished between uses to account for potential plating effects during testing.

A series circuit configuration is produced by connecting a reference resistor with known resistance to the specimen. The current is constant through a series circuit. The current is computed by measuring the voltage drop over the known reference resistor and applying Ohm's Law (equation A3-4):

$$i = \frac{V_{ref}}{R_{ref}} \quad \text{A3-4}$$

Where i is the current, V_{ref} is the voltage drop over the reference resistor and R_{ref} is the known resistance. Ohm's Law is again applied (equation A3-5) to compute the resistance across two points in the specimen by measuring the voltage drop using either the 2- or 4- probe techniques.

$$R_{specimen} = \frac{V_{probe}}{i} \quad A3-5$$

Where $R_{specimen}$ is the specimen resistance, V_{probe} is the voltage drop over the specimen measurement probes, and i is the current through the series circuit computed previously (equation A3-4).

The specimen resistivity is computed using equation A3-1 by setting $R = R_{probe}$, and knowing the measurement geometry including the probe separation length, L , and area of voltage application, A .

Temperature is important. Slight changes in brine concentration change the conductivity by appreciable amounts. For example, Queeney (2003) reports that just a 1 ppm change in salt concentration changes the slope of the log conductivity vs. temperature curve from 5%/°C for pure water to 2.5%/°C for water with 1 ppm NaCl. Therefore, all resistivity measurements should be referenced to a specific temperature.

1.2.1 2-Probe Resistivity

The 2-probe technique applies a differential voltage across the two electrodes and measures the voltage drop across the same two electrodes. Soil resistance and resistivity are computed using the measured voltage drop and known current through the system.

The 2-probe technique is advantageous for high resistivity (low conductivity) specimens because the errors associated with the unknown interface resistance are minimized. However, polarization and plating of the electrodes is of high concern because the measurement electrodes are the same electrodes that apply the voltage and current to the specimen. As a result, the 2-probe technique is generally avoided in the MIT Geotechnical Laboratory.

1.2.2 4-Probe Resistivity

The 4-probe technique is illustrated in Figure A3-1. The voltage and current is applied to the specimen through the plate probes V1 and V4, as in the two probe technique. The voltage drop across a portion of the specimen is measured using the measurement electrodes V2 and V3. There is no current flow through V2 and V3, limiting polarization effects. The 4-probe technique differs in that the voltage drop across the specimen is measured using different electrodes from which the differential voltage is applied to the specimen.

1.3 Frequency

Both low and high frequency has been applied to measure the resistivity of soils (McCarter et al, 2005). Despite numerous studies applying varying frequencies, the frequency effect on mudrock resistivity is still relatively unclear.

Blewett et al (2001) show the effects of electrode polarization as a function of frequency for 2-probe resistivity measurements using an Argand plot (Figure A3-2). An Argand plot, also known as a Nyquist plot, plots the imaginary component of the electrical impedance vs. the real component. As the frequency increases (from right to left) the imaginary component decreases to a minimum value and then increases again as the real component decreases. For 2-probe measurements, increasing the frequency reduces the effects of electrode polarization but in turn can lead to errors associated with double layer capacitance. The bulk resistivity of a mudrock or clay slurry is given when the imaginary component of the resistivity is minimized; the frequency required to obtain this minimum varies based on the measurement set up and material. Therefore, for 2-probe measurements it is important to measure the frequency response of the resistivity.

Contrarily, Waxman and Smits (1968) note a lack of resistivity-frequency dependence for 2-probe measurements in the range of 0.5 to 20 kHz.

To avoid difficulties associated with electrode polarization, 4-probe measurements are used for this research. Denicol and Jing (1998) measured the effects of varying frequency on oil field reservoir rocks using the 4-probe resistivity technique. They found that the measurements are frequency dependent only within specific frequency ranges. Measurements made at frequencies lower than 10 kHz are strongly influenced by electrode polarization as in the 2-probe case. The resistivity measurement is stable and independent of frequency in the range of 10 to 100 kHz, deemed the intermediate frequency range. Above 100 kHz, the measured resistivity decreases substantially with increasing measurement frequency. The resistivity measurement system (described in Section 2) is designed to make measurements at a default of just above 10 kHz, within the stable frequency independent range.

Many more studies using the 2-probe configuration are available than those the 4-probe configuration. Researchers have used fixed frequencies, or studied the resistivity – frequency response with no clear conclusions. The industry standard, if any, is unknown, and company standards are often proprietary. For simplicity, and resultant from discussions with UT Geofluids sponsors, a fixed frequency of 10 kHz was chosen for use in this research. This frequency is within the intermediate frequency range and falls within the stable range shown by Denicol and Jing (1998).

2 Resistivity Measurement System

Laboratory resistivity measurements have been intermittently published in the literature. Common techniques include 2-probe (e.g. McCarter 1984, McCarter et al 2005, Blewett et al 2001) and 4-probe methods (e.g. Gao et al 2003, Brannan and Von Gonten 1973, Abu-hassanein et al 1996), as well as variations of these. Most systems described in the literature are experiment-specific and authors rarely specify exactly how the measurements are made. Commercial measurement systems are available and are sometimes used to measure soil resistivity (e.g. Blewett et al 2001, Gao et al

2003), however the inner workings of these commercial 'black boxes' are often poorly presented, proprietary, and non-customizable.

Depending on the setup and measurement requirements, soil resistivity can be easily measured using basic knowledge of electric circuits and simple equations such as Ohm's law relating the current, voltage and resistance in an electrical circuit. Consequently, a custom resistivity measurement system was designed for this research. This system consists of a measurement box that contains all of the electronic circuitry required to measure the resistivity using either the 2- or 4- probe techniques. The measurement box has a user interface with a variety of electrical connections allowing control of various parameters.

The resistivity measurement system is designed with standard input connections that make it versatile and reusable. Instead of varying the measurement system by experiment, the resistivity probes themselves are varied depending on experiment. Each set of probes is custom designed to connect to the multi-use resistivity measurement box. The following sections describe the resistivity measurement system and three measurement configurations used for this research: bench top measurements, triaxial cell measurements, and CRS specimen measurements.

The resistivity measurement system is designed to measure the resistance of a specimen between two points using either the 2-probe or 4-probe resistivity measurement techniques. The 2-probe technique measures the voltage drop between two plates through which a current is applied. The 4-probe setting measures the voltage drop between two measurement probes through which no current is applied to the system. Polarization is less of a concern using the 4-probe technique because the probes are used only for measurement of voltages applied via the 2-probe plates.

Figure A3-3 shows the ideal specimen circuit. The specimen is connected in series to two resistors, a current drop and a reference resistor. The current drop resistor controls the current in the system and therefore the voltage drops over the subsequent two resistors. The reference resistor has a known resistance. Measuring the voltage drop over this resistor allows calculation of the current using Ohm's Law (equation A3-4). The specimen is considered to be a resistor, and the specimen resistance is computed using Ohm's law and the measured 2- or 4-probe voltage drop. A non-ideal specimen circuit occurs when the measurement method requires electrification of other resistor analogs, for example during measurement in the triaxial device. This is discussed in Section 3.1.

2.1 PCB Design Summary

The resistivity measurement system consists of a custom made PCB board with two 20-pin IDC connectors. Ribbon cable connects the PCB board to the user interface box. Figure A3-4 shows the user interface with all electrical terminals and switches. Both the schematic diagram and the PCB layout were created using the commercial PCBArtist version 1.4 software available free from Advanced Circuits (4pcb.com). Figure A3-5 gives the schematic circuit diagram in PCB Artist; this drawing showing all electrical components and wiring. Figure A3-6 and Figure A3-7 provide simplified, larger scale schematic drawings of the signal generator circuit, specimen circuit and

measurement circuit. Figure A3-8 gives the PCB layout. A list of all PCB board components is provided in Table A3-1. Finally, Figure A3-9 is the resistivity user interface box wiring diagram showing pin connections from the circuit and straight wired connections between terminals.

The circuit consists of three distinct sub circuits: A signal generator circuit, a specimen circuit, and a measurement circuit.

The signal generator circuit produces an AC sine wave using an ICL8038 precision waveform generator, two LF351 Operational Amplifiers (Op-Amp), two switches and W171DIP-21 relay.

The specimen circuit consists of a bank of current drop and reference resistors connected to a selector switch on the user interface box. These drop and reference resistors are in turn connected to banana connectors on the user interface box allowing external connection to the specimen probes. Because this forms a series circuit, the current through each resistor is the same and can be computed using Ohms Law knowing either the resistance or the voltage drop.

The measurement circuit measures the voltage drop across two points in the specimen circuit using an AD524 Precision Amplifier and an AD637 High Precision RMS-to-DC converter. The output is routed through to banana connectors on the user interface box for output to a voltmeter. The voltage output is used to compute the soil resistivity.

The circuit requires both +/- 15V DC power. An AD949 analogue DC/DC converter with a +5 V DC power supply is used. The box is connected to both +5 V and ground as inputs. The maximum input and output currents are 600 mA and 60 mA, respectively. The circuit is designed to have an operating input current in the range of 300 – 400 mA for most soils.

The following sections provide more detailed descriptions of the signal generator, specimen and measurement circuits.

2.2 Signal Generator Circuit

The purpose of the signal generator circuit is to produce a sinusoidal AC voltage signal for specimen excitation. An AC signal is required to prevent polarization of the electrodes exposed to ionic solutions. The resistivity meter offers two methods for signal generation: internal and external. The signal is buffered via an Op Amp and fed through the specimen circuit. An on/off switch connected to a W171DIP-21 Relay separates the signal generator circuit from the specimen circuit and allows the user to control when current is applied to the specimen.

2.2.1 Internal Signal Generation

The internal signal generator consists of an ICL8038 precision waveform generator amplified by an LF351 Op-Amp. The ICL8038 can be set to produce either a sine, square or triangular wave with a

frequency varying from 0.001 Hz to more than 300Hz and varying duty cycle. Frequency and duty cycle variation are controlled by two resistors and a capacitor. These correspond to R2, R3 and C1, respectively, in Figure A3-5. For a 50% duty cycle, which corresponds to symmetrical sine wave, R2= R3. The frequency is determined by equation A3-6:

$$f = \frac{0.33}{RC} \quad \text{A3-6}$$

Where f is the output frequency, R is the resistance and C is the capacitance. R2 and R3 are fixed at 33 k Ω , and C1 is 1.0 nF (see Figure A3-5), resulting in a sine wave with a frequency of approximately 10 kHz and a peak to peak voltage of approximately 6 V.

The voltage of the internally generated signal is amplified using an LF351 Op-Amp. The amplification is set by the ratio of R6 to R5 (Figure A3-5). As designed, R5 is 10 k Ω and R6 is 38 k Ω , yielding an amplification of ~ 3.8. Through experimentation, it was found that a higher gain value resulted in railing of the reference and specimen signals in the AD524 amplifier.

The net output voltage of the internally generated signal is approximately 24 volts peak to peak (+/- 12 volts AC).

2.2.2 External Signal Generation

External signal generation is enabled by connecting a function generator to both the external function generator terminal and ground and switching the function switch to 'EXT'. The function generator is set to the desired wave form, frequency and voltage. The externally generated signal is not internally amplified within the circuit, therefore, the voltage must be carefully selected. The voltage must be high enough to provide sufficient voltage drop across each of the reference and specimen resistors, allowing an accurate measurement to be made, but also low enough that the signal measured by the AD524 is not railed (see section 2.3.1). Selection of the appropriate current drop resistor, R_{drop}, (see section 2.3) can help avoid this problem.

As a rule of thumb, a signal voltage less than that of the amplified internally generated signal, 24 volts peak to peak (+/- 12 V AC), is ideal.

2.2.3 Buffer Amplifier

There are two Op Amps in the signal generator circuit. The Op Amps are separated by a Function switch. The first Op Amp (see U3 in Figure A3-5), acts as an amplifier and is applied only to the internally generated signal, previously described in section 2.2.1.

The second LF351 Op-Amp (see U6 in Figure A3-5) wired as a voltage follower. This acts as a buffer amplifier and has no effect on the internally generated signal. Rather, this second amplifier provides the circuit current. The internal signal generator or the external signal generators provide

the voltage signal only, and the buffer amplifier provides the current generating the power of the circuit.

This amplifier becomes railed if the input voltage is greater than 30 volts peak to peak (+/- 15 V AC). Railing occurs when the amplified input voltage into an operational amplifier exceeds the power supply voltage to the amplifier. The output voltage is limited by the +/- power supply voltages, called the rails. If the amplified input voltage is too high, the output voltage is the rail voltage instead of the amplified input voltage. Railing a sine wave truncates the peaks and makes it appear closer to a square wave.

2.3 Specimen Circuit

The specimen circuit consists of three resistors in series: a current drop resistor, R_{drop} , a reference resistor, R_{ref} , and the specimen to be measured which acts as the third resistor. The ideal specimen circuit is shown in Figure A3-3. The specimen circuit is connected to the buffered AC voltage at one end and to ground at the other end. Different key points of the specimen circuit are set up as measurement points for use in resistivity calculations.

2.3.1 Drop Resistor

The purpose of the drop resistor is twofold. First, the drop resistor reduces the voltage of the AC signal such that further voltage reduction by the reference resistor brings the total signal voltage below the supply voltage (rails) of the AD524 amplifier. Secondly, the drop resistor reduces the signal voltage so that the AS524 can accurately compute the differential signal with minimal error.

Experiments have revealed that the AD524 becomes railed when the amplification causes the RMS output voltage (output of the resistivity measurement box) to exceed 8.5 V. The drop resistor should be selected in combination with amplification to produce an RMS output in the range of 1.2 to 8.5 V. The upper limit of 8.5 V is set to prevent railing. The lower limit of 1.2 V ensures that the proper amplification is applied. A signal that is 0.7 V should be further amplified to be 7 V to reduce errors. A signal that is 1.0 V cannot be further amplified without causing railing (10 V > 8.5 V railing limit) however, a signal lower than 1.2 V results in larger errors.

Even when railing is avoided, the AD524 is unable to accurately compute the difference between two very high signals; experiments revealed that the error band was too high. Initially, the reference resistor was wired as first in series, followed by the drop resistor. This configuration requires the AD524 amplifier to compute the difference between two very high voltage input signals leading to large errors. Reversing the order of the drop and reference resistors solved this problem. The drop resistor is installed first, followed by the reference resistor, and the specimen.

R_{drop} should be selected to keep the current in the range of 1 - 6 mA when possible. Currents lower than 1 mA result in very low voltage drops over the reference and specimen resistors translating to

poor measurements. Experiments show that currents higher than 6 mA lead to specimen effects that increase measurement errors.

There are six possible settings on the drop rotary switch for R_{drop} : 0.971, 0.775, 2.39, 2.94 and 3.5 k Ω , as well as an external setting allowing the user to select and install any resistor. R_{drop} should be selected in combination with a reference resistor such that the voltage drop over the reference resistor and the specimen are as close as possible, and the current is within the range of 1-6 mA. Section 4 gives procedures for making measurements and selecting proper drop resistor values. R_{drop} does not affect the resistivity calculation except to drop the signal voltage and control the current through the specimen circuit.

2.3.2 Reference Resistor

The reference resistor, R_{ref} , is used to compute the current through the circuit. The resistance of each reference resistor is known and measured using an ohm-meter. The voltage drop over the resistor is measured the current through the resistor computed using Ohm's Law (equation A3-4, section 1.2).

There are six possible settings on the reference rotary switch for R_{ref} : 50.6, 99.2, 273, 506 and 998 ohms, as well as an external setting allowing the user to select and install any resistor. R_{ref} should be selected such that the resistance is close to the resistance of the soil specimen being measured.

2.3.3 Specimen Resistor

The specimen resistor is the specimen being measured and has a resistance that varies with the mudrock mineralogy, porosity and fabric structure, the pore fluid salinity and ionic composition, and the length, area and temperature of measurement. The specimen resistance is measured using two or four probes which are connected to the user interface box electrical terminals (Figure A3-4). The AC voltage is applied across the specimen via plate probes connected to the 2 probe banana terminals on the user interface box. The 2-probe resistivity technique measures the voltage drop across the specimen using these same two probes. The 4-probe resistivity technique measures the voltage drop between two pin probes which protrude into the specimen and are connected to the 4-probe banana terminals on the user interface box. The specimen resistor is the last resistor in series; therefore one of the 2-probe plate electrodes is grounded.

2.4 Measurement Circuit

The measurement circuit actually measures the voltage drop across two points in the specimen circuit. The 4 possible measurement points (reference, 2-probe specimen, 4-probe specimen and shunt) can be connected to the measurement system via the measurement rotary switch. This rotary switch is a 2 pole switch with commons connected to the inputs of the AD524 amplifier. The amplifier computes the difference between the two input signals and amplifies the differential

signal to 1, 10, 100 or 1000 times based on the selection of the amplifier rotary switch. The output of the amplifier is input to an AD637 High Precision RMS-to-DC converter through a high pass filter to reduce noise. The RMS-to-DC converter computes the RMS voltage of the amplified differential signal and outputs it to a voltmeter connected through the measurement terminals on the user interface box. The RMS voltage corresponds to the voltage drop across the selected measurement points.

2.4.1 Specimen Circuit Measurement Points

The resistivity calculation inputs include the voltage drop and measurement amplification for the reference and specimen resistors, as well as the zero voltage (shunt voltage) of the system at the same amplification. These values are measured using the rotary switch on the user interface box (Figure A3-4).

The voltage drop over the reference resistor allows computation of the current in the specimen circuit using Ohm's law (eqn. A3-3).

The voltage drop over the specimen can be measured using either a 2- or 4- probe technique, described in section 1.2. There are terminals for each of these measurement connections on the user interface box (Figure A3-4). The 2-probe terminals are used to measure the plate to plate voltage drop and double as the voltage source for the specimen. These terminals must be connected to the specimen for all measurements. The 4-probe terminals are used to measure the voltage drop between any 2 points in the specimen as determined by the location of the probes. The 4-probe terminals need only be connected when the 4-probe technique is applied.

The 2-probe measurement technique should be avoided due to polarization effects, as noted in Section 1.2.1. However, measurement of the 2-probe or plate to plate voltage drop is useful to correct for current loss, such as that due to electrification of the triaxial cell during measurement of cubic specimens (see Section 3.1). Therefore, both the 2-probe and 4-probe voltage drop measurements should be recorded for quality control purposes.

The shunt voltage is the zero of the measurement system at a given amplification. It is used to compute the real voltage given the measured voltage; it is not part of the specimen circuit but is required to reduce error in the resistivity calculations. When set to measure the shunt voltage, the measurement rotary switch effectively disconnects the measurement circuit from the specimen circuit. The shunt voltage is measured for each voltage measurement (reference, 2-probe and 4-probe) at the corresponding amplification. The shunt voltage is typically < 0.050 and varies with the gain. For a constant gain, all measurements made at the same time will have the same shunt voltage within ± 0.005 , based on the accuracy of the voltmeter used to measure the voltage and the steadiness of the signal. The real voltage is equal to the measured voltage minus the corresponding shunt voltage, all divided by the gain used for measurement:

$$V = \frac{V_{meas} - V_{shunt}}{G} \quad A3-7$$

Where V is the corrected voltage, V_{meas} is the measured voltage drop at amplification G across any two points, and V_{shunt} is the shunt or zero voltage of the system measured at the same amplification G .

3 Measurement Electrodes

The Resistivity measurement System can be connected to any number of electrode configurations to measure the resistivity of soils, saline solutions, or other materials. Three primary electrode configurations have been constructed to measure the resistivity of 1) flowable materials on the bench top (e.g. saline solutions, sands and clay slurries); 2) cubic specimens in the flexible wall permeameter (consolidated clay specimens); and 3) solid specimens on the bench top (e.g. wet or dry consolidated clay specimens). The third configuration can also be used to measure the resistivity of compacted Constant Rate of Strain (CRS) specimens making it useful for other projects that rely extensively on CRS measurement techniques. The following sections describe the equipment design and methods relevant to each electrode configuration.

3.1 Triaxial Configuration

The cubic resistivity end adapters are a modification to existing cubic end adapters already in use to measure the permeability of cubic specimens in the flexible wall permeameter (Figure A3-10, described in Chapter 4 and Appendix 2). Figure A3-11 shows a solid view of the modified cubic end adapters with the probes. Appendix 6 provides dimensioned drawings for the end adapters. The following paragraphs describe the key modifications to the end caps, as well as the fabrication methods.

The cubic resistivity end adapters are constructed with 4 brass electrodes, two each on the top and bottom platens. Two plate probes cover the square surfaces of the end adapters in contact with the specimen and serve to apply the current to the specimen; these probes are connected to the 2-probe terminals on the resistivity measurement box. Two pin probes protrude into the specimen to measure the voltage drop across the specimen; these probes are connected to the 4-probe terminals on the resistivity measurement box.

Electrical connections from these probes to the resistivity box are wired through two 9 pin connectors already present in the flexible wall permeameter device (Figure A3-10). Electrical wires in the end adapters are epoxied in place to create leak proof seal. Loctite E-30CL Hysol ultra clear low viscosity epoxy (29329) was used to bond the brass plates, wires and fittings to the end caps. This epoxy is non-conductive, has a long working life, cures hard and strong, and flows easily into the small holes in the end adapters.

The plate probe consists of a brass plate 0.020" thick with a drainage hole attached to the cubic face of each end adapter using epoxy. A braided wire is soldered to the base of the brass plate and fed through a hole in the end cap. This hole is filled with epoxy, leaving a few millimeters gap at the end of the wire opposite the brass plate. This gap is filled with more flexible RTV silicone sealant to minimize the potential for wire breakage with use. Figure A3-12 shows the set up for attaching the plate probe and infilling the wire holes in the end adapters. A 0.040" diameter brass pin is soldered to the end of the wire leaving at least an inch of flexible wire between the pin and the end cap. This pin connects to a length of wire with dual end sockets which in turn connects to one of the pins of a 9 pin connector in the base of the permeameter cell. Outside the cell, a length of braided wire with a socket at one end connects the corresponding pin in the 9 pin connector to one of the 2-probe terminals on the resistivity box. Both the top and bottom end adapters are fitted with brass plate probes.

A similar system is employed for the pin probe. A brass pin, acting as the probe, is installed in one corner of the end cap. This pin must be electrically disconnected from the brass plate. To achieve this goal, the pin is epoxied in a cylindrical acrylic pin adapter that fits into a hole drilled into the end cap. The pin is soldered at one end to a braided wire fed through a hole in the end cap. A portion of the braided wire that will be epoxy encased within the end adapter is stripped; the epoxy will fill in this section and prevent leakage through the wire. Figure A3-13 shows fabrication of the specimen pin plugs and pin probes prior to insertion into the cubic end adapters. Fabrication of the pin adapter is not trivial; O ring spaces are used to ensure correct positioning of the pin during epoxying. The solder connection must be correctly placed within the pin adapter for protection.

The pin adapter rises 0.25" above the brass plate to be flush with a porous stone when placed. The pin extends an additional 0.1562" (5/32") beyond the porous stone into the specimen. The epoxy must entirely fill the wire connection hole to ensure a leak proof product. Various set ups similar to that shown in Figure A3-12 were used to correctly position the components during the multi-stage epoxy process. Despite the low viscosity of the Loctite epoxy, vacuum saturation of the wire lead holes through the end caps was necessary for correct assembly. O-rings were used as necessary for positioning and centering.

The non-conductive epoxy is used to fix the pin, pin adapter and braided wire in place, filling the hole and electrically disconnecting the pin from the brass plate. This wire is connected in the same manner as is the brass plate, with a gap filled with RTV, followed by an external pin connected to a double ended socket connector that fits on a pin on the 9 pin connector. Outside the cell, a socket and wire connects the corresponding pin in the 9 pin connector to one of the 4-probe terminals resistivity box. Both the top and bottom end adapters are fitted with brass pin probes.

Porous stones with holes slightly bigger than the pin adapter are used on both ends of the specimen. Table 2 summarizes the wire colour coding used for the end caps. Note that as wired, assuming black as ground, current flow is from bottom to top of the specimen in the same direction as fluid flow for the permeability measurements and the top cap is grounded. However, it has been found that this setup makes disassembly of the permeameter and removal of the specimen difficult

because the O-ring seal in the bottom end adapter sticks to the triaxial end platen following excitation. Therefore, the current flow for resistivity measurements is reversed to ground the bottom end adapter and the O-ring seal. This is done by reversing the connections to the resistivity measurement box: connect the black plate probe to the red two probe connection and the red plate probe to the black 2-probe connection.

The flexible wall permeameter (Figure A3-10) is made of metal, primarily steel, brass and copper. Copper tubing with brass and stainless steel fittings are used for the cell plumbing, delivering silicone oil to apply the cell pressure and brine to apply the pore pressure to the specimen. The brine salinity, and hence conductivity, varies with each specimen. When a current is applied to the top and bottom of the specimen installed in the permeameter it is also applied to the conductive brine that saturates the porous stones, the pore system plumbing and, via direct contact with the metal connections and fittings, the entire permeameter apparatus. The apparatus has a fixed resistance and essentially adds a parallel resistor to the specimen circuit. Figure A3-14 gives the modified specimen circuit with an additional resistor representing the system or cell resistance. The cell resistance is in parallel with the specimen resistance, with the applied current being split between the cell and the specimen.

Measurement of the cell resistance is required to compute the current in each of the cell and specimen resistors and in turn compute the specimen resistance and resistivity. The cell resistance is measured by setting up the apparatus without a specimen with the top and base end adapters connected to the cell but disconnected from each other. All lines are saturated and all probes are covered with a brine solution. The cell resistance was found to be constant over the current range tested and does not vary significantly with changes in brine salinity (Table A3-3). A standard cell resistance of 6820 Ω representative of 16 g/L brine salinity was used in all calculations. The current through the specimen is computed using equation A3-8:

$$i_{specimen} = i_{ref} - i_{cell} = \frac{V_{ref}}{R_{ref}} - \frac{V_{2-probe}}{R_{cell}} \quad A3-8$$

Where $i_{specimen}$ is the current through the specimen, i_{ref} is the total system current computed using the reference resistor, i_{cell} is the current through permeameter cell including the conductive brine and all connected metal fittings, V_{ref} is the voltage drop over the reference resistor, R_{ref} is the known resistance of the reference resistor, $V_{2-probe}$ is the voltage drop over the entire specimen, from plate to plate, and R_{cell} is the cell resistance measured using the setup with no specimen as described above. All voltages in equation A3-8 should be corrected for the applied gain and shunt (measurement system zero) by subtracting the shunt value at the same gain and dividing by the gain value to obtain the real voltage. Section 5.1 gives detailed instructions and equations for the calculation of specimen resistivity.

3.2 Bench Top Configuration – Unconsolidated specimens

Unconsolidated specimens (e.g. saline solutions, sands etc.) are measured using a simple apparatus (Figure A3-15) constructed using readily available materials to mimic the elements of a 4-probe resistivity set up (Figure A3-1). Two brass triaxial end caps act as the 2-probe plate electrodes that apply voltage across the specimen. The specimen is contained within a plastic sleeve that exactly overlaps each end cap. The overlap is sealed by wrapping Teflon tape around the brass end cap beneath the plastic sleeve and placing an O ring over the plastic sleeve, as shown in Figure A3-14. Regular electrical wires (one green, one white) are stripped for a known length (typically ¼”) at one end and inserted into the drainage hole of each end cap. These wires create the 4-probe pin electrodes to measure the voltage drop across two points in the specimen. Heat shrink tubing is used to seal the holes around the electrical wires to prevent leaks and subsequent drainage of the specimen. An additional hole is drilled in one of the triaxial end caps to allow assembly and vacuum de-airing of the specimen; this hole remains open and unsealed.

The specimen is electrically connected to the resistivity measurement box via alligator clips. A worm drive hose clamp is installed around the end of each end cap to create an easy connection point (Figure A3-15). Two alligator clips (typically red and black) are used to connect the 2-probe terminals of the resistivity measurement box to the hose clamps on the brass end clamps. Two additional alligator clips (typically green and yellow) are used to connect the 4-probe terminals of the resistivity measurement box to each of the two wires protruding from the end cap drainage holes.

The area of voltage application is fixed; for standard triaxial end caps the area is 10 cm². The length between the pin probes must be accurately measured and will vary from specimen to specimen. The porosity, where applicable, is computed using specimen length and mass measurements.

3.3 Bench top Configuration - Consolidated Specimens

The resistivity of small consolidated specimens (e.g. mudrock specimens) is measured on the bench top using a CRS trimming alignment frame to stabilize the specimen. This method allows measurement of both the resistivity and the resistivity anisotropy; resistivity anisotropy is obtained by measuring the specimen resistivity in different directions. For consolidated specimens, the 4-probe measurement pins are inserted into the side of the specimen, either 1) protruding into the specimen for soft specimens, or 2) contacting the surface of the specimen for dense specimens.

The measurement set up is shown in Figure A3-16, with a close up of the specimen configuration given in Figure A3-17. Figure A3-18 shows the electrode equipment, including drilling and trimming templates, surface and protrusion electrodes, 4- and 2- pin probe wire connections, and 2-pin probe electrodes.

For simplicity and ease of measurement, the specimen is cut into a rectangular prism shape. The specimen is trimmed such that the prism axis aligns with the desired measurement directions; the resistivity is measured between parallel faces. This shape provides as near to a uniform electric field as possible, with voltage drops parallel to the specimen faces connected to the 2-probe electrodes and current flowing perpendicular to the 2-probe electrodes.

The specimen size depends on the size of the parent specimen, with the constraint that any face being measured must be fully covered by the 2-probe electrode. Given the setup shown in Figure A3-16, all specimen faces should fit within a circle of area 10 cm², equal to the contact area of the triaxial end cap used to apply the stabilizing load to the top of the specimen. Long slender specimens are not stable, and it is equally hard to measure very thin specimens. Ideal specimens are nearly cubic and fit within the triaxial end cap area profile. A steel specimen trimming template (shown in Figure A3-18) can be used as a guide to trim specimens to the maximum sized square profile to fit within the 10 cm² circular triaxial end cap area.

The 2-Probe plate electrodes are fashioned out of any available conductive material paired with a soft non-conductive cushioning layer. This construction helps the electrode conform to the uneven specimen surface and create a good contact. The electrodes are sized to be big enough to fully cover the specimen surface to be measured, but not to be so big as to bend or droop down the sides of the specimen, affecting the uniformity of the applied electric field. Good results have been obtained using 2-probe electrodes fashioned out of the top, coarse layer of a standard Scotch Brite brand kitchen scrub pad that is cut to the required size and wrapped in a double layer of aluminum foil. A piece of folded aluminum foil is left protruding off one side for attachment to the resistivity measurement system via an alligator clip. This can be seen in Figure A3-16, Figure A3-17, and Figure A3-18.

Because the size and shape of consolidated specimens varies, the area of voltage application is given by the specimen dimensions, measured using calipers.

The 4-pin electrodes (shown in Figure A3-18) consist of a machined acrylic housing with two precision holes with fixed spacing. A length of 1 mm brass rod is fed through the holes and used as the pin electrodes, similar to the pin probes in the cubic resistivity end adapters. One end of the brass rod fits into a similarly sized end socket connected to a length of wire for connection to the resistivity measurement box. Probes with 4 different center-to-center spacing were fabricated to fit an array of specimen sizes: 9.6 mm, 5.1 mm, 4.0 mm, and 2.75 mm.

It is difficult, if not impossible to drill holes and insert 4-probe pin electrodes into very small (i.e. thin CRS specimens) or very dense wet or oven dried specimens without ruinously cracking the specimens (see Figure A3-19). Therefore, two different 4-probe electrode designs are available: protruding and surface. Both designs are shown in Figure A3-18. The protruding electrodes have pin probes that protrude approximately 1/8 to 1/4" into the specimen. The surface mount probes have very short probe lengths that make contact with the surface of the specimen only. Because the specimen is a rectangular prism with a uniform electric field, the voltage measured using either of

these techniques (surface or protruding) should be the same, providing the length parameter in equation A3-1 is the same.

Surface electrodes are easily applied, and are held in contact with the specimen using a rubber band. They are best suited for dense specimens because the use of a rubber band may damage soft specimens. For the softest specimens, the protruding electrodes can be carefully pushed into the specimen. For somewhat denser specimens, holes must be drilled to aid with insertion of the protruding electrodes. Drilling templates (shown in Figure A3-18) with the same design as the acrylic housings, are made of out steel and are carefully clamped to the specimen using a parallel clamp. A hole is drilled into the specimen, through the drilling template using a Dremel fitted with a No. 69 drill bit. Care must be taken not to 1) drill the hole too deep or too fast (leading to cracking) or 2) get the drill bit stuck in the specimen. The best method is to drill to a depth of 1 mm, remove and clean the drill bit, and then repeat until the required depth has been achieved.

Appendix 6 contains drawings of the acrylic housings used to form both surface and protruding pin electrodes, as well as the drilling templates and the specimen trimming guide.

The measured resistivity varies with goodness of the electrical contacts. The cut specimen surfaces often have very small scale irregularities and may not be parallel. To ensure good electrical contacts, as well as to stabilize the specimen during measurement, the specimen is installed in a makeshift alignment frame shown in Figure A3-16. The alignment frame is in reality a CRS trimming frame. A clamp is attached to the top of the piston to make it easier to grab, as well as to prevent it from falling on the specimen. First, the 4-probe electrodes are attached to the specimen, either via elastic bands (surface probes) or by inserting the probes (protruding probes). The specimen sits on the bottom 2-probe electrode in the load frame. On top of the specimen is the top 2-probe electrode, followed by a triaxial end cap for rigidity. This is followed by a ball bearing to aid with alignment, and a spacer before contacting the top cap fitting of the trimming frame. Figure A3-17 gives a close up of the assembly to this point. The load frame top cap is a circular acrylic plate attached to a steel piston. A metal adapter sits on top of the piston converting the spherical profile to a flat surface upon which 2 kg mass is placed. 2 kg is typically sufficient to provide a good contact without harming the specimen.

As mentioned, the resistivity or conductivity anisotropy can be measured using the bench top method for consolidated specimens. However, for wet specimens, these measurements must be done quickly to obtain representative measurements in both directions without significant specimen drying. The specimen will rapidly dry when exposed to the air, forming a dry outer shell that will affect measurements. A typical procedure would be to:

- 1) Prepare the 2-probe electrodes;
- 2) Select the 4 probe electrodes;
- 3) Trim the specimen to the required size;
- 4) Measure all required dimensions for area calculation (length parameter dictated by choice of 4-probe electrodes);

- 5) If using protruding electrodes, drill all 4 holes (2 each for each direction of measurement) in one step;
- 6) Set up the specimen for measurement in one direction;
- 7) Measure the resistivity quickly (2-4 minutes);
- 8) Take down the assembly;
- 9) Rotate the specimen and re-set up the specimen for measurement in the other direction;
- 10) Measure the resistivity quickly (2-4 minutes); and
- 11) Take down the specimen.

A good quality control check would be to repeat the first directional measurement to verify that the resistivity has not changed as a result of drying.

4 User Manual

4.1 Connecting the Box

This section describes the basic steps required to connect the resistivity measurement box to power, the specimen, and the output voltmeter.

1. Connect +5V and ground to the labeled terminals.
2. Connect a voltmeter to the "Output" terminals. Black is ground, red is signal.
3. Connect the electrodes on the end of the specimen to the "2 Probe" terminals on the box. Black is ground, red is signal. If using the cubic resistivity end adapters, connect the top of the specimen (black wires) to the signal (red terminal) and the base of the specimen (red wires) to the ground (black terminal). The colours may not match the wires on the end adapters. Though the measurements will not be affected if the power is applied to the bottom cubic adapter instead of the top, the O-ring in the base end adapter will stick to the brass end platen. This will make removing the base end adapter during apparatus disassembly extremely difficult, and may lead to specimen damage during removal if excessive force is used.
4. Determine the type of function generation:
 - a. Internal Generation - set function switch to Auto
 - b. External Function generation - set function switch to 'Ext' and connect an external waveform generator to the green "Ext Function" terminal and ground terminal. Set waveform generator to desired wave form, frequency and voltage. Rule of thumb: Keep peak to peak voltage below 24V.
5. Determine the type of measurement
 - a. 2-Probe Measurement: Do nothing. Note: 2-probe measurement is not advised.
 - b. 4-Probe Measurement: Connect the "4 Probe" terminals to the specimen measurement (pin) probes.

4.2 Measuring Resistivity

This section describes steps required to measure the resistivity of a specimen using either the ideal specimen circuit (Figure A3-3) or the modified specimen circuit in the flexible wall permeameter (Figure A3-14).

1. Connect the box following section 4.1.
2. Select a reference resistor, a current drop resistor, and a gain value. These values will be adjusted for the measurement. A good starting point for saturated, consolidated mudrocks is a reference resistor of 50 Ohms and a current drop resistor of 1 k Ω . Set the gain to 1.
3. Turn the power on.
4. Set the measurement dial to '4-Probe'. Adjust the amplification until the value is within the range of 1.2 to 8.5 V. A voltage higher than 8.5 V will rail the AD converter. A voltage reading lower than 1.2 V is too low in relation to the shunt or zero value of the system and will result in too high of an error on the measurement. Try to avoid using an amplification of 1000.
5. Repeat step 4 to read the voltage drops over the '2-Probe' and 'Reference' resistors. Adjust only the gain values, do not adjust the value of either the current drop or reference resistor.
6. If all of the '4-probe', '2-probe' and 'reference' resistor voltage drops yielded amplified measurements within the range of 1.2 to 8.5 V, proceed to step 7 to record the measurements. If not, return to step 2 and select a different combination of reference and drop resistor.
7. Record the value of the reference resistor and the current drop resistor.
8. Set the measurement dial to "4-Probe". Adjust the amplification until the value is within the range of 1.2 to 8.5 V. Record the 4-probe voltage drop and gain. Without adjusting the gain, turn the measurement dial to 'Shunt' and record the measurement system zero value corresponding to the 4-probe voltage drop.
9. Repeat Step 8 to measure the voltage drop, gain and shunt for the reference resistor.
10. You should now have a table with 11 values:
 - a. Drop resistor value, Reference resistor value
 - b. $V_{4\text{-probe}}$, Gain, Shunt
 - c. $V_{2\text{-probe}}$, Gain, Shunt
 - d. V_{ref} , Gain, Shunt
11. Turn the box off. Avoid having current running through the specimen more than necessary.
12. Repeat steps 2 to 11 using a number of reference resistor - drop resistor combinations. Try to get at least 10 different measurements. Ensure that all voltage measurements are correctly amplified and fall within the range of 1.2 to 8.5V.

4.3 Troubleshooting and Rules of Thumb

1. All voltage measurements need to be amplified as high as possible to reduce error associated with subtraction of the shunt. All voltage measurements should fall in the range of 1.2 to 8.5 V. A voltage higher than 9 V will rail the AD converter. A voltage lower than 0.9 V is too small compared to the shunt or zero value of the system and will result in too high of an error on the measurement. Voltages between 8.5 and 9 V and 0.9 and 1.2 V are difficult to determine the correct amplification (i.e. 0.9 V – should you amplify it by 10 times?)
2. The current should be below 10 mA. The combination of drop and reference resistor is used to control both the current through the system and the output voltage readings.
3. The A/D converter has a minimum output of about 0.25 V.
4. Some combinations of drop resistors and reference resistors just won't work. They produce RMS voltages in the range of 0.9 V - in the range of high computation error and amplification error. In this case, try a different drop resistor.
5. There should be no trend in resistivity with current. Apparent trends are resultant from measurement errors. These measurement errors include railed signals and unamplified signals that have large error bars. Correctly done, a plot of resistivity vs. current should be flat over the range of 1 to 6 mA current.
6. The total system current draw, as shown on the power supply, should be within the range of 300 mA. Higher currents indicate a short in the system.
7. When using an external function generator, ensure that low resistance connectors are used to connect the function generator to the box. Do not use high resistance oscilloscope probes for the connections.
8. When using the cubic end adapters in the flexible wall permeameter, ensure that all pin and socket wire connections don't touch parts of the cell and short out. Use plastic tubing to cover connections as required.
9. Make sure the power supply is set to +5V. Insufficient input voltage causes unsteady readings.

5 Data Analysis

5.1 Resistivity Calculation

Compute the current and resistivity using the following equations:

$$i_{system} = \frac{V_{ref} - V_{shunt}}{R_{ref}G} \quad A3-9$$

$$R_{probe} = \frac{V_{4-probe} - V_{shunt}}{i_{system}G} \quad A3-10$$

Where R is the resistance, V is the measured voltage drop, i is the current and G is the gain. Subscript 'ref' denotes the reference resistor and shunt the measurement system zero.

Compute the specimen resistivity knowing the area of voltage application, A, and the length of probe separation, L, using equation A3-11.

$$\rho = \frac{R_{probe}A}{L} \quad \text{A3-11}$$

If multiple measurements are made, plot the resistivity vs. current. The specimen resistivity is taken as the average of the flat part of the curve which should be the average of the highest values.

Compute the current and resistivity using the following equations:

$$i_{system} = \frac{V_{ref} - V_{shunt}}{R_{ref}G} \quad \text{A3-12}$$

$$i_{cell} = \frac{V_{2-probe} - V_{shunt}}{R_{cell}G} \quad \text{A3-13}$$

$$i_{specimen} = i_{system} - i_{cell} \quad \text{A3-14}$$

$$R_{probe} = \frac{V_{4-probe} - V_{shunt}}{i_{specimen}G} \quad \text{A3-15}$$

5.2 Current Effect

There is no effect of current on resistivity within the range of 0.2 - 10 mA. During initial testing of the resistivity measurement system an apparent current effect was noted. This apparent current effect was characterized by resistivity minimum in the range of 2 mA. The resistivity increased linearly above and below 2 mA and reached a apparent asymptote value ~ 1 mA and above 6 mA. Further analysis proved that the apparent current effect was resultant from improper amplification of the output signals.

In the resistivity calculation, the shunt voltage is subtracted from the measured output signal (2-probe, reference or 4-probe voltage drop) e.g. equations A3-12 to A3-15. The shunt is a constant value typically in the range of 0.020 to 0.080 V. If the output signal is in the range of ~ 0.25 V to 0.9 V it can be recorded as is or amplified. Amplification does not affect the shunt voltage. Use of the lower, unamplified signal (<1V) introduces unnecessary error into the measurement. The error is a function of output voltage which is turn a function of current, leading to an apparent current effect.

The use of proper amplification and use of current – reference resistor combinations that yield output voltages in the range of 1.2 to 8.5V removes the apparent current effect and significantly reduces the error in resistivity measurement.

5.3 Frequency effect

The resistivity measurement system uses a fixed 10 kHz signal frequency. A brief investigation into the effect of frequency on the conductivity anisotropy was undertaken using the benchtop electrode configuration (Section 3.3) during the design phases of the resistivity measurement system. Three specimens of 39% clay RBBC and one specimen of RGOM-EI were measured (Figure A3-20). The results of this study were inconclusive. Two specimens showed an increase in conductivity anisotropy and two a decrease in conductivity anisotropy over a frequency range of 1- 20 kHz. The conductivity anisotropy of the RGOM-EI specimen was most affected by changing input frequency, likely due to the higher clay content and Smectite rich mineralogy vs. the siltier and more Illite rich 39% Clay RBBC specimens.

Future work could include a more in depth and systematic study of the frequency effect on the conductivity anisotropy by performing measurements in the triaxial cell with the cubic resistivity end adapters.

Table A3-1: Resistivity Measurement System Circuit Components (Page 1 of 2)

Component ID	Component / Value	Parent Chip / Function
Chips		
N/A	AD949	+5V to +/-15V power converter
U1	ICL8030	Precision Waveform Generator
U2	AD524	Amplifier
U3	LF351	Operational Amplifier
U4	AD637	RMS-to-DC Converter
U5	W171DIP-21	Relay
U6	LF351	Operational Amplifier - Voltage Follower
Conn1	20-pin IDC	Connections to ribbon cable
Conn2	20-pin IDC	Connections to ribbon cable
Capacitors		
C1	1.0 nF	ICL8038 - sets frequency and duty of waveform
C2	4.7 uF	AD637
C3	0.1 uF	LF351 - noise reduction
C4	0.1 uF	LF351 - noise reduction
C5	0.1 uF	AD524 - noise reduction
C6	10 uF	AD524 - noise reduction
C7	0.1 uF	AD524 - noise reduction
C8	10 uF	AD524 - noise reduction
C11	0.1 uF	AD637 - noise reduction
C12	10 uF	AD524 - high pass filter
C13	0.1 uF	AD637 - noise reduction
C14	0.1 uF	AD637
C17	0.1 uF	LF351 - noise reduction
C18	0.1 uF	LF351 - noise reduction

Table A3-1: Resistivity Measurement System Circuit Components (page 2/2)

Component ID	Component / Value	Parent Chip / Function
Resistors		
R1	10 k Ω	ICL8038
R2	33 k Ω	ICL8038 - sets frequency and duty of waveform
R3	33 k Ω	ICL8038 - sets frequency and duty of waveform
R4	120 k Ω	ICL8038
R5	10 k Ω	LF351- sets gain
R6	38 k Ω	LF351- sets gain
R7	10 k Ω variable	AD542 - provides stability not used
R8	1 M Ω	AD524 - high pass filter
R9	22 k Ω	AD637
R10	51 Ω	Reference Resistor
R11	100 Ω	Reference Resistor
R12	270 Ω	Reference Resistor
R13	510 Ω	Reference Resistor
R14	1 k Ω	Reference Resistor
R15	1 k Ω	Drop resistor
R16	1.7 k Ω	Drop resistor
R17	2.4 k Ω	Drop resistor
R18	3 k Ω	Drop resistor
R19	3.6 k Ω	Drop resistor
R20	82 k Ω	ICL8038

Table A3-2: Wiring Colour Codes for End Cap Adapters

Item	Function	Wire Colour
Top Plate	2 probe, Top	Black*
Bottom Plate	2 probe, Bottom	Red*
Top Pin Probe	4 probe, Top	White
Bottom Pin Probe	4 probe, Bottom	Green

* This table gives current wiring configurations. The bottom plate should be grounded. To solve this problem, when connected to the resistivity measurement system, the top plate black wire is connected to power and the bottom plate red wire is connected to ground. In future development this error should be corrected and the top plate wire should be red, and the bottom plate wire should be black.

Table A3-3: MIT06 Cell Resistance Measurements

Brine Salinity	Cell Resistance	Current Range
g/L	Ω	mA
0	6860 +/- 148	0.65 - 0.84
16	6820 +/- 115	0.60 - 0.93

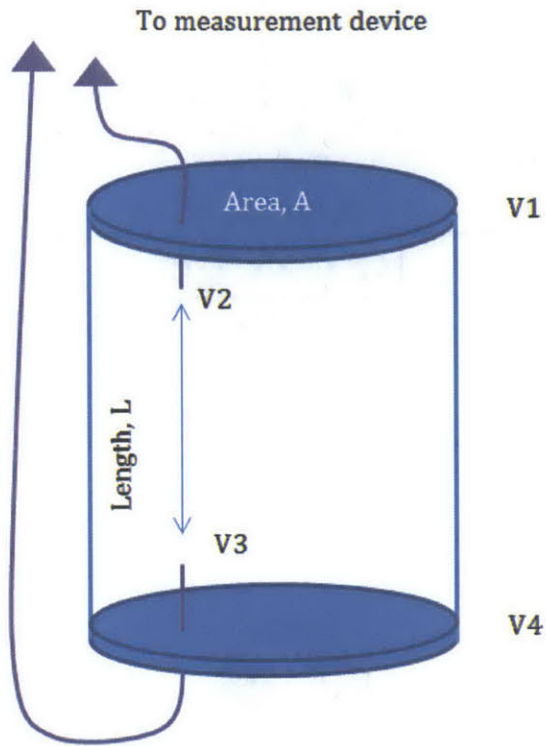


Figure A3-1: 4-Probe resistivity diagram

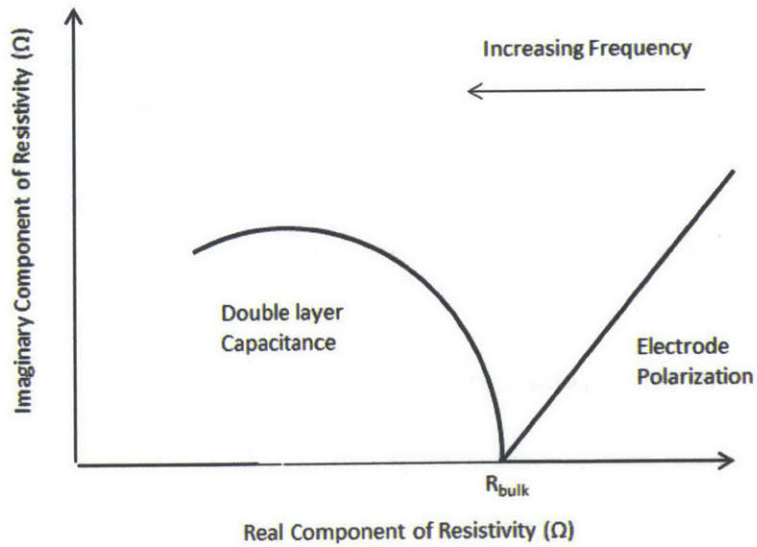


Figure A3-2: Frequency effect for 2-probe resistivity measurements (after Blewett et al, 2001)

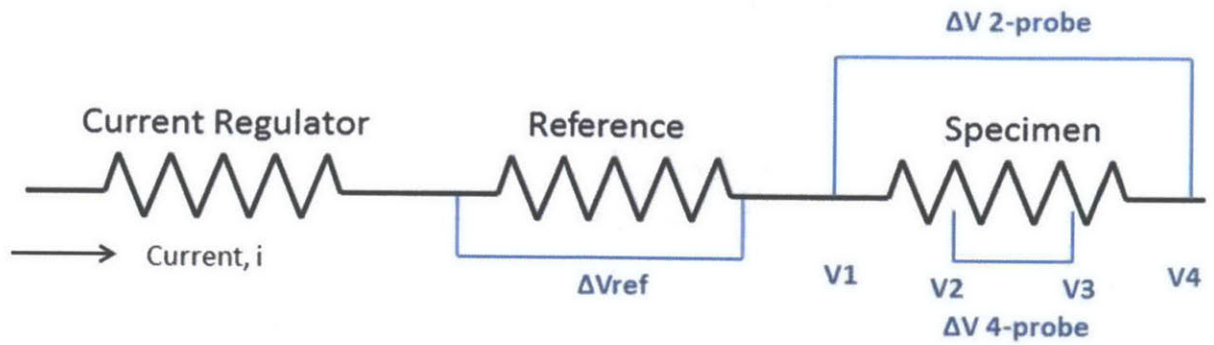


Figure A3-3: Ideal specimen circuit

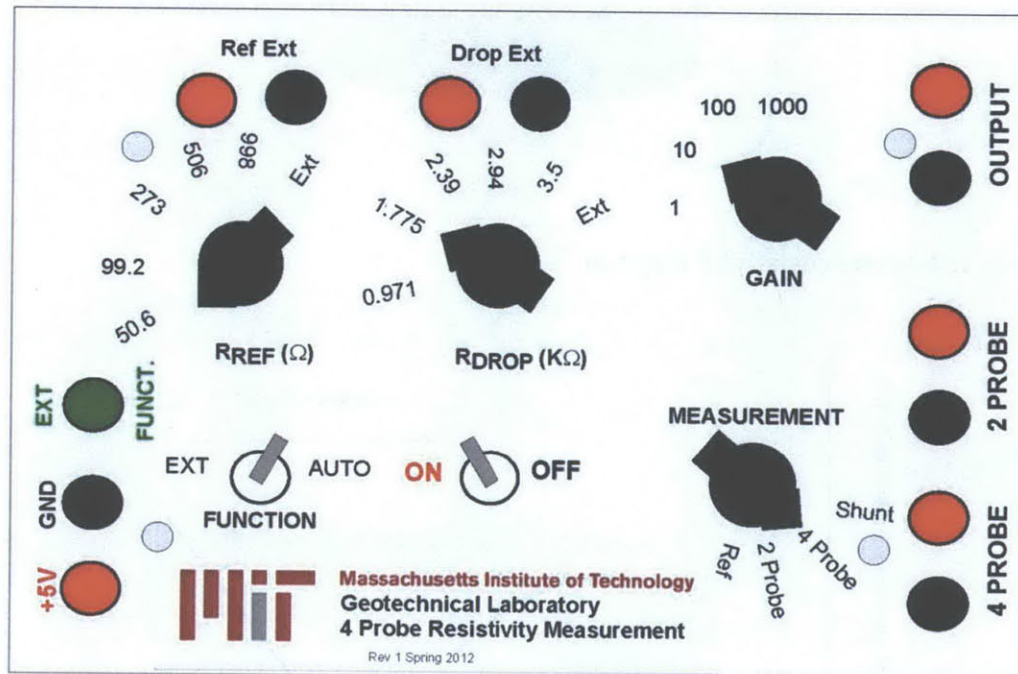


Figure A3-4: Resistivity measurement system user interface

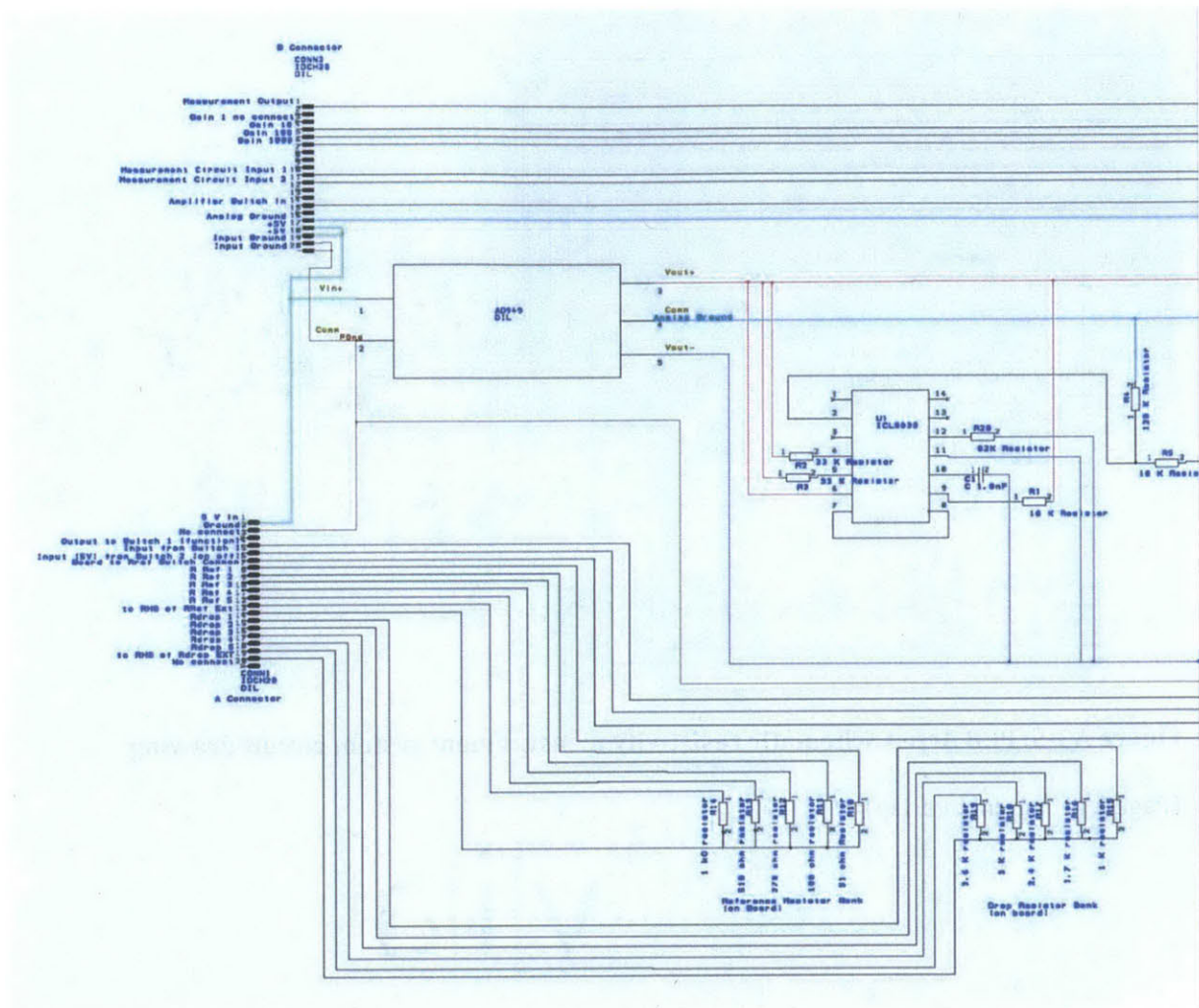


Figure A3-5: PCB Artist Schematic resistivity measurement system circuit drawing

(Page 1 of 2, 1 cm overlap)

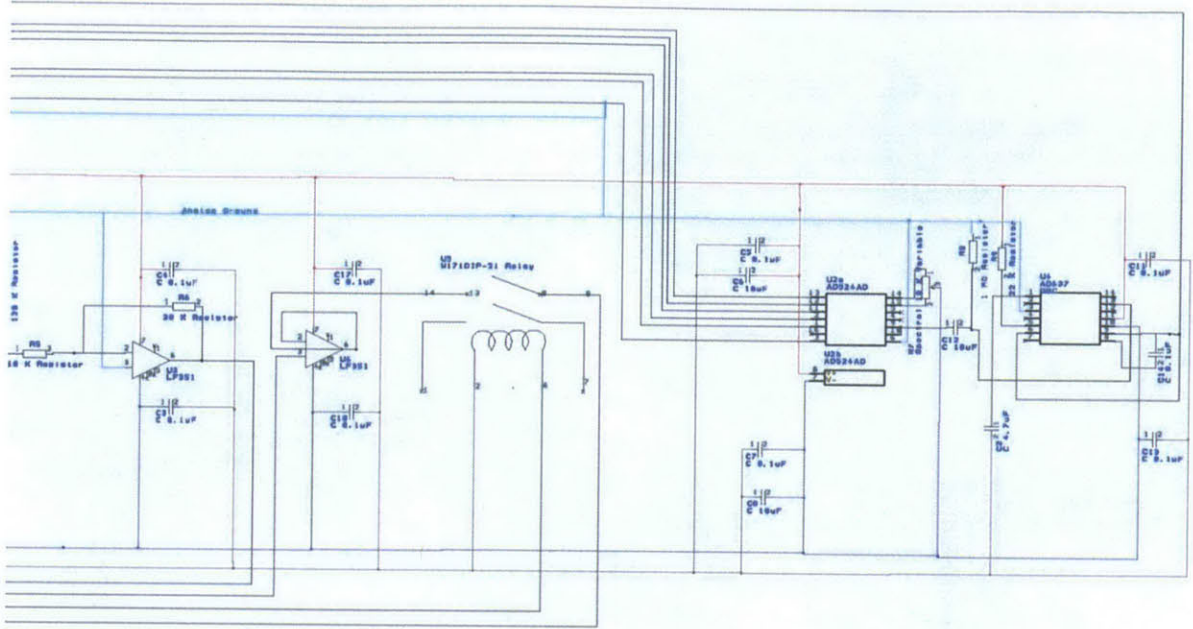


Figure A3-5: PCB Artist Schematic resistivity measurement system circuit drawing

(Page 2 of 2, 1 cm overlap)

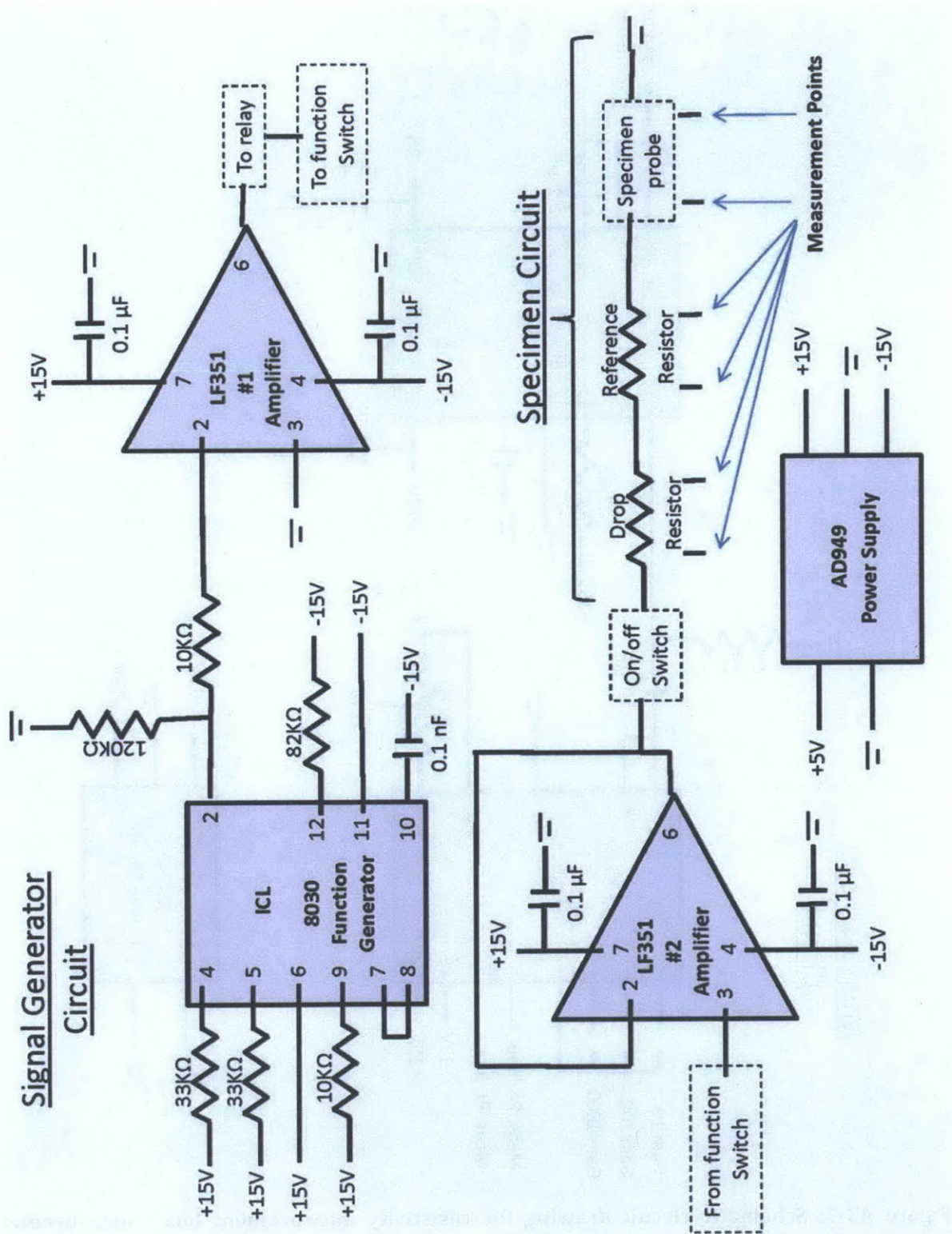


Figure A3-6: Schematic circuit drawing for resistivity measurement box - signal generator circuit and specimen circuit

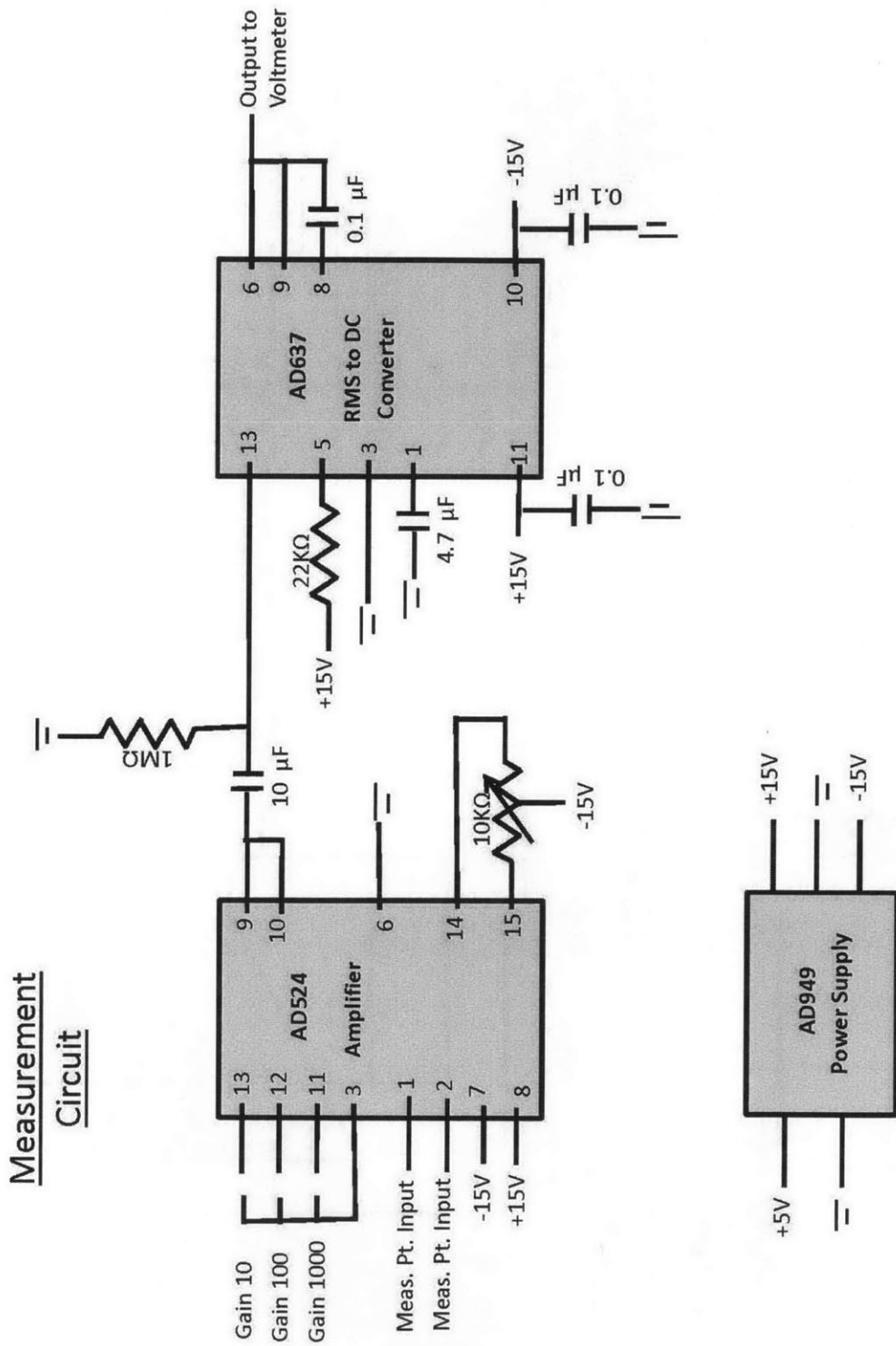


Figure A3-7: Schematic circuit drawing for resistivity measurement box - measurement circuit

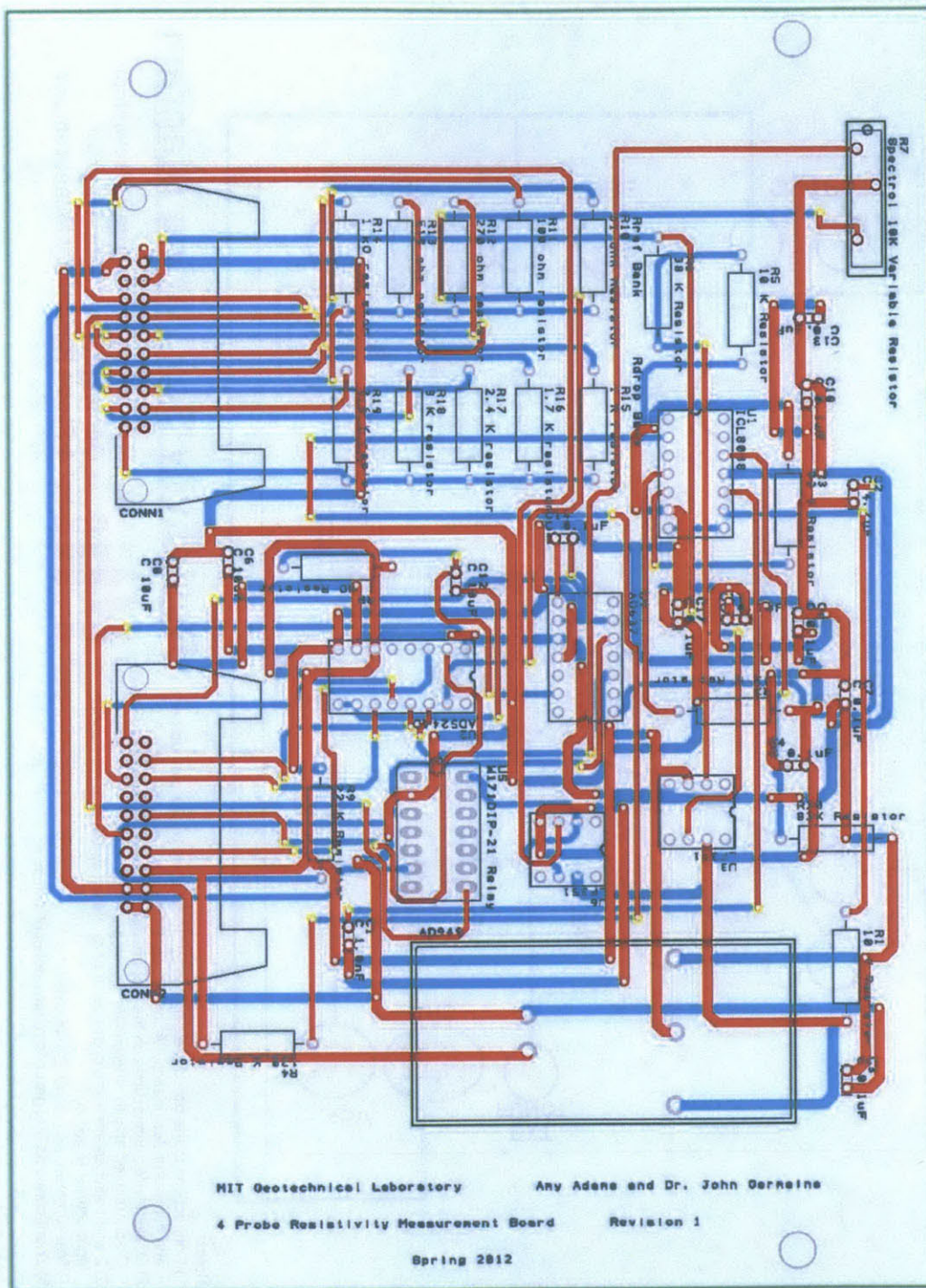
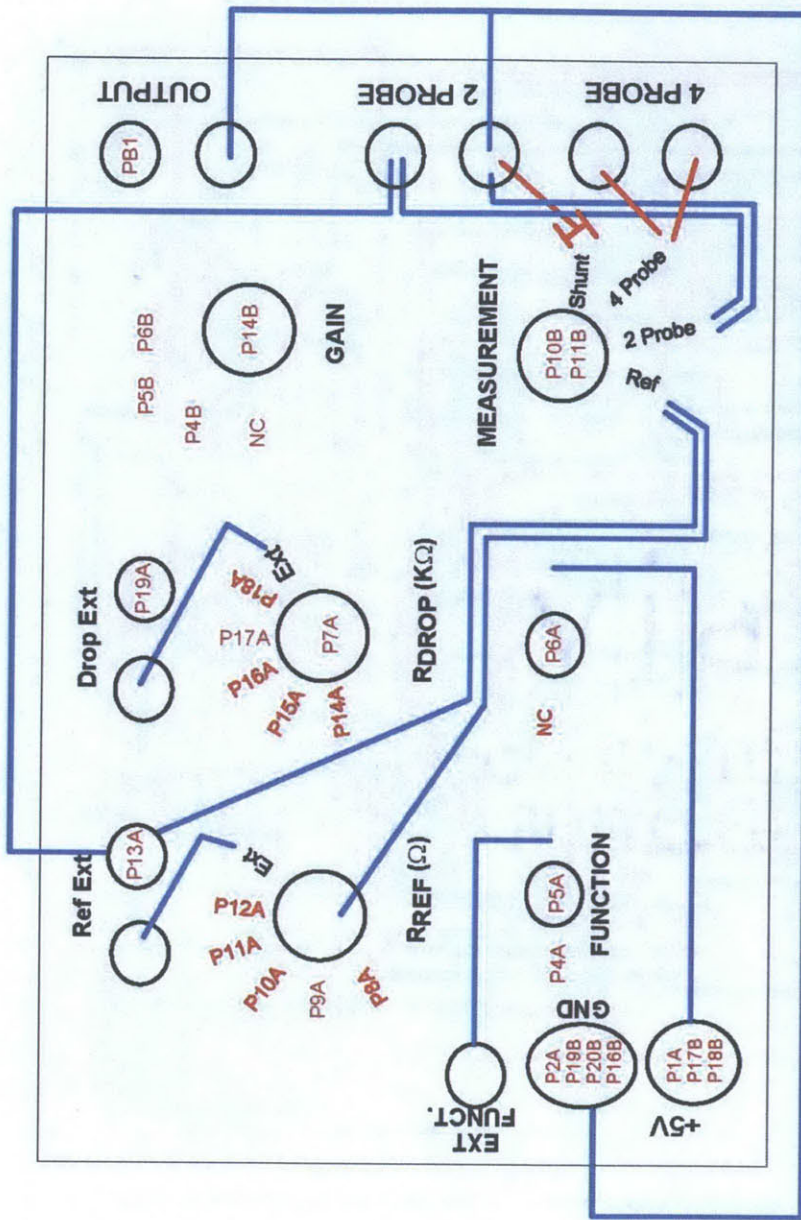


Figure A3-8: PCB board layout



Resistivity Box Wiring Diagram

Massachusetts Institute of Technology
Geotechnical Laboratory
4 Probe Resistivity Measurement

Rev 1 Spring 2012

- Notes:
- 1) Connections to the board are denoted by "P" followed by the pin number and connector designation, "A" or "B", eg. P1A is pin 1 on connector A.
 - 2) Straight wired connections on the box are denoted by solid blue or red lines. Colour is used only to differentiate crossing paths.
 - 3) 2 way switches are wired opposite on back. When switch is in left position, right contact is active.
 - 4) Measurement switch is a 2 pole switch.
 - 5) Shunt connects and grounds related poles of switch.

Figure A3-9: Resistivity box wiring diagram

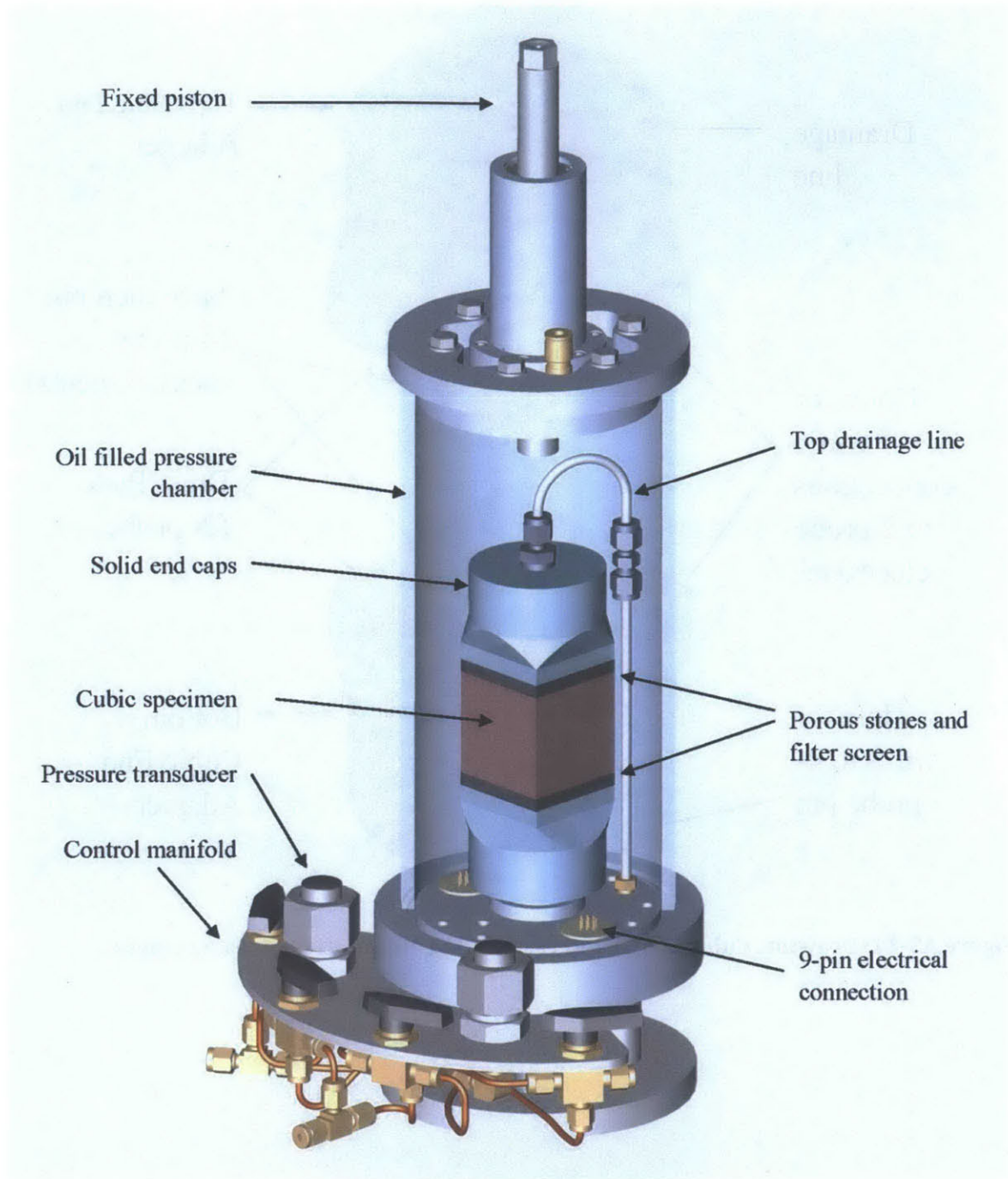


Figure A3-10: Flexible wall permeameter with cubic end adapters

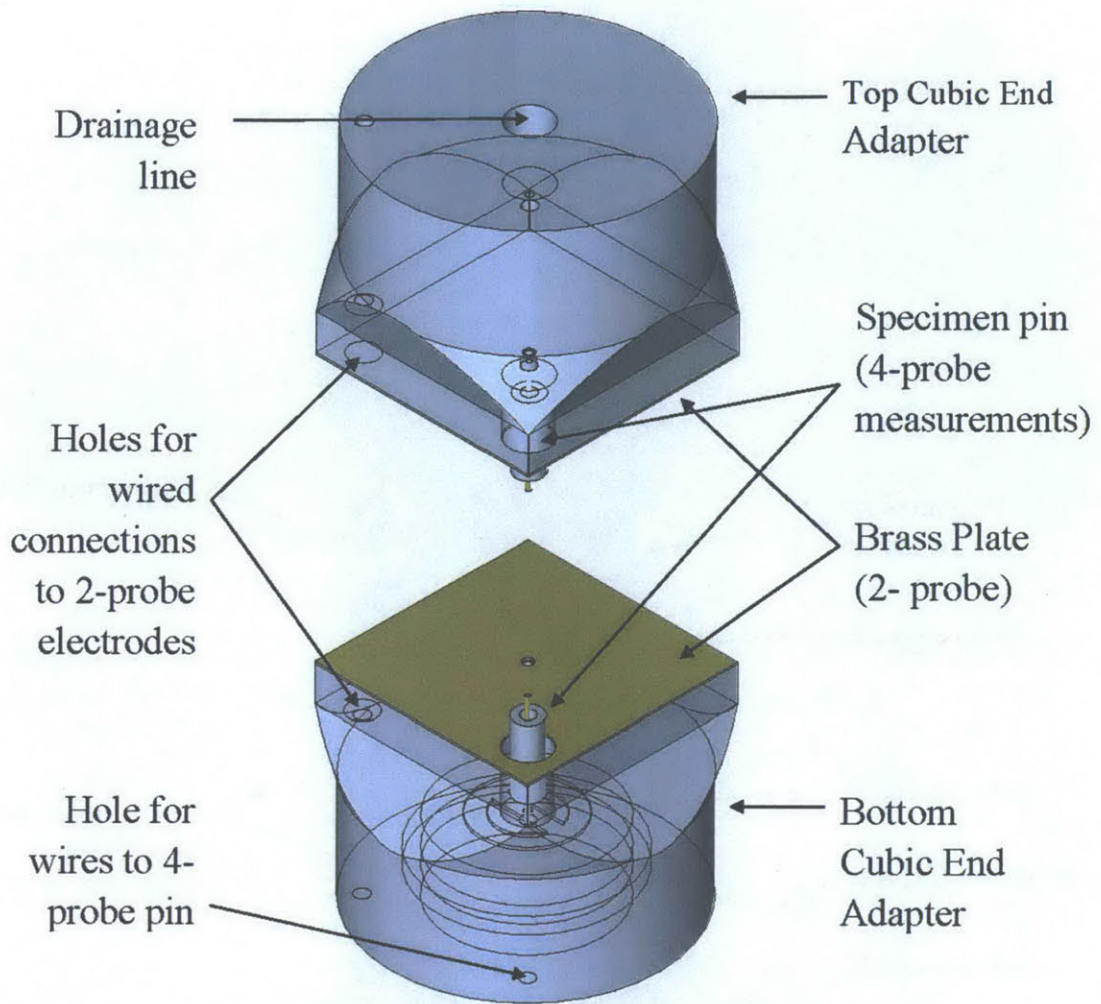


Figure A3-11: Drawing: Cubic end adapters modified for resistivity measurements

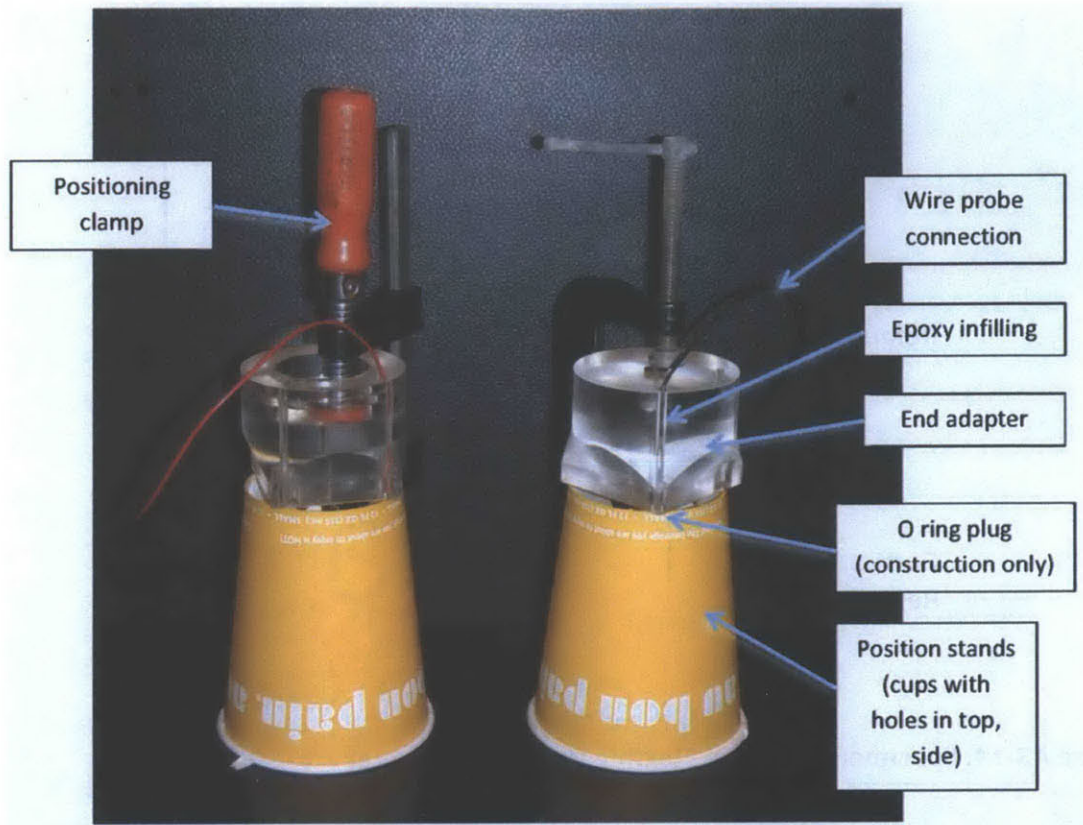


Figure A3-12: Construction of cubic resistivity end adapters: plate probe wire connections

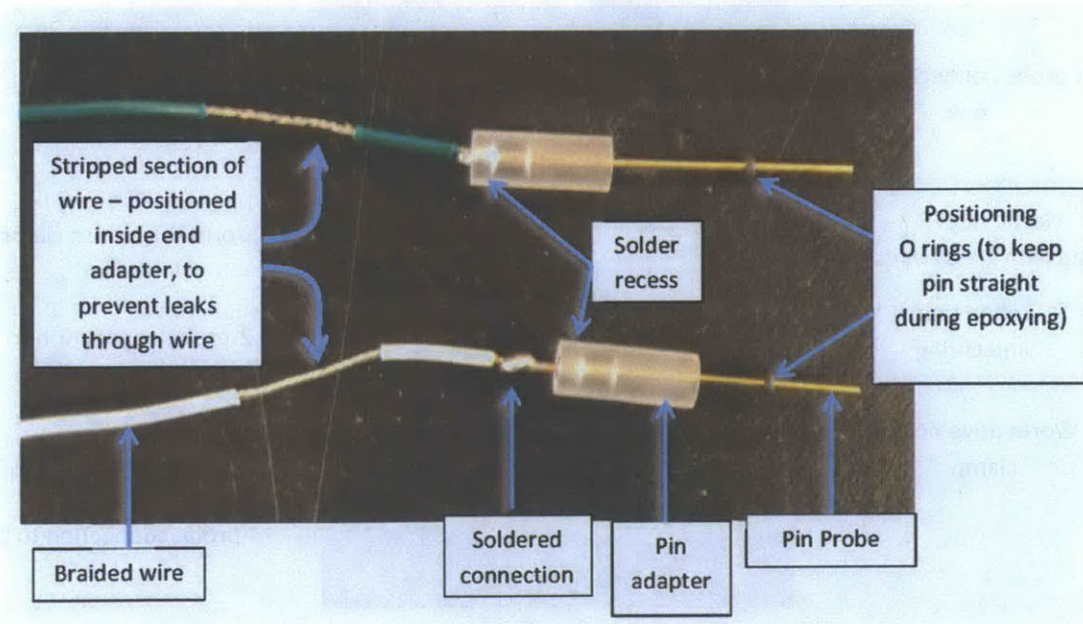


Figure A3-13: Construction cubic resistivity end adapters: specimen pin probes

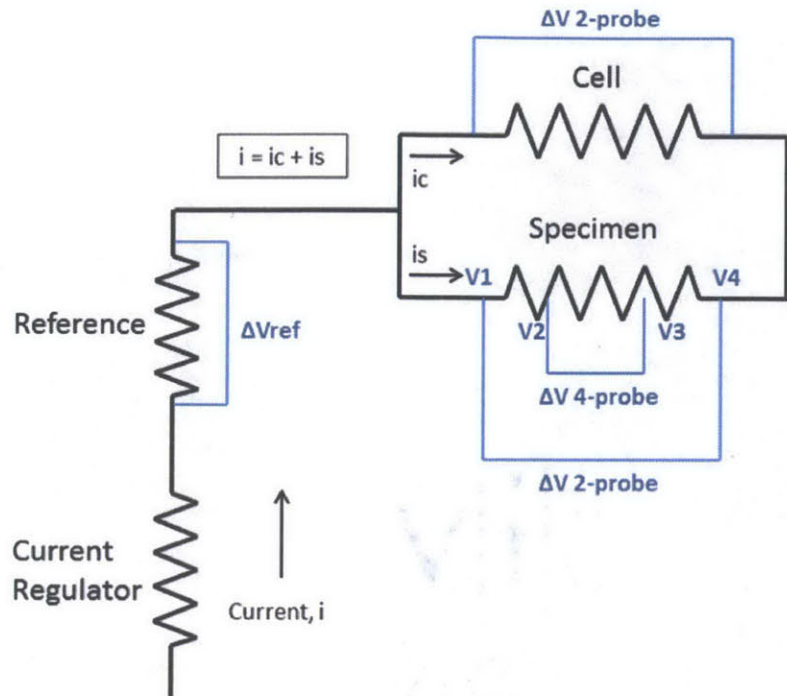


Figure A3-14: Specimen Circuit in Flexible Wall Permeameter

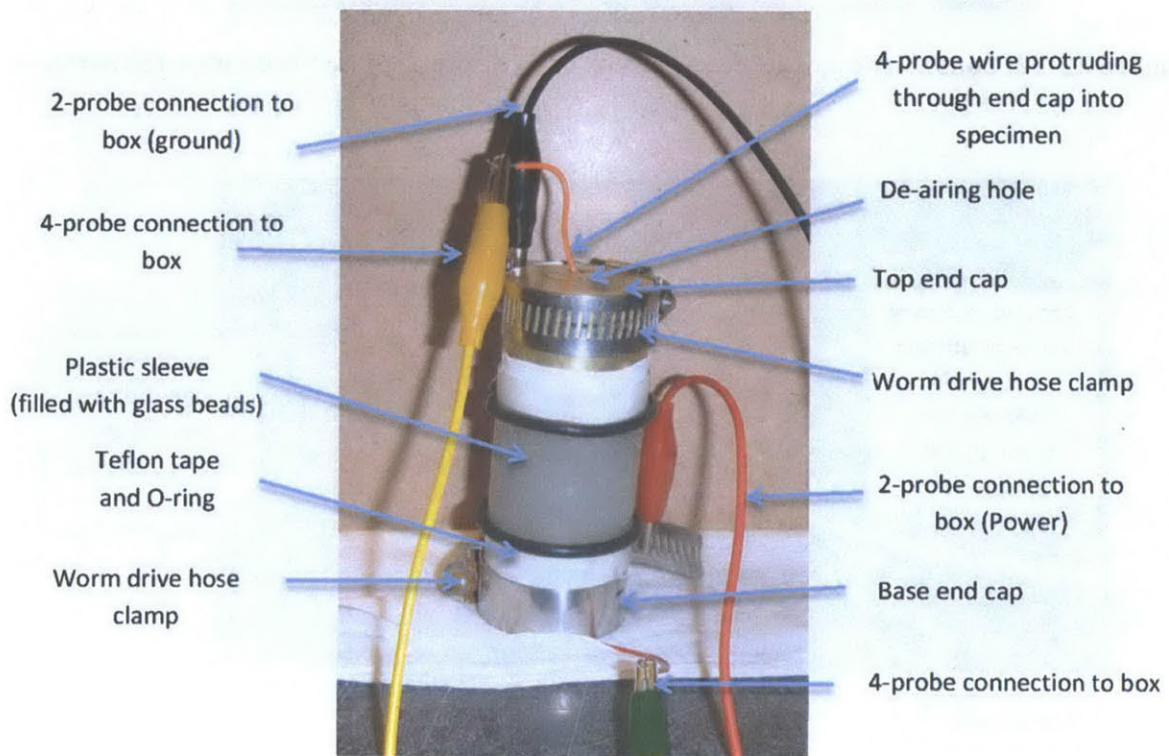


Figure A3-15: Bench top electrode configuration for unconsolidated materials

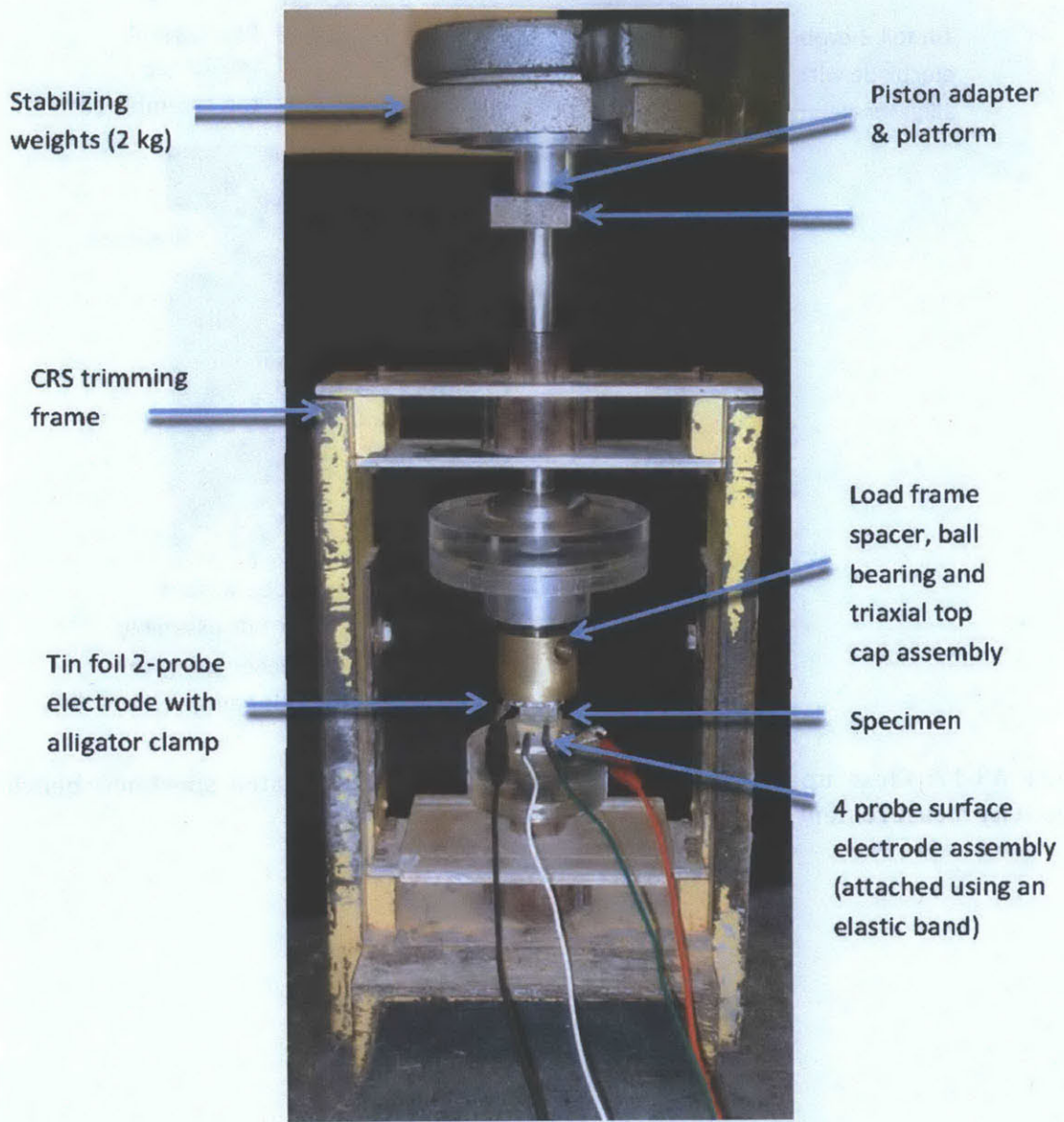


Figure A3-16: Consolidated specimen bench top resistivity measurement configuration

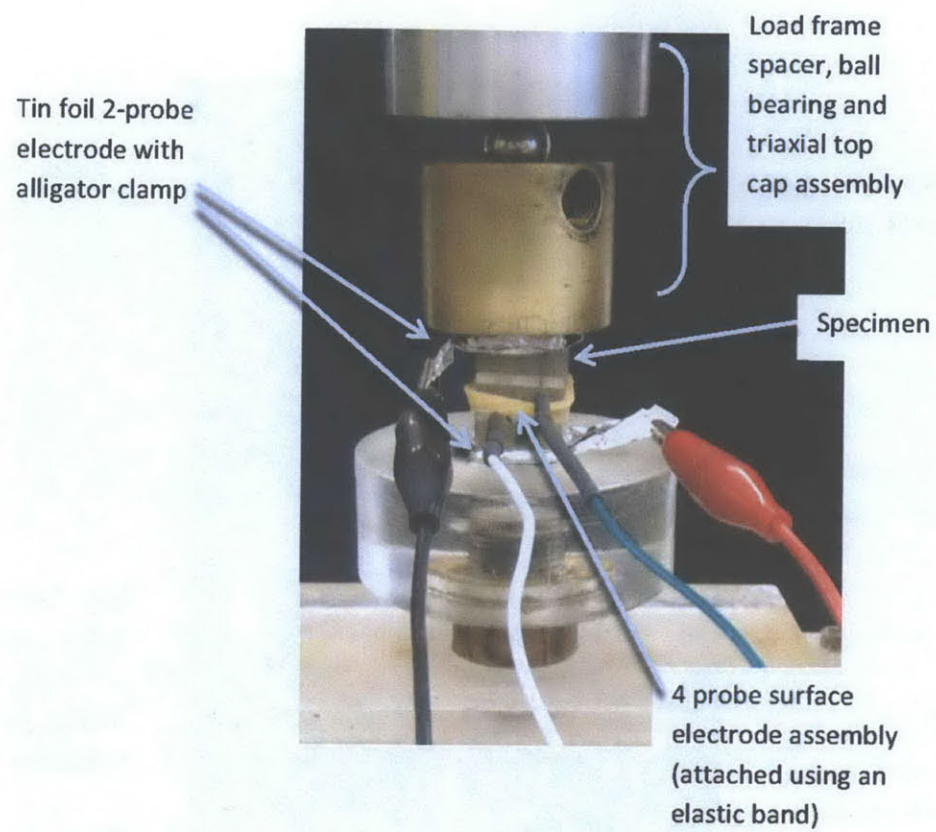


Figure A3-17: Close up of specimen configuration for consolidated specimen bench top resistivity measurement

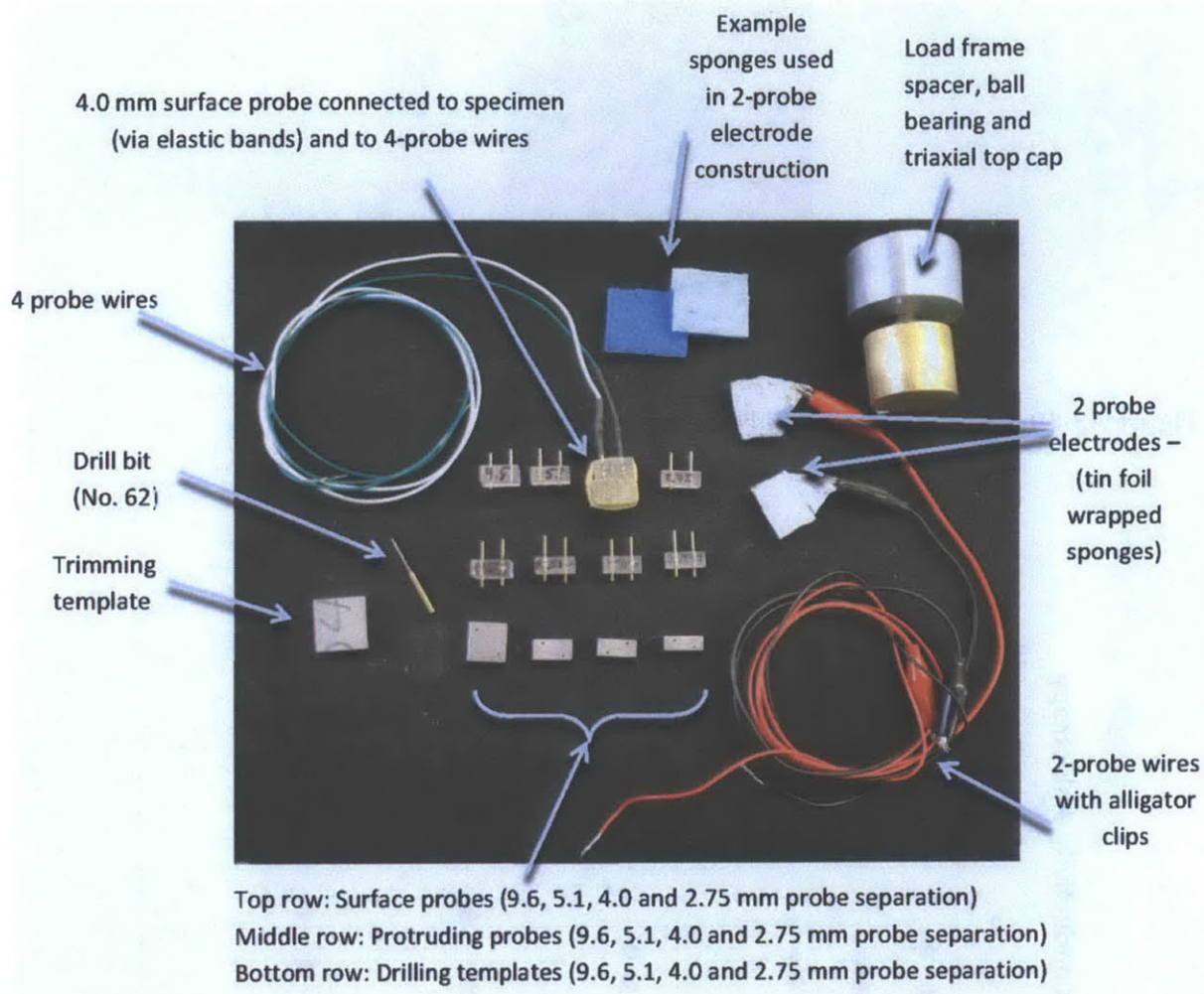


Figure A3-18: Consolidated specimen bench top resistivity electrode equipment



Figure A3-19: CRS specimen cracked during 4-probe pin insertion

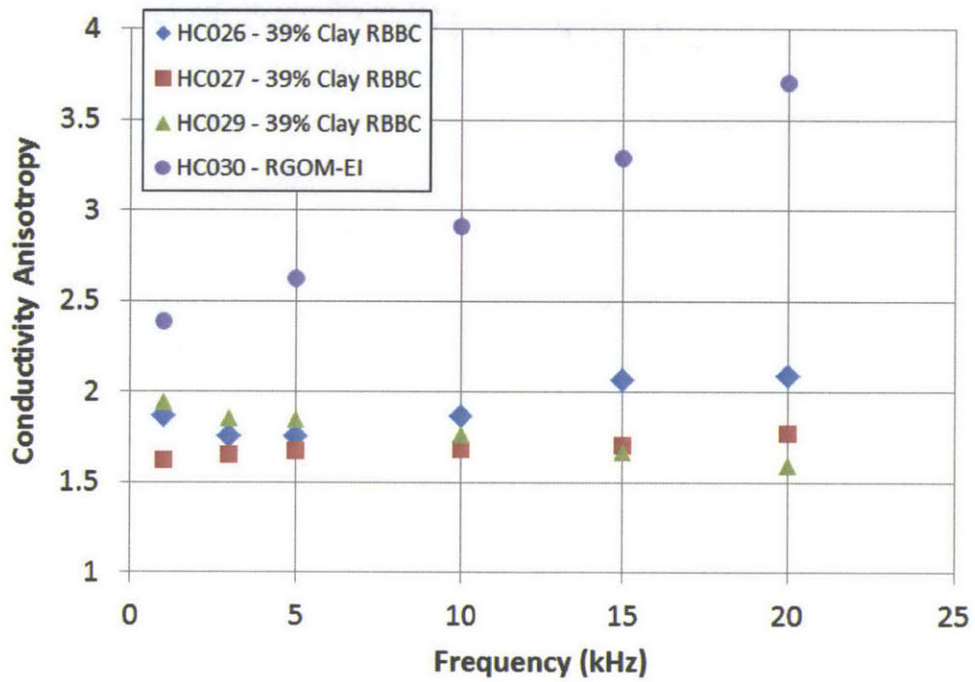


Figure A3-20: Frequency vs. Conductivity Anisotropy for Four Specimens

Appendix 4: Bench Top Resistivity Measurements: Summary of Results

This short report summarizes a number of bench top resistivity measurements that were undertaken by various researchers over the course of two years. Materials tested ranged from saline solutions, to glass beads and sands, to both wet and dry consolidated clay specimens. The purpose of this study was many fold:

- 1) To test the system abilities, troubleshoot the methodology, and define fixed parameters (e.g. reference and drop resistor values) for the resistivity measurement box;
- 2) To measure the resistivity of the specific salt water solutions used in our laboratory. Measuring this relationship is more accurate than using published tables which may be based on a different chemistry;
- 3) To gauge sources of error in the measurement method. Simple materials were measured first, and the complexity of the measurement set up was progressively increased;
- 4) To assess the repeatability of the method;
- 5) To determine the magnitude and significance of surface conductivity and its relationship with grain size and material for non-clayey materials.
- 6) To determine the effects of back pressure, saturation and loading conditions, if any by comparing bench top measurements with triaxial measurements of the same specimen.

The following sections summarize the methods and materials, divided into three key sub projects: saline solutions, sand and glass beads, and consolidated clays. The experiments were performed with the help of Mun Nghah Cheong, a UROP in the MIT Geotechnical Laboratory from September 2012 – May 2013.

Contents

Appendix 4: Bench Top Resistivity Measurements: Summary of Results	461
1 Basic Equations and Concepts.....	463
2 Experimental set up.....	464
3 Saline Solutions	464
4 Glass Beads and Sands.....	465
4.1 Glass Beads.....	465
4.2 Sands.....	466
4.3 Discussion.....	466
5 Mudrocks.....	467

List of Tables

Table A4-1: Saline Solution Mixing Guide	469
Table A4-2: Resistivity of Saline Solutions.....	469
Table A4-3: Summary of Resistivity Measurements on Glass Beads	470
Table A4-4: Resistivity and formation factor as a function of grain size and salinity for glass beads	471
Table A4-5: Resistivity and formation factor as a function of grain size and salinity for sands.....	471
Table A4-6: Comparison between bench top and triaxial cell resistivity measurements.....	472

List of Figures

Figure A4-1: Patnode and Wyllie (1950) Method for determining formation factor (after Huntley, 1986)	473
Figure A4-2: Waxman and Smits (1968) Method for determining intrinsic formation factor (after Waxman and Smits, 1968).....	473
Figure A4-3: Bench top electrode configuration for unconsolidated materials.....	474
Figure A4-4: Example plot of electrical resistivity vs. measurement current for a 1 g/L saline solution.....	474
Figure A4-5: Relationship between electrical resistivity and salinity for sea salt solutions	475
Figure A4-6: Relationship between electrical conductivity and salinity for sea salt solutions	475
Figure A4-7: Formation factor vs. pore fluid conductivity for glass beads	476
Figure A4-8: Formation factor vs. pore fluid conductivity for fine sand	476
Figure A4-9: Formation factor vs. pore fluid conductivity for concrete sand	477
Figure A4-10: Consolidated specimen bench top resistivity measurement configuration	478
Figure A4-11: Close up of specimen configuration for consolidated specimen bench top resistivity measurement	479
Figure A4-12: Flexible wall permeameter with cubic end adapters	480
Figure A4-13: Drawing: Cubic end adapters modified for resistivity measurements	481
Figure A4-14: Comparison of horizontal resistivity, ρ_H , measured using bench top and triaxial cell methods for RBBC.....	482
Figure A4-15: Comparison of vertical resistivity, ρ_V , measured using bench top and triaxial cell methods for RBBC.....	482
Figure A4-16: Comparison of conductivity anisotropy, r_o , measured using bench top and triaxial cell methods for RBBC and Leached RBBC	483

1 Basic Equations and Concepts

The basic resistivity equations are described in detail in Section 2 and Appendix 3. The following is a summary of the relevant equations for this work.

Resistivity (ρ) is the length (L) and area (A) normalized resistance (R) of a material and has units of ohm meters (Ωm):

$$\rho = \frac{RA}{L} \quad \text{A4-1}$$

The inverse of the resistivity is the conductivity (σ) with units of Siemens per meter (S/m):

$$\sigma = \frac{1}{\rho} \quad \text{A4-2}$$

The formation factor normalizes the resistivity by the pore fluid resistivity and allows comparison between mudrocks of varying pore fluid salinity and ionic composition:

$$F = \frac{\rho}{\rho_w} \quad \text{A4-3}$$

Where F is the formation factor, ρ is the resistivity of the mudrock and ρ_w is the resistivity of the pore fluid.

There are two formation factors: the apparent or measured formation factor, and the intrinsic or true formation factor. The apparent formation factor is computed using the measured resistivity and includes all possible conductive pathways through the specimen. The intrinsic formation factor is the corrected or true formation factor and is representative of electrical flow through the fluid filled pores only.

Particle surface conductivity causes the difference between measured and apparent formation factor. At low pore fluid salinities (low pore fluid conductivity), electric current flows dominantly along charged particle surfaces. As the pore fluid salinity increases a higher percentage of electric current flows through the fluid filled pore space - yielding formation factor measurements closer to the intrinsic formation factor.

The intrinsic formation factor is determined by measuring the material at varying pore fluid salinities, or by applying correction factors (discussed in Section 2). There are two key graphical methods presented in the literature that are commonly applied to determine intrinsic formation factor of a granular material, and in turn the degree of surface conductivity: the Patnode and Wyllie (1950) method (Figure A4-1), and the Waxman and Smits (1968) method (Figure A4-2).

In the Patnode and Wyllie (1950) method (Figure A4-1), the apparent formation factor is plotted as a function of pore fluid conductivity. Materials with non-conductive grains (low surface conductivity) will have an apparent formation factor that does not vary with salinity; thus the apparent formation factor is equal to the intrinsic formation factor. More commonly, as the pore fluid salinity increases (conductivity increases), the apparent formation factor will increase and asymptote. Such materials are influenced by a higher particle surface conductivity. In this case, the measured formation factor is equal to the apparent formation factor, and the asymptote is equal to the intrinsic formation factor. In some cases, the measured formation factor at a high pore fluid salinity will be very close to the intrinsic formation factor.

In the Waxman and Smits (1968) method (Figure A4-2), the measured conductivity is plotted as a function of pore fluid conductivity. Materials with non-conductive grains (low surface conductivity) will have a constant slope where the measured conductivity varies linearly with the increasing pore fluid conductivity as the salinity is increased. More commonly the surface conductivity is higher; as the pore fluid salinity increases (conductivity increases), the slope of the line will increase until it becomes constant. The slope increases because as the pore fluid conductivity increases, the cationic mobility increases and the path of least resistance changes through the soil fabric.

Though both methods are applied in the literature, the Waxman and Smits (1968) method requires more data points to ascertain the correct slope. Further, it can be confusing to differentiate between changing formation factor and errors in measurement. The Patnode and Wyllie (1950) method makes the differences between apparent and intrinsic formation factor much more visually evident and easier to interpret.

2 Experimental set up

Various experimental setups were used to measure the resistivity of saline solutions, unconsolidated sediments, and consolidated mudrocks. These experimental setups are described in Appendix 3. The geometry of each set up is designed to provide a uniform current path through the specimen, eliminating the need for complex geometry correction factors that are sometimes discussed in the literature.

3 Saline Solutions

The resistivity of saline solutions was measured using the bench top configuration for unconsolidated specimens, described in Appendix 3 and shown in Figure A3-15. Saline solutions of 1 g/L, 16 g/L and 80 g/L were prepared using the Laboratory Salt mixing guide (described in Section 3). Table A4-1 summarizes the mass of water and mass of sea salt used to mix each solution.

Seven separate saline solutions were mixed: Three 1 g/L, two 16 g/L and two 80 g/L. Multiple measurements with an applied current varying from 1.5 up to 10 mA were made (> 9) to determine the resistivity of each saline solution. Figure A4-4 gives a typical plot of resistivity vs. measurement

current for a 1 g/L saline solution; no trend in resistivity with current was noted. The coefficient of variation in measured resistivity for a single measurement set up ranged from 1 to 3 %. Table A4-2 summarizes the measured resistivity results. The results show excellent repeatability with a low standard deviation across multiple setups (different specimens).

Figure A4-5 plots the results in terms of resistivity, and Figure A4-6 in terms of conductivity. The resistivity of the sea salt water in the MIT Geotechnical Laboratory is given by:

$$\text{Log}(\rho) = 0.9221 \text{Log}(S) + 0.7914 \quad \text{A4-4}$$

And the conductivity by:

$$\text{Log}(\sigma) = 0.9221 \text{Log}(S) - 0.7914 \quad \text{A4-5}$$

Where ρ is the resistivity in Ωm , σ is the conductivity in S/m, and S is the solution salinity in g/L.

4 Glass Beads and Sands

The resistivity of glass beads and clay -free sands was measured using the bench top method for unconsolidated specimens (Figure A3-15) to determine the effect of grain size on formation factor, as well as the effect of salinity on the measurement.

4.1 Glass Beads

Three sizes of glass beads were measured:

- 1) #4 - #10 - Those beads passing the #4 sieve and retained on the #10 sieve
- 2) #20 to #40 - Those beads passing the #20 sieve and retained on the #40 sieve
- 3) < #100 - those beads passing the # 100 sieve.

Measurements were conducted at three salinities: 1 g/L, 16 g/L and 80 g/L. These salinities were selected to be reflective of the range of common working mudrock salinity in the MIT Geotechnical Laboratory.

Table A4-3 summarizes the resistivity measurements on glass beads. In total, 20 different specimens were constructed and measured with varying salinity and grain size. The porosity varied only slightly with grain size. The resistivity varied slightly, with the 1 g/L specimens being the most resistive. The coefficient of variation ranged from 1% to 13% and was highest for the 80 g/L specimens. Table A4-4 summaries the average resistivity and porosity of all measurements with the same salinity and grain size and the computed formation factor. The formation factor was computed using the pore fluid resistivity from Section 3 (eq. A4-4)

The formation factor is plotted vs. the pore fluid conductivity (determined using eq. A4-5) as a function of size, applying the Patnode and Wyllie (1950) method. In this case, the formation factors measured at a pore fluid salinity of 80 g/L are very close to the intrinsic formation factor.

4.2 Sands

The resistivity of a total of twelve specimens of sand was measured. Two different types of sand were investigated, each with two different grain sizes:

- 1) Fine sand
 - a. #10- #20: Those grains passing the #10 sieve but retained on the #20 sieve
 - b. #20- #40: Those grains passing the #20 sieve but retained on the #40 sieve
- 2) Concrete Sand
 - a. #4 - #10: Those grains passing the #4 sieve but retained on the #10 sieve
 - b. #10- #20: Those grains passing the #10 sieve but retained on the #20 sieve

Specific properties of the sands (grain size, uniformity, particle angularity) are unavailable. One specimen of size of each type of sand was prepared for the three different pore fluid salinities: 1 g/L, 16 g/L and 80 g/L. Table A4-5 summaries the porosity, resistivity and formation factor measurements for the sand and concrete sand.

For the fine sand, the porosity does not vary as a function of grain size. For the concrete sand, the porosity of the larger grain size (#4-#10) was slightly larger (0.03) than that of the smaller grain size.

The variation in formation factor with increasing pore fluid conductivity (after the Patnode and Wyllie, 1950) method is plotted in Figure A4-8 for fine sand and in Figure A4-9 for concrete sand.

4.3 Discussion

Interestingly, there is no consistent trend in formation factor with increasing pore fluid conductivity, as suggested by Patnode and Wyllie (1950, Huntley, 1986), or with increasing grain size, as suggested by Huntley, 1986.

The glass beads (Figure A4-7) exhibit the expected behavior (shown in Figure A4-1), with the formation factor increasing with increasing pore fluid conductivity, eventually forming an asymptote. For the glass beads, the highest formation factor measured, corresponding to the specimen with a pore fluid salinity of 80 g/L, is roughly equal to the asymptote value suggested as the intrinsic formation factor. There does not seem to be any trend between intrinsic formation factor and increasing grain size for the glass beads. The excellent repeatability of the measurements (shown in Table A4-3) suggests that this finding is not the result of experimental error. Further, some of the repeated measurements in were carried out with weeks or even months' time separation and every effort was made to minimize errors associated with the method.

The expected behavior given in Figure A4-1 is not seen for the sand specimens. The concrete sand results show that the formation factor varies only slightly (0.2) with increasing pore fluid conductivity. This indicates that the measured formation factor is very close to the intrinsic formation factor regardless of pore fluid salinity. Surface conductivity is therefore not as important for the concrete sand as it is for the glass beads.

Finally, the sand specimen behavior is the most unexpected. The smallest grain size measured (#20 to #40) behaves similarly to the concrete sand, exhibiting only a slight increase in formation factor (0.3) with increasing pore fluid conductivity and salinity. However, the largest grain size measured (#10 to #20) exhibits behavior more similar to the glass beads, with the formation factor increasing significantly as the pore fluid salinity is increased from 1 g/L to 80 g/L. These results suggest that the behavior of the sand is grain size dependent, with smaller grains having a lower surface conductivity and larger grains having a higher surface conductivity. This experiment was not repeated; therefore this could be the result of an experimental error, or may be due to size dependent mineralogy variations.

Overall, these results indicate that surface conductivity is not negligible, even for materials with non-conductive grains such as glass beads and clean sands.

5 Mudrocks

The resistivity of mudrocks was measured using the bench top method for consolidated specimens shown in Figure A3-16 and Figure A3-17 and described in Appendix 3.

The directional resistivity of eight RBBC specimens and two leached RBBC specimens was measured using bench top methods. The resistivity was measured using protruding pin electrodes for soft mudrock specimens, and using surface contact pin electrodes for dense specimens to avoid issues associated with cracking.

The directional resistivity of the same specimens was also measured in the flexible wall permeameter using the cubic resistivity end adapters (shown in Figure A3-10 and Figure A3-11). This method is referred to as the triaxial cell method. Table A4-6 summarizes the bench top and triaxial cell resistivity measurements for these 10 specimens.

One specimen of RBBC (HC044) was measured using the bench top method by two different users using two different versions of the bench top resistivity electrodes – surface and protruding. These variations in measurement parameters resulted in different vertical and horizontal resistivity, and slightly different conductivity anisotropy (1.28 vs. 1.52). This variability illustrates the increased susceptibility of the bench top method to problems with electrical contacts, variations in temperature and changing resistivity due to specimen drying as compared to the triaxial measurement method.

Figure A4-14 and Figure A4-15 compare the horizontal and vertical resistivity measured using the bench top and triaxial measurement methods for RBBC. These figures illustrate that the resistivity measured using the bench top measurement method is consistently higher, on average by 20 – 30%, than that measured in the triaxial cell. As suggested above, differences in specimen temperature or specimen saturation may account for some of this variation. The leached RBBC results are not included in this plot because the resistivity is significantly higher than that of RBBC and there is significantly more variation in the results between measurement methods.

Figure A4-16 compares the conductivity anisotropy measured using the bench top and triaxial measurement methods for RBBC and Leached RBBC. Despite some scatter in individual specimens, on average across 10 specimens the conductivity anisotropy measured using the two methods is the same. The difference in conductivity anisotropy for individual specimens is in the second or third significant digit. The largest variation in conductivity anisotropy measured using the two methods is 0.6 with the bench top method predicting the higher conductivity anisotropy.

Bench top measurements are tricky to set up, but once set up, are significantly quicker to perform than measurements in the triaxial cell. These results indicate that the conductivity anisotropy measured using the bench top method is representative of the specimen. However, the measured resistivity varies based on a number of factors and should not be used except to calculate the conductivity anisotropy. There is significantly more error incorporated into the bench top resistivity measurements compared to the triaxial resistivity measurements. Sources of error include specimen drying during measurement, variations in temperature, the increased influence of length and area measurement errors due to the small specimen size, non-uniform electrical fields due to imperfect specimen shape that are amplified by small specimen size, and poor electrical contacts. These sources of error are isotropic; this fact is highlighted by the agreement between the conductivity anisotropy measured using the bench top and triaxial methods and the disagreement in the resistivity measured using these two methods.

Table A4-1: Saline Solution Mixing Guide

Solution Salinity (g/L)	Mass of Sea Salt (g)	Mass of Distilled Water (20°C) (g)
1	1	997.96
16	16	994.26
80	80	976.25

Table A4-2: Resistivity of Saline Solutions

Salinity	Measured Resistivity (Ωm)		
	1 g/L	16 g/L	80 g/L
Solution 1	6.21	0.47	0.11
Solution 2	6.39	0.46	0.11
Solution 3	6.21	--	--
Average	6.27	0.46	0.11
Standard Deviation	0.10	0.01	0.00
Coefficient of Variation	1.6%	2.2%	0.0%

Table A4-3: Summary of Resistivity Measurements on Glass Beads

Size	Salinity (g/L)	Porosity	Resistivity, ρ (Ωm)			
			Measured	Average	Standard Deviation	Coefficient of Variation
#4 to #10	1	0.39	22.56	22.90	0.34	1.5%
	1	0.40	23.24			
	1	0.40	22.91			
	16	0.40	1.78	1.75	0.03	1.6%
	16	0.39	1.75			
	16	0.40	1.73			
	80	0.40	0.44	0.43	0.02	3.7%
	80	0.41	0.42			
#20 to #40	1	0.38	24.11	24.49	1.14	4.7%
	1	0.37	25.77			
	1	0.37	23.58			
	16	0.37	1.93	1.93	N/A	
	80	0.38	0.41	0.45	0.03	7.4%
	80	0.37	0.48			
	80	0.38	0.45			
less than #100	1	0.39	18.60	18.60	N/A	
	16	0.39	1.83	1.83	N/A	
	80	0.40	0.37	0.41	0.05	13.3%
	80	0.38	0.44			

Table A4-4: Resistivity and formation factor as a function of grain size and salinity for glass beads

Material	Size	Salinity, S	Porosity, n	Pore Fluid Resistivity, ρ_w	Measured Resistivity, ρ	Formation Factor, F
		g/L		Ωm	Ωm	
Glass Beads	#4 to #10	1	0.40	6.27	22.90	3.65
		16	0.40	0.46	1.75	3.79
		80	0.40	0.11	0.43	3.83
	#20 to #40	1	0.37	6.27	24.49	3.91
		16	0.37	0.46	1.93	4.17
		80	0.37	0.11	0.48	4.30
	less than #100	1	0.39	6.27	18.60	2.97
		16	0.39	0.46	1.83	3.95
		80	0.38	0.11	0.44	3.98

Table A4-5: Resistivity and formation factor as a function of grain size and salinity for sands

Material	Size	Salinity, S	Porosity, n	Pore Fluid Resistivity, ρ_w	Measured Resistivity, ρ	Formation Factor, F
		g/L		Ωm	Ωm	
Sand	#10 to #20	1	0.42	6.27	14.36	2.29
		16	0.42	0.46	1.84	3.97
		80	0.42	0.11	0.42	3.74
	#20 to #40	1	0.42	6.27	23.62	3.77
		16	0.42	0.46	1.75	3.78
		80	0.41	0.11	0.46	4.13
Concrete Sand	#4 to #10	1	0.47	6.27	22.72	3.62
		16	0.47	0.46	1.65	3.57
		80	0.45	0.11	0.42	3.77
	#10 to #20	1	0.44	6.27	23.20	3.70
		16	0.44	0.46	1.66	3.59
		80	0.44	0.11	0.42	3.79

Table A4-6: Comparison between bench top and triaxial cell resistivity measurements

Specimen ID	Material	User	Method	Bench top Measurements						Triaxial Cell Measurements					
				ρ_H		ρ_V		r_G		ρ_H		ρ_V		r_G	
				Avg. Ωm	Stdev. Ωm	Avg. Ωm	Stdev. Ωm	Avg. Ωm	Stdev. Ωm	Avg. Ωm	Stdev. Ωm	Avg. Ωm	Stdev. Ωm	Avg. Ωm	Stdev. Ωm
HC045	Leached RBBC	Amy	Surface	20.39	0.08	48.75	0.27	2.39	18.27	0.30	44.45	0.00	2.43	0.04	
HC047	Leached RBBC	Amy	Protruding	13.80	0.03	19.05	0.11	1.38	30.14	0.00	36.84	0.36	1.22	0.03	
HC036	RBBC	Amy	Surface	1.78	0.01	3.03	0.02	1.70	1.67	0.11	2.93	0.23	1.76	0.13	
HC037	RBBC	Amy	Surface	1.86	0.01	4.24	0.06	2.28	1.86	0.07	3.01	0.16	1.62	0.10	
HC038	RBBC	Amy	Surface	1.57	0.01	3.25	0.08	2.07	1.09	0.06	1.61	0.04	1.47	0.08	
HC040	RBBC	Amy	Surface	4.00	0.03	3.53	0.12	0.88	2.78	0.01	3.70	0.03	1.33	0.01	
HC044	RBBC	Amy	Surface	3.70	0.03	4.75	0.14	1.28	2.37	0.01	3.61	0.01	1.52	0.01	
HC044	RBBC	Mun	Protruding	2.84	0.10	4.32	0.06	1.52	2.37	0.01	3.61	0.01	1.52	0.01	
HC048	RBBC	Mun	Protruding	1.72	0.04	3.08	0.06	1.80	1.42	0.03	2.68	0.03	1.89	0.04	
HC049	RBBC	Amy	Protruding	1.94	0.01	3.77	0.03	1.94	1.73	0.02	3.17	0.03	1.83	0.03	
HC050	RBBC	Amy	Surface	1.62		2.51	0.04	1.55	1.59	0.02	2.81	0.04	1.76	0.03	

Notes:

- 1) All TX Measurements are adjusted for measurement sequence bias using either the global specimen or single specimen adjustment methods
- 2) Pertinent specimen data including maximum effective stress and porosity can be found in Chapter 5.

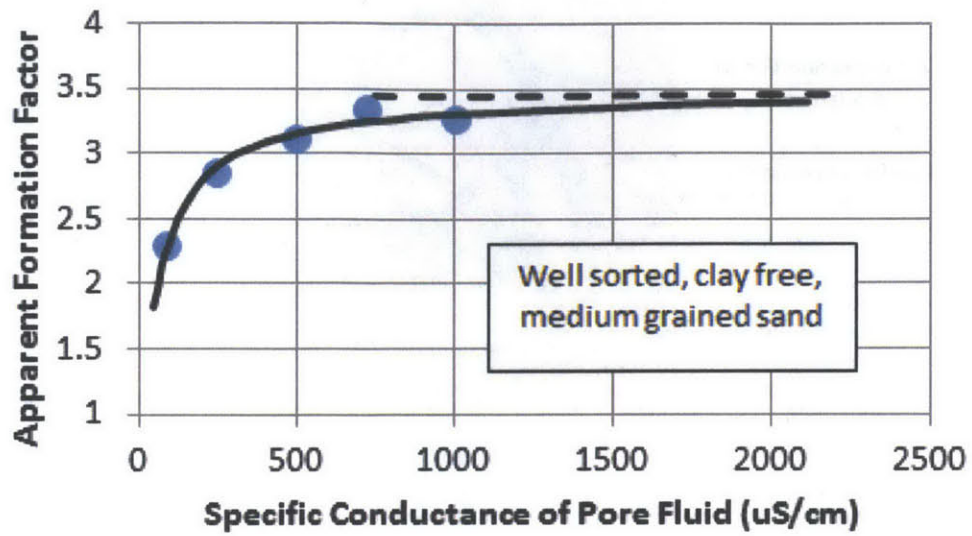


Figure A4-1: Patnode and Wyllie (1950) Method for determining formation factor (after Huntley, 1986)

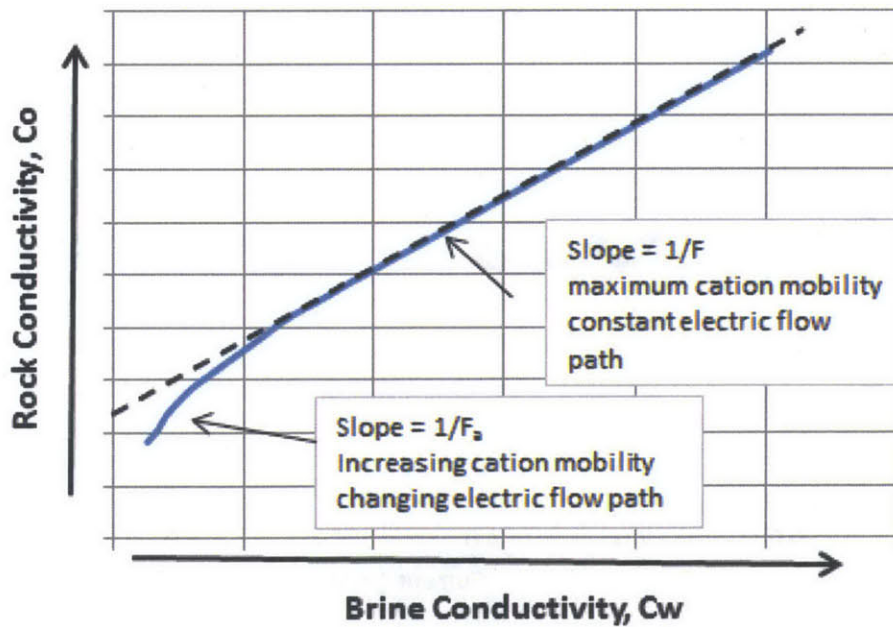


Figure A4-2: Waxman and Smits (1968) Method for determining intrinsic formation factor (after Waxman and Smits, 1968)

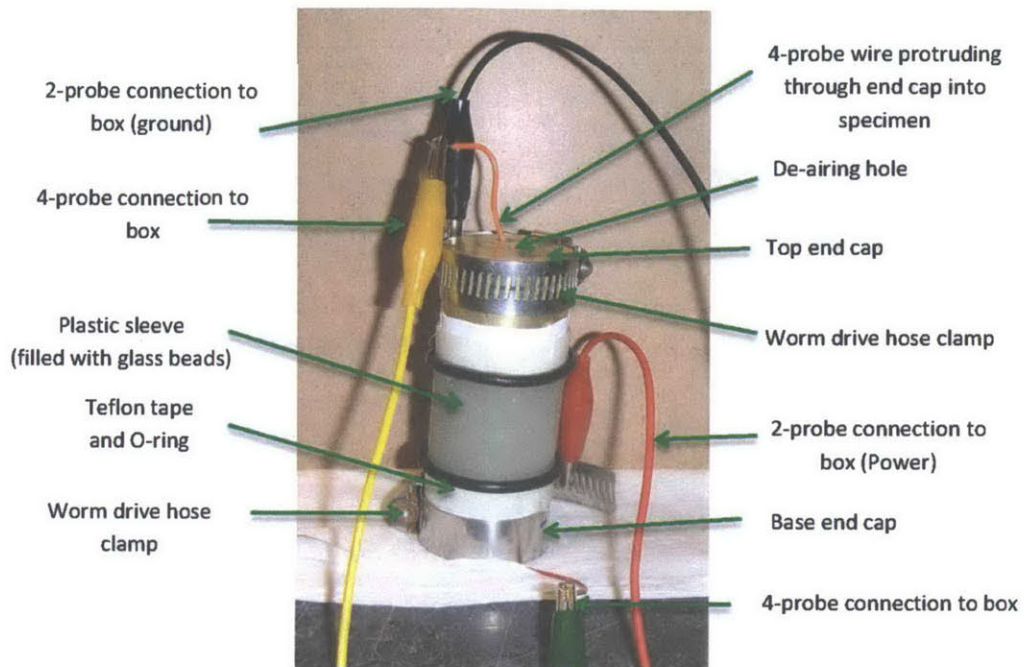


Figure A4-3: Bench top electrode configuration for unconsolidated materials

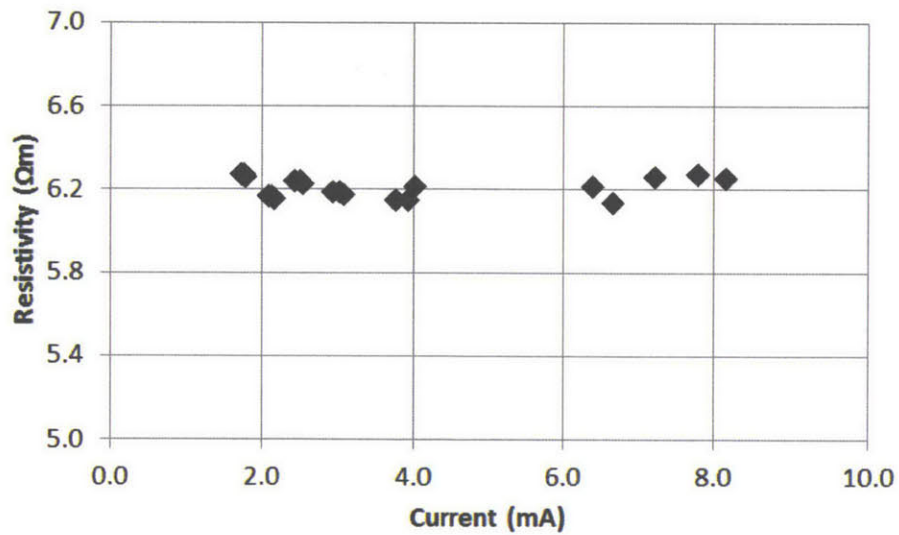


Figure A4-4: Example plot of electrical resistivity vs. measurement current for a 1 g/L saline solution

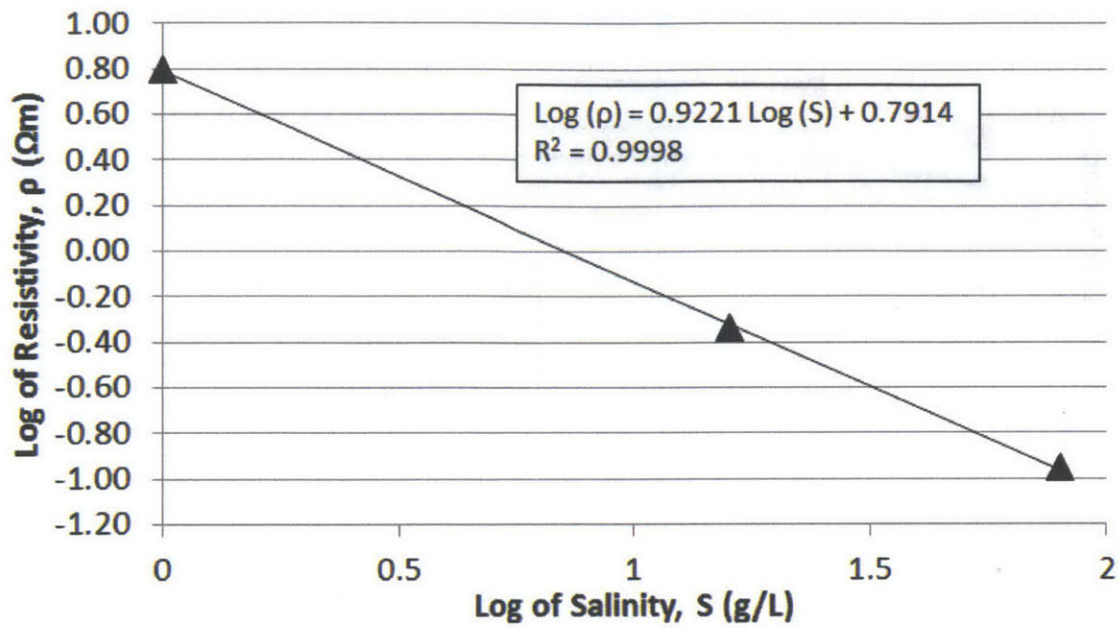


Figure A4-5: Relationship between electrical resistivity and salinity for sea salt solutions

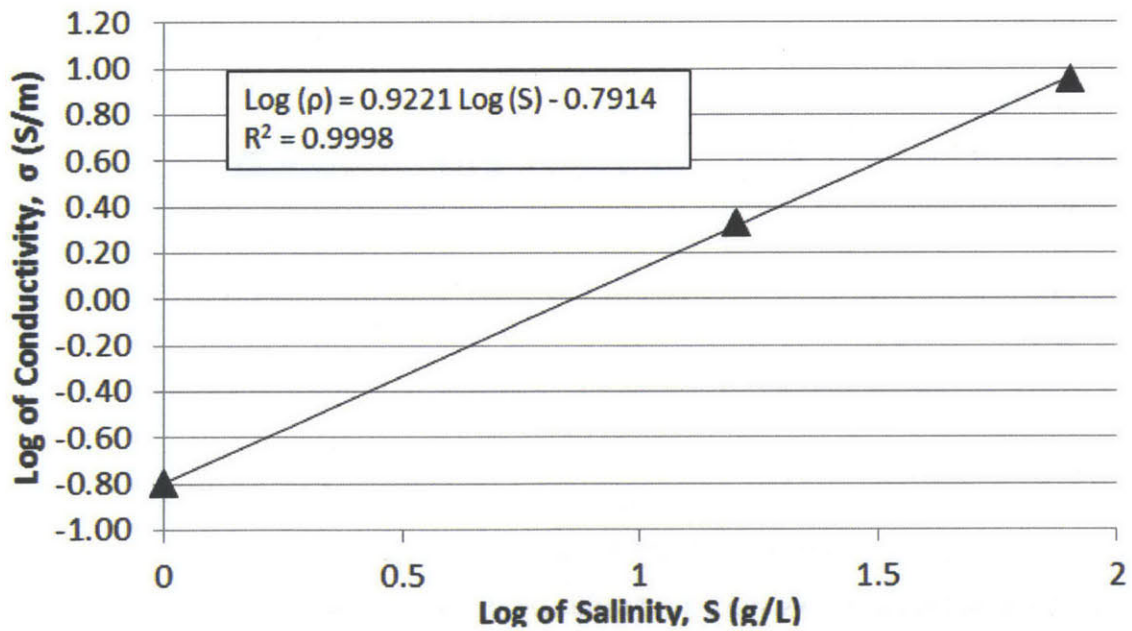


Figure A4-6: Relationship between electrical conductivity and salinity for sea salt solutions

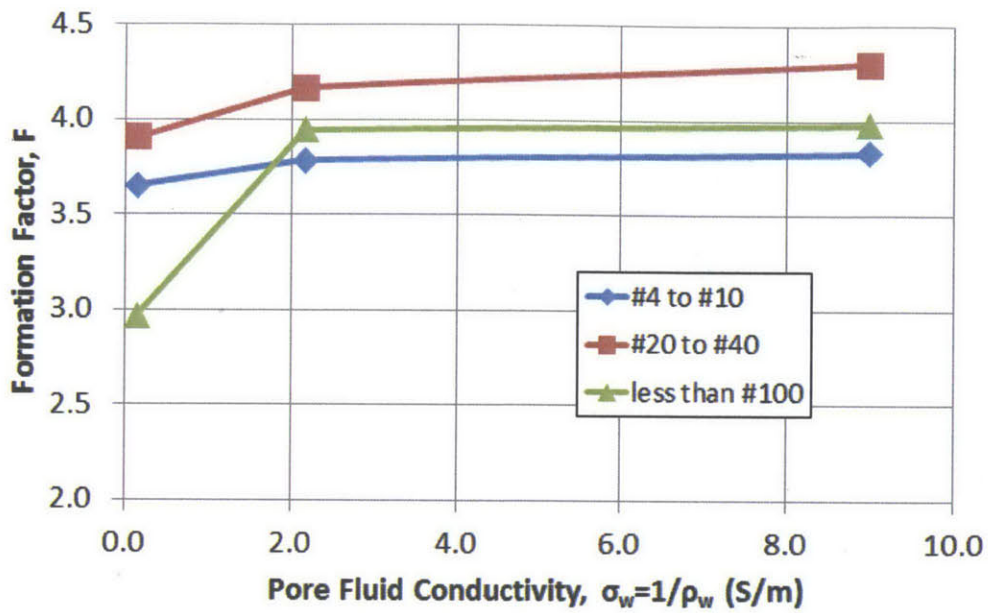


Figure A4-7: Formation factor vs. pore fluid conductivity for glass beads

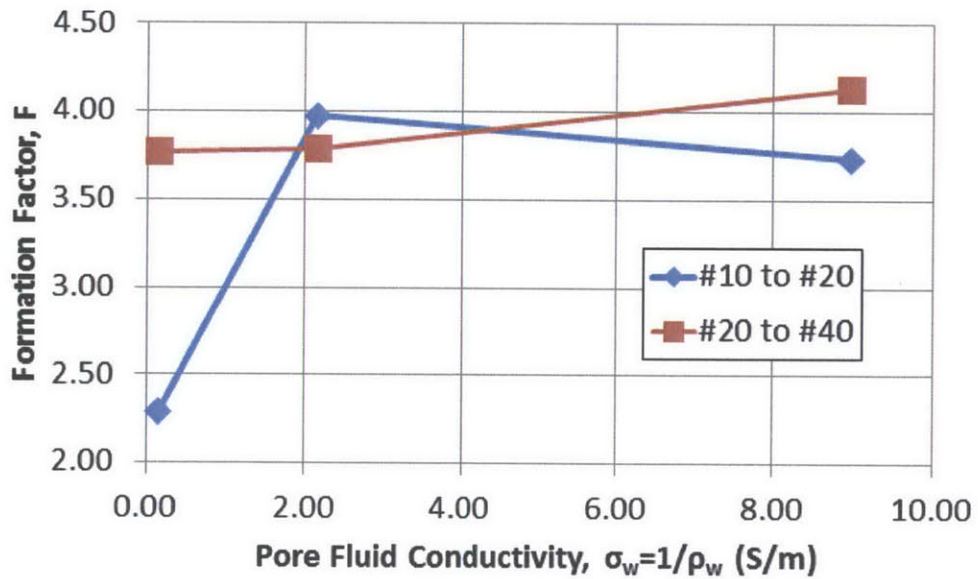


Figure A4-8: Formation factor vs. pore fluid conductivity for fine sand

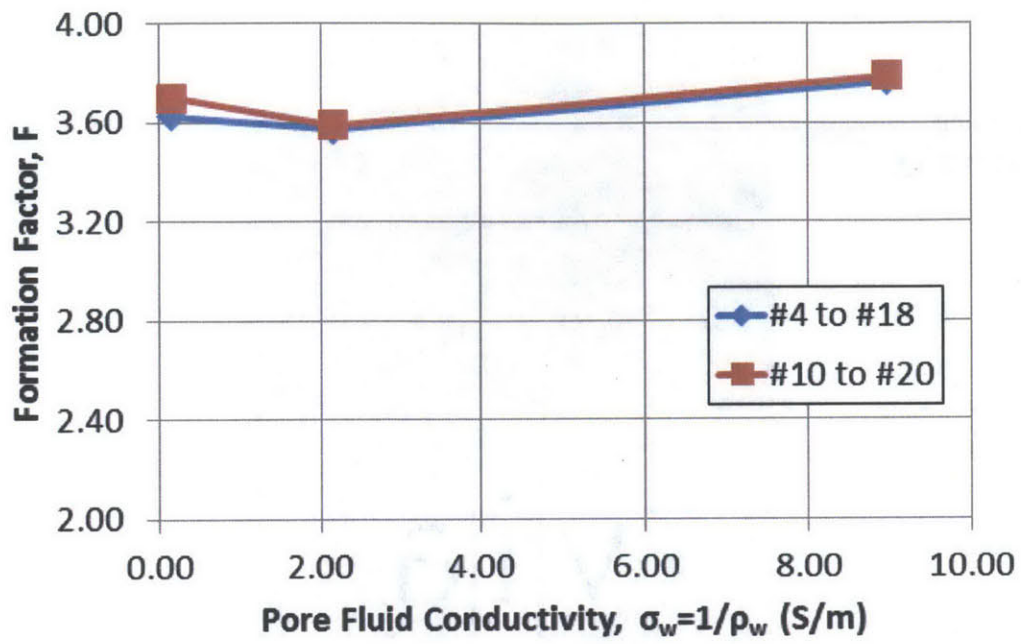


Figure A4-9: Formation factor vs. pore fluid conductivity for concrete sand

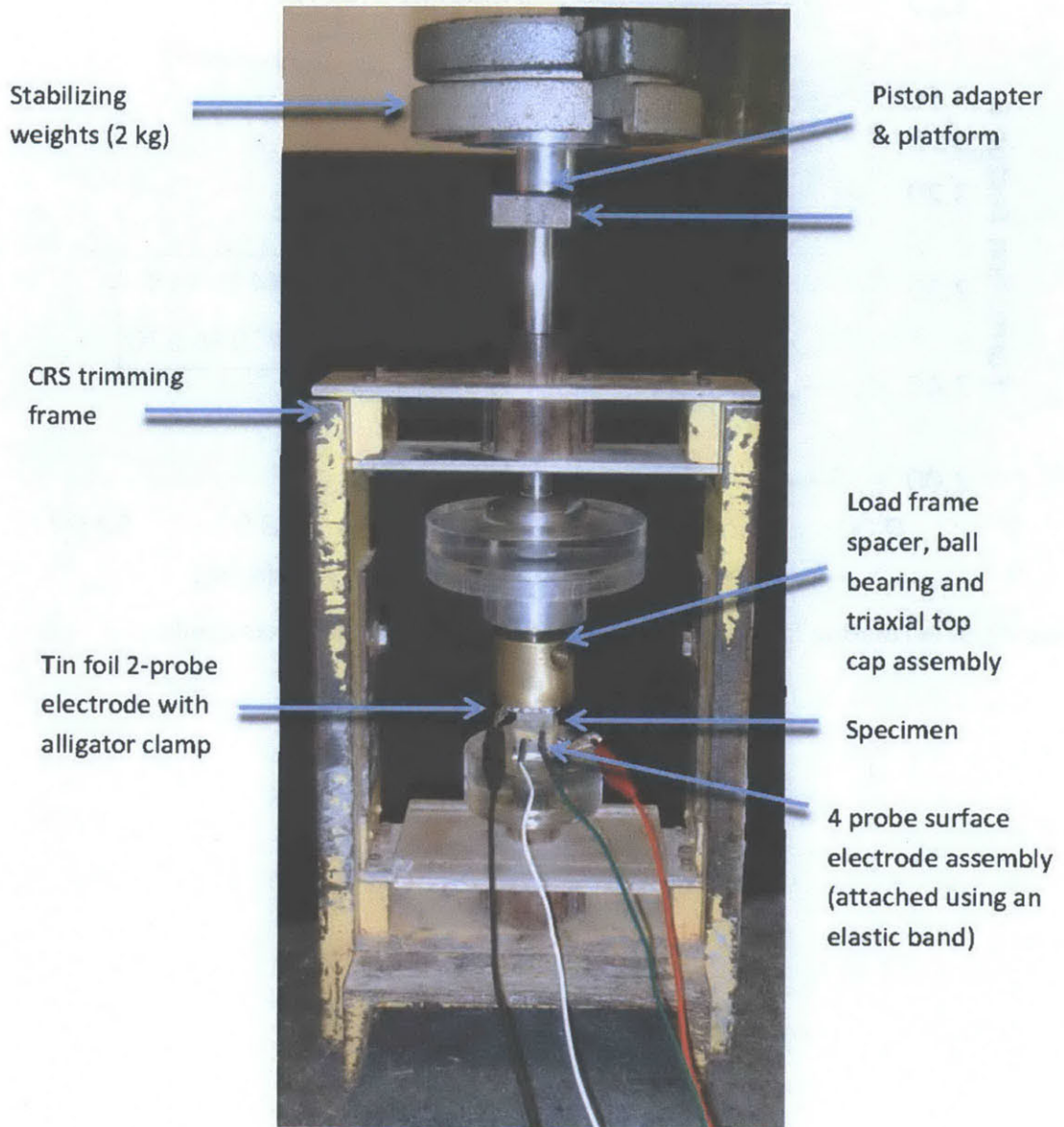


Figure A4-10: Consolidated specimen bench top resistivity measurement configuration

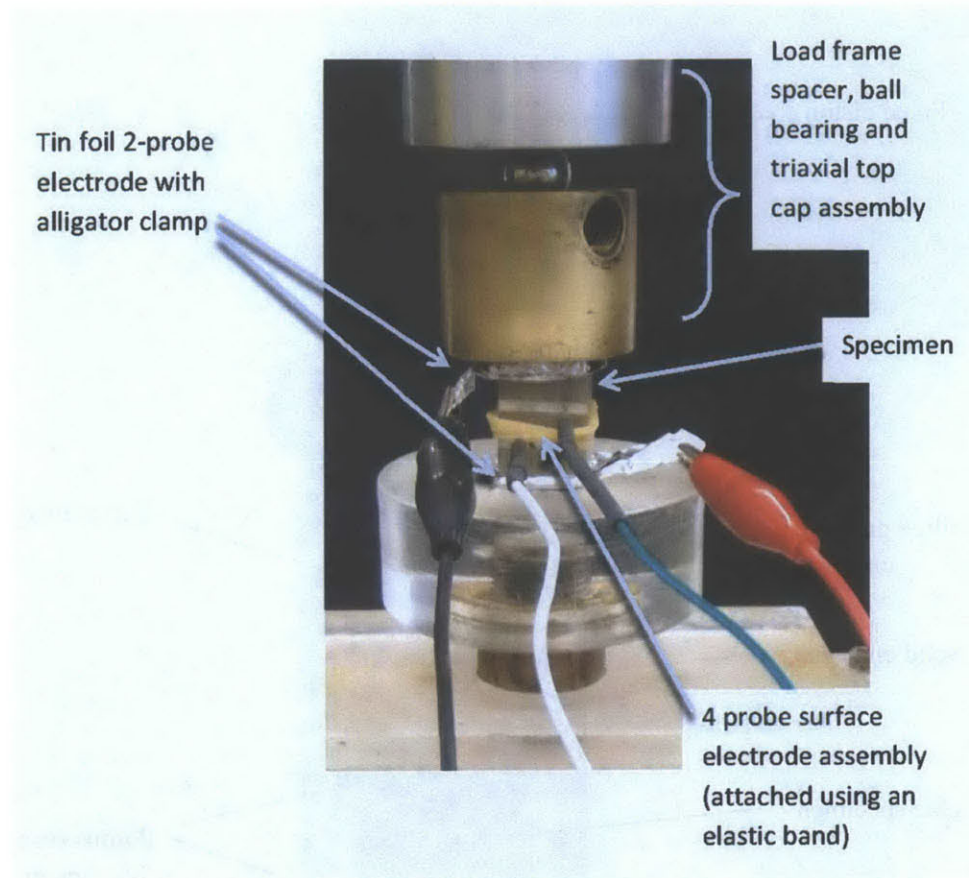


Figure A4-11: Close up of specimen configuration for consolidated specimen bench top resistivity measurement

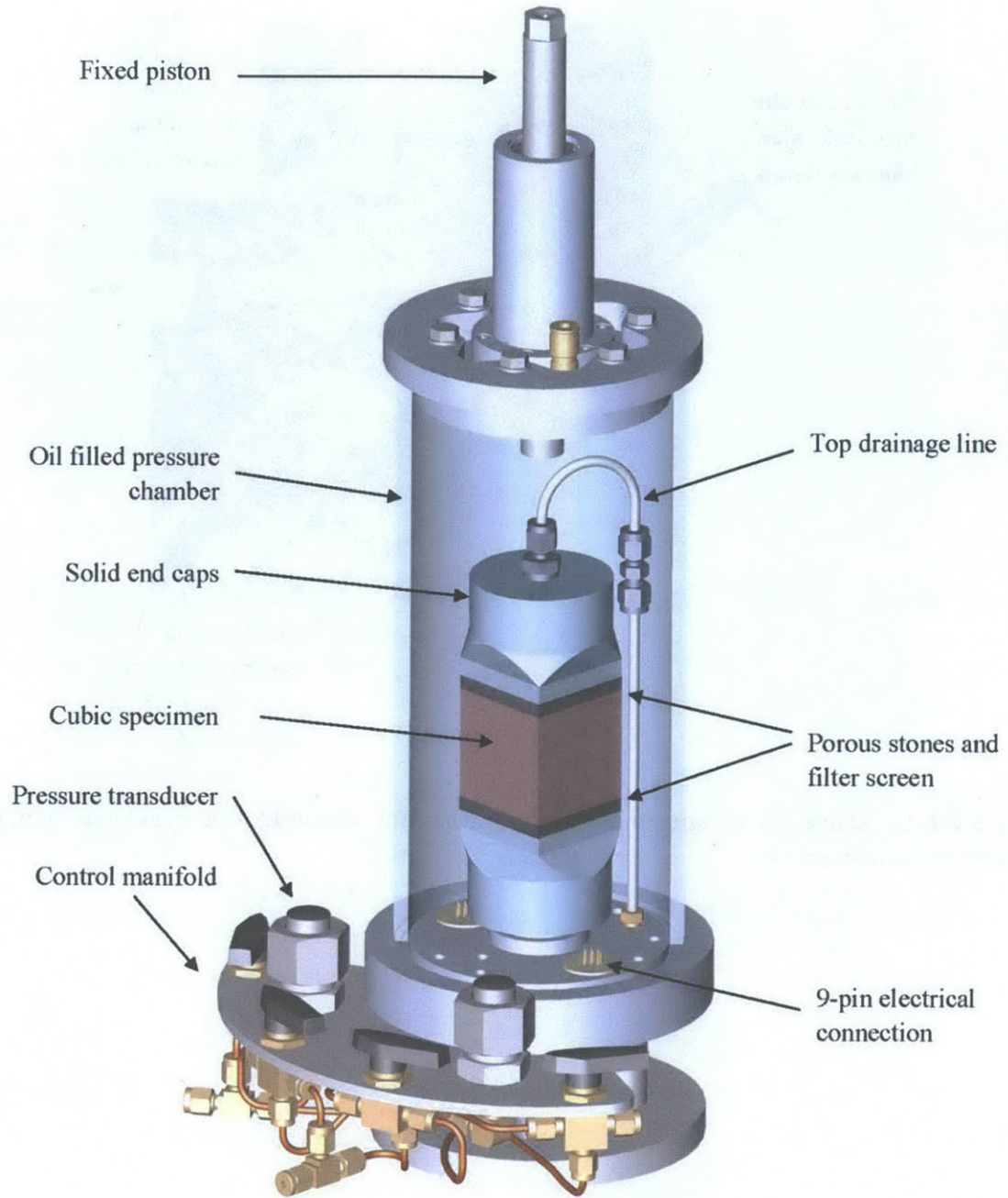


Figure A4-12: Flexible wall permeameter with cubic end adapters

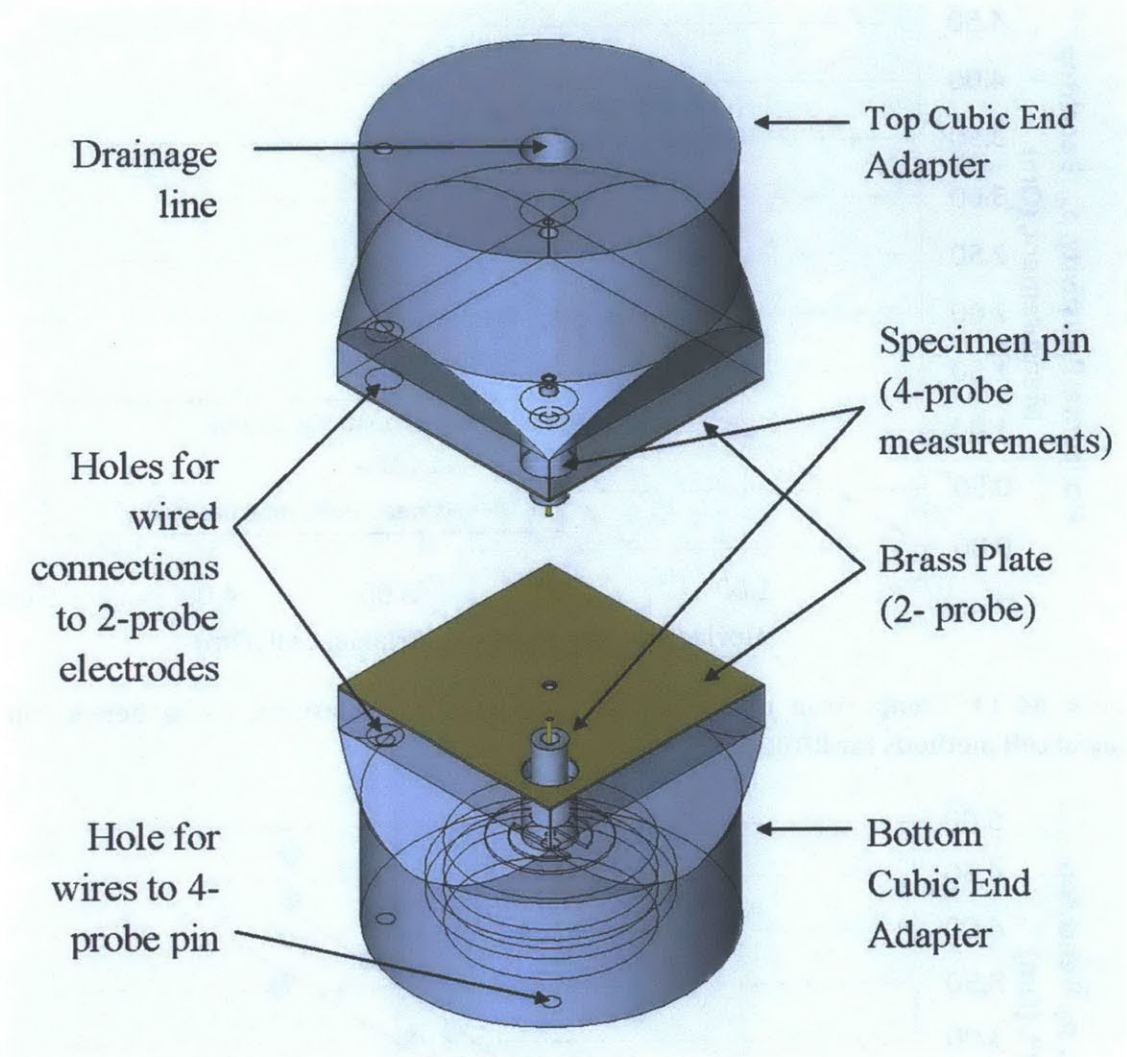


Figure A4-13: Drawing: Cubic end adapters modified for resistivity measurements

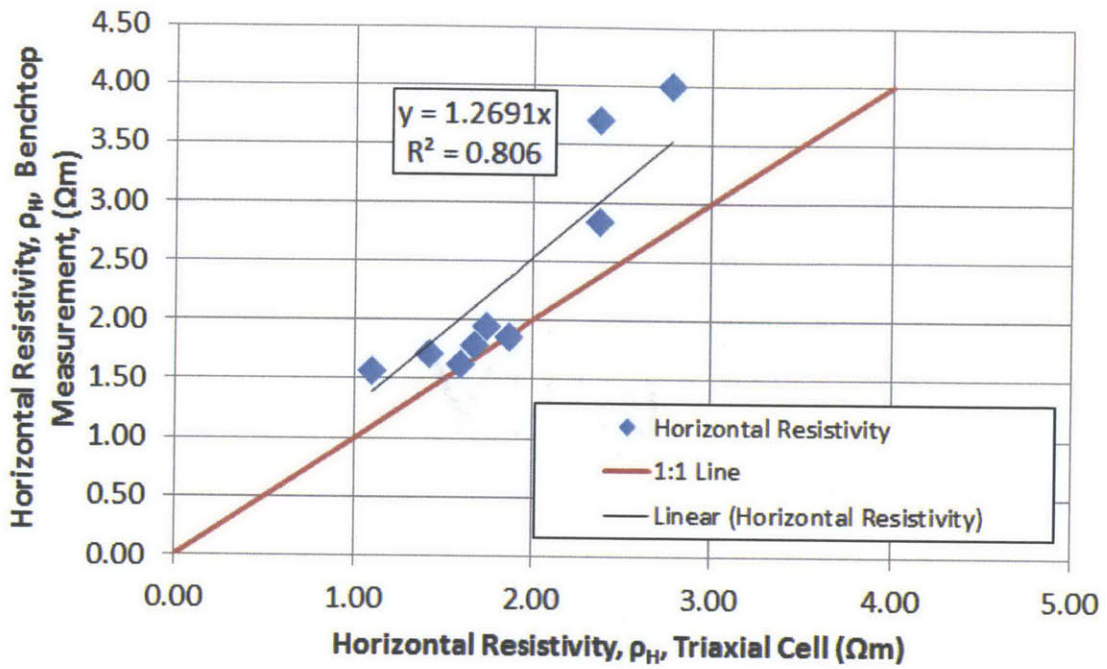


Figure A4-14: Comparison of horizontal resistivity, ρ_H , measured using bench top and triaxial cell methods for RBBC

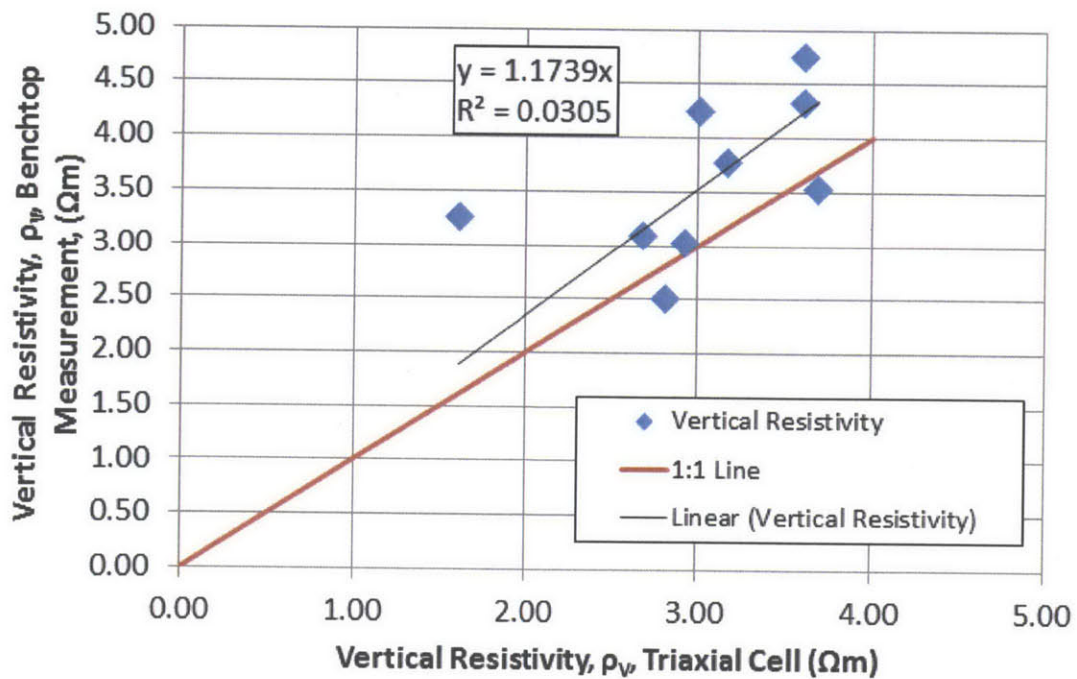


Figure A4-15: Comparison of vertical resistivity, ρ_V , measured using bench top and triaxial cell methods for RBBC

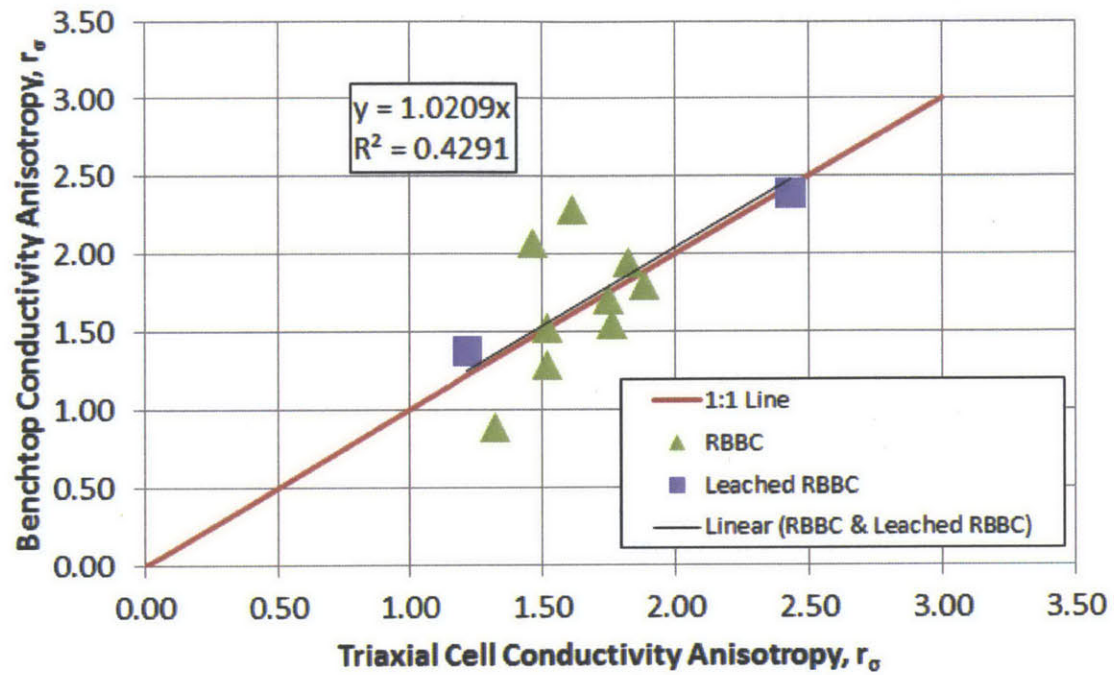


Figure A4-16: Comparison of conductivity anisotropy, r_{σ} , measured using bench top and triaxial cell methods for RBBC and Leached RBBC

(Page intentionally left blank)

Appendix 5: Cation Exchange Capacity (CEC) and Specific Surface Area (SSA) Analysis

This appendix summarizes the methods and results of Cation Exchange Capacity (CEC) and Specific Surface Area (SSA) analysis for Boston Blue Clay (BBC), San Francisco Bay Mud (SFBM) and Gulf of Mexico Clay from the Eugene Island Block (GoM-EI).

Contents

Appendix 5: Cation Exchange Capacity (CEC) and Specific Surface Area (SSA) Analysis.....	485
1 Cation Exchange Capacity	486
2 Specific Surface Area	486
2.1 External SSA - BET Method	486
2.2 Total SSA – Methylene Blue (MB) Spot Test Method.....	486
2.3 Comparison of methods.....	489
3 Results	490
4 Cation Exchange Capacity - Relevant Emails:	491
5 Micromeritics SSA Reports	493

List of Tables

Table A5-1 – CEC results.....	490
Table A5-2- SSA Results.....	490

List of Figures

Figure A5-1: Increments 1 – 10 of GoM-EI MB spot test (no halo, no end point).....	488
Figure A5-2: Increment 11 of GoM-EI MB spot test showing formation of halo that remains with time.....	489

1 Cation Exchange Capacity

Cation Exchange Capacity (CEC) analysis was performed by Dr. Ross Giese at the University at Buffalo, SUNY. The CEC analysis reports are included in Section 4.

The CEC was measured using a copper saturation technique. The oven dried powdered sample is exposed to a Cu-complex in aqueous solution. The sample normally is 100 mg. The Cu-complex is strongly adsorbed to cationic sites on the sample. The amount of copper in the solution before exposure is known. The amount of copper remaining following exposure is determined via a spectroscopic measurement. The difference gives the CEC (Bergaya and Vayer, 1997; see Section 4).

2 Specific Surface Area

The Specific Surface Area (SSA) was measured using two different methods. The external SSA was measured by Micromeritics using the BET method (Brunauer et al, 1938). The total SSA was measured in house using the Methylene Blue drop test method (adapted from Santamarina, 2002). The internal SSA is computed as the difference between the total SSA and the external SSA (Cerato, 2001).

2.1 External SSA - BET Method

The external SSA was measured on 1 g samples of oven dried clay powder by Micromeritics using the Brunauer, Emmett and Teller (BET) surface area method. This method, based on work by Brunauer et al (1938), measures the adsorption of gas (N₂) molecules onto the external surfaces of the soil particles. The N₂ molecules are not able to penetrate the intralayer surface area of the clay particles, yielding an external measurement only. Other methods measuring the adsorption of polar liquids (e.g. ethylene glycol monomethyl ether) are better able to penetrate the intralayer surface layer of clay particles and may yield surface area measurements up to an order of magnitude higher (e.g. Machta et al, 2011). Finally, because the measurements are performed on dry mudrock powder, this method is not suited to measure the surface area of expandable clays that swell in water.

2.2 Total SSA – Methylene Blue (MB) Spot Test Method

The total SSA was measured using the Methylene Blue Spot Test Method. This method is a quick bench top method using relatively safe chemicals that measures the SSA of clay particles in water suspensions, allowing full measurement of the SSA of expansive minerals. Methylene Blue (MB, C₁₆H₁₈ClN₃S) is a cationic dye whose molecules strongly adsorb to negatively charged clay particle surfaces. The specific surface area of clay particles can therefore be determined by measuring the amount of MB required to saturate the clay particles surfaces. MB has a molecular weight of 319.87 g/mol and a surface area of 130 Å² (Santamarina et al, 2002).

Many adaptations of this method are available in the literature. The general procedure is as follows: First, a strong solution of methylene blue is mixed; Second, a known mass of oven dried clay is mixed with water to form a slurry; Third, incremental volumes of MB solution are added to the clay slurry and thoroughly mixed for a period of time. Following each addition, a drop of the blue clay solution is removed and deposited on a piece of low flow filter paper and evaluated for the end point. The end point is indicated by the formation of a light blue halo around the clay droplet. At this point, all clay surfaces are saturated with MB and excess MB is available to leach onto the filter paper. Once this point has been obtained, the solution should be further mixed for 2 – 5 more minutes and re-tested to ensure that adequate mixing and time was given for full absorption. A more specific method, adapted from Santamarina et al (2002), follows.

2.2.1 Modified Methodology

Santamarina et al (2002) provide a method for measuring the SSA of clay suspensions. The following procedure improves upon their methodology:

1. Prepare a methylene blue solution by mixing 1.0 g of dry powder with 200 mL of deionized water. Mix this solution well and let sit overnight to ensure complete mixing.
2. Prepare the soil suspension by mixing 5 or 10 g of oven dried soil powder with water in a blender for 1 minute. Sufficient deionized water should be added to form a thin slurry; adding more water to facilities blending will not affect the measurement. Pour the blended clay slurry into a flask and cap with a rubber stopper. Let sit overnight to hydrate.
3. For best results, prepare at least two identical soil suspensions. The first will be used to quickly bracket the SSA, and the second to more accurately measure the SSA.
4. Add MB solution in increments. Use titration equipment to precisely measure the volume of MB solution added. Record the volume of MB added per increment.
5. After each increment of MB is added, thoroughly mix the clay suspension for at least two minutes. Ensure that the clay particles do not settle to the bottom of the flask. Place a drop of the suspension on to low flow filter paper (Fisher Brand P5). If a light blue halo forms, mix the solution for an additional 2 minutes and place another drop of suspension. If a halo is still formed after the second drop, the clay surfaces are saturated with MB solution and the endpoint has been reached.
6. Continue adding increments of MB solution until the halo is formed. Take a picture of the filter paper with halo for record keeping. Once dry, the drops will flake off and the halo will not be as visible. Figure XX gives a photograph showing s filter paper with incremental droplets identifying the end point indicated by a light blue halo measured using GoM-EI.
7. Compute the SSA using equation A5-1:

$$SSA = \frac{1}{M_w} \frac{M_{MB}}{V_s} V A_v A_{MB} \frac{1}{M_s} \quad A5-1$$

Where M_w is the molecular weight of MB (319.87 g/mol), M_{MB} is the mass of MB in the solution (1 g), V_s is the solution volume (200 mL), V is the volume of solution added, A_v is

Avogadro's number (6.02×10^{23} molecules / mol), AMB is the area of the MB molecule (130 \AA^2) and M_s is the dry mass of soil in the suspension. The volume of water added to the soil suspension is irrelevant in the calculation.

8. For best results, measure the SSA of one soil suspension at a time. The first soil suspension is used to bracket the volume of MB required to be added, and the second soil suspension is used to more precisely identify the volume of MB and the SSA. This procedure will increase the speed and accuracy of the measurement. First estimate the SSA of the material and the volume of MB solution that should be added to achieve this SSA using equation A5-1. When measuring the first soil suspension, design the increments such that the first increment is large and results in a lower SSA than estimated, with following increments gradually reduced in volume as the total volume approaches the estimated volume. The final increment volumes should be in the range of 1 – 2 mL, resulting in SSA increments of $< 2 \text{ m}^2$ for 10 g of oven dried material. The first volume increment of the second soil suspension should be very large and get close to the measured SSA of the first suspension, with subsequent volume additions being very small, in the range of 0.5 to 1.0 mL to more accurately measure the SSA.

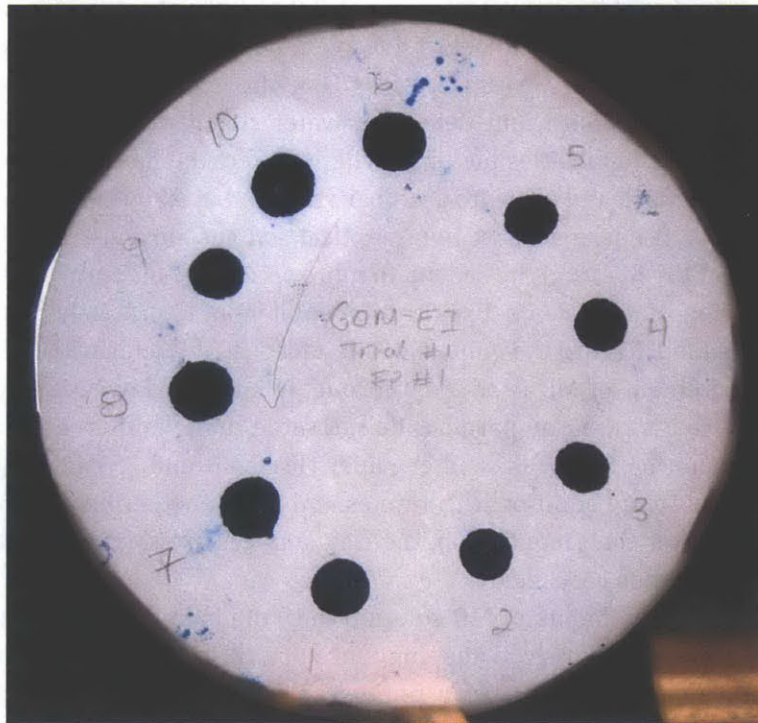


Figure A5-1: Increments 1 – 10 of GoM-EI MB spot test (no halo, no end point)

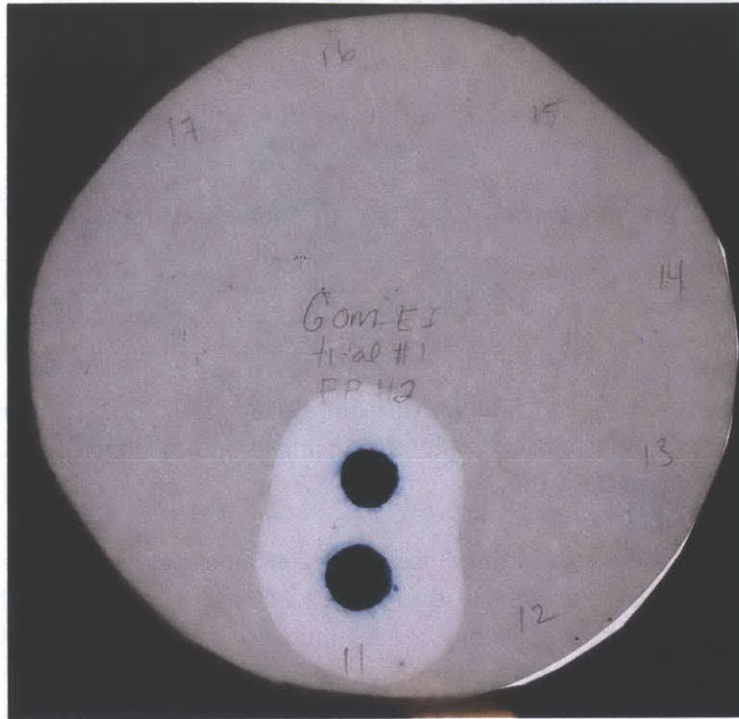


Figure A5-2: Increment 11 of GoM-EI MB spot test showing formation of halo that remains with time

2.3 Comparison of methods

Both the BET (external SSA) and MB spot test (total SSA) methods measure different surface areas and may be affected by different sources of error.

The BET method uses large N_2 molecules which cannot penetrate pores or intralayer surfaces, and results in very small surface areas. The MB spot test method relies on the adsorption of rectangular shaped MB particles to clay surfaces. The surface area of the MB molecules itself varies depending on which face is contacted, and how the molecules are packed onto the surfaces. The area covered by one MB molecule may vary and can affect the results by up to 100%.

Further, the chemistry of the solution including the pH and temperature can affect ionic adsorption. Santamarina (2002) describes these sources of error in more detail.

Finally, the BET method measures the external SSA, and the MB spot test method measures the total SSA. The internal SSA is the difference between the two measurements (Cerato, 2001). For non-swelling clays, the difference is small, however for swelling clays such as Smectite, this difference is significant.

3 Results

Table A5-1 provides a summary of the CEC results for BBC, SFBM and GoM-EI.:

Table A5-1 - CEC results

Mudrock	Cation Exchange Capacity (CEC) (meq / 100 g)
Boston Blue Clay (BBC)	10.7
San Francisco Bay Mud (SFBM)	28.1 +/- 2.4
Gulf of Mexico – Eugene Island (GoM-EI)	32.4 +/- 1.7

Multiple measurements were performed for the GoM-EI and SFBM CEC. The San Francisco Bay Mud is inhomogeneous at the fine particle scale and includes millimeter sized particles, leading to a relatively high CEC standard deviation.

CEC data for different minerals including Illite, Kaolinite, Smectite and Chlorite are available in the literature (e.g. Carroll 1959, Cerato and Lutenegeger 2005, Das 2008). The CEC computed as a weighted average based on the mineralogy of each mudrock agrees well with the measured values. The mineralogy of BBC, SFBM and GoM-EI is provided in Chapter 3.

Table A5-2 provides the SSA results for BBC, SFBM and GoM-EI where available. For comparison a measurement of the total SSA of pure gold gel, a commercial drilling mud product that is nearly pure Montmorillonite, is also provided. Relevant data on the clay fraction and clay mineralogy are also included for interpretation; these data are discussed in more detail in Chapter 3.

Table A5-2- SSA Results

Mudrock	(a) External SSA BET Method	(b) Internal SSA Difference (c-a)	(c) Total SSA MB Spot Test Method	Clay Fraction (%)	Smectite in < 2 μ m fraction
	m ² /g	m ² /g	m ² /g	%	%
Boston Blue Clay (BBC)	24	25	49	53	1
39% Clay BBC	N/A	N/A	43	39	<1
Leached BBC	N/A	N/A	60	53	1
San Francisco Bay Mud (SFBM)	21	100	121	52	45
Gulf of Mexico – Eugene Island (GoM- EI)	43	224	267	65	65
Pure gold Gel (Montmorillonite)	N/A	N/A	788	76	high

The external SSA results are in the range expected from the BET method for external surface area and agree with results obtained by Schneider (2011). Cerato and Lutenegeger (2004) give the SSA of BBC as 48 using the BET method. It is interesting to note that the external SSA of SFBM is lower than BBC despite having a higher Smectite content (45% for SFBM vs. 1.4% for BBC). This result

could be due to the noted SFBM inhomogeneity because the BET method uses a very small sample size (<1 g) similar to the CEC measurement.

The total SSA and internal SSA increase with increasing Smectite content, as is expected. The total SSA of the pure gold gel is in the range (~ 800 m²/g) suggested by Ladd (1996) for pure Montmorillonite. The difference between the external and internal surface also increases with increasing Smectite content. This is a result of the different measurement procedures. The BET method measures a dry specimen without allowing for double layer expansion. Further, the N₂ molecules used to measure the surface area are large and cannot penetrate small intralayer spaces. The MB method, on the other hand, measures the specimens in the wet state, allowing the double layers to fully expand. The smaller MB particles are able to better penetrate and adhere to the intralayer surfaces.

4 Cation Exchange Capacity - Relevant Emails:

Dr. Ross Giese
University at Buffalo, SUNY
Department of Geology
411 Cooke Hall
Buffalo, NY 14260-1350
Ross Giese <glgclay@buffalo.edu>

We do CEC measurements on clay-rich soils and rocks (black shales). The measurement is done by exposing the powdered sample to a Cu-complex in aqueous solution. The sample normally is 100 mg. The Cu-complex is strongly adsorbed to cationic sites on the sample. We know how much copper is in the solution to start with and determine the amount remaining in solution after exposure to the sample via a spectroscopic measurement. The difference gives us the CEC.

We have examined a range of standard clay minerals and our CEC values are in agreement with a number of published results using several different techniques. The things we look at typically have CEC values in the .02 to 1.10 mE/gram. For samples outside this range, we would have to modify the procedure which we can do. It helps if you have some rough estimate of the CECs. We do this on a fee per sample basis. Our rate for commercial work is \$75/sample, academic is \$50/sample and we quote 2 weeks turn around. Normally we beat that, but it depends on what else is going on in my lab (exam grading, graduation, equipment problems, the flu).

For surface areas, are you looking at BET measurements? We tried analyzing organic content but I was never satisfied that we had a reliable procedure. We also provide quantitative mineral analysis based on powder X-ray diffraction if you have such an interest.

Ross

Jana: Here are the results for your three samples. It took a bit longer than usual because of the semester ending and exams.

San Francisco Bay	.027	mEq/gram	→ <i>See below note!</i>
Gulf of Mexico	.316		
Boston blue clay	.107		

The problem is that the sample from SF Bay is not homogeneous. There are millimeter-sized particles which are mixed with a fine grained clay-like material. The larger particles are hard and impervious so they have almost no absorption. This lowers the measured cec and it is not possible to weigh out 0.1 g samples with the same proportion of the large particles so the variation in multiple cec measurements is large. I did the cec measurements on three samples of SFB and for comparison three samples of GOM. Here are the numbers. You will notice that these SFB values are larger than the number I sent you - I mistyped the number (0.027 instead of 0.270). How embarrassing. Sorry.

SFB	1	0.315	meq/g
SFB	2	0.260	
SFB	3	0.278	
GOM	1	0.349	
GOM	2	0.312	
GOM	3	0.318	

The variation in the SFB cecs is greater than for the GOM samples. I suggest that the higher cec values you mentioned for SFB samples were measured on the fine fraction of mud w/o the coarse particles.

Ross

5 Micromeritics SSA Reports



Analysis Report Summary

MIT
MECHANICAL ENGINEERING, 32 VASSAR
ST
CAMBRIDGE, MA 02139
Sheila Fay

Report Number: PR130529-008

PO Number: VISA/Sheila Fay

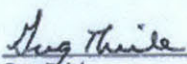
On May 29, 2013 3 sample(s) as shown below were submitted for analysis as shown. The samples were all included
Project Number PR130529-008

Client Sample ID	Sample Number	Test Name
Gulf of Mexico Clay-EI	1302824	005-01 MAS Multi-point surface area with N2
Boston Blue Clay	1302825	005-01 MAS Multi-point surface area with N2
San Francisco Bay Mud	1302826	005-01 MAS Multi-point surface area with N2

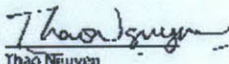
The individual results for each sample and each test are attached to the same email you just received. Details regarding the sample preparation and analysis conditions can be found on these reports. If you have any additional questions, please contact us at your convenience.

The signatures at the bottom of this page attest that all of the reports associated with this project have been reviewed and approved in accordance with our quality system.

Thank you for your business and we look forward to working with you again.

Lab Management: 
Greg Thiele
MAS General Manager

Date: 6/7/2013

Quality Management: 
Thao Nguyen
Lab Compliance Specialist

Date: 6/7/2013

MICROMERITICS
ANALYTICAL SERVICES *The Particle Testing Authority*

TriStar II 3020 V1.04 (V1.04)

Unit 1 Port 1

Serial #: 831

Page 1

Sample: San Francisco Bay Mud J9/A5
Operator: MM/AS
Submitter: MIT
File: C:\...\06JUN\1302826.SMP

Started: 6/7/2013 8:30:36AM
Completed: 6/7/2013 11:23:48AM
Report Time: 6/7/2013 1:14:53PM
Warm Free Space: 7.5178 cm³ Measured
Equilibration Interval: 10 s
Sample Density: 1.000 g/cm³

Analysis Adsorptive: N2
Analysis Bath Temp.: 77.350 K
Sample Mass: 2.6403 g
Cold Free Space: 21.5717 cm³ Measured
Low Pressure Dose: None
Automatic Degas: Yes

Sample Prep: Stage	Temperature (°C)	Ramp Rate (°C/min)	Time (min)
1	110	10	960

Summary Report

Surface Area

Single point surface area at P/P₀ = 0.300189303: 20.9197 m²/g

BET Surface Area: 21.3696 m²/g

MICROMERITICS

ANALYTICAL SERVICES

The Particle Testing Authority

TriStar II 3020 V1.04 (V1.04)

Unit 1 Port 1

Serial #: 831

Page 2

Sample: San Francisco Bay Mud J9/A5
 Operator: MM/AS
 Submitter: MIT
 File: C:\...06JUN1302826.SMP

Started: 6/7/2013 8:30:36AM
 Completed: 6/7/2013 11:23:48AM
 Report Time: 6/7/2013 1:14:53PM
 Warm Free Space: 7.5178 cm³ Measured
 Equilibration Interval: 10 s
 Sample Density: 1.000 g/cm³

Analysis Adsorptive: N2
 Analysis Bath Temp.: 77.350 K
 Sample Mass: 2.6403 g
 Cold Free Space: 21.5717 cm³ Measured
 Low Pressure Dose: None
 Automatic Degas: Yes

Sample Prep: Stage 1
 Temperature (°C) 110
 Ramp Rate (°C/min) 10
 Time (min) 960

Isotherm Tabular Report

Relative Pressure (P/Po)	Absolute Pressure (mmHg)	Quantity Adsorbed (cm ³ /g STP)	Elapsed Time (h:min)	Saturation Pressure (mmHg)
0.051206782	37.550892	4.5301	00:58	732.77771
0.077117247	56.555447	4.8432	01:20	733.318726
0.098680923	72.374718	5.0658	01:29	733.369629
0.123632366	90.675285	5.3012	01:36	733.421570
0.148948342	109.145218	5.5266	01:43	733.426758
0.174099917	127.665108	5.7460	01:50	733.264587
0.199392385	146.208908	5.9641	01:56	733.286438
0.224716762	164.802505	6.1830	02:02	733.272278
0.250054633	183.398560	6.4062	02:07	733.378784
0.274801169	201.568100	6.6299	02:13	733.433960
0.300189303	220.215256	6.8670	02:18	733.505249
			02:23	733.587952

TriStar II 3020 V1.04 (V1.04)

Unit 1 Port 1

Serial #: 831

Page 3

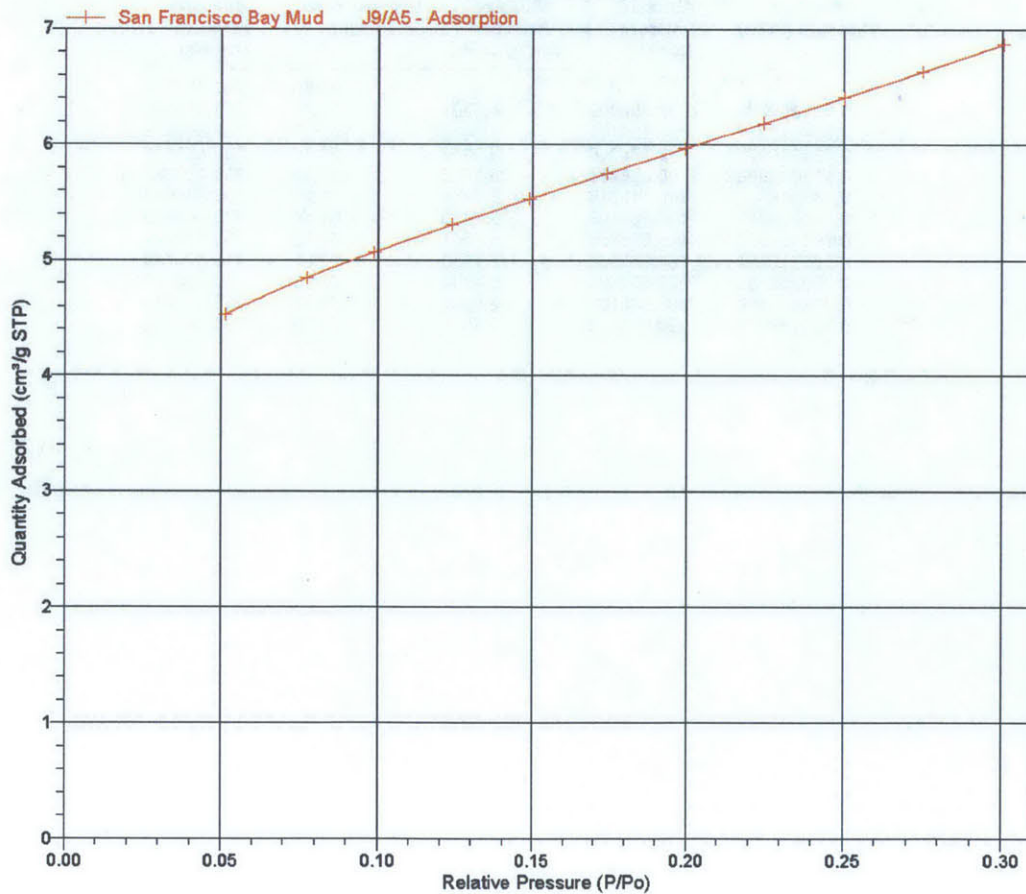
Sample: San Francisco Bay Mud J9/A5
 Operator: MM/AS
 Submitter: MIT
 File: C:\...\06JUN\1302826.SMP

Started: 6/7/2013 8:30:36AM
 Completed: 6/7/2013 11:23:48AM
 Report Time: 6/7/2013 1:14:53PM
 Warm Free Space: 7.5178 cm³ Measured
 Equilibration Interval: 10 s
 Sample Density: 1.000 g/cm³

Analysis Adsorptive: N2
 Analysis Bath Temp.: 77.350 K
 Sample Mass: 2.6403 g
 Cold Free Space: 21.5717 cm³ Measured
 Low Pressure Dose: None
 Automatic Degas: Yes

Sample Prep: Stage	Temperature (°C)	Ramp Rate (°C/min)	Time (min)
1	110	10	960

Isotherm Linear Plot



MICROMERITICS

ANALYTICAL SERVICES

The Particle Testing Authority

TriStar II 3020 V1.04 (V1.04)

Unit 1 Port 1

Serial #: 831

Page 4

Sample: San Francisco Bay Mud J9/A5
 Operator: MM/AS
 Submitter: MIT
 File: C:\...06JUN\1302826.SMP

Started: 6/7/2013 8:30:36AM
 Completed: 6/7/2013 11:23:48AM
 Report Time: 6/7/2013 1:14:53PM
 Warm Free Space: 7.5178 cm³ Measured
 Equilibration Interval: 10 s
 Sample Density: 1.000 g/cm³

Analysis Adsorptive: N2
 Analysis Bath Temp.: 77.350 K
 Sample Mass: 2.6403 g
 Cold Free Space: 21.5717 cm³ Measured
 Low Pressure Dose: None
 Automatic Degas: Yes

Sample Prep: Stage	Temperature (°C)	Ramp Rate (°C/min)	Time (min)
1	110	10	960

BET Surface Area Report

BET Surface Area: 21.3696 ± 0.0443 m²/g
 Slope: 0.202129 ± 0.000414 g/cm³ STP
 Y-Intercept: 0.001581 ± 0.000079 g/cm³ STP
 C: 128.885485
 Qm: 4.9090 cm³/g STP
 Correlation Coefficient: 0.9999811
 Molecular Cross-Sectional Area: 0.1620 nm²

Relative Pressure (P/Po)	Quantity Adsorbed (cm ³ /g STP)	1/[Q(Po/P - 1)]
0.051206782	4.5301	0.011914
0.077117247	4.8432	0.017253
0.098680923	5.0658	0.021613
0.123632366	5.3012	0.026612
0.148848342	5.5266	0.031643
0.174099917	5.7460	0.036686
0.199392385	5.9641	0.041758
0.224716762	6.1830	0.046879
0.250054633	6.4062	0.052048
0.274801169	6.6299	0.057155
0.300189303	6.8670	0.062467

TriStar II 3020 V1.04 (V1.04)

Unit 1 Port 1

Serial #: 831

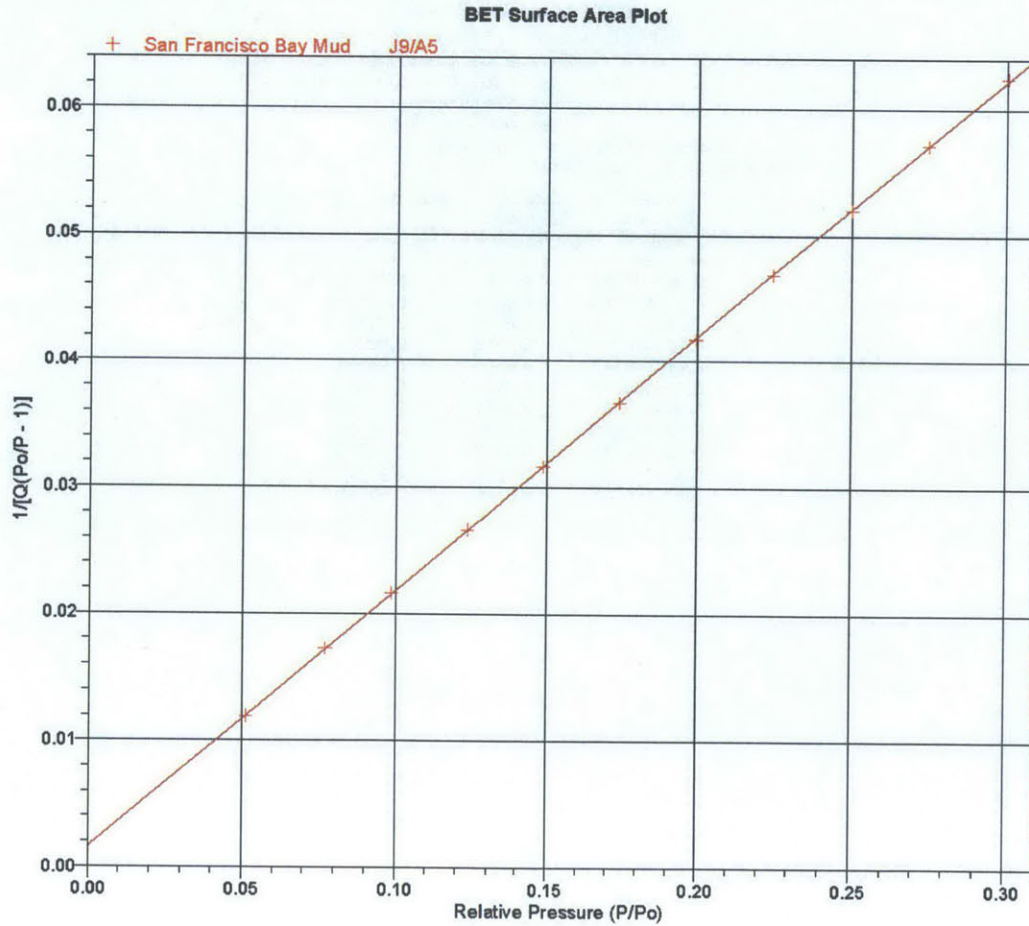
Page 5

Sample: San Francisco Bay Mud J9/A5
 Operator: MM/AS
 Submitter: MIT
 File: C:\...\06JUN1302826.SMP

Started: 6/7/2013 8:30:36AM
 Completed: 6/7/2013 11:23:48AM
 Report Time: 6/7/2013 1:14:53PM
 Warm Free Space: 7.5178 cm³ Measured
 Equilibration Interval: 10 s
 Sample Density: 1.000 g/cm³

Analysis Adsorptive: N2
 Analysis Bath Temp.: 77.350 K
 Sample Mass: 2.6403 g
 Cold Free Space: 21.5717 cm³ Measured
 Low Pressure Dose: None
 Automatic Degas: Yes

Sample Prep: Stage	Temperature (°C)	Ramp Rate (°C/min)	Time (min)
1	110	10	960



MICROMERITICS
ANALYTICAL SERVICES *The Particle Testing Authority*

TriStar II 3020 V1.04 (V1.04)

Unit 1 Port 3

Serial #: 831

Page 1

Sample: Gulf of Mexico Clay-EI 2M/C5
Operator: MM/AS
Submitter: MIT
File: C:\...06JUN1302824.SMP

Started: 6/7/2013 8:30:36AM
Completed: 6/7/2013 11:23:48AM
Report Time: 6/7/2013 1:19:42PM
Warm Free Space: 7.0439 cm³ Measured
Equilibration Interval: 10 s
Sample Density: 1.000 g/cm³

Analysis Adsorptive: N2
Analysis Bath Temp.: 77.350 K
Sample Mass: 1.6820 g
Cold Free Space: 19.8477 cm³ Measured
Low Pressure Dose: None
Automatic Degas: Yes

Sample Prep: Stage	Temperature (°C)	Ramp Rate (°C/min)	Time (min)
1	110	10	960

Summary Report

Surface Area

Single point surface area at P/Po = 0.300779776: 42.0037 m²/g

BET Surface Area: 42.9599 m²/g

MICROMERITICS ANALYTICAL SERVICES

*The Particle
Testing
Authority*

TriStar II 3020 V1.04 (V1.04)

Unit 1 Port 3

Serial #: 831

Page 2

Sample: Gulf of Mexico Clay-EI 2M/C5
 Operator: MM/AS
 Submitter: MIT
 File: C:\...\06JUN1302824.SMP

Started: 6/7/2013 8:30:36AM
 Completed: 6/7/2013 11:23:48AM
 Report Time: 6/7/2013 1:19:42PM
 Warm Free Space: 7.0439 cm³ Measured
 Equilibration Interval: 10 s
 Sample Density: 1.000 g/cm³

Analysis Adsorptive: N2
 Analysis Bath Temp.: 77.350 K
 Sample Mass: 1.6820 g
 Cold Free Space: 19.8477 cm³ Measured
 Low Pressure Dose: None
 Automatic Degas: Yes

Sample Prep: Stage 1 Temperature (°C) 110 Ramp Rate (°C/min) 10 Time (min) 960

Isotherm Tabular Report

Relative Pressure (P/P ₀)	Absolute Pressure (mmHg)	Quantity Adsorbed (cm ³ /g STP)	Elapsed Time (h:min)	Saturation Pressure (mmHg)
			00:58	732.777771
0.049984790	36.659904	9.0786	01:31	733.421204
0.073719281	54.072121	9.6733	01:44	733.486816
0.102644179	75.273918	10.2713	01:54	733.348145
0.123555137	90.602234	10.6681	02:02	733.293945
0.147760485	108.364937	11.1106	02:10	733.382385
0.172757766	126.714584	11.5555	02:17	733.481262
0.198061767	145.294601	11.9944	02:24	733.582275
0.223399262	163.881180	12.4332	02:31	733.579773
0.249035525	182.667801	12.8808	02:38	733.500977
0.274890606	201.668365	13.3379	02:45	733.631348
0.300779776	220.682236	13.7996	02:51	733.700378

MICROMERITICS

ANALYTICAL SERVICES

The Particle Testing Authority

TriStar II 3020 V1.04 (V1.04)

Unit 1 Port 3

Serial #: 831

Page 3

Sample: Gulf of Mexico Clay-EI 2M/C5
 Operator: MM/AS
 Submitter: MIT
 File: C:\...06JUN\1302824.SMP

Started: 6/7/2013 8:30:36AM
 Completed: 6/7/2013 11:23:48AM
 Report Time: 6/7/2013 1:19:42PM
 Warm Free Space: 7.0439 cm³ Measured
 Equilibration Interval: 10 s
 Sample Density: 1.000 g/cm³

Analysis Adsorptive: N2
 Analysis Bath Temp.: 77.350 K
 Sample Mass: 1.6820 g
 Cold Free Space: 19.8477 cm³ Measured
 Low Pressure Dose: None
 Automatic Degas: Yes

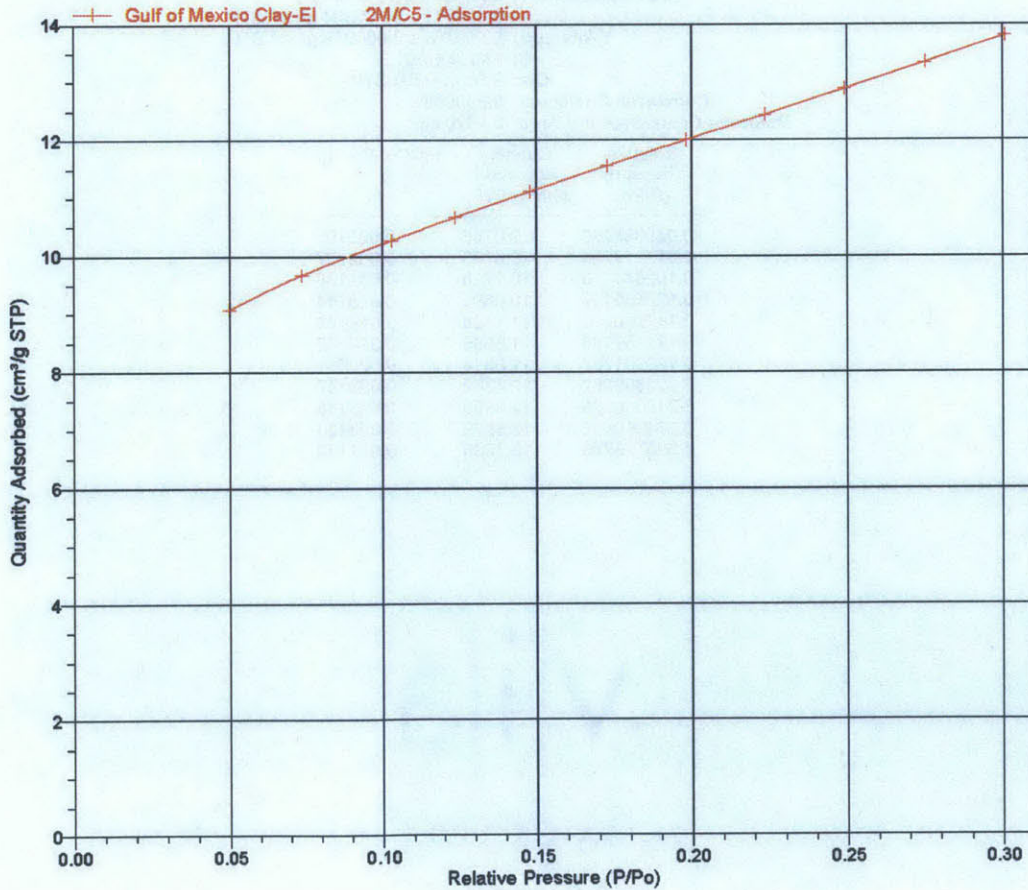
Sample Prep: Stage
 1

Temperature (°C)
 110

Ramp Rate (°C/min)
 10

Time (min)
 960

Isotherm Linear Plot



MICROMERITICS

ANALYTICAL SERVICES

The Particle Testing Authority

TriStar II 3020 V1.04 (V1.04)

Unit 1 Port 3

Serial #: 831

Page 4

Sample: Gulf of Mexico Clay-EI 2M/C5
 Operator: MM/AS
 Submitter: MIT
 File: C:\...06JUN\1302824.SMP

Started: 6/7/2013 8:30:36AM
 Completed: 6/7/2013 11:23:48AM
 Report Time: 6/7/2013 1:19:42PM
 Warm Free Space: 7.0439 cm³ Measured
 Equilibration Interval: 10 s
 Sample Density: 1.000 g/cm³

Analysis Adsorptive: N2
 Analysis Bath Temp.: 77.350 K
 Sample Mass: 1.6820 g
 Cold Free Space: 19.8477 cm³ Measured
 Low Pressure Dose: None
 Automatic Degas: Yes

Sample Prep: Stage	Temperature (°C)	Ramp Rate (°C/min)	Time (min)
1	110	10	960

BET Surface Area Report

BET Surface Area: 42.9599 ± 0.1312 m²/g
 Slope: 0.100571 ± 0.000304 g/cm³ STP
 Y-Intercept: 0.000761 ± 0.000058 g/cm³ STP
 C: 133.241932
 Qm: 9.9686 cm³/g STP
 Correlation Coefficient: 0.9999589
 Molecular Cross-Sectional Area: 0.1620 nm²

Relative Pressure (P/Po)	Quantity Adsorbed (cm ³ /g STP)	1/[Q(Po/P - 1)]
0.049984790	9.0786	0.005795
0.073719281	9.6733	0.008227
0.102644179	10.2713	0.011136
0.123555137	10.6681	0.013214
0.147760485	11.1106	0.015605
0.172757766	11.5555	0.018072
0.198061767	11.9944	0.020591
0.223399262	12.4332	0.023137
0.249035525	12.8808	0.025745
0.274890606	13.3379	0.028423
0.300779776	13.7996	0.031172

TriStar II 3020 V1.04 (V1.04)

Unit 1 Port 3

Serial #: 831

Page 5

Sample: Gulf of Mexico Clay-EI 2M/C5
 Operator: MM/AS
 Submitter: MIT
 File: C:\...06JUN1302824.SMP

Started: 6/7/2013 8:30:36AM
 Completed: 6/7/2013 11:23:48AM
 Report Time: 6/7/2013 1:19:42PM
 Warm Free Space: 7.0439 cm³ Measured
 Equilibration Interval: 10 s
 Sample Density: 1.000 g/cm³

Analysis Adsorptive: N2
 Analysis Bath Temp.: 77.350 K
 Sample Mass: 1.6820 g
 Cold Free Space: 19.8477 cm³ Measured
 Low Pressure Dose: None
 Automatic Degas: Yes

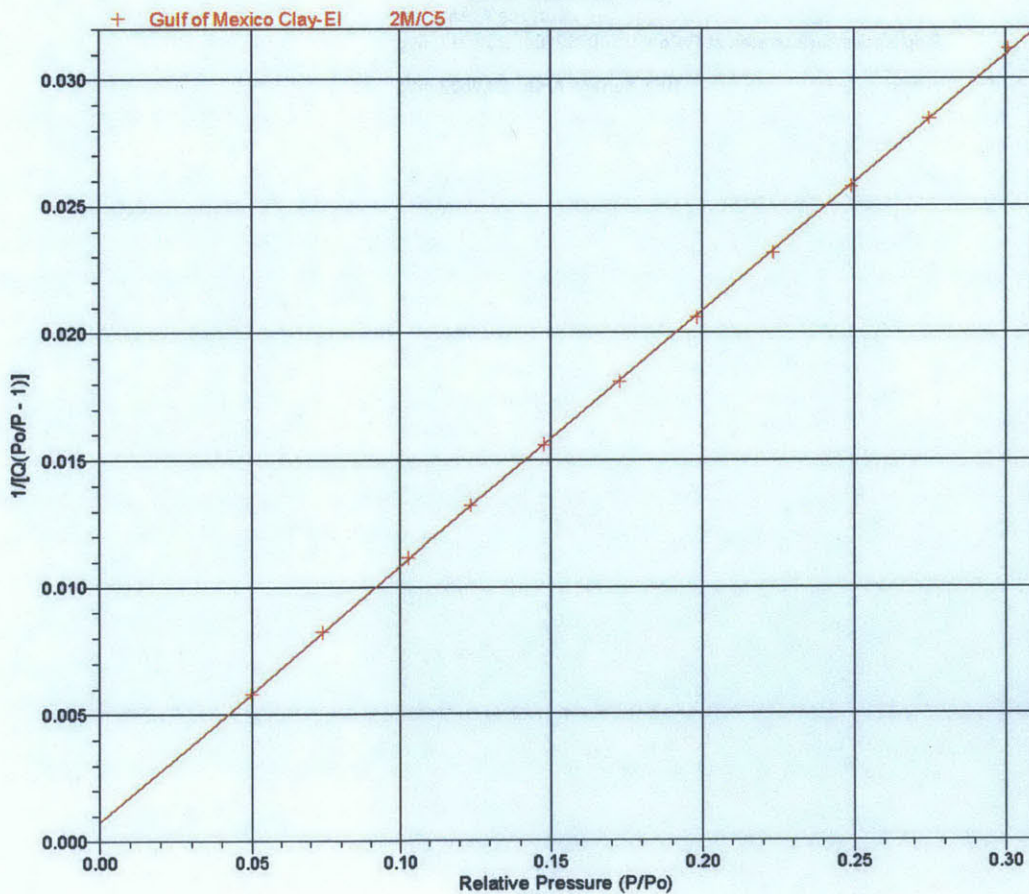
Sample Prep: Stage
 1

Temperature (°C)
 110

Ramp Rate (°C/min)
 10

Time (min)
 960

BET Surface Area Plot



MICROMERITICS
ANALYTICAL SERVICES *The Particle Testing Authority*

TriStar II 3020 V1.04 (V1.04)

Unit 1 Port 2

Serial #: 831

Page 1

Sample: Boston Blue Clay AKM
Operator: MM/AS
Submitter: MIT
File: C:\...06JUN1302825.SMP

Started: 6/7/2013 8:30:36AM	Analysis Adsorptive: N2
Completed: 6/7/2013 11:23:48AM	Analysis Bath Temp.: 77.350 K
Report Time: 6/7/2013 1:17:06PM	Sample Mass: 1.6933 g
Warm Free Space: 7.8967 cm ³ Measured	Cold Free Space: 22.9333 cm ³ Measured
Equilibration Interval: 10 s	Low Pressure Dose: None
Sample Density: 1.000 g/cm ³	Automatic Degas: Yes

Sample Prep: Stage	Temperature (°C)	Ramp Rate (°C/min)	Time (min)
1	110	10	960

Summary Report

Surface Area

Single point surface area at P/Po = 0.300262184: 23.4217 m²/g

BET Surface Area: 23.8532 m²/g

MICROMERITICS

ANALYTICAL SERVICES

The Particle Testing Authority

TriStar II 3020 V1.04 (V1.04)

Unit 1 Port 2

Serial #: 831

Page 2

Sample: Boston Blue Clay AKM
 Operator: MM/AS
 Submitter: MIT
 File: C:\...\06JUN\1302825.SMP

Started: 6/7/2013 8:30:36AM
 Completed: 6/7/2013 11:23:48AM
 Report Time: 6/7/2013 1:17:06PM
 Warm Free Space: 7.8967 cm³ Measured
 Equilibration Interval: 10 s
 Sample Density: 1.000 g/cm³

Analysis Adsorptive: N2
 Analysis Bath Temp.: 77.350 K
 Sample Mass: 1.6933 g
 Cold Free Space: 22.9333 cm³ Measured
 Low Pressure Dose: None
 Automatic Degas: Yes

Sample Prep: Stage 1
 Temperature (°C) 110
 Ramp Rate (°C/min) 10
 Time (min) 960

Isotherm Tabular Report

Relative Pressure (P/Po)	Absolute Pressure (mmHg)	Quantity Adsorbed (cm ³ /g STP)	Elapsed Time (h:min)	Saturation Pressure (mmHg)
			00:58	732.777771
0.051606812	37.844402	5.1638	01:21	733.321838
0.079729648	58.471119	5.5171	01:28	733.376526
0.099063263	72.647812	5.7260	01:33	733.347656
0.123764794	90.772049	5.9741	01:38	733.423828
0.149087878	109.350862	6.2177	01:43	733.464478
0.174328572	127.838013	6.4558	01:49	733.316467
0.199318287	146.176849	6.6909	01:54	733.384033
0.224583772	164.684097	6.9308	01:59	733.285828
0.249783175	183.182297	7.1761	02:04	733.365234
0.274726749	201.463577	7.4244	02:09	733.323486
0.300262184	220.221786	7.6891	02:14	733.431641

TriStar II 3020 V1.04 (V1.04)

Unit 1 Port 2

Serial #: 831

Page 3

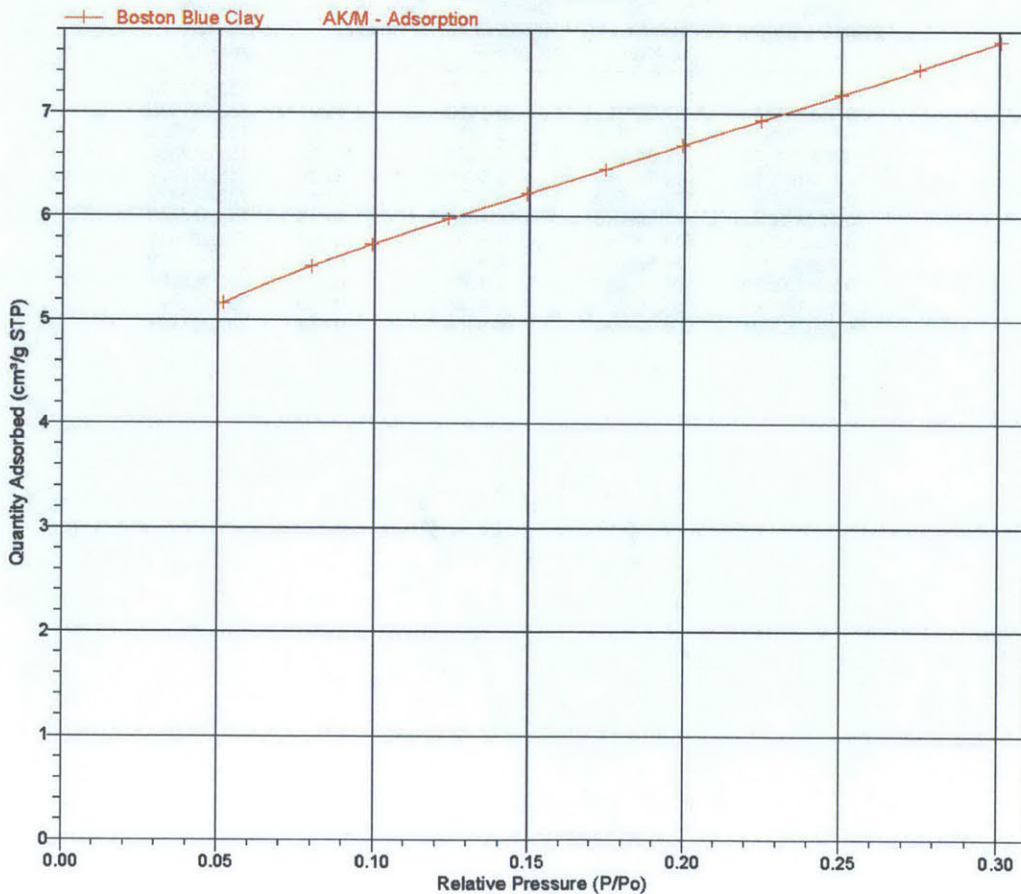
Sample: Boston Blue Clay AKM
 Operator: MM/AS
 Submitter: MIT
 File: C:\...06JUN1302825.SMP

Started: 6/7/2013 8:30:36AM
 Completed: 6/7/2013 11:23:48AM
 Report Time: 6/7/2013 1:17:06PM
 Warm Free Space: 7.9967 cm³ Measured
 Equilibration Interval: 10 s
 Sample Density: 1.000 g/cm³

Analysis Adsorptive: N2
 Analysis Bath Temp.: 77.350 K
 Sample Mass: 1.6933 g
 Cold Free Space: 22.9333 cm³ Measured
 Low Pressure Dose: None
 Automatic Degas: Yes

Sample Prep: Stage	Temperature (°C)	Ramp Rate (°C/min)	Time (min)
1	110	10	960

Isotherm Linear Plot



MICROMERITICS

ANALYTICAL SERVICES

The Particle Testing Authority

TriStar II 3020 V1.04 (V1.04)

Unit 1 Port 2

Serial #: 831

Page 4

Sample: Boston Blue Clay AKM
 Operator: MM/AS
 Submitter: MIT
 File: C:\...06JUN1302825.SMP

Started: 6/7/2013 8:30:36AM
 Completed: 6/7/2013 11:23:48AM
 Report Time: 6/7/2013 1:17:06PM
 Warm Free Space: 7.8967 cm³ Measured
 Equilibration Interval: 10 s
 Sample Density: 1.000 g/cm³

Analysis Adsorptive: N2
 Analysis Bath Temp.: 77.350 K
 Sample Mass: 1.6933 g
 Cold Free Space: 22.9333 cm³ Measured
 Low Pressure Dose: None
 Automatic Degas: Yes

Sample Prep: Stage	Temperature (°C)	Ramp Rate (°C/min)	Time (min)
1	110	10	960

BET Surface Area Report

BET Surface Area: 23.8532 ± 0.0490 m²/g
 Slope: 0.181326 ± 0.000368 g/cm³ STP
 Y-Intercept: 0.001173 ± 0.000071 g/cm³ STP
 C: 155.533547
 Qm: 5.4795 cm³/g STP
 Correlation Coefficient: 0.9999814
 Molecular Cross-Sectional Area: 0.1620 nm²

Relative Pressure (P/Po)	Quantity Adsorbed (cm ³ /g STP)	1/[Q(Po/P - 1)]
0.051606812	5.1638	0.010538
0.079728648	5.5171	0.015703
0.099063263	5.7260	0.019203
0.123764794	5.9741	0.023643
0.149087878	6.2177	0.028179
0.174328572	6.4558	0.032705
0.199318287	6.6909	0.037205
0.224583772	6.9308	0.041789
0.249783175	7.1761	0.046396
0.274726749	7.4244	0.051020
0.300262184	7.6891	0.055807

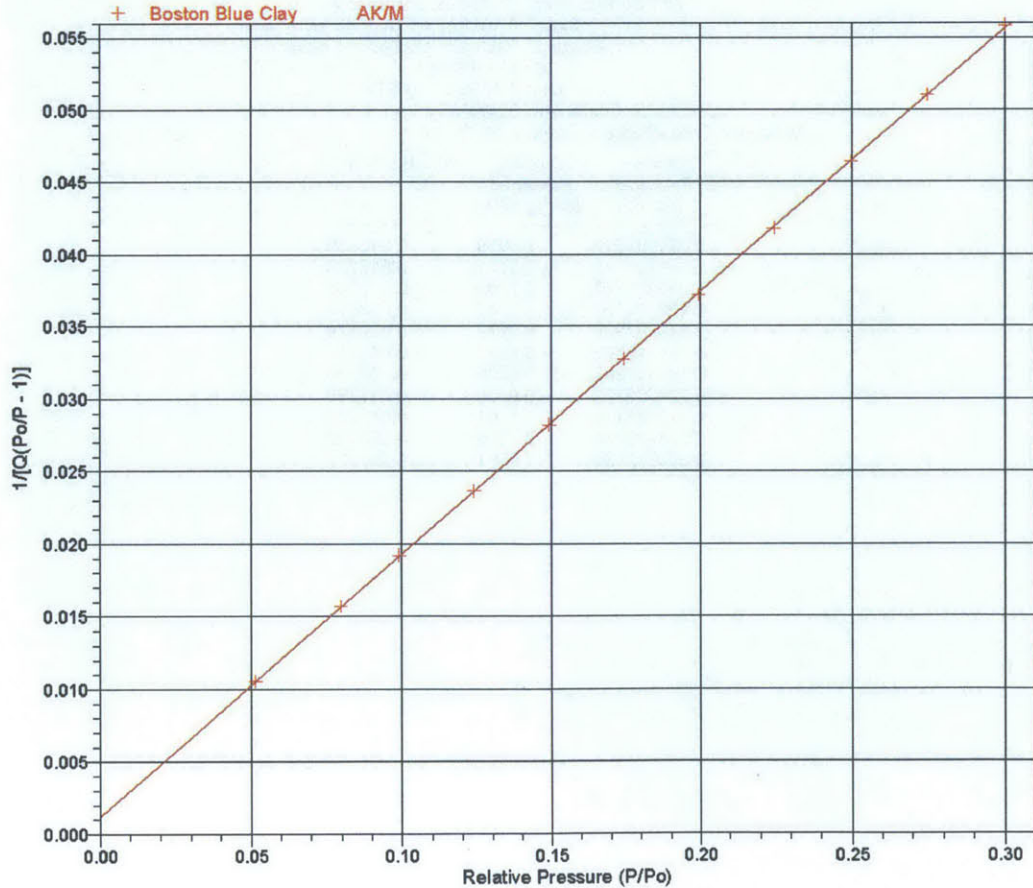
Sample: Boston Blue Clay AKM
 Operator: MM/AS
 Submitter: MIT
 File: C:\...106JUN1302825.SMP

Started: 6/7/2013 8:30:36AM
 Completed: 6/7/2013 11:23:48AM
 Report Time: 6/7/2013 1:17:06PM
 Warm Free Space: 7.8967 cm³ Measured
 Equilibration Interval: 10 s
 Sample Density: 1.000 g/cm³

Analysis Adsorptive: N2
 Analysis Bath Temp.: 77.350 K
 Sample Mass: 1.6933 g
 Cold Free Space: 22.9333 cm³ Measured
 Low Pressure Dose: None
 Automatic Degas: Yes

Sample Prep: Stage	Temperature (°C)	Ramp Rate (°C/min)	Time (min)
1	110	10	960

BET Surface Area Plot



Appendix 6: Equipment CAD Drawings

This appendix contains CAD drawings for 1) the cubic end adapters (section A1) used to measure the resistivity of mudrocks in the triaxial cell in parallel with the permeability measurement, and 2) the bench top electrodes that were used to measure the resistivity of mudrocks on the bench top, outside of the triaxial cell.

Contents

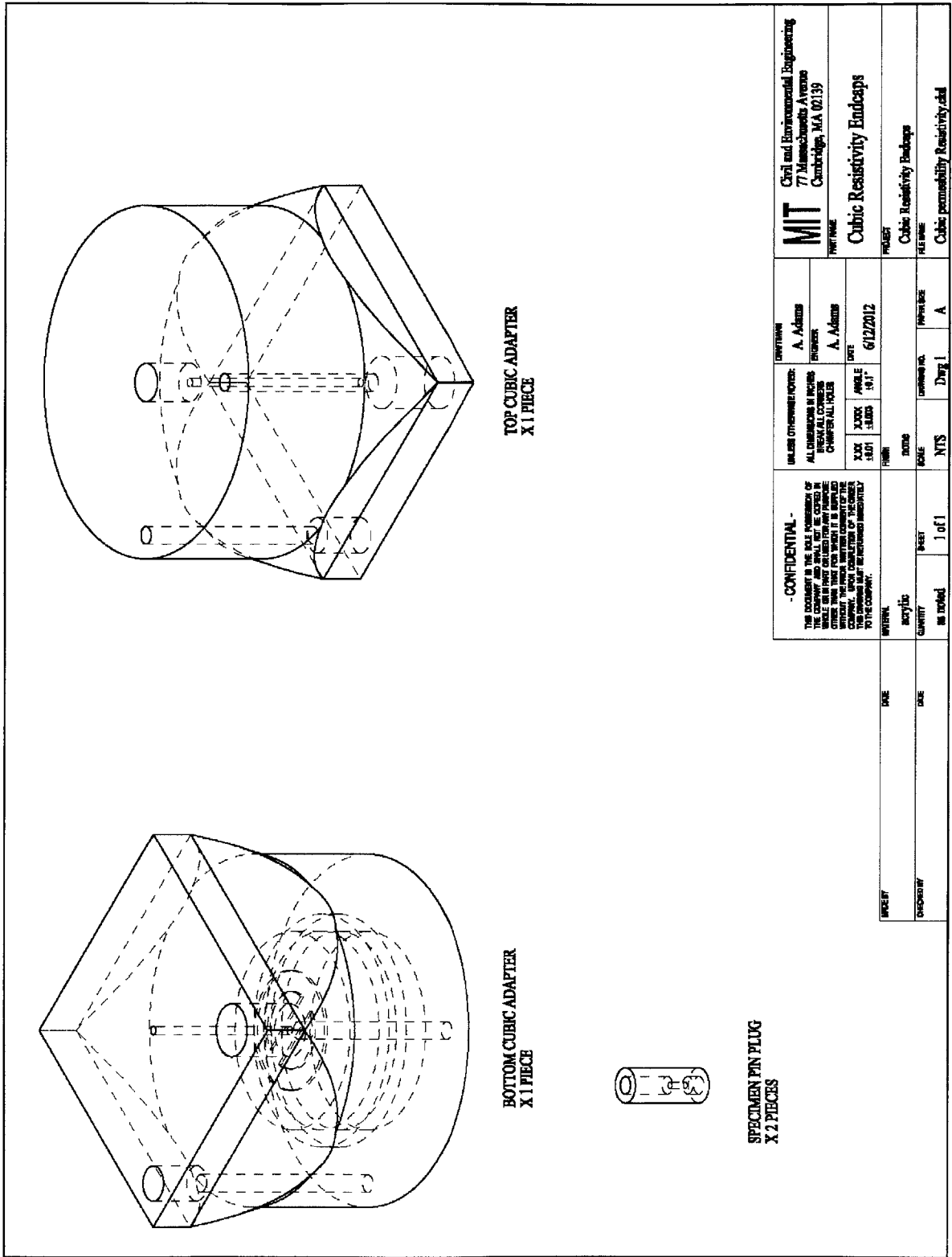
Appendix 6: Appendix 6: Equipment CAD Drawings.....	509
A1: Cubic End Adapters with Resistivity Electrodes	511
A2: Bench top Electrodes for Measurement of Consolidated Specimens (CRS Specimen Electrodes).....	519

List of Figures

Figure A6-1: Cubic resistivity end adapters: Drawing 1, isometric view.....	512
Figure A6-2: Cubic resistivity end adapters: Drawing 2, bottom cubic adapter	513
Figure A6-3: Cubic resistivity end adapters: Drawing 3, top cubic adapter	514
Figure A6-4: Cubic resistivity end adapters: Drawing 4, specimen pin plug.....	515
Figure A6-5: Cubic resistivity end adapters: Drawing 5, brass plate.....	516
Figure A6-6: Cubic resistivity end adapters: Drawing 6, porous stone	517
Figure A6-7: CRS Electrodes: Drawing 1, 9.5 mm probe.....	520
Figure A6-8: CRS Electrodes: Drawing 2, 9.5 mm drilling guide	521
Figure A6-9: CRS Electrodes: Drawing 3, 5.1 mm probe.....	522
Figure A6-10: CRS Electrodes: Drawing 4, 5.1 mm drilling guide.....	523
Figure A6-11: CRS Electrodes: Drawing 5, 4.0 mm probe	524
Figure A6-12: CRS Electrodes: Drawing 6, 4.0 mm drilling guide.....	525
Figure A6-13: CRS Electrodes: Drawing 7, 2.75 mm probe	526
Figure A6-14: CRS Electrodes: Drawing 8, 2.75 mm drilling guide	527
Figure A6-15: CRS Electrodes: Drawing 9, specimen trimming template	528

(Page intentionally left blank)

A1: Cubic End Adapters with Resistivity Electrodes



<p>MIT Civil and Environmental Engineering 77 Massachusetts Avenue Cambridge, MA 02139</p>		<p>DESIGNER A. Adams</p>		<p>DATE 6/12/2012</p>		<p>PROJECT Cubic Resistivity Endcaps</p>
		<p>UNLESS OTHERWISE NOTED: ALL DIMENSIONS IN INCHES DIMENSIONS IN PARENTHESES ARE DIMENSIONS IN MILLIMETERS</p>		<p>DATE 6/12/2012</p>		
<p>CONFIDENTIAL - THE DESIGN IS THE SOLE PROPERTY OF THE COMPANY AND SHALL NOT BE COPIED, REPRODUCED, OR TRANSMITTED IN ANY FORM OR BY ANY MEANS, ELECTRONIC OR MECHANICAL, INCLUDING PHOTOCOPYING, RECORDING, OR BY ANY INFORMATION STORAGE AND RETRIEVAL SYSTEM, WITHOUT THE WRITTEN PERMISSION OF THE COMPANY. ANY VIOLATION OF THIS NOTICE SHALL BE PROSECUTED IMMEDIATELY BY THE COMPANY.</p>		<p>SCALE NTS</p>		<p>DATE 6/12/2012</p>		<p>REVISION Cubic Resistivity Endcaps</p>
<p>DATE 6/12/2012</p>		<p>DATE 6/12/2012</p>		<p>DATE 6/12/2012</p>		
<p>DATE 6/12/2012</p>		<p>DATE 6/12/2012</p>		<p>DATE 6/12/2012</p>		<p>DATE 6/12/2012</p>
<p>DATE 6/12/2012</p>		<p>DATE 6/12/2012</p>		<p>DATE 6/12/2012</p>		
<p>DATE 6/12/2012</p>		<p>DATE 6/12/2012</p>		<p>DATE 6/12/2012</p>		<p>DATE 6/12/2012</p>
<p>DATE 6/12/2012</p>		<p>DATE 6/12/2012</p>		<p>DATE 6/12/2012</p>		

Figure A6-1: Cubic resistivity end adapters: Drawing 1, isometric view

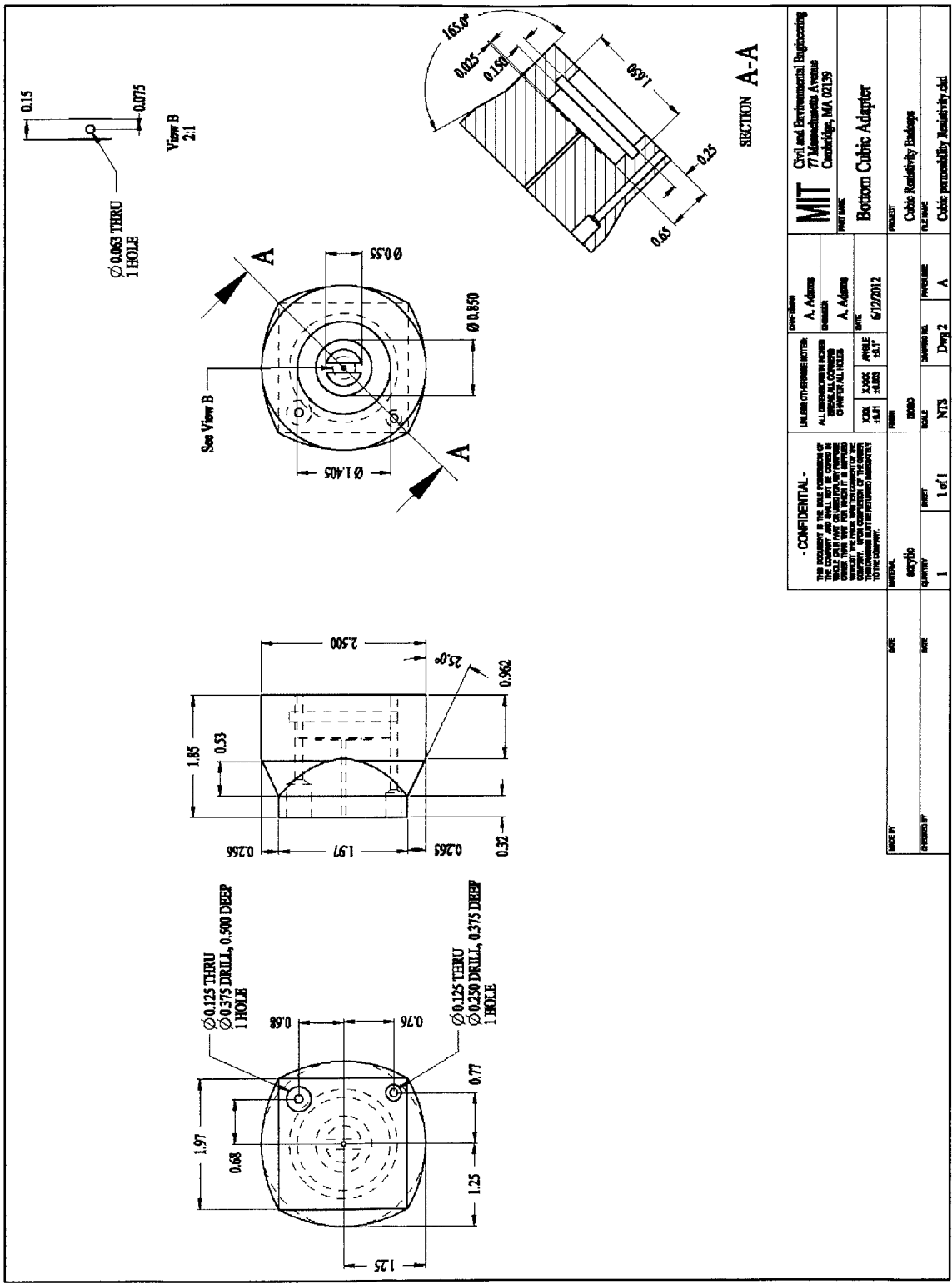


Figure A6-2: Cubic resistivity end adapters: Drawing 2, bottom cubic adapter

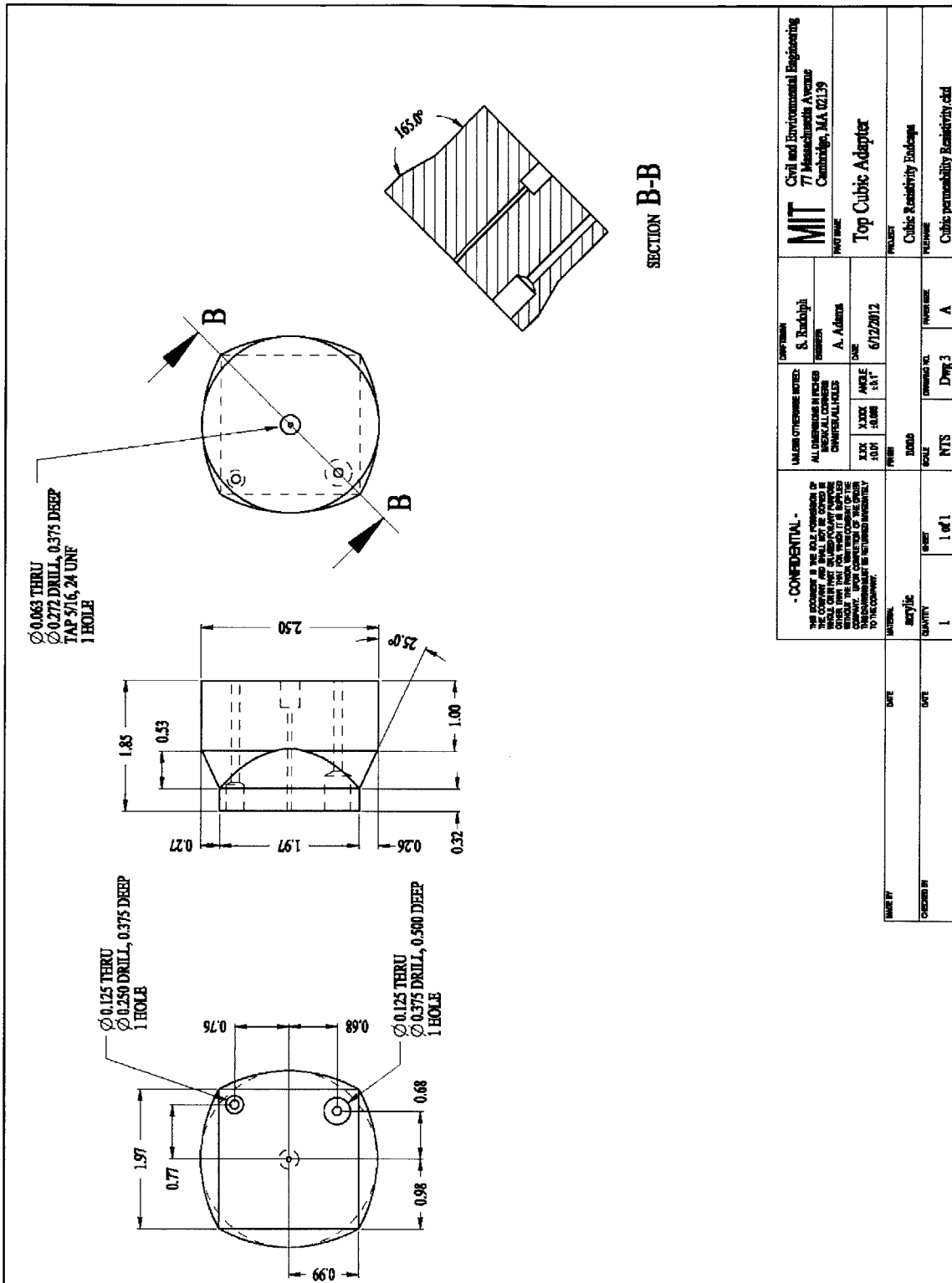


Figure A6-3: Cubic resistivity end adapters: Drawing 3, top cubic adapter

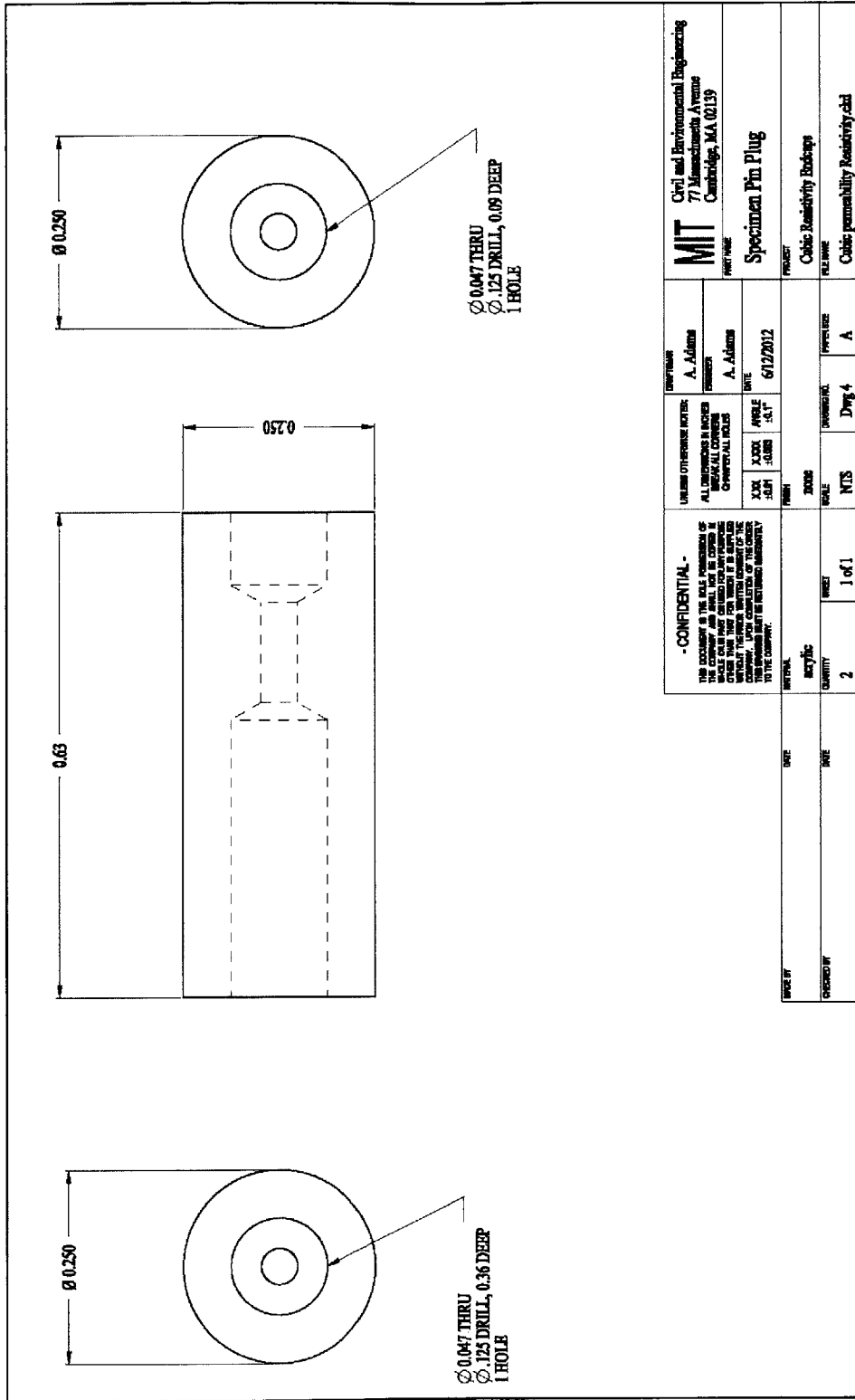


Figure A6-4: Cubic resistivity end adapters: Drawing 4, specimen pin plug

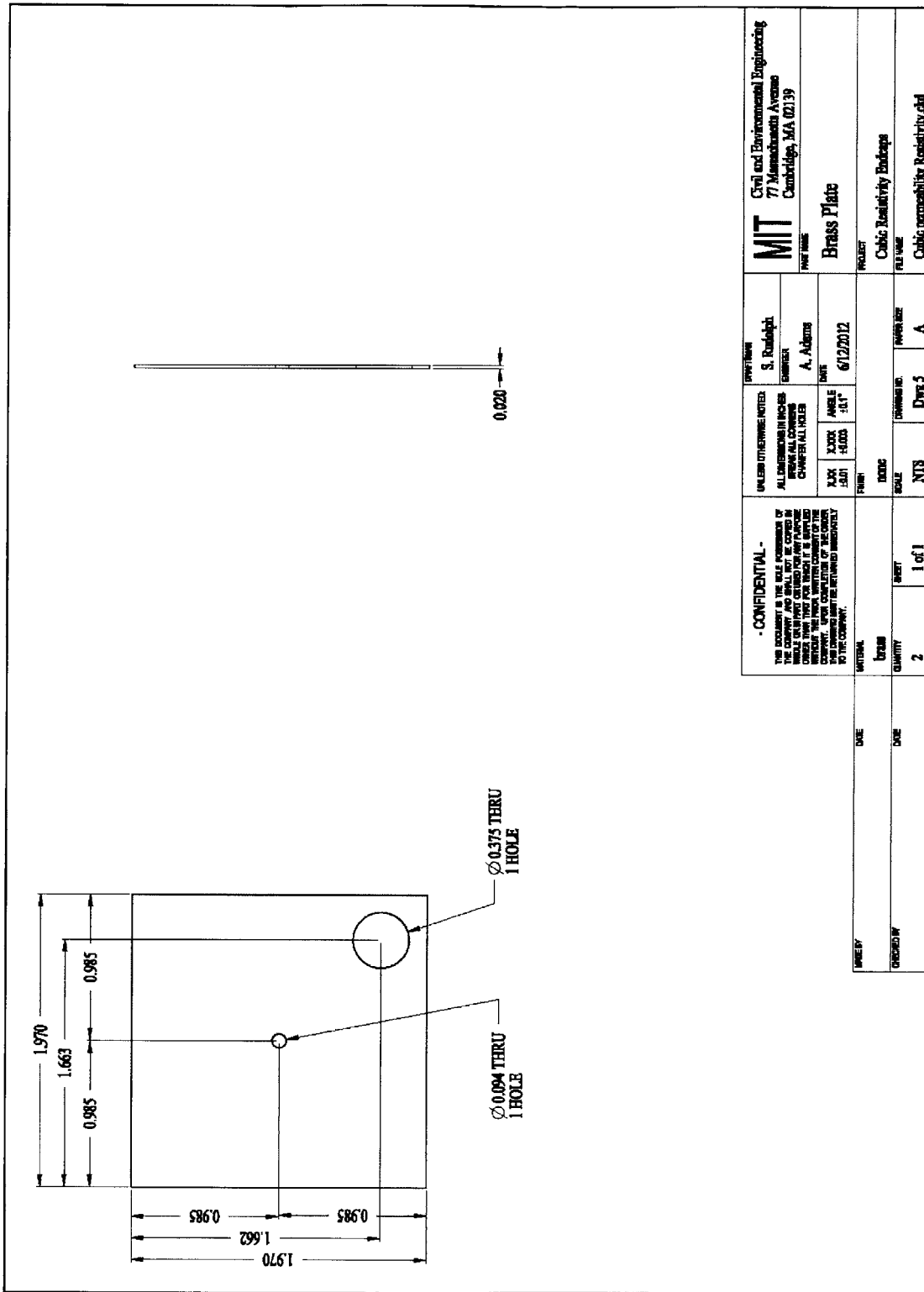


Figure A6-5: Cubic resistivity end adapters: Drawing 5, brass plate

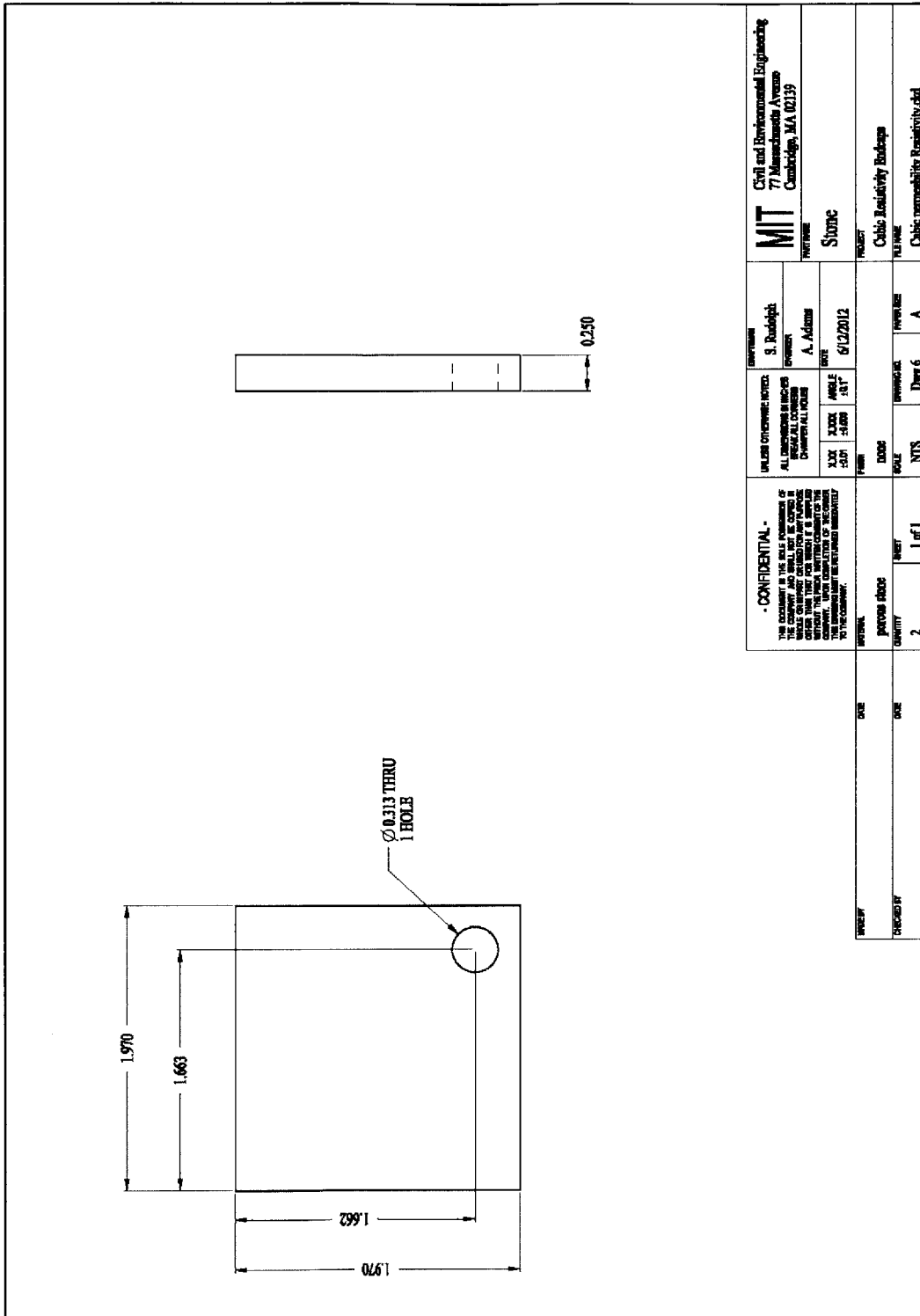


Figure A6-6: Cubic resistivity end adapters: Drawing 6, porous stone

(Page intentionally left blank)

A2: Bench top Electrodes for Measurement of Consolidated Specimens (CRS Specimen Electrodes)

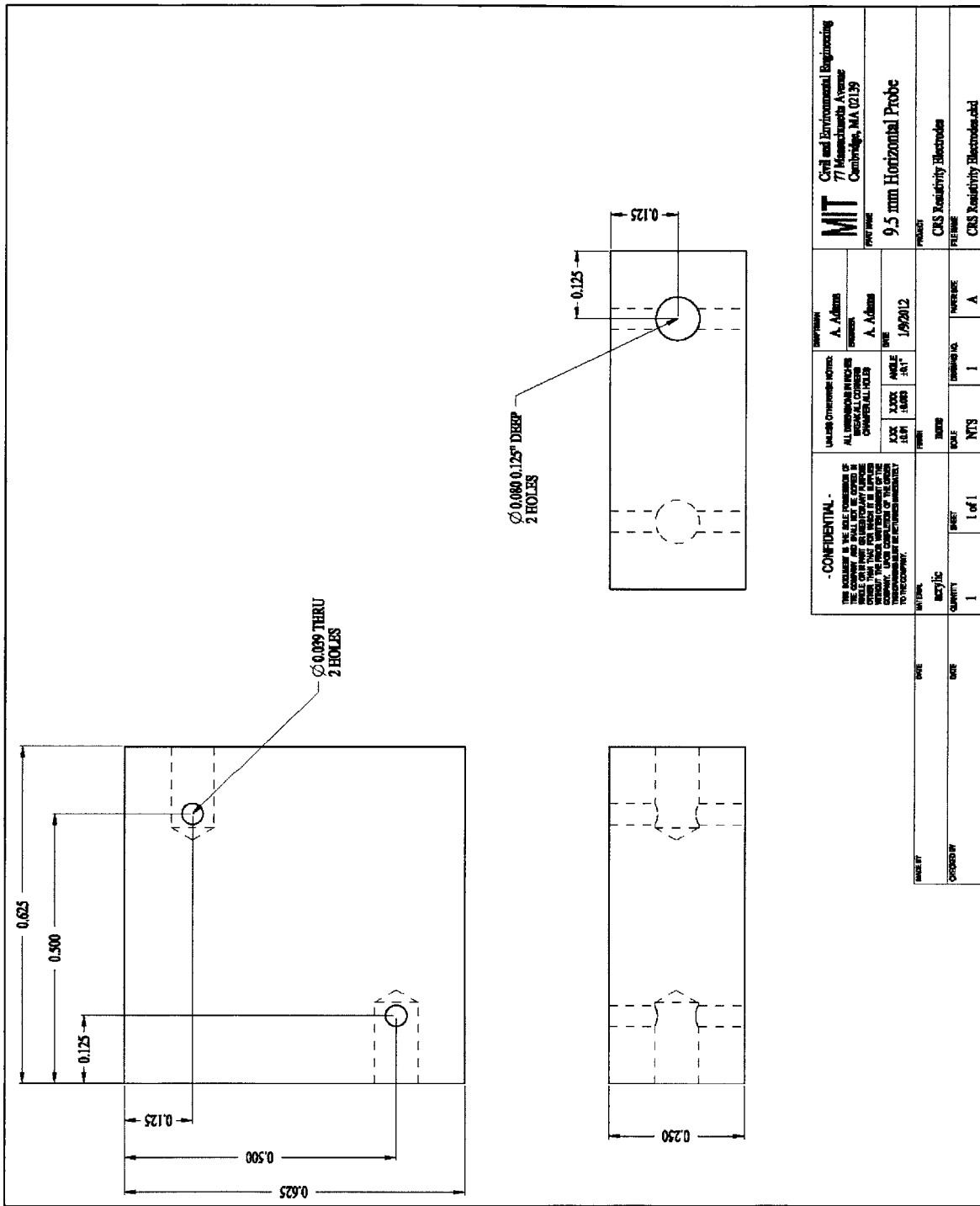


Figure A6-7: CRS Electrodes: Drawing 1, 9.5 mm probe

<p>MIT Civil and Environmental Engineering 77 Massachusetts Avenue Cambridge, MA 02139</p>		<p>MIT PROJECT: CRS Resistivity Electrodes</p>	
<p>DATE: 1/9/2012</p>		<p>PREPARED BY: CRS Resistivity Electrodes.cad</p>	
<p>DESIGNED BY: A. Adams</p>		<p>DATE: 1/9/2012</p>	
<p>CHECKED BY: A. Adams</p>		<p>SCALE: NTS</p>	
<p>DATE: 1/9/2012</p>		<p>ISSUE NO: 1</p>	
<p>DESCRIPTION: 9.5 mm Horizontal Probe</p>		<p>REVISION: A</p>	
<p>QUANTITY: 1</p>		<p>SHEET: 1 of 1</p>	

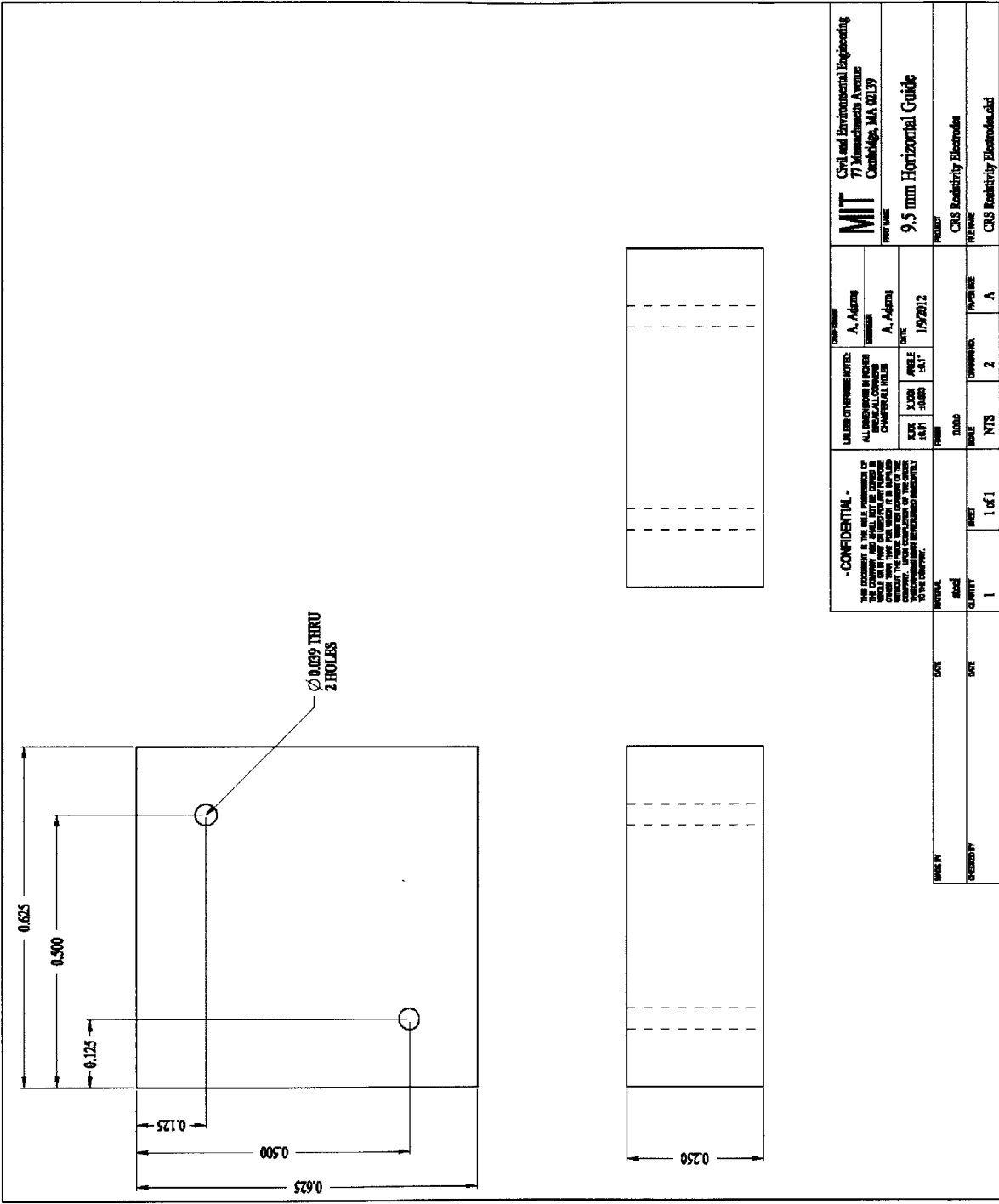


Figure A6-8: CRS Electrodes: Drawing 2, 9.5 mm drilling guide

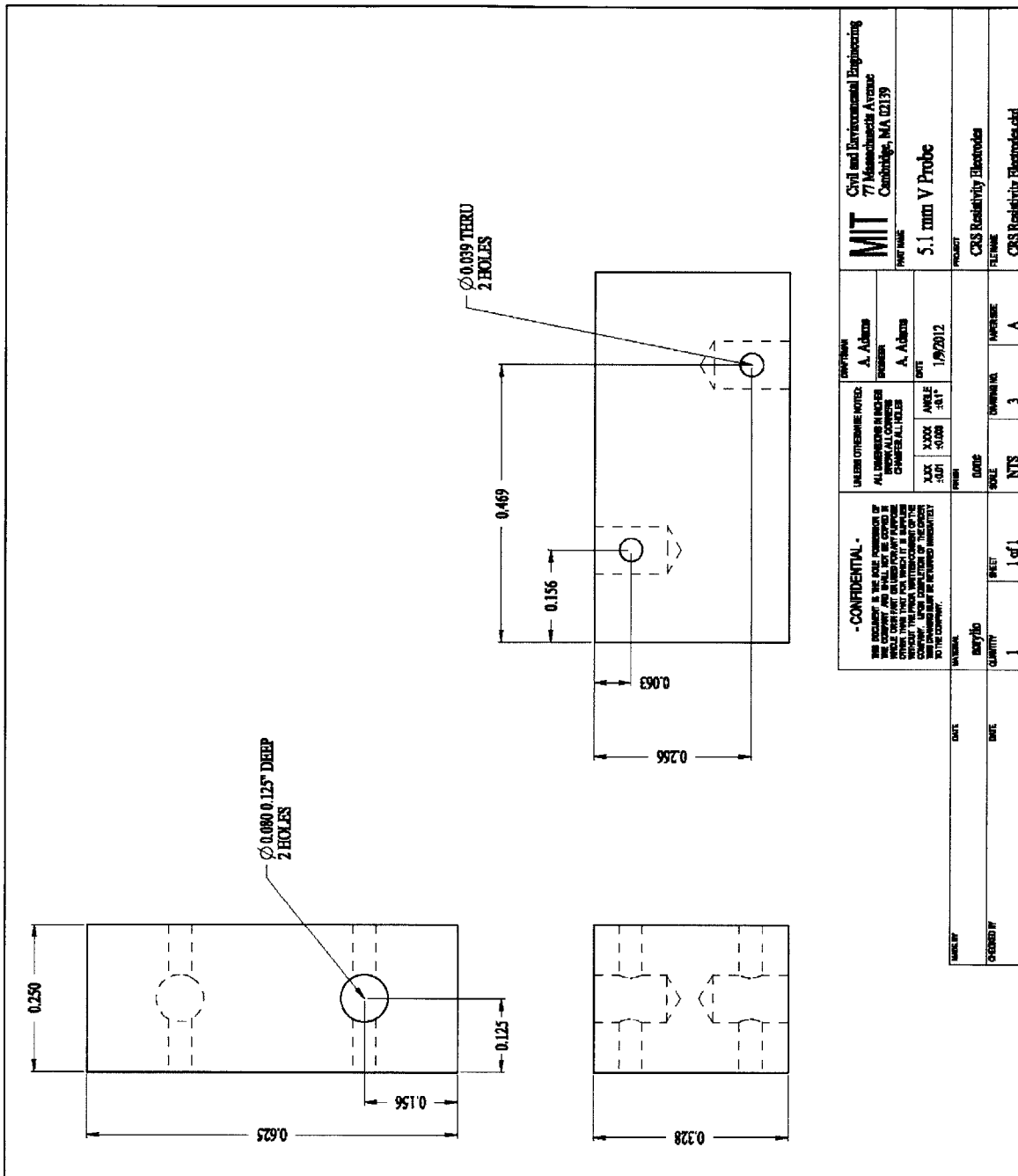


Figure A6-9: CRS Electrodes: Drawing 3, 5.1 mm probe

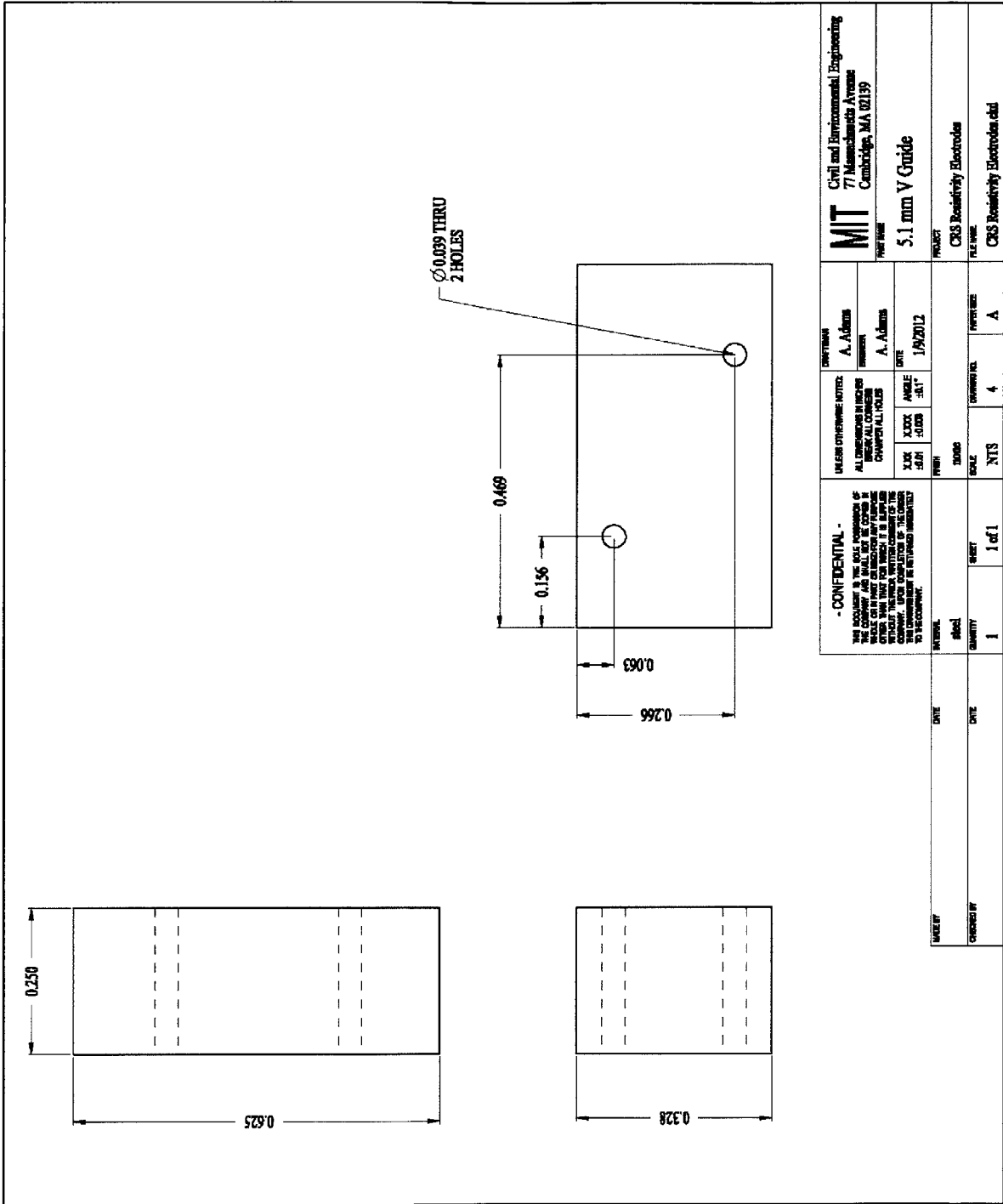


Figure A6-10: CRS Electrodes: Drawing 4, 5.1 mm drilling guide

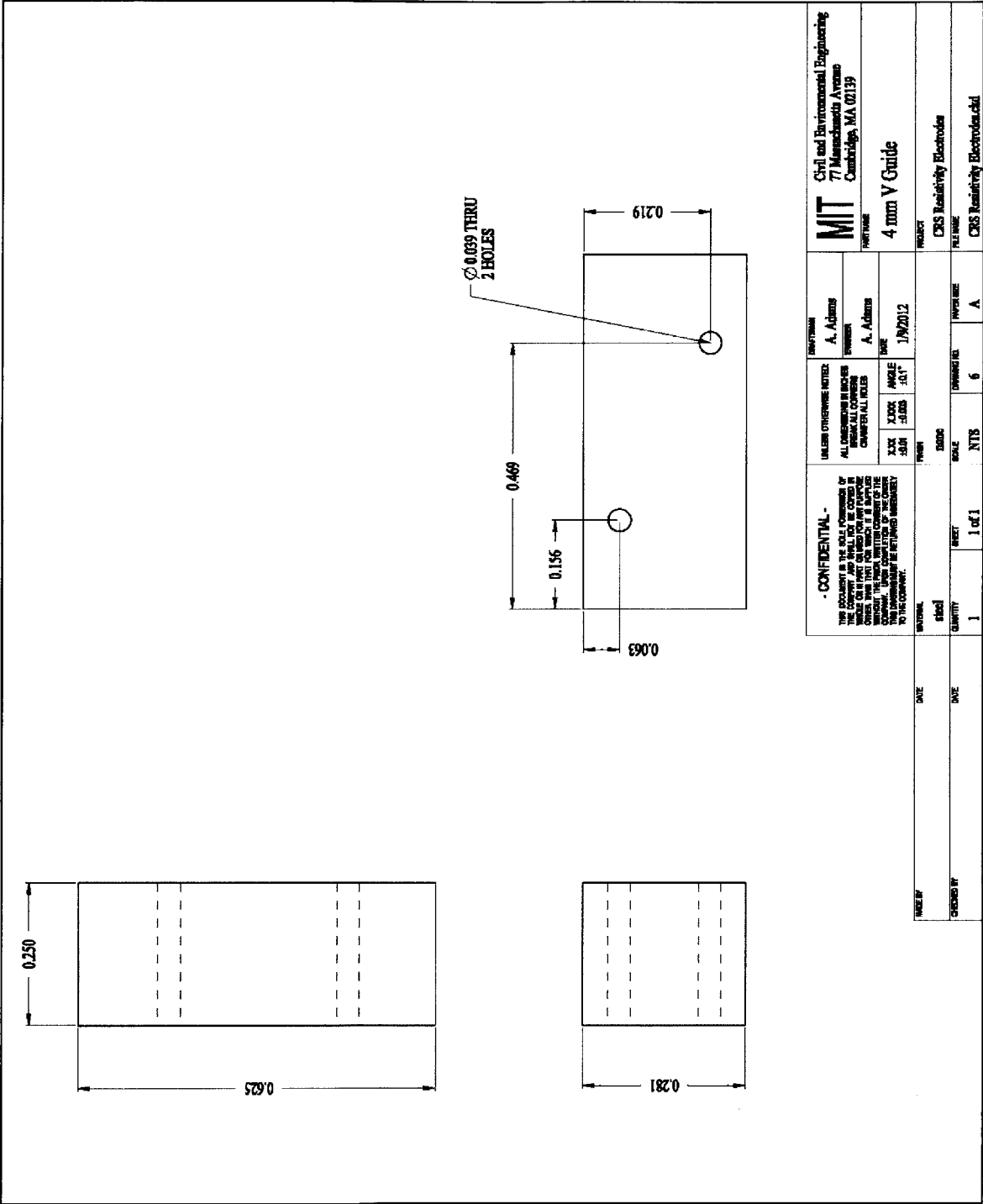


Figure A6-12: CRS Electrodes: Drawing 6, 4.0 mm drilling guide

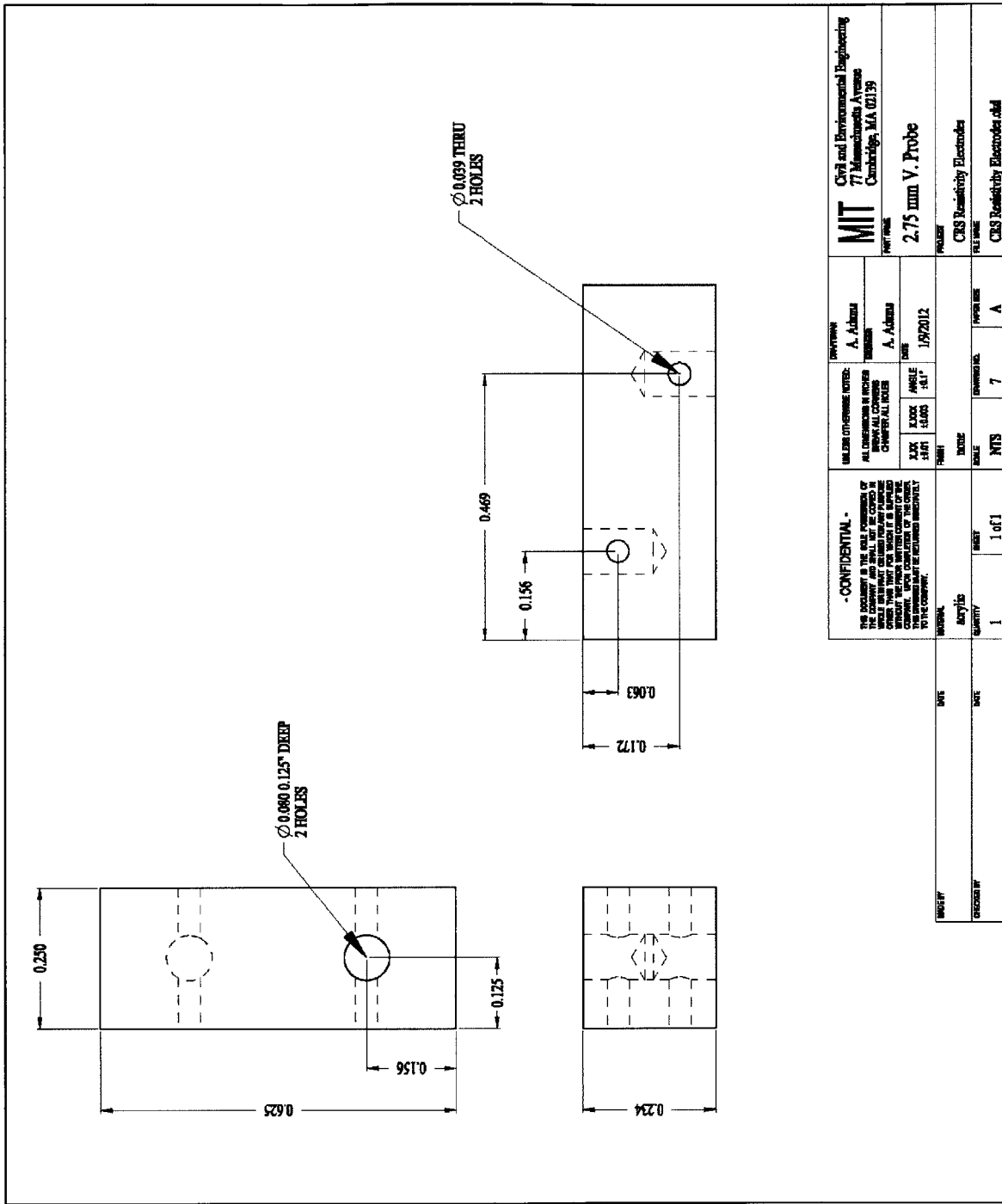


Figure A6-13: CRS Electrodes: Drawing 7, 2.75 mm probe

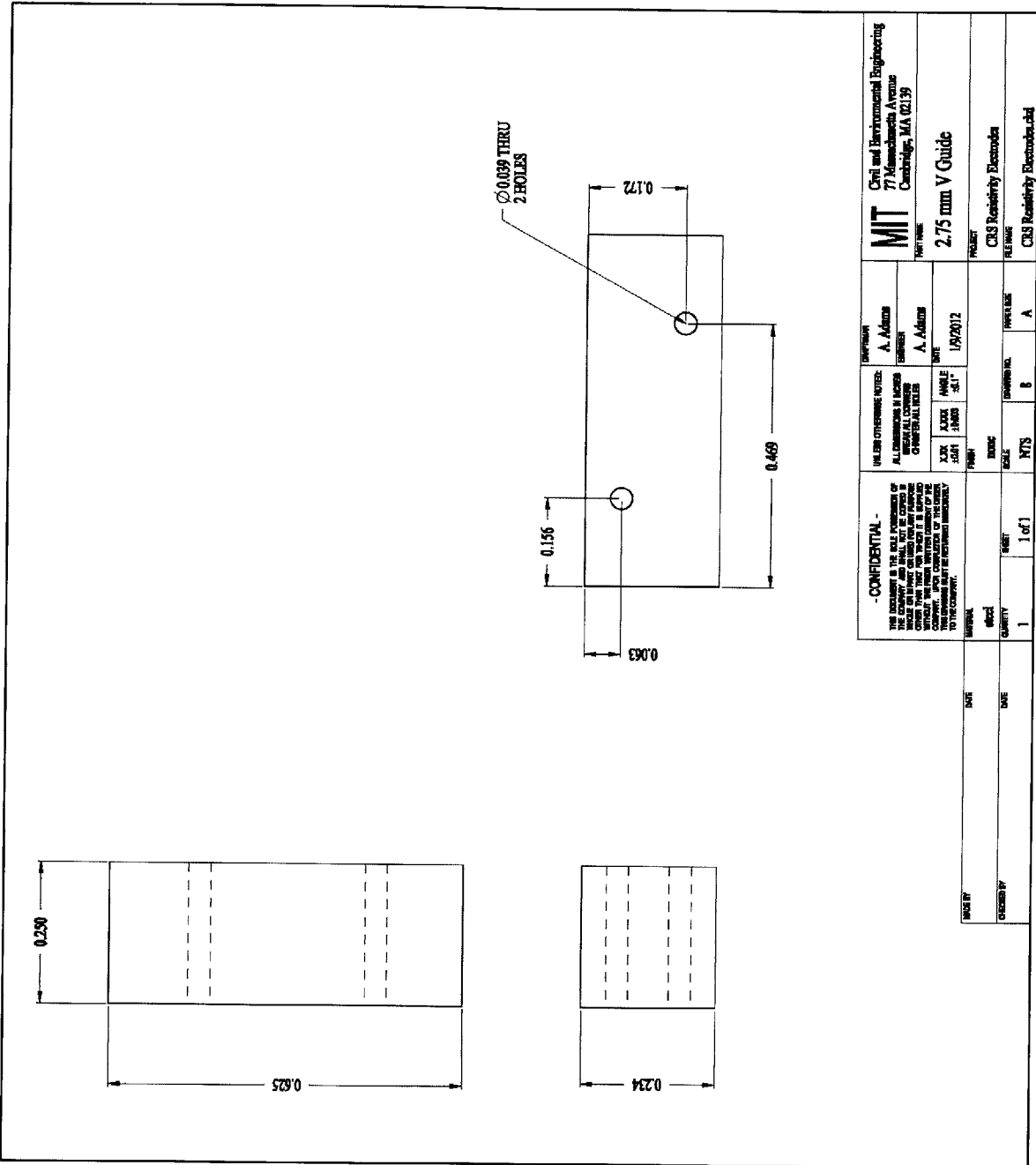


Figure A6-14: CRS Electrodes: Drawing 8, 2.75 mm drilling guide

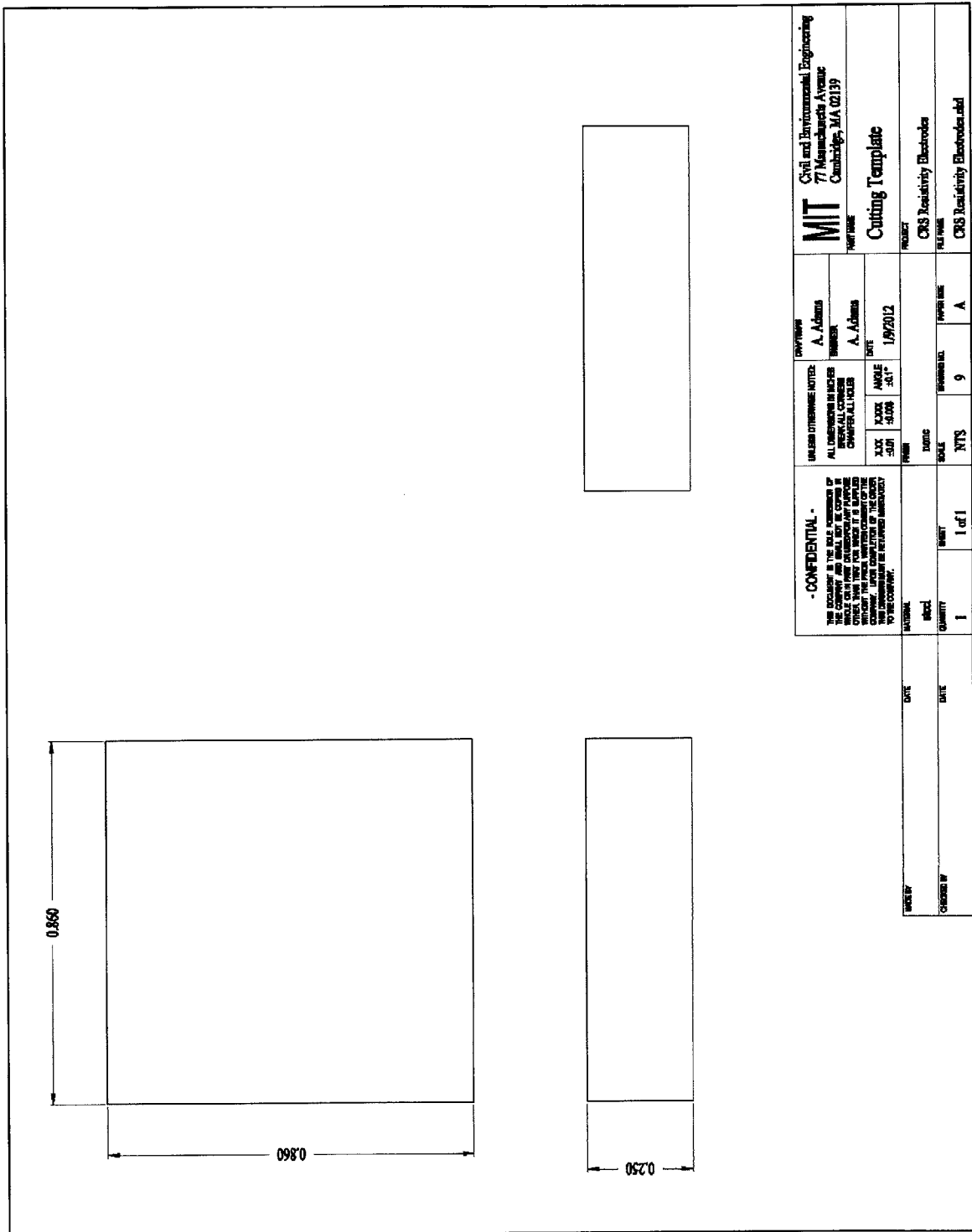


Figure A6-15: CRS Electrodes: Drawing 9, specimen trimming template

Appendix 7: Sample Data Sheets

This appendix contains samples of the data sheets that were used to record laboratory data during experiments performed for this research. The following sample data sheets are included: cubic permeability and resistivity measurement, resedimentation log, salinity measurement and constant rate of strain measurement.

MIT
 GEOTECHNICAL LABORATORY
 CUBIC HYDRAULIC CONDUCTIVITY REFERENCE DATA SHEET

Test No. _____ Direction _____ Test Date _____ Test By _____
 Project _____ Boring _____ Depth _____ Sample _____

1.0 SPECIMIN DATA

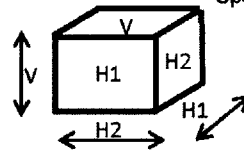
Weights and Measures							
Location							
Tare No.							
Tare							
Tare + Wet							
Tare + Dry							
WC %							

Specimin Dimensions

Meas. No.	Height (V)	Length (H1)	Width (H2)
Marker			
1			
2			
3			
4			
Avg			

Specimin Mass

Tare + Specimin _____
 Tare _____
 Specimin _____



2.0 TRANSDUCER DATA

Component	ID	Channel	CF	Units	Comments
Top Volume					
Top Pressure					
Back Pressure					
Cell Pressure					
Back Volume					
Vin					

Zeros

	Volt Meter / Data Acq		Computer		
	Zero	Vin	Zero	Vin	Zero (v/v)
Top Volume					
Top Pressure					
Back Pressure					
Cell Pressure					
Back Volume					

3.0 INITIAL SET UP AND DIRECTION TRACKING

Orient.	Top Cap	FP Marker
Vertical		
H1		
H2		

Top cap has marks ||. Use this to track direction during test. When trimming sample, use Aluminum foil V, H, H tags. Use labelled rectangular glass plate to track direction at all other times.

Applied Cell Pressure _____ Initial u_b _____ Final u_b _____
 $\sigma_s =$ _____

7.0 Resistivity Measurements

Date: _____ Time: _____

Temperature: _____ Stress Level: _____ Measurement # _____

	Rdrop	Rref	V 4-Probe	Vshunt	Gain	V 2-Probe	Vshunt	Gain	Vref	Vshunt	Gain
1											
2											
3											
4											
5											
6											
7											
8											
9											
10											
11											
12											
13											
14											
15											
16											
17											
18											
19											
20											
21											
22											
23											
24											

Comments:

MIT GEOTECHNICAL LABORATORY

Resedimentation Sample Data Sheet

Project: _____ Tested By: _____
 Sample No.: _____ Start Date: _____
 Source Material: _____ Consolidometer: _____
 Water Content: _____ Data Acq Channels: LVDT: _____ Vin: _____ Area (cm²): _____
 Salt Conc.: _____ (g/l) Salt Type/Ratios: _____ Reference Height (mm): _____

INC No.	Mass Added (g or kg)	Mass Type	Total Mass (g or kg)	Starting		Ending		Data Acq. File Name	Remarks
				Date	Time	Input (volts)	LVDT (volts)		
s									
1									
2									
3									
4									
5									
6									
7									
8									
9									
10									
11									
12									
13									
14									
15									

Comments: _____
 Final Extruded Height (mm): _____

MIT Geotechnical Laboratory
Salinity Data Sheet

Sample: _____ Natural Water Content: _____ Test Date: _____
 Testing Done _____ Test By: _____

Boston Blue Clay	Sample 1	Sample 2	Sample 3	Sample 4	Average
Location					
Tube ID	1	2	3	8	
Oven Tare ID					
Tare					
Tare + Dry					
Mass tube and cap					
Mass of soil wet (g)					
Water content % (g)					
Mass of dry soil (g)					
Mass of water in soil (g)					
Mass of water added (g)					
Total water (g)					
water content:soil (g)					
Try 1					
Try 2					
Try 3					
Result					
Corrected for 2:1 Water Soil ratio					
Co at 1g/L try 1					
Co at 1g/L try 2					
Co at 1g/L try 3					
Co at 1g/L					
Normalized result					
Salt Concentration g/l					
	average =				
	st. Dev =				
Natural Water content					
Natural Wc g					
Salt g					
Salt g/1000cc pore fluid					

MIT GEOTECHNICAL LABORATORY
CONSTANT RATE OF STRAIN CONSOLIDATION TEST
REFERENCE DATA

Project _____ Boring No. _____ Date Start _____
 Test No. _____ Sample No. _____ Date End _____
 Device No. _____ Sample Depth _____ Tested By _____

Instruments	DAQ Chan.	Make/No.	Cal. Factor	Zero @ Start	Norm. Zero	Zero @ end
Vertical Load						
Vertical Disp.						
Pore Pressure						
Cell Pressure						
Input Voltage						
Time/Date						

Water Contents

Location					Final	Washing
Tare No.						
Mass Tare+Wet Soil (gm)						
Mass Tare+Dry Soil (gm)						
Mass Tare (gm)						
Mass Dry Soil (gm)						
Water Content (%)						
From Trimmings (%)	Average =		Std. Dev. =			

Measurements

Mass Stone (gm)	
Mass Top Cap and Piston (gm)	
Mass Recess Tool (RT) (gm)	
Mass Specimen Ring w/FP (gm)	
Mass Initial Ring, Soil, FP, RT (gm)	
Mass Final Ring and Soil (gm)	

Torvanes

Vane Size and Factor	@	Readings
Small Shoe x 2.5		
Std. Shoe x 1.0		
Large Shoe x 0.2	Avg. and S. D.	

Location of Specimen (x-ray Markers) _____

Material Description

Set-Up Dimensions

Thickness of Specimen Ring				Avg (cm):
Initial Dist. of Spec. into Ring w/FP				Avg (cm):
Final Dist. of Spec. into Ring w/FP				Avg (cm):
Diameter of Ring				Avg (cm):
Thickness of FP (cm):	Initial Area (cm ²):		Initial Height (cm):	

File Name	Description

Test Remarks _____

Appendix 8: Constant Head Hydraulic Conductivity Program Code

The constant head hydraulic conductivity program is a modified version of the Triaxial program used in the MIT Geotechnical laboratory. It allows up to three axis of control: two pore pressures (axis 1 and 3) and one cell pressure (axis 2). The program contains six routines that are used to pressure up, back pressure, measure B values and hold stress on the specimen. Consolidation, B value measurement and permeability measurement are accomplished mainly using the hold stress routine by varying the parameters. Many routines that are standard in the triaxial program have been removed because they control a piston which is not used for constant head hydraulic conductivity measurement. Further, the constant head hydraulic conductivity program measures volume change but does not compute strain and therefore cannot control based on strain.

The program code may require calibration of the Proportional-Integrative-Derivative (PID) constants from time to time. These are found on lines 150 – 164 in Section 3.

The code for the constant head hydraulic conductivity program follows.

```
1   'rev 6.0 4/18/10 ala change to work with 3 pressure transducers, 3PVT's and 2 stringpots
2   ' for flexible wall hydraulic conductivity testing
3   'rev 5.3 5/17/06 change to work with clamp configuration
4   'rev 5.2 7/25/05 small edits to make consistent
5   'rev 5.1 this has a pressure sensitivity zero adjustment to the internal LC
6   'rev 5.0 10/24/00 jtg major rehaul of the basic program
7   'rev 4.0 8/1/00 jtg converted to quickbasic
8   'rev 3.1 8/06/91 jtg
9   '
10  ' Revision 1 written by Tom Sheahan to control stepper motors.
11  ' Revision 2 written by Jack germaine to control dc servo motors.
12  '
13  ' *****
14  '
15  ' The following hardware is required:
16  '   -Strawberrytree d to a converter
17  '   -The Sheahan a to d converter
18  '   -The MIT three axis dc controller box with;
19  '     -channel 1 for axial force
20  '     -channel 2 for cell pressure
21  '     -channel 3 for pore pressure
```

```

22
23 ' Relay switches are used for the following
24 '   -1 is to turn off motor 1
25 '   -2 is to turn off motor 2
26 '   -3 is to turn off motor 3
27 '   -4 is to reverse the direction of motor 1 when using the 352 controller
28 '   -5 is to turn on and off the input voltage relay
29
30
31 '*** Information shared with the setup program ****
32
33 COMMON FILENAME$, DAT$, INITIALS$, BLANK0, BLANK1, BLANK2, BLANK3, BLANK7
34 COMMON BLANK4, BLANK5, BLANK6, ZLOAD, CFLOAD, ZDCDT, CFDCDT
35 COMMON ZCELL, CFCELL, ZPORE, CFPORE, ZVOLDCDT, CFVOLDCDT, LOADCHANNEL
36 COMMON DCDTCHANNEL, CELLCHANNEL, PORECHANNEL, VOLDCDTCHANNEL,
37 DUMMY1
38 COMMON DUMMY2, VINCHANNEL
39
40 'convert some variables for use in conductivity
41 'Z = Zero, CF = Cal Factor, Channel = Channel
42 'set top pressure = Load
43 'set back volume = VolDCDT
44 'set top volume = DCDT
45
46 ZTOP = ZLOAD      'top pressure
47 CFTOP = CFLOAD
48 TOPCHANNEL = LOADCHANNEL
49 ZBVOL = ZVOLDCDT 'Bottom volume
50 CFBVOL = CFVOLDCDT
51 BVOLCHANNEL = VOLDCDTCHANNEL
52 ZTVOL = ZDCDT     'Top volume
53 CFTVOL = CFDCDT
54 TVOLCHANNEL = DCDTCHANNEL
55
56 DIM CELL(25), TOP(25), BACK(25), time(25), VOLTS(10)
57 DIM MFLAG$(3), control!(3), SGAIN(3), DGAIN(3), mvolts(3), zvolts(3), Amp(6)
58 DIM k(3, 5, 2), e(3, 3), mdir(3)
59 ' for k(motor, constant,controltype)
60
61
62 ' *****
63 ' AD1170$ = "N" 'used as flag to allow debugging the program
64 AD1170$ = "Y" 'comment this line out when card is not in machine

```

```

65 ' *****
66 ' MOTOR1$ = "Y" 'use this setting when using reversing relay on motor1
67   MOTOR1$ = "N" 'default condition when not using the relay
68
69 ***** Constants which are used throughout the program *****
70   rev$ = "6.0"
71   blk$ = SPACE$(79)           'line eraser
72   H1$ = "TRANSDUCER READINGS in volts"
73   H2$ = "  T.Vol  Cell  T.Pore  B.Pore  B.Vol  input"
74
75   H3$ = "Top      Cell  Back  T.Vol  B.Vol"
76   H4$ = "  ksc   ksc   ksc   cm3   cm3"
77   P1$ = "####.#": P2$ = "###.##": P3$ = "##.###"
78
79
80   'V0 = A0 * H0           'initial volume *****DONT NEED
81   VINREAD = 10           'period to read vin & update screen
82   VINFLAG = VINREAD      'input voltage counter
83   Refreshrate = 3       'number of readings between updating screen
84   STEPTIME = 1           'time for each motor step in sec.
85
86 ' ***** Set up function keys and be sure keyboard is set correctly ***
87   CLS
88   X = 1
89   GOSUB 3890             'lock out keyboard
90 260 GOSUB 4160           'set enter key
91 270 a$ = INKEY$
92   IF ENTERFLAG = 1 THEN GOTO 340
93   IF a$ <> CHR$(13) THEN GOTO 270
94   CLS
95   LOCATE 15 + 2 * X, 2
96   PRINT "turn off both the NUMBER LOCK and CAPS LOCK keys"
97   PRINT "      and"
98   X = X + 1
99   GOTO 260
100
101 340 CLS
102   LOCATE 10, 5
103   PRINT "This will take two seconds"
104   GOSUB 3750           'calibrate steptime
105
106 ***** SET UP GAINS, ARRAYS, VARIABLES AND CURRENT READINGS *****
107

```

```

108 ' set the A/D converter up and define performance variables
109 INTTIME = 21 'to specify the integraion time of the A/D converter
110     'inttime=16+N where N=0 1 msec  N=4 100 msec
111     '      N=1 10 msec  N=5 166.7 msec
112     '      N=2 16.7 msec  N=6 300 msec
113     '      N=3 20 msec
114     ' can set a variable integration time using the EIS command
115 INTBIT = 13 ' specify the bit precision  INTBIT=(bit precision-7)
116 AD1170 = 768 ' the decimal I/O address of the A/D converter
117 MUX! = 776 ' decimal I/O of channel selector
118 '      CORRESPONDS TO SWITCH SETTING 00001
119
120 ***** set default values and flags *****
121
122 row = 2      ' for what
123 Tadjust = 0  ' to adjust time for a change in date during test
124 ENTERFLAG = 0  ' for breaking a loop on the enter key
125 NUMCHANNELS = 6  ' for input channel loop for data acq card
126 MAXINCS = 25  ' for saturation steps
127 STARTDATE$ = DATE$ ' get todays date for rate calculations
128 GNDCHANNEL = 15  ' location of the ground connection on ad card
129 REFCHANNEL = 14  ' location of the 5 volt reference voltage on A/D card
130 tolerance = .1  ' stress (ksc) condition to move to next step
131 feedback = 0  ' variable to specific equations used for computer error
132
133
134 GOSUB 10000      'this sets up the A/D card
135
136 ' ***** Setup the DC servo motors *****
137
138 motors! = 6928      'decimal I/O address of analog out card
139 STOPDEVICE! = 0      'variable to specify motors to stop;0=all
140 OUT motors! + 4, 0      'open relays and lock all motors
141
142 ***** specify the gain values to control the motors *****
143
144     FOR I = 1 TO 3
145     FOR j = 1 TO 4
146     k(I, j, 0) = 0
147     NEXT j
148     NEXT I      '= 3 integration
149                 '=4 memory
150

```

```

151 k(1, 0, 1) = 1 'volt-sec/ksc '
152 k(1, 1, 1) = 0.4 '
153 k(1, 2, 1) = -.03 ' control type=0 off
154 k(1, 3, 1) = .1 'was 0.8 =1 pressure
155 k(1, 4, 1) = .95 '
156 k(2, 0, 1) = 10 'v-s/ksc '
157 k(2, 1, 1) = 1 ' motor=1 top
158 k(2, 2, 1) = -.03 ' =2 cell
159 k(2, 3, 1) = .5 ' =3 pore
160 k(2, 4, 1) = .7 'was 0.9
161 k(3, 0, 1) = 1 'v-s/ksc
162 k(3, 1, 1) = .4
163 k(3, 2, 1) = -.03
164 k(3, 3, 1) = .1 'was 0.2
165 k(3, 4, 1) = 1 'was 0.95
166
167 ***** Hardware settings for the interface *****
168
169 Amp(1) = 1 'amplifier gains on the ad524 by channel
170 Amp(2) = 10
171 Amp(3) = 10
172 Amp(4) = 10
173 Amp(5) = 1
174 Amp(6) = 1
175
176 DEVICE!(1) = 14 'set motor 1 to top *****why 14, 13 and 11? Because
177 with Mode, they add to 15!
178 DEVICE!(2) = 13 'set motor 2 to cell
179 DEVICE!(3) = 11 'set motor 3 to pore
180
181 mdir(1) = 1 'program assumes positive sign convention
182 mdir(2) = 1 'so a positive voltage causes increase stress
183 mdir(3) = 1 'and positive strain. mdir reverses the
184 'convention to account for wiring changes
185
186 zvolts(1) = 0 'voltage offset to stop each motor
187 zvolts(2) = -.04 'changed for mit06 from 0
188 zvolts(3) = 0
189
190
191 control!(1) = 0 'set top to off 1=stress ' *****
192 SHOULD ALL CONTROLS BE EITHER OFF OR ON ONLY? DON'T NEED DISP OR STRAIN
193 CONTROL, ONLY STRESS CONTROL

```

```

194 control!(2) = 0      'set cell to off
195 control!(3) = 0      'set pore to off
196
197 Mode(1) = 0          'determines method of control
198 Mode(2) = 0          '0=step,1=continuous open loop, 2=continuous pid loop
199 Mode(3) = 0
200
201
202 *** Reminders to set up the load frame for testing ***
203
204
205 PRINT "Ensure that ""
206 PRINT "   The PVC reservoirs are closed"
207 PRINT "   -the back pressure valves are closed"
208 PRINT "   -and the control box is on ""
209 PRINT
210 PRINT " This is program revision "; rev$
211 IF AD1170$ = "N" THEN PRINT " The AD1170 card is DISABLED"
212 IF MOTOR1$ = "Y" THEN PRINT " The reversing switch for motor 1 is ENABLED"
213 INPUT " press ENTER to continue ", a$
214
215 ' ***** Collect a set of readings and set the target values *****
216 GOSUB 3260          'get set of readings
217 newcell = CELL      'set target values
218 newback = BACK
219 newtop = TOP
220
221 *****
222 890 ***** This is the starting point of the control program *****
223 *****
224 control(1) = 1 'needed to print target values on screen
225 control(2) = 1
226 control(3) = 1
227
228 feedback = 0
229
230 CLS : GOSUB 4463      'data set and basic screen
231 GOSUB 3880           'turn off motors and zero control
232
233 PRINT
234 PRINT "Please select the next phase of test;": PRINT
235 PRINT " 1. Undrained Hydrostatic Initial Stress ";
236 PRINT " 2. Drained Hydrostatic Stress Change  ";

```

```

237 PRINT " 3. Hold Current State of Stress ";
238 PRINT " 4. Hold Target State of Stress ";
239 PRINT " 5. Enter New Target State of Stress ";
240 PRINT " 6. Measure 'B' Value 7. End Program"
241 900 LOCATE 19, 1: PRINT blk$ 'ERASES LINE
242 LOCATE 19, 1: INPUT " Enter OPTION number ", CHOICE$
243 CH = VAL(CHOICE$)
244 IF CH < 1 OR CH > 7 THEN GOTO 900
245 ON CH GOTO 930, 1100, 2040, 2050, 2060, 2140, 2100
246
247 *****
248 930 ***** PRESSURE-UP TO GET INITIAL EFFECTIVE STRESS *****
249 *****
250
251
252 control(1) = 0 'turned off
253 control(2) = 1 'stress control
254 control(3) = 0 'turned off
255 Mode(1) = 0
256 Mode(2) = 0 'off between steps
257 Mode(3) = 0
258 Reverse(1) = 0
259 Reverse(2) = 0
260 Reverse(3) = 0
261 feedback = 1
262
263
264 KEYFLAG = 0
265 LOCATE 23, 1: PRINT blk$ 'ERASES LINE
266 PRINT "NOTE-Be sure the back pressure valves are closed"
267 960 INPUT "Initial pressure-up desired (yes or no) ? ", Z$
268 IF Z$ = "YES" OR Z$ = "yes" THEN GOTO 990
269 IF Z$ = "no" OR Z$ = "NO" THEN GOTO 890 ELSE GOTO 960
270 990 CLS : GOSUB 4463 'read & basic screen
271 LOCATE 16, 1
272 1001 INPUT "What cell pressure should be applied (ksc) ? ", newcell
273 1002 LOCATE 16, 1: PRINT SPACE$(65)
274 1030 KEY(1) ON: ON KEY(1) GOSUB 2600
275 1040 CLS : LOCATE 25, 1: PRINT blk$
276 1050 LOCATE 25, 1: PRINT "<F1> TO END PRESSURE UP";
277 1060 LOCATE 25, 65: COLOR 0, 7: PRINT "PRESSURE UP"; : COLOR 3, 8
278 1065 GOSUB 4450 'print screen
279 1066 PTRFLAG! = 1

```

```

280
281 1070 WHILE (KEYFLAG <> 1)
282 1080 GOSUB 2720
283 1090 WEND
284
285 GOSUB 3880 'stop motors and lock relays
286
287 1095 GOTO 890
288
289 *****
290 1100 ***** DRAINED STRESS STEP APPLICATION *****
291 *****
292 control(1) = 0 'all stress control *****TURNED TOP PRESSURE
293 OFF*****8
294 control(2) = 1
295 control(3) = 1
296 Mode(1) = 0 'all turned off between steps
297 Mode(2) = 0
298 Mode(3) = 0
299 Reverse(1) = 0
300 Reverse(2) = 0
301 Reverse(3) = 0
302 feedback = 1
303
304 1140 CLS : GOSUB 4465 'readings and basic screen
305 1150 PRINT
306 R = CSRLIN
307 LOCATE 23, 1: PRINT blk$
308 COLOR 0, 7
309 LOCATE R, 11
310 PRINT "DRAINED CONSOLIDATION STRESS INCREMENTS"
311 COLOR 3, 8
312 PRINT "For each STRESS STEP specify the CELL PRESSURE, BACK PRESSURE and
313 DURATION"
314 PRINT "Enter a '99' for cell pressure when finished."
315 PRINT "Enter a '999' for cell pressure to return to MAIN MENU"
316 NUMINCS = 0
317 FOR I = 1 TO MAXINCS
318 CELL(I) = -1
319 BACK(I) = -1
320 time(I) = -1
321 NEXT I
322 PRINT "Increment #"; TAB(18); "Cell"; TAB(34); "Back"; TAB(60); "Time (minutes)"

```



```

323
324 1250 WHILE (CELL(NUMINCS) <> 999 AND CELL(NUMINCS) <> 99 AND NUMINCS <>
325 MAXINCS)
326     NUMINCS = NUMINCS + 1
327     row = CSRLIN
328     IF row < 24 THEN GOTO 1360
329     I = 23 - NUMINCS
330     LOCATE 17, 1
331     FOR row = 17 TO 22
332         PRINT row - I; TAB(18); CELL(row - I); TAB(34); BACK(row - I); TAB(60);
333 time(row - I)
334     NEXT row
335     PRINT SPACE$(70)
336
337 1360 LOCATE row, 1: PRINT NUMINCS; TAB(20); : INPUT CELL(NUMINCS)
338     IF CELL(NUMINCS) < 0 THEN 1360
339     IF CELL(NUMINCS) = 99 THEN 1250 'Finished entering data
340     IF CELL(NUMINCS) = 999 THEN 1250 'Finished entering data
341 1380 LOCATE row, 34: PRINT ""; : INPUT BACK(NUMINCS)
342     IF BACK(NUMINCS) < 0 THEN 1380
343     IF BACK(NUMINCS) > CELL(NUMINCS) THEN 1380
344 1390 LOCATE row, 60: PRINT ""; : INPUT time(NUMINCS)
345     IF time(NUMINCS) < 1 THEN 1390
346     IF NUMINCS = MAXINCS THEN PRINT "Max # increments ="; MAXINCS: GOTO
347 1250
348     WEND
349     IF CELL(NUMINCS) = 99 THEN NUMINCS = NUMINCS - 1
350     IF CELL(NUMINCS) = 999 THEN GOTO 890
351
352     CLS : PRINT
353     PRINT "Increment #"; TAB(18); "Cell"; TAB(34); "Back"; TAB(60); "Time (minutes)"
354     FOR I = 1 TO NUMINCS
355         PRINT I; TAB(20); CELL(I); TAB(34); BACK(I); TAB(60); time(I)
356         time(I) = time(I) * 60
357     NEXT I
358     LOCATE 24, 1
359 1550 INPUT "Is this schedule okay (yes or no) ?"; a$
360     IF a$ = "yes" OR a$ = "YES" THEN 1600
361     IF a$ = "NO" OR a$ = "no" THEN GOTO 1100
362     GOTO 1550
363
364 1600 ' ***** APPLY THE DRAINED STRESS INCREMENTS *****
365

```

```

366
367 1650 INCR = 1          ' loop to apply the large increments
368
369 1660 CLS : GOSUB 4450      'readings & basic screen
370   PTRFLAG! = 1
371   GOSUB 4160              'enter flag for next inc
372   GOSUB 4290              'esc flag to abort inc
373   LOCATE 25, 55: COLOR 0, 7: PRINT "STRESS APPLICATION"; : COLOR 3, 8
374   OLDCELL = CELL: OLDBACK = BACK:
375   LOCATE 16, 57: PRINT "Increasing Pressure "
376   LOCATE 18, 57: PRINT "of Increment "; INCR
377   DCELL = (CELL(INCR) - CELL) / 10          'DIVIDE BY 10 B/C APPLIES IN 10
378 STRESS INCREMENTS IN MINOR INCREMENT LOOP
379   DBACK = (BACK(INCR) - BACK) / 10
380   t0 = TIMER: Tadjust = 0  'set the start time for the increment
381   Lasttime = t0
382   Delttime = 0
383   newcell = OLDCELL: newback = OLDBACK
384
385
386 '++++++ This section is the minor increment loop +++++++
387
388   CTR = 0
389   WHILE (ENTERFLAG = 0 AND CTR <> 10) 'Loop to apply the split increment
390     CTR = CTR + 1
391     LOCATE 17, 57: PRINT "for Step "; CTR
392     newcell = newcell + DCELL
393     newback = newback + DBACK
394     IF CTR = 10 THEN
395       newcell = CELL(INCR)
396       newback = BACK(INCR)
397
398     END IF
399 1770   GOSUB 2720
400     IF ENTERFLAG <> 0 THEN GOTO 1800
401     IF ABS(CELL - newcell) > tolerance THEN GOTO 1770 'tolerance check
402     IF ABS(BACK - newback) > tolerance THEN GOTO 1770
403
404 1800 WEND
405
406 '++++ This section continously monitors cell, pore and load
407
408   NEWTIME = TIMER

```

```

409     IF ENTERFLAG <> 0 THEN GOTO 1960
410     LOCATE 16, 57: PRINT "Holding pressure  "
411     WHILE (Deltime <= time(INCR) AND ENTERFLAG = 0)
412         GOSUB 2720
413         now = TIMER
414         IF now < Lasttime THEN Tadjust = Tadjust + 86400
415         Deltime = now - t0 + Tadjust
416         Lasttime = now
417         LOCATE 17, 57
418         T! = INT(Deltime / 60)
419         PRINT "for "; T!; " of "; INT(time(INCR) / 60); " MIN"
420     WEND
421
422 1960 'Process the end of increment
423
424     IF ENTERFLAG <> 1 THEN GOTO 1970     'not enter key
425     ENTERFLAG = 0
426     KEY(19) ON: KEY(20) ON           'reset keys
427     GOTO 2010                         'next inc
428 1970 IF ENTERFLAG = 2 THEN GOTO 2015     'abort the mission
429     GOSUB 2150                         'Do a B-value check
430     control(3) = 1                     'return to stress control
431     GOSUB 2720
432
433 2010 IF INCR = NUMINCS THEN GOTO 2050     'goto hold stress
434     INCR = INCR + 1
435     GOTO 1660                         'continue to next increment
436
437 2015 '**** manage action on abort increment ****
438
439     KEY(19) OFF: KEY(20) OFF
440     GOSUB 3880                         'close relays
441     GOTO 890                           'return to main menu
442
443     *****
444 2040 '***** HOLD CURRENT STRESS SUBROUTINE *****
445     *****
446
447 2042 newback = BACK 'enter if all new values but limit motor direction
448 2044 newcell = CELL
449 2046 newtop = TOP
450
451

```

```

452      '*****
453 2050 '***** HOLD EXISTING TARGET STATE OF STRESS SUBROUTINE *****
454      '*****
455
456      control(1) = 1          '*****CAN'T REALLY CHANGE*****
457      control(2) = 1
458      control(3) = 1
459      Mode(1) = 2          'set to pid
460      Mode(2) = 2
461      Mode(3) = 2
462      Reverse(1) = 0
463      Reverse(2) = 0
464      Reverse(3) = 0
465      feedback = 1
466
467 2053 CLS : GOSUB 4450      'enter using existing control settings
468 2055 PTRFLAG! = 1
469      GOSUB 4290
470      LOCATE 25, 65: COLOR 0, 7: PRINT "HOLD STRESS"; : COLOR 3, 8
471      t0 = TIMER
472      Tadjust = 0
473      Lasttime = t0
474      WHILE (ENTERFLAG = 0)
475          GOSUB 2720
476          now = TIMER
477          IF now < Lasttime THEN Tadjust = Tadjust + 86400
478          INctime = now - t0 + Tadjust
479          Lasttime = now
480          LOCATE 17, 56: PRINT "Time (hrs) =";
481          PRINT USING " ###.##"; INctime / 3600!
482
483      WEND
484
485      GOSUB 3880          'close relay and stop motors
486      GOTO 890          'go to main
487
488      '*****
489 2060 '***** Manually set a new set of target values *****
490      '*****
491
492      CLS : GOSUB 4463
493      row = 11
494      COLOR 0, 7: LOCATE row, 11

```

```

495     PRINT "Manually Input a NEW SET of TARGET VALUES"
496     COLOR 3, 8
497     PRINT
498     PRINT "The current target values are displayed above"
499     PRINT " You can enter new target values for each stress"
500     PRINT " or press ENTER to keep the current value"
501 2062 LOCATE 17, 1
502     INPUT " Enter the new target top pressure (ksc) ", a$
503     IF a$ = "" THEN a = newtop: GOTO 2064
504     a = VAL(a$)
505
506 2064 LOCATE 17, 1
507     PRINT SPACE$(65)
508     PRINT SPACE$(65)
509     LOCATE 17, 1
510     INPUT " Enter the new cell pressure (ksc) ", a$
511     IF a$ = "" THEN b = newcell: GOTO 2066
512     b = VAL(a$)
513
514 2066 LOCATE 17, 1
515     PRINT SPACE$(65)
516     PRINT SPACE$(65)
517     LOCATE 17, 1
518     INPUT " Enter the new back pressure (ksc) ", a$
519     IF a$ = "" THEN c = newback: GOTO 2068
520     c = VAL(a$)
521     IF c >= b THEN GOTO 2066
522
523 2068 LOCATE 12, 1
524     FOR I = 1 TO 7
525     PRINT SPACE$(65)
526     NEXT I
527     LOCATE 13, 1
528     PRINT "The following values will be used as the new target values"
529     PRINT
530     PRINT "    Top Pressure = "; a
531     PRINT "    Cell Pressure = "; b
532     PRINT "    Back Pressure = "; c
533     PRINT
534     INPUT " Is it okay to continue (yes or no) ", a$
535     IF a$ <> "yes" THEN GOTO 890
536     newtop = a
537     newcell = b

```

```

538     newback = c
539
540     GOTO 2050
541     '-----
542     '---- THE FOLLOWING SECTIONS ARE ALL UTILITY ROUTINES ----
543     '-----
544
545     2100 '***** END PROGRAM *****
546
547     OUT motors! + 4, 0           'LOCK MOTORS
548     LOCATE 10, 1
549     FOR j = 1 TO 10
550         PRINT blk$
551     NEXT j
552     LOCATE 13, 1
553     PRINT "Enter 'a' to return to the setup program => "
554     PRINT "  'b' to continue running this program =>"
555     INPUT " or just press <Enter> to stop program ", Z$
556     IF Z$ = "a" OR Z$ = "A" THEN CHAIN "qbsetup3.bas"
557     IF Z$ = "B" OR Z$ = "b" THEN GOTO 890
558     STOP: END
559
560     '*****
561     2140 '***** Measurement of B value subroutine *****
562     '*****
563     GOSUB 2150           'this allows the B value routine to be entered using a got
564     GOTO 890
565     ' *****
566     '                                     *****HAVEN'T TOUCHED THIS ROUTINE
567
568     2150 FOR I = 1 TO 5: BEEP: NEXT I
569     control(1) = 0       'stress control
570     control(2) = 1       'stress control
571     control(3) = 1       'stress control
572     Mode(1) = 0
573     Mode(2) = 0          'off between steps
574     Mode(3) = 0
575     Reverse(1) = 0
576     Reverse(2) = 0
577     Reverse(3) = 0
578     feedback = 1
579
580     2190 CLS : GOSUB 4450

```

```

581 2200 LOCATE 25, 65: COLOR 0, 7: PRINT "B-VALUE CHECK"; : COLOR 3, 8
582 2210 TIMER ON: ON TIMER(60) GOSUB 4230 'Time out ==> set flag
583 2220 GOSUB 4160 'set enter flag
584 2221 GOSUB 4290 'set esc flag
585 2222 PTRFLAG! = 1
586 2230 WHILE (ENTERFLAG = 0)
587 2235 GOSUB 2720
588 2237 WEND
589 2238 TIMER OFF
590 2240 IF ENTERFLAG = 1 THEN GOTO 2270 'measure B-value
591 2250 RETURN 'time up or esc key
592 2270 CLS : GOSUB 4465
593 2271 LOCATE 25, 65: COLOR 0, 7: PRINT "B-VALUE CHECK"; : COLOR 3, 8
594 2280 LOCATE 14, 1: INPUT "Enter cell pressure increment (ksc) to apply: ", CELLINCR
595 2290 INPUT "Close pore pressure valves,press <Enter>."; a$
596 2291 RETURNCELL = CELL: RETURNBACK = BACK' pressures to return to at end
597 2295 GOSUB 4290 'set esc flag
598 2296 LOCATE 14, 1: PRINT blk$: PRINT blk$
599 2300 GOSUB 4465 'new readings
600 2301 PTRFLAG! = 1
601 2302 LOCATE 12, 1: PRINT H3$; " B-value"
602 2303 row = CSRLIN
603 2304 LOCATE 21, 20: PRINT H1$: PRINT H2$; " B-value"
604 2310 ZROCELL = CELL: ZROBACK = BACK 'start values for b-value
605
606 2360 '
607 2370 ' This is a loop to do the B-value check
608 Extraprint$ = "bvalue"
609 2400 newcell = RETURNCELL + CELLINCR' set the target cell pressure
610 2405 TIMER ON: ON TIMER(120) GOSUB 4230
611 control(3) = 0 'lock off pore motor
612 2410 WHILE (ENTERFLAG = 0)
613 2420 GOSUB 2720
614 2425 IF (CELL - ZROCELL) <= 0 THEN BVALUE = 0: GOTO 2440
615 2430 BVALUE = (BACK - ZROBACK) / (CELL - ZROCELL)
616 2440 '
617 2460 WEND
618 2480 Extraprint$ = ""
619 2490 TIMER OFF
620 2491 'LOCATE 12, 1': PRINT H3$; " "
621 2492 'FOR i = 1 TO 7: PRINT SPACE$(60): NEXT i
622 2493 'Row = 13
623 2500 CLS

```

```

624     GOSUB 4440
625     LOCATE 17, 60: PRINT "The final B-value"
626     LOCATE 18, 65: PRINT "is "; : PRINT USING "#.##"; BVALUE
627     2510 newcell = RETURNCELL
628     2520 GOSUB 4160
629     2521 GOSUB 4290
630     2529 WHILE (ENTERFLAG = 0)
631     2530   GOSUB 2720
632     2540 WEND
633     2550 CLS : PRINT : PRINT
634     2560 INPUT "OPEN drainage valves and press <ENTER> "; a$
635
636     2590 RETURN
637     2600 '
638     2610 '** SET THE FLAG
639     2620 '
640     2630 ' Needed to maintain the syntax of the ON KEY() statements
641     2640 '
642     2650 KEYFLAG = 1
643     2660 RETURN
644
645     '*****
646     2720 '***** CONTROL THE MOTORS *****
647     '*****
648
649     2750 ' The big control loop
650     '
651     2770   GOSUB 3260 ' take a set of readings
652     '+++++
653     IF AD1170$ = "N" THEN   'this is here to allow program development
654         FOR I = 1 TO stepinc
655             X = X
656         NEXT I
657         RETURN
658     END IF
659     '+++++
660
661     2790 ' Calculate the difference between readings and target values
662
663     e(3, 1) = newback - BACK   'use for all situations
664     row(3) = 5
665
666     2730 '*** this is feedback 1 (all stress control)

```



```

667
668     e(1, 1) = newtop - TOP
669     row(1) = 3
670     e(2, 1) = newcell - CELL
671     row(2) = 4
672     GOTO 2760
673     feedback = 1
674
675 2760 Enable = 7           'unlocks only motors in use
676     IF control(1) = 0 THEN Enable = Enable - 1
677     IF control(2) = 0 THEN Enable = Enable - 2
678     IF control(3) = 0 THEN Enable = Enable - 4
679     ' STOP
680
681     '*****
682     FOR I = 1 TO 3       'loop over motors this initial loop figures out the error for each
683     axis of control
684         IF control!(I) <> 0 THEN
685             LOCATE row(I), 63
686             PRINT "      "
687             LOCATE row(I), 63
688             PRINT USING P3$; mvolts(I);
689         END IF
690
691     'compute the PID constants
692
693         IF Mode(I) <> 2 THEN 'not PID control
694             mvolts(I) = 0
695             stiff = 0
696             PID = 0
697             GOTO 2765
698         END IF 'not PID control
699         stiff = 1
700         sume(I) = sume(I) * k(I, 4, control!(I)) + e(I, 1)
701         diffe(I) = e(I, 1) - e(I, 2)
702         PID = diffe(I) * k(I, 2, control!(I)) + sume(I) * k(I, 3, control!(I))
703
704 2765 mvolts(I) = PID + e(I, 1) * k(I, stiff, control(I))
705
706         IF mvolts(I) > 4.95 THEN mvolts(I) = 4.95
707         IF mvolts(I) < -4.95 THEN mvolts(I) = -4.95
708         IF control!(I) <> 0 THEN
709             LOCATE row(I), 72

```

```

710         PRINT USING P3$; mvolts(I)
711         END IF
712         e(I, 2) = e(I, 1)      'e is the error
713     NEXT I
714
715     FOR I = 1 TO 3
716         cvolts(I) = mvolts(I) + zvolts(I)      'apply offset
717         IF cvolts(I) > 4.99 THEN cvolts(I) = 4.99 'constrain limits
718         IF cvolts(I) < -4.99 THEN cvolts(I) = -4.99
719     NEXT I
720     'STOP
721     2800 FOR j = 1 TO 2          'loop to start, run and stop each motor
722
723     2840 OUT motors! + 4, Enable + Enable4      'close motor relays and open relay #4
724
725     GOSUB 2950 'output to the motors
726
727     IF j = 2 THEN GOTO 2900      'skip out of routine
728
729     FOR I = 1 TO stepinc: NEXT I  'run time delay
730
731     ' set voltage for selected motors to stop value
732
733     IF Mode(1) = 0 THEN cvolts(1) = zvolts(1)
734     IF Mode(2) = 0 THEN cvolts(2) = zvolts(2)
735     IF Mode(3) = 0 THEN cvolts(3) = zvolts(3)
736
737     2900 NEXT j
738
739     OUT motors! + 4, Mode(1) + Mode(2) + Mode(3) + Enable4 'close relays to lock motors
740     'change above line original was Mode*2*2, mode 3 * 4
741     RETURN
742
743     2950 'this section of code coverts voltage and sends to motor
744
745     ' ***** Calculate the bit output required for each motor
746     FOR I = 1 TO 3
747         BITS! = INT((cvolts(I) * mdir(I) + 5) * 409.5)
748         HIBIT!(I) = INT(BITS! / 256)
749         LOBIT!(I) = BITS! - HIBIT!(I) * 256
750     NEXT I
751
752     ' Send voltage to motors

```

```

753     FOR I = 1 TO 3           'loop over motors
754         OUT motors!, LOBIT!(I)   'set voltage register
755         OUT motors! + 1, HIBIT!(I)
756         OUT motors! + 2, DEVICE!(I) 'activate motor
757         OUT motors! + 2, 255     'close register
758     NEXT I
759
760     RETURN
761
762     3190 ' ***** ADJUST FOR CHANGE IN DATE DURING TEST *****
763     3210 '
764     3220 Tadjust = 86400! - TINC + Tadjust
765     3230 TINC = 0: 'WON'T NEED THIS ANYMORE AFTER THE FIRST ADJUSTMENT
766     3240 STARTDATE$ = DATE$
767     3250 RETURN
768     3260 '
769     3270 ' ***** TAKE SET OF READINGS AND CONVERT TO ENGINEERING UNITS *****
770     3280 '
771     3290 ' This routine takes the transducer readings from NUMCHANNELS number
772     3300 ' of channels and converts volts to engineering units.
773     3310 ' The input voltage should only be checked periodically.
774     3320 ' Automatic background calibration is enabled whenever this
775     3330 ' routine is not active.
776     3340 '
777     '+++++
778     '+++++ Create readings when no card in computer +
779     '+++++
780     IF AD1170$ = "Y" THEN GOTO 3350
781     FOR L = 1 TO NUMCHANNELS
782         VOLTS(L) = SIN(TIMER)
783     NEXT L
784     VOLTS(VINCHANNEL) = 1
785     GOTO 3500
786     '+++++
787
788     3350 OUT AD1170, 184: WAIT AD1170, 1, 1 'disable the background calibration
789     3370 FOR L = 1 TO NUMCHANNELS           'all channels plus ground
790     3380 CHANNEL = (L - 1)
791     3390 OUT MUX!, CHANNEL                 'select the mux channel
792     3400 IF VINFLAG = VINREAD AND L = VINCHANNEL THEN GOTO 3600
793     3410 IF L = VINCHANNEL THEN GOTO 3490 'skip the loop and keep old value
794     3420 OUT AD1170, INTTIME: WAIT AD1170, 1, 1 'conversion using preset time
795     3430 OUT MUX!, GNDCHANNEL             'ground the input to the AD1170

```

```

796 3440 ' read the three data bytes
797 3450     LOWBYTE = INP(AD1170 + 1); MIDBYTE = INP(AD1170 + 2); HIBYTE =
798 INP(AD1170 + 3)
799 3460 CTS = LOWBYTE + 256 * MIDBYTE + 65536! * HIBYTE ' total number of bits
800 3470 VTS = (CTS * 10 / 2 ^ (INTBIT + 7) - 5) ' convert to volts
801 3480 VOLTS(L) = VTS / Amp(L)
802 3485 IF VINFLAG = -1 AND L = VINCHANNEL THEN VOLTS(L) = VOLTS(L) + 5
803 3490 NEXT L
804 3492 OUT AD1170, 176: WAIT AD1170, 1, 1 'reenable background calibration
805 3495
806 3500 LOCATE 23, 1: PRINT SPACE$(80);
807 3510 LOCATE 23, 7: PRINT USING "#.##### "; VOLTS(DCDTCHANNEL);
808 VOLTS(CELLCHANNEL); VOLTS(LOADCHANNEL); VOLTS(PORECHANNEL);
809 VOLTS(VOLDCDTCHANNEL); VOLTS(VINCHANNEL);
810 IF Extraprint$ = "bvalue" THEN PRINT USING "### "; BVALUE;
811 3530 '
812 3540 ' convert to engineering units
813 3550 '
814 3555 TVOL = (VOLTS(TVOLCHANNEL) / VOLTS(VINCHANNEL) - ZTVOL) * CFTVOL
815 3560 CELL = (VOLTS(CELLCHANNEL) / VOLTS(VINCHANNEL) - ZCELL) * CFCELL
816 3565 BACK = (VOLTS(PORECHANNEL) / VOLTS(VINCHANNEL) - ZPORE) * CFPORE
817 3570 TOP = (VOLTS(TOPCHANNEL) / VOLTS(VINCHANNEL) - ZTOP) * CFTOP
818 3575 BVOL = (VOLTS(BVOLCHANNEL) / VOLTS(VINCHANNEL) - ZBVOL) * CFBVOL
819 '****BVOL CHANGED FROM VOLU
820 3585 'someday add corrections
821
822 IF PTRFLAG! > 0 THEN GOTO 3590 'no screen display for is step
823 GOSUB 4500
824 row = row + 1: IF row = 20 THEN row = 13
825 LOCATE row + 1, 1: PRINT SPACE$(53);
826 IF Extraprint$ = "bvalue" THEN PRINT SPACE$(10);
827 PRINT
828 LOCATE row, 1: PRINT USING " ###.## "; TOP; CELL; BACK; TVOL; BVOL;
829 IF Extraprint$ = "bvalue" THEN PRINT USING " ###.##"; BVALUE;
830 3590 PTRFLAG! = PTRFLAG! - 1
831 VINFLAG = VINFLAG + 1
832 RETURN
833 3600 '
834 3610 'nested subroutine to read the input voltage of the transducers
835
836 3620 OUT MUX!, REFCHANNEL 'mux to AD1170 reference voltage
837 3630 OUT AD1170, 112: WAIT AD1170, 1, 1 'measure the null signal
838 3640 OUT AD1170, 120: WAIT AD1170, 1, 1 'enable the null

```

```

839 3650 OUT MUX!, CHANNEL      'set mux to input voltage channel
840 3660 OUT AD1170, INTTIME: WAIT AD1170, 1, 1 'convert using preset time
841 3670 OUT AD1170, 128: WAIT AD1170, 1, 1  'disable the null
842 3680 VINFLAG = -1          'reset the flag
843 3730 GOTO 3430
844
845 3750 '***** Set counter for delay loop *****
846      '*****
847      'this is done only once
848      I = 1
849      ON TIMER(2) GOSUB 3810  '2 second sample
850      TIMER ON
851      3800 I = I + 1: GOTO 3800
852      3810 stepinc = (I / 2) * STEPTIME
853      TIMER OFF
854      RETURN 3870
855
856 3870 '***** generic return center *****
857
858      RETURN
859
860 3880 '***** Set the control functions to off *****
861      control(1) = 0
862      control(2) = 0
863      control(3) = 0
864      cvolts(1) = zvolts(1)
865      cvolts(2) = zvolts(2)
866      cvolts(3) = zvolts(3)
867      GOSUB 2950  'send zero command to motors
868      GOSUB 4430  'reset PID values to zero
869      OUT motors + 4, 0
870      RETURN
871
872 3890 '***** Subroutine to set soft function keys *****
873
874      KEY OFF: FOR I = 1 TO 10: KEY I, "": NEXT I  'disable F-keys
875      KEY 15, CHR$(0) + CHR$(84)  'pause key
876      KEY 16, CHR$(0) + CHR$(83)
877      KEY 17, CHR$(0) + CHR$(70)  'control break  changwe 0 to 4
878      KEY 18, CHR$(12) + CHR$(83)  'reset sequence
879      KEY 19, CHR$(0) + CHR$(81)  'ENTER KEY
880      KEY 20, CHR$(0) + CHR$(8)  'ESC KEY
881      ON KEY(1) GOSUB 4380  '/'

```

```

882     ON KEY(2) GOSUB 4390     '/'
883     ON KEY(3) GOSUB 4400     '\ motor stop/start keys
884     ON KEY(10) GOSUB 4410    '\
885     ON KEY(15) GOSUB 3870
886     ON KEY(16) GOSUB 3870
887     ON KEY(17) GOSUB 3870
888     ON KEY(18) GOSUB 3870
889     ON KEY(19) GOSUB 4100
890     ON KEY(20) GOSUB 4230
891     FOR I = 15 TO 19: KEY(I) ON: NEXT I
892     RETURN
893
894 4100 '***** GENERIC enter deactivation ****
895
896     ENTERFLAG = 1
897     KEY(19) OFF
898     KEY(20) OFF
899     RETURN
900
901 4160 '***** generic enter activation ****
902 4170 '
903 4175 LOCATE 25, 1
904 4180 PRINT "ENTER to continue";
905 4190 ENTERFLAG = 0
906 4200 KEY(19) ON
907 4210 RETURN
908 4220 '
909 4230 '***** generic ESC deactivation ****
910 4240 '
911 4250 ENTERFLAG = 2
912 4260 KEY(20) OFF
913 4265 KEY(19) OFF
914 4270 RETURN
915 4280 '
916 4290 '***** generic ESC activation ****
917 4300 '
918 4305 LOCATE 25, 20
919 4310 PRINT "ESC to abort";
920 4320 ENTERFLAG = 0
921 4330 KEY(20) ON
922 4340 RETURN
923 4350 '
924 4360 '***** toggle to turn on and off motors with f-keys ****

```

```

925 4370 '
926 4380 II = 1: GOTO 4420
927 4390 II = 2: GOTO 4420
928 4400 II = 3: GOTO 4420
929 4410 FOR II = 1 TO 3: GOSUB 4420: NEXT II
930 4420 IF MFLAG$(II) = "start" THEN MFLAG$(II) = "stop " ELSE MFLAG$(II) = "start"
931     RETURN
932
933 4430 '***** routine to reset the PID registers *****
934
935     FOR I = 1 TO 3
936         e(I, 1) = 0
937         e(I, 2) = 0
938         sume(I) = 0
939         mvolts(I) = 0
940         PID = 0
941     NEXT I
942     RETURN
943 4440 '*****
944 4450 '***** print basic screen and collect readings*****
945 4460 '*****
946
947 4461 LOCATE 11, 1: PRINT H3$: PRINT H4$
948 4462 row = CSRLIN
949 4463 LOCATE 21, 20: PRINT H1$: PRINT H2$
950 4465 'PTRFLAG! = 0
951 4470 VINFLAG = VINREAD      ' get an initial input voltage
952 4480 GOSUB 3260 ' get an initial set of readings and convert to eng. units
953     '*****
954 4500 '***** print screen only *****
955     '*****
956     PTRFLAG! = Refreshrate
957 4502 LOCATE 1, 1
958 4503 FOR I = 1 TO 10: PRINT blk$: NEXT I
959 4504 LOCATE 1, 1
960 4510 PRINT
961 4520 PRINT "   CURRENT READINGS   TARGET VALUES   GAIN RATES   CONTROL
962 SIGNALS "
963 4552 PRINT " Top  = "; : PRINT USING P2$; TOP; : PRINT " Ksc  ";
964
965 4553
966 4554 IF control(1) = 1 THEN
967     PRINT USING P2$; newtop; : PRINT " Ksc  ";

```

```

968         IF feedback > 0 THEN
969             PRINT USING P3$; k(1, 0, 1); : PRINT " v-sec/ksc ";
970         END IF
971     END IF
972 4556 PRINT
973 4557 '
974
975     PRINT " Cell = "; : PRINT USING P2$; CELL; : PRINT " Ksc ";
976
977 4575
978 4580 IF control(2) = 1 THEN
979         PRINT USING P2$; newcell; : PRINT " Ksc ";
980         IF feedback > 0 THEN
981             PRINT USING P3$; k(2, 0, 1); : PRINT " v-sec/ksc ";
982         END IF
983     END IF
984
985 4586 PRINT
986
987 4590 PRINT " Back = "; : PRINT USING P2$; BACK; : PRINT " Ksc ";
988
989 4595
990 4602 IF control(3) = 1 THEN
991         PRINT USING P2$; newback; : PRINT " Ksc ";
992         IF feedback > 0 THEN
993             PRINT USING P3$; k(3, 0, 1); : PRINT " v-sec/ksc ";
994         END IF
995     END IF
996
997 4610 PRINT
998 4611 '
999 4620 PRINT " T.Vol = "; : PRINT USING P2$; TVOL; : PRINT " cm^3 ";
1000 4640 PRINT
1001 4641 '
1002 4650 PRINT " B.Vol = "; : PRINT USING P2$; BVOL; : PRINT " cm^3 ";
1003
1004 4670 PRINT
1005 4680 RETURN
1006 10000 'this is the setup routine for the a/d converter'
1007
1008     IF AD1170$ = "N" THEN RETURN 'No card in computer
1009
1010     OUT AD1170, 60: WAIT AD1170, 1, 1'set the default calibration time

```



```

1011     OUT AD1170 + 1, INTBIT 'load the data format into the 2nd byte
1012     OUT AD1170, 48: WAIT AD1170, 1, 1 ' lock in the data format loaded
1013     OUT AD1170, 176: WAIT AD1170, 1, 1 ' begin background calibration
1014     OUT MUX!, GNDCHANNEL      ' set input to AD1170 to ground
1015     RETURN
1016
1017     10100 '***** END PROGRAM *****
1018
1019     OUT motors! + 4, 0          'LOCK MOTORS
1020     LOCATE 10, 1
1021     FOR j = 1 TO 10
1022         PRINT blk$
1023     NEXT j
1024     LOCATE 13, 1
1025     PRINT "Enter 'a' to return to the setup program => "
1026     PRINT "      'b' to continue running this program =>"
1027     INPUT " or just press <Enter> to stop program ", Z$
1028     IF Z$ = "a" OR Z$ = "A" THEN CHAIN "qbsetup3.bas"
1029     IF Z$ = "B" OR Z$ = "b" THEN GOTO 890
1030     STOP: END

```